Synthese und Modifizierung poröser aluminiumhaltiger Gerüstverbindungen auf der Basis aromatischer Dicarbonsäurederivate

Kumulative Dissertation

zur Erlangung des Doktorgrades
der Mathematisch-Naturwissenschaftlichen Fakultät
der Christian-Albrechts-Universität zu Kiel

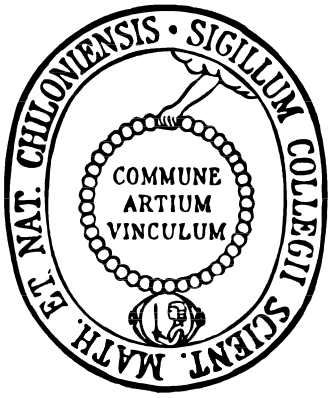

vorgelegt von

Tim Ahnfeldt

Institut für Anorganische Chemie
der Christian-Albrechts-Universität zu Kiel
Kiel, 2011

Referent/in: Prof. Dr. Norbert Stock
Koreferent/in: Prof. Dr. Wolfgang Bensch
Tag der mündlichen Prüfung: 22.05.2012
Zum Druck genehmigt: Kiel, Prof. Dr. Lutz Kipp

Der Dekan

Synthese und Modifizierung poröser aluminiumhaltiger Gerüstverbindungen auf der Basis aromatischer Dicarbonsäurederivate

Metall-organische Gerüstverbindungen (MOFs) haben sich im vergangenen Jahrzehnt zu einer der am intensivsten erforschten Materialklassen zur Trennung von Stoffgemischen und Gasspeicherung entwickelt. Da viele dieser Verbindungen aufgrund geringer chemischer Stabilität oder schwacher Adsorbat/Adsorbens Wechselwirkungen für eine potentielle Anwendung nicht geeignet sind, besteht ein großes Interesse an alternativen Verbindungen. Die Darstellung neuer MOFs ist oft ein aufwendiger „trial and error"-Prozess. Hochdurchsatzmethoden stellen ein ausgezeichnetes Werkzeug zur Entdeckung und Syntheseoptimierung neuer metall-organischer Gerüstverbindungen dar. Unter Verwendung der Hochdurchsatzmethode wurden im Rahmen dieser Arbeit die Reaktionssysteme Al^{3+}/H_2BDC-X/Lsgm./Base (X= -NH_2, -$(OH)_2$, -NO_2, -H) und Al^{3+}/H_2NDC/MeOH/NaOH untersucht. Im Zuge dieser Untersuchungen konnten eine Vielzahl neuer und isoretikulärer Verbindungen erhalten werden. Alle Verbindungen konnten durch eine Aufskalierung des Reaktionsansatzes im Gramm-Maßstab dargestellt werden. Als besonders aufwendig erwies sich die Aktivierung der Verbindungen, deren Poren und Käfige häufig durch nicht umgesetzte Reaktanden blockiert waren. Für fast alle Verbindungen mussten individuelle Aktivierungsprozesse in Abhängigkeit von ihrer Stabilität und der Löslichkeit der nicht umgesetzten Reaktanden durchgeführt werden. Die Charakterisierung der Verbindungen erfolgte durch folgende Methoden: Röntgenpulverdiffraktometrie, Sorptionsmessungen, IR- und Raman-Spektroskopie, Thermogravemetrie, NMR-Spektroskopie und Elementaranalyse. Der Einbau unterschiedlicher funktioneller Gruppen in die Poren und Kanäle der Verbindungen Al-MIL-53 und CAU-1 führte zu einer drastischen Veränderung des Sorptionsverhaltens. Die Porenwände der aminofunktionalisierten MOFs CAU-1-NH_2 und Al-MIL-53-NH_2 konnten des Weiteren durch eine Umsetzung mit Essigsäureanhydrid bzw. Ameisensäure chemisch postsynthetisch modifiziert werden, was ebenfalls zu einem veränderten Sorptionsverhalten der Verbindungen führte.

Mithilfe von in-situ-Röntgenbeugungsexperimenten wurde das Kristallwachstum zweier isoretikulärer CAU-1-X-Verbindungen (X = $-NH_2$, $-(OH)_2$) in Abhängigkeit von der verwendeten Heizmethode - konventioneller elektrischer Ofen und Mikrowellenofen - untersucht und kinetisch ausgewertet. Die Synthese im Mikrowellenreaktor führte im Vergleich zu der konventionellen Heizmethode zu einer Beschleunigung der Reaktion.

Synthesis and Modification of Porous Aluminium-Containing Frameworks Based on Aromatic Dicarboxylic Acids

Metal-organic frameworks (MOFs) have evolved over the past decade into one of the most investigated class of materials for the separation of gas mixtures and gas storage. Since many of these compounds exhibit low chemical stability or weak adsorbate/adsorbent interactions, they are not suitable for a potential application. Therefore, there is a considerable interest in alternative compounds. A tedious trial and error approach is often required for the synthesis of new MOFs. High-throughput methods present a valuable tool for the discovery and synthesis optimization of new and isoreticular MOFs. Applying this method, the reaction systems Al^{3+}/H_2BDC-X/Solvent/Base (X= -NH_2, -$(OH)_2$, -NO_2, -H) and Al^{3+}/H_2NDC/MeOH/NaOH were investigated. Under solvothermal conditions new compounds were discovered and a large number of isoreticular compounds could be synthesized. All MOFs could be obtained in gram-scale by scaling up the reaction mixture. A special task was the activation of the pores and cages, which were often blocked by free acid molecules. Almost every compound needed to be activated by an individual activation process, which was dependent on the stability and the solubility of the unconverted reactants. The characterization of the compounds was carried out by the following methods: X-ray powder diffraction, sorption measurements, IR- and Raman-spectroscopy, thermogravimetry, NMR spectroscopy and elemental analysis. The incorporation of different functional groups in the pores and channels of CAU-1 and Al-MIL-53 led to a drastic change in the sorption behaviour. In addition, the sorption properties of the amino functionalized CAU-1-NH_2 and Al-MIL-53-NH_2 were also varied by post-synthetic modification using acetic anhydride and formic acid, respectively. Applying in situ energy dispersive X-ray diffraction the crystal growth of two isoreticular CAU-1-X (X = -NH_2, -$(OH)_2$) compounds was investigated as a function of the applied heating method, i. e. conventional and microwave-assisted heating. The obtained data were also kinetically evaluated. The syntheses using microwave-assisted heating led to an acceleration of the reaction compared to the conventional syntheses.

für meine Familie und Julia

Danksagung

An dieser Stelle möchte ich denjenigen danken, die mir bei der Durchführung und Fertigstellung der Arbeit unterstützt haben.

Mein ganz besonderer Dank gilt meinem Doktorvater Prof. Dr. N. Stock für die hervorragende wissenschaftliche Betreuung und den mir gewährten Freiraum bei der Erstellung dieser Arbeit, sowie der uneingeschränkten Unterstützung bei der Interpretation meiner Ergebnisse und dem Schreiben der Publikationen – sei es auch am Sonntagnachmittag in einem Café auf dem Kieler Bahnhof.

Herrn Prof. Dr. Wolfgang Bensch und Herrn Prof. Dr. Christian Näther danke ich für die Nutzung ihrer experimentellen Ausstattung – insbesondere für das Bereitstellen der in situ-Apparatur.

Der gesamten Arbeitsgruppe danke ich für das gesellige Miteinander und das tolle Arbeitsklima. Ein besonders großer Dank gebührt dabei meinen Freunden Dr. Palanikumar Maniam und Dr. Andreas Sonnauer für die immerwährende Diskussions- und Hilfsbereitschaft bei wissenschaftlichen Fragestellungen sowie den gemeinsamen Unternehmungen neben der Uni.

Ebenfalls bedanke ich mich bei Mark Feyand, Beatrix Seidelhofer und Dr. Nicole Pienack für die interessanten und hilfreichen Diskussionen über die in situ Röntgenbeugung.

Meinen Kooperationspartnern Florian Hinterholzinger, Jens Möllmer, Matthias Mendt und Daniel Gunzelmann danke ich für die ausgezeichnete und produktive Zusammenarbeit. Ich danke außerdem Herrn Prof. Jürgen Senker für die Möglichkeit, ein paar interessante Projekte in seinem Arbeitskreis fortzuführen.

Weiterhin gilt mein Dank:

Frau Uschi Cornelissen und Frau Stephanie Phelke für die Durchführung der Elementaranalysen und der Aufnahme zahlloser IR- und Raman-Spektren

Dr. Frank Sönnichsen für die Messung der ^{1}H-NMR-Spektren

Meinem ewigen Wegbegleiter und guten Freund Dr. Adam Wutkowski sowie Frau Inke Jess für Durchführung der DTA/TG Messungen

dem Werkstattteam für die gute Unterstützung, bei der Betreuung des Röntgenpulverdiffraktometers

Antje Modrow und Christian Stoltenberg für die Durchführung der Sorptionsexperimente

Dr. Sönke Ziesmer und Klaus Beneke für das Aufspüren von Fehlern in dieser Arbeit

Felicitas Niekiel für die stetige Hilfsbereitschaft und die Unterstützung bei den DLS-Messungen

den F-Praktikanten Andreas Griebe, Ellen Mark, Ina Herber, Karin Geisel, Nele Reimer, Selda Halis, und Sascha Krüger

Dr. Alexandra Lieb für die Gastfreundschaft bei meinem Aufenthalt in Paris

den Sekretärinnen Brita Bahn, Ute Sabotta und Cornelia Möller.

Sehr herzlich bedanke ich mich bei meiner gesamten Familie, insbesondere bei meinen Eltern, die mich besonders während meines Studiums großzügig in finanzieller und moralischer Hinsicht unterstützt haben. Julia danke ich für – um es kurz zu machen – einfach alles.

1 Einleitung

1.1 Motivation und Zielsetzung

Die Entwicklung von porösen Materialien mit einem geordneten Porensystem ist von hohem wissenschaftlichen und wirtschaftlichen Interesse. Die Anwendungen dieser Materialien reichen dabei von dem Einsatz als Katalysator[1] bei der Aufarbeitung fossiler Brennstoffe, über die Verwendung als Molekularsieb[2] und Ionenaustauscher[3] bis hin zum Gebrauch als Nanoreaktor.[4] Die Darstellung neuer poröser Materialien mit der für die Anwendung benötigten Eigenschaften, wie eine ausreichende thermische und chemische Stabilität sowie klar definierte Porengrößen und Porenfunktionalitäten, ist daher von enormer Bedeutung.

Poröse Materialien können neben der äußeren Oberfläche auch mit der inneren Oberfläche des Bulkmaterials, den Porenwänden, mit Gastmolekülen und Ionen wechselwirken.[5] Die Stärke der sogenannten Wirts-Gast-Wechselwirkungen wird durch die Größe, Topologie und chemische Umgebung der Poren bestimmt. In der Regel weisen beispielsweise kleinere Poren (Mikroporen) ein wesentlich höheres Adsorptionspotential auf als größere (Mesoporen und Makroporen).[6] Durch eine chemische oder thermische Behandlung der porösen Verbindungen ist es zudem möglich die Wirts-Gast-Wechselwirkung im Nachhinein gezielt zu verändern. So können die katalytischen Eigenschaften von porösen Materialien verbessert werden, indem kleinere funktionalisierte Moleküle kovalent an die Porenwände gebunden[7] oder durch Erhitzen Lewissäurezentren im Gerüst generiert werden.[1]

Die porösen Verbindungen mit dem größten industriellen Nutzen sind Zeolithe, aus SiO_4^{4-} und AlO_4^{5-}-Baueinheiten zusammengesetzte Alumosilicate. Zeolithe zeichnen sich durch ein definiertes Porensystem aus, welches eine sehr enge Porenradienverteilung besitzt.[8] Selektiv können dadurch nur Moleküle bis zu einer bestimmten Größe in die Poren der Zeolithe eindringen. Aufgrund der geringen Größe der Tetraederbaueinheiten sowie ihrer limitierten Verknüpfungsmöglichkeiten besitzen die Zeolithe nur sehr kleine Poren und sind für größere Moleküle nicht zugänglich. Seit Beginn der 1990er Jahre können durch templatgesteuerte

Synthesen die Porengrößen poröser SiO_2-Verbindungen nahezu stufenlos eingestellt werden.[9] Diese Materialien, zu denen die bekannten Vertreter MCM-41[10] und SBA-15[11] gehören, besitzen mesoporöse Poren. Im Gegensatz zu den Zeolithen haben diese Verbindungen amorphe Porenwände und weisen dadurch eine deutlich größere Porenradienverteilung auf.

Neben diesen rein anorganischen Materialien haben sich Metall-organische Gerüstverbindungen (MOF = englische Abkürzung für Metal-Organic-Framework) zu einer bedeutenden Klasse innerhalb der porösen Materialien entwickelt.[12] Die MOFs kombinieren die klar definierte Gerüststruktur der Zeolithe mit der einstellbaren Porengröße der mesoporösen SiO_2-Verbindungen. Bei den MOFs werden die anorganischen Baueinheiten, die aus isolierten Metallatomen, Metall-Sauerstoff-Clustern, -Ketten oder -Ringen bestehen können, durch funktionalisierte organische Moleküle, sogenannte Linker, zu dreidimensionalen Gerüststrukturen miteinander verbrückt.[13] Die Linkermoleküle werden dabei durch die Ausbildung starker koordinativer Bindungen zu einem festen Bestandteil der Struktur. Häufig eingesetzte Linker sind polyfunktionalisierte aromatische Carbonsäuren[14] sowie stickstoffhaltige Heteroaromaten.[15]

Das modulare Bauprinzip der MOFs ermöglicht es die Größe, Form und Funktionalität der Poren gezielt einzustellen.[16] Dabei kann auf einen großen Pool organischer Linker und Metallionen zurückgegriffen werden. Durch den Einsatz größerer Linkermoleküle können die Poren aufgeweitet werden.[17] Die Verwendung von Linkermolekülen mit zusätzlichen funktionellen Gruppen (z. B. $-NH_2$, -OH, -COOH) ermöglicht die nahezu beliebige Modifizierung der Porenwände.[18] Dadurch sind eine Vielzahl potentieller Anwendungen von MOFs denkbar. Zurzeit wird versucht MOFs als Wirkstoffspeicher in der Medizin,[19] bei der Speicherung und Trennung von Gasen[20] oder in der Katalyse[21] einzusetzen. Für den Einsatz als Speichermaterial ist eine möglichst geringe Gerüstdichte anzustreben. So sind MOFs, die auf Leichtmetallen wie Magnesium[22] oder Aluminium[23] basieren, besonders vielversprechend.

Ziel der vorliegenden Arbeit war es, funktionalisierte aluminiumhaltige Gerüstverbindungen darzustellen, diese chemisch zu modifizieren und zu

charakterisieren. Im Mittelpunkt des Interesses stand dabei die Synthese isoretikulärer Strukturen unter Verwendung funktionalisierter Linker. Außerdem sollte der Einfluss unterschiedlicher Heizmethoden (konventionell und Mikrowelle) auf die Produktbildung der im Rahmen dieser Arbeit entdeckten Verbindungen, CAU-1 und CAU-1-OH_2, mit in situ-Methoden untersucht werden.

1.2 Aluminiumhaltige MOFs

Das große Interesse an aluminiumhaltigen MOFs (Al-MOFs) beruht vor allem auf der hohen thermischen und chemischen Stabilität sowie der bemerkenswerten Porosität vieler dieser Verbindungen. Diese können mit günstigen Basischemikalien wie Terephthalsäure, Trimesinsäure oder Naphthalindicarbonsäure aus den entsprechenden Aluminiumsalzen hergestellt werden, wobei häufig dreidimensionale Netzwerke mit hohen scheinbaren spezifischen Oberflächen und geringen Dichten erhalten werden. Neben der Synthese neuer Verbindungen in aufwändigen „trial and error"-Prozessen wurde bei der Herstellung von Al-MOFs sehr oft auf das modulare Aufbauprinzip zurückgegriffen. Auf diesem Wege konnten isostrukturelle Verbindungen dargestellt werden, die auf den dreiwertigen Metallionen Fe^{3+} (Fe-MIL-101-NH_2[24] (MIL = Materiaux de l`Institut Lavoiser)) und Cr^{3+} (MIL-53[25]) basieren. Zudem ließen sich durch den Einsatz größerer oder zusätzlich funktionalisierter Linkermoleküle die Adsorptions- und Katalyseeigenschaften des MOFs Al-MIL-53,[26] dem bekanntesten Vertreter der Al-MOFs, verändern (vgl. Kap. 1.2.1). Bei beiden Synthesestrategien ist die reproduzierbare Darstellung der anorganischen Baueinheit von entscheidender Bedeutung.

In allen Al-MOFs sind die anorganischen Baueinheiten aus AlO_6-Oktaedern zusammengesetzt, die isoliert oder zu Clustern, Ringen bzw. Ketten verknüpft vorliegen. Die Sauerstoffatome dieser Oktaeder werden durch die Lösungsmittelmoleküle und die verbrückenden Linkermoleküle gestellt. Als Linker wurden ausschließlich aromatische Di-, Tri- und Tetracarbonsäuren eingesetzt, welche zudem zusätzliche funktionelle Gruppen aufweisen können.

In diesem Unterkapitel werden die anorganischen Baueinheiten der Al-MOFs vorgestellt sowie die dazugehörigen Netzwerkstrukturen beschrieben. Die Bildung der jeweiligen anorganischen Baueinheit bzw. die Art der Verknüpfung dieser Einheiten über die organischen Linkermoleküle hängt sehr stark von den gewählten Reaktionsbedingungen ab. Bei der Synthese von Al-MOFs spielt, neben dem verwendeten Lösemittel und der Reaktionsdauer, besonders der pH-Wert eine entscheidende Rolle. In Abbildung 1.1 sind alle in der Literatur bekannten anorganischen Baueinheiten aluminiumhaltiger MOFs dargestellt und den jeweiligen Verbindungen zugeordnet.

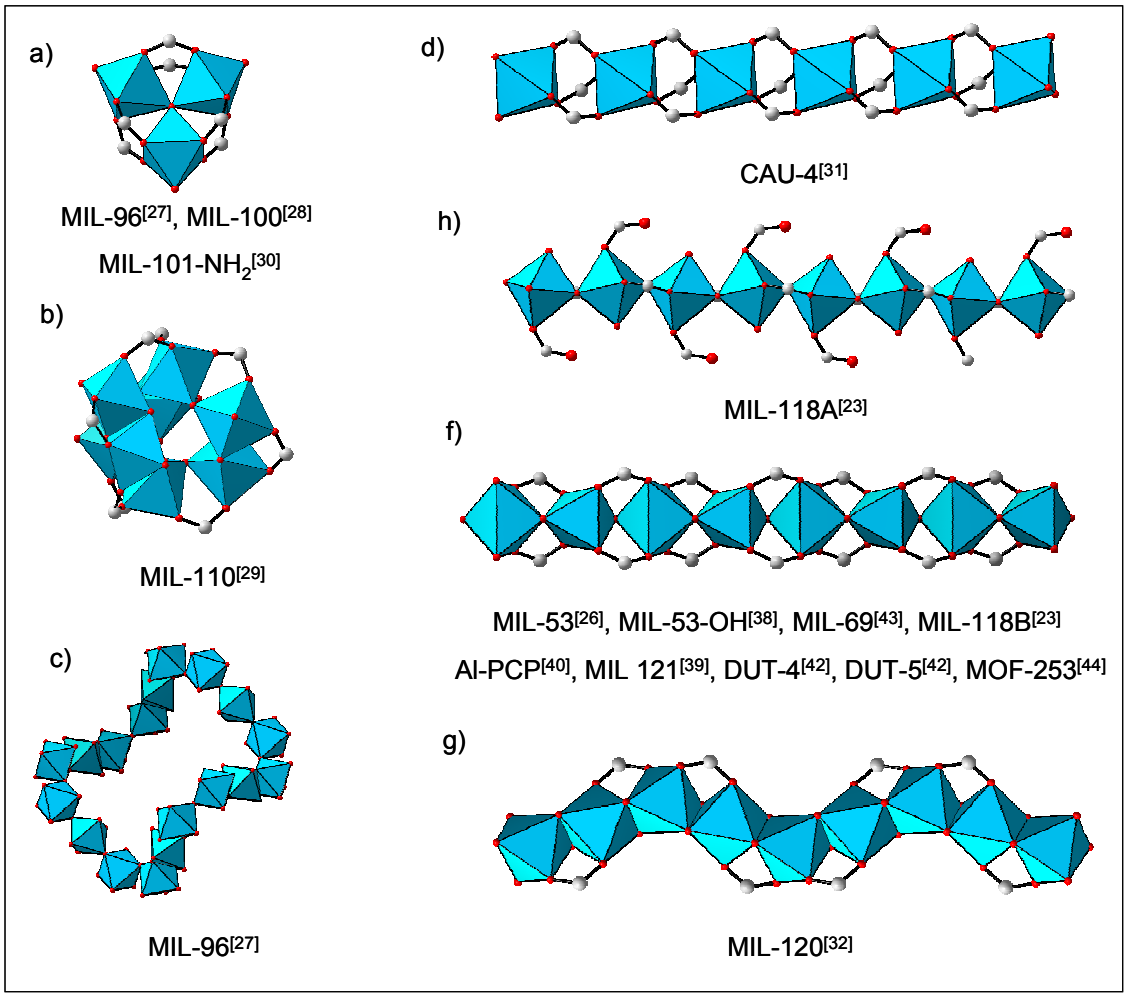

Abb. 1.1 Anorganische Baueinheiten aluminiumhaltiger MOFs

Durch Variation des pH-Wertes und der Reaktionsdauer konnten in dem System $Al^{3+}/H_3BTC/H_2O$ (H_3BTC = Benzol-1,3,5-tricarboxysäure) die drei Verbindungen MIL-96,[27] MIL-100[28] und MIL-110[29] erhalten werden. MIL-96 ($[Al_{12}O(OH)_{18}(H_2O)_3(Al_2(OH)_4)(BTC)_6]\cdot 24H_2O$) bildet sich innerhalb des pH-Bereichs von 1-3 nach einer Reaktionszeit von 24 h. Das Gerüst von MIL-96 ist aus isolierten μ_3-O-verbrückten Aluminiumclustern ($\{Al_3(\mu_3\text{-}O)(O_2CR)_6\}^+$) sowie eckenverknüpften $Al(OH)_2O_4$- und $Al(OH)_4O_2$-Oktaedern aufgebaut. Letztere sind untereinander zu einem honigwabenartigen Netzwerk verknüpft, welches 18-gliedrige Ringe enthält. MIL-110 ($[Al_8(OH)_{12}(OH)_3(H_2O)_3(BTC)_3]\cdot nH_2O$) wurde dagegen unter stark sauren Bedingungen (pH ~ 0-0.3) bei einer Reaktionszeit von 72 h gebildet. Das Netzwerk von MIL-110 weist isolierte Al_8-Sauerstoffcluster ($\{Al_8(OH)_{15}(O_2CR)_9\}$) auf, die ebenfalls in einer Honigwabenstruktur angeordnet sind. MIL-100 ($[Al_3O(OH)(H_2O)_2(BTC)_2]\cdot nH_2O$) konnte bei sehr kurzen Reaktionszeiten (3-4 h) und in einem sehr engen pH-Bereich (0.5-0.7) synthetisiert werden.[28] Das Gerüst von Al-

MIL-100 weist die gleichen trimeren Cluster auf wie MIL-96. Verknüpft über die BTC-Linker bilden vier solcher Cluster sogenannte Supertetraeder aus. In einem Supertetraeder nehmen die trimeren Einheiten die Eckpositionen ein, während die organischen Baueinheiten an den Flächen lokalisiert sind. Über die gemeinsamen Ecken verknüpft bilden die Supertetraeder ein dreidimensionales Netzwerk mit der von den Zeolithen bekannten MTN-Topologie aus. In dem Lösemittel DMF konnte mit 2-Aminoterephthalsäure (H_2BDC-NH_2 (BDC = 1,4-Benzoldicarboxylat)) als Linker die Verbindung MIL101-NH_2[30] erhalten werden. Das Gerüst von MIL101-NH_2 ist nahezu identisch mit dem von MIL-100 und weist baugleiche trimere Oxocluster und Supertetraeder auf.

In dem honigwabenartigen Netzwerk von CAU-4 ([Al(BTB)]·1.6DMF·4.7H_2O (CAU = Christian-Albrechts-Universität)) liegen die AlO_6-Oktaeder isoliert vor und werden in einer kettenförmigen Anordnung über 4,4´,4´´-Benzol-1,3,5-triyl-tribenzoat (BTB)-Linker miteinander verknüpft.[31] Der prozentuale Anteil der anorganischen Komponente ist dadurch für CAU-4, im Vergleich zu den anderen wabenförmigen Netzwerken MIL-96 und MIL-110, wesentlich geringer (Abb. 1.2).

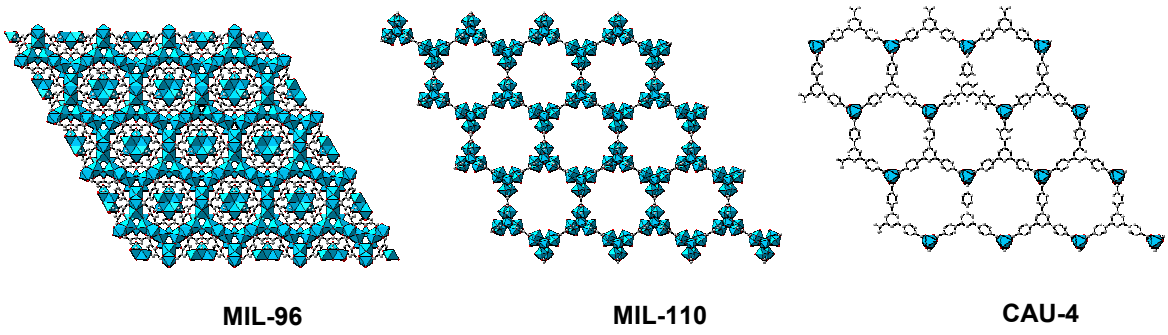

Abb. 1.2 Al-MOFs mit einem honigwabenartigen Netzwerk. Für ein besseres Verständnis der Strukturen wurden die eingelagerten Gastmoleküle aus den Abbildungen entfernt.

Alle weiteren in der Literatur bekannten Al-MOFs weisen kettenförmige Baueinheiten auf, bei denen die AlO_6-Oktaeder direkt über gemeinsame Ecken oder Kanten miteinander verknüpft sind. Die Ketten sind über die Carboxylatreste der organischen Linker zu dreidimensionalen Netzwerken mit eindimensionalen Kanälen verbrückt.

In dem System Al^{3+}/H_4BTEC/H_2O (H_4BTEC = Benzol-1,2,4,5-tetracarbonsäure) tritt in Abhängigkeit des pH-Wertes ein unterschiedliches Verknüpfungsmuster der AlO_6-Oktaeder in den Ketten auf. Bei der Synthese im basischen Milieu sind AlO_6-Oktaeder über μ_2-OH Gruppen zu kantenverknüpften Ketten verbunden (MIL-120

([$Al_4(OH)_8(BTEC)$]·~$5H_2O$)).[32] Eine Kette wird über die BTEC-Einheiten mit vier weiteren Ketten verknüpft. Alle acht Carboxylatsauerstoffatome des BTEC-Linkers sind dabei an die Aluminiumionen koordiniert. Dadurch wird ein dreidimensionales Gerüst gebildet, welches kleine eindimensionale Kanäle enthält.

Bei niedrigen pH-Werten wird eine Eckenverknüpfung der AlO_6-Oktaeder beobachtet (MIL-118A ([$Al_2(OH)_2(H_2O)_2(BTEC)$])).[23] In MIL-118A sind die Aluminiumionen jeweils von drei Carboxylatsauerstoffatomen, einem Wassermolekül sowie zwei μ_2-OH Gruppen umgeben. Die Verknüpfung der AlO_6-Oktaeder erfolgt über trans-eckenverknüpfte Hydroxygruppen. Anders als bei MIL-120 sind nur sechs der acht Carboxylatsauerstoffatome des BTEC-Linkers an die Aluminiumionen koordiniert. Je ein nicht koordiniertes Carboxylatsauerstoffatom zweier gegenüberliegender Carboxylatgruppen bildet Wasserstoffbrückenbindungen mit den an die Aluminiumionen gebundenen Wassermolekülen aus. Beim Erhitzen von MIL-118A entweichen die Wassermoleküle aus dem Gerüst und das zuvor ungebundene Carboxylatsauerstoffatom nimmt an der Koordination mit den Aluminiumionen teil. Diese, als MIL-118B ([$Al_2(OH)_2(BTEC)$]) bezeichnete Verbindung,[23] weist ein flexibles Gerüst mit eindimensionalen Kanälen auf. Bei MIL-118A bzw. MIL-118B ist jede Kette mit acht anstelle von vier Ketten (MIL-120) direkt über die BETC-Linker miteinander verbrückt. Durch die erhöhte Verknüpfung der Ketten innerhalb des Gerüstes weist das Netzwerk eine geringere Porosität auf (Abb. 1.3).

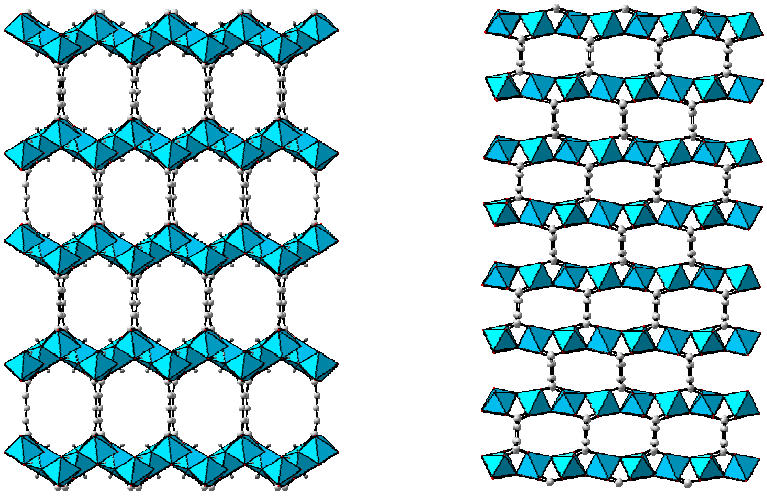

MIL 120 **MIL-118C**

Abb. 1.3 Darstellung der Strukturen von MIL-120 (links) und MIL-118C (rechts) entlang der c-Achse (die in den Poren eingelagerten Wassermoleküle wurden für eine bessere Übersicht aus den Abbildungen entfernt).

Beim Abkühlen von MIL-118B lagern sich Wassermoleküle aus der Luft in das Gerüst ein und es wird die hydratisierte Verbindung MIL-118C ($[Al_2(OH)_2(BTEC)]\cdot 2.75H_2O$) gebildet.[23] Aufgrund von Wechselwirkungen des Gerüstes mit den eingelagerten Wassermolekülen ändert sich das Zellvolumen um ca. 6%. Dieses Phänomen wird als „Breathing Effect“ bezeichnet und verläuft in diesem Fall vollkommen reversibel.

Die Verbindung MIL-53[26] ($[Al(OH)(BDC)]\cdot H_2O$) besitzt die gleiche anorganische Baueinheit wie MIL-118C. Jeweils vier dieser eckenverknüpften Ketten sind über Terephthalateinheiten (BDC^{2-}) miteinander verbrückt. Diese Verknüpfung führt zu einem dreidimensionalen Netzwerk mit eindimensionalen, rhombisch geformten Kanälen. In die Kanäle können kleinere Gastmoleküle (z. B. Xylol, DMF, CH_4) eingelagert werden. Je nach Art der Wechselwirkungen der Gäste mit dem Gerüst ziehen sich die Kanäle dabei zusammen (geschlossene Form) oder werden aufgeweitet (offene Form). Der bei MIL-53 beobachtete „Breathing Effekt“ ist im Vergleich zu MIL-118C wesentlich stärker. Bei der Rehydratisierung von thermisch aktivierten MIL-53 nimmt das Zellvolumen um 33% ab. Die Kanäle gehen dabei von der offenen Form (8.5 x 8.5 $Å^2$) in die geschlossene Form (13.6 x 2.6 $Å^2$) über (Abb. 1.4). Interessanterweise kann der „Breathing Effect“ bei MIL-53 auch ohne die Adsorption beziehungsweise Desorption von Gastmolekülen beobachtet werden. Bei extrem tiefen Temperaturen (ca. -150 °C) findet ein Phasenübergang von der offenen Form in die geschlossene Form statt (vgl. Kap. 4.1.3).[33]

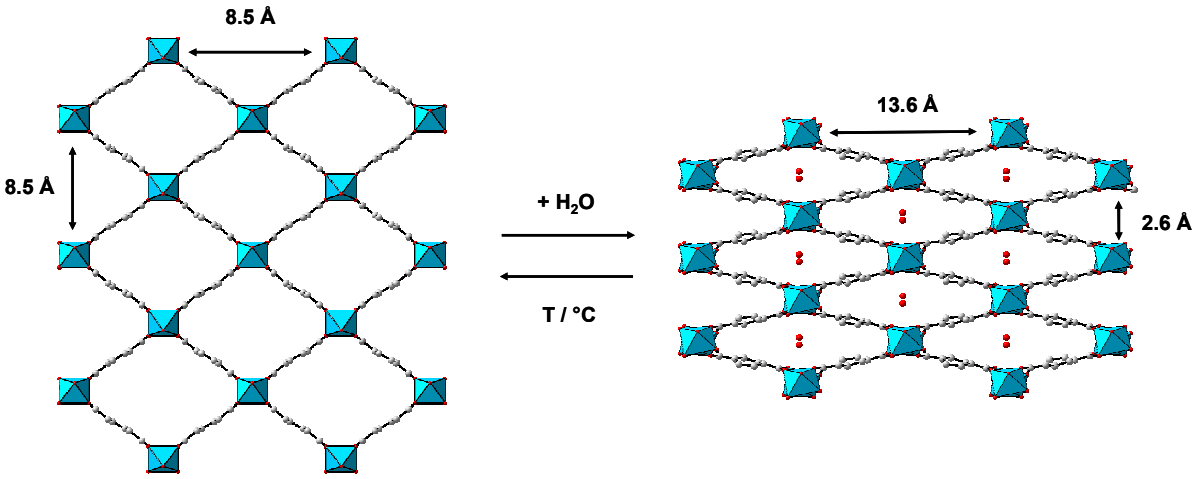

Abb.1.4 „Breathing Effekt“ von Al-MIL-53.

In der folgenden Tabelle sind Vertreter von Al-MOFs mit unterschiedlichen Gerüststrukturen sowie deren scheinbaren spezifischen Oberflächen zusammengefasst. Die Materialien weisen im Vergleich zu anderen porösen aluminiumhaltigen Verbindungen (Zeolithe und Alumophosphate) eine deutlich höhere Porosität auf.

Tab. 1. 1 Ausgewählte Al-MOFs mit unterschiedlichen Gerüststrukturen und deren scheinbare spezifische Oberfläche.

Al-MOF	Summenformel	$S_{BET}(m^2 \cdot g^{-1})$[a]	Lit.
Al-MIL-53	$[Al(OH)(BDC)] \cdot H_2O$ [b]	1235	[26], [34]
MIL-96	$[Al_{12}O(OH)_{18}(H_2O)_3(Al_2(OH)_4)(BTC)_6] \cdot 24H_2O$	532	[27], [35]
MIL-100	$[Al_3O(OH)(H_2O)_2(BTC)_2] \cdot nH_2O$	2152	[28]
MIL-101-NH_2	k. A.[c]	2100	[30]
MIL-110	$[Al_8(OH)_{12}(OH)_3(H_2O)_3(BTC)_3] \cdot nH_2O$	1400	[29]
MIL-118	$[Al_2(OH)_2(BTEC)] \cdot 2.75H_2O$ (MIL-118 C) [b]	k. A.	[23]
MIL-120	$[Al_4(OH)_8(BTEC)] \cdot \sim 5H_2O$	308	[32]
CAU-4	$[Al(BTB)] \cdot 1.6DMF \cdot 4.7H_2O$	1520	[31]

mit BDC = 1,4-Benzoldicarboxylat, BTC = Benzol-1,3,5-tricarboxylat, BTEC = Benzol-1,2,4,5-tetracarboxylat, BTB = 4,4´,4´´-Benzol-1,3,5-triyltribenzoat

[a] Spezifische Oberfläche berechnet aus der N_2-Sorptionsisorptionsisotherme mithilfe der BET-Theorie. Für diese Messungen wurden alle Verbindungen thermisch aktiviert.
[b] Summenformeln der thermisch aktivierten Verbindung bei Raumtemperaturbedingungen.
[c] Für MIL-101-NH_2 ist in der entsprechenden Literatur keine Summenformel angegeben. Anhand der XRPD-Daten der Verbindung wurde postuliert, dass MIL-101-NH_2 eine isoretikulare Verbindung von MIL-101 ist. Die Summenformel von MIL-101 ist $[Cr_3O(H_2O)_2(F,OH)(BDC)_3]$.[36]

In Rahmen dieser Arbeit konnten mit CAU-1 (vgl. Kap. 4.2.1) und CAU-3-NDC (vgl. Kap. 4.2.4) zwei weitere poröse, aluminiumhaltige Gerüststrukturen dargestellt werden. CAU-1 und CAU-3-NDC besitzen zwölffach verknüpfte Netzwerke mit bisher unbekannten anorganischen Baueinheiten. Bemerkenswert an diesen Verbindungen ist, dass das organische Lösemittel (Methanol) in Form von Methoxygruppen zum Ladungsausgleich in die anorganischen Baueinheiten eingebaut wurde.

Zu Beginn dieser Arbeit waren mit MIL-53, MIL-96 und MIL-110 erst drei poröse Al-MOFs in der Literatur bekannt. Ausgehend von MIL-53 konnten in den Folgejahren unter Verwendung unterschiedlicher Linkermoleküle weitere Al-MOFs mit gleicher Netzwerktopologie hergestellt werden. Da eine wesentliche Aufgabe dieser Dissertation darin bestand, funktionelle Gruppen (-NH_2, -NO_2, -OH) in das Gerüst von MIL-53 einzubauen, werden die bislang aus der Literatur bekannten Al-MIL-53-Verbindungen in dem nächsten Kapitel (1.1.2) kurz vorgestellt. Der Schwerpunkt liegt

dabei auf den neuen Eigenschaften der Materialien, die durch die verschiedenen Linker in das Gerüst von MIL-53 eingebracht werden konnten.

1.2.1 Isoretikuläre aluminiumhaltige MOFs

Metall-organische Gerüstverbindungen ermöglichen durch ihr modulares Aufbauprinzip die gezielte Herstellung von isoretikulären Verbindungen mit neuen physikalischen und chemischen Eigenschaften. Isoretikuläre Verbindungen weisen die gleiche Netzwerktopologie auf und können durch den Einsatz unterschiedlicher Linkermoleküle synthetisiert werden. Auf diese Weise können zusätzliche funktionelle Gruppen (z. B. -NH_2, -OH, -COOH) in ein bekanntes Gerüst eingebracht sowie dessen Poren oder Kanäle aufgeweitet bzw. verkleinert werden (Größe der Linkermoleküle).

Bei den Al-MOFs sind bislang nur von MIL-53 und MIL-118 isoretikuläre Verbindungen in der Literatur bekannt. Die isoretikuläre Verbindung von MIL-118, MIL-122,[37] ($Al_2(OH)_2$[NTC]) (NTC = 1,4,5,8-Naphthalintetracarboxylat) konnte in dem System M^{3+}/H_4NTC/H_2O außer mit Aluminium auch mit den Elementen Gallium und Indium dargestellt werden. Der Einsatz des im Vergleich zu MIL-118 größeren Linkermoleküls (H_4NTC > H_4BTEC) führte, aufgrund einer Verschiebung der Ketten innerhalb des Gerüstes, entgegen der Erwartung zu keiner signifikanten Erhöhung der Porosität.

Isoretikuläre Al-MOFs mit MIL-53 Topologie konnten mit insgesamt sechs Linkermolekülen dargestellt werden (Abb. 1.5).

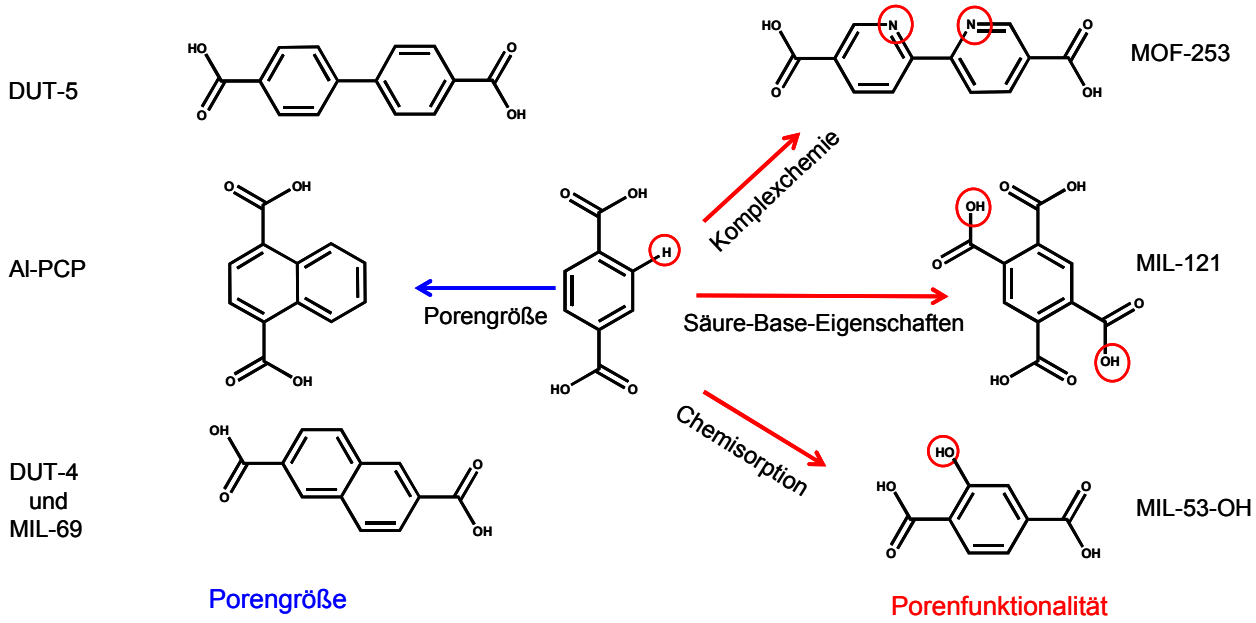

Abb. 1.5 Zur Synthese isoretikulärer MIL-53-Verbindungen eingesetzte Dicarbonsäuren. Die in das Gerüst eingebrachten funktionellen Gruppen sind rot eingekreist.

Bei der Synthese von isoretikulären MIL-53-Verbindungen wurden zwei Strategien verfolgt. Zum einen die Modifizierung der Porengröße und zum anderen das Einbringen von Funktionalität in die Poren.

Letzteres gelang Himsl et. al,[38] indem unter Verwendung von 2-Hydroxyterephthalsäure (H_2BDC-OH) Hydroxygruppen in das Gerüst von MIL-53 eingeführt wurden. Die leicht sauren Hydroxygruppen von MIL-53-OH wurden im Anschluss in einer Säure-Base Reaktion mit LDA in Lithiumalkoxidgruppen umgewandelt. Obwohl nicht alle aziden Protonen gegen Lithiumkationen ausgetauscht werden konnten, führte diese Behandlung zu einer Erhöhung der gravimetrischen Wasserstoffspeicherdichte des Materials.

Volkringer et al. konnten nichtkoordinierte Carboxylgruppen in das Netzwerk von MIL-53 einbauen.[39] Bei der als MIL-121 bezeichneten Verbindung wurde, wie für die Synthese von MIL-118 und MIL-120, der H_4BTEC-Linker eingesetzt. Eine Erniedrigung des pH-Wertes führte dazu, dass bei MIL-121 (Al(OH)[H_2BTEC]) anstelle von acht (MIL-120) bzw. sechs (MIL-118A) Carboxylsauerstoffatomen nur vier an der Koordination mit den Aluminiumionen beteiligt sind. Jeweils zwei von den vier Carboxylgruppen des BTEC-Linkers ragen in ihrer protonierten Form in die Kanäle hinein. Dadurch liegen die Kanäle von MIL-121 auch bei Raumtemperatur in der offenen Form vor.

Die Verbindung Al-PCP[40] (PCP = engl. Abk. Porous Coordination Polymer) ($Al(OH)_2$(1,4-NDC) (NDC^{2-} = Naphthalindicarboxylat) stellt eine Besonderheit dar. Die aromatischen Naphthalinreste sind über intermolekulare π··π Wechselwirkungen zum Poreninneren ausgerichtet, wodurch zwei Sorten eindimensionaler, quadratisch geformter Kanäle im Gerüst gebildet werden. Die größeren Kanäle besitzen eine Öffnung von 7.7 × 7.7 $Å^2$ und sind damit mehr als doppelt so groß wie die kleineren Kanäle (3.0 × 3.0 $Å^2$). Kürzlich wurde Al-PCP erfolgreich als Templat zur Herstellung von mikroporösen Kohlenstofffasern eingesetzt.[41] Dazu wurde Al-PCP zusammen mit Furfurylalkohol unter Inertgasatmosphäre karbonisiert und die übriggebliebenen Al-Spezies wurden mit HF entfernt.

Eine Aufweitung der Kanäle des MIL-53 Netzwerkes konnte durch die Darstellung der Verbindungen DUT-4 ([Al(OH)(NDC)]) (DUT = Dresden University of Technology) und DUT-5 ([Al(OH)(BPDC)]) (H_2BPDC = 4,4`-Biphenyldicarbonsäure)) erreicht werden.[42] Dazu wurden anstelle von Terephthalsäure die größeren Linker 1,6-H_2NDC (DUT-4) und H_2BPDC (DUT-5) zur Synthese eingesetzt. DUT-4 und DUT-5

besitzen Kanäle mit einer Öffnung von 8.5 × 8.5 $Å^2$ bzw. 11.1 × 11.1 $Å^2$. Interessant ist, dass bereits vier Jahre zuvor eine unporöse Modifikation von DUT-4 mit der Bezeichnung MIL-69[43] (Al(OH)[NDC]·H_2O) hergestellt wurde. Zur Synthese von MIL-69 wurde Wasser, statt des bei der Herstellung von DUT-4 verwendeten DMF, eingesetzt. Erstaunlich ist, dass beide Verbindungen nicht flexibel sind und durch Lösemittelaustauschexperimente nicht ineinander überführt werden konnten. Daher wird davon ausgegangen, dass in diesem System die Wahl des Lösemittels die Porosität des erhaltenen Produktes entscheidend beeinflussen kann.

Ein eleganter Weg zugängliche Metallzentren in das Gerüst von DUT-5 einzufügen wurde von Yaghi et. al aufgezeigt.[44] Diese ersetzten bei der Synthese von MOF-253 den Linker 4,4`-Biphenyldicarbonsäure durch 2,2`-Bipyridin-5,5`-dicarbonsäure ($H_2$BPYDC). Unter Erhalt der Porosität der Verbindungen konnte so erstmalig eine 2,2`-Bipyridin (BPy)-Einheit in ein MOF eingebaut werden, welche aufgrund ihres „Chelat-Effektes“ Metallionen koordinativ an das Gerüst binden kann. Die Koordination von $Cu(BF_4)_2$ an die BPy-Einheit des MOFs führte zu einer signifikanten Änderung der Sorptionseigenschaften des Gerüstes. Unter anderem stieg in einem Experiment unter einem typischen Gasstrom der Selektivitätsfaktor für eine bevorzugte Bindung von CO_2 über N_2 nach der Modifizierung von 2.8 auf 12 an.

In Tabelle 1.2 sind die derzeit aus der Literatur bekannten Al-MIL-53-Strukturanaloga mit den dazugehörigen scheinbaren spezifischen Oberflächen zusammengefasst.

Tab. 1.2 Zusammenstellung derzeit bekannter Al-MIL-53-Strukturanaloga sowie deren scheinbaren spezifischen Oberflächen.

Al-MOF	**Summenformel**	**S_{BET}(m^2·g^{-1})[a]**	**Lit.**
MIL-53	[Al(OH)(BDC)]·H_2O	1235	[26], [34]
MIL-53-OH	[Al(OH)(BDC-OH)]·H_2O	1566	[38]
MIL-121	[Al(OH)(H_2BTEC)]·nH_2O·nH_4BTEC	162	[39]
MOF-253	[Al(OH)(BPYDC)]	2160	[44]
MIL-69	[Al(OH)(NDC)]·H_2O	-	[43]
DUT-4	[Al(OH)(NDC)]·1.5DMF·1.5H_2O	1308	[42]
DUT-5	[Al(OH)(BPDC)] 1.8DMF·3.5H_2O	1613	[42]
Al-PCP	[Al$(OH)_2$(1,4-NDC)]·2H_2O	513[41]	[40]

mit BDC = 1,4-Benzoldicarboxylat, H_4BTEC = Benzol-1,2,4,5-tetracarbonsäure, BPYDC = 2,2`-bipyridin-5,5`-dicarboxylat, NDC = Naphthalindicarboxylat, BPDC = Biphenyl-4,4´-dicarboxylat

1.3 Postsynthetische Modifizierung von MOFs

Dem Konzept, die Porengröße oder die Porenfunktionalität der MOFs durch die Wahl des Linkers zu variieren, sind Grenzen gesetzt. Zum einen nimmt die Löslichkeit der Linker mit zunehmender Größe meist rapide ab, was die Synthese von MOFs deutlich erschwert. Zum anderen kann es bei Verwendung von größeren Linkern zur Katenation kommen, d. h. zwei oder mehrere Netze sind ineinander verstrickt. Der Einsatz von funktionalisierten Linkermolekülen birgt die Gefahr, dass sich die zusätzlichen funktionellen Gruppen an der Koordinationschemie der Metallionen beteiligen oder dass diese unter den meist solvothermalen Reaktionsbedingungen nicht stabil sind.
Aus eben genannten Gründen wird häufig eine nachträgliche Modifizierung des Gerüstes in Betracht gezogen, um eine gewünschte Funktionalität einzuführen. Bei einer nachträglichen Modifizierung wird das Gerüst des MOFs nach der Synthese in einem anschließenden Schritt unter Erhalt der Struktur thermisch oder chemisch verändert. Letzteres wurde erstmals 1990 von Robson[45] für anorganisch-organische Hybridverbindungen vorgeschlagen:

„*Eine relativ ungehinderte Diffusion einer Spezies durch ein Gitter sollte die chemische Funktionalisierung des Gerüstes nach dem Aufbau des Netzwerkes ermöglichen*."

Erfolgreich angewendet werden konnte dieses Konzept bereits bei der Modifizierung von mesoporösen Silicatverbindungen[7] und Zeolithen[46]. Über die an den Porenoberflächen befindlichen -OH-Gruppen konnten so postsynthetisch chirale organische Moleküle im Gerüst dieser Verbindungen verankert und die katalytischen Eigenschaften der Materialien verbessert werden. Im Gegensatz zu diesen Materialien bieten die Metall-organischen Gerüstverbindungen den Vorteil, dass neben der anorganischen Komponente im Gerüst auch die verbrückenden organischen Linker-Moleküle nachträglich modifiziert werden können. In der Regel wird eine dauerhafte chemische Modifizierung (PSM) (englisch für Post-Synthetic-Modification) des Gerüstes angestrebt, bei der häufig kleinere Moleküle kovalent bzw. koordinativ ans Gerüst gebunden oder durch thermische Abspaltung aus diesem entfernt werden. Zum ersten Mal wurde im Jahr 2000 von einer PSM an

MOFs berichtet.[47] Kim et al. wandelten Pyridin-Einheiten, die koordinativ an die Metallzentren der homochiralen Verbindung POST-1 gebunden waren, mit Methyliodid in N-Methylpyridinumionen um. Erstaunlich ist, dass erst sieben Jahre später wieder verstärkt über die PSM von MOFs berichtet wurde. Hintergrund hierfür ist u. a. die vermehrte Entdeckung stabiler, zur PSM einsetzbarer Gerüste. Zu diesen zählen Verbindungen bei denen die anorganische Baueinheit ein koordinativ ungesättigtes Metallzentrum besitzt. Als bekannteste Vertreter sind HKUST-1 und MIL-101 zu nennen, deren Baueinheiten aus mehrkernigen Metallclustern bestehen. Die Verbindung HKUST-1 beruht auf dem zweikernigen Cluster $\{Cu_2(O_2CR)_4\}$. Jedes Kupferion ist quadratisch-planar von Carboxylateinheiten sowie von einem Lösungsmittelmolekül umgeben. Die trimere $\{Cr_3(\mu_3\text{-}O)(O_2CR)_6\}^+$-Baueinheit von MIL-101 enthält zwei terminal gebundene Lösemittelmoleküle. Aus beiden Clustern lassen sich die Lösemittel entfernen und Metallzentren mit freien Bindungsstellen generieren. An diesen Bindungsstellen können im Anschluss Moleküle koordiniert werden, die über funktionelle Gruppen mit freien Elektronenpaaren verfügen, wie Alkohole oder Amine. Da die Mehrzahl der MOFs keine koordinativ ungesättigten Metallzentren besitzen, sind nur sehr wenige Verbindungen[48] auf diese Weise modifizierbar. Die meisten PSM erfolgen daher an zusätzlichen funktionellen Gruppen wie $-NH_2$ oder -OH an den organischen Linker-Molekülen. Diese funktionellen Gruppen können durch die Synthese isoretikulärer Verbindungen gezielt in das Gerüst eingebracht (vlg. Kapitel 4.1.1, 4.1.2, 4.2.3, 4.2.4 und 4.3.1) und im Anschluss chemisch modifiziert werden. Besonders häufig wird die Aminogruppe ($-NH_2$) in den MOF eingebaut. Die Aminogruppe ist basisch und ermöglicht durch das freie Elektronenpaar am Stickstoff-Atom eine Vielzahl an chemischen Reaktionen (z. B. nukleophile Substitutions- oder Säure-Base-Reaktionen). Weiter ist die Aminogruppe in den meisten Lösemitteln chemisch inert und beteiligt sich nicht an der Koordinationschemie der eingesetzten Metallionen. Einer der am häufigsten modifizierten aminofunktionalisierten MOFs ist IRMOF-3.[49] IRMOF-3 wird aus $H_2BDC\text{-}NH_2$ hergestellt und ist isoretikulär zu MOF-5 ($[Zn_4O(BDC)_3]$). In dem Gerüst von MOF-5 werden $\{Zn_4O\}^{6+}$-Cluster sechsfach durch Terephthalationen zu einem dreidimensionalen Netzwerk verknüpft. Weitere Beispiele für aminofunktionalisierte MOFs sind MIL-101-NH_2[24,30] (Fe^{3+},Al^{3+}), MIL-68-NH_2[50] ($[In(OH)(BDC\text{-}NH_2)]$) und die ebenfalls auf den $\{Zn_4O\}^{6+}$-Cluster basierenden Verbindungen UMCM-1-NH_2[51] ($[Zn_4O(BDC\text{-}NH_2)(BTB)_{4/3}]$) und DMOF-$NH_2$[52] ($[Zn(BDC\text{-}NH_2)(DABCO)]$).

Im Rahmen dieser Arbeit konnten mit MIL-53-NH_2 (vgl. 4.1.1) und CAU-1-NH_2 (vgl. 4.2.1) zwei weitere aminofunktionalisierte MOFs dargestellt und die Aminogruppen im Gerüst chemisch modifiziert werden.

Durch eine PSM können einzelne Stoffeigenschaften dieser Verbindungen, wie die chemische Stabilität, die Adsorptionskapazität oder die katalytische Wirkung entscheidend verbessert werden. Die PSM kann in Abhängigkeit von den aktiven Zentren (funktionellen Gruppen bzw. ungesättigte Metallionen) und der Beschaffenheit des Netzwerks über verschiedene Wege durchgeführt werden. Die zurzeit gängigsten Methoden zur PSM sind in Abbildung 1.6 schematisch dargestellt und werden nachfolgend anhand von Beispielen kurz erläutert.

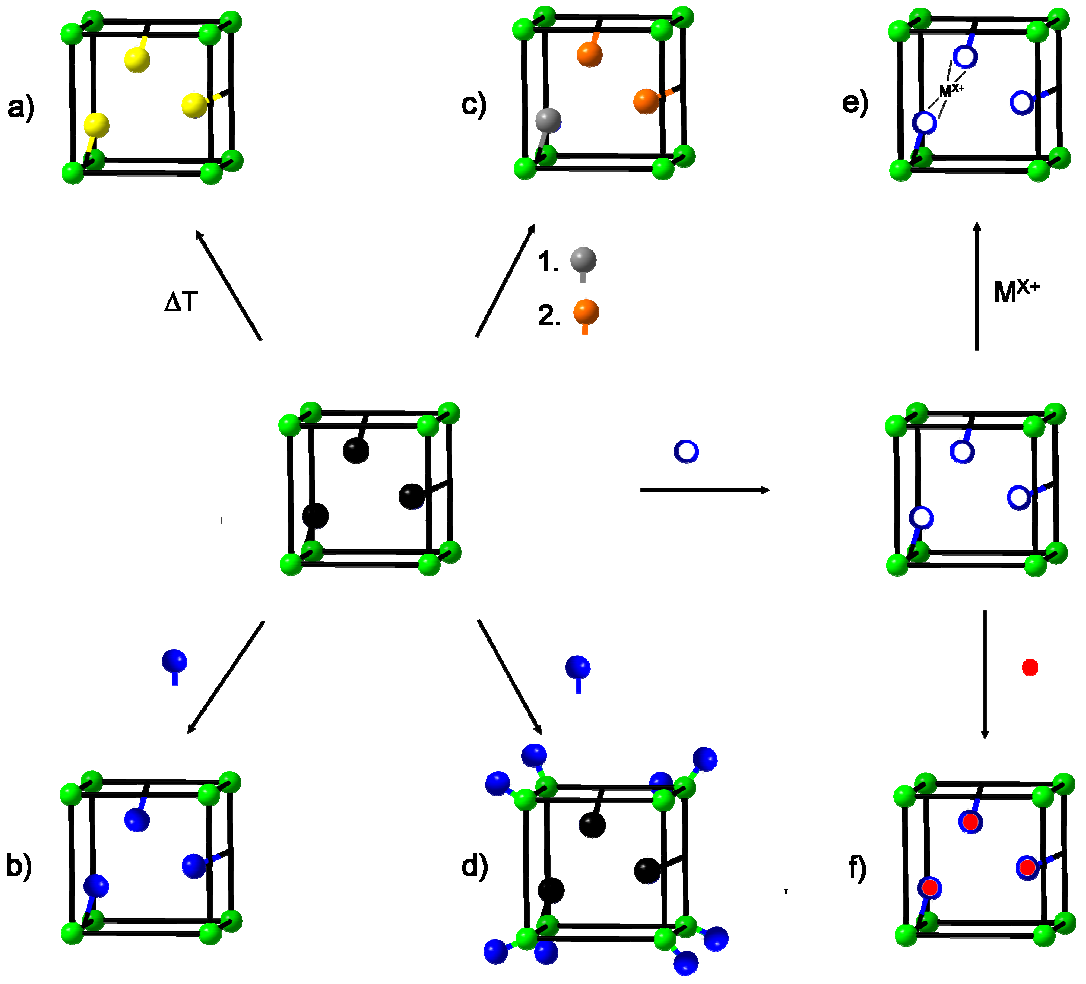

Abb. 1.6 Unterschiedliche Ansätze zur PSM Metall-organischer Gerüstverbindungen: a) thermische Mod., b) kovalente Mod., c) Tandem-Mod., d) koordinative kovalente Mod., e) Komplexierungsreaktion, f) Darstellung reaktiver funktioneller Gruppen im Gerüst (e) und f) werden häufig in zwei Syntheseschritten durchgeführt). Abbildung in Anlehnung an Referenz [53].

(a) Modifizierung von thermolabilen organischen Gruppen am Linker durch Erhitzen: Im Gerüst vorhandene funktionelle Gruppen können durch Erhitzen des MOFs teilweise zerfallen, wobei die chemischen und physikalischen Eigenschaften der Poren grundlegend verändert werden. Beispiel: Die Verwendung eines 4,4`-Biphenyllinkers mit der sterisch anspruchsvollen NHBoc-Gruppe verhinderte bei der Synthese eines Zn-MOFs eine Katenation des MOF-Netzwerkes. Durch eine thermische Behandlung des MOFs konnten die Boc-Gruppen entfernt und die reaktive Aminogruppe entschützt werden.[54]

(b) Kovalente Umsetzung funktioneller Gruppen im Gerüst mit reaktiven organischen Molekülen: Bei der am häufigsten verwendeten PSM-Methode lassen sich neben Amidkupplungen, N-Alkylierungen und Iminkondensationen auch Harnstoffderivate innerhalb des MOFs generieren. Funktionelle Gruppen an den Linkermolekülen können zudem protoniert, reduziert oder bromiert werden. Beispiel: Das Einführen aromatischer Gruppen in das Gerüst von IRMOF-3 durch Amidkupplungen bzw. Bildung von Harnstoffderivaten verbesserte die Wasserstoffspeicherkapazität bei niedrigen Drücken.[51]

(c) Einbringen unterschiedlicher funktioneller Gruppen in ein Gerüst durch eine sogenannte Tandem-PSM: Die unter b) vorgestellten Reaktionen werden zunächst gequencht. Anschließend werden die nicht umgesetzten funktionellen Gruppen an den Linkermolekülen mit einem anderen Reagenz versetzt. Beispiel: In das Gerüst von IRMOF-3 konnten nebeneinander eine Alkyl- und eine Olefin-Funktion eingebaut werden. Dazu wurde der MOF nacheinander mit Essigsäureanhydrid und Crotonanhydrid behandelt. Der Modifizierungsgrad der eingeführten Gruppen ließ sich über die Reaktionszeit sowie die Konzentration der Reaktanden reproduzierbar einstellen.[55]

(d) Substitution mit Lösungsmittelmolekülen besetzter Koordinationsstellen der anorganischen Baueinheiten: An der anorganischen Baueinheit koordinierte Lösungsmittelmoleküle können entweder thermisch entfernt oder direkt in einer Flüssig-fest-Reaktion gegen im Überschuss eingesetzte Substituenten ausgetauscht werden. Lediglich sehr wenige MOFs, wie MIL-100, MIL-101 oder HKUST-1 besitzen solche zugänglichen Koordinationsstellen in der

anorganischen Baueinheit. Beispiel: Férey et al. koordinierten die multifunktionalen Liganden Etylendiamin, Diethylentriamin und 3-Aminiopropyltrialkoxylsilan an die Cr(III)-Trimere von MIL-101. Die aminofunktionalisierten MIL-101-Verbindungen zeigten eine verbesserte katalytische Wirkung bei der Knoevenagelkondensation von Benzaldehyd und Ethylcyanoacetat.[56]

(e) Kovalentes „Verankern“ von komplexbildenden Liganden im Gerüst: MOFs die mit mehrzähnigen Liganden modifiziert wurden, können Metallionen komplexieren und als heterogene Katalysatoren eingesetzt werden. Beispiel: In einer Iminkondensation konnten zweizähnige Salicylaldehydeinheiten in IRMOF-3 eingebaut werden. Anschließend wurde die Spezies V(O)acac (acac = Acetylacetonat) an die Salicylidengruppen koordiniert.[57]

(f) Darstellung neuer funktioneller Gruppen im Gerüst über reaktive Zwischenstufen: Wenn die im Gerüst vorliegenden funktionellen Gruppen die gewünschte Modifizierung nicht ermöglichen, können diese über reaktivere bzw. besser geeignete Zwischenstufen, wie z. B. Azide oder Isocyanate, generiert werden. Beispiel: In einer Ein-Topf-Synthese wurde DMOF-1-NH_2 mit tBuONO und $TMSN_3$ in das Azidintermediat DMOF-3-N_3 überführt, welches im Anschluss im Überschuss mit Phenylacetylen, in Gegenwart eines Kupferkatalysators, in die triazolmodifizierte Verbindung DMOF-fun umgewandelt wurde.[58]

Zusammenfassend kann aus den letzten beiden Kapiteln das Fazit gezogen werden, dass neben dem Einsatz zusätzlich funktionalisierter Linker bei der Synthese die PSM eine sehr variable und effiziente Methode ist, um funktionelle Gruppen in ein Gerüst einzubauen. Letztere bietet zudem den Vorteil, dass im selben MOF eine Reihe von unterschiedlichen funktionellen Gruppen eingebracht und der Grad der Modifizierung über die Reaktionsbedingungen kontrolliert werden kann.

1.4 In situ-Untersuchungen von MOFs

Zeitaufgelöste Untersuchungen der Produktbildung Metall-organischer Gerüstverbindungen erlauben nahezu den gesamten Kristallisationsprozess zu durchleuchten. Dieser erstreckt sich von der Deprotonierung der Linkermoleküle und Bildung der anorganischen Baueinheiten über die Nukleation bis hin zum Kristallwachstum der Verbindungen. Zurzeit sind noch sehr wenige Details über den Ablauf der einzelnen Reaktionsschritte bekannt. Besonders für die Synthese isoretikulärer Verbindungen ist jedoch ein besseres Verständnis der Produktbildung essentiell: Neben den unterschiedlichen Säure-Baseeigenschaften und Löslichkeiten der Reaktanden können einzelne Reaktionsparameter wie beispielsweise die Temperatur,[59,60] der pH-Wert,[61] die Reaktionsdauer[62] und die verwendete Heizmethode[63] die Produktbildung unvorhergesehen beeinflussen. Mittels zeitaufgelöster Untersuchungsmethoden kann der Einfluss einzelner Reaktionsparameter gezielt untersucht und mögliche Intermediate bei der Reaktion beobachten werden. Bei einer entsprechenden Zeitauflösung der Experimente kann neben den Geschwindigkeitskonstanten und Aktivierungsenergien auch eine Idee über den Reaktionsmechanismus des untersuchten Systems erhalten werden.

Die zeitaufgelöste Untersuchung der MOF Kristallisation kann mit ex situ- und in situ-Methoden durchgeführt werden. Da die Synthesen von MOFs in der Regel unter solvothermalen Bedingungen in Glas- oder Stahlautoklaven durchgeführt werden, kann der Kristallisationsprozess nur mit sehr hohem präparativen Aufwand in situ verfolgt werden. Die energiedispersive Röntgenbeugung (EDXRD) hat sich hierfür als besonders geeignete Untersuchungsmethode etabliert. Die bei dieser Methode verwendete hochenergetische Synchrotronstrahlung ist in der Lage, die Reaktorwände zu durchdringen und erlaubt eine hohe Zeitauflösung des untersuchten Systems. Aufgrund des begrenzten Zugangs zu Laboren mit einer Synchrotronstrahlungsquelle werden allerdings viele Experimente ex situ oder unter veränderten Synthesebedingungen (z. B. bei Raumtemperatur in übersättigter Lösung) durchgeführt. Für die ex situ-Untersuchungen von Reaktionen unter solvothermalen Bedingungen werden die Reaktionen in vorher definierten Zeitintervallen gequencht, die Reaktionsprodukte charakterisiert und der Reaktionsfortschritt gegen die Zeit aufgetragen. Dieser Ansatz hat den Nachteil, dass

der wahre Reaktionszustand durch das benötigte Abkühlen der Reaktionsmischung und die Probenpräparation verfälscht wird.[64] Bei kristallinen Produkten wird der Reaktionsfortschritt häufig aus der relativen Intensität der Produktreflexe mittels Röntgenpulverdiffraktometrie bestimmt. Mithilfe dieser Methode untersuchten Jhung et al. den Einfluss der Metallionen bei der Synthese isostruktureller Metall(III)-terephthalate [65] bzw. Lanthanterephthalate.[66] In beiden Fällen war die Geschwindigkeit der Nukleation und des Kristallwachstums direkt proportional zu der Labilität bzw. chemischen Inertheit der Metallionen ($r_{Cr\text{-}MIL\text{-}53} < r_{Al\text{-}MIL\text{-}53} < r_{V\text{-}MIL\text{-}47}$; $r_{Ce\text{-}BTC} > r_{Tb\text{-}BTC} > r_{Y\text{-}BTC}$ mit r = 1/t, t = Dauer des Nukleations- bzw. Kristallwachstums). Im Umkehrschluss bedeutet dies, dass die Deprotonierung der organischen Linker viel schneller ablaufen muss, als die Komplexierung der Metallionen. Letztere stellt daher den geschwindigkeitsbestimmenden Schritt der Reaktionen dar (Abb.1.7).

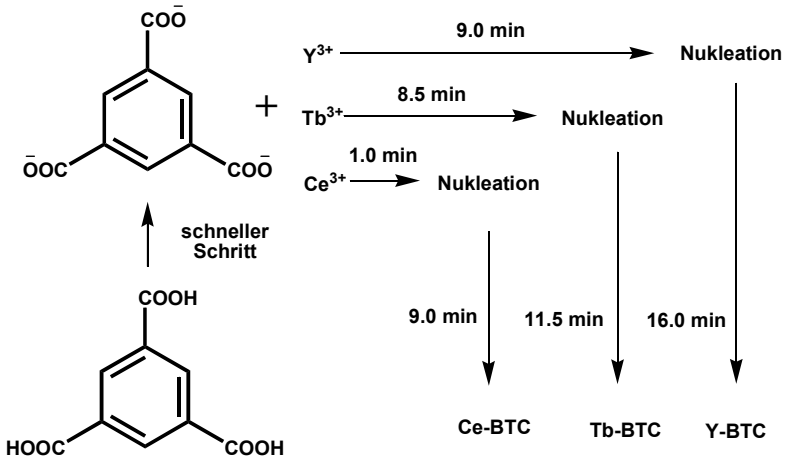

Abb. 1.7 Reaktionszeiten der Nukleation und des Kristallwachstums bei der Produktbildung isostruktureller Lanthan-MOFs.[66]

Neben den eingesetzten Metallionen besitzt auch die verwendete Heizmethode einen großen Einfluss auf die Geschwindigkeit solvothermaler Synthesen. Dieser wurde von Jhung et al. anhand der Produktbildung von Fe-MIL-53 untersucht. Hierfür wurden Reaktionen in einem konventionellen elektrischen Ofen (CE) sowie unter dem Einfluss von Mikrowellen (MW) - und Ultraschall- (US) Strahlung durchgeführt.[67] Der Einsatz von US- bzw. MW-Strahlung führte zu einer drastischen Beschleunigung der Synthesen ($r_{US} > r_{MW} > r_{CE}$). Die Beschleunigung unter US-Strahlung wird durch das Auftreten von akustischer Kavitation erklärt, die zu lokal stark erwärmten Bereichen in der Reaktionslösung, den sogenannten „Hot-spots“, führt. Die höheren Syntheseraten für die MW-unterstützten Synthesen werden

hingegen den schnellen Aufheizraten sowie einer gleichmäßigen Erwärmung der Reaktionslösungen zugeschrieben.

Für eine Aufklärung der bei der Synthese ablaufenden Reaktionsmechanismen ist eine lückenlose Verfolgung des Kristallisationsprozesses nahezu unabdingbar. Ex situ-Experimente sind aufgrund des dafür benötigten hohen präparativen Aufwandes hierfür eher ungeeignet, so dass auf in situ-Methoden zurückgegriffen wird.

Mithilfe von in situ-EDXRD-Experimenten untersuchten Walton et al. die solvothermale Synthese von HKUST-1 und Fe-MIL-53.[68] Dabei konnten zwei unterschiedliche Reaktionsverläufe beobachtet werden. Die Produktbildung von Fe-MIL-53 verläuft demnach über ein kristallines Intermediat, während HKUST-1 direkt aus einer klaren Lösung gebildet wird. Durch Quenchen der Reaktion konnte der metastabile Präkursor bei der Synthese von Fe-MIL-53 isoliert und als MOF-235 identifiziert werden (Abb. 3).

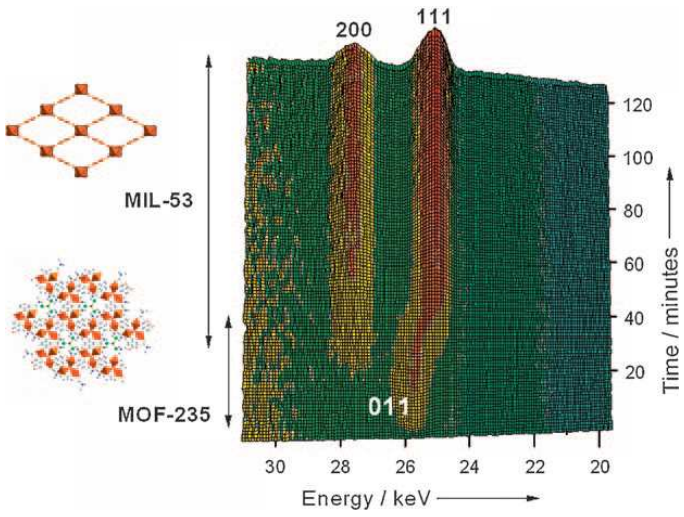

Abb. 3 Zeitaufgelöste EDXRD-Messung während der Kristallisation von Fe-MIL-53 bei 150°C. Abbildung aus Referenz [68] mit freundlicher Genehmigung von Wiley & Sons, © 2010.

Das Kristallwachstum von HKUST-1 wurde kinetisch ausgewertet und einer klassischen nukleationskontrollierten Reaktion aus einer Lösung zugeordnet. Dabei wurde das ursprünglich aus der Festkörperchemie bekannte Avrami-Eroféev-Modell[69] verwendet. Mit diesem Modell konnten bereits neue Erkenntnisse und Tendenzen der Kristallisationskinetik solvothermaler Synthesen von Zeolithen,[70] Alumophosphaten[71] und Thiometallaten[72] erhalten werden.

In der folgenden Tabelle sind ausgewählte Beispiele von ex situ und in situ-Untersuchungen solvothermaler MOF-Synthesen stichwortartig zusammengestellt (Tab. 1.3).

Tab. 1.3 Ausgewählte ex situ- und in situ-Untersuchungen solvothermaler MOF-Synthesen.

MOF	Methode	Untersuchung
ex situ-Methoden		
MOF-76	XRD	Beschleunigte Produktbildung isostruktureller Ln-MOF-76 Verbindungen (Ln = Ce, Tb, und Y) bei Verwendung von US-Strahlung.[66]
MIL-53	XRD	Einfluss der Metallionen auf die Reaktionsgeschwindigkeit isostruktureller Me-MIL-53 Verbindungen (Me = V^{3+}, Al^{3+}, Cr^{3+}).[65]
HKUST-1	XRD	Beschleunigte Produktbildung durch MW-unterstützte Synthese.[73]
Fe-MIL-53	XRD	Einfluss der Heizmethode (CE, US, MW) auf die Syntheseraten.[68]
in situ-Methoden		
HKUST-1	EDXRD	Kinetische Auswertung der Produktbildung nach der Sharp-Hancock sowie der Gualtieri Methode.[68,74]
Fe-MIL-53	EDXRD	Entdeckung und Isolierung des Intermediats MOF-235 bei der Synthese von Fe-MIL-53.[68]
MOF-14	EDXRD	Kinetische Auswertung der Produktbildung nach der Gualtieri Methode sowie die Untersuchung des Zerfalls unter hydrothermalen Bedingungen.[74]
Al-MIL-53-NH_2, Al-MIL-101-NH_2, Al-MOF-235-NH_2	SAXS/ WAXS	Untersuchung der Produktbildung in dem System Al^{3+}/H_2BDC-NH_2/Lsgm. unter Verwendung der Gualtieri Methode.[75]

Der Großteil der ex situ-Untersuchungen beschäftigt sich mit dem Einfluss einzelner Syntheseparameter wie der verwendeten Heizmethode und der Labilität der eingesetzten Metallionen. Die in situ-Untersuchungen konzentrieren sich hingegen mehr auf den bei der Reaktion ablaufenden Mechanismus sowie auf das Auffinden von Intermediaten. Im Rahmen dieser Arbeit wurde der Einfluss von MW-Strahlung sowie des verwendeten Linkers auf die Kristallisation zweier CAU-1-Derivate (CAU-1-NH_2 und CAU-1-$(OH)_2$ mittels in situ-EDXRD-Methode untersucht (vgl. 4.3.1, 4.3.2). Für diese Untersuchungen wurde erstmalig ein kommerziell erhältlicher MW-Ofen in einen Synchrotronstrahlengang implementiert.

Literatur

[1] A. Corma, *J. Catal.* **2003**, *216*, 298.

[2] M. E. Davis, R. F. Lobo*, Chem. Mater*. **1992**, *4*, 756.

[3] K. Tanabe, W. F. Hölderich, *Appl. Catal. A: Gen.* **1999**, *181*, 399.

[4] M. T. Ravanchi, T. Kaghazchi, *Desalination* **2009**, *235*, 199.

[5] M. E. Davis, *Nature* **2002**, *417*, 813.

[6] S. Storck, H. Bretinger, W. F. Maier, *Appl. Catal. A: Gen:* **1998**,*174*, 137.

[7] D. Brunel*, Microporous Mesoporous Mater.* **1999***, 27,* 329.

[8] A. K. Cheetham, G. Férey, T. Loiseau, *Angew. Chem. Int. Ed.* **1999,** *38*, 3268.

[9] U. Ciesla, F. Schüth, *Microporous Mesoporous Mater.* **1999***, 27,* 131.

[10] J. S. Beck, J. C. Vartuli, W. J. Roth, M. E. Leonowicz, C. T. Kresge, K. D. Schmitt, C. T. W. Chu, D.H. Olson, E. W. Sheppard, S. B. McCullen, J. B. Higgins, J. L. Schlenker, *J. Am. Chem. Soc.* **1992**, *114*, 10834.

[11] D. Y. Zhao, J. L. Feng, Q. S. Huo, N. Melosh, G. H. Fredrickson, B. F. Chmelka, G. D. Stucky, *Science* **1998,** *279,* 548.

[12] U. Mueller, M. Schubert, F. Teich, H. Puetter, K. Schierle-Arndt, J. Pastre, *J. Mater. Chem*. **2006**, *16*, 626.

[13] G. Férey, *Chem. Soc. Rev.* **2008**, *37*, 191.

[14] N. L. Rosi, J. Kim, M. Eddaoudi, B. Chen, M. O`Keeffe, O. M. Yaghi, *J. Am. Chem. Soc.* **2005,** *127,* 1504.

[15] J. R. Li, Y. Tao, Q. Yu, X. H. Bu, H. Sakamoto, S. Kitagawa, *Chem. Eur. J.* **2008,** *14*, 2771.

[16] M. Eddaoudi, J. Kim, N. Rosi, D. Vodak, J. Wachter, M. O`Keeffe, O. M. Yaghi, *Science* **2002**, *295*, 469.

[17] A. Sonnauer, F. Hoffmann, M. Fröba, L. Kienle, V. Duppel, M. Thommes, C. Serre, G. Férey, N. Stock, *Angew. Chem. Int. Ed.* **2009**, *48*, 3791.

[18] T. Devic, P. Horcajada, C. Serre, F. Salles, G. Maurin, B. Moulin, D. Heurtaux, G. Clet, A. Vimont, J. M. Greneche, B. Le Ouay, F. Moreau, E. Magnier, Y. Filinchuk, J. Marrot, J. C. Lavalley, M. Daturi, G. Férey, *J. Am. Chem. Soc.* **2010**, *132,* 1127.

[19] P. Horcajada, C. Serre, M. Vallet-Reg, M. Sebban, F. Taulelle, G. Férey, *Angew. Chem. Int. Ed.* **2006**, *45*, 5974.

[20] J. Li, R. Kuppler, H. Zhou, *Chem. Soc. Rev.* **2009**, *38*, 1477.

[21] J. Y. Lee, O. K. Farha, J. Roberts, K. A. Scheidt, S. T. Nguyen, J. T. Hupp, *Chem. Soc. Rev.* **2009**, *38*, 1450.

[22] Z. Guo, G. Li, L. Zhou, S. Su, Y. Lei, S. Dang, H. Zhang, *Inorg. Chem.* **2009**, *48*, 8069.

[23] C. Volkringer, T. Loiseau, N. Guillou, G. Férey, M. Haouas, F. Taulelle, N. Audebrand, I. Margiolaki, D. Popov, M. Burghammer, C. Riekel, *Cryst. Growth Des.* **2009**, 9, 2927.

[24] S. Bauer, C. Serre, T. Devic, P. Horcajada, J. Marrot, G. Férey, N. Stock, *Inorg. Chem.* **2008**, *47*, 7568.

[25] C. Serre, F. Millange, C. Thouvenot, M. Nogues, G. Marsolier, D. Louer, G. Férey, *J. Am. Chem. Soc.* **2002**, *124,* 13519.

[26] T. Loiseau, C. Serre, C. Huguenard, G. Fink, F. Taulelle, M. Henry, T. Bataille G. Férey, *Chem. Eur. J*. **2004**, *10*, 1373.

[27] T. Loiseau, L. Lecroq, C. Volkringer, J. Marrot, G. Férey, M. Haouas, F. Taulelle, S. Bourrelly, P. L. Llewellyn, M. Latroche, *J. Am. Chem. Soc.* **2006**,*128,* 10223.

[28] C. Volkringer, D. Popov, T. Loiseau, G. Férey, M. Burghammer, C. Riekel, M. Haouas, F. Taulelle, *Chem. Mater.* **2009**, *21,* 5695.

[29] C. Volkringer, D. Popov, T. Loiseau, N. Guillou, G. Férey, M. Haouas, F. Taulelle, C. Mellot-Drazniek, M. Burghammer, C. Riekel, *Nat. Mater*. **2007**, *6*, 760.

[30] P. Serra-Crespo, E. V. Ramos-Fernandez, J. Gascon, F. Kapteijn, *Chem. Mater.* **2011,** *23*, 2565.

[31] H. Reinsch, M. Krüger, J. Wack, J. Senker, F. Salles, G. Maurin, N. Stock, *Microporous Mesoporous Mater.* DOI: 10.1016/j.micromeso.2011.05.029

[32] C. Volkringer, T. Loiseau, M. Haouas, F. Taulelle, D. Popov, M. Burghammer, C. Riekel, C. Zlotea, F. Cuevas, M. Latroche, D. Phanon, C. Knöfelv, P. L. Llewellyn, G. Férey, *Chem. Mater.* **2009**, *21*, 5783.

[33] Y. Liu, J.-H. Her, A. Dailly, J. A. Ramirez-Cuesta, D. A. Neumann, C. M. Brown. *J. Am. Chem. Soc.* **2008**, *130*, 11813.

[34] J. P. Rallapalli, K. P. Prasanth, D. Patil, R. S. Somani , R. V. Jasra, H. C. Bjaj, *J. Porous Mater.* **2011**, *118*, 205.

[35] J. S. Lee, S. H. Jhung, *Microporous and Mesoporous Mater.* **2010**, *129*, 274.

[36] G. Férey, C. Mellot-Draznieks, C. Serre, F. Millange, J. Dutour, S. Surblé, I. Margiolaki, *Science*, **2005**, *309*, 2040.

[37] C. Volkringer, T. Loiseau, N. Guillou, G.Ferey, E. Elkaïm, *Solid State Sci.* **2009**, *11*, 1507.

[38] D. Himsl, D. Wallacher, M. Hartmann, *Angew. Chem. Int. Ed.* **2009**, *48*, 4639.

[39] C. Volkringer, T. Loiseau, N. Guillou, G. Ferey, M. Haouas, F. Taulelle, E. Elkaim, N. Stock, *Inorg. Chem.* **2010**, *49*, 9852.

[40] A. Comotti, S. Bracco, P. Sozzani, S. Horike, R. Matsuda, J. Chen, M. Takata, Y. Kubota, S. Kitagawa, *J. Am. Chem. Soc.* **2008**, *130*, 13664.

[41] L. Radhakrishnan, J. Reboul, S. Furukawa, P. Srinivasu, S. Kitagawa, Y. Yamauchi, *Chem. Mater*. **2011**, *23*, 1225.

[42] I. Senkovska, F. Hoffmann, M. Fröba, J. Getzschmann, W. Böhlmann, S. Kaskel, *Microporous Mesoporous Mater.* **2009**, *122*, 93.

[43] T. Loiseau, C. Mellot-Draznieks, H. Muguerra, G. Férey, M. Haouas, F. Taulelle*, C. R. Chim*. **2005**, 8, 765.

[44] E. D. Bloch, D. Britt, C. Lee, C. J. Doonan, F. J. Uribe-Romo, H. Furukawa, J. R. Long, O. M. Yaghi, *J. Am. Chem. Soc.* **2010**,132, 14382.

[45] B. F Hoskins, R. Robson, *J. Am. Chem. Soc*. **1990**, *112*,1546.

[46] G. J. Hutchings, *Chem. Commun.* **1999**, 301.

[47] J. S. Seo, D. Whang, H. Lee, S. I. Jun, J. Oh, Y. J. Jeon, K. Kim, *Nature*, **2000**, *404*, 982.

[48] M. Dincă, J. R. Long, *Angew*. *Chem*. Int. Ed. **2008**, *47*, 6766.

[49] M. Eddaoudi, J. Kim, N. Rosi, D. Vodak, J. Wachter, M. O'Keefe, O. M. Yaghi, *Science* **2002**, *295*, 469.

[50] M. Savonnet, D. Bazer-Bachi, C. Pinel, V. Lecocq, N. Bats, D. Farrusseng, 2009, FR Patent 09/05.101, **2009**.

[51] Z. Wang, K. K. Tanabe, S. M. Cohen, *Chem. Eur. J.* **2010**, *16*, 212.

[52] Q. Wang, K. K. Tanabe, S. M. Cohen, *Inorg. Chem.* **2009**, 48, 296.

[53] K. K. Tanabe, S. M. Cohen, *Chem. Soc. Rev.* **2011**, *40*, 498.

[54] R. K. Deshpande, J. L. Minnaar, S. G. Telfer, *Angew. Chem. Int. Ed.* **2010**, *49*, 4598.

[55] Z. Wang, S. M. Cohen, *Angew. Chem. Int. Ed.* **2008**, *47*,4699.

[56] Y. K. Hwang, D. Y. Hong, J. S. Chang, S. H. Jhung, Y. K. Seo, J. Kim, A. Vimont, M. Daturi, C. Serre, G. Férey, *Angew. Chem. Int. Ed.* **2008**, *47*, 4144.

[57] M. J. Ingleson, J. P. Barrio, J. B. Guilbaud, Y. Z. Khimyak, M. J. Rosseinsky, *Chem. Commun.* **2008**, 2680.

[58] M. Savonnet, D. Bazer-Bachi, N. Bats, J. Perez-Pellitero, E. Jeanneau, V. Lecocq, C. Pinel, D. Farrusseng, *J. Am. Chem.Soc.* **2010**, *132*, 4518.

[59] P. M. Forster, A. R. Burbank, C. Livage, G. Férey, A. K. Cheetham, *Chem. Commun.* **2004**, 368.

[60] P. Mahata, M. Prabu, S. Natarajan, *Inorg. Chem.* **2008**, *47*, 8451.

[61] Y. B. Go, X. Wang, E. V. Anokhina, A. J. Jacobson, *Inorg. Chem*. **2005**, *44*, 8265.

[62] A. K. Cheetham, C. N. R. Rao and R. K. Feller, *Chem. Commun*. **2006**, 4780.

[63] N. A. Khan, S. H. Jhung, *Cryst. Growth Des.* **2010**, *10*, 1860.

[64] N. Pienak, W. Bensch, *Angew. Chem. Int. Ed.* **2011**, *123*, 2062.

[65] E. Haque, J. H. Jeong, S. H. Jhung, *CrystEngComm.* **2010**, *12*, 2749.

[66] N. A. Khan, E. Haque, S. H. Jhung, *Phys. Chem. Chem. Phys.* **2010**, *12*, 2625.

[67] E. Haque, N. A. Khan, J. H. Park, S. H. Jhung, *Chem. Eur. J*. **2010**, *16*, 1046.

[68] F. Millange, I. M. Medina, N. Guillou, G. Férey; K. M. Golden, R. I. Walton, *Angew. Chem. Int. Ed.* **2010**, *49*, 763.

[69] B. V. Eroféev, *C. R. (Dokl.) Acad. Sci. URSS*, **1946**, *52*, 511.

[70] R. I. Walton, F. Millange, D. O'Hare, A. T. Davies, G. Sankar, C. R. A. Catlow, *J. Phys. Chem. B* **2001**, *101*, 83.

[71] G. Sankar, T. Okubo, W. Fan and F. Meneau, *Faraday Discuss*. ***2007***, *136*, 157.

[72] R. Kiebach, N. Pienack, M. E. Ordolff, F. Studt, W. Bensch, *Chem. Mater.* **2006**, *18*, 1196.

[73] N. A. Khan, E. Haque, S. H. Jhung, *Phys. Chem. Chem. Phys.* **2010**, *12*, 2625.

[74] F. Millange, R. El Osta, M. E. Medina, R. I. Walton, *CrystEngComm.* **2011**, *13*, 103.

[75] E. Stavitski, M. Goesten, J. Juan-Alcañiz, A. Martinez-Joaristi, P. Serra-Crespo, A. V. Petukhov, J. Gascon, F. Kapteijn, *Angew. Chem. Int. Ed.* **2011**, *50*, 1.

2 Charakterisierungsmethoden

Zur Charakterisierung der im Rahmen dieser Arbeit dargestellten Verbindungen wurden die in Tab. 2.1 aufgeführten Geräte und Methoden routinemäßig verwendet. Die von den Kooperationspartnern eingesetzten Geräte und Methoden sowie das experimentelle Setup für die in situ-EDXRD-Untersuchungen sind in den jeweiligen Veröffentlichungen beschrieben.

Tab. 2.1 Zusammenfassung der in der Arbeit verwendeten Geräte.

Methode	Gerätetyp / Hersteller	Anmerkungen
Pulverdiffraktometrie	HT-STOE Stadi-P Kombi	Transmissionsgeometrie, Cu-$K\alpha_1$ (λ = 154.056 pm), IP-PSD- bzw. lin. PSD-Detektor, xy-Probentisch
	STOE Stadi-P Kombi	Transmissionsgeometrie, Cu-$K\alpha_1$ (λ = 154.056 pm), lin. PSD-Detektor
Gassorptionsmessung	BEL JAPAN INC. Belsorpmax	Sorption von N_2 bei -196.15 °C H_2O und CO_2 bei 25 °C
TG-DTA	Netsch STA-409CD	Luft und N_2 (75 ml/min), Heizrate 4 °C/min
Elementaranalyse	Eurovektor Euro EA Elemental Analyzer	C-, H-, N-, S-Analyse, He-Trägergas, Verbrennung in O_2 bei 1010 °C, Detektion über Wärmeleitzelle
EDX-Analyse	Philips ESEM XL 30	Rasterelektronenmikroskop mit EDAX-EDX-Detektor
MAS-NMR-Spektroskopie	BRUKER Avance II 300	Probe in 4 mm ZrO_2 Rotor
^{1}H-NMR-Spektroskopie	Bruker DRX500 mit Probenwechsler	500 MHz
FT-Raman-Spektroskopie	Bruker IFS 66 FRA 106	0-3300 cm^{-1}, Nd/YAG Laser (1064 nm).
MIR-Spektroskopie	ATI Matheson Genesis	4000-400 cm^{-1}, KBr-Matrix
	ALPHA-ST-IR Bruker	4000-375 cm^{-1}, ATR-Einheit
DLS-Untersuchung	DelsaNano C apparatus Beckman & Coulter	in Methanol, 70 Zyklen

3 Experimenteller Teil

Dieser Abschnitt behandelt kurz die Grundlagen der Solvothermalsynthese. Im Anschluss daran wird das experimentelle Setup für die Hochdurchsatzuntersuchungen und die MW-unterstützten Synthesen beschrieben.

3.1 Solvothermalsynthese

Fast alle im Rahmen dieser Arbeit erhaltenen Verbindungen wurden durch Solvothermalsynthesen dargestellt. Diese sind im Allgemeinen definiert als heterogene Reaktionen, die in einem geschlossenen Reaktor oberhalb des Siedepunktes des Reaktionsmediums durchgeführt werden.[1,2,3]

Solvothermale Reaktionen werden im Vergleich zu den in der Festkörperchemie sonst üblichen Reaktionstemperaturen bei wesentlich niedrigeren Temperaturen durchgeführt. Dementsprechend werden häufig kinetisch stabile Produkte anstatt der thermodynamisch stabilen Produkte erhalten. Neben Wasser und Ammoniak werden auch organische Lösemittel, wie z. B. Alkohole oder Amine als Reaktionsmedien eingesetzt. Unter solvothermalen Bedingungen können sich die physikalisch-chemischen Eigenschaften der Lösemittel (z. B Viskosität, Dichte Dielektrizitätskonstante) drastisch verändern, was häufig zu einer erhöhten Löslichkeit der Reaktanden führt. Die Zugabe von Mineralisatoren, wie Säuren, Basen oder Komplexbildnern, kann die Löslichkeit zusätzlich erhöhen. Dadurch können auch sonst schwerlösliche Stoffe als Komplexe in Lösung gehen, wobei die Gesetzmäßigkeiten chemischer Transportreaktionen gelten.[2] Eine der bekanntesten Solvothermalsynthesen ist die Darstellung von Quarzkristallen, die wegen ihrer piezoelektrischen Eigenschaften zum Erzeugen hochfrequenter Schwingungen benutzt werden.[4] Ebenfalls von Bedeutung sind die solvothermalen Synthesen von Zeolithen, Alumosilicaten und TiO_2-Nanopartikeln.[5,6]
Die Synthese der in dieser Arbeit dargestellten Verbindungen wurde sowohl unter Verwendung konventioneller Methoden (Stahlautoklaven und Glasreaktoren) als auch unter Einsatz von Hochdurchsatzmultiklaven und einem MW-Ofen durchgeführt. Die Hochdurchsatzmethode ermöglicht es, den Einfluss einzelner

Reaktionsparameter auf die Synthese schnell und systematisch zu untersuchen. MW-unterstützte Synthesen solvothermaler Reaktionen können oft bei drastisch verkürzten Reaktionszeiten durchgeführt werden.[7,8,9] Ferner kann die Verwendung eines MW-Ofens zu engeren Teilchengrößenverteilungen,[10,11] höherer Phasenreinheit und Phasenselektivität führen.[11,12] Viele dieser positiven Eigenschaften werden 1) einer höheren Aufheizrate des Lösemittels, 2) dem gleichmäßigen Aufheizen der Lösung, 3) dem Auftreten von Hot-spots, 4) einem Überhitzen des Reaktionsmediums oder 5) der besseren Löslichkeit der Präkursoren unter MW-Strahlung zugeschrieben.[13]

3.2 Hochdurchsatzmethode

Die Hochdurchsatzmethode erlaubt es, in sehr kurzer Zeit eine große Anzahl von Reaktionen durchzuführen und die erhaltenden Produkte zeitnah zu untersuchen. Von entscheidender Bedeutung sind dabei die Parallelisierung einzelner Reaktionen und Miniaturisierung der Reaktionsgefäße, die effiziente Aufarbeitung der Produkte sowie automatisierte Charakterisierungsmethoden. Ein typischer Arbeitsablauf eines Hochdurchsatzversuches ist in Abb. 3.1 schematisch dargestellt.

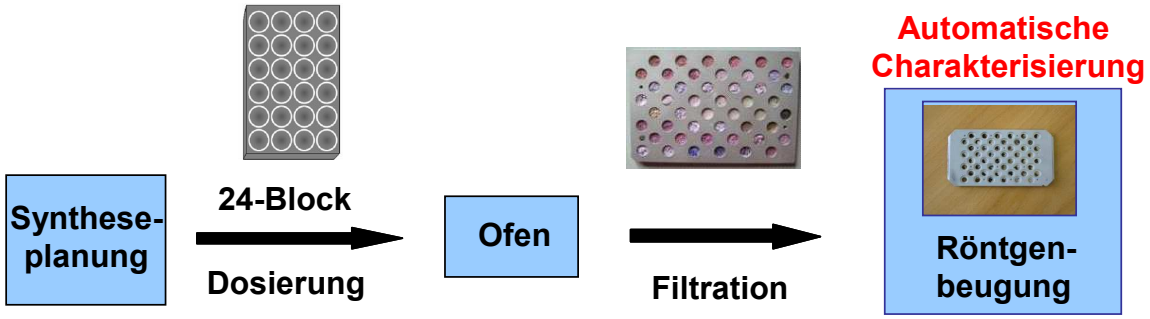

Abb. 3.1 Typischer Arbeitsablauf eines Hochdurchsatzversuches unter solvothermalen Bedingungen.

Die Hochdurchsatzsynthesen können in einem 24er- bzw. 48er-Reaktorsystem durchgeführt werden. Letzteres ermöglicht die gleichzeitige Umsetzung von 48 Reaktionen mit einem maximalen Reaktionsvolumen von 200 µl. Im 24er-Reaktorsystem können zeitgleich 24 Reaktionen mit einem maximalen Reaktionsvolumen von 2 ml untersucht werden. Ein 24er-Reaktorblock mit dazugehörigen Teflonreaktoren ist in Abb. 3.2 exemplarisch gezeigt. Die für den Hochdurchsatzsansatz berechneten Eduktmengen werden direkt in die

Teflonreaktoren eingewogen. Flüssige Edukte sowie Lösungsmittel werden mit einer Mikropipette dosiert. Nach dem Befüllen der Teflonreaktoren wird der Reaktorblock mit zwei Teflonfolien abgedeckt, durch einen Stahlautoklaven verschlossen und in den Ofen überführt.

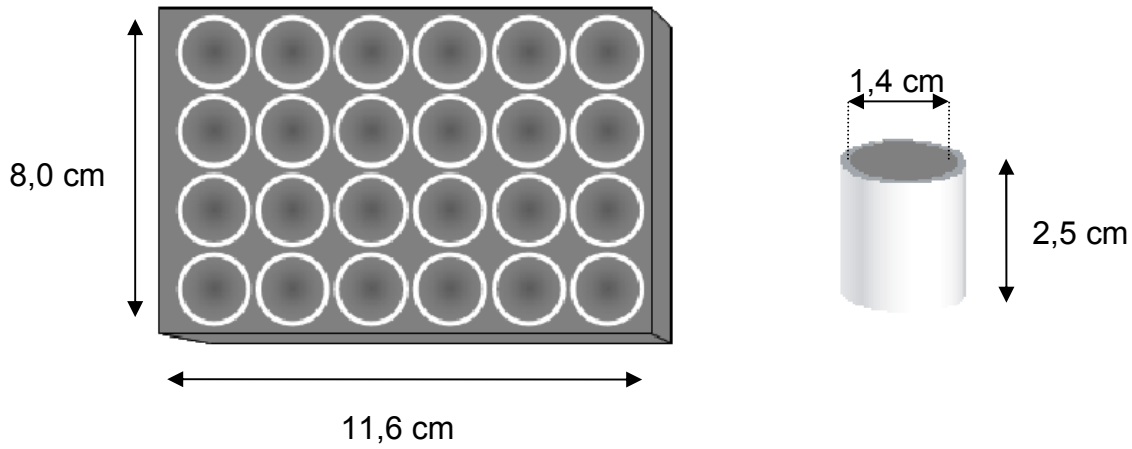

Abb. 3.2 Schematische Darstellung des Reaktorblocks und eines Teflonreaktors.

Die bei der Synthese ausgefallenen Produkte werden nebeneinander mit einer HD-Filtrationsapparatur abfiltriert und gewaschen. Nach dem Transfer der Produkte auf einen Hochdurchsatzprobenträger können diese in einem automatisierten Prozess mittels Röntgenpulverbeugung charakterisiert werden. Die Messzeit beträgt 3 min pro Probe. Die Filterstation sowie das Setup des Röntgendiffraktometers basieren auf dem 96-well-plate-Format, was das Überführen und Archivieren der Proben in handelsübliche Mikrotiterplatten erleichtert. Weitere Details zur verwendeten Hochdurchsatz-Methodik sind in den Referenzen [14], [15] sowie in den Dissertationen von S. Bauer[16] und A. Sonnauer[17] zu finden.

3.3 Mikrowellensynthese

Mitte der achtziger Jahre hat die MW-unterstützte Synthese vermehrt den Einzug in den modernen Laboralltag gefunden.[18] Die stetig weiterentwickelte MW-Technik ermöglicht heutzutage die Herstellung kommerziell erhältlicher Geräte.
Zur Durchführung der MW-unterstützten Synthesen wurde in dieser Arbeit der MW-Reaktor „Initiator“ der Firma Biotage benutzt. Die MW-Strahlung wird über ein

Magnetron bei einer Leistung von bis zu 400 Watt mit einer Frequenz von 2.45 GHz erzeugt. Die Reaktionsgefäße sind aus Quarzglas hergestellt und besitzen maximale Füllvolumina von 0.2-20 mL. Während der Synthese sorgt ein Magnetrührer (300-900 U/min) für eine ausreichende Durchmischung der Reaktionslösung. Die Synthesen können in einem Temperaturbereich von 40-250 °C und bei einem Druck bis zu 20 bar durchgeführt werden. Die Reaktionstemperatur wird über einen IR-Sensor reguliert, der an das Magnetron gekoppelt ist. Der sich bei der Reaktion einstellende Druck wird in situ über einen Drucksensor aufgezeichnet. Abb. 3.3 zeigt exemplarisch die Daten einer MOF-Synthese in dem Lösemittel Methanol. Zum Erhitzen der Reaktionsmischung wird zunächst mit hoher MW-Leistung eingestrahlt, die nach dem Erreichen der Reaktionstemperatur rasch abgesenkt wird. Bis zum Ende der Reaktion kann so die Reaktionstemperatur nahezu konstant gehalten werden. Danach kann die Reaktionsmischung mit Druckluft innerhalb weniger Minuten abgekühlt werden.

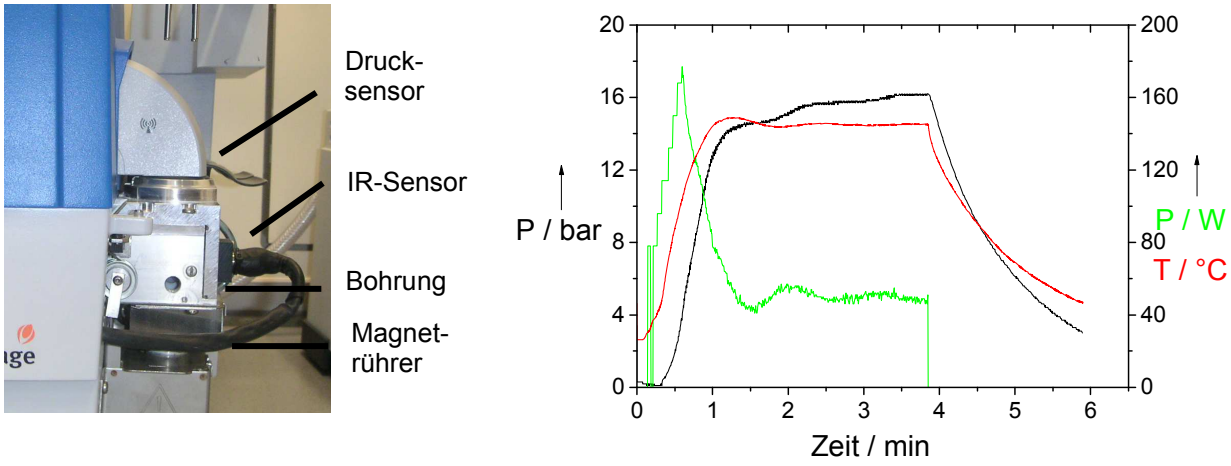

Abb. 3.3 Seitenansicht des Biotage MW-Reaktors (links) sowie das Druck- und Temperaturprofil einer typischen Synthese (rechts) (Reaktionstemperatur: 145 °C, Reactionszeit: 3 min).

Für die in situ-EDXRD-Untersuchungen am Hasylab in Hamburg, Messplatz F3, musste der MW-Reaktor modifiziert werden. Aufgrund der Stahlumkleidung der Reaktionszelle waren sehr hohe Intensitätsverluste zu erwarten. Für einen ungehinderten Strahlendurchgang wurden auf der Höhe des Strahls die Vorder- und Rückseite der Reaktionszelle durchbohrt. Die Implementierung des MW-Reaktors in den Strahlengang des Messplatzes F3 ist in Abb. 4 gezeigt. Über eine Kamera lassen sich während der Reaktion die eingestrahlte MW-Leistung, der Druck und die Reaktionstemperatur auf einem Monitor außerhalb der Messzelle verfolgen.

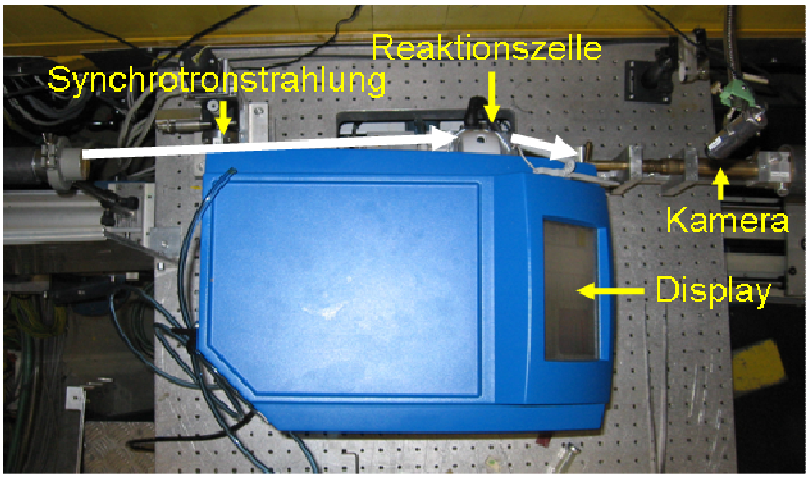

Abb. 3.4 Implementierung des MW-Reaktors in den Strahlengang des Messplatzes F3 am HASYLAB. Zur Verdeutlichung ist die Synchrotronstrahlung mit weißen Pfeilen in die Abbildung eingezeichnet.

Literatur

[1] G. Demazea, *J. Mater. Sci.* **2008**, *43*, 2104.

[2] A. Rabenau, *Angew. Chem. Int. Ed.* **1985**, *12*, 1026.

[3] W. S. Sheldrick, M. Wachhold, *Angew. Chem. Int. Ed.* **1997**, *36*, 450.

[4] L. Smart, E. Moore, *Einführung in die Festkörperchemie*, 1. Aufl., Springer, Berlin, **1997**.

[5] A. K. Cheetham, G. Ferey, T. Loiseau, *Angew. Chem. Int. Ed.* **1999**, *38*, 3268.

[6] R. K. Wahi, Y. Liu, J. C. Falkner, V. L. Colvin, *J. Coll. Inter. Sci.* **2006,** *302,* 530.

[7] S. H. Jhung, J.-H. Lee, J. W. Yoon, C. Serre, G. Férey, J.-S. Chang, *Adv. Mater.* **2007**, *19*, 121.

[8] Z. Ni, R. I. Masel, *J. Am. Chem. Soc.* **2006**, *128*, 12394.

[9] E. Haque, N. A. Khan, J. H. Park, S. H. Jhung, *Chem. Eur. J.* **2010**, *16*, 1046.

[10] X. Xu, W. Yang, J. Liu, L. Lin, *Adv. Mater.* **2000**, *12*, 195.

[11] S. H. Jhung, J. H. Lee and J.-S. Chang, *Microporous Mesoporous Mater.* **2008**, *112*, 178.

[12] S. H. Jhung, J.-S. Chang, J.-S. Hwang, S.-E. Park, *Microporous Mesoporous Mater.* **2003**, *64*, 33.

[13] S. H. Jhung, T. Jin, Y. K. Hwang, J.-S. Chang, *Chem. Eur. J.* **2007**, *13*, 4410.

[14] N. Stock, T. Bein, *Angew. Chem. Int. Ed.* **2004**, *43*, 749.

[15] S. Bauer, T. Bein, N. Stock, *Inorg. Chem.* **2005**, *44*, 5882.

[16] S. Bauer, *Dissertation*, Universität Kiel, **2007**.

[17] A. Sonnauer, *Dissertation*, Universität Kiel, **2009**.

[18] C . Kappe, *Angew*. *Chem*. *Int. Ed*. **2004**, *43*, 6250.

4 Kumulativer Teil

Ein Großteil der in dieser Dissertation enthaltenen Artikel wurde in Kooperation mit anderen Arbeitsgruppen angefertigt. Die folgende Tabelle gibt einen Überblick über den in dieser Arbeit geleisteten Eigenanteil an diesen Artikeln.

Tab. 1 Auflistung des Eigenanteils der im Rahmen dieser Dissertation publizierten Artikel und Manuskripte.

Kap.	Publikation	Seite	Eigenanteil
4.1.1	Synthesis and Modification of a Functionalized 3D Open-Framework Structure with MIL-53 Topology	35	Gesamter Artikel-exklusive Messung der NMR-Spektren, sowie Diskussion des MQMAS-NMR-Sektrums
4.1.2	New Functionalized Flexible Al-MIL-53-X (X = -Cl, -Br, -Me, -NO_2, -$(OH)_2$) Solids: Syntheses, Characterization, Sorption and Breathing Behavior	45	Darstellung aller Verbindungen; Optimierung und Charakterisierung von Al-MIL-53-$(OH)_2$ und Al-MIL-53–NO_2, Durchführung der „Breathing-Experimente“
4.1.3	Structural Phase Transitions and Thermal Hysteresis in the Metal-Organic Framework Compound MIL-53 as Studied by Electron Spin Resonance	56	Darstellung und Röntgenbeugungsexperimente an $[Al_{1-y}/Cr_y(OH)(BDC)]\cdot xH_2BDC$
4.2.1	$[Al_4(OH)_2(OCH_3)_4(H_2N\text{-}BDC)_3]\cdot xH_2O$: A 12-Connected Porous Metal–Organic Framework with an Unprecedented Aluminum-Containing Brick	66	Gesamter Artikel-exklusive der Strukturlösung und Verfeinerung
4.2.2	Oriented growth of the functionalized metal-organic framework CAU-1 on –OH- and –COOH-terminated self-assembled monolayers	72	Hilfestellung bei der Synthese
4.2.3	Controlled modification of the inorganic and organic brick in an Al-based MOF by direct and post-synthetic synthesis routes	79	Gesamtes Manuskript-exklusive der Durchführung der MAS-NMR-Spektren
4.2.4	A new family of porous MOFs with a new Al-based brick: $[Al_2(OCH_3)_4(O_2C\text{-}X\text{-}CO_2)]$ (X=aryl)	92	Auffinden der Synthesebedingungen von CAU-3, Synthese und Charakterisierung von CAU-3-NDC-exklusive Rietveld-Verfeinerung bzw. dessen Diskussion
4.3.1	High-throughput and time-resolved EDXRD Study of the Formation of CAU-1-$(OH)_2$ – Microwave and Conventional	102	Gesamter Artikel-exklusive der Durchführung der Hochdruck-Sorptionsmessungen
4.3.2	Synthesis of isoreticular CAU-1 compounds: Effects of linker and heating methods on the kinetics of the synthesis	112	Gesamter Artikel
4.4.4	3-D coordination polymers based on the TetraThiaFulvaleneTetraCarboxylate (TTF-TC) derivative: synthesis, characterization and oxidation issues	121	Hilfestellung bei der Synthese

4.1 Darstellung, Modifizierung und Charakterisierung aluminiumhaltiger MIL-53-Verbindungen auf der Basis von Terephthalsäurederivaten

Auf der Suche nach neuen Metall-organischen Gerüstverbindungen wurden unter Verwendung aromatischer Dicarboxylate und Tricarboxylate eine Vielzahl von Verbindungen hergestellt. Viele dieser Verbindungen besitzen ein dreidimensionales Netzwerk, dessen Poren und Kanäle für Gastmoleküle und Gase zugänglich sind. Ein häufig verwendeter organischer Linker ist die Terephthalsäure, durch deren Einsatz u. a. die Verbindung MIL-53 dargestellt werden konnte. Die Verbindung MIL-53 besitzt ein flexibles Gerüst mit eindimensionalen Kanälen und weist interessante Sorptionseigenschaften auf. Das modulare Bauprinzip der MOFs sollte es ermöglichen, die Wirt-Gast-Wechselwirkungen durch Verwendung funktionalisierter Terephthalsäurederivate zu modifizieren. Um dies zu untersuchen, sollten isoretikuläre Verbindungen von MIL-53 unter Verwendung von H_2BDC-X (mit X= $-NH_2$, $-NO_2$, $-(OH)_2$) dargestellt und charakterisiert werden.

4.1.1 Synthesis and Modification of a Functionalized 3D Open-Framework Structure with MIL-53 Topology

Der folgende Artikel wurde 2009 im Journal „Inorganic Chemistry“ veröffentlicht und beschreibt die Synthese und Charakterisierung der Verbindung MIL-53-NH_2 unter Verwendung von 2-Aminoterephthalsäure (H_2BDC-NH_2), sowie deren postsynthetische Modifizierung. Zusätzliche Informationen zu dieser Publikation befinden sich im Anhang 1 auf Seite 148.

Durch Einsatz der Hochdurchsatzmethode erfolgte die Entdeckung und die Syntheseoptimierung der Verbindung Al-MIL-53-NH_2 ([Al(OH)(BDC-NH_2)]·0.9H_2O). Als Ausgangsparameter wurden die Synthesebedingungen der aus der Literatur bekannten Verbindung Al-MIL-53 verwendet. Die optimierte Synthese von Al-MIL-53-NH_2 konnte im Vergleich zu Al-MIL-53 bei niedrigeren Temperaturen und kürzeren Reaktionszeiten durchgeführt werden. Im Rohprodukt von Al-MIL-53-NH_2 waren die Kanäle durch nicht umgesetzte Aminoterephthalsäuremoleküle blockiert. Aufgrund

der geringeren thermischen Stabilität von Al-MIL-53-NH_2 konnten die Linkermoleküle, anders als bei Al-MIL-53, nicht durch Kalzinierung aus den Kanälen entfernt werden. In einem Zwischenschritt wurden die in den Kanälen eingeschlossenen Aminoterephthalsäuremoleküle bei 150 °C gegen DMF-Moleküle ausgetauscht. Die DMF-Moleküle konnten im Anschluss bei relativ milden Temperaturen vollständig und unter Erhalt der Struktur entfernt werden. Nach der Aktivierung waren die Kanäle von Al-MIL-53-NH_2 für eine Vielzahl von Gastmolekülen zugänglich, so dass sogar eine chemische Modifizierung der Aminogruppen im Gerüst erfolgen konnte. Durch Umsetzung von Ameisensäure mit Al-MIL-53-NH_2 wurde ein Großteil der Aminogruppen in Formamidgruppen umgewandelt. Alle Zwischenprodukte sowie das durch die chemische Modifizierung erhaltende Al-MIL-53-NHCHO [Al(OH)(BDC-NHCOH)]·H_2O) wurden mittels IR-Spektroskopie, Thermogravimetrie und Elementaranalyse untersucht. Al-MIL-53-NH_2 konnte phasenrein und im Gramm-Maßstab hergestellt werden. Besonders hervorzuheben ist die Charakterisierung der Zwischenstufen bzw. der Endprodukte mittels Festkörper-NMR-Spektroskopie, mit der die eingelagerten Gastmoleküle sowie die abschließende chemische Modifizierung von Al-MIL-53-NH_2 zweifelsfrei nachgewiesen wurden.

Inorg. Chem. **2009**, *48*, 3057−3064

Synthesis and Modification of a Functionalized 3D Open-Framework Structure with MIL-53 Topology

Tim Ahnfeldt,[†] Daniel Gunzelmann,[‡] Thierry Loiseau,[§] Dunja Hirsemann,[‡] Jürgen Senker,[‡] Gerard Férey,[§] and Norbert Stock*[,†]

Institute of Inorganic Chemistry, Christian-Albrechts-Universität, Otto-Hahn-Platz 6/7, 24118 Kiel, Germany, Institute of Inorganic Chemistry, University of Bayreuth, Universitätsstrasse 30, 95447 Bayreuth, Germany, and Institut Lavoisier, UMR CNRS 8180, Université de Versailles St-Quentin en Yvelines, 45 Avenue des Etats-Unis, 78035 Versailles, France

Received December 4, 2008

Aluminum aminoterephthalate Al(OH)[H_2N−BDC]·0.3(H_2N−H_2BDC (denoted MIL-53−NH_2(as)) was synthesized under hydrothermal conditions. The activation of the compound can be achieved in two steps. The treatment with DMF at 150 °C leads to Al(OH)[H_2N−BDC]·0.95DMF (MIL-53−NH_2(DMF)). In the second step, DMF is thermally removed at 130 °C. Upon cooling in air, the hydrated form Al(OH)[H_2N−BDC]·0.9H_2O (MIL-53−NH_2(lt)) is obtained. The dehydration leads to a porous compound that exhibits hysteresis behavior in the N_2 sorption experiments. The MIL-53−NH_2(lt) can be modified by postsynthetic functionalization using formic acid, and the corresponding amide Al(OH)[HC(O)N(H)−BDC]·H_2O (MIL-53−NHCHO) is formed. All four phases were thoroughly characterized by X-ray powder diffraction, solid-state NMR and IR spectroscopy, and sorption measurements, as well as thermogravimetric and elemental analysis. Based on the refined lattice parameter similar breathing behavior of the framework as found in the unfunctionalized MIL-53 can be deduced. Solid-state NMR spectra unequivocally demonstrate the presence of the guest species, as well as the successful postsynthetic functionalization.

Introduction

Inorganic−organic hybrids have developed into an important class in the family of porous materials.[1−3] This is due to their interesting magnetic[4,5] or optical properties,[6,7] their potential application in the fields of gas and liquid separation[8,9] and storage,[10,11] their catalysis,[12,13] as well as their drug delivery.[14] The success of hybrid frameworks is based on the diversity of metal oxide clusters that can be connected with innumerous functionalized organic linkers. In the field of metal carboxylates, the use of linear organic linkers, especially terephthalic acid (BDC), is very popular since it gives rise to the formation of many open-framework structures with interesting features.[15] The combination of trivalent metal cations, such as Al^{3+}, V^{3+}, Cr^{3+}, Fe^{3+}, Ga^{3+}, and In^{3+}, and terephthalic acid under solvothermal synthetic conditions results in the formation of at least five crystalline

* To whom correspondence should be addressed. E-mail: stock@ac.uni-kiel.de.
[†] Christian-Albrechts-Universität.
[‡] University of Bayreuth.
[§] Université de Versailles St-Quentin en Yvelines.

(1) Kitagawa, S.; Uemara, K. *Chem. Soc. Rev.* **2005**, *34*, 109.
(2) Rowsell, J. L. C.; Yaghi, O. M. *Microporous Mesoporous Mater.* **2004**, *73*, 15.
(3) Cheetham, A. K.; Rao, C. N. R.; Feller, R. K. *Chem. Commun.* **2006**, 4780.
(4) Maspoch, D.; Ruiz-Molina, D.; Wurst, K.; Domingo, N.; Cavallini, M.; Biscarini, F.; Tejada, J.; Rovira, C.; Veciana, J. *Nat. Mater.* **2003**, *2*, 190.
(5) Halder, G. J.; Kepert, C. J.; Moubaraki, B.; Murray, K. S.; Cashion, J. D. *Science* **2002**, *298*, 1762.
(6) Holman, K. T.; Pivovar, A. M.; Swift, J. A.; Ward, M. D. *Acc. Chem. Res.* **2001**, *34*, 107.
(7) Evans, O. R.; Lin, W. B. *Acc. Chem. Res.* **2002**, *35*, 511.
(8) Alaerts, L.; Maes, M.; Giebeler, L.; Jacobs, P. A.; Martens, J. A.; Denayer, J. F. M.; Kirschhock, C. E. A.; De Vos, D. E. *J. Am. Chem. Soc.* **2008**, *130*, 14170.
(9) Chen, B.; Liang, C.; Yang, J.; Contreras, D. S.; Clancy, Y. L.; Lobkovsky, E. B.; Yaghi, O. M.; Dai, S. *Angew. Chem., Int. Ed.* **2006**, *45*, 1390.
(10) Férey, G.; Latroche, M.; Serre, C.; Millange, F.; Loiseau, T.; Percheron-Guégan, A. *Chem. Commun.* **2003**, 2976.
(11) Rowsell, J. L. C.; Millward, A. R.; Park, K. S.; Yaghi, O. M. *J. Am. Chem. Soc.* **2004**, *126*, 5666.
(12) Fujita, M.; Kwon, Y. J.; Washizu, S.; Ogura, K. *J. Am. Chem. Soc.* **1994**, *116*, 1151.
(13) Evans, O. R.; Ngo, H. L.; Lin, W. *J. Am. Chem. Soc.* **2001**, *123*, 10395.
(14) Horcajada, P.; Serre, C.; Vallet-Regí, M.; Sebban, M.; Taulelle, F.; Férey, G. *Angew. Chem., Int. Ed.* **2006**, *45*, 5974.
(15) Férey, G. *Chem. Soc. Rev.* **2008**, *37*, 191.

10.1021/ic8023265 CCC: $40.75
Published on Web 02/26/2009

phases MIL-53 (M(OH)BDC·guest),[16−18] MIL-68 (M(OH)BDC·guest),[19,20] MIL-71 ($M_2(OH)_2F_2BDC$·guest),[21,22] MIL-88 (M_3OBDC_3·X·guest),[23] and MIL-101 (M_3OBDC_3·X·guest).[24] Among these, MIL-53 and MIL-88 (MIL = Materials of Institute Lavoisier) exhibit exceptional framework flexibility, and MIL-101 shows an unusually large pore volume and surface area. Due to its stability, the Al- and Fe-containing MIL-53 have been investigated intensively, for example in the fields of liquid−liquid separation,[8] gas sorption,[25,26] thin-film growth,[27] and drug delivery[28] and for Li-insertion reactions.[29] Recently, the amino-functionalized Fe form of MIL-53 ($Fe(OH)H_2N$−BDC·guest) has been described.[30]

In addition to the use of large linker molecules for the synthesis of isoreticular compounds containing larger pores, another main topic in MOF (metal−organic framework) chemistry is the functionalization of the pores. This is especially of interest for applications such as gas separation, gas storage, or host−guest chemistry, since it can lead to more selective materials or higher storage capacity. This can be achieved using reticular chemistry and employing functionalized organic molecules, such as derivatives of terephthalic acid.[31] For example, NH_2-, Br-, and CH_3-functionalized terephthalic acid has been employed in these investigations. An even more important aspect is the possibility to use these functional groups for postsynthetic modification reactions.[32] This has recently been demonstrated for the amino-functionalized MOFs, IRMOF-3[33−35] and IRMOF-16,[36] and a Gd-based framework[37] by acylation reaction with isonitriles, in some cases followed by metal complexation or bromination. ZIF-90 containing a carboxyaldehyde group has been modified by reduction with $NaBH_4$ and reaction with ethanolamine to yield an alcohol derivative and an imine functionality, respectively.[38] This synthetic strategy is expected to facilitate the generation of functional properties not directly accessible through conventional MOF synthesis. We have focused our research on the investigation of hybrid materials belonging to the MIL family, since these are thermally and chemically very stable compared to most other MOFs.

Table 1. Comparison of the Lattice Parameters of MIL-53,[16] and Fe−MIL-53−NH_2(as)[30] with the Results Obtained in This Work

sample	*a*/Å	*b*/Å	*c*/Å	*β*/°	*V*/Å^3
MIL-53(as)[16]	17.129(2)	6.628(1)	12.182(1)		1383.0(2)
MIL-53(lt)[16]	19.513(2)	7.612(1)	6.576(1)	104.24(1)	946.5(2)
MIL-53−NH_2(as)	16.898(20)	12.539(18)	6.647(8)	−	1408.4(4)
MIL-53−NH_2(DMF)	17.578(17)	11.483(9)	6.630(6)	−	1338.9(25)
MIL-53−NH_2(lt)	19.722(7)	7.692(3)	6.578(4)	105.1(3)	961.5(10)
MIL-53−NHCHO	17.156(5)	12.246(5)	6.604(13)		1387.4(8)
Fe−MIL-53−NH_2(as)[30]	17.668(3)	12.120(3)	6.9177(14)		1481.3(6)

Here, we report the synthesis of amino-functionalized, Al-containing MIL-53 and the activation by solvothermal and thermal treatment, as well as the postsynthetic modification using formic acid. For the detailed characterization of all the compounds powder XRD, IR, TG, and solid-state NMR measurements, as well as elemental analyses, were performed. In addition, results on N_2 sorption measurements are presented.

Experimental Section

Chemicals. $AlCl_3$·$6H_2O$ (Riedel−de Haen, ≥99%), NH_2−H_2BDC (Fluka, ≥98%), formic acid (Merck), and *N,N*-dimethylformamide (BASF, tech.) were used as obtained.

Methods. X-ray powder diffraction patterns were recorded with a STOE STADI P diffractometer equipped with a linear position-sensitive detector using monochromated Cu $K\alpha_1$ radiation. Lattice constants were determined using the DICVOL program[39] and refined using the STOE software package. Temperature-dependent X-ray diffraction experiments were performed in the Θ−Θ mode in air with the sample in the furnace (Anton Paar HTK 16 high-temperature chamber) of a Siemens D5000 diffractometer (Co radiation). Each powder pattern was recorded in the 8−25° range (2θ) at intervals of 10 °C up to 400 °C and 25 °C up to 500 °C with a 2 s/step scan, corresponding to an approximate duration of 1 h. The temperature ramp between two patterns was 10 °C min^{-1}. Thermogravimetric (TG) analyses were carried out in air or nitrogen (75 mL/min, 25−900 °C, 4 °C/min) on a Netzsch STA-409CD. Carbon, hydrogen, and nitrogen contents were determined by

(16) Loiseau, T.; Serre, C.; Huguenard, C.; Fink, G.; Taulelle, F.; Henry, M.; Bataille, T.; Férey, G. *Chem. Eur. J.* **2004**, *10*, 1373.
(17) Serre, C.; Millange, F.; Thouvenot, C.; Nogúes, M.; Marsolier, G.; Louër, D.; Férey, G. *J. Am. Chem. Soc.* **2002**, *124*, 13519.
(18) Millange, F.; Guillou, N.; Walton, R. I.; Grenèche, J.-M.; Margiolaki, I.; Férey, G. *Chem. Commun.* **2008**, 4732.
(19) Barthelet, K.; Marrot, J.; Ferey, G.; Riou, D. *Chem. Commun.* **2004**, 520.
(20) Volkringer, C.; Meddouri, M.; Loiseau, T.; Guillou, N.; Marrot, J.; Férey, G.; Haouas, M.; Taulelle, F.; Audebrand, N.; Latroche, M. *Inorg. Chem.* **2009**, in press.
(21) Barthelet, K.; Adil, K.; Millange, F.; Serre, C.; Riou, D.; Ferey, G. *J. Mater. Chem.* **2003**, *13*, 2208.
(22) Vougo-Zanda, M.; Anokhina, E. V.; Duhovic, S.; Liu, L.; Wang, X.; Oloba, O. A.; Albright, T.; Jacobson, A. J. *Inorg. Chem.* **2008**, *47*, 4746.
(23) Mellot-Draznieks, C.; Serre, C.; Surblé, S.; Audebrand, N.; Férey, G. *J. Am. Chem. Soc.* **2005**, *127*, 16273.
(24) Férey, G.; Mellot-Draznieks, C.; Serre, C.; Millange, F.; Dutour, J.; Surblé, S.; Margiolaki, I. *Science* **2005**, *309*, 2040.
(25) Bourrelly, S.; Llewellyn, P. L.; Serre, C.; Millange, F.; Loiseau, T.; Férey, G. *J. Am. Chem. Soc.* **2005**, *127*, 13519.
(26) Llewellyn, P. L.; Bourrelly, S.; Serre, C.; Filinchuk, Y.; Férey, G. *Angew. Chem.* **2006**, *118*, 7915.
(27) Scherb, C.; Schödel, A.; Bein, T. *Angew. Chem., Int. Ed.* **2008**, *120*, 5861.
(28) Horcajada, P.; Serre, C.; Guillaume, M.; Ramsahye, N. A.; Balas, F.; Vallet-Regí, M.; Sebban, M.; Taulelle, F.; Férey, G. *J. Am. Chem. Soc.* **2008**, *130*, 6774.
(29) Férey, G.; Millange, F.; Morcrette, M.; Serre, C.; Doublet, M.-L.; Grenèche, J.-M.; Tarascon, J.-M. *Angew. Chem., Int. Ed.* **2007**, *46*, 3259.
(30) Bauer, S.; Serre, C.; Devic, T.; Horcajada, P.; Marrot, J.; Férey, G.; Stock, N. *Inorg. Chem.* **2008**, *47*, 7568.
(31) Yaghi, O. M.; O'Keefe, M.; Ockwig, N. W.; Chae, H. K.; Eddaoudi, M.; Kim, J. *Nature* **2003**, *423*, 705.
(32) Wang, Z.; Cohen, S. M. *J. Am. Chem. Soc.* **2007**, *129*, 12368.
(33) Dugan, E.; Wang, Z.; Okamura, M.; Medina, A.; Cohen, S. M. *Chem. Commun.* **2008**, *29*, 3366.
(34) Wang, Z.; Cohen, S. M. *Angew. Chem., Int. Ed.* **2008**, *120*, 4777.
(35) Ingleson, M. J.; Barrio, J. P.; Guilbaud, J.-B.; Yaroslav, Z.; Khimyak, Y. Z.; Rosseinsky, M. J. *Chem. Commun.* **2008**, *23*, 2680.
(36) Goto, Y.; Sato, H.; Shinkai, S.; Sada, K. *J. Am. Chem. Soc.* **2008**, *130*, 14354.
(37) Costa, J. S.; Gamez, P.; Black, C.; Roubeau, O.; Teat, S. J.; Reedijk, J. *Eur. J. Inorg. Chem.* **2008**, 1551.
(38) Morris, W.; Doonan, C. J.; Furukawa, J. H.; Banerjee, R.; Yaghi, O. M. *J. Am. Chem. Soc.* **2008**, *130*, 12626.
(39) Boultif, A.; Louer, D. *J. Appl. Crystallogr.* **1991**, *24*, 987.

elemental chemical analysis on an Eurovektor EuroEA Elemental Analyzer. IR spectra were recorded on an ATI Matheson Genesis in the spectral range 4000−400 cm^{-1} using the KBr disk method. EDX analysis was performed on a Philips ESEM XL 30. ^{15}N, ^{13}C, ^{27}Al and ^{1}H solid-state NMR studies were performed on a commercial BRUKER Avance II 300 spectrometer operating at 7.05 T with resonance frequencies of 30.4, 75.5, 78.2 and 300.1 MHz, respectively. ^{1}H and ^{13}C shifts were referenced relative to TMS, ^{15}N shifts with respect to nitromethane, and ^{27}Al shifts relative to $AlCl_3$ in an acidic aqueous solution. Samples for ^{13}C and ^{15}N measurements were filled in standard 4 mm ZrO_2 rotors and mounted in a triple-resonance probe (Bruker). For all ^{13}C and ^{15}N experiments, spinning frequencies between 4.5 and 12 kHz were set. ^{1}H and ^{27}Al spectra were recorded with a triple resonance 2.5 mm MAS probehead and spinning frequencies of 25 kHz and 30 kHz, respectively. A ramped cross-polarization sequence with contact times between 3 and 5 ms was employed to excite ^{13}C and ^{15}N nuclei via the proton bath, where the power of the ^{1}H radiation was linearly varied from 100 to 50%. For the acquisition of the ^{1}H spectra, three back-to-back 90° pulses were used in order to eliminate unwanted contributions from the probe.[30] The 90° pulse length was adjusted to 3 μs, and the recycle delay varied between 2.5 and 10 s to guarantee total rebuild of magnetization due to spin−lattice relaxation. ^{27}Al spectra were recorded with a Hahn−Echo sequence with pulse lengths of 1.0 and 2.0 μs for the first and second impulses and a nutation frequency of 65 kHz. All 1D experiments were recorded using broadband proton decoupling via the SPINAL64 sequence.[29] The ^{27}Al MQ-MAS spectra were measured in standard 4 mm ZrO_2 rotors with a rotation frequency of 12.5 kHz, using a three-pulse sequence[40] with nutation frequencies of 100 and 13 kHz for the excitation, conversion, and selective 90° pulses, respectively. The coherence pathway 0 ± 30−1 was selected via a cog-wheel phase cycle[41] COG60{11,1,0;30}, and the repetition delay was set to 0.5 s.

The sorption behavior of the dehydrated MIL-53−NH_2(lt) (lt = activated, low temperature phase)[16,30] and MIL-53−NHCHO was determined measuring the N_2 sorption isotherms at 77 K using a Bellsorp Max apparatus. Based on the TG data, activation at 130 °C under vacuum for 3 h was used. Due to the presence of a strong hysteresis in the initial sorption measurements, the same sample was measured four times with a repeated activation at 130 °C for 3 h in between the measurements.

Synthesis. Al−MIL-53−NH_2(as), Al(OH)[H_2N−BDC]·0.3-(H_2N−H_2BDC). The discovery, as well as the optimization under solvothermal conditions, was done using our high-throughput methodology.[42−44] Thus, syntheses were performed in the range of 110−180 °C. The following aluminum salts were employed in the investigation: $Al(NO_3)_3 \cdot 9H_2O$, $Al(ClO_4)_3 \cdot 9H_2O$, and $AlCl_3 \cdot 6H_2O$. Different protic as well as aprotic solvents (acetonitrile, DMF, methanol, and water) were used. From more than 350 experiments, the following optimal reaction conditions were extracted: (1) H_2O is the best solvent; (2) the molar ratio Al^{3+}:H_2N−H_2BDC of 1:1 is the best; (3) the temperature should be around 150 °C since lower temperatures lead to less crystalline products, while at higher temperatures the decomposition of H_2N−H_2BDC is observed. The optimized synthesis parameters were employed for the scale-up reaction. This reaction was carried out in a 27 mL Teflon-lined steel bomb under autogenous pressure for 5 h at 150 °C. The molar ratio Al^{3+}:H_2N−H_2BDC:H_2O of 1:1:153 was used ($AlCl_3 \cdot 6H_2O$ (493.6 mg), H_2BDC−NH_2 (375.6 mg), and 5 mL H_2O). After filtering and washing with deionized water, the resulting yellow product (yield: 50% based on H_2BDC−NH_2) was first identified by X-ray powder diffraction analysis (Table 1). The amount of included H_2N−H_2BDF was determined by TG analysis.

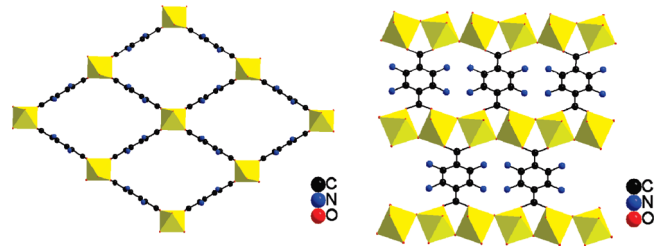

Figure 1. View along (left) and perpendicular to (right) the pore system in MIL-53−NH_2 (disordered H_2N−H_2BDC molecules in the pores have been omitted for clarity). The MO_6-octahedra are presented in yellow. N positions are only occupied by one-fourth.

Activation of MIL-53−NH_2(as), Al(OH)[H_2N−BDC]·0.3-(H_2N−H_2BDC). The as form contains free aminoterephthalic acid, which could not be removed by thermal activation. This could be due to stronger host−guest interactions owing to the NH_2 groups. A two-step procedure led to the activated form. In the first step, aminoterephthalic acid in pores was exchanged by DMF at 150 °C. Thus, MIL-53−NH_2(DMF), Al(OH)[H_2N−BDC]·0.95DMF, was formed (calcd C: 44.5, H: 4.4, N: 9.3; obsd C: 44.7, H: 4.4, N: 9.3). The DMF molecules were removed by thermal treatment in air at 130 °C in a muffle furnace. Upon cooling in air, MIL-53−NH_2(lt), Al(OH)[H_2N−DC]·0.9H_2O, was obtained (calcd C: 40.1, H: 3.3, N: 5.8; obsd: C: 40.1, H: 3.2, N: 5.7). For the postsynthetic modification, the lt-form was used.

Postsynthetic Modification of MIL-53−H_2(lt). To 200 mg of Al(OH)[H_2N−DC]·0.9H_2O (0.8 mmol), 200 μL of formic acid (5.3 mmol) was added in a glass flask. The reaction at 70 °C for 3 h, followed by washing with H_2O and heating in air (130 °C, 2 days), leads to the formation of formamide groups (Al−MIL-53−NHCHO, Al(OH)[OHCN−BDC]·H_2O) (elemental analysis, calcd: C: 40.2, H: 3.0, N: 5.2; obsd: C: 40.2, H: 3.2, N: 5.2).

Results and Discussion

The synthesis of amino-functionalized Al−MIL-53 was accomplished. The activation of the pores was carried out by solvent exchange and thermal treatment. The activation of the water-containing form at elevated temperatures leads to a porous compound, and the postsynthetic modification using formic acid as a reactant is possible (Scheme 1).

Structure Description. The framework topology of all title compounds is identical, and they correspond to the MIL-53 structure (Figure 1). This structure contains chains of μ-OH corner-sharing AlO_6-octahedra, which are interconnected by aminoterephthalic acid molecules to form one-dimensional pores. Based on results of the lattice constant determinations, the structures of the different forms of MIL-53−NH_2 were found to correspond to the ones observed in the nonfunctionalized system (Al−MIL-53) and the other known amino-functionalized compound, Fe−MIL-53−NH_2(as) (Table 1). Similar breathing behavior of the frameworks is observed, which is due to host−guest interactions.

(40) Amoureux, J. P.; Fernandez, C.; Steuernagel, S. *J. Magn. Reson. A* **1996**, *123*, 116.
(41) Jerschow, A.; Kumar, R. *J. Magn. Reson.* **2003**, *160*, 59.
(42) Bauer, S.; Stock, N. *Angew. Chem., Int. Ed.* **2007**, *46*, 6857.
(43) Bauer, S.; Bein, T.; Stock, N. *Inorg. Chem.* **2005**, *44*, 5882.
(44) Stock, N.; Bein, T. *Angew. Chem., Int. Ed.* **2004**, *43*, 749.

Scheme 1. Postsynthetic Modification of MIL-53−NH_2 by Reaction with Formic Acid

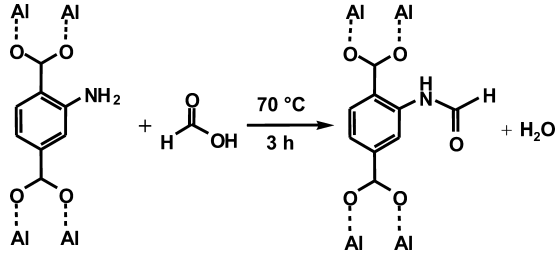

As observed for the Fe-containing compound, the as-synthesized MIL-53−NH_2(as), Al(OH)[H_2N−BDC]·0.3-(H_2N−H_2BDC), contains free aminoterephthalic acid molecules in the pores, and the NH_2 group is disordered over four crystallographically equivalent positions. The free aminoterephthalic acid molecules can be exchanged by treatment with DMF, and MIL-53−NH_2(DMF), Al(OH)-[H_2N−BDC]·0.95DMF, is formed. This guest exchange leads only to minor changes in the cell parameters. After thermal removal of the DMF molecules, followed by cooling to RT under ambient conditions, a drastic change in cell symmetry from orthorhombic to monoclinic and in cell parameters is observed. The same results are found for MIL-53, and the contraction of the rhombic channels is due to the formation of strong hydrogen bonds between the water molecules and the carboxylate groups of the framework. Thus, the presence of NH_2 seems to have only minor influence on the structure. Upon postsynthetic modification, the unit cell symmetry changes back from monoclinic to orthorhombic symmetry, and cell parameters are similar to the ones found for MIL-53−NH_2(as) and MIL-53−NH_2(DMF).

Thermal Behavior. The thermal behavior of the four compounds was studied by TG measurements (Figure 2). In addition, an X-ray thermodiffractogram of MIL-53−NH_2(as) in air (Figure 3) is presented. All TG curves show a two-step weight loss. The first step corresponds to the release of the guest molecules within the pores, and the second weight loss is due to the decomposition of the aminoterephthalic acid from the framework. The first steps in these diagrams, as well as the CNHS analyses, were used to calculate the amount of different guest molecules.

In contrast to MIL-53(as) and Cr−MIL-53(as), the free acid molecules depart at lower temperatures (220 vs 275 °C). The observed weight loss of 20% (0.30 mol of H_2BDC per formula unit) is smaller than the one observed in the pure terephthalic acid compounds, but it is in accordance with results from Fe−MIL53(as). The departure is accompanied by a structural change and followed by the decomposition of the structure. This is clearly observed in the X-ray thermodiffractogram (Figure 3), where two structural changes occur upon heating. Up to 250 °C, almost no changes of the reflex intensities and positions of MIL-53−NH_2(as) are detectable. This temperature is slightly higher than the one from the TG study. Around 250 °C, a drastic shift of the reflection positions is found, which is accompanied by peak broadening. Above 410 °C, no crystalline products are observed. MIL-53−NH_2(as) is transformed into an X-ray amorphous product.

The solvent-exchanged sample MIL-53−NH_2(DMF), Al(OH)[H_2N−BDC]·0.95DMF, releases the DMF molecules upon heating up to 320 °C (Figure 2 top right). The observed weight loss (23%) corresponds to 0.95 equiv of DMF molecules, which is also confirmed by elemental analysis. The solvent-free structure is stable up to approximately 400 °C, and it collapses at higher temperatures.

The water-containing samples, MIL-53−NH_2(lt), Al(OH)-[H_2N−BDC]·0.9H_2O, and MIL-53−NHCHO, Al(OH)-[HC(O)N(H)−BDC]·H_2O, show very similar TG curves. The dehydration of both compounds is observed up to 150 °C. The weight loss corresponds to 0.9 and 1 mol equivalent water molecules per formula unit for MIL-53−NH_2(lt) and MIL-53−NHCHO, respectively. The framework structures are stable up to 400 °C. Thus, the exceptional thermal stability of the nonfunctionalized MIL-53(lt), where a decomposition temperature of 500 °C is observed, is not found.

Sorption Experiments. MIL-53−NH_2(lt) was activated at 130 °C in vacuum for 3 h. In contrast to MIL-53, the sorption curves of MIL-53−NH_2 (Figure 4) show hysteresis behavior, which strongly depends on the number of sorption/desorption cycles and activation steps. While in the first two measurements sorption occurs at higher partial pressures, reproducible results are obtained starting with the third measurement. This could be due to the presence of guest molecules that are only removed after repeated measurements and activation.

Infrared Spectroscopy. The IR spectra of MIL-53−NH_2-(as), MIL-53−NH_2(DMF), and Al−MIL-53−NH_2(lt) are shown in Figure 5. The activation steps can clearly be followed. The spectrum of MIL-53−NH_2(as) exhibits the typical vibrational bands in the region of 1400−1700 cm^{-1} for the carboxylic acid function of the Al-coordinating and free aminoterephthalic acid.[16,30] The different O−H and N−H groups can be clearly seen. The bands at 3656 and 3497/3385 cm^{-1} and the broad signals between 3000 and 2500 cm^{-1} are due to the bridging OH and the NH_2 group, as well as the aminoterephthalic acid in the pores, respectively. The latter bands are absent in the spectrum of MIL-53−NH_2(DMF), and additional bands due to the presence of CH_3 groups are observed. The C═O band of the free acid (1687 cm^{-1}) in the pores is replaced by the C═O band of the DMF molecules (1670 cm^{-1}). These bands vanish upon thermal treatment under formation of Al−MIL-53NH_2(lt).

The postsynthetic modification under formation of the formamide functionality (Figure 6) is clearly demonstrated by the appearance of bands that are due to the formation of an amide.[45] The two sharp bands of the NH_2 group vanish and one broad band is observed. New signals at 1690, 1296 cm^{-1} are caused by the C═O and the C−N stretching vibration of the formamide. At the same time, the bands due to the C−N(NH_2) vibration at 1254 and 1334 cm^{-1} appear with much lower intensities. This indicates a partial functionalization of the NH_2 groups.

(45) Socrates, G. *Infrared and Raman Characteristic Group Frequencies: Tables and Charts*, 3rd ed.; Wiley & Sons: West Sussex, U.K., 2004.

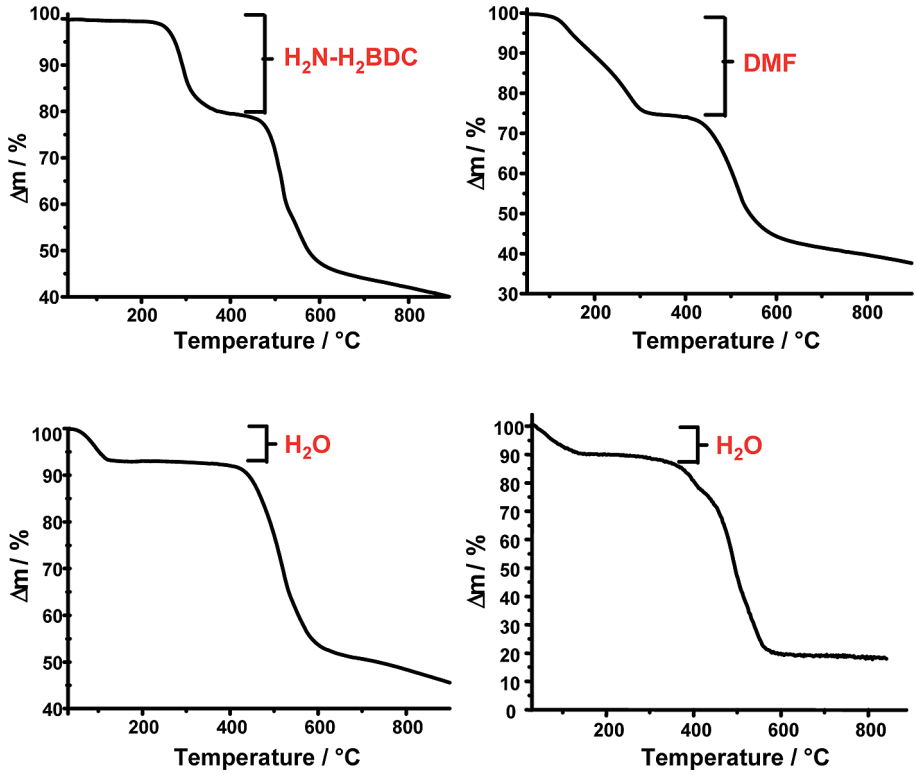

Figure 2. TG curves of MIL-53−NH_2(as), MIL-53−NH_2(DMF), MIL-53−NH_2(lt) under nitrogen, and TG curves of MIL-53-NHCHO under oxygen.

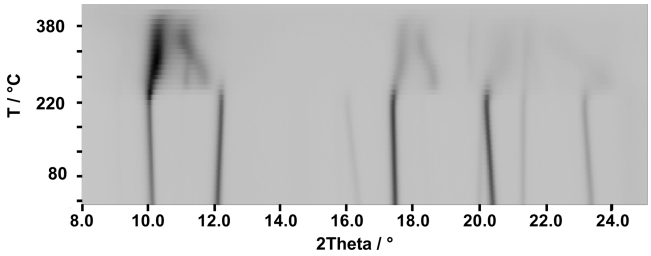

Figure 3. Results of the temperature-dependent X-ray powder XRD study of MIL-53−NH_2(as) in air (20−500 °C).

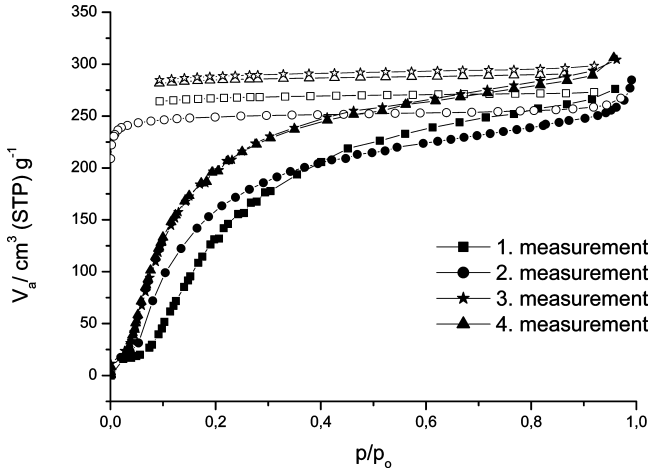

Figure 4. N_2 sorption isotherms of MIL-53−NH_2(lt) activated for 3 h at 130 °C before each measurement. The same sample was measured four times, applying the same activation procedure prior to the measurements. Black symbol denotes sorption and white symbol denotes desorption curves.

Solid-State NMR Studies. The ^{1}H, ^{13}C, ^{15}N, and ^{27}Al MAS NMR spectra of MIL-53−NH_2(as,DMF,lt) and MIL-53−NHCHO are displayed in Figures 7−10. The assignment of the bands is based on literature data.[16,46,47] The NMR spectra show signals due to the different guest species in the pores. Figure 7 displays the ^{1}H spectra of the four compounds. The as form exhibits three signals at $\delta = 2.3$, 6.4, and 12.2 ppm due to the μOH bridging hydroxide groups, the aromatic CH atoms, and the COOH groups, respectively. The ^{1}H spectrum of the DMF form shows peaks at $\delta = 1.5$, 2.3, and 7.3 ppm attributable to the CH_3 groups of the DMF, the μOH bridging hydroxide groups, and the aromatic CH atoms. No signals due to the free aminoterephthalic acid are observed. The spectrum of MIL-53−NH_2(lt) shows three signals at $\delta = 2.6$, 4.5, and 6.4 ppm that can be assigned to the μOH, H_2O, and aromatic CH atoms, respectively. In accordance with MIL-53(lt), the last two signals are poorly resolved and broad.[16] It should be noted that the ^{1}H resonances arising from the amino groups for MIL-53−NH_2(as,DMF,lt) are expected between 6 and 8 ppm and are, thus, obscured by the proton signals in the aromatic region. The ^{1}H spectrum of MIL-53−NHCHO exhibits one broad signal at 10.9 ppm that can be assigned to the formamide group. Its low-field shift may be caused by hydrogen bond interactions with two water molecules in the cages. In addition, the signals of the phenyl ring and the μOH bridging hydroxide groups at 7.4 and 2.7 ppm, respectively, are observed.

The ^{13}C and ^{15}N NMR spectra clearly demonstrate the postsynthetic modification under formation of the formamide group. The ^{13}C NMR spectrum of MIL-53−NH_2(as) (Figure 8a) exhibits five broad signals, four between $\delta = 149.6$ and

(46) Jürgens, B.; Irran, E.; Senker, J.; Kroll, P.; Müller, H.; Schnick, W. *J. Am. Chem. Soc.* **2003**, *125*, 10288.
(47) Smernik, R. J.; Baldock, J. A. *Plant Soil* **2005**, *275*, 271.

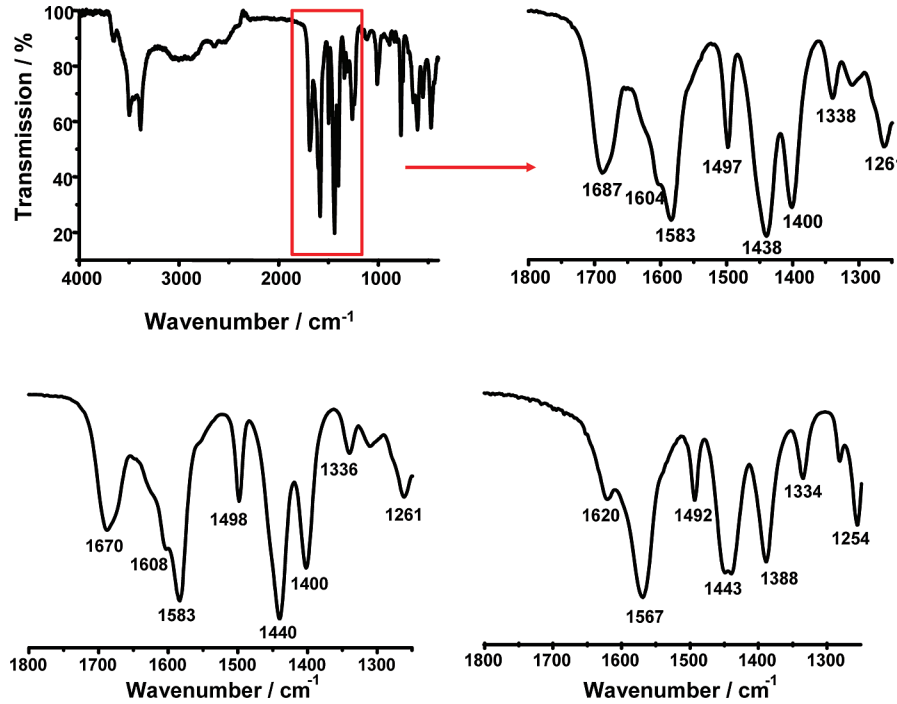

Figure 5. Top: IR spectrum of MIL-53−NH_2(as). Bottom: MIL-53−NH_2(DMF) (left) and MIL-53−NH_2(lt) (right).

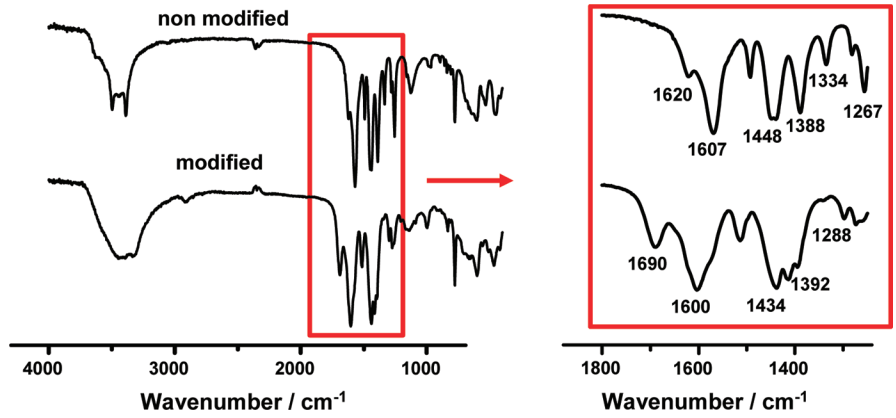

Figure 6. IR spectra of MIL-53−NH_2(lt) (top) and modified MIL-53−NHCHO (bottom).

117 ppm, due to the C atoms of the phenyl ring and one signal at $\delta = 172$ ppm, which is caused by the carboxylic groups. The ^{13}C spectrum of the DMF form shows three additional signals at $\delta = 29.1$, 35.2, and 163.4 ppm attributable to the DMF molecules. In the ^{13}C spectrum of the lt form, these signals are not present. The peak of the carboxylate group is shifted in the lt form from $\delta = 172.4$ to 176.7 ppm due to the presence of water molecules and the change in the crystallographic symmetry.[16] The signals of the phenyl rings are much better resolved. Upon postsynthetic modification, a new signal at 160.8 ppm is observed, which is caused by the presence of the formamide functionality. The other signals show only minor changes.

The ^{15}N NMR spectra of the as, DMF and lt form exhibit a signal in the region from $\delta = -312$ to -315 ppm, which can be unequivocally assigned to the NH_2 group. An additional sharp intensive signal in the spectrum of the DMF form is observed at $\delta = -274.2$ ppm and is attributed to the DMF molecules in the pores. The ^{15}N MAS NMR spectrum of MIL-53−NHCHO exhibits two signals at -315.2 and -248.8 ppm. The former is due to the presence of unreacted NH_2 groups, while the latter gives evidence to the successful postsynthetic modification under formation of the formamide.[46] Considering the cross-polarization time of 3 ms, which overemphasizes the NH_2 group, the functionalization can be regarded as almost complete.

The 1D ^{27}Al NMR spectra are shown in Figure 10. All spectra can be interpreted in accordance with a single resonance with an isotropic shift around 0 ppm, and a shape which is dominated by a second order quadrupole interaction. As for MIL-53, this is consistent with only one type of AlO_6 octahedra present in the crystal structure for all compounds.[16] Due to the local disorder caused by the functionalization of the terephthalic acid molecules, the ^{27}Al MAS spectra acquired for MIL-53−NH_2(as,DMF,lt) and MIL53−NHCHO are much more featureless than for the pure MIL-53.[16] The distribution of chemical shift values and quadrupolar coupling constants is also reflected in the TQ dimension of MQMAS spectra (shown only for MIL-53−NHCHO in Figure 11). The lack of other aluminum species especially

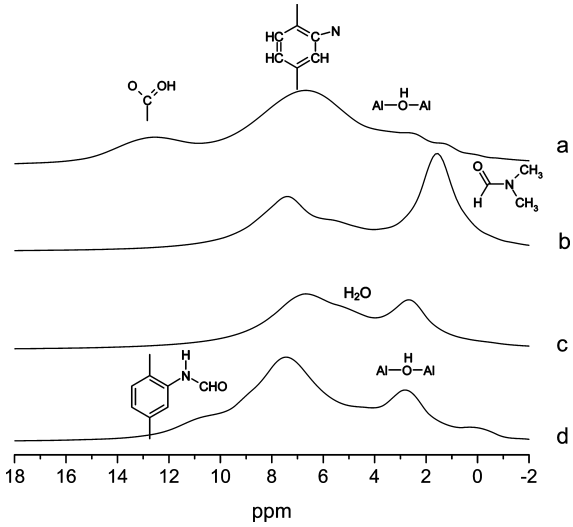

Figure 7. ^{1}H MAS NMR spectra of (a) MIL-53−NH_2(as), (b) MIL-53−NH_2(DMF), (c) MIL-53−NH_2(lt) and (d) MIL-53−NHCHO.

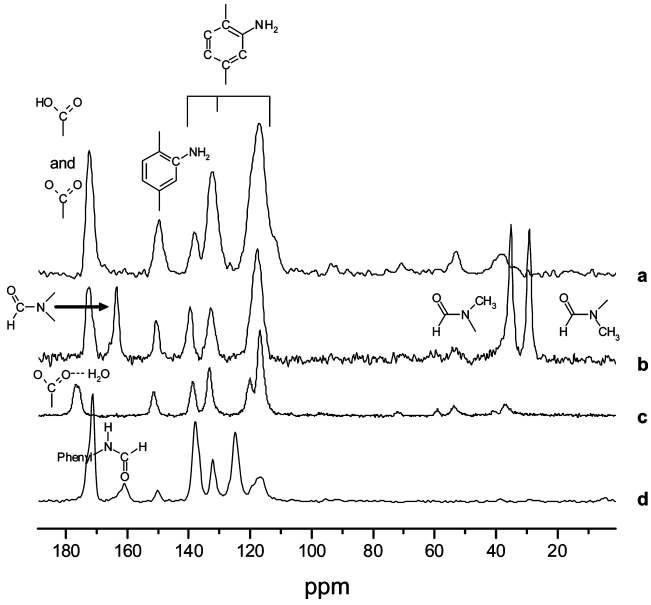

Figure 8. ^{13}C MAS NMR spectra of (a) MIL-53−NH_2(as), (b) MIL-53−NH_2(DMF), (c) MIL-53−NH_2(lt) and (d) MIL-53−NHCHO.

in the MQMAS spectrum of MIL-53−NHCHO, however, indicates that the postsynthetic functionalization can be carried out without formation of side products. The trends for the line width of the ^{27}Al spectra, which increases from MIL-53−NH_2(as) (QCC = 2.3 MHz) over MIL-53−NHCHO (QCC = 2.4 MHz) and MIL-53−NH_2(DMF) (QCC = 2.5 MHz) over MIL-53−NH_2(lt) (QCC = 2.7 MHz), are correlated with an increasing distortion of the channels in the MIL-53 structure, leading to a more anisotropic environment of the AlO_6 octahedra. Thus, the overall line width can be used as a simple probe for the space requirement of the incorporated guest molecules.

Conclusion

The chemically and thermally very stable MOF MIL-53-containing NH_2 groups, i.e. MIL-53−NH_2, has been obtained and used in the postsynthetic modification by reaction with

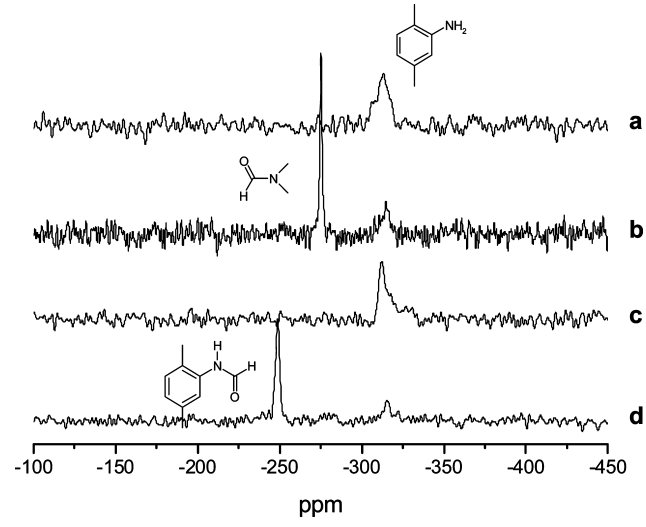

Figure 9. ^{15}N MAS NMR spectra of (a) MIL-53−NH_2(as), (b) MIL-53−NH_2(DMF), (c) MIL-53−NH_2(lt) and (d) MIL-53−NHCHO.

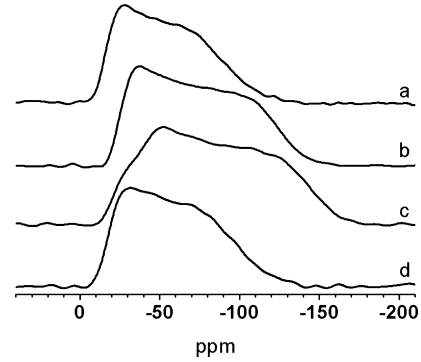

Figure 10. ^{27}Al MAS NMR spectra of (a) MIL-53−NH_2(as), (b) MIL-53−NH_2(DMF), (c) MIL-53−NH_2(lt) and (d) MIL-53−NHCHO.

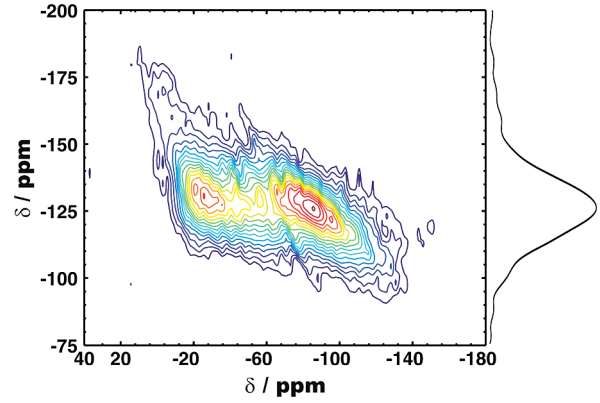

Figure 11. ^{27}Al MQMAS NMR spectrum of MIL-53−NHCHO.

formic acid. The activation of the as synthesized compound containing free aminoterephthalic acid molecules is accomplished in a two-step process. Thus, three forms of MIL-53−NH_2 have been obtained and thoroughly characterized. In comparison to MIL-53, the thermal stability of the amino-functionalized MIL-53−NH_2 is decreased. As shown by powder XRD measurements, the presence of the NH_2 group has no obvious influence on the breathing behavior of the aluminum carboxylate framework. This is only influenced by the presence of hydrogen bonds between the water molecules and the carboxylate groups. A strong difference

is observed in the N_2 sorption behavior. Strong hysteresis is found in the amino-functionalized compound. The postsynthetic modification of the activated MIL-53−NH_2 was accomplished by reaction with formic acid and verified by a combination of NMR and IR analysis.

Acknowledgment. The work has been supported by the German Science Foundation (DFG) via the DFG priority program SPP 1362 Porous Metal-Organic Frameworks under grants STO 643/5-1 and SE 1417/4-1.

Supporting Information Available: Powder XRD pattern results for (a) MIL-53−NH_2(as), (b) MIL-53−NH_2(DMF), (c) MIL-53−NH_2(lt) and (d) MIL-53−NHCHO. This material is available free of charge via the Internet at http://pubs.acs.org.

IC8023265

4.1.2 New Functionalized Flexible Al-MIL-53-X (X = -Cl, -Br, -Me, -NO_2, -$(OH)_2$) Solids: Syntheses, Characterization, Sorption and Breathing Behavior

Der Artikel wurde 2011 in der Zeitschrift „Inorganic Chemistry“ veröffentlicht. Die Zusatzinformation zu diesem Artikel befindet sich im Anhang 2 auf Seite 151.

In dem Artikel werden die Herstellung und die Charakterisierung fünf isoretikulärer Al-MIL-53-Verbindungen beschrieben. Durch den Einsatz verschiedener Terephthalsäurederivate (H_2BDC-X X= -Cl, -Br, -Me, -NO_2, -$(OH)_2$) konnten insgesamt fünf funktionelle Gruppen mit unterschiedlicher Größe, Polarität und Acidität in das Gerüst von Al-MIL-53 eingebaut werden. Ausgehend von den Synthesebedingungen des aminofunktionalisierten Al-MIL-53-NH_2 ließen sich die Verbindungen Al-MIL-53-Cl ([Al(OH)(BDC-Cl)])·0.5H_2O), Al-MIL-53-Br ([Al(OH)(BDC-Br)]·0.5H_2O), Al-MIL-53-Me ([Al(OH)(BDC-Me)]·0.1H_2O) und Al-MIL-53-NO_2 ([Al(OH)(BDC-NO_2)]·0.6H_2O) unter hydrothermalen Bedingungen herstellen. Die Synthese von Al-MIL-53-$(OH)_2$ ([Al(OH)(BDC-$(OH)_2$)]·H_2O) erfolgte hingegen in DEF. Durch eine anschließende Optimierung der Synthesen konnten alle Rohprodukte im Gramm-Maßstab und mit hoher Kristallinität erhalten werden. Zur Aktivierung der Rohprodukte wurden die in den Kanälen eingelagerten oder als kristalline Nebenphasen anfallenden Linkermoleküle durch DMF-Moleküle ausgetauscht. Dazu wurden die Verbindungen mit einem Überschuss an DMF versetzt und 24 h bei 150 °C erwärmt. Die in den Kanälen eingelagerten DMF Moleküle konnten in einem zweiten Aktivierungsschritt unter solvothermalen Bedingungen durch Methanol ausgetauscht werden. Nach dem Trocknen an der Luft wurde das in dem Gerüst verbliebene Methanol thermisch entfernt. Beim Abkühlen der Substanzen lagerten sich Wassermoleküle aus der Luft in die Gerüste ein. Aufgrund starker Wechselwirkungen mit den Wassermolekülen gingen die Verbindungen in die geschlossene Form von Al-MIL-53 über. Für die Verbindungen Al-MIL-53-Cl, Al-MIL-53-Br und Al-MIL-53-Me erfolgte dieser Übergang nicht vollständig. In den Pulverdiffraktogrammen der Verbindungen traten zusätzliche Reflexe auf, die der offenen Form der jeweiligen Verbindung zugeordnet werden konnten.

Temperaturabhängige Röntgenbeugungsexperimente zeigten, dass die Temperatur des Phasenübergangs von der geschlossen- in die offenporige Form von den funktionellen Gruppen abhängig ist. Für Al-MIL-53-$(OH)_2$ und Al-MIL-53-NH_2 konnte durch eine rein thermische Behandlung der Probe kein Öffnen der Kanäle beobachtet werden. Im Überschuss von Wasser (Al-MIL-53-$(OH)_2$) oder beim Versetzen mit DMF (Al-MIL-53-$(OH)_2$ und Al-MIL-53-NH_2) kam es jedoch auch hier zu einem Übergang in die offenporige Form. Demnach wiesen alle Verbindungen flexible Netzwerke auf, deren Gitterparameter bzw. Porendurchmesser stark von den funktionellen Gruppen und eingelagerten Gastmolekülen im Gerüst beeinflusst werden. Die Adsorptionseigenschaften der Gerüste wurden mittels Sorptionsexperimenten unter Verwendung unterschiedlicher Gase qualitativ untersucht. Als Messgase wurden Stickstoff, Kohlendioxid und Wasserdampf eingesetzt. Je nach funktioneller Gruppe im Gerüst variierte die Aufnahmekapazität der unterschiedlichen Verbindungen stark. Al-MIL-53-$(OH)_2$ beispielsweise adsorbierte unter den verwendeten Messbedingungen keinen Stickstoff, nahm jedoch im Vergleich zu allen anderen untersuchten Verbindungen die größte Menge an Wassermolekülen auf.

Inorganic Chemistry

ARTICLE

pubs.acs.org/IC

New Functionalized Flexible Al-MIL-53-X (X = -Cl, -Br, -CH_3, -NO_2, -$(OH)_2$) Solids: Syntheses, Characterization, Sorption, and Breathing Behavior

Shyam Biswas, Tim Ahnfeldt, and Norbert Stock*

Institut für Anorganische Chemie, Christian-Albrechts-Universität, Max-Eyth-Strasse 2, 24118 Kiel, Germany

Supporting Information

ABSTRACT: Five new flexible functionalized aluminum hydroxo terephthalates [Al(OH)(BDC-X)]·*n*(guests) (BDC = 1,4-benzene-dicarboxylate; X = -Cl, **1-Cl**; -Br, **2-Br**; -CH_3, **3-CH_3**; -NO_2, **4-NO_2**; -$(OH)_2$, **5-OH_2**) were synthesized under solvothermal conditions. The as synthesized (Al-MIL-53-X-AS) as well as the activated compounds were characterized by X-ray powder diffraction (XRPD), IR spectroscopy, thermogravimetric (TG), and elemental analysis. Activation, that is, removal of unreacted H_2BDC-X molecules and/or occluded solvent molecules, followed by hydration in air at room temperature, led to the narrow pore (NP) form of the title compounds [Al(OH)(BDC-X)]·*n*(H_2O) (Al-MIL-53-X). Thermogravimetric analysis (TGA) and temperature-dependent XRPD (TDXRPD) experiments performed on the NP-form of the compounds indicate high thermal stability in the range 325−500 °C. As verified by N_2, CO_2, or H_2O sorption measurements, most of the thermally activated compounds exhibit significant microporosity. Similar to pristine Al-MIL-53, the present compounds retain their structural flexibility depending on the nature of guest molecules and temperature, as verified by cell parameter determination from XRPD data. The breathing behavior of the functionalized frameworks upon dehydration−rehydration, investigated by temperature and time-dependent XRPD measurements, differs significantly compared to parent Al-MIL-53.

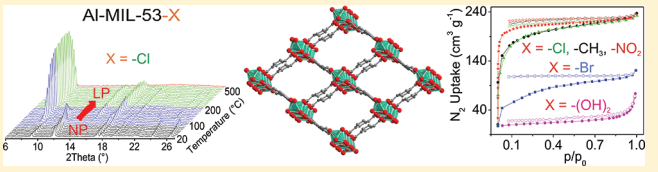

INTRODUCTION

Metal−organic frameworks (MOFs),[1−3] which are constructed of inorganic building units and organic linkers, are attracting considerable interest because of their potential applications in areas such as catalysis,[4,5] gas storage/separation,[6−8] and drug delivery.[9,10]

Because of the modular character of MOFs various pore shapes and functionalities can be achieved by varying the metal as well as the organic linker molecules. A series of compounds based on the MIL-53 topology has been reported, where various trivalent metal ions as well as different ditopic organic linker molecules varying in size and functionality have been incorporated.[11−15] The MIL-53 structure contains chains of *trans* corner-sharing [$MO_4(OH)_2$] polyhedra that are connected to each other by aryldicarboxylate linker molecules, $(O_2C-C_6H_4-CO_2)^{2-}$, and thus one-dimensional channels are formed (Figure 1). The compounds have the general composition [M(OH)($O_2C-C_6H_4-CO_2$)] with M = Cr,[11] Fe,[12] Al,[13] Ga,[14] and In.[15] One outstanding property of these compounds is their reversible framework flexibility, also denoted as breathing,[16] which depends strongly on the incorporated metal ion,[17,18] size and functionality of the linker molecules,[19] the temperature[17,18] as well as the nature of the guest molecules.[11,13,20] Thus many studies have been performed with carbon dioxide,[21−29] linear alkanes,[30−33] or xylenes[34,35] as guest molecules. Depending on these parameters a narrow or a large pore form is observed (Figure 1), and the transformation can lead to a change in unit cell volume up to 40%.[19]

The iron series has been investigated in great depth. Thus, seven functionalized Fe-MIL-53 compounds[19,36,37] have been reported. The effect on the structure flexibility of the dry as well as guest containing forms was evaluated using various characterization methods ranging from X-ray powder diffraction and IR spectroscopy to computational studies. Through the use of chemical groups differing in polarity, hydrophilicity, and acidity, the authors were able to demonstrate that the presence of intraframework interactions dominate the geometry of the pore opening rather than their steric properties.

Al-based MOFs are lightweight, nontoxic, and most of these materials are stable against hydrolysis.[38−40] Compared to the Fe-MIL-53 compounds the number of known functionalized Al-based analogues is smaller and little is know about the temperature dependent structural properties. Thus Al-MIL-53-NH_2,[41−43] Al-MIL-53-OH,[44] Al-MIL-53-$(CO_2H)_2$,[45] and Al-MIL-53-C_4H_4 (Al-PCP)[46] have been reported, and the amino as well as the hydroxyl derivative have been employed for post-synthetic modification reactions.[44−49] The unfunctionalized compound Al-MIL-53 was also used as a host material.[50−52]

Inspired by the advantages of Al-based MOFs, and the interest that the known Al-MIL-53 based compounds have attracted, we have introduced five different functional groups (polar: -Cl, -Br, -NO_2; acidic: -OH; nonpolar: -CH_3) into parent Al-MIL-53 framework to evaluate by X-ray diffraction, IR spectroscopy,

Received: June 7, 2011
Published: September 07, 2011

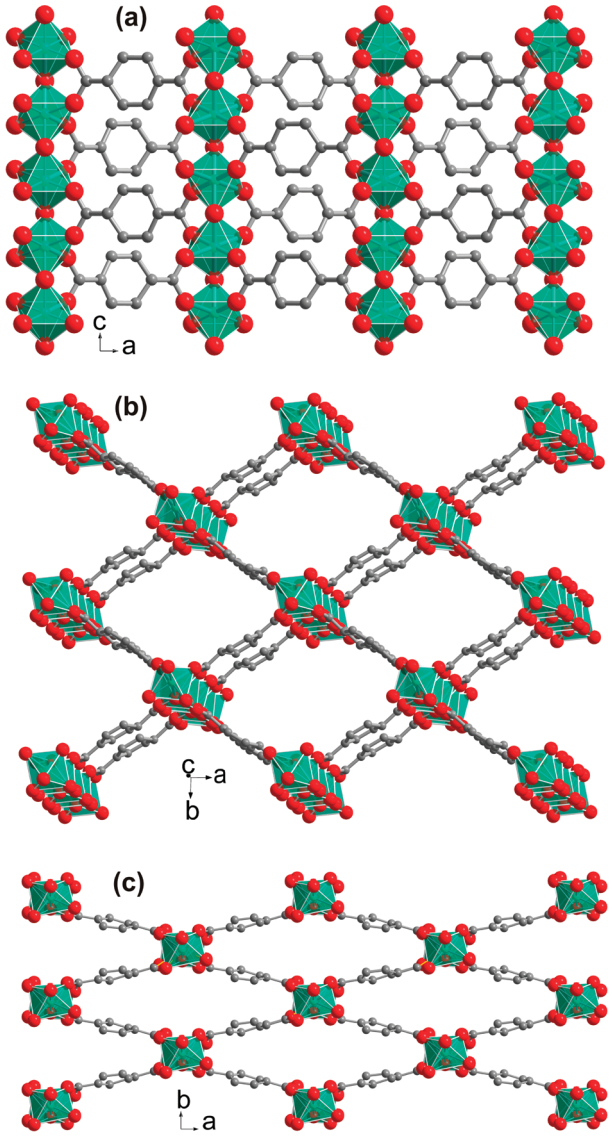

Figure 1. Ball-and-stick representations of the 3D framework structure of Al-MIL-53 with Al atoms displayed as octahedra (color codes: Al, bluish green; C, gray; O, red). (a) Infinite chains of corner-sharing octahedral $[AlO_4(OH)_2]$ units interconnected by the BDC linkers. (b, c) The large pore (LP) and narrow pore (NP) forms of the framework viewed along the crystallographic *c*-axis. For clarity, hydrogen atoms and guest molecules have been omitted from all structural plots. The figure was drawn using structural data taken from ref 13.

TG, and sorption analysis the effect of such organic modifications (Scheme 1) both on the pore surface properties and breathing behavior. In this article, we report on the syntheses, characterization, sorption and breathing properties of the above-mentioned flexible functionalized Al-MIL-53-X solids (X = -Cl, -Br, $-CH_3$, $-NO_2$, $-(OH)_2$).

EXPERIMENTAL SECTION

Materials and General Methods. The H_2BDC-Cl and H_2BDC-CH_3 ligands were synthesized according to previously published procedures.[19] All other starting materials were of reagent grade and used as received from the commercial supplier. Fourier transform infrared (FTIR) spectra were recorded in the range 4000−400 cm^{-1} on an ALPHA-ST-IR Bruker spectrometer with an ATR unit. Elemental analyses (C, H, N) were carried out on a Eurovektor EuroEA Elemental Analyzer. Thermogravimetric analysis (TGA) was performed with a Netzsch STA-409CD thermal analyzer in a temperature range of 25−800 °C under air atmosphere at a heating rate of 4 °C min^{-1}. Ambient temperature X-ray powder diffraction (XRPD) patterns were measured using CuKα radiation (λ = 1.5406 Å) with a STOE STADI P diffractometer equipped with a linear position-sensitive detector (LPSD) or a STOE high-throughput powder diffractometer equipped with an image-plate position-sensitive detector (IPPSD). Lattice parameters were determined using the DICVOL program[53] and refined using STOE's WinXPow[54] software package. Temperature-dependent X-ray powder diffraction (TDXRPD) experiments were performed under air atmosphere with a STOE STADI P diffractometer equipped with an IPPSD detector and a STOE capillary furnace (version 0.65.1) using CuKα radiation. For **4-NO_2-AS**, each pattern was recorded at intervals of 15 °C. For all the other compounds, the patterns below and above 200 °C were collected at intervals of 10 and 25 °C, respectively. The N_2, CO_2, and H_2O sorption isotherms up to 1 bar were measured using a Belsorp Max apparatus at −196, 25, and 25 °C, respectively. The NP-forms of the compounds were heated (155 °C, 12 h for **1-Cl**, **2-Br**, and **3-CH_3**; 130 °C, 6 h for **4-NO_2** and **5-$(OH)_2$**) under dynamic vacuum prior to sorption experiments.

Caution! *Perchlorate salt is potentially explosive, and caution should be exercised when dealing with such material. However, the small quantities used in this study were not found to present a hazard.*

Elemental analyses and frequencies of infrared bands for all the compounds are presented in Supporting Information, Tables S2 and S3, respectively.

Al-MIL-53[13,33] and Al-MIL-53-NH_2[43] were synthesized and activated according to literature methods. The usual characterization experiments (XRPD, TGA, IR spectroscopy, and sorption analysis) were performed to confirm their purity.

Synthesis of Al-MIL-53-Cl-AS (1-Cl-AS). A mixture of $AlCl_3 \cdot 6H_2O$ (1.0 g, 4.14 mmol), H_2BDC-Cl (0.83 g, 4.14 mmol), and water (40 mL) was placed in a 100 mL Teflon liner, and the resulting mixture was heated in a conventional oven at 210 °C for 12 h and cooled to room temperature. The white product was obtained by filtration. The yield was 0.74 g (2.84 mmol, 69%) based on the Al salt.

Synthesis of Al-MIL-53-Br-AS (2-Br-AS). A mixture of $Al(NO_3)_3 \cdot 9H_2O$ (1.5 g, 3.99 mmol), H_2BDC-Br (0.98 g, 3.99 mmol), benzoic acid (0.25 g, 2.04 mmol) and water (60 mL) was placed in a 100 mL Teflon liner, and the resulting mixture was heated in a conventional oven at 210 °C for 12 h and cooled to room temperature. The white product was collected by filtration. The yield was 0.95 g (2.49 mmol, 63%) based on the Al salt.

Synthesis of Al-MIL-53-CH_3-AS (3-CH_3-AS). A mixture of $AlCl_3 \cdot 6H_2O$ (1.0 g, 4.14 mmol), H_2BDC-CH_3 (0.75 g, 4.16 mmol), and water (40 mL) was placed in a 100 mL Teflon liner, and the resulting mixture was heated in a conventional oven at 210 °C for 12 h and cooled to room temperature. The white product was obtained by filtration. The yield was 0.65 g (1.66 mmol, 40%) based on the Al salt.

Scheme 1. Modified Terephthalic Acid Ligands H_2BDC-X Used for Synthesizing Al-MIL-53-X Materials

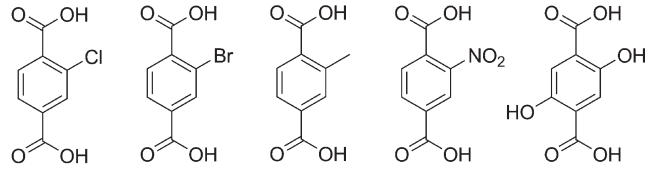

dx.doi.org/10.1021/ic201219g |*Inorg. Chem.* 2011, 50, 9518–9526

Synthesis of Al-MIL-53-NO_2-AS (4-NO_2-AS). A mixture of $Al(NO_3)_3 \cdot 9H_2O$ (1.49 g, 3.97 mmol), $H_2BDC\text{-}NO_2$ (0.92 g, 4.37 mmol) and water (50 mL) was placed in a 100 mL Teflon liner, and the resulting mixture was heated in a conventional oven at 170 °C for 12 h and cooled to room temperature. The white microcrystalline product was obtained by filtration. The yield was 0.52 g (1.92 mmol, 48%) based on the Al salt.

Synthesis of Al-MIL-53-$(OH)_2$-AS (5-OH_2-AS). A mixture of $Al(ClO_4)_3 \cdot 9H_2O$ (0.98 mg, 2.01 mmol), $H_2BDC\text{-}(OH)_2$ (0.40 g, 2.01 mmol) and *N,N′*-diethylformamide (DEF; 5 mL) was placed in a 27 mL Teflon liner, and the resulting mixture was heated in a conventional oven at 125 °C for 5 h and cooled to room temperature. The yellow product was collected by filtration. The yield was 0.78 g (3.02 mmol, 67%) based on the Al salt.

Activation of Al-MIL-53-X-AS Materials. All the AS-materials were activated in two steps.

Each (1.0 g) of **1-Cl-AS**, **2-Br-AS**, and **3-CH_3-AS** was heated in *N,N′*-dimethylformamide (DMF; 60 mL) at 155 °C for 24 h in a conventional oven. The filtered solids (denoted Al-MIL-53-X-DMF) were heated at 155 °C for 24 h in a conventional oven.

Compound **4-NO_2-AS** (0.5 g) was heated in methanol (2 × 60 mL) at 80 °C in a conventional oven for 48 h, during which period the solvent was discarded and fresh solvent was added after 24 h. The filtered white solid was heated at 150 °C for 12 h in a conventional oven.

Compound **5-$(OH)_2$-AS** (0.2 g) was heated in 200 mL of methanol/water (50:50, v/v) at 100 °C in a conventional oven for 12 h. The yellow solid was collected by filtration, washed with water (named **5-$(OH)_2$-H_2O** or water-rich form) and heated at 130 °C for 12 h in a conventional oven.

RESULTS AND DISCUSSION

Syntheses and Activation. The synthesis procedures adopted for the functionalized compounds differ significantly with respect to the one previously reported for pristine Al-MIL-53.[13] To optimize synthesis conditions for the Al-MIL-53-X solids, stoichiometric mixtures (1:1) of aluminum salts (nitrate, chloride, perchlorate, and sulfate) and H_2BDC-X ligands were heated in polar solvents such as H_2O, methanol, DMF, DEF, or DMA (*N,N′*-dimethylacetamide). Water was found as the best solvent for the preparation of all compounds, except **5-$(OH)_2$**. The use of DEF instead of water led to the formation of highly crystalline **5-$(OH)_2$-AS**. Whereas **1-Cl-AS**, **3-CH_3-AS**, and **4-NO_2-AS** can be synthesized with $Al(NO_3)_3 \cdot 9H_2O$ and $AlCl_3 \cdot 6H_2O$, **2-Br-AS** and **5-$(OH)_2$-AS** with high crystallinity were only obtained with $Al(NO_3)_3 \cdot 9H_2O$ and $Al(ClO_4)_3 \cdot 9H_2O$, respectively.

The AS-forms of the compounds contain guest molecules (H_2BDC-X linkers, H_2O or DEF) trapped in the pores which could not be removed by direct thermal treatment (see Thermal Behavior section). They were activated in a two-step procedure similar to that reported for Al-MIL-53[33] and Al-MIL-53-NH_2.[43] At first, the guest molecules were exchanged by heating the AS-compounds with polar solvents such as DMF (**1-Cl-AS**, **2-Br-AS**, and **3-CH_3-AS**), methanol (**4-NO_2-AS**), or a methanol/water (50:50, v/v) mixture (**5-$(OH)_2$-AS**). In a second step, the polar solvent molecules were removed by heating the exchanged solids under air atmosphere. After cooling to room temperature, the activated compounds adsorb different amounts of water (Supporting Information, Table S1) from air depending on the attached functional groups.

Structure Description. The framework topology of all the functionalized compounds is identical, and they correspond to the pristine Al-MIL-53 structure (Figure 1).[13] The 4^4 net of Al-MIL-53 contains infinite tilted *trans* chains (Figure 1a) of corner-sharing (via μ_2-OH group) $[AlO_4(OH)_2]$ octahedra, which are connected through the carboxylate groups of the BDC linkers to form a three-dimensional (3D) framework possessing one-dimensional (1D) rhombic-shaped pores. In the AS-forms of the functionalized solids, the 1D channels are occupied by guest molecules (solvent molecules or H_2BDC-X linkers) at ambient conditions. Depending on both the nature of guest molecules[11,13,20] and the temperature,[17,18] the frameworks reversibly change from a narrow pore (NP; crystal system: monoclinic; unit cell volume: ~1000 Å^3) to a large pore (LP; crystal system: orthorhombic; unit cell volume: ~1400−1500 Å^3) form (Figures 1b,c, Table 1 and Breathing Behavior section) with up to 50% variation of their unit cell volume without breaking any bond and changing the framework topology.

Infrared Spectroscopy. The FT-IR spectra of AS, guest-exchanged and NP-forms of each of the Al-MIL-53-X compounds (Supporting Information, Figures S6−S10 and Tables S3−S4) are very similar, as expected. In the IR spectra of the AS-forms of all the compounds, the strong absorption bands due to asymmetric and symmetric $-CO_2$ stretching vibrations of the coordinated BDC-X linkers are located in the regions 1597−1616 cm^{-1} and 1415−1463 cm^{-1}, respectively.[13] The additional strong absorption bands in the region 1694−1711 cm^{-1}, observed in the IR spectra of AS-forms of **1-Cl**, **2-Br**, **3-CH_3**, and **4-NO_2**, can be attributed to the protonated form ($-CO_2H$) of unreacted or occluded BDC-X ligands.[13] The medium absorption band at 1659 cm^{-1} in the IR spectra of **5-$(OH)_2$-AS** can be assigned to the carbonyl stretching vibration of occluded DEF molecules. The characteristic strong absorption band of the carbonyl stretching vibration of guest DMF molecules appears in the range 1663−1673 cm^{-1} in the IR spectra of DMF-form of all the compounds. The absence of the absorption bands of noncoordinated H_2BDC-X linkers, DMF, and DEF molecules in the IR spectra of NP-form confirms complete activation of the compounds. The C−H stretching vibration of the -CH_3 group attached with the BDC-CH_3 linker exhibits weak absorption bands at about 2970 and 2930 cm^{-1} in the IR spectra of AS, DMF and NP-forms of **3-CH_3**.[55] The characteristic broad absorption band due to stretching vibration of the −OH group appended to BDC-$(OH)_2$ linker is located in the region 3300−3350 cm^{-1} in the IR spectra of AS, guest-exchanged and NP-forms of **5-$(OH)_2$**.[55] The stretching vibration of the μ_2-OH group displays weak absorption band in the region 3630−3680 cm^{-1} in the IR spectra of AS, guest-exchanged and NP-forms of all the compounds.[19]

Thermal Stability. To examine the thermal stability of all Al-MIL-53-X compounds, thermogravimetric analyses (TGA) were performed on both AS and NP-forms of the compounds in air atmosphere. On the basis of the TG analyses, all the compounds are thermally stable up to 325−500 °C. The descending order of thermal stability of the compounds is **1-Cl** (500 °C) > **2-Br** (410 °C) > **4-NO_2** (380 °C) > **3-CH_3** (370 °C) > **5-$(OH)_2$** (325 °C). The highest thermal stability of **1-Cl** equals to that of the nonmodified Al-MIL-53 solid.[13] The lowest thermal stability of **5-$(OH)_2$** can be related to the redox reactivity of the BDC-$(OH)_2$ linker.[56] It is noteworthy that an even lower thermal stability has been reported for Fe-MIL-53-$(OH)_2$ (150−160 °C).[19]

In the TG curves of the AS-forms of all the compounds (Supporting Information, Figures S11−S15), any weight loss step that occurs below the decomposition temperature of the frameworks can be assigned to the removal of the occluded guest molecules (H_2O, H_2BDC-X linkers or DEF). Below the decomposition

Table 1. Molecular Formulae, Refined Lattice Parameters,[a] and Pore Types[b] of the Different Forms of the Al-MIL-53-X Solids

compound	molecular formula	a (Å)	b (Å)	c (Å)	β (deg)	V (Å^3)	pore type
1-Cl-AS	[Al(OH)(BDC-Cl)]·0.85(H_2BDC-Cl)	16.580(7)	13.243(5)	6.666(6)		1453.2(12)	LP
1-Cl-DMF	[Al(OH)(BDC-Cl)]·1.1(DMF)	17.03(4)	12.36(3)	6.616(20)		1392.0(89)	LP
1-Cl	[Al(OH)(BDC-Cl)]·0.5(H_2O)	19.776(4)	7.9371(16)	6.6010(17)	106.589(13)	993.0(5)	NP
1-Cl-HT	[Al(OH)(BDC-Cl)]	16.604(7)	12.985(8)	6.623(4)		1428.1(19)	LP
2-Br-AS	[Al(OH)(BDC-Br)]·0.4(H_2BDC-Br)·0.5(H_2O)	16.532(12)	13.092(14)	6.637(5)		1453.1(25)	LP
2-Br-DMF	[Al(OH)(BDC-Br)]·1.1(DMF)	16.438(15)	13.368(11)	6.653(3)		1462.0(11)	LP
2-Br	[Al(OH)(BDC-Br)]·0.5(H_2O)	19.567(14)	8.532(12)	6.616(5)	107.22(6)	1055.1(23)	NP
1-Br-HT	[Al(OH)(BDC-Br)]	16.372(12)	13.181(11)	6.608(6)		1426.1(26)	LP
3-CH_3-AS	[Al(OH)(BDC-CH_3)]·0.9(H_2BDC-CH_3)·0.2(H_2O)	16.404(5)	13.335(3)	6.649(3)		1456.8(31)	LP
3-CH_3-DMF	[Al(OH)(BDC-CH_3)]·1.1(DMF)	16.93(3)	12.61(4)	6.663(15)		1422.6(86)	LP
3-CH_3	[Al(OH)(BDC-CH_3)]·0.1(H_2O)	19.700(17)	7.999(7)	6.603(5)	106.40(5)	998.1(19)	NP
3-CH_3-HT	[Al(OH)(BDC-CH_3)]	16.545(13)	12.981(14)	6.613(8)		1420.4(30)	LP
4-NO_2-AS	[Al(OH)(BDC-NO_2)]·0.22(H_2BDC-NO_2)·1.4(H_2O)	16.545(6)	13.120(5)	6.670(3)		1447.8(13)	LP
4-NO_2-DMF	[Al(OH)(BDC-NO_2)]·1.0(DMF)	17.367(6)	11.868(5)	6.662(4)		1373.1(8)	LP
4-NO_2	[Al(OH)(BDC-NO_2)]·0.6(H_2O)	19.687(10)	8.257(5)	6.635(3)	106.87(4)	1032.1(12)	NP
4-NO_2-HT	[Al(OH)(BDC-NO_2)]	16.382(7)	13.320(10)	6.6490(17)		1450.8(8)	LP
5-$(OH)_2$-AS	[Al(OH)(BDC-$(OH)_2$)]·0.7(H_2BDC-$(OH)_2$)	17.212(14)	12.284(8)	6.670(7)		1410.4(28)	LP
5-$(OH)_2$-DMF	[Al(OH)(BDC-$(OH)_2$)]·1.0(DMF)	17.62(3)	11.579(8)	6.628(4)		1352.2(34)	LP
5-$(OH)_2$-H_2O	[Al(OH)(BDC-$(OH)_2$)]·5.5(H_2O)	17.397(4)	11.832(4)	6.6284(22)		1364.5(4)	LP
5-$(OH)_2$	[Al(OH)(BDC-$(OH)_2$)]·1.0 (H_2O)	19.762(4)	7.6320(16)	6.5786(14)	105.768(13)	954.9(5)	NP
Al-MIL-53-AS[13]	[Al(OH)(BDC)]·0.7(H_2BDC)	17.129(2)	12.182(1)	6.628(1)		1383.1(2)	LP
Al-MIL-53-DMF	[Al(OH)(BDC)]·1.1(DMF)	17.55(6)	11.396(17)	6.615(13)		1322.8(74)	LP
Al-MIL-53[13]	[Al(OH)(BDC)]·1.0(H_2O)	19.513(2)	7.612(1)	6.576(1)	104.24(1)	946.8(1)	NP
Al-MIL-53-HT[13]	[Al(OH)(BDC)]	16.675(3)	12.813(2)	6.608(1)		1411.9(4)	LP
Al-MIL-53-NH_2-AS[43]	[Al(OH)(BDC-NH_2)]·0.3(H_2BDC-NH_2)	16.898(20)	12.539(18)	6.647(8)		1408.4(4)	LP
Al-MIL-53-NH_2-DMF[43]	[Al(OH)(BDC-NH_2)]·0.95(DMF)	17.578(17)	11.483(9)	6.630(6)		1338.9(25)	LP
Al-MIL-53-NH_2[43]	[Al(OH)(BDC-NH_2)]·0.9(H_2O)	19.722(7)	7.692(3)	6.578(4)	105.1(3)	961.5(10)	NP
Al-MIL-53-NHCHO-AS[43]	[Al(OH)(BDC-NHCHO)]·1.0(H_2O)	17.156(5)	12.246(5)	6.604(13)		1387.4(8)	LP
Al-MIL-53-$(COOH)_2$-AS[45]	[Al(OH)(BDC-$(COOH)_2$)]·0.1(H_2BDC-$(COOH)_2$))·1.5(H_2O)	17.54483(8)	13.57813(8)	6.66420(4)	113.1956(5)	1459.25(2)	LP

[a] Lattice parameters were determined from room temperature XRPD data, except the four high-temperature (HT) forms that were derived from the TDXRPD data. [b] LP: large-pore, NP: narrow-pore.

temperatures, the TG traces of the NP-forms of the compounds (Supporting Information, Figures S11−S15) display only one weight loss step owing to the removal of adsorbed water molecules. The observed weight losses of the NP-forms are consistent with the calculated ones as well as the elemental analyses (Supporting Information, Tables S1 and S2), indicating phase purity of the compounds. The removal of free water molecules from the channels occurs at about 100 °C for NP-forms of all the compounds. Evidently, the introduction of functional groups does not lead to a dramatic change of thermal stability or large activation barriers for the removal of H_2O molecules.

The high thermal stability of the Al-MIL-53-X compounds has also been verified by temperature-dependent XRPD (TDXRPD) measurements. From the TDXRPD patterns of the AS-form of **4-NO_2**- (Supporting Information, Figure S16), it becomes obvious that the compound is stable up to 380 °C. Since the AS-forms of the compounds do not switch to their high-temperature (HT) forms upon heating, they could not be activated by direct thermal treatment.

According to the TDXRPD patterns (Figures 2, 3 and Supporting Information, Figures S17−S19) recorded in capillary geometry, the NP-forms of **1-Cl**, **2-Br**, **3-CH_3**, **4-NO_2**, and **5-$(OH)_2$** are stable up to 525, 450, 500, 475, and 400 °C, respectively. The

dx.doi.org/10.1021/ic201219g |Inorg. Chem. 2011, 50, 9518–9526

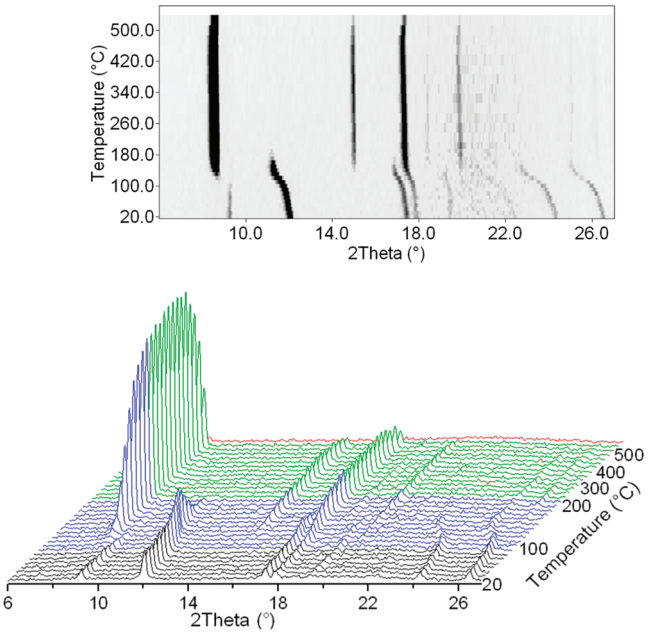

Figure 2. TDXRPD patterns of **1-Cl** under air atmosphere (Cu Kα radiation, λ = 1.5406 Å) in the range 20−550 °C. The top view of the patterns is shown on the top. Black patterns: NP-form; blue patterns: mixture of NP and HT-forms; green patterns: HT-form; red pattern: decomposed form.

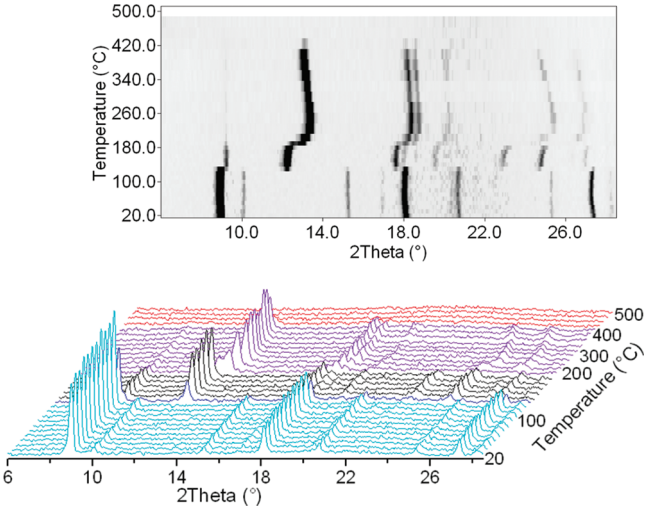

Figure 3. TDXRPD patterns of the water-rich form of **5-(OH)$_2$** under air atmosphere (CuKα radiation, λ = 1.5406 Å) in the range 20−500 °C. The top view of the patterns is shown on the top. Cyan patterns: water-rich (LP) form; black patterns: NP-form; violet patterns: NP-form with Bragg peaks shifted toward higher 2θ values; red patterns: decomposed form.

observation of higher decomposition temperatures during TDXRPD measurements compared to TGA can be assigned to the lower outer diameter (0.30 mm) of the thin-walled (thickness: 0.01 mm) capillaries which prevent sufficient air flow around the samples filled into them.

Breathing Behavior. On the basis of results of the unit cell determinations (Table 1), the structures of the different forms of Al-MIL-53-X were found to correspond to the ones observed in the nonfunctionalized[13] and amino-functionalized[43] Al-MIL-53. However, the modification of the pore environments with different functional groups results in different breathing behavior of the frameworks. The unit cell volumes of all the AS, guest-exchanged and HT-forms of the compounds vary in the ranges 1410−1457, 1352−1462, and 1420−1451 Å^3, respectively. Obviously, the AS, guest-exchanged and HT-forms of the compounds differ slightly from each other in terms of unit cell volumes, and all of these forms correspond to the LP-version of the frameworks. In sharp contrast, the unit cell volumes (955−1055 Å^3) of the hydrated compounds vary significantly from those of AS, guest-exchanged, and HT-forms, and thus the frameworks adopt the NP-forms. Conclusively, the breathing effect of the functionalized solids is dependent on both the nature of guest molecules and the temperature. Whereas some guest molecules (H_2BDC-X and DMF) allow the frameworks to exist in the LP-form, the others (H_2O) force them to adopt the NP-form.

To investigate the breathing properties of the Al-MIL-53-X compounds upon dehydration−rehydration, both temperature and time-dependent XRPD experiments were carried out on the NP-forms of the compounds. A typical TDXRPD analysis of the NP-form is illustrated in Figure 2 (here **1-Cl**, see Supporting Information, Figures S17−S19 for all the other compounds). The Bragg peaks of the NP-forms of all the compounds are exclusively observed below 80 °C. With increase in temperature, the Bragg reflections of the NP-forms gradually disappear, and new reflections of the HT-phases start to appear at different temperatures (**1-Cl**, 110 °C; **2-Br**, 80 °C; **3-CH$_3$**, 120 °C; **4-NO$_2$**, 130 °C) depending on the appended functional groups, as a consequence of both the departure of water and the thermal expansion.[57] The Bragg peaks of only the HT-forms are noticed in the following ranges: **1-Cl**, 210−525 °C; **2-Br**, 140−450 °C; **3-CH$_3$**, 325−500 °C; **4-NO$_2$**, 160−475 °C. The diffraction peaks of the HT-forms finally vanish above the range 400−525 °C, leading to the decomposition of the compounds into X-ray amorphous materials.

To examine the flexibility of the **5-(OH)$_2$** framework, a TDXRPD measurement was carried out on its water-rich (LP) form, that is, **5-(OH)$_2$-H$_2$O** (Figure 3). Therefore, **5-(OH)$_2$** was treated with an excess of water before the measurement. This leads to an uptake of water accompanied by the opening of the pores, which has been also observed in the unmodified Cr-MIL-53 material.[58] Below 120 °C, the LP-form is observed in the TDXRPD patterns. At 140 °C, the LP-form transforms completely into the NP-form which continues to exist up to 180 °C. In the range 190−400 °C, the positions of some of the Bragg reflections of the NP-form shift toward higher 2θ values. Slight shift of the positions of few of the diffraction peaks has also been observed in the TDXRPD patterns of the NP-form of Al-MIL-53-NH$_2$ (Supporting Information, Figure S20) in the range 120−450 °C. This alteration of the peak positions for both compounds can be attributed to the removal of water molecules from the pores. Evidently, the NP-forms of both compounds remains closed after heating.

A graphical summary of the results on the temperature-dependent breathing behavior of the different functionalized Al-MIL-53 compounds is given in the Supporting Information, Figure S21.

To determine the time needed for rehydration of the HT forms, the NP-forms of **1-Cl**, **2-Br**, **3-CH$_3$**, and **4-NO$_2$** were heated at 180 °C under vacuum for 2 h and subsequently the powder patterns in flat-plate geometry were collected at room temperature under air atmosphere. The mixtures of HT and NP-forms of **4-NO$_2$**, **1-Cl**, and **2-Br** (Supporting Information,

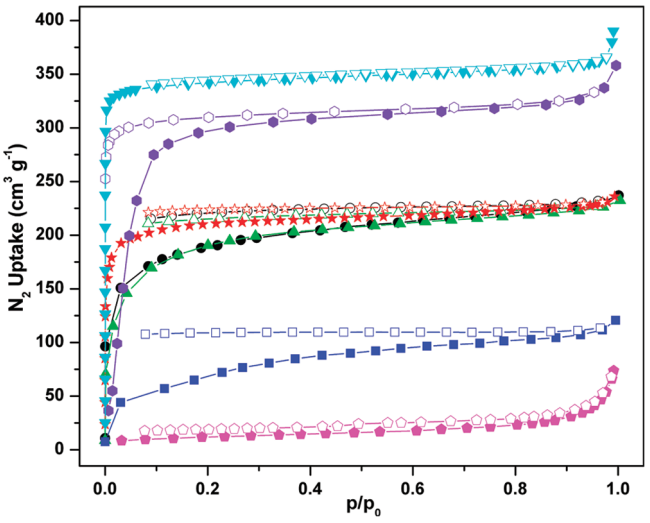

Figure 4. Low pressure N_2 adsorption (solid symbols) and desorption (empty symbols) isotherms of the thermally activated **1-Cl** (black, circles), **2-Br** (blue, squares), **3-CH_3** (green, triangles), **4-NO_2** (red, stars), **5-$(OH)_2$** (magenta, pentagons), Al-MIL-53-NH_2 (violet, hexagons), and Al-MIL-53 (cyan, upside-down triangles) measured at −196 °C.

Figures S21−S23) transform almost completely into their NP-forms after staying at room temperature for 0.15, 20, and 25 h, respectively. However, the transformation of a mixture of HT and NP-forms of **3-CH_3** (Supporting Information, Figure S24) into its NP-form remains incomplete, even after staying at ambient conditions for 23 h.

The introduction of different functionalities into the organic linkers of the frameworks thus influences the breathing phenomena of Al-MIL-53-X compounds. Notably, molecular mechanics simulations on the recently reported Fe-MIL-53-X compounds show that materials which easily convert from NP to LP-form (-CH_3, -$(CF_3)_2$) have free μ_2-OH groups, whereas the more energetically stable NP materials (-Cl, -Br, -NH_2, -$(OH)_2$) possess μ_2-OH groups that are involved in inorganic−organic intraframework H-bonds.[19] Therefore, a combination of guest-framework and intraframework H-bonding interactions effected by the attached functional groups may be attributed for the different breathing properties of the Al-MIL-53-X compounds. Compared to the here presented compounds, no significant breathing behavior during TDXRPD experiments was observed for the Fe-MIL-53-X compounds, which remain in their NP-forms in both dry and hydrated states, rendering the pores inaccessible to N_2.[19]

Sorption Properties. With the exception of **5-$(OH)_2$** the N_2 sorption measurements performed with the thermally activated Al-MIL-53-X compounds reveal type-I adsorption isotherms, but hysteresis is present for all functionalized compounds (Figure 4). The micropore volumes (Table 2) derived from the N_2 adsorption isotherms exhibit considerable porosities, which are lower than the one reported for nonfunctionalized Al-MIL-53.[13] Among the presented five compounds, **4-NO_2** adsorbs the highest amount of N_2. The N_2 accessible micropore volumes at a p/p_0 value of 0.9 decrease in the sequence: **4-NO_2** > **1-Cl** = **3-CH_3** > **2-Br** > **5-$(OH)_2$**. The lower N_2 uptake of **2-Br** compared to **1-Cl** and **3-CH_3** is probably due to the steric bulkiness of the −Br group compared to the −Cl and −CH_3

Table 2. Micropore Volumes[c] of the Al-MIL-53-X Solids Determined from N_2 and H_2O Adsorption Isotherms

compound	micropore volume (N_2; $cm^3\ g^{-1}$)	micropore volume (H_2O; $cm^3\ g^{-1}$)
1-Cl	0.32	0.14
2-Br	0.14	0.11
3-CH_3	0.32	0.11
4-NO_2	0.34	0.12
5-$(OH)_2$	0.07	0.42
Al-MIL-53	0.54	
Al-MIL-53-NH_2	0.44	0.10

[c] The micropore volumes of the Al-MIL-53-X compounds have been calculated at a p/p_0 value of 0.9.

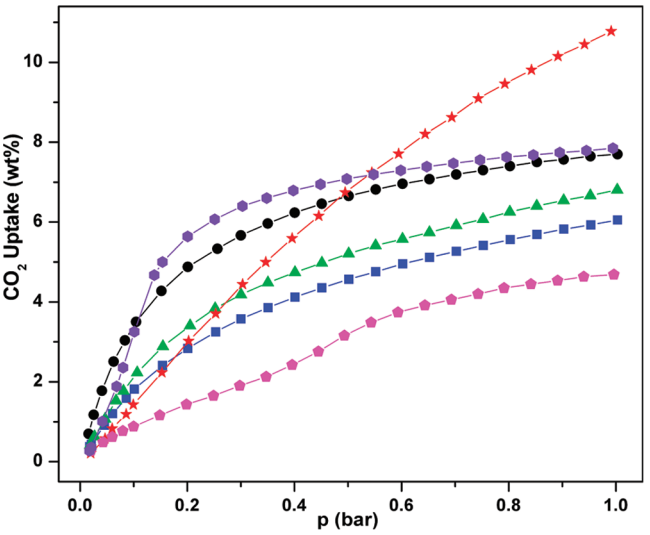

Figure 5. CO_2 adsorption isotherms of the thermally activated **1-Cl** (black, circles), **2-Br** (blue, squares), **3-CH_3** (green, triangles), **4-NO_2** (red, stars), **5-$(OH)_2$** (magenta, pentagons), and Al-MIL-53-NH_2 (violet, hexagons) measured at 25 °C.

functionalities. The inability of **5-$(OH)_2$** to show any N_2 uptake can be attributed to strong intraframework interactions [see TDXRPD patterns (Figure 3)]. Noticeably, **5-$(OH)_2$** has the smallest unit cell volume (Table 1) among the NP-forms of the five title compounds. The pores of the NP-form of **5-$(OH)_2$**, which are inaccessible to N_2, becomes clearly accessible to other gases having smaller kinetic diameters[59] and different adsorptive-framework interactions compared to N_2 (e.g., CO_2 and H_2O, Figures 5 and 6). Notably, the previously reported Al-MIL-53-NH_2 compound showed N_2 uptake higher than that of the presented five compounds.

The CO_2 adsorption properties of the thermally activated Al-MIL-53-X compounds were investigated at 25 °C up to 1 bar. As shown in Figure 5, the CO_2 adsorption isotherms of all compounds, except **5-$(OH)_2$**, follow type-I behavior in the pressure range from 0 to 1 bar. The deviation of the CO_2 adsorption isotherm of **5-$(OH)_2$** from type-I can be tentatively assigned to the breathing effect of its framework, which depends on the CO_2 pressure.

Adsorption isotherm of similar shape have been previously observed for parent M-MIL-53 (M = Al or Cr)[21−23] and Al-MIL-

dx.doi.org/10.1021/ic201219g |Inorg. Chem. 2011, 50, 9518–9526

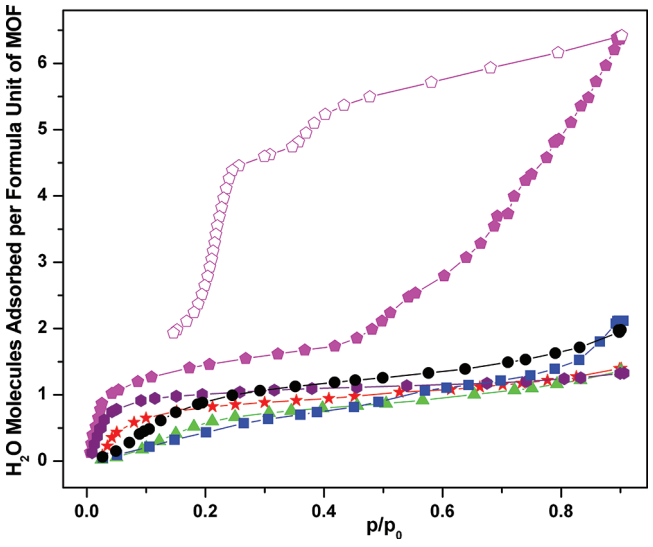

Figure 6. H_2O adsorption (solid symbols) and desorption (empty symbols) isotherms of the thermally activated **1-Cl** (black, circles), **2-Br** (blue, squares), **3-CH_3** (green, triangles), **4-NO_2** (red, stars), **5-$(OH)_2$** (magenta, pentagons), and Al-MIL-53-NH_2 (violet, hexagons) measured at 25 °C. The H_2O desorption isotherms for the thermally activated **1-Cl**, **2-Br**, **3-CH_3**, and **4-NO_2** (Supporting Information, Figure S25) are omitted for clarity.

53-NH_2[25,29] during high pressure CO_2 sorption studies. The descending order of CO_2 uptake values (wt %) at 1 bar is **4-NO_2** (10.8) > **1-Cl** (7.7) > **3-CH_3** (6.8) > **2-Br** (6.0) > **5-$(OH)_2$** (4.7). This CO_2 uptake sequence is in good agreement with the N_2 uptake trend of the compounds. In the pressure range 0.01−0.5 bar, Al-MIL-53-NH_2 captures the highest amount of CO_2 compared to the other compounds. This is due to the availability of CO_2 adsorption sites provided by the appended -NH_2 groups, as recently suggested by Stavitski et al.[28] and Torrisi et al.[60] based on computational studies. At 1 bar, the CO_2 uptake (7.85 wt %) of Al-MIL-53-NH_2, which has higher micropore volume than the presented compounds, exceeds that of **1-Cl**, **2-Br**, **3-CH_3**, and **5-$(OH)_2$**, but falls below that of **4-NO_2**. This fact can be attributed to the difficulty of opening the pores of Al-MIL-53-NH_2 at 1 bar and room temperature, which is in agreement with the temperature versus CO_2 pressure phase diagram of the compound derived by Denayer and co-workers.[29] Compared to unfunctionalized Al-MIL-53, the phase diagram of Al-MIL-53-NH_2 shows a larger stability domain of the NP form, which has been attributed to the increased affinity of the $-NH_2$ groups for CO_2. The computer simulations of Torrisi et al.[60] also claim that **5-$(OH)_2$** in its LP-form should adsorb the maximum amounts of CO_2 in the pressure range 0.01−0.5 bar, which is contrary to our observation. It should be noted that the simulations were performed on the LP-form of **5-$(OH)_2$**. However, both N_2 sorption and TDXRPD measurements show that the pores of **5-$(OH)_2$** are difficult to open probably because of several H-bonding interactions involving −OH functionalities. The fact that the NP-form of MIL-53 structure bearing BDC-$(OH)_2$ as a bridging ligand is energetically more stable than its LP-form has recently been predicted and in fact observed by Devic et al.[19] for Fe-MIL-53-$(OH)_2$ compound.

The H_2O adsorption−desorption properties (Figures 6 and Supporting Information, Figure S25) of the thermally activated Al-MIL-53-X compounds were examined at 25 °C. The H_2O accessible micropore volumes ($cm^3\ g^{-1}$) at a p/p_0 value of 0.9 decrease in the sequence: **5-$(OH)_2$** > **1-Cl** > **4-NO_2**> **2-Br** = **3-CH_3** (Table 2). This H_2O uptake trend is contrary to that observed during the N_2 and CO_2 sorption analyses of the compounds. The water-framework interactions (H-bonds) rather than availability of N_2 accessible micropore volume may be attributed for this trend. Whereas the less hydrophilic pore surfaces of **1-Cl**, **2-Br**, **3-CH_3**, **4-NO_2**, and Al-MIL-53-NH_2 show lower H_2O uptake (1−2 molecules per formula unit at p/p_0 = 0.9), the more hydrophilic pore surface of **5-$(OH)_2$** allows to capture six H_2O molecules per formula unit at p/p_0 = 0.9. The high H_2O uptake capacity of **5-$(OH)_2$** is consistent with the possibility of H-bonds between attached −OH groups and adsorbed water molecules. Upon adsorption of large amounts of H_2O, **5-$(OH)_2$** transforms from a NP-form (unit cell volume: 955 $Å^3$) into a water-rich (**5-$(OH)_2$-H_2O**) or LP-form (unit cell volume: 1365 $Å^3$) (Table 1). It is noteworthy that high water uptake comparable to that of **5-$(OH)_2$** has recently been reported by Devic et al. for Fe-MIL-53-$(OH)_2$ compound.[19]

The H_2O adsorption−desorption isotherms of **5-$(OH)_2$** display a wide hysteresis loop. The adsorption of H_2O on **5-$(OH)_2$** proceeds in two steps: after a very fast uptake (one H_2O molecule per formula unit) below the p/p_0 value of 0.1, the isotherm reaches its first plateau between the p/p_0 values 0.1 and 0.4, followed by an adsorption of five additional H_2O molecules per formula unit between the p/p_0 values 0.4 and 0.9. This type of unusual phenomenon has been previously observed during the high-pressure CO_2 sorption analysis of nonmodified M-MIL-53 (M = Al or Cr)[21−23] and Al-MIL-53-NH_2[25,29] can be interpreted based on the following hypothesis. After adsorption of the first portion of water, the degassed solid remains in NP-form similar to the hydrated material. At higher vapor pressures, the framework opens up and takes up additional H_2O molecules into the pores.

CONCLUSIONS

The synthesis, characterization, and structural analysis of five isoreticular functionalized flexible Al-MIL-53-X hybrid solids have been demonstrated. TGA and TDXRPD experiments carried out on the NP-form of the compounds show high thermal stability in the range 325−500 °C. Compared to the isotypic functionalized Fe-MIL-53-X solids,[19] most of the present compounds display significant microporosity toward N_2, CO_2, or H_2O. As expected from previous studies on the nonmodified parent Al-MIL-53,[13] all the functionalized frameworks retain their structural flexibility upon dehydration−rehydration. However, a complex combination of guest-framework and possible intraframework H-bonding interactions caused by the grafted functional groups leads to different breathing behavior. Finally, the study of the adsorption of various gases and water showed that the pore opening is selective and strongly depends on intraframework H-bonding and adsorptive-framework interactions, making these inexpensive, nontoxic, lightweight, and hydrolytically stable solids potential candidates for applications such as gas storage, catalysis, separations, drug delivery, and sensors, which can be envisaged from the larger accessibility of the pores in their open forms.

ASSOCIATED CONTENT

Supporting Information. XRPD patterns, IR spectra, TG curves, detailed H_2O sorption isotherms, tables containing TGA

results, elemental analysis, and IR frequencies. This material is available free of charge via the Internet at http://pubs.acs.org.

AUTHOR INFORMATION

Corresponding Author

*E-mail: stock@ac.uni-kiel.de. Phone: (+)49-4318801675. Fax: (+)49-4318801775.

ACKNOWLEDGMENT

The State of Schleswig-Holstein and the Deutsche Forschungsgemeinschaft (DFG, SPP 1362 "Porous Metal-Organic Frameworks" under the grant STO 643/5-1) are gratefully acknowledged for the financial support. We thank Dr. Thomas Devic (UVSQ, Versailles) for fruitful discussion concerning the results of the MIL-53-$(OH)_2$ data. The research leading to these results has received funding from the European Community's Seventh Framework Programme (FP7/2007-2013) under grant agreement no. 228862.

REFERENCES

(1) Férey, G. *Chem. Soc. Rev.* **2008**, *37*, 191.
(2) Kitagawa, S.; Kitaura, R.; Noro, S. *Angew. Chem., Int. Ed.* **2004**, *43*, 2334.
(3) Yaghi, O. M.; O'Keeffe, M.; Ockwig, N. W.; Chae, H. K.; Eddaoudi, M.; Kim, J. *Nature* **2003**, *423*, 705.
(4) Lee, J.; Farha, O. K.; Roberts, J.; Scheidt, K. A.; Nguyen, S. T.; Hupp, J. T. *Chem. Soc. Rev.* **2009**, *38*, 1450.
(5) Ma, L.; Abney, C.; Lin, W. *Chem. Soc. Rev.* **2009**, *38*, 1248.
(6) Murray, L. J.; Dinca, M.; Long, J. R. *Chem. Soc. Rev.* **2009**, *38*, 1294.
(7) Li, J.-R.; Kuppler, R. J.; Zhou, H.-C. *Chem. Soc. Rev.* **2009**, *38*, 1477.
(8) Hamon, L.; Llewellyn, P. L.; Devic, T.; Ghoufi, A.; Clet, G.; Guillerm, V.; Pirngruber, G. D.; Maurin, G.; Serre, C.; Driver, G.; van Beek, W.; Jolimaitre, E.; Vimont, A.; Daturi, M.; Férey, G. *J. Am. Chem. Soc.* **2009**, *131*, 17490.
(9) Taylor-Pashow, K. M. L.; Della Rocca, J.; Xie, Z. G.; Tran, S.; Lin, W. B. *J. Am. Chem. Soc.* **2009**, *131*, 14261.
(10) Horcajada, P.; Chalati, T.; Serre, C.; Gillet, B.; Sebrie, C.; Baati, T.; Eubank, J. F.; Heurtaux, D.; Clayette, P.; Kreuz, C.; Chang, J. S.; Hwang, Y. K.; Marsaud, V.; Bories, Y.-N.; Cynober, L.; Gil, S.; Férey, G.; Couvreur, P.; Gref, R. *Nat. Mater.* **2010**, *9*, 172.
(11) Serre, C.; Millange, F.; Thouvenot, C.; Nogues, M.; Marsolier, G.; Louer, D.; Ferey, G. *J. Am. Chem. Soc.* **2002**, *124*, 13519.
(12) Whitfield, T. R.; Wang, X.; Liu, L.; Jacobson, A. J. *Solid State Sci.* **2005**, *7*, 1096.
(13) Loiseau, T.; Serre, C.; Huguenard, C.; Fink, G.; Taulelle, F.; Henry, M.; Bataille, T.; Férey, G. *Chem.—Eur. J.* **2004**, *10*, 1373.
(14) Vougo-Zanda, M.; Huang, J.; Anokhina, E.; Wang, X.; Jacobson, A. J. *Inorg. Chem.* **2008**, *47*, 11535.
(15) Anokhina, E. V.; Vougo-Zanda, M.; Wang, X.; Jacobson, A. J. *J. Am. Chem. Soc.* **2005**, *127*, 15000.
(16) Férey, G.; Serre, C. *Chem. Soc. Rev.* **2009**, *38*, 1380.
(17) Millange, F.; Guillou, N.; Walton, R. I.; Grenèche, J. M.; Margiolaki, I.; Férey, G. *Chem. Commun.* **2008**, 4732.
(18) Volkringer, C.; Loiseau, T.; Guillou, N.; Férey, G.; Elkaïm, E.; Vimont, A. *Dalton Trans.* **2009**, 2241.
(19) Devic, T.; Horcajada, P.; Serre, C.; Salles, F.; Maurin, G.; Moulin, B.; Heurtaux, D.; Clet, G.; Vimont, A.; Grenèche, J.-M.; Le Ouay, B.; Moreau; Magnier, E.; Filinchuk, Y.; Marrot, J.; Lavalley, J.-C.; Daturi, M.; Férey, G. *J. Am. Chem. Soc.* **2010**, *132*, 1127.
(20) Millange, F.; Serre, C.; Guillou, N.; Férey, G.; Walton, R. I. *Angew. Chem., Int. Ed.* **2008**, *47*, 4100.
(21) Serre, C.; Bourrelly, S.; Vimont, A.; Ramsahye, N. A.; Maurin, G.; Llewellyn, P. L.; Daturi, M.; Filinchuk, Y.; Leynaud, O.; Barnes, P.; Férey, G. *Adv. Mater.* **2007**, *19*, 2246.
(22) Bourrelly, S.; Llewellyn, P. L.; Serre, C.; Millange, F.; Loiseau, T.; Férey, G. *J. Am. Chem. Soc.* **2005**, *127*, 13519.
(23) Boutin, A.; Coudert, F.-X.; Springuel-Huet, M.-A.; Neimark, A. V.; Férey, G.; Fuchs, A.-H. *J. Phys. Chem. C* **2010**, *114*, 22237.
(24) Boutin, A.; Couck, S.; Coudert, F.-X.; Serra-Crespo, P.; Gascon, J.; Kapteijn, F.; Fuchs, A. H.; Denayer, J. F. M. *Microporous Mesoporous Mater.* **2011**, *140*, 108.
(25) Couck, S.; Denayer, J. F. M.; Baron, G. V.; Rémy, T.; Gascon, J.; Kapteijn, F. *J. Am. Chem. Soc.* **2009**, *131*, 6326.
(26) V. Finsy, V.; Maa, L.; Alaerts, L.; De Vos, D. E.; Baron, G. V.; Denayer, J. F. M. *Microporous Mesoporous Mater.* **2009**, *120*, 221.
(27) Salles, F.; Ghoufi, A.; Maurin, G.; Bell, R. G.; Mellot-Draznieks, C.; Férey, G. *Angew. Chem., Int. Ed.* **2008**, *47*, 8487.
(28) Stavitski, E.; Pidko, E. A.; Couck, S.; Remy, T.; Hensen, E. J. M.; Weckhuysen, B. M.; Denayer, J.; Gascon, J.; Kapteijn, F. *Langmuir* **2011**, *27*, 3970.
(29) Boutin, A.; Couck, S.; Coudert, F.-X.; Serra-Crespo, P.; Gascon, J.; Kapteijn, F.; Fuchs, A. H.; Denayer, J. F. M. *Microporous Mesoporous Mater.* **2011**, *140*, 108.
(30) Llewellyn, P. L.; Maurin, G.; Devic, T.; Loera-Serna, S.; Rosenbach, N.; Serre, C.; Bourrelly, S.; Horcajada, P.; Filinchuk, Y.; Férey, G. *J. Am. Chem. Soc.* **2008**, *130*, 12808.
(31) Couck, S.; Rémy, T.; Baron, G. V.; Gascon, J.; Kapteijn, F.; Denayer, J. F. M. *Phys. Chem. Chem. Phys.* **2010**, *12*, 9413.
(32) Llewellyn, P. L.; Horcajada, P.; Maurin, G.; Devic, T.; Rosenbach, N.; Bourrelly, S.; Serre, C.; Vincent, D.; Loera-Serna, S.; Filinchuk, Y.; Férey, G. *J. Am. Chem. Soc.* **2009**, *131*, 13002.
(33) Trung, T. K.; Trens, P.; Tanchoux, N.; Bourrelly, S.; Llewellyn, P. L.; Loera-Serna, S.; Serre, C.; Loiseau, T.; Fajula, F.; Férey, G. *J. Am. Chem. Soc.* **2008**, *130*, 16926.
(34) Alaerts, L.; Maes, M.; Giebeler, L.; Jacobs, P. A.; Martens, J. A.; Denayer, J. F. M.; Kirschhock, C. E. A.; De Vos, D. E. *J. Am. Chem. Soc.* **2008**, *130*, 14170.
(35) Finsy, V.; Kirschhock, C. E. A.; Vedts, G.; Maes, M.; Alaerts, L.; De Vos, D. E.; Baron, G. V.; Denayer, J. F. M. *Chem.—Eur. J.* **2009**, *15*, 7724.
(36) Bauer, S.; Serre, C.; Devic, T.; Horcajada, P.; Marrot, J.; Férey, G.; Stock, N. *Inorg. Chem.* **2008**, *47*, 7568.
(37) Sanselme, M.; Grenèche, J.-M.; Riou-Cavellec, M.; Férey, G. *Solid State Sci.* **2004**, *6*, 853.
(38) Volkringer, C.; Popov, D.; Loiseau, T.; Férey, G.; Burghammer, M.; Riekel, C.; Haouas, M.; Taulelle, F. *Chem. Mater.* **2009**, *21*, 5695.
(39) Loiseau, T.; Lecroq, L.; Volkringer, C.; Marrot, J.; Férey, G.; Haouas, M.; Taulelle, F.; Bourrelly, S.; Llewellyn, P. L.; Latroche, M. *J. Am. Chem. Soc.* **2006**, *128*, 10223.
(40) Volkringer, C.; Popov, D.; Loiseau, T.; Guillou, N.; Férey, G.; Haouas, M.; Taulelle, F.; Mellot-Draznieks, C.; Burghammer, M.; Riekel, C. *Nat. Mater.* **2007**, *6*, 760.
(41) Gascon, J.; Aktay, U.; Hernandez-Alonso, M. D.; van Klink, G. P. M.; Kaptejin, F. *J. Catal.* **2009**, *261*, 75.
(42) Stavitski, E.; Pidko, E. A.; Couck, S.; Remy, T.; Hensen, E. J. M.; Weckhuysen, B. M.; Denayer, J.; Gascon, J.; Kapteijn, F. *Langmuir* **2011**, *27*, 3970.
(43) Ahnfeldt, T.; Gunzelmann, D.; Loiseau, T.; Hirsemann, D.; Senker, J.; Férey, G.; Stock, N. *Inorg. Chem.* **2009**, *48*, 3057.
(44) Himsl, D.; Wallacher, D.; Hartmann, M. *Angew. Chem., Int. Ed.* **2009**, *48*, 4639.
(45) Volkringer, C.; Loiseau, T.; Guillou, N.; Férey, G.; Haouas, M.; Taulelle, F.; Elkaim, E.; Stock, N. *Inorg. Chem.* **2010**, *49*, 9852.
(46) Comotti, A.; Bracco, S.; Sozzani, P.; Horike, S.; Matsuda, R.; Chen, J.; Takata, M.; Kubota, Y.; Kitagawa, S. *J. Am. Chem. Soc.* **2008**, *130*, 13664.
(47) Garibay, S. J.; Wang, Z.; Cohen, S. M. *Inorg. Chem.* **2010**, *49*, 8086.
(48) Volkringer, C.; Cohen, S. M. *Angew. Chem., Int. Ed.* **2010**, *49*, 4644.

(49) Nguyen, J. G.; Cohen, S. M. *J. Am. Chem. Soc.* **2010**, *132*, 4560.
(50) Meilikhov, M.; Yusenko, K.; Fischer, R. A. *J. Am. Chem. Soc.* **2009**, *131*, 9644.
(51) Meilikhov, M.; Yusenko, K.; Fischer, R. A. *Dalton Trans.* **2010**, *39*, 10990.
(52) Meilikhov, M.; Yusenko, K.; Fischer, R. A. *Dalton Trans.* **2009**, 600.
(53) Boultif, A.; Louer, D. *J. Appl. Crystallogr.* **1991**, *24*, 987.
(54) *STOE WinXPOW*, version 2.11; Stoe & Cie GmbH: Darmstadt, Germany, 2005.
(55) Banwell, C. N.; McCash, E. M. *Fundamentals of Molecular Spectroscopy*; McGraw Hill: New York, 1994.
(56) Costentin, C.; Robert, M.; Saveant, J. M. *J. Am. Chem. Soc.* **2006**, *128*, 8726.
(57) Barthelet, K.; Marrot, J.; Riou, D.; Férey, G. *Angew. Chem., Int. Ed.* **2002**, *41*, 281.
(58) Guillou, N.; Millange, F.; Walton, R. I. *Chem. Commun.* **2011**, *47*, 713.
(59) Li, J.-R.; Kuppler, R. J.; Zhou, H. C. *Chem. Soc. Rev.* **2009**, *38*, 1477.
(60) Torrisi, A.; Bell, R. G.; Mellot-Draznieks, C. *Cryst. Growth Des.* **2010**, *10*, 2839.

4.1.3 Structural Phase Transitions and Thermal Hysteresis in the Metal-Organic Framework Compound Al-MIL-53 as Studied by Electron Spin Resonance Spectroscopy

Der Beitrag wurde in „The Journal of Physical Chemistry“ im Jahr 2010 veröffentlicht und beschreibt die Untersuchung des temperaturgesteuerten Phasenübergangs einer dehydratisierten Al-MIL-53-Verbindung mittels ESR-Spektroskopie. Die Zusatzinformation zu diesem Beitrag befindet sich im Anhang 3 auf Seite 177.

Zur Untersuchung des Phasenüberganges von Al-MIL-53 (geschlossenporige Form/ offenporige Form) wurde Al-MIL-53 mit einem geringen Anteil an Chrom(III)-Ionen dotiert. Das Einbringen der Chrom(III)-Ionen in das Gerüst von Al-MIL-53 konnte mittels ESR und ENDOR-Spektroskopie (Elektron-Kern Doppelresonanz) nachgewiesen werden. Die charakteristische Feinstrukturaufspaltung der Chrom(III)-Ionen im Magnetfeld in Abhängigkeit von ihrer chemischen Umgebung ermöglichte es, mithilfe der ESR-Spektroskopie den temperaturgesteuerten Phasenübergang von der offen- in die geschlossenporige Form zu untersuchen. Der Übergang wurde in dem Temperaturbereich von 150 – 60 K beobachtet, während die Rückumwandlung in die offenporige Form in einem wesentlich kleineren Temperaturfenster von 330 – 375 K auftrat. Diese Ergebnisse sind konsistent mit unabhängig durchgeführten Neutronenbeugungsexperimenten an undotierten Al-MIL-53. Für die Herstellung des Cr(III)-dotierten Al-MIL-53 wurden die aus der Literatur bekannten Syntheseparameter von Al-MIL-53 verwendet und 3 Prozent des eingesetzten $Al(NO_3)_3 \cdot 6H_2O$ durch $Cr(NO_3)_3 \cdot 9H_2O$ ersetzt. Das erhaltene Produkt Al/Cr-MIL-53 (as) ($[Al_{1-y}/Cr_y(OH)(BDC)] \cdot xH_2BDC$ (mit $y < 0.1$)) wurde im Anschluss zur Entfernung der in den Poren eingelagerten freien Terephthalsäureeinheiten bei 430 °C kalziniert und mittels Röntgenpulverbeugung charakterisiert.

Structural Phase Transitions and Thermal Hysteresis in the Metal−Organic Framework Compound MIL-53 As Studied by Electron Spin Resonance Spectroscopy

Matthias Mendt,[†] Bettina Jee,[†] Norbert Stock,[‡] Tim Ahnfeldt,[‡] Martin Hartmann,[§] Dieter Himsl,[§] and Andreas Pöppl*,[†]

Fakultät für Physik und Geowissenschaften, Universität Leipzig, Linnéstr. 5, D-04103 Leipzig, Germany, Institut für Anorganische Chemie, Christian-Albrechts-Universität Kiel, Max-Eyth-Str. 2, D-24118 Kiel, Germany, and Erlangen Catalysis Resource Center (ECRC), Friedrich-Alexander Universität Erlangen-Nürnberg, Egerlandstr. 3, D-91058 Erlangen, Germany

Received: August 9, 2010; Revised Manuscript Received: September 30, 2010

The dehydrated aluminum form of the metal−organic framework compound MIL-53 shows a temperature-driven phase transition with pronounced structural hysteresis as recently shown by neutron diffraction and scattering experiments (Liu et al. *J. Am. Chem. Soc.* **2008**, *130*, 11813). Thereby, the structure of the corner-sharing metal $AlO_4(OH)_2$ octahedra differs in terms of local symmetry for the dehydrated MIL-53(Al) material in its high- and low-temperature form with open or closed pore structure, respectively. In this work, some of the framework aluminum ions were exchanged by chromium(III) to introduce an electron spin resonance (ESR) active probe ion. The resulting material was investigated by means of ESR and electron nuclear double resonance (ENDOR) spectroscopy to verify the incorporation of chromium at the octahedral framework sites. In addition, variable-temperature ESR measurements were performed to analyze the temperature-dependent phase behavior of the doped MIL-53 material. The Cr(III) ions have an electron spin $S = {}^3/_2$ which shows a characteristic fine structure interaction depending very sensitively on the local symmetry of the chromium site. Therefore, the fine structure splitting of the Cr(III) probe ions allows for a concise elucidation of changes in the local symmetry at the $CrO_4(OH)_2$ octahedra which occur upon structural transitions. In agreement with results from neutron experiments, the transformation from the open to the closed pore structure was found to occur in the temperature range between 150 and 60 K whereas the back transformation is taking place within a smaller temperature interval between 330 and 375 K.

1. Introduction

Metal−organic framework (MOF) compounds have triggered considerable research efforts in the past decade since the pioneering work by Yaghi et al.,[1,2] Férey et al.,[3] and Kitagawa et al.[4] In general, these coordination polymers are composed of two basic structural building units, an inorganic node (usually a single metal center or a multinuclear moiety) and connecting organic linker molecules, such as di- or tricarboxylic acid.[4] Characteristic features of these porous coordination polymers are a crystalline three-dimensional open framework with usually large specific surface area and pore volume as well as a high degree of structural diversity. These specific material properties can be controlled by use of countless combinations of different organic linkers and inorganic building units making MOFs attractive materials in particular for potential applications in gas storage,[5,6] separation by selective adsorption,[7−9] and catalysis.[10,11] In these application areas, MOF compounds are promising alternatives for conventional inorganic zeolite or porous carbon-based molecular sieves. However, MOF compounds offer new additional material properties that go beyond those of the above-mentioned conventional classes of porous materials. The possibility to synthesize MOFs with a variety of main group, transition or rare earth metals as structure metal and a broad range of different organic linker molecules allows the fabrication of tailor-made porous materials with, e.g., selected magnetic, optical, or electrical properties for various sensing applications.[4,12]

Besides these prospects, one of the most astonishing features of certain MOF compounds is the so-called "breathing" effect that has been observed for a number of porous coordination polymers.[13] Famous examples are MIL-47,[14] MIL-53,[15−20] and MIL-88.[21] Although all of the aforementioned crystalline porous materials feature a three-dimensional framework, their crystal structure changes upon adsorption and desorption of guest molecules. These adsorption/desorption-driven structural phase transitions are reversible and lead to a drastic decrease or increase of the shape, size, and related volume of the internal pores. So far, the most intensive studies concerning the breathing effect were concentrated on MIL-53-type materials.[15] MIL-53(M) is built from infinite chains of corner-sharing metal $MO_4(OH)_2$ (M = Cr(III),[15,16] Fe(III),[17] or Al(III)[19]) octahedra interconnected by benzenedicarboxylate (bdc) linkers resulting in a 3D metal−organic framework featuring porous channels. Here, the corner-sharing metal octahedra in the chains are linked by μ_2-OH bridging hydroxy groups.[15−20] The as-synthesized MIL-53 material has an orthorhombic crystal structure with space group *Pnma*[15,16,19] where the pores are occupied by disordered uncoordinated terephthalic acid molecules. These can be removed together with residual solvent or water molecules by calcination at 330 °C in air, yielding a material with an orthorhombic crystal structure (*Imma*, except for the Fe analogue of MIL-53) featuring a porous structure with free diameters of 0.85 nm (Figure 1a).[15,16,19] However, after readsorption of water, MIL-53(M = Al, Cr) adopts a monoclinic crystal structure

* Corresponding author. E-mail: poeppl@physik.uni-leipzig.de.
[†] Universität Leipzig.
[‡] Christian-Albrechts-Universität Kiel.
[§] Friedrich-Alexander Universität Erlangen-Nürnberg.

10.1021/jp107487g
Published on Web 10/26/2010

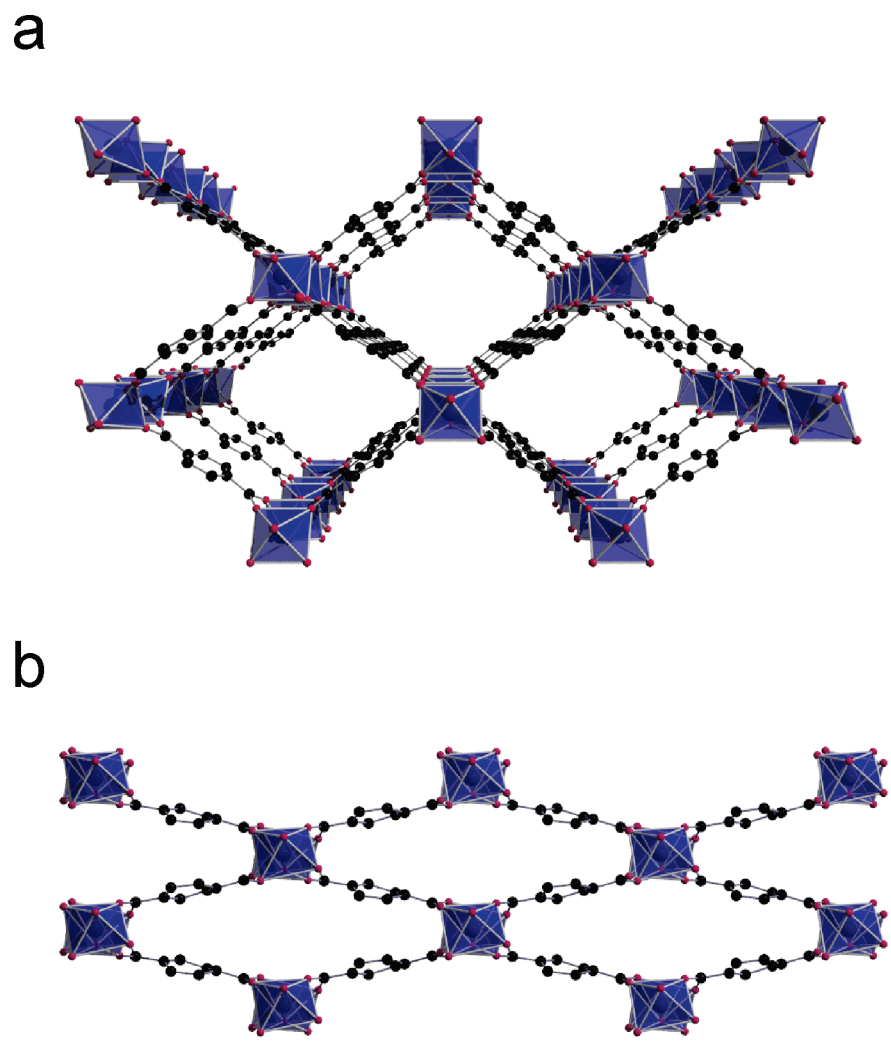

Figure 1. Schematic representation of the MIL-53(Al) structure with its 1D channel system: (a) HT phase, and (b) LT phase (blue, AlO_6 octahedra; red, oxygen; black, carbon; hydrogens have been omitted). Structural data were taken from Liu et al.[20]

(space group *C*2/*c*) accompanied by a shrinkage of the unit cell and a substantial contraction of the pores[15,16,19] (Figure 1b), presumably caused by an hydrogen-bond interaction between the water molecules and the framework oxygens of the carboxylate and the μ_2-OH bridging hydroxy groups.[8] In line with previous publications,[15,16,19] we denote the open structure of MIL-53 as the high-temperature (HT) phase and the contracted structure as the low-temperature (LT) phase.

Recently, Liu et al.[22] showed by neutron powder diffraction (NPD) and inelastic neutron scattering (INS) experiments that the transformation between the HT and LT phase of dehydrated MIL-53 (Al) can be reversibly triggered by temperature variation alone without adsorption and desorption of guest molecules. The phase transition shows a large temperature hysteresis. The transition from the HT into LT phase occurred upon cooling from room temperature between 125 and 150 K, whereas temperatures up to 325−375 K were required for the back transformation from the LT to the HT phase. Adsorbate and also temperature-induced phase transitions in MIL-53 (Al) have been likewise observed by ^{129}Xe nuclear magnetic resonance (NMR) spectroscopy[23] at low Xe loading and allowed a spectroscopic quantification of this phenomenon for the first time.

In this work, a chromium(III)-doped structural analogue of MIL-53(Al), i.e., where some of the framework aluminum ions were exchanged by chromium to incorporate an electron spin resonance (ESR) active probe ion in the otherwise ESR silent material, was synthesized. The successful substitution of some octahedral aluminum sites by chromium was explored and verified by ESR and electron nuclear double resonance (ENDOR) spectroscopy. The Cr(III) ions have an electron spin $S = {}^3/_2$ which shows a characteristic zero-field splitting (zfs) for a Cr(III) site of lower than cubic symmetry.[24] Crystal structure analyses[16,22] revealed that the local symmetry of the corner-sharing metal $MO_4(OH)_2$ octahedra differ for the as-synthesized MIL-53 (M = Al, Cr) and the HT and LT phases of the dehydrated materials. Therefore, for low Cr(III) concentrations, the zfs is an excellent tool to monitor the local symmetry at the $CrO_4(OH)_2$ octahedra which is closely related to the overall 3D structure of the MIL-53(Al) framework. This feature is utilized to examine the temperature-triggered structural transition of the dehydrated coordination polymer in variable-temperature ESR experiments.

2. Experimental Section

Sample Preparation. The synthesis of Cr(III)-doped aluminum-based MIL-53, in the following denoted by MIL-53(Al/Cr), was performed in a 27 mL Teflon-lined steel bomb. A mixture of $AlCl_3 \cdot 6H_2O$ (1.30 g, 5.4 mmol), $CrNO_3 \cdot 9H_2O$ (0.0139 g, 3.4 mmol), and terephthalic acid (0.5 g, 3.0 mmol) in 5 mL of water (313 mmol) was heated at 210 °C for 48 h.

After filtration, a slightly purple-colored microcrystalline product was obtained.

These as-synthesized MIL-53(Al/Cr)as materials were calcined at 603 K in air for 72 h. For further sample preparation, calcined MIL-53(Al/Cr) material was placed in ESR quartz glass tubes and heated under vacuum (0.01 Pa) at 393 K for 20 h. Subsequently, the sample tubes with the dehydrated MOF materials, denoted by MIL-53(Al/Cr)deh, were cooled down to room temperature and sealed.

Structural and Chemical Characterization. The n_{Al}/n_{Cr} ratio of the sample MIL-53(Al/Cr)deh was determined as 99:1 by inductively coupled plasma optical emission spectroscopy (ICP-OES). The powder X-ray diffraction PXRD patterns of the as-synthesized and the calcined MIL-53(Al/Cr) materials were obtained in the Debye−Scherrer mode on a STADI-P (STOE) equipped with a linear PSD and a Ge(111) monochromator using Cu Kα1 radiation ($\lambda = 154.060$ pm). The samples were placed in 0.5 mm capillaries (No. 14, Hilgenberg). The PXRD pattern of as-synthesized and calcined materials are presented in Figures S1 and S2 in the Supporting Information. The MIL-53(Al/Cr)as sample was measured under ambient conditions and shows in addition to the expected reflections of MIL-53 one weak reflection (marked by an asterisk) which is due to minor impurities of γ-AlOOH (Figure S1, Supporting Information). After calcination, the MIL-53(Al/Cr) sample was likewise measured under ambient conditions and exhibits the typical diffractogram of the narrow pore LT phase of MIL-53(Al) (Figure S2a, Supporting Information). Dehydration of these materials under ambient pressure at 393 K for 20 h results in the typical PXRD pattern of the open pore HT phase of MIL-53(Al) (Figure S2b, Supporting Information). After having performed a complete set of temperature-dependent ESR measurements and finishing with the HT phase, the samples were quickly transferred into capillaries under ambient conditions again and immediately sealed for further XRD measurements. The obtained PXRD patterns (Figure S2c, Supporting Information) demonstrate the presence of the open pore HT phase and some traces of a minor LT phase.

Spectroscopic Measurements. Continuous wave (CW) ESR experiments have been performed on Bruker EMX 10-40 (Q-band, 34 GHz) and ELEXYS E580 (X-band, 9.5 GHz) spectrometers fitted with a cylindrical cavity for Q-band and a rectangular cavity for X-band experiments. For low-temperature experiments (5 K < T < 298 K), Oxford Instruments He cryostats ESR 910 and CF935 were used at X- and Q-band, respectively, whereas measurements at $T > 298$ K have exclusively been done at X-band using a Bruker N_2 flow cryostat ER 4118CV equipped with a ER 4131VT temperature controller. Spectral simulations of the Cr(III) CW ESR powder patterns were performed using the EasySpin ESR simulation package[25] that employs exact numerical diagonalization of the full-spin Hamiltonian matrix. Davies and Mims pulsed ENDOR experiments[26] were performed at Q-band frequencies using a spectrometer with a home-built microwave (mw) pulse unit[27] and the commercial magnet system of the Bruker EMX CW Q-band instrument. For the Davies ENDOR sequence, microwave (mw) pulse lengths of $t_{\pi/2} = 90$ ns and $t_{\pi} = 130$ ns with a pulse delay $\tau = 300$ ns between the second and third mw pulse were used. In the case of Mims ENDOR experiments, the mw pulse lengths were $t_{\pi/2} = 90$ ns and pulse delays $\tau = 300$ ns between the first and second mw pulse were employed. The length of the radiofrequency (rf) pulse was $t_{rf} = 10$ μs in both experiments.

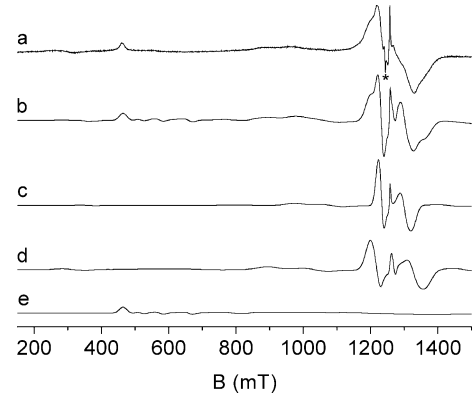

Figure 2. Q-band ESR spectra of MIL-53(Al/Cr)as at 6 K: (a) experimental spectrum, (b) sum of simulated Cr(III) spectra, (c) simulated Cr(III) species A(as), (d) simulated Cr(III) species B(as), and (e) simulated Cr(III) species C(as). The asterisk indicates a free-radical signal.

3. Results and Discussion

As-Synthesized MIL-53(Al/Cr). Cw ESR spectra of the as-synthesized material MIL-53(Al/Cr)as were recorded at X- and Q-band frequencies at 6 and 300 K in order to verify the successful incorporation of the Cr(III) ions into the octahedral framework sites of MIL-53. Figure 2a displays the Q-band CW ESR powder spectrum of MIL-53(Al/Cr)as recorded at 6 K. The spectrum is dominated by the central Cr(III) transition, $M_S = -1/2 \leftrightarrow +1/2$ (M_S = magnetic spin quantum number), at about 1260 mT of a major chromium species A(as), which is split within the limit $D \ll \nu_{mw}$ by second-order perturbation theory[21] into three singularities corresponding to $\theta = 0°$ (1260 mT), $\theta = 42°$ (1320 mT), and $\theta = 90°$ (1210 mT). Here, the microwave frequency is $\nu_{mw} = 34$ GHz, θ defines the angle between the z principal axis of the zfs tensor **D** and the external magnetic field vector $\boldsymbol{B}$, $D_{xx,yy} = 1/3D \pm E$ and $D_{zz} = -2/3D$ are the principal values of the zfs tensor **D** with the axial and rhombic zfs splitting parameters D and E. In the case of transition metal ions such as Cr(III), the zfs splitting is mainly caused by the local crystal field at the ion sites due to spin−orbit coupling.[24] For the MIL-53 structure with its $MO_4(OH)_2$ units the zfs parameters D and E can be considered as a measure for the deviation of the crystal field at Cr(III) sites from octahedral symmetry. Here the axial zfs parameter D measures the tetragonal distortion of the octahedra whereas the rhombic zfs parameter E is very sensitive with respect to orthorhombic distortions or perturbations of even lower symmetry of the local crystal field. In the spectral range of the central $M_S = -1/2 \leftrightarrow +1/2$ Cr(III) transition a further weak signal at 1241 mT is observed from a free radical with $g = 2.005$, presumably caused by some minor traces of residual organic reactants. The broad spectral features from 900 to 1050 mT can be assigned to the $\theta = 90°$ singularities of one of the outer $M_S = \pm 3/2 \leftrightarrow \pm 1/2$ transitions of the spectrum of species A(as). However, a close inspection reveals three bumps in this field range and further bumps at the wings of the central $M_S = -1/2 \leftrightarrow +1/2$ transition. This indicates that the tensor **D** of species A(as) has orthorhombic symmetry, i.e., $E \neq 0$, and, in addition the observed spectrum is actually a superposition of the ESR spectra of the Cr(III) species A(as) with that of a second Cr(III) species B(as) having a somewhat larger zfs parameter D. An additional signal at about 460 mT suggests the presence of a further third Cr(III) species C(as) with considerably larger D values ($D > 20$ GHz). Spectral simulations were performed in order to determine the spin Hamiltonian parameters of the Cr(III) centers in MIL-53(Al/Cr)as more precisely. The Cr(III) powder

TABLE 1: Spin Hamiltonian Parameters g, D, and E of Cr(III) Species and Zfs Strain Parameters ΔD and ΔE (FWHH of Gaussian Distributions) in As-Synthesized MIL-53(Al/Cr)as and Their Relative Contributions P at $T = 6$ K, and $T = 300$ K

Cr^{3+} species	T (K)	g	D (GHz)	E (GHz)	E/D	ΔD (GHz)	ΔE (GHz)	P (%)
A(as)	6	1.978(3)	6.5(4)	0.55(3)	0.085(6)	1.5(4)	0.30(3)	*57(6)*
B(as)	6	1.978(3)	8.5(5)	0.72(5)	0.085(7)	2.0(4)	0.30(3)	*29(5)*
C(as)	6	1.978(3)	>20	>4.9	0.33	>5	–	*14(5)*
A(as)	295	1.978(3)	6.5(4)	0.29(5)	0.044(8)	3.0(4)	0.30(3)	*54(7)*
B(as)	*295*	*1.978(3)*	*8.5(5)*	*0.37(8)*	*0.044(12)*	*2.0(4)*	*0.30(3)*	*31(6)*

spectra were simulated by an exact matrix diagonalization of the conventional spin Hamiltonian

$$\hat{H} = \beta_e \mathbf{B}\mathbf{g}\hat{\mathbf{S}} + \hat{\mathbf{S}}\mathbf{D}\hat{\mathbf{S}} \quad (1)$$

of an $S = {}^3/_2$ ion using the EasySpin ESR simulation package[25] where the hyperfine interaction with the ^{53}Cr isotope (natural abundance 9.55%) was omitted. Here, β_e is the Bohr magneton and $\hat{\mathbf{S}}$ defines the electron spin operator. The electron Zeeman splitting tensor **g** was found to be isotropic within the accuracy (0.2%) of our spectral simulations. For the simulations, uncorrelated Gaussian distributions of the zfs parameters D and E have been assumed with distribution widths ΔD and ΔE (FWHH). The simulated Q-band ESR spectra of the three chromium species A(as), B(as), and C(as) at 6 K are displayed in Figure 2 in comparison to the experimental spectrum. The determined spin Hamiltonian parameters together with relative contribution of each species to the overall spectrum are given in Table 1. The X-band ESR spectra of MIL-53(Al/Cr)as at 6 K can be fitted with the same set of parameters (see Figure S2, Supporting Information), except that a minor impurity signal of Fe(III) ions in their high spin state ($S = {}^5/_2$) with $D > 30$ GHz and $E/D = 0.145$ could be observed at this frequency in addition to the three above-described Cr(III) centers. The Cr(III) species A(as) and B(as) could be likewise detected in the Q-band ESR spectra at 295 K (see Figure S3, Supporting Information) with comparable D but slightly smaller E parameters (Table 1). The poor signal-to-noise ratio prevented the observation of the third species C(as) at 295 K.

According to the crystal structure analysis of both as-synthesized MIL-53(Al)[19] and MIL-53(Cr),[15] the $MO_4(OH)_2$ (M = Cr(III), Al(III)) octahedra have C_i symmetry with three distinctly different M−O bond lengths and slight deviations of the (O, M, O) bond angles from 90°. Thus, we expect a rhombic zfs parameter $E \neq 0$ for the sample MIL-53(Al/Cr)as. The estimated value of the axial zfs parameter D of the two Cr(III) species A(as) and B(as) (Table 1) is typical for distorted (CrO_6) octahedra in crystalline solids.[28] Therefore, it is natural to assign the two species to Cr(III) ions incorporated into the MIL-53 framework at octahedral metal lattice sites. The slightly different zfs parameters D of species A(as) and B(as) indicate some variation in the axial distortion of the $CrO_4(OH)_2$ octahedra. One explanation might be a nonuniform distribution of free terephthalic acid and solvent molecules across the pores resulting in a modulation of the local crystal field exerted upon the chromium ions. The obtained broad distributions in D and E (D and E strains, see Table 1) indicate likewise a substantial variation in the local crystal fields at the Cr(III) octahedron sites due to some structural disorder in the MIL-53(Al/Cr)as sample. At lower temperatures, the ratio E/D is somewhat higher, indicating an increase of the rhombic distortion of the octahedra. Unfortunately, crystal structure data of MIL-53as at low temperatures have not been published yet and an interpretation of the effects described above solely on the basis of ESR data would go beyond the scope of this method. The third species, C(as), has very large values of D and E/D (Table 1) which is indicative of a very distorted Cr(III) site of low coordination symmetry. Therefore, we assign species C(as) to extraframework Cr(III) ions that have not been incorporated in the MIL-53 lattice.

Additional Q-band pulsed ENDOR experiments have been performed at the $\theta = 0°$ edge singularity of the powder pattern of the central $M_S = -{}^1/_2 \leftrightarrow +{}^1/_2$ transition of the Cr^{3+} species A(as) and B(as) in order to probe the nuclear spin environment of the chromium centers and, additionally, to unambiguously prove the assignment of the species A(as) and B(as) to Cr(III) ions incorporated at the metal sites of the corner-sharing $MO_4(OH)_2$ octahedra. For such chromium sites, we expect ^{27}Al ENDOR signals from the aluminum nuclei in the two neighboring octahedra at a distance of about 0.34 nm from the Cr(III). For the ^{1}H ENDOR signals from the bridging benzenedicarboxylate linkers at a shortest distance to the Cr(III) of 0.42 nm can be expected.[15,19] These distances translate into dipolar aluminum and proton hyperfine (hf) coupling parameters[26] of $T^{Al} = 0.53$ MHz and $T^H = 1.11$ MHz, respectively. ^{27}Al and ^{1}H Mims ENDOR spectra of the sample MIL-53(Al/Cr)as (Figure 3) display aluminum and proton ENDOR signals at their respective nuclear Larmor frequencies $\nu_{Al} = 14.02$ MHz and $\nu_H = 53.81$ MHz from weakly coupled nuclei which correspond to hf coupling values of $A^{Al} = 1.25$ MHz and $A^H = 1.3$ MHz. If we assume that the isotropic hf interaction between the chromium ion and the protons of the next but one benzenedicarboxylate linkers can be neglected because of the large Cr−H distances, the measured ^{1}H hf coupling is in good agreement with the calculated value of $T^H = 1.11$ MHz. In the case of aluminum the experimental ^{27}Al hf coupling is larger than the dipolar hf coupling $T^{Al} = 0.53$ MHz calculated from the Cr−Al distances. This suggests that a weak spin density transfer occurs from the Cr(III) ions to the aluminum nuclei in the neighboring $AlO_4(OH)_2$ octahedra resulting in a small isotropic ^{27}Al hf interaction.

In comparison to the remote benzenedicarboxylate protons, the protons from the bridging μ_2-hydroxy groups are at a considerably shorter distance in the second coordination sphere to the chromium ions and allow for some direct overlap of the spin bearing Cr(III) 3d atomic orbitals and the hydrogen 1s orbital. Therefore, such OH moieties coordinating to a paramagnetic transition metal ion may result in significantly larger isotropic proton hf coupling. Indeed, the Davies ENDOR spectrum illustrated in Figure 4 reveals besides the ^{1}H signals from the benzenedicarboxylate protons close to the proton Larmor frequency ν_H two signals from protons with substantial larger hf coupling, $A^H = 12.3$ MHz, that we can assign to the μ_2-OH bridging hydroxy groups. Therefore, we conclude that the ENDOR experiments likewise indicate the successful incorporation of Cr(III) at the octahedral metal sites in the MIL-53 framework. Unfortunately, the very poor signal-to-noise ratio prevented ENDOR experiments at other spectral positions of the Cr(III) ESR spectrum and, consequently, a complete

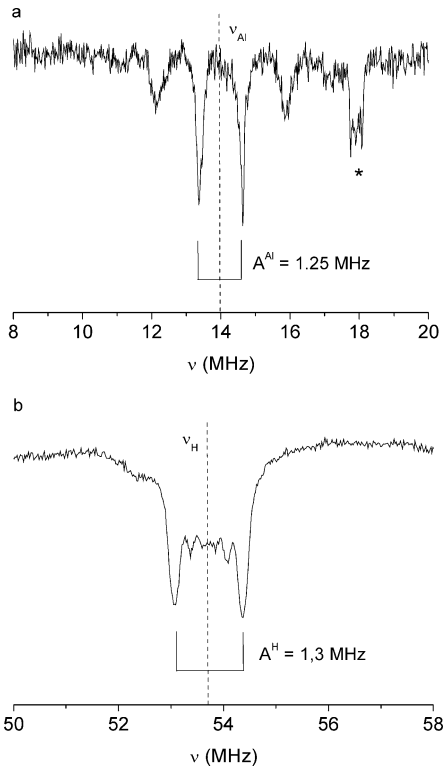

Figure 3. Q-band Mims ENDOR spectra of MIL-53(Al/Cr)as at 8 K recorded at the central $M_S = -1/2 \leftrightarrow +1/2$ transitions of the Cr^{3+} species A(as) and B(as) at 1262.8 mT: (a) ^{27}Al and (b) ^{1}H ENDOR spectrum. The asterisk indicates higher harmonics of the proton ENDOR signals at the free Larmor frequency at $\nu_H = 45.7$ MHz.

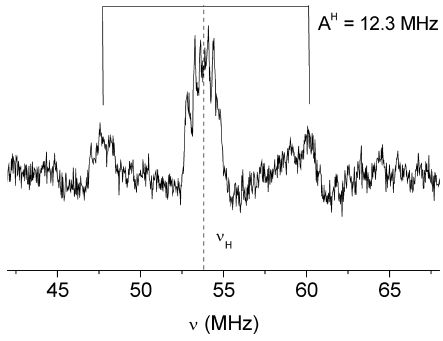

Figure 4. Q-band Davies ENDOR spectrum of MIL-53(Al/Cr)as at 8 K recorded at the central $M_S = -1/2 \leftrightarrow +1/2$ transitions of the Cr^{3+} species A(as) and B(as) at 1262.8 mT.

determination of the ^{1}H and ^{27}Al hf coupling tensor by orientation selective ENDOR spectroscopy[26] was not feasible.

HT and LT Phases of Calcined Dehydrated MIL-53(Al/Cr). Upon removal of free terephthalic acid and residual solvent and water molecules by calcination of MIL-53, the ESR spectra of the resulting dehydrated solid, MIL-53(Al/Cr)deh, change drastically. At room temperature, MIL-53(Al/Cr)deh is initially present in its HT phase as shown by its PXRD pattern (Figure S2b, Supporting Information). Figure 5a,b illustrates the corresponding experimental and simulated Q-band CW ESR spectra of MIL-53(Al/Cr)deh at 295 K. Again, the limit $D \ll \nu_{mw}$ is met at Q-band frequencies. The spectrum shows a well-resolved Cr(III) zfs pattern of a single major chromium species with sharp features of the three singularities ($\theta = 0°$, $\theta = 42°$, and $\theta = 90°$) of the central $M_S = -1/2 \leftrightarrow +1/2$ transition between 1170 and 1320 mT. Furthermore, two single $\theta = 90°$ edge singularities of the $M_S = \pm 3/2 \leftrightarrow \pm 1/2$ transitions are observed at

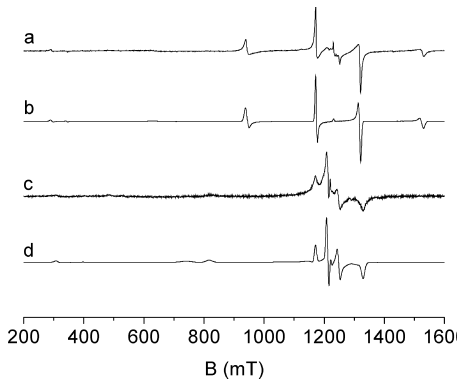

Figure 5. Q-band ESR spectra of MIL-53(Al/Cr)deh at various temperatures: (a) experimental and (b) simulated spectrum at 295 K; (c) experimental and (d) simulated spectrum at 5 K.

940 and 1520 mT without noticeable splitting, indicating an almost axially symmetric zfs tensor ($E \approx 0$). The less intense peak at 630 mT is assigned to the $\theta = 0°$ edge singularities of one of the $M_S = \pm 3/2 \leftrightarrow \pm 1/2$ transitions whereas the low-field signals at 300 mT are due to forbidden transitions ($\Delta M_S = \pm 3$). The spin Hamiltonian parameters of the Cr(III) ions in the HT phase at 295 K as determined from spectral simulations are given in Table 2. The ratio E/D amounts to almost 0, indicating that only small deviations of the $CrO_4(OH)_2$ octahedra from axial symmetry (D_{4h}) occur. Indeed, the crystal structure data of the HT phase of MIL-53(Cr)[15] and MIL-53(Al)[19,22] at 300 K indicate C_{2h} symmetric $MO_4(OH)_2$ octahedra. But the deviation from D_{4h} symmetry is very small and only the bond angles between the four equatorial and the two axial oxygen atoms differ slightly from 90°, whereas the bond lengths between the central metal atom and all four equatorial oxygens are identical according to the reported structural data.[15,19] Therefore, our ESR spectroscopic results are in line with the crystal structure data and it is justified to assign the observed almost axially symmetric Cr(III) signal to the $CrO_4(OH)_2$ octahedra in the HT phase of MIL-53(Al/Cr)deh. It is noteworthy that the D and E strain effects are smaller by 1 order of magnitude for the HT phase of the calcined and dehydrated material with its empty pore system in comparison to the as-synthesized samples having filled pores. This highlights a very uniform structure for the HT phase whereas in the as-synthesized MIL-53 the free terephthalic acid and residual solvent molecules located in the pores obviously disturb the MIL-53 framework significantly.

At 5 K, the Cr(III) Q-band spectrum transforms into a rhombic spectrum (Figure 5, c and d) as indicated by $E/D > 0$ with a smaller D value compared to the spectrum recorded at 295 K (Table 2). The large ratio $E/D = 0.236$ suggests a substantial lowering of the local symmetry of the $CrO_4(OH)_2$ octahedrons. Indeed, calcined dehydrated MIL-53(Al) is reported to be present in its LT phase for temperatures below 125 K.[22] For the LT phase of MIL-53(Al) the $AlO_4(OH)_2$ octahedra become highly distorted and their symmetry is lowered to C_1.[19] All Al−O bond lengths and (O, Al, O) bond angles are different from each other.[19,22] In the case of the LT phase of MIL-53(Cr), C_i symmetry of the $CrO_4(OH)_2$ moieties has been reported[15] with the inversion center at the Cr position and three different Cr−O bond lengths. On the basis of this reported lowering of the local symmetry of the metal oxygen octahedra, we assign the observed Cr(III) species at 5 K with a pronounced rhombic zfs tensor with $E/D = 0.236$ to $CrO_4(OH)_2$ octahedra in the LT phase of MIL-53(Al/Cr)deh. Besides the spectrum of this major Cr(III) species, a faint signal of the extraframework Cr(III) centers C(as) at 470 mT is also observed in the Q-band spectrum

TABLE 2: Spin Hamiltonian Parameters g, D, and E of Cr(III) Ions and Zfs Strain Parameters ΔD and ΔE (FWHH of Gaussian Distributions) in the HT and LT Phases of Calcined and Dehydrated MIL-53(Al/Cr)deh at $T = 10$, 300, and 473 K

phase	T (K)	g	D (GHz)	E (GHz)	E/D	ΔD (GHz)	ΔE (GHz)
HT	10	1.973(5)	8.55(9)	0.39(1)	0.046(1)	0.4(2)	0.04(4)
HT	295	1.973(4)	8.30(5)	0.008(8)	0.001(1)	0.3(1)	0.04(4)
HT	473	1.973(5)	8.27(7)	0.210(3)	0.025(1)	0.23(7)	0.05(5)
LT	10	1.976(2)	6.82(5)	1.61(6)	0.236(7)	0.55(1)	0.15(10)
LT	295	1.976(2)	7.03(6)	1.62(8)	0.230(9)	0.55(15)	0.15(10)

of MIL-53(Al/Cr)deh at 5 K. Unfortunately, short electron spin−lattice relaxation times of the Cr(III) ions in the LT phase prevented further pulsed ENDOR investigations of the dehydrated materials.

Our experimental setup did not allow for Q-band measurements above room temperature. In order to explore also the local structure of the $CrO_4(OH)_2$ octahedra in MIL-53(Al/Cr)deh materials at $T > 300$ K, we performed additional experiments at X-band frequencies in the temperature range 9 K $\leq T \leq$ 473 K. In the X-band experiments (Figure 6), the condition $D \ll \nu_{mw}$ is no longer met and the Cr(III) spectra of MIL-53(Al/Cr)deh are dominated by intense asymmetric signals in the low-field range from 100 to 200 mT caused by the $\theta = 90°$ edge singularities of the Cr(III) zfs powder patterns. The shape and field position of these spectral features are extremely sensitive in particular with respect to small changes in the rhombic zfs parameter E. The spectrum of the HT phase measured at 295 K and illustrated in Figure 6a displays a single intense asymmetric low-field signal at 183 mT with $E/D \approx 0$ in accordance with the Q-band results. Also the less intense high-field features are convincingly reproduced by spectral simulations (Figure 6b) using the parameter set from Table 2. However, at 473 K the low-field line at 183 mT splits into two signals (Figure 6, c and d) and consequently the ratio E/D becomes larger (Table 2), suggesting an increase of the rhombic distortion of the $CrO_4(OH)_2$ octahedra with rising temperature.

Upon lowering the temperature to 9 K, the MIL-53(Al/Cr)deh sample transforms into its LT phase. In the X-band spectra the characteristic low-field signals of the Cr(III) centers shift downfield to 124 and 140 mT and show a larger spitting (Figure 6e) due to a substantially enhanced E/D ratio in the LT phase (Table 2). We have to note that in particular in this spectral region additional signals from the extraframework Cr(III) species C(as) and Fe(III) impurity ions (see for comparison Figure S2, Supporting Information) are expected to interfere with the low-field signals of the Cr(III) spectrum in the LT phase. Indeed, a comparison of the experimental X-band spectrum at 9 K and the simulated Cr(III) spectrum of the LT phase (Figures 6, e and f) using the parameters in Table 2 shows that most spectral features can be reproduced satisfactorily by the Cr(III) parameter set of the LT phase in accordance with the Q-band analysis with two noticeable exceptions. There is an additional signal at 349.3 mT corresponding to $g = 1.965$. As this signal has not been observed for the as-synthesized material at low temperatures (see Figure S2, Supporting Information) and the g value is less than 2, thus within the typical range of Cr(V) ions in distorted octahedral environments[29] we assign the signal to Cr(V) species that have been formed by partial oxidation of Cr(III) during the calcination and dehydration of the sample. At Q-band frequencies the Cr(V) signal is hidden by the intense central $M_S = -1/2 \leftrightarrow +1/2$ transition of the Cr(III) ions in the LT phase. The second signal which is not covered by simulation of the Cr(III) spectrum of the LT phase appears at 177 mT and originates from a Cr(III) species having parameters comparable to the Cr(III) center in the HT phase but with $E > 0$. Therefore, we assume that the conversion from the HT into the LT phase is not complete and even at 9 K a fraction of the sample remains in the HT phase. This is in accordance to previous NPD and INS investigations[22] and strongly supported by the temperature dependency of the Cr(III) X- and Q-band spectra (see Figures S4 and S5, Supporting Information) that show a gradual but incomplete transformation from the Cr(III) spectrum of the HT phase into that of the LT phase. When lowering the temperature from room temperature to 9 K, the E/D ratio of the zfs tensor **D** of the Cr(III) ions in the HT phase rises as indicated by the increasing splitting of both the peak at 183 mT in the X-band spectra and the $\theta = 90°$ edge singularity of one of the $M_S = \pm 3/2 \leftrightarrow \pm 1/2$ transition in the Q-band spectra. At room temperature, a minimum in the E/D ratio is obtained whereas for $T > 315$ K it rises again with temperature (see Figure S6, Supporting Information). The low-temperature behavior of the temperature course of the E/D ratio is in agreement with a recent publication[22] where likewise a drastic increase of the distortion of the $AlO_4(OH)_2$ octahedra of the HT phase in terms of the octahedral angle variance[30] was observed with decreasing temperature. For the high-temperature part $T > 315$ K we suggest that increasing amplitudes of the vibrational modes of the bdc linkers lead to larger asymmetries and distortions of the $MO_4(OH)_2$ octahedra on the ESR time scale (determined by $E^{-1} \approx 1-10$ ns) and in that way to rising E/D ratios. However, a precise analysis of these effects is beyond the scope of this study.

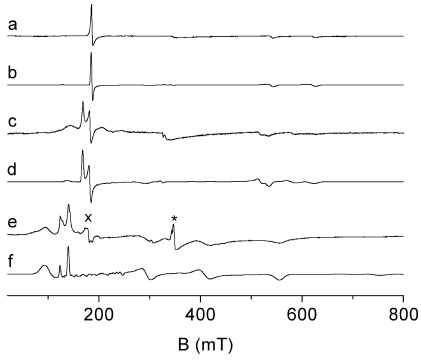

Figure 6. X-band ESR spectra of MIL-53(Al/Cr)deh at various temperatures: (a) experimental and (b) simulated spectrum at 295 K, (c) experimental and (d) simulated spectrum at 473 K, and (e) experimental and (f) simulated spectrum at 9 K. The asterisk indicates the Cr(V) signal and the cross the residual signal from Cr(III) ions in the HT phase.

HT−LT Phase Transition and Thermal Hysteresis in Calcined Dehydrated MIL-53(Al/Cr). After the two distinct Cr(III) ESR spectra from chromium ions of the HT and LT phase of MIL-53(Al/Cr)deh have been indentified, the Cr(III) ions can be employed as local probes to monitor the phase behavior of the MIL-53 framework. In that way the Cr(III) ESR spectra can be employed to quantify the phase fractions of HT and LT phase at varying temperatures.

In the first experiment, a MIL-53(Al/Cr)deh sample, which was initially in its HT phase as ensured by the presence of the

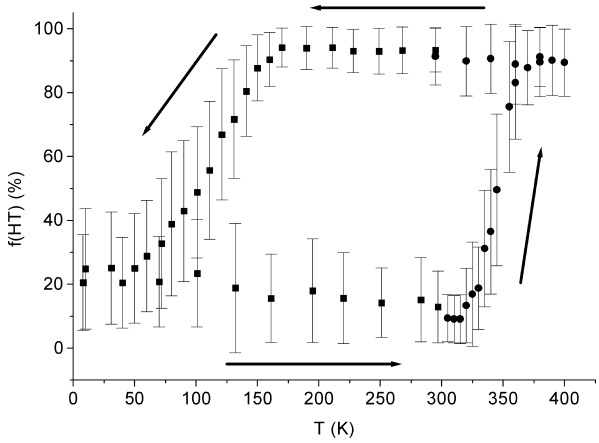

Figure 7. Temperature-driven structural hysteresis of the HT−LT phase transition in MIL-53(Al/Cr)deh as evaluated from the Cr(III) ESR spectra. The diagram shows the relative fraction *f*(HT) of Cr(III) ions in the HT phase. Data presented here were obtained from X-band ESR spectra using an ESR 910 He cryostat for $T < 298$ K and an ER 4118CV Bruker N_2 flow cryostat (squares) at $T > 298$ K. The error bars are based on the accuracy of the determination of the intensity ratio between the Cr(III) spectra in the HT and LT phase in the spectral simulations.

Cr(III) ESR pattern of the HT phase and its corresponding PXRD pattern (Figure S2b, Supporting Information), was slowly cooled down from 295 to 8 K in temperature steps of 10 K with an equilibration time of 10 min each (see below for a rationale). After reaching 8 K, the sample was heated to room temperature again while ESR spectra were recorded every 30 K. These low-temperature experiments were performed at both X- and Q-band with two different samples. Subsequently, the X-band sample was studied at temperatures above 295 K where the sample was heated in steps at minimum of 5−400 K and subsequently cooled down to room temperature. Again, X-band ESR spectra were recorded at every temperature step (for the temperature dependencies of the ESR spectra, see Figures S4 and S5, Supporting Information). For every temperature, the Cr(III) ESR spectra were simulated and the relative fractions *f*(HT) and *f*(LT) of the Cr(III) ions in the HT and LT phases were determined. In this approach, the total Cr(III) ESR spectrum S_{total} was obtained by the sum of the simulated subspectra S_{HT} and S_{LT} from Cr(III) ions in the HT and LT phase weighted with corresponding intensity factors I_{HT} and I_{LT}

$$S_{total} = I_{HT}S_{HT} + I_{LT}S_{LT}; \quad I_{HT} + I_{LT} = 1 \qquad (2)$$

The relative phase fractions *f*(HT) and *f*(LT) at a given temperature can be evaluated according to

$$f(\mathrm{HT,LT}) = \frac{I_{HT,LT}}{I_{HT} + I_{LT}} \qquad (3)$$

Figure 7 displays the fraction *f*(HT) of the HT phase in MIL-53(Al/Cr)deh during the above-described temperature run. Obviously, there is an extremely wide structural hysteresis as already reported by Liu et al.[22] covering a temperature range of approximately 200 K. The transition from the HT into the LT phase starts at about 150 K and covers a broad temperature range of about 90 K where both phases coexist with a decreasing contribution of the HT phase. The superposition of the Q- and X- band Cr(III) ESR spectra from the LT and HT phase and their decomposition into the subspectra corresponding to the two phases is illustrated in Figures S7 and S8 in the Supporting Information. Even below 60 K, where no further temperature-induced spectral changes have been observed, a significant fraction of the sample (∼20%) remains in the HT phase (Figure 6e), indicating an incomplete conversion from the HT to the LT phase as already reported previously.[22] No significant spectral changes have been observed for the subsequent heating of MIL-53(Al/Cr)deh from 8 to 295 K. Therefore, it is concluded that the phase composition achieved by cooling to 8 K is not significantly altered upon warming the sample to 295 K within the error of analysis of the Cr(III) ESR spectra (±18%). Thus, the LT phase prevails to be the majority phase up to a 295 K. As an illustrative example, Figure 8 presents the corresponding Q-band ESR spectrum which has been recorded at 295 K after heating the sample from 8 K. The spectrum displays the coexistence of the Cr(III) spectra from both the LT and the HT phase. We would like to emphasize that the amplitudes of the two subspectra are misleading since the substantial larger rhombic zfs parameters *E* and related strain ΔE (Table 2) lead to larger line widths and consequently smaller signal amplitudes concerning the LT phase spectrum. In contrast, the total intensity of the LT phase spectrum deduced from spectral simulations is 4.5 times higher than for the HT phase spectrum at 295 K.

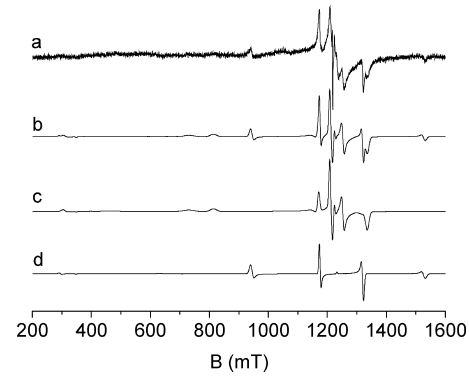

Figure 8. Q-band ESR spectra of MIL-53(Al/Cr)deh recorded at 295 K after the sample was heated up from 8 K: (a) experimental spectrum, (b) sum of simulated Cr(III) spectra, and simulated Cr(III) spectra of (c) LT and (d) HT phase.

If the temperature is increased above room temperature, the back transformation of the LT into the HT phase takes place starting at ca. 330 K. This phase transition occurs within a narrower temperature range ($\Delta T < 45$ K) than the LT transition. At $T > 370$ K no further spectral changes can be observed and the majority of the sample has been converted back to the HT phase. Only a minor fraction of the sample remains in the LT phase (<10%). Decreasing the temperature again to 295 K does not affect the phase composition of MIL-53(Al/Cr)deh and provides the initial phase composition with the HT phase dominating after a full hysteresis cycle as indicated by the corresponding Cr(III) ESR spectrum (Figure S9, Supporting Information).

This temperature-driven structural hysteresis can be reproduced, and no significant aging or memory effects were observed even after several consecutive temperature runs. The first information about such a structural hysteresis for dehydrated MIL-53(Al) materials has been obtained from NPD data and low-energy excitations of twisting modes of the benzene rings in INS experiments.[22] The reported principal features of the hysteresis are comparable to our results in Figure 7. For the high-temperature phase transition LT → HT, both techniques ESR and INS provide comparable values for the onset temperature, $T_{c2} \approx 330$ K, of the phase transformation. The same is

true for the temperature range of about 45 K for the LT → HT phase transition. Likewise, the onset of the low-temperature phase transitions, HT → LT, is observed approximately at the same temperature, $T_{c1} \approx 150$ K. However, there are two noticeable discrepancies between our results and the results from neutron experiments. The width of the HT → LT phase transition appears to be much broader based on the ESR experiments ($\Delta T = 90$ K) in comparison with the INS data ($\Delta T = 25$ K).[22] We also note that the INS and further hydrogen adsorption experiments[22] suggest a slow transition rate (<0.05 min^{-1}) for the HT → LT transformation at 77 K, whereas the ESR measurements employing the Cr(III) probes indicate a much faster transformation rate (>0.3 min^{-1}) at the same temperature. In our ESR experiment a sample initially prepared in its HT phase was immediately inserted into the ESR cryostat and exposed to a temperature of 77 K. We found that the transformation from the HT to the LT phase was completed already 3 min after the sample was inserted into the cryostat and no further changes of the phase composition occurred (Figure S10, Supporting Information). Furthermore, this experiment provides an unambiguous proof that our applied delay time of 10 min between subsequent spectra in the temperature-dependent measurements was sufficient to reach thermodynamic equilibrium.

It seems to be difficult to give a sound interpretation for the differences observed for transformation rates by ESR spectroscopy in comparison with INS and H_2 adsorption experiments at this point. It is obvious that the investigated samples differ, e.g., with respect to the number of structural defects present which may influence the dynamics of the transformation. Furthermore, we cannot rule out that even a low substitution as small as 1% or less of Al(III) by Cr(III) as was used in our ESR experiments may influence the phase transformation of the very flexible MIL-53 framework. It is well-known that the doping may influence phase transition temperatures of crystalline solids as well as the dynamics of the lattice constituents in the vicinity of the transition.[31] Additionally, the discrepancies in the results derived from ESR and INS experiments might be caused by the time scales probed by the two experiments that differ by 3 orders of magnitude. However, further studies are necessary to elucidate these differences between INS and ESR results.

4. Conclusions

The aluminum and chromium analogues of MIL-53 exhibit the same framework topology. Therefore, our results that chromium ions are incorporated at aluminum sites in the MIL-53(Al) framework is reasonable and not surprising. However, low doping with Cr(III) ions offers new perspectives for the study and characterization of the phase transformations of the aluminum form of calcined dehydrated MIL-53. The temperature-driven phase transitions between the open pore HT structure and the closed pore LT topology of the MIL-53(Al) framework can be monitored by the Cr(III) ESR spectra. Here, the chromium zfs interaction carries the relevant information about the respective framework topology, as this spin interaction is very sensitive to even small variances in the structure of the $CrO_4(OH)_2$ octahedra. It is worth noting that the ESR-active chromium-substituted octahedra take part in the collective structural transformations of the MIL-53(Al) framework and can be considered as proper local probes to elucidate the phase transitions of the material. Using Cr(III) ESR spectroscopy, we found in agreement with previous neutron diffraction and inelastic neutron scattering experiments[22] that the dehydrated MIL-53(Al) transforms from its HT into the LT phase between 150 and 60 K. The back transformation from the LT to the HT phase occurs at considerably higher temperatures between 330 and 375 K, indicating a large thermal hysteresis. However, the phase transformation of the material is not complete. A fraction of up to 20% of the material does not undergo the HT → LT phase transition and remains in its HT phase even at temperatures as low as 8 K.

We propose that the presented approach based on ESR spectroscopy on paramagnetic Cr(III) probes is a cost- and in particular time-efficient alternative to the more expensive neutron diffraction and scattering experiments for the elucidation of such phase transformations in MIL-53(Al) materials. Moreover, this spectroscopic approach does not rely on the use of probe molecules as in case of ^{129}Xe NMR methods.[23] We like to emphasize that the adsorption of the probe molecules may already significantly influence by themselves the phase transformation of the material. By use of ESR spectroscopy, the phase transformations can be studied in a wide temperature interval between 4 and 673 K with commercially available equipment. Besides the temperature-induced phase transformation studied here, phase transitions of the MIL-53(Al) framework triggered by guest molecules can easily be examined by this approach. Here, in situ experiments are feasible and currently in progress. In principle, such ESR spectroscopic studies can be done parallel, for instance, to adsorption experiments to monitor the respective structural composition of the material, a necessary information for a correct analysis of the adsorption data.

Acknowledgment. The authors thank the DFG for financial support in the frame of the Priority Program 1362.

Supporting Information Available: Powder X-ray diffraction patterns of MIL-53(Al/Cr)as and MIL-53(Al/Cr)deh, X-band spectrum at 6 K and Q-band spectra at 295 K of MIL-53(Al/Cr)as, Q- and X-band temperature-dependent ESR spectra of MIL-53(Al/Cr)deh, temperature dependence of the ratio *E*/*D* of the Cr(III) ions in the HT phase of MIL-53(Al/Cr)deh, Q- and X-band ESR spectra of MIL-53(Al/Cr)deh at 117 K showing the superposition of the Cr(III) ESR spectra from the HT and LT phases, X-band ESR spectra of MIL-53(Al/Cr)deh at 295 K after a full hysteresis cycle, and X-band ESR spectra of MIL-53(Al/Cr)deh recorded at 77 K immediately after the sample was exposed to low temperatures. This material is available free of charge via the Internet at http://pubs.acs.org.

References and Notes

(1) Yaghi, O. M.; Davids, C. E.; Li, G. M.; Li, H. L. *J. Am. Chem. Soc.* **1991**, *119*, 2861.
(2) Li, H. L.; Eddaoudi, M.; O'Keeffe, M.; Yaghi, O. M. *Nature* **1999**, *402*, 276.
(3) Férey, G.; Mellot-Draznieks, C.; Serre, C.; Millange, F.; Dutour, J.; Surblé, S.; Margiolaki, I. *Science* **2005**, *309*, 2040.
(4) Kitagawa, S.; Kitaura, R.; Nore, S. *Angew. Chem., Int. Ed.* **2004**, *43*, 2334.
(5) Dinca, N.; Long, J. R. *Angew. Chem., Int. Ed.* **2008**, *47*, 6766.
(6) Panella, B.; Hönes, K.; Müller, U.; Trukhan, N.; Schubert, M.; Pütter, H.; Hirscher, M. *Angew. Chem., Int. Ed.* **2008**, *47*, 2138.
(7) Hartmann, M.; Kunz, S.; Himsl, D.; Tangermann, O.; Ernst, S.; Wagener, A. *Langmuir* **2008**, *24*, 8634.
(8) Bourelly, S.; Llewellyn, P. L.; Serre, C.; Millange, F.; Loiseau, T.; Férey, G. *J. Am. Chem. Soc.* **2005**, *127*, 13519.
(9) Llewellyn, P. L.; Bourelly, S.; Serre, C.; Filinchuk, Y.; Férey, G. *Angew. Chem., Int. Ed.* **2006**, *45*, 7751.
(10) Wu, C. D.; Hu, A.; Zhang, L.; Lin, W. *J. Am. Chem. Soc.* **2005**, *127*, 8940.
(11) Henschel, A.; Kedrich, K.; Kraehnert, R.; Kaskel, S. *Chem. Commun.* **2008**, 4192.

(12) Rowsell, J. L. C.; Yaghi, O. M. *Microporous Mesoporous Mater.* **2004**, *73*, 3.

(13) Kitagawa, S.; Uemura, K. *Chem. Soc. Rev.* **205**, *34*, 109.

(14) Barthelet, K.; Marrot, J.; Riou, D.; Férey, G. *Angew. Chem., Int. Ed.* **2002**, *41*, 281.

(15) Serre, C.; Millange, F.; Thouvenot, F.; Noguès, C.; Marsolier, M.; Louër, D.; Férey, G. *J. Am. Chem. Soc.* **2002**, *124*, 13519.

(16) Millange, F.; Serre, C.; Férey, G. *Chem. Commun.* **2002**, 822.

(17) Whitfield, T. R.; Wang, X.; Liu, L.; Jacobson, A. J. *Solid State Sci.* **2005**, *7*, 1096.

(18) Millange, F.; Serre, C.; Guillon, N.; Férey, G.; Walton, R. I. *Angew. Chem., Int. Ed.* **2008**, *47*, 4100.

(19) Loiseau, T.; Serre, C.; Huguenard, C.; Fink, G.; Taulelle, F.; Henry, M.; Bataille, T.; Férey, G. *Chem. Eur. J.* **2004**, *10*, 1373.

(20) Boutin, A.; Springuel-Huet, M. A.; Nossov, A.; Gédéon, A.; Loiseau, T.; Volkringer, C.; Férey, G.; Coudert, F.-X.; Fuchs, A. H. *Angew. Chem., Int. Ed.* **2009**, *48*, 8314.

(21) Serre, C.; Mellot-Draznieks, C.; Surbé, S.; Audebrand, N.; Filinchuk, Y.; Férey, G. *Science* **2007**, *315*, 1828.

(22) Liu, Y.; Her, J.-H.; Dailly, A.; Ramirez-Cuesta, A. J.; Neumann, D. A.; Brown, C. M. *J. Am. Chem. Soc.* **2008**, *130*, 11813.

(23) Springuel-Huet, M.-A.; Nossov, A.; Adom, Z.; Guenneau, F.; Volkringer, C.; Loiseau, T.; Férey, G. A. *J. Am. Chem. Soc.* **2010**, *132*, 11599.

(24) Pilbrow, J. R. *Transition Ion Electron Paramagnetic Resonance*; Clarendon Press: Oxford, UK; 1990.

(25) Stoll, S.; Schweiger, A. *J. Magn. Reson.* **2006**, *178*, 42.

(26) Schweiger, A.; Jeschke, G. *Principles of Pulse Electron Paramagnetic Resonance*; Oxford University Press: Oxford, UK, 2001.

(27) Hoentsch, J.; Rosentzweig, Yu.; Köhler, K.; Gutjahr, M.; Pöppl, A.; Völkel, G.; Böttcher, R. *Appl. Magn. Reson.* **2003**, *25*, 249.

(28) Xiao-Yu, K.; Ai-Jie, M.; Hue, W. *Phys. Chem. A,* **2008**, *112*, 737. Wu, S.-Y.; Gao, X.-Y.; Dong, H.-N. *Mater. Lett.* **2006**, *60*, 1319.

(29) Böttcher, R.; Pöppl, A.; Hoetsch, J.; Rakhmatullin, R. M. *J. Phys.: Condens. Matter* **2010**, *22*, 065902.

(30) Thomas, N. W. *Acta Crystallogr.* **1989**, *B45*, 337.

(31) Lines, M. E.; Glass, A. M. *Principles and Applications of Ferroelectrics and Related Materials*; Clarendon: Oxford, UK, 2001.

JP107487G

4.2 Zwölffach-verknüpfte poröse aluminiumhaltige Metall-organische Gerüstverbindungen: CAU-1 und CAU-3

Bei Betrachtung der aus der Literatur bekannten Synthesen aluminiumhaltiger MOFs ist besonders auffällig, dass viele Verbindungen im wässrigen Medium dargestellt wurden. Aufgrund der geringen Löslichkeit der aromatischen Linkermoleküle im Wasser müssen die Reaktionen deshalb häufig bei hohen Temperaturen und langen Reaktionszeiten durchgeführt werden. Unter diesen Reaktionsbedingungen werden bevorzugt thermodynamisch stabile Produkte gebildet. Mögliche kinetisch stabile Produkte sind somit kaum zugänglich. Ein weiterer Nachteil hydrothermaler Synthesen ist, dass durch die sehr geringe Löslichkeit der Linkermoleküle die Poren nach der Reaktion oft durch nicht umgesetzte Linkermoleküle blockiert sind. Um Zugang zu diesen Poren zu erhalten, müssen die Linkermoleküle zunächst durch eine Lösungsmittelextraktion und/oder thermisch aus den Poren entfernt werden. Eine direkte Synthese in den für die Extraktion benötigten organischen Lösemitteln, wie Alkohole, DMF oder Acetonitril, kann daher viele Vorteile bieten. Zum einen erhöht sich die Löslichkeit der organischen Linkermoleküle im Reaktionsmedium deutlich, so dass die Synthesen bei niedrigeren Temperaturen und kürzeren Reaktionszeiten durchgeführt werden können. Zum anderen sind die Poren nach der Synthese leichter zugänglich, da keine Linkermoleküle mehr in den Poren vorliegen sollten. Die Verwendung der Hochdurchsatzmethode sollte zu einem raschen Aufdecken von Reaktionstrends und neuen Verbindungen führen.

4.2.1 $[Al_4(OH)_2(OCH_3)_4(BDC\text{-}NH_2)_3]\cdot xH_2O$: A 12-Connected Porous Metal–Organic Framework with an Unprecedented Aluminum-Containing Brick

Der Artikel wurde in dem Journal „Angewandte Chemie“ im Jahr 2009 veröffentlicht und beschreibt die Struktur und Charakterisierung der Verbindung CAU-1 (CAU = Christian-Albrechts Universität) $[Al_4(OH)_2(OCH_3)_4(BDC\text{-}NH_2)_3]\cdot xH_2O$. Zusätzliche Informationen zu diesem Artikel befinden sich im Anhang 4 ab Seite 188.

Die systematische Hochdurchsatzuntersuchung des Systems Al^{3+}/H_2BDC-NH_2/Lsgm. führte zu insgesamt drei Verbindungen. Im Rahmen dieser Studie wurde H_2BDC-NH_2 in verschiedenen molaren Verhältnissen mit $AlCl_3 \cdot 6H_2O$ sowie $Al(NO_3)_3 \cdot 9H_2O$ in den Lösemitteln Ethanol, Methanol, DMF und Acetonitril umgesetzt. In jedem dieser Lösemittel, mit Ausnahme von Acetonitril, konnte die Phase Al-MIL-53-NH_2 synthetisiert werden. Während mit $Al(NO_3)_3 \cdot 9H_2O$ ausschließlich Al-MIL-53-NH_2 hergestellt werden konnte, traten unter Verwendung von $AlCl_3 \cdot 6H_2O$ zwei weitere, bislang unbekannte Verbindungen auf. In Methanol wurde bei einem molaren Verhältnis von $AlCl_3 \cdot 6H_2O$: H_2N-H_2BDC = 3:1 die neue Verbindung CAU-1 erhalten, während bei den Synthesen in DMF neben Al-MIL-53-NH_2 vereinzelt die Nebenphase Al-MIL-101-NH_2 auftrat. Unter Verwendung der Hochdurchsatzmethode wurden die Synthesen aller drei Verbindungen optimiert. CAU-1 konnte im Glasreaktor (250 mL) phasenrein und in größerem Maßstab synthetisiert und anschließend mittels Infrarotspektroskopie, Sorptionsexperimenten, Festkörper-NMR-Spektroskopie und Thermogravimetrie charakterisiert werden. Da CAU-1 bei der Synthese als mikrokristallines Produkt anfällt, erfolgte die Strukturlösung und Strukturverfeinerung aus Röntgenpulverdaten. In der Struktur von CAU-1 sind die Aluminiumionen verzerrt oktaedrisch von Sauerstoffatomen umgeben. Diese AlO_6-Oktaeder sind untereinander über Methoxygruppen zu kantenverknüpften dimeren Einheiten verbunden. Vier eckenverknüpfte Dimere bilden ein Oktamer der Zusammensetzung $\{Al_8(OH)_4(OCH_3)_8\}^{12+}$ aus, welches die anorganische Baueinheit der Verbindung darstellt. Ein Oktamer wird über zwölf Aminoterephthalationen mit zwölf weiteren Oktameren zu einem dreidimensionalen Netzwerk verknüpft. In diesem sind die Oktamere in einem quasi kubisch-innenzentrierten Gitter angeordnet, welches leicht tetragonal verzerrt ist. Das Netzwerk weist zwei unterschiedlich große Hohlräume auf, die den entsprechenden Oktaederlücken und Tetraederlücken in der kubisch-innenzentrierten Anordnung gleichkommen. Die Durchmesser der oktaedrisch und tetraedrisch umgebenen Hohlräume betragen ca. 10 Å bzw. ca. 4.5 Å. Der Zugang zu diesen Hohlräumen ist durch eine Öffnung mit einem Durchmesser von 3-4 Å beschränkt. Die N_2-Adsorptionsisotherme von CAU-1 entspricht dem Typ-1 nach IUPAC-Klassifizierung und bestätigt das Vorliegen von Mikroporen.

Metal–Organic Frameworks

DOI: 10.1002/ange.200901409

$[Al_4(OH)_2(OCH_3)_4(H_2N\text{-}bdc)_3]\cdot x\,H_2O$: A 12-Connected Porous Metal–Organic Framework with an Unprecedented Aluminum-Containing Brick**

*Tim Ahnfeldt, Nathalie Guillou, Daniel Gunzelmann, Irene Margiolaki, Thierry Loiseau, Gérard Férey, Jürgen Senker, and Norbert Stock**

The search for new, highly porous, and thermally and chemically stable compounds has been one of the main objectives of many investigations in recent years.[1–3] Metal–organic frameworks (MOFs) present the ideal class of compounds to achieve this target, as they are built up from inorganic bricks and organic complexing molecules. Their modular assembly provides the possibility to adjust pore sizes and to fine-tune the shape and functionality of the pores.[4] One important requirement is the reproducible formation of the inorganic bricks.[1] Once the reaction conditions for the inorganic unit have been established, the variation of the organic linker should in principle allow the synthesis of isoreticular compounds using larger or functionalized organic molecules. Thus, many MOF structures depend on the presence of defined inorganic building units. Often paddle-wheel units (e.g. $\{Cu_2(O_2CR)_4\}$), for example in HKUST-1,[5] or tetranuclear $\{Zn_4O\}$ tetrahedra (as in the IRMOF series or MOF-177)[6,7] are observed. Trimeric building units $\{M_3(\mu_3\text{-}O)(O_2CR)_6\}$ are found in a series of MOFs, for instance those based on the MIL-88 topology as well as MIL-100 and MIL-101.[8,9] Recently, rigid carboxylate linkers were used to connect substituted polyoxotungstates under hydrothermal conditions to form inorganic–organic frameworks.[10] We were able to synthesize iron-containing MIL-53, MIL-88, and MIL-101 based on Fe^{III} and aminoterephthalate[11] as well as the large-pore analogue of MIL-101, which contains naphthyldicarboxylic acid instead of terephthalic acid as the organic unit.[12] In this context, the use of high-throughput methods has been shown to be a valuable tool for the systematic and efficient investigation of hydrothermal reaction systems. Such systematic investigations in the field of inorganic–organic hybrid compounds are still rare,[13–17] although different reagents, reaction stoichiometries, and process parameters have a strong influence on the product formation.

Aluminum-based MOFs are known to show good thermal stabilities (up to 450–500 °C for Al-MIL-53).[18] From a structural point of view, different Al-based MOFs can be formed from distinct inorganic bricks (Figure 1). MIL-96 is built up from isolated trinuclear $\{Al_3(\mu_3\text{-}O)(O_2CR)_6\}$ clusters and corrugated chains of corner-sharing aluminum octahedra, which form a honeycomb lattice containing 18-membered rings.[19] MIL-110 contains octanuclear $\{Al_8(OH)_{15}(O_2CR)_9\}$ clusters arranged in a honeycomb lattice.[20] A number of compounds, such as MIL-53[18,21] and MIL-69,[22,23] are based on chains of corner-sharing aluminum octahedra that are connected to form one-dimensional rhombic channels. We have been able to synthesize amine-functionalized Al-MIL-53 and to use it in a postsynthetic modification reaction.[24] Recently, Al-MIL-53-NH_2 was shown to be a stable, highly active, basic catalyst in a Knoevenagel condensation, and to be well-suited for CO_2/CH_4 separation.[25,26]

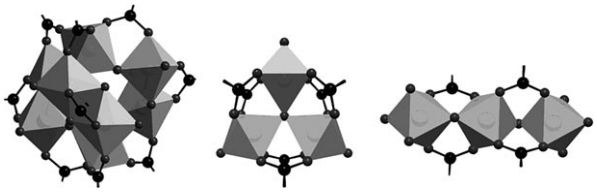

Figure 1. Inorganic Al-containing bricks in Al-containing MOFs. Left: octanuclear $\{Al_8(OH)_{15}(O_2CR)_9\}$ cluster in MIL-110. Center: trinuclear $\{Al_3(\mu_3\text{-}O)(O_2CR)_6\}$ cluster in MIL-96. Right: corner-sharing $\{AlO_6\}$ octahedra in MIL-96, MIL-69, and MIL-53.

Herein we present the results of our systematic investigation of the system Al^{3+}/aminoterephthalic acid ($H_2N\text{-}H_2bdc$)/solvent, which led to the new 12-connected, highly porous, and stable metal–organic framework $[Al_4(OH)_2(OCH_3)_4(H_2N\text{-}bdc)_3]\cdot x\,H_2O$ (named CAU-1; CAU = Chris-

[*] T. Ahnfeldt, Prof. Dr. N. Stock
Institut für Anorganische Chemie, Christian-Albrechts-Universität
Max-Eyth-Strasse 2, 24118 Kiel (Germany)
Fax: (+49) 431-880-1775
E-mail: stock@ac.uni-kiel.de
Dr. N. Guillou, Dr. T. Loiseau, Prof. Dr. G. Férey
Institute Lavoisier, UMR 8637 CNRS
Université de Versailles-Saint Quentin
45 Avenue des États-Unis, 78035 Versailles (France)
D. Gunzelmann, Prof. Dr. J. Senker
Anorganische Chemie I, Universität Bayreuth
Universitätsstrasse 30, 95447 Bayreuth (Germany)
Dr. I. Margiolaki
European Synchrotron Radiation Facilities, ID31
Materials Science Group, Inorganic Chemistry I
6, rue Jules Horowitz, BP 220, 38043 Grenoble (France)

[**] The work has been supported by the State of Schleswig-Holstein and the Deutsche Forschungsgemeinschaft (DFG) through the priority program SPP 1362 "Porous Metal–Organic Frameworks" under grants STO 643/5-1 and SE 1417/4-1. bdc = benzene dicarboxylate.

Supporting information for this article is available on the WWW under http://dx.doi.org/10.1002/anie.200901409.

tian-Albrechts-University), containing the new Al-containing octameric brick $\{Al_8(OH)_4(OCH_3)_8\}^{12+}$.

In the course of the systematic investigation of the formation of new or functionalized isoreticular aluminum-containing MOFs, high-throughput experiments were performed with various chemical and process parameters.[11,14,17] Thus, the influence of the molar ratios of starting compounds, the solvents, and the use of different aluminum salts on the product formation in the system $Al^{3+}/H_2N\text{-}H_2bdc$/solvent was studied (Figure 2). Three $Al^{3+}/H_2N\text{-}H_2bdc$ molar ratios (1:2, 1:1, and 2:1) were used in four different solvents. On the basis of the results of previous studies,[24] a reaction temperature of 125 °C and reaction time of 5 h were chosen as starting parameters.

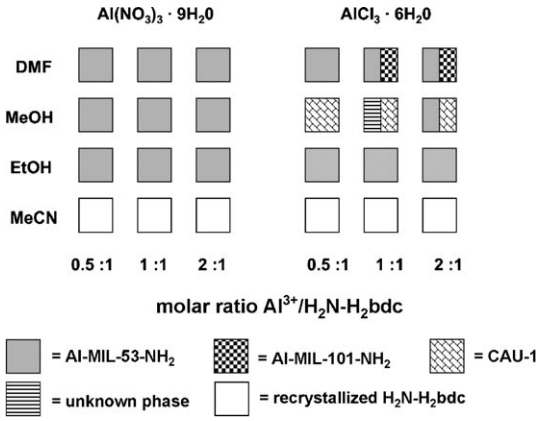

Figure 2. Results of the high-throughput investigation of the system $Al^{3+}/H_2N\text{-}H_2bdc$/solvent at 125 °C.

The solvents have the most profound influence on product formation. In acetonitrile, only recrystallized aminoterephthalic acid is recovered, while in ethanol poorly crystalline Al-MIL-53-NH_2 is formed. The use of DMF or methanol as the reaction medium increases the complexity of the system. With $Al(NO_3)_3{\cdot}9H_2O$ as the starting material, the formation of Al-MIL-53-NH_2 is observed in both solvents. Reaction mixtures containing $AlCl_3{\cdot}6H_2O$ as the starting material result in the formation of new phases. In addition to the well-known phase Al-MIL-53-NH_2,[24] for the first time Al-containing MIL-101 is observed. The latter is formed in DMF at molar ratios $Al^{3+}/H_2N\text{-}H_2bdc \geq 1$. The reactions in methanol yielded an unidentified phase and the title compound CAU-1, $[Al_4(OH)_2(OCH_3)_4(H_2N\text{-}bdc)_3]{\cdot}x\,H_2O$ (see Figure S1 in the Supporting Information for all XRD patterns). The synthesis procedure was optimized using high-throughput methods (see the Supporting Information), and a procedure for gram-scale reactions was established.

The crystal structure of CAU-1 was determined from powder X-ray diffraction data (Figure 3, Tables S1 and S2 in the Supporting Information).[27] High-precision powder X-ray diffraction data were collected on ID31 of the European Synchrotron Radiation Facilities (ESRF). Extractions of the peak positions, pattern indexing, Fourier calculations, and Rietveld refinements were carried out with the TOPAS program.[28] A tetragonal unit cell was found unambiguously

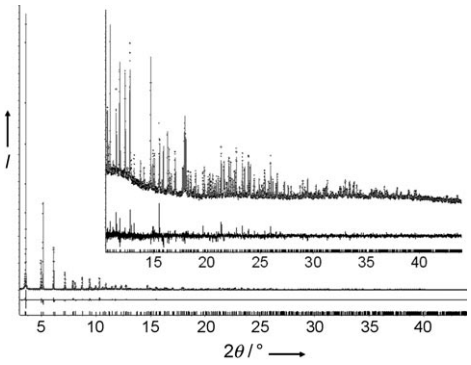

Figure 3. Final Rietveld plot of the structure refinement of $[Al_4(OH)_2(OCH_3)_4(H_2N\text{-}bdc)_3]{\cdot}x\,H_2O$ (CAU-1). The observed data are shown by dots and the calculated pattern by a solid line. The difference curve is represented below; vertical bars mark the Bragg reflection positions. The inset shows a plot enlargement for $2\theta > 12°$.

with satisfactory figure of merit (GoF = 110) using the LSI indexing method. Systematic extinctions were consistent with the *I* Bravais lattice, and the *I*4/*mmm* space group was chosen to solve the structure. Calculations were performed with the EXPO package,[29] using EXTRA[30] for extracting integrated intensities and SIR*97*[31] for direct-methods structure solution.

The tetragonal structure of CAU-1 is built up from a pseudo-body-centered-cubic arrangement of the 8-ring building blocks $\{Al_8(OH)_4(OCH_3)_8\}^{12+}$ (Figure 4), which are linked by 12 aminoterephthalate ions.[32] The wheel-shaped 8-rings are built from corner- and edge-sharing $\{AlO_6\}$ polyhedra

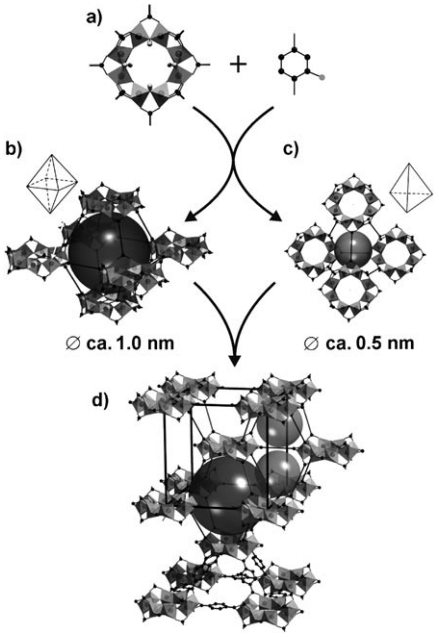

Figure 4. Structure of CAU-1. The brick $\{Al_8(OH)_4(OCH_3)_8\}^{12+}$ is formed by corner- and edge-sharing AlO_6 octahedra (a). These wheel-shaped bricks are connected to 12 other units through the aminoterephthalate linker. Thus, distorted octahedral (b) and tetrahedral (c) cages are formed. The structure (d) can be derived from a tetragonally distorted cubic centered cell. For clarity, some of the phenyl rings are replaced by straight lines, and the disordered NH_2 groups are omitted.

through the hydroxide and methoxide groups, respectively. The Al^{3+} ion resides on a unique crystallographic site and is coordinated to three carboxylate oxygen atoms, one hydroxide, and two methoxide ions. Each wheel is connected to 12 other units by aminoterephthalate linkers with four linkers in the plane of the 8-ring as well as four above and four below the ring. Thus, a three-dimensional microporous framework is formed with two types of cages, distorted octahedral and distorted tetrahedral, with effective accessible diameters of approximately 1 and 0.45 nm, respectively, taking into account the van der Waals radii of the carbon atoms. Access to the cages is only possible through small triangular windows with a free aperture of 0.3–0.4 nm. The disordered water molecules are located close to the middle of the 8-ring units and are involved in hydrogen bonds.

Both the occurrence of an 8-ring unit and the presence of a 12-connected net are notable. Very similar octameric rings with edge- and corner-sharing alternation have been observed for vanadium, chromium, and iron in vanadium hydroxide carboxylates $[V_8(OH)_4(OEt)_8(O_2Ac)_{12}]$[33] and $[V_8(OH)_4(OEt)_8(O_2CPh)_{12}]$,[34] chromium hydroxide acetate $[Cr_8(OH)_{12}(O_2Ac)_{12}]\cdot 34\,H_2O$,[35] and iron hydroxide carboxylate $[Fe_8(OH)_8(OPh)_8(O_2CR)_{12}]$ (R = Bu or Ph),[36] but it is novel in aluminum chemistry. Moreover, the wheel-type analogues involving transition metals are isolated as discrete molecular clusters, whereas the octanuclear Al-based unit in CAU-1 is fully connected to generate an infinite three-dimensional framework. Such 12-connected metal–organic frameworks are very rare,[37–39] and recently such a net was observed in the zirconium-based MOF UiO-66, which contains $\{Zr_6O_4(OH)_4(CO_2)_{12}\}$ units. This structure represents an expanded version of the cubic close-packed structure.[40]

For a more detailed characterization, IR, Raman, and multinuclear solid-state NMR spectroscopic studies (Figures S2 and S3 in the Supporting Information) as well as thermogravimetric analysis (TGA) and elemental analysis were carried out. Especially the high-resolution ^{13}C and ^{15}N NMR spectra unequivocally demonstrate the incorporation of methoxide ions (^{13}C H_3CO^- $\delta = 48$ ppm) and aminoterephthalate (^{15}N NH_2 $\delta = -327$ ppm) into the structure of CAU-1. The methyl groups of the methoxide ions are also clearly detectable in the IR and Raman spectrum.

The TGA data of CAU-1 show a two-step weight loss. The first step, with a weight loss of 6.3 % in the temperature range of 25–100 °C, corresponds to the release of three water molecules per formula unit, whereas only one water molecule could be located in the pores from powder diffraction data. This discrepancy could be explained by a high dependence of the water content of CAU-1 on environmental conditions. The second weight loss is due to the decomposition of the aminoterephthalic acid from the framework and starts at approximately 310 °C (Figure S4 in the Supporting Information). These results are in good agreement with the elemental analysis and with the temperature-dependent XRD measurements, which do not indicate any change in crystallinity or phase transitions up to 360 °C. Above this temperature the framework collapsed. In comparison to flexible MOFs such as MIL-53, CAU-1 shows no structural changes upon dehydration. This thermal stability and the rigidity of CAU-1 could be due to the presence of exclusively triangular windows in combination with the presence of the trivalent metal ions.

The permanent porosity has been confirmed by gas sorption measurements. The sorption isotherm (Figure 5) of CAU-1 exhibits type 1 behavior. The Langmuir surface area is approximately 1700 $m^2 g^{-1}$, and a micropore volume of 0.52 $cm^3 g^{-1}$ was determined.

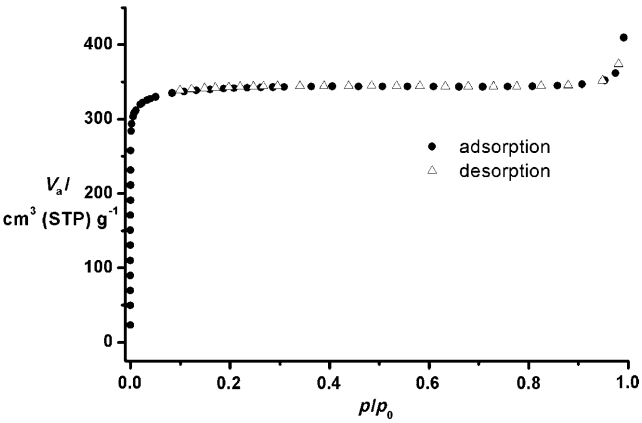

Figure 5. N_2 sorption isotherm of CAU-1 activated overnight at 130 °C before measurement.

In conclusion, the field of formation of the new Al-based MOF $[Al_4(OH)_2(OCH_3)_4(H_2N\text{-}bdc)_3]\cdot x\,H_2O$ (CAU-1) has been determined using high-throughput methods. The structure contains unprecedented octameric $\{Al_8(OH)_4(OCH_3)_8\}^{12+}$ building units, which are connected through the aminoterephthalate ions to a 12-connected net. CAU-1 exhibits high porosity and thermal stability. These properties in combination with the presence of the amino groups allow postsynthetic modification reactions. These results will be presented in a separate publication.

Experimental Section

The discovery and optimization of the synthesis of CAU-1 was investigated using our 24 multiclave (for details, see the Supporting Information). The optimized synthesis of CAU-1 in the 24-reactor system is as follows: a mixture of $AlCl_3\cdot 6\,H_2O$ (92.7 mg, 0.384 mmol) and $H_2N\text{-}H_2bdc$ (23.32 mg, 0.129 mmol) was suspended in methanol (1.235 mL) and heated at 125 °C for 5 h. Scale-up of the reaction to the gram scale was performed in a 250 mL Duran screw-cap glass bottle (Schott). $H_2N\text{-}H_2bdc$ (2.33 g, 12.9 mmol) and $AlCl_3\cdot 6\,H_2O$ (9.27 g, 38.4 mmol) were suspended in methanol (123 mL). The resulting dispersion was heated at 125 °C for 5 h.

After filtration, a yellow microcrystalline product was obtained. The as-synthesized product contains large amounts of chloride ions, which can be removed by stirring the microcrystalline product three times in deionized water (2000 mL per 0.5 g CAU-1) overnight. The product was isolated and dried at room temperature in air. Elemental analysis of the dehydrated phase $[Al_4(OH)_2(OCH_3)_4(H_2N\text{-}bdc)_3]$ ($M = 803\ g\,mol^{-1}$) calcd (%): C 42.35, H 3.83, N 5.32; found (%): C 41.85, H 3.64, N 5.23. Thermogravimetric analysis of the hydrated phase $[Al_4(OH)_2(OCH_3)_4(H_2N\text{-}bdc)_3]\cdot 3\,H_2O$: calcd weight loss 6.3 %; found: 6.2 %.

High-throughput X-ray analysis was carried out using a STOE high-throughput powder diffractometer. High-resolution X-ray

powder diffraction data used for the structural determination were collected on ID31 of the ESRF from a powdered sample.

^{15}N, ^{13}C, and ^{1}H solid-state NMR spectroscopic studies were performed on a commercial BRUKER DSX Avance 400 spectrometer operating at 9.4 T with resonance frequencies of 40.5, 100.7, and 400.1 MHz. ^{1}H and ^{13}C shifts were referenced relative to TMS and ^{15}N shifts to nitromethane. The samples were filled in 4 mm ZrO_2 rotors, mounted in a double-resonance probe (Bruker), and rotated with spinning frequencies of 8–12 kHz. A ramped cross-polarization sequence with contact times between 5 and 20 ms was employed to excite both the ^{13}C and ^{15}N nuclei via the proton bath. All 1D experiments were recorded using broadband proton decoupling by the SPINAL64 sequence.

Carbon, hydrogen, and nitrogen contents were determined by elemental chemical analysis on a Eurovektor EuroEA Elemental Analyzer. For more details, see the Supporting Information.

Received: March 13, 2009
Published online: June 5, 2009

Keywords: organic–inorganic hybrid composites · high-throughput methods · metal–organic frameworks · microporous materials · solvothermal synthesis

[1] G. Férey, *Chem. Soc. Rev.* **2008**, *37*, 191.
[2] S. Kitagawa, R. Kitaura, S. Noro, *Angew. Chem.* **2004**, *116*, 2388; *Angew. Chem. Int. Ed.* **2004**, *43*, 2334.
[3] J. L. C. Rowsell, O. M. Yaghi, *Microporous Mesoporous Mater.* **2004**, *73*, 3.
[4] G. Férey, C. Mellot-Draznieks, C. Serre, F. Millange, J. Dutour, S. Surblé, I. Margiolaki, *Science* **2005**, *309*, 2040.
[5] S. S.-Y. Chui, S. M.-F. Los, J. P. H. Charmant, A. G. Open, I. D. Williams, *Science* **1999**, *283*, 1148.
[6] M. Eddaoudi, J. Kim, N. Rosi, D. Vodak, J. Wachter, M. O'Keeffe, O. M. Yaghi, *Science* **2002**, *295*, 469.
[7] H. Li, M. Eddaoudi, M. O'Keeffe, O. M. Yaghi, *Nature* **1999**, *402*, 276.
[8] S. Surblé, C. Serre, C. Mellot-Draznieks, F. Millange, G. Férey, *Chem. Commun.* **2006**, 284.
[9] C. Serre, C. Mellot-Draznieks, S. Surblé, N. Audebrand, Y. Filinchuk, G. Férey, *Science* **2007**, *315*, 1828.
[10] S.-T. Zheng, J. Zhang, G.-Y. Yang, *Angew. Chem.* **2008**, *120*, 3903; *Angew. Chem. Int. Ed.* **2008**, *47*, 3843.
[11] S. Bauer, C. Serre, T. Devic, P. Horcajada, J. Marrot, G. Férey, N. Stock, *Inorg. Chem.* **2008**, *47*, 7568.
[12] A. Sonnauer, F. Hoffmann, M. Fröba, L. Kienle, V. Duppel, M. Thommes, C. Serre, G. Férey, N. Stock, *Angew. Chem.* **2009**, *121*, 3849; *Angew. Chem. Int. Ed.* **2009**, *48*, 3791.
[13] S. Bauer, N. Stock, *Angew. Chem.* **2007**, *119*, 6981; *Angew. Chem. Int. Ed.* **2007**, *46*, 6857.
[14] A. Sonnauer, N. Stock, *Eur. J. Inorg. Chem.* **2008**, 5038.
[15] R. Banerjee, A. Phan, B. Wang, C. Knobler, H. Furukawa, M. O'Keeffe, O. M. Yaghi, *Science* **2008**, *319*, 939.
[16] M. P. Forster, N. Stock, K. A. Cheetham, *Angew. Chem.* **2005**, *117*, 7780; *Angew. Chem. Int. Ed.* **2005**, *44*, 7608.
[17] N. Stock, T. Bein, *Angew. Chem.* **2004**, *116*, 767; *Angew. Chem. Int. Ed.* **2004**, *43*, 749.
[18] T. Loiseau, C. Serre, C. Huguenard, G. Fink, F. Taulelle, M. Henry, T. Bataille, G. Férey, *Chem. Eur. J.* **2004**, *10*, 1373.
[19] T. Loiseau, L. Lecroq, C. Volkringer, J. Marrot, G. Férey, M. Haouas, F. Taulelle, S. Bourrelly, P. L. Llewellyn, M. Latroche, *J. Am. Chem. Soc.* **2006**, *128*, 10223.
[20] C. Volkringer, D. Popov, T. Loiseau, N. Guillou, G. Férey, M. Haouas, F. Taulelle, C. Mellot-Draznieks, M. Burghammer, C. Riekel, *Nat. Mater.* **2007**, 6, 760.
[21] A. Comotti, S. Bracco, P. Sozzani, S. Horike, R. Matsuda, J. Chen, M. Takata, Y. Kubota, S. Kitagawa, *J. Am. Chem. Soc.* **2008**, *130*, 13664.
[22] T. Loiseau, C. Mellot-Draznieks, H. Muguerra, G. Férey, M. Haouas, F. Taulelle, *C. R. Chim.* **2005**, *8*, 765.
[23] I. Senkovska, F. Hoffmann, M. Fröba, J. Getzschmann, W. Böhlmann, S. Kaskel, *Microporous Mesoporous Mater.* **2009**, *122*, 93.
[24] T. Ahnfeldt, D. Gunzelmann, T. Loiseau, D. Hirsemann, J. Senker, G. Ferey, N. Stock, *Inorg. Chem.* **2009**, *48*, 3057.
[25] J. Gascon, U. Aktay, M. D. Hernandez-Alonso, G. P. M. van Klink, F. Kapteijn, *J. Catal.* **2009**, *261*, 75.
[26] S. Couck, J. F. Denayer, G. V. Baron, T. Rémy, J. Gascon, F. Kapteijn, *J. Am. Chem. Soc.* **2009**, *131*, 6326.
[27] CCDC 723320 contains the supplementary crystallographic data for this paper. These data can be obtained free of charge from The Cambridge Crystallographic Data Centre via www.ccdc.cam.ac.uk/data_request/cif. Crystal data for $[Al_4(\mu\text{-}OH)_2(\mu\text{-}OCH_3)_4(H_2N\text{-}bdc)_3]\cdot H_2O$ (check 821.5 g mol^{-1}): tetragonal, *I4/mmm*, $a = b = 1835.17(1)$, $c = 1777.20(1)$ pm, $V = 5985.33(8) \times 10^6$ pm^3, $Z = 4$. At the final stage, the Rietveld refinement involved the following parameters: 30 atomic coordinates, 5 thermal factors, 1 scale factor, 1 zero point, 2 cell parameters, 20 background parameters, and 8 parameters to model the evolution of diffraction lines shape. Soft restraints were maintained on the C–N and a few C–C bond lengths and C-C-N angles. The final Rietveld plot (Figure 3) corresponds to satisfactory crystal structure model indicator ($R_{Bragg} = 0.025$) and profile factors ($R_P = 0.053$ and $R_{WP} = 0.070$).
[28] Topas V4.1: General Profile and Structure Analysis Software for Powder Diffraction Data Bruker AXS Ltd, **2004**.
[29] A. Altomare, M. C. Burla, M. Camalli, B. Carrozzini, G. L. Cascarano, C. Giacovazzo, A. Guagliardi, A. G. G. Moliterni, G. Polidori, R. Rizzi, *J. Appl. Crystallogr.* **1999**, *32*, 339.
[30] A. Altomare, M. C. Burla, G. Cascarano, C. Giacovazzo, A. Guagliardi, A. G. G. Moliterni, G. Polidori, *J. Appl. Crystallogr.* **1995**, *28*, 842.
[31] A. Altomare, M. C. Burla, M. Camalli, G. L. Cascarano, C. Giacovazzo, A. Guagliardi, A. G. G. Moliterni, G. Polidori, R. Spagna, *J. Appl. Crystallogr.* **1999**, *32*, 115.
[32] A more detailed description of the crystal structure is given in the Supporting Information.
[33] H. Kumagai and S. Kitagawa, *Chem. Lett.* **1996**, 471.
[34] R. H. Laye, M. Murrie, S. Ochsenbein, A. R. Bell, S. J. Teat, J. Raftery, H.-U. Güdel, E. J. L. McInnes, *Chem. Eur. J.* **2003**, *9*, 6215.
[35] M. Eshel, A. Bino, I. Felner, D. C. Johnston, M. Luban, L. L. Miller, *Inorg. Chem.* **2000**, *39*, 1376.
[36] C. Canada-Vilalta, M. Pinkand G. Christou, *Chem. Commun.* **2003**, 1240.
[37] X.-M. Zhang, R.-Q. Fang, H.-S. Wu, *J. Am. Chem. Soc.* **2005**, *127*, 7670.
[38] D. Li, R. Wu, X.-P. Zhou, R. Zhou, X.-C. Huang, *Angew. Chem.* **2005**, *117*, 4247; *Angew. Chem. Int. Ed.* **2005**, *44*, 4175.
[39] J. Jia, X. Lin, C. Wilson, A. J. Blake, N. R. Champness, P. Hubberstey, G. Walker, E. J. Cussen, M. Schröder, *Chem. Commun.* **2007**, 840.
[40] J. H. Cavka, S. Jakobsen, U. Olsbye, N. Guillou, C. Lamberti, S. Bordiga, K. P. Lillerud, *J. Am. Chem. Soc.* **2008**, *130*, 13850.

4.2.2 Oriented growth of the functionalized metal-organic framework CAU-1 on –OH- and –COOH-terminated self-assembled monolayers

Der folgende Artikel wurde 2010 im Journal „Physical Chemistry Chemical Physics“ veröffentlicht und beschreibt das orientierte Kristallwachstum von CAU-1 auf selbstanordnenden Monoschichten (SAMs). Zusätzliche Informationen zu diesem Beitrag befinden sich im Anhang 5 ab Seite 201.

In dieser Arbeit wurden unter Verwendung von 16-Mercaptohexadecanol und 16-Mercaptohexadecanoicsäure zwei selbstanordnende Monoschichten auf Goldsubstraten abgeschieden und jeweils mit einer Kristallisationslösung von CAU-1 versetzt. In Abhängigkeit von den endständigen funktionellen Gruppen und der Syntheseparameter wurde ein orientiertes Wachstum auf den Goldoberflächen beobachtet. Für die carbonsäurefunktionalisierten SAMs konnte selektiv ein hoch orientiertes Kristallwachstum senkrecht zu (002) beobachtet werden. Endständige, hydroxyfunktionalisierte SAMs führten je nach Reaktionsbedingungen entweder zu einer Kristallisation entlang der [011] oder [002] Richtung. Die Ergebnisse dienen als Ausgangspunkt für die Darstellung von dünnen Filmen funktionalisierter MOFs, die in Zukunft zum Bau chemischer Sensoren eingesetzt werden sollen.

Oriented growth of the functionalized metal–organic framework CAU-1 on –OH- and –COOH-terminated self-assembled monolayers†

Florian Hinterholzinger,[a] Camilla Scherb,[a] Tim Ahnfeldt,[b] Norbert Stock[b] and Thomas Bein*[a]

Received 23rd November 2009, Accepted 24th March 2010
First published as an Advance Article on the web 13th April 2010
DOI: 10.1039/b924657f

The oriented growth of the amino-functionalized metal–organic framework $[Al_4(OH)_2(OCH_3)_4(H_2N\text{-}bdc)_3]\cdot xH_2O$ (named CAU-1; CAU = Christian-Albrechts-University) on different self-assembled monolayers (SAMs) is reported. Gold substrates were modified with both 16-mercaptohexadecanol and 16-mercaptohexadecanoic acid SAMs and immersed in a pre-treated crystallization solution. The different terminal functionalities and synthesis parameters result in the direct surface growth of CAU-1 crystals along preferred crystallographic orientations. While for the OH-terminated SAMs a preferential attachment of the CAU-1 crystals either in [011] or [002] direction is observed (depending on the reaction conditions), highly oriented crystal growth in [002] orientation was obtained on the carboxylic acid functionalized SAMs.

Introduction

In recent years, inorganic–organic hybrid materials or metal–organic frameworks (MOFs) have emerged as an important class of porous materials.[1–5] The interest in this field of research is caused by the chemical versatility of their different inorganic and organic building blocks. The modular assembly of these blocks provides the possibility to adjust pore sizes, to design materials with suitable structural properties and to implement different functionalities within the pores.[6] MOFs are thus envisaged to overcome some limitations of inorganic porous materials with respect to possible applications in catalysis,[7,8] adsorption,[9,10] gas storage,[11–13] sensors[14] and drug release.[15,16]

In particular, nanotechnological devices such as smart membranes, catalytic coatings or sensors demand the fabrication of porous thin films. The intriguing properties of MOFs led to a number of studies on the preparation of MOF thin films for these possible applications, as recently outlined by Zacher *et al.*[17] The existing reports are mainly based on synthesis approaches following the route of direct growth of MOFs on self-assembled monolayers (SAMs). The direct nucleation or growth of MOF crystals was achieved by immersing functionalized substrates in the differently treated crystallization solutions. Fischer and co-workers were able to demonstrate the selective nucleation and deposition of different MOFs under solvothermal conditions on modified supports such as alumina and silica.[18,19] First results showing the tunable, oriented growth on SAM-functionalized gold substrates were obtained for HKUST-1 in the group of T. Bein.[20] Scherb *et al.*[21] extended the concept of direct growth to the flexible Fe^{III}/bdc (bdc = 1,4-benzenedicarboxylic acid or terephthalic acid) system providing evidence for the structure directing properties of functionalized organic interfaces. In contrast to the direct growth from solvothermally treated synthesis solutions, Shekhah *et al.*[22] demonstrated a step-by-step approach for the synthesis of MOF thin films. Repeated immersion cyles resulted in a layer-by-layer growth of the MOF crystals on the SAM-functionalized gold substrates. Employing the layer-by-layer approach led to novel insights into the nucleation and the growth mechanism of MOFs. It was found that the presence of pre-formed molecular building units is essential for the crystallization of the MOF HKUST-1.[23]

So far, the fabrication of thin films is limited to a small number of well-known MOFs without any additional functionality within the framework. Here, we wish to focus on the preparation of porous thin films of functionalized MOFs, offering potential for gas separation or chemical sensing purposes.

We report on the deposition of the microporous amino-functionalized MOF CAU-1 (Christian-Albrechts-University; $[Al_4(OH)_2(OCH_3)_4(H_2N\text{-}bdc)_3]\cdot xH_2O$)[24] on modified gold substrates. This functionalized metal–organic framework consists of trivalent aluminium ions and aminoterephthalic acid ligands. The metal ions are coordinated to three carboxylate oxygen atoms from the ligands, one hydroxide ion, and two methoxide ions. CAU-1 is built from unprecedented aluminium-based octameric building units, which are connected through twelve aminoterephthalate linkers to form a three-dimensional framework. The functionality of the framework provided by the uncoordinated amino groups within the pores in combination with the novel structural

[a] *Department of Chemistry and Center for NanoScience (CeNS), University of Munich (LMU), Butenandtstr. 11 (Gerhard-Ertl-Building, E), 81377 Munich, Germany. E-mail: bein@lmu.de; Fax: +49 (0) 89 2180 77622; Tel: +49 (0) 89 2180 77621*
[b] *Department of Inorganic Chemistry, Christian-Albrechts-University of Kiel, Otto-Hahn-Platz, 6/7, 24098 Kiel, Germany. E-mail: stock@ac.uni-kiel.de; Fax: +49 (0) 431 880 1775; Tel: +49 (0) 431 880 1675*

† Electronic supplementary information (ESI) available: RAIR, IR and Raman spectra of film samples and bulk material, respectively as well as TGA/DSC and sorption data of powder samples. See DOI: 10.1039/b924657f

properties prompted us to study the direct growth of CAU-1 crystals on functionalized gold surfaces.

Experimental

All chemicals are available commercially and were used as received.

Bulk CAU-1 synthesis

In a glass reactor, 1.50 g (6.22 mmol) $AlCl_3 \cdot 6\ H_2O$ (p.a., *Riedel-de Haen*) was added to 0.38 g (2.07 mmol) of 2-amino-1,4-benzenedicarboxylic acid (99%, *Aldrich*). The solids were suspended in 20 mL methanol (MeOH, p.a., *Merck*) using an ultrasonic bath. The sealed glass reactor was left for 5 h in a preheated oven at 125 °C. After cooling down to room temperature, the yellow microcrystalline product was centrifuged, washed with methanol, dried and stored for further characterization. See Fig. S3 and S4 for TGA analysis and nitrogen sorption of bulk CAU-1, Fig. S5 for H_2 and S6 for CO_2 sorption, and Fig. S7 for IR and S8 for Raman spectra of CAU-1, respectively.†

Analytical characterization of the SAMs and the deposited CAU-1 crystals

X-Ray diffraction (XRD) measurements of powders were performed on a STOE powder diffractometer in transmission geometry (Cu Kα1, λ = 1.5406 Å), those of films using a Bruker D8 in theta-theta geometry (Cu-Kα1, λ = 1.5406 Å; Cu Kα2, λ = 1.5444 Å). Characterization of the self-assembled monolayers was performed by RAIR spectroscopy, using a Bruker IFS 66v FTIR spectrometer. The sample chamber with a high performance variable angle reflection accessory (A-513) was maintained at 2 mbar during the entire measurement by means of an Edwards rotary-pump. In a typical measurement on gold surfaces, an incidence angle of 83° to the surface normal was used. Furthermore, a cleaned gold slide was measured as background prior to the measurements. The morphology of the crystals was studied using a JEOL JSM-6500F scanning electron microscope. The volumetric sorption measurements were performed on a Quantachrome Nova 4000 e using nitrogen at 77 K to determine BET surface area, pore volume and pore size. The samples were degassed at 120 °C for at least 10 h before sorption measurements were carried out. A confocal LabRAM HR UVVis (HORIBA Jobin Yvon) Raman Microscope (Olympus BX41) with a symphony CCD detection system and a He–Ne laser (λ = 632.8 nm) was used for powder measurements.

SAM preparation

The gold-coated glass slides (glass slides (10 × 13 mm^2) coated with 10 nm Ti/100 nm Au by electron-beam evaporation (*Olympus* AG) were cleaned in ethanol and methanol. The cleaned gold slides were immersed in a 1 mM ethanolic solution (6 pieces in 30 mL) of either 16-mercaptohexadecanoic acid (MHDA; 90%, *Aldrich*) or 16-mercaptohexadecanol and left at room temperature for 48 h. The SAM-functionalized gold slides were repeatedly washed with ethanol and stored in fresh, absolute ethanol until needed.

Preparation of the crystallization solution for the growth of CAU-1 (A) crystals on different functionalized surfaces

In a glass reactor, 1.50 g (6.22 mmol) $AlCl_3 \cdot 6\ H_2O$ (p.a., *Riedel-de Haen*) was added to 0.38 g (2.07 mmol) of 2-amino-1,4-benzenedicarboxylic acid (99%, *Aldrich*). The solids were dissolved in a total volume of 20 mL of methanol (MeOH, p.a., *Merck*) in ethanol mixture (3 : 1 v/v) using an ultrasonic bath. The sealed glass reactor was left for 5 h in a preheated oven at 125 °C. The filtrated solution (**A**) was used for the growth of thin films.

Preparation of the crystallization solution for the growth of CAU-1 (B) crystals on different functionalized surfaces

In a glass reactor, 1.01 g (4.20 mmol) $AlCl_3 \cdot 6\ H_2O$ (p.a., *Riedel-de Haen*) was added to 0.25 g (1.40 mmol) of 2-amino-1,4-benzenedicarboxylic acid (99%, *Aldrich*). The solids were dissolved in a total volume of 20 mL of methanol (MeOH, p.a., *Merck*) in ethanol mixture (1 : 2 v/v) using an ultrasonic bath. The sealed glass reactor was left for 5 h in a preheated oven at 125 °C. The filtrated solution (**B**) was used for the growth of thin films.

Film growth of CAU-1

The SAM-functionalized gold-slides were placed upside-down on Teflon® supports into the filtered synthesis solutions of CAU-1 (3 pieces in 20 mL). The growth was performed at room temperature in a closed glass reactor. Immersion times were varied between 16 h and 14 d.

Results and discussion

Modification of Au(111) substrates

As described in the Experimental section, gold substrates were modified with monolayers of 16-mercaptohexadecanoic acid ($HS(CH_2)_{15}COOH$) and 16-mercaptohexadecanol ($HS(CH_2)_{16}OH$) according to literature procedures[25,26] in order to direct the nucleation and orientation of the amino-functionalized CAU-1 crystals. The formation of the self-assembled monolayers was studied with the help of RAIR spectroscopy, as shown in the ESI (Fig. S1, S2).† A strong and characteristic absorption band at 1712 cm^{-1} corresponding to the C=O stretching vibration validates the presence of the 16-mercaptohexadecanoic acid on the surface. A further characteristic band occurs at 1565 cm^{-1}, associated with the asymmetric stretching vibration of carboxylate groups. The formation of the 16-mercaptohexadecanol SAM is shown by the absorption band at 1058 cm^{-1}, indicating the characteristic C–O stretching vibration of primary alcohols. For both the 16-mercaptohexadecanoic acid and 16-mercaptohexadecanol SAMs, the methylene groups of the aliphatic chains present high-frequency modes at 2920 and 2850 cm^{-1} associated with the asymmetric and symmetric stretching vibrations, respectively. The adsorption and covalent bonding of the organic alkane chains to the gold substrate is confirmed by the band at 721 cm^{-1}, which can be assigned to the stretching vibration of the S–C bond.

Direct growth of CAU-1 (A) on –OH-terminated SAM-functionalized gold substrates

The concept of direct growth of MOFs on SAM-modified interfaces is based on the assumption that a certain functional terminus is directly coordinating to the metal centres or SBUs from solution.[19–23,27] Once the metal centres or SBUs are attached to the surface, subsequent coordination of the organic ligand from the crystallization solution will lead to the crystal growth of the MOF on the SAM-functionalized substrate. Based on this concept, the growth of CAU-1 crystals on functionalized organic interfaces was investigated. The different coordination sites present within the inorganic building blocks of CAU-1 (see Fig. 1) have given rise to the idea to control the crystal growth by using SAMs terminated with different functional groups. Here, the particular functionalities of the SAMs are presumed to mimic either the methoxide or carboxylate groups coordinated to the aluminium ions of CAU-1.

For the following approach Au (111) substrates were functionalized with 16-mercaptohexadecanol SAMs as described in the Experimental section. The SAM-modified supports were placed in the crystallization solution of **A** at room temperature. After 6 d the substrates were taken out, rinsed with ethanol and dried. The crystal growth of the amino-functionalized CAU-1 (**A**) on 16-mercaptohexadecanol modified gold substrates was studied and characterized by X-ray diffraction (Fig. 2) and scanning electron microscopy (SEM, Fig. 4).

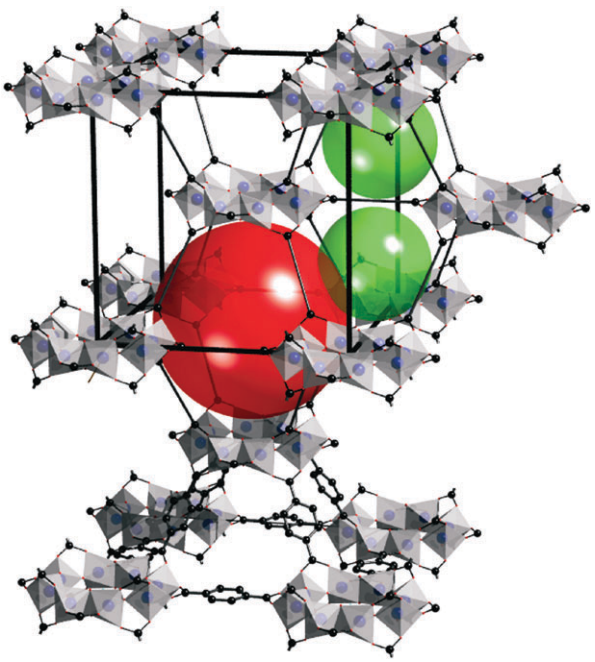

Fig. 1 The crystal structure of CAU-1 is built from wheel-shaped $[Al_8(OH)_4(OCH_3)_8]^{12+}$ bricks, formed by corner- and edge-sharing $[AlO_6]$ octahedra and connected to 12 other units through the amino-terephthalate linker. The two types of pores show distorted octahedral (red) and tetrahedral (green) geometries, respectively. For clarity, most of the phenyl rings are replaced by straight lines, and the disordered NH_2 groups are omitted.[24]

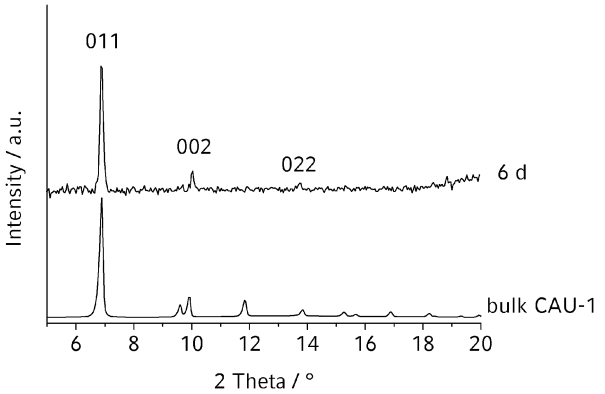

Fig. 2 XRD pattern (background corrected) of CAU-1 (**A**) crystals grown on a 16-mercaptohexadecanol (MHD) SAM after an immersion time of 6 days (top). Compared to the powder pattern of bulk CAU-1 crystals (bottom).

The comparison of the XRD data of the CAU-1 (**A**) thin film with a polycrystalline reference powder sample indicates the oriented growth of CAU-1 crystals along the [011] direction, which can be seen from the 011 reflection and the 022 reflection at $2\theta = 6.9°$ and at $2\theta = 13.8°$, respectively. However, the attachment of an additional population of CAU-1 crystals at the –OH-terminated interface with [002] orientation can be seen from the reflection at $2\theta = 9.9°$ The two differently oriented attachments of CAU-1 crystals on the functionalized surface can be explained by the different accessible coordination sites of the inorganic building blocks. In Fig. 3 a schematic representation of the crystal growth on the SAM modified gold substrate as well as the unit cell of CAU-1 showing the (011) lattice planes are depicted. The aluminium ions present within the wheel-shaped building block are presumed to serve as coordination sites. As the hydroxyl groups are located close to (011) lattice planes, we might anticipate a preferred attachment of the SBUs to the terminal functional groups of the SAM in this direction (although there are differences in the binding modes of hydroxyl *vs.* alcohol). The formation of a molecular interface can thus lead to the oriented growth of CAU-1 crystals along the [011] direction.

In addition to the XRD measurements, the oriented film of CAU-1 (**A**) was further characterized by scanning electron microscopy (Fig. 4). As revealed by the micrographs, a loosely packed coating of CAU-1 (**A**) crystals on the functionalized gold suface was obtained for an immersion time of 6 days. The SEM image (Fig. 4, right) shows the growth of well-defined and tetragonally shaped crystals. The CAU-1 crystals exhibit a size between 150 and 400 nm in length and 50 to 100 nm in width. We conclude that the major population of CAU-1 crystals on the surface has a preferred orientation along the [011] direction, as in the SEM images only very few differently oriented crystals can be detected.

Highly oriented growth of CAU-1 (B) on different SAM-functionalized gold substrates

Since no crystal growth was observed for the carboxylic terminated SAM in the former approach with synthesis

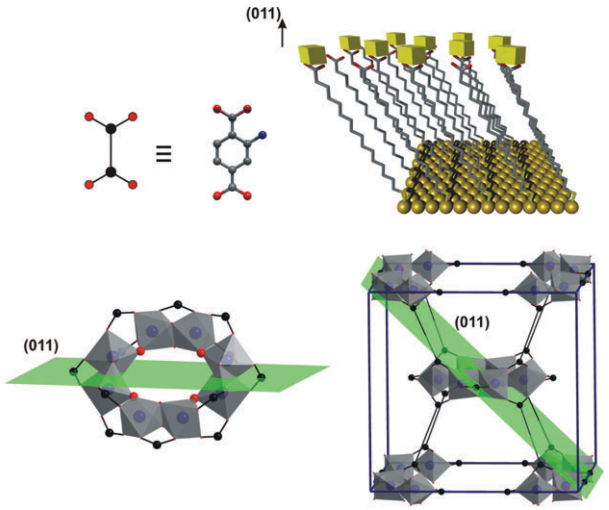

Fig. 3 Top: Schematic representation of the linker and of CAU-1 crystals deposited on the organic monolayer. Bottom: Unit cell of CAU-1 showing the wheel-shaped $[Al_8(OH)_4(OCH_3)_8]^{12+}$ building block and the (011) lattice planes. The aluminium ions are viewed as potential coordination centres, while the terminal hydroxyl groups of the SAM are assumed to mimic the coordinated hydroxide units (bottom, red spheres) of the $[AlO_6]$ polyhedra. The amino-terephthalate linkers and carbon atoms of the methoxy groups are omitted for clarity.

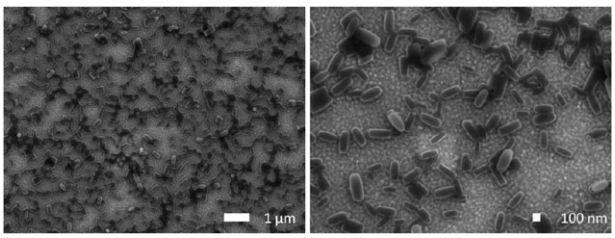

Fig. 4 Scanning electron micrographs showing the oriented growth of CAU-1 crystals on –OH-terminated SAMs in preferred [011] direction after an immersion time of 6 days.

solution **A**, synthesis parameters such as the concentration and the solvent ratio were varied in order to achieve the growth of CAU-1 crystals on both –COOH and –OH-functionalized organic interfaces. The SAM-modified gold substrates were now immersed for 16 h in the crystallization solution **B** and worked up as described before (see Experimental section). A shorter crystallization time was implemented to investigate the initial stage of the growth of CAU-1 crystals. The resulting films were again characterized *via* XRD (Fig. 5) and SEM (Fig. 7).

The X-ray diffraction patterns of surface-grown CAU-1 (**B**) crystals on –OH and –COOH SAMs are compared to the powder pattern of bulk CAU-1 (Fig. 5). The obtained XRD data show one respectively two reflections at $2\theta = 9.9°$ and $2\theta = 19.9°$, indicating the oriented growth of $[Al_4(OH)_2(OCH_3)_4(H_2N\text{-bdc})_3]\cdot xH_2O$ in [001] direction for both functionalized substrates. This indicates that in the CAU-1 system the synthesis parameters have a greater influence on the orientation of the crystals than the functionalization of the SAM for the applied reaction conditions.

Fig. 6 shows the schematic representation of CAU-1 crystals grown on the COOH-terminated SAM as well as

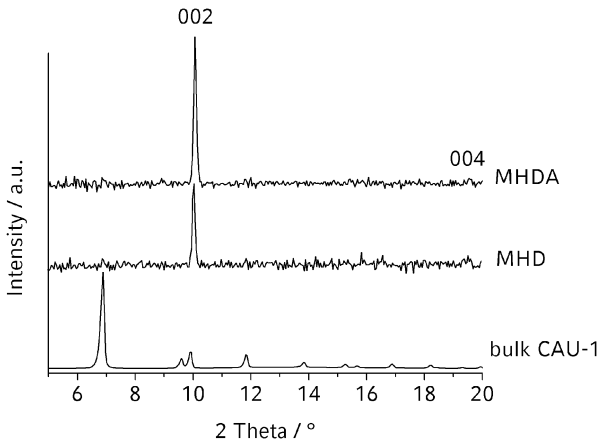

Fig. 5 XRD patterns (background corrected) of CAU-1 crystals grown on a 16-mercaptohexadecanol (MHD) and 16-mercaptohexadecanoic acid (MHDA) SAMs after immersion times of 16 h in solution **B** (top) compared to the powder pattern of bulk CAU-1 crystals (bottom).

the unit cell of CAU-1 with the centred wheel-shaped $[Al_8(OH)_4(OCH_3)_8]^{12+}$ building unit, intersected with the horizontal (002) lattice plane. The aluminium ions, which act as potential coordination sites, as well as the hydroxyl groups, which connect the $[AlO_6]$ octahedra, are located within the (002) lattice plane. Thus, a perpendicular attachment of the growth species to the hydroxyl groups of the SAM along the [002] direction can be envisaged in addition to the aforementioned attachment in [011] direction. It is assumed that the coordination of the terminal hydroxyl groups of the

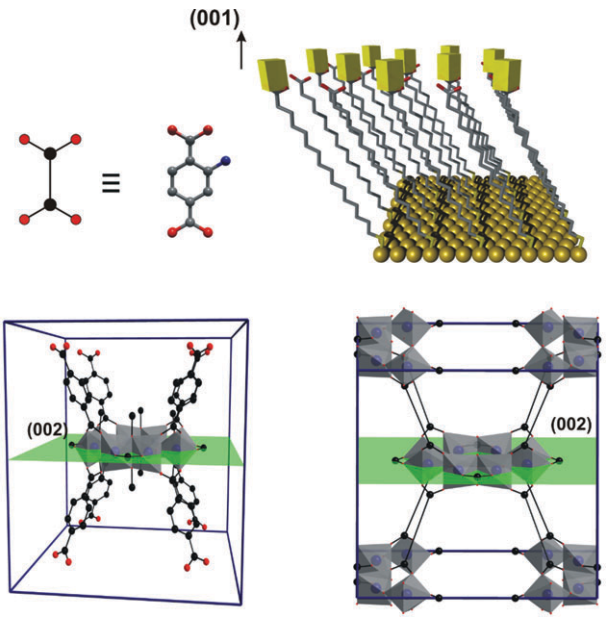

Fig. 6 Top: Schematic representation of the linker and of CAU-1 crystals deposited on the organic monolayer. Bottom: Unit cell of CAU-1 showing the wheel-shaped $[Al_8(OH)_4(OCH_3)_8]^{12+}$ building block with different accessible coordination sites. The hydroxyl groups are located within the (002) lattice plane (green shaded). The amino-terephthalic acid molecules are replaced with straight lines for clarity (bottom, right).

organic monolayer to the aluminium takes place during the formation of the crystals. Oriented crystal growth on the molecular layer follows, resulting in well-grown and highly oriented CAU-1 crystals.

Contrary to our expectations of the terminal carboxylate groups mimicking the functionality of organic linkers present in the plane of the wheel-shaped $[Al_8(OH)_4(OCH_3)_8]^{12+}$ building block, a preferred orientation in [002] direction parallel to the gold surface was obtained. However, the oriented growth of CAU-1 crystals on the carboxylate-terminated self-assembled monolayer can be explained by a chelating coordination of the carboxylate to the aluminium ion. A closer consideration of the building unit of CAU-1, which is connected to 12 other SBUs by coordinating amino-terephthalate linkers, shows the potential binding sites of the inorganic brick (Fig. 6) Since the aminoterephthalate linkers are partially aligned along the [002] direction, the substitution of the carboxylates of the aminoterephthalic acid through carboxylates of the SAM can lead to the preferential [002] orientation. The reproducibility of the oriented growth of CAU-1 was shown using the crystallization solution, as described in the Experimental section.

The scanning electron micrographs, depicted in Fig. 7 (top) show the morphology of several well-defined CAU-1 crystals. The rectangular top face of the crystals is in good agreement with the [002] orientation, deduced from the XRD data. An average crystal size of approximately 150 nm can be determined from the SEM images. In addition, a small population of crystals grown in a different orientation is observed (Fig. 7, top/left). However, in the X-ray diffraction pattern of CAU-1 (**B**) crystals, which are deposited on the MHD-SAM interface, no additional reflections are seen that could be assigned to crystals grown in different orientations; this is attributed to the very small density of the other crystals on the substrate.

Both SEM micrographs shown in Fig. 7 (bottom) illustrate the growth of CAU-1 crystals on the –COOH-terminated self-assembled monolayer. The crystal size varies between 100 and 150 nm in diameter, which was also observed for crystals grown on hydroxyl-terminated MHD SAMs. The SEM images show the crystal faces of CAU-1 aligned along the [002] direction, in agreement with the [002] orientation shown by X-ray diffraction.

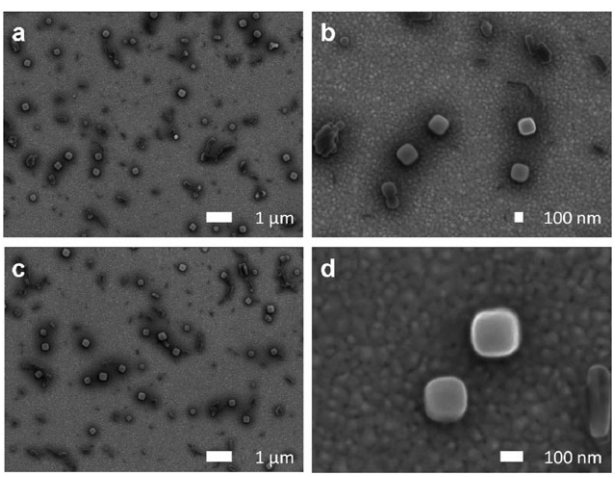

Fig. 7 Scanning electron micrographs showing the oriented growth of CAU-1 crystals grown on MHD-SAM (a, b) and MHDA-SAM (c, d) functionalized gold substrates in preferred [002] direction after an immersion time of 16 h in solution (B).

Direct growth of CAU-1 (A) crystals on SAM modified QCM electrodes—ethanol sorption isotherms

For studies on the sorption behavior of CAU-1 thin films, QCM-gold electrodes were functionalized with MHDA SAMs. The preparation of CAU-1 thin films on functionalized QCM devices was carried out in the same way as it was done for the surface growth on gold substrates (see Experimental section). Prior to the adsorption measurement, X-ray diffraction was performed in order to determine the presence and the preferred orientation of CAU-1 crystal growth (see ESI, Fig. S9).†

The porosity and sorption behavior of CAU-1 were studied by performing ethanol sorption measurements on a coated QCM device. Fig. 8 illustrates the QCM isotherms using ethanol as adsorptive.

The sorption of ethanol on CAU-1 shows the shape of a Type I analogous isotherm. In Fig. 8 the isotherm of CAU-1 shows a steep and characteristic increase of ethanol-loading at low relative pressures, which indicates the microporous character of CAU-1,[24] followed by further adsorption attributed to the textural porosity of the thin film. A total amount of approximately 5.0 mmol g^{-1} of ethanol is adsorbed before condensation is reached. The isotherm shows good reversibility and reproducibility (Fig. S8).† Nitrogen sorption measurements at 77 K on powder samples of CAU-1 show a greater pore volume and a steeper rise at low pressures (Fig. S4).† A micropore volume of 0.52 cm^3 g^{-1} was determined for bulk CAU-1 using nitrogen sorption data,[24] while the adsorbed amount of ethanol in the thin film at a relative pressure of 0.99 p/p_0 was calculated to be only 0.26 cm^3 g^{-1}, based on the density of liquid ethanol at room temperature. We tentatively attribute these differences to the larger ethanol molecule that cannot fill all volume elements in the cages. Further information on the porosity of the films and on their molecular sorption selectivity is expected from the measurement of sorption data of adsorbates featuring different cross sections and different polarities.

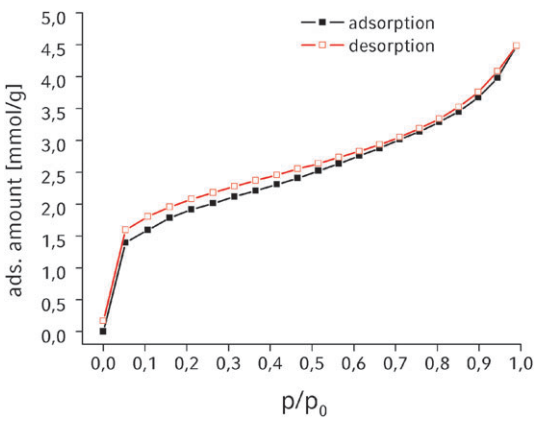

Fig. 8 EtOH sorption isotherms recorded on a CAU-1 thin film.

Conclusions

The deposition of the microporous amino-functionalized $[Al_4(OH)_2(OCH_3)_4(H_2N\text{-}bdc)_3]\cdot xH_2O$ (denoted as CAU-1) on SAM-functionalized gold substrates has been studied. It was shown that by adopting the concept of direct crystal growth for the metal–organic framework CAU-1, control of oriented crystal growth on SAM-functionalized gold substrates can be realized. The results show evidence of the mimicry of characteristic structural features by different terminal functionalities of the SAM leading to highly oriented crystal growth of CAU-1.

We demonstrate that the molecular functionalities of the self-assembled monolayers induce oriented growth of CAU-1 crystals along the preferred [002] direction. As the thermal pre-treatment of the crystallization solution results in the formation of bulk CAU-1 crystals, we assume that either colloidal or (capped) molecular building blocks of the CAU-1 structure are present in solution. Thus, selective interactions between the molecular building blocks and the terminal functional groups of the self-assembled monolayer can be anticipated. Based on the structural features of the wheel-shaped $[Al_8(OH)_4(OCH_3)_8]^{12+}$ building block, the available aluminium centres in combination with different coordinating groups are considered as potential binding sites for the self-assembled monolayer functional groups. Thus, either chelating or monodentate coordination modes of the carboxylic or the alcoholic groups, respectively, might control the selective nucleation/binding on the substrate. While the –OH terminus of the SAM is viewed to mimic the coordinating hydroxyl groups, which leads to corner-sharing $[AlO_6]$ polyhedra, mimicry of the aminoterephthalic acid is anticipated by a chelating coordination of the carboxylate groups of the SAM.

The primary amino functionality of CAU-1 is anticipated to impart selective adsorption behavior with respect to polar molecules. In this context, the sorption behavior of ethanol on CAU-1 thin films was studied by measurements performed with a quartz-crystal microbalance (QCM). The isotherms show the signature of micropore adsorption. Future work will address the potential of these and similar thin films for the design of selective chemical sensors combining molecular sieving with different affinities towards analyte molecules.

Acknowledgements

Financial assistance from DFG (SPP 1362) is gratefully acknowledged.

Notes and references

1 O. M. Yaghi, M. O'Keeffe, N. W. Ockwig, H. K. Chae, M. Eddaoudi and J. Kim, *Nature*, 2003, **423**, 705–714.
2 S. Kitagawa, R. Kitaura and S.-i. Noro, *Angew. Chem., Int. Ed.*, 2004, **43**, 2334–2375.
3 J. L. C. Rowsell and O. M. Yaghi, *Microporous Mesoporous Mater.*, 2004, **73**, 3–14.
4 M. Eddaoudi, J. Kim, N. Rosi, D. Vodak, J. Wachter, M. O'Keeffe and O. M. Yaghi, *Science*, 2002, **295**, 469–472.
5 G. Ferey, C. Mellot-Draznieks, C. Serre, F. Millange, J. Dutour, S. Surble and I. Margiolaki, *Science*, 2005, **309**, 2040–2042.
6 G. Ferey, *Chem. Soc. Rev.*, 2008, **37**, 191–214.
7 J. S. Seo, D. Whang, H. Lee, S. I. Jun, J. Oh, Y. J. Jeon and K. Kim, *Nature*, 2000, **404**, 982–986.
8 R.-Q. Zou, H. Sakurai and Q. Xu, *Angew. Chem., Int. Ed.*, 2006, **45**, 2542–2546.
9 B. Chen, N. W. Ockwig, A. R. Millward, D. S. Contreras and O. M. Yaghi, *Angew. Chem., Int. Ed.*, 2005, **44**, 4745–4749.
10 A. Torrisi, C. Mellot-Draznieks and R. G. Bell, *J. Chem. Phys.*, 2009, **130**, 194703.
11 N. L. Rosi, J. Eckert, M. Eddaoudi, D. T. Vodak, J. Kim, M. O'Keeffe and O. M. Yaghi, *Science*, 2003, **300**, 1127–1130.
12 U. Mueller, M. Schubert, F. Teich, H. Puetter, K. Schierle-Arndt and J. Pastre, *J. Mater. Chem.*, 2006, **16**, 626–636.
13 L. J. Murray, M. Dinca and J. R. Long, *Chem. Soc. Rev.*, 2009, **38**, 1294–1314.
14 S. Achmann, G. Hagen, J. Kita, I. M. Malkowsky, C. Kiener and R. Moos, *Sensors*, 2009, **9**, 1574–1589.
15 J. An, S. J. Geib and N. L. Rosi, *J. Am. Chem. Soc.*, 2009, **131**, 8376–8377.
16 P. Horcajada, C. Serre, M. Vallet-Regi, M. Sebban, F. Taulelle and G. Ferey, *Angew. Chem., Int. Ed.*, 2006, **45**, 5974–5978.
17 D. Zacher, O. Shekhah, C. Woell and R. A. Fischer, *Chem. Soc. Rev.*, 2009, **38**, 1418–1429.
18 D. Zacher, A. Baunemann, S. Hermes and R. Fischer, *J. Mater. Chem.*, 2007, **17**, 2785.
19 S. Hermes, D. Zacher, A. Baunemann, C. Woell and R. A. Fischer, *Chem. Mater.*, 2007, **19**, 2168–2173.
20 E. Biemmi, C. Scherb and T. Bein, *J. Am. Chem. Soc.*, 2007, **129**, 8054–8055.
21 C. Scherb, A. Schoedel and T. Bein, *Angew. Chem., Int. Ed.*, 2008, **47**, 5777–5779.
22 O. Shekhah, H. Wang, S. Kowarik, F. Schreiber, M. Paulus, M. Tolan, C. Sternemann, F. Evers, D. Zacher, R. A. Fischer and C. Woell, *J. Am. Chem. Soc.*, 2007, **129**, 15118–15119.
23 O. Shekhah, H. Wang, D. Zacher, R. A. Fischer and C. Woell, *Angew. Chem., Int. Ed.*, 2009, **48**, 5038–5041.
24 T. Ahnfeldt, N. Guillou, D. Gunzelmann, I. Margiolaki, T. Loiseau, G. Ferey, J. Senker and N. Stock, *Angew. Chem., Int. Ed.*, 2009, **48**, 5163–5166.
25 A. Ulman, *Chem. Rev.*, 1996, **96**, 1533–1554.
26 J. C. Love, L. A. Estroff, J. K. Kriebel, R. G. Nuzzo and G. M. Whitesides, *Chem. Rev.*, 2005, **105**, 1103–1169.
27 S. Hermes, F. Schroeder, R. Chelmowski, C. Woell and R. A. Fischer, *J. Am. Chem. Soc.*, 2005, **127**, 13744–13745.

4.2.3 Controlled modification of the inorganic and organic brick in an Al-based MOF by direct and post-synthetic synthesis routes

Das Manuskript wird in die Zeitschrift CrystEngComm eingereicht. In dem Manuskript wird die detaillierte Untersuchung der Synthese von CAU-1 in einem MW-Ofen sowie dessen postsynthetische Modifizierung beschrieben. Zusätzliche Informationen zu diesem Beitrag befinden sich im Anhang 6 ab Seite 207.

In der ersten Veröffentlichung zu CAU-1 in der Zeitschrift „Angewandte Chemie“ wurde ein ^{13}C-MAS-NMR-Spektrum der Verbindung gezeigt. In diesem trat bei ~27 ppm ein zusätzliches Signal auf, welches nicht zugeordnet werden konnte. Genauere Untersuchungen unter Berücksichtigung des verwendeten Reaktortyps und der Heizmethode zeigten, dass, in Abhängigkeit von der Reaktionstemperatur sowie der Reaktionszeit, bei der Synthese von CAU-1-NH_2 eine Methylierung der in das Gerüst eingebauten Aminogruppen auftritt. Dies wurde mithilfe von ^{1}H-NMR-Spektroskopie nachgewiesen. Dazu wurden alle aktivierten Reaktionsprodukte in einer 20% NaOD/H_2O-Lösung aufgelöst. Die Untersuchungen lieferten folgende Ergebnisse:

- Eine längere Reaktionszeit sowie eine höhere Reaktionstemperatur förderten eine Methylierung der Aminogruppen.
- Unter Einsatz von konventionellen Heizmethoden wurde der Methylierungsgrad der Aminogruppen stark von dem verwendeten Reaktortyp beeinflusst. Während im Teflonautoklaven bei den verwendeten Reaktionsbedingungen (125 °C/5 h) nur eine geringe Methylierung der Aminogruppen beobachtet wurde, führte die Synthese im Glasreaktor zu einem wesentlich höheren Methylierungsgrad sowie einer Zweifachmethylierung der Aminogruppen.
- Bei der Verwendung eines MW-Ofens ließ sich der Methylierungsgrad gezielt einstellen. Bei einer Reaktionszeit von zehn Stunden und einer Reaktionstemperatur von 135 °C wurde die nahezu vollständig einfachmethylierte Verbindung CAU-1-$NHCH_3$ ($[Al_4(OH)_2(OCH_3)_4(BDC\text{-}NHCH_3)_3]\cdot xH_2O$) erhalten. Eine drastische Verkürzung der Reaktionszeit auf 3

min führte bei einer Reaktionstemperatur von 145 °C zu der unmethylierten Verbindung CAU-1-NH_2 ($[Al_4(OH)_2(OCH_3)_4(BDC\text{-}NH_2)_3]\cdot xH_2O$).

- Sehr kurze Reaktionszeiten führten zu Defekten in der Struktur. Die Ergebnisse der ^{1}H-NMR-Untersuchungen zeigten, dass bei einer Reaktionsdauer von 3 min nur 88% der zu erwartenden OCH_3^- Gruppen in den anorganischen Cluster von CAU-1-NH_2 eingebaut wurden.
- Synthesen im Mikrowellen-Ofen sowie Synthesen bei höheren Reaktionstemperaturen führten zu kleineren Produktpartikeln (siehe Kapitel 4.3.2).

In einer postsynthetischen Modifizierung von CAU-1-NH_2 konnten die Aminogruppen durch Reaktion mit Essigsäureanhydrid fast vollständig in die entsprechenden Amidgruppen überführt werden (CAU-1-$NHCOCH_3$ ($[Al_4(OH)_2(OCH_3)_4(BDC\text{-}NHCOCH_3)_3]\cdot xH_2O$)). Alle drei Verbindungen wurden mittels Röntgenpulverbeugung, Sorptionsexperimenten, Elementaranalysen und IR-Spektroskopie charakterisiert. Die in das Gerüst von CAU-1 eingebrachten funktionellen Gruppen (-NH_2, -$NHCH_3$ und -$NHCOCH_3$) beeinflussen die Sorptionseigenschaften des Gerüstes stark. Durch die Methylierung der Aminogruppen ist CAU-1-$NHCH_3$ im Vergleich zu CAU-1-NH_2 deutlich hydrophober, was mittels H_2O-Sorptionsexperimenten nachgewiesen wurde. Neben der organischen Baueinheit konnte bei CAU-1-NH_2 zudem die chemische Zusammensetzung der Al-haltigen anorganischen Baueinheiten variiert werden. Bei einer thermischen Behandlung von CAU-1-NH_2 an Luft wurde ein Austausch der OCH_3^-- durch OH^--Gruppen in den $\{Al_8(OH)_4(OCH_3)_8\}^{12+}$-Clustern beobachtet. Wurde die thermische Aktivierung hingegen unter Vakuum durchgeführt, so fand kein Austausch der OCH_3^-- durch OH^--Gruppen statt. Unter Erhalt der Kristallinität ließen sich an Luft bei einer Temperatur von 190 °C binnen 24 Stunden alle Methoxygruppen aus der anorganischen Baueinheit entfernen und durch Hydroxygruppen ersetzen. Es entsteht CAU-1-NH_2(OH) mit der Zusammensetzung ($[Al_4(OH)_6(BDC\text{-}NH_2)_3]\cdot xH_2O$).

CrystEngComm

Cite this: DOI: 10.1039/c2ce06620c

www.rsc.org/crystengcomm

PAPER

Controlled modification of the inorganic and organic bricks in an Al-based MOF by direct and post-synthetic synthesis routes†

Tim Ahnfeldt,[a] Daniel Gunzelmann,[b] Julia Wack,[b] Jürgen Senker*[b] and Norbert Stock*[a]

Received 2nd December 2011, Accepted 26th January 2012
DOI: 10.1039/c2ce06620c

Four new porous CAU-1 derivatives CAU-1–NH_2 ($[Al_4(OH)_2(OCH_3)_4(BDC–NH_2)_3]\cdot xH_2O$, $BDC–NH_2^{2-}$ = aminoterephthalate), CAU-1–NH_2(OH) ($[Al_4(OH)_6(BDC–NH_2)_3]\cdot xH_2O$), CAU-1–$NHCH_3$ ($[Al_4(OH)_2(OCH_3)_4(BDC–NHCH_3)_3]\cdot xH_2O$) and CAU-1–$NHCOCH_3$ ($[Al_4(OH)_2(OCH_3)_4(BDC–NHCOCH_3)_3]\cdot xH_2O$) all containing an octameric $[Al_8(OH)_{4+y}(OCH_3)_{8-y}]^{12+}$ cluster, with $y = 0–8$, have been obtained by MW-assisted synthesis and post-synthetic modification. The inorganic as well as the organic unit can be modified. Heteronuclear $^1H–^{15}N$, $^1H–^{13}C$ and homonuclear $^1H–^1H$ connectivities determined by solid-state NMR spectroscopy prove the methylation of the NH_2 groups when conventional heating is used. Varying reaction times and temperatures allow controlling the degree of methylation of the amino groups. Short reaction times lead to non-methylated CAU-1 (CAU-1–NH_2), while longer reaction times result in CAU-1–$NHCH_3$. CAU-1–NH_2 can be modified chemically by using acetic anhydride, and the acetamide derivative CAU-1–$NHCOCH_3$ is obtained. Thermal treatment permits us to change the composition of the Al-containing unit. Methoxy groups are gradually exchanged by hydroxy groups at 190 °C in air. Solid-state NMR spectra unequivocally demonstrate the presence of the amino groups, as well as the successful post-synthetic modification. Furthermore $^1H–^1H$ correlation spectra using homonuclear decoupling allow the orientation of the $NHCOCH_3$ groups within the pores to be unravelled. The influence of time and temperature on the synthesis of CAU-1 was studied by X-ray powder diffraction, elemental analyses, and ^1H liquid-state NMR and IR spectroscopy.

1. Introduction

Metal–organic frameworks (MOFs) have evolved over the past decade into the most investigated class of porous materials.[1] Based on their high thermal stability, well defined pore systems and high porosity, some MOFs are suitable for a number of potential applications, such as controlled drug release,[2] storage and separation of gases,[3] as catalysts[4] and in sensing devices.[5] For most of the applications very low framework density and/or additional functional groups in the pores are required. To achieve a low framework density, MOFs which are based on light metals such as magnesium or aluminium are promising.[6] In the last decade aluminium-containing MOFs (Al-MOFs) have been investigated intensively.[7] Al-based MOFs are known for their high thermal and chemical stability, non-toxicity and large apparent specific BET surface areas.[8] Al-MOFs can be synthesised using common linker molecules, such as terephthalic acid,[9] naphthalenedicarboxylic acid[10] and trimesic acid.[11] Starting from the terephthalic acid linker additional functional groups, like hydroxy-, nitro-, chloro-, bromo-, and methyl-groups, were successfully incorporated into Al-MOFs *via* isoreticular synthesis strategies.[12] The modified frameworks show often different sorption[13] and improved catalytic properties,[14] which are based on different host–guest interactions. The most common functional group in Al-MOFs is the amino group. The amino group is chemically inert in most solvents and does not participate in the coordination chemistry of the metal ions. Furthermore, the amino group allows post-synthetic modification reactions on the pore surfaces such as nucleophilic substitution, acid–base reactions or condensation reactions.[15] Modified linker molecules can change properties like the accessibility of the pores and thus sorption behaviour depending on their orientation within the pores. The orientation of linker residues, however, is difficult to determine and mostly unknown. Solid-state NMR spectroscopy is a powerful tool for this task. It enables the determination of distances, angles and orientation

[a]*Institut für Anorganische Chemie Christian-Albrechts-Universität, Max-Eyth Strasse 2, 24118 Kiel, Germany. E-mail: stock@ac.uni-kiel.de; Fax: +49 4318801775; Tel: +49 4318801675*
[b]*Anorganische Chemie III, Universität Bayreuth, Universitätsstraße 30, 95447 Bayreuth, Germany. E-mail: juergen.senker@uni-bayreuth.de; Tel: +49 921552532*

† Electronic supplementary information (ESI) available: Additional results of solid state and solution-based NMR spectroscopic studies, X-ray powder diffraction and temperature dependent X-ray powder diffraction patterns and results of the thermogravimetric measurements. See DOI: 10.1039/c2ce06620c

correlations. Based on the aminoterephthalic acid linker the amino group could be successfully incorporated into the structures of MIL-53 (ref. 16) and MIL-101.[17,18] Very recently we synthesised CAU-1 using the aminoterephthalic acid linker.[17] The CAU-1 framework[19] contains $[Al_8(OH)_4(OCH_3)_8]^{12+}$ clusters composed of eight distorted AlO_6-octahedra that are connected through hydroxy groups (corner-sharing) and two methoxy groups (edge-sharing). The arrangement of these clusters can be derived from a tetragonally distorted bcc arrangement. These clusters are twelve-fold connected *via* amino terephthalate ions. The structure possesses two kinds of cavities with effective diameters of approximately 1 and 0.45 nm. Twelvefold connected networks, such as UiO-66 (ref. 20) and MIL-125,[21] are known for their stability and high porosity. CAU-1 has been intensively investigated, for example in the field of thin-film crystal growth,[22] N_2-, H_2-, and CO_2-sorption[23,24] and post-synthetic modification,[25] and its formation has been studied by *in situ* EDXRD measurements.[12a,26] The first publication on CAU-1 (ref. 17) depicts a signal at ~27 ppm in the ^{13}C CP MAS solid-state NMR spectrum, which could not be assigned at that time. This prompted us to carry out an in-depth investigation which also revealed the origin of the ^{13}C signal. Herein we show that the signal is due to the methylation of the amino group. We also demonstrate the influence of the reaction time and temperature on the *in situ* methylation of CAU-1–NH_2. In addition, the post-synthesis modification by reaction with acetic anhydride is shown and the influence of thermal activation on the composition of the Al-based building unit is identified.

2. Experimental

2.1 Chemicals

$AlCl_3 \cdot 6H_2O$ (Riedel-de Haen, ≥99%), H_2BDC–NH_2 (Fluka, ≥98%), methanol (BASF, purum), and acetic anhydride (Fluka, ≥99%).

2.2 Methods

X-Ray powder diffraction patterns were recorded with a STOE STADI P diffractometer equipped with a linear position sensitive detector using monochromatic Cu-$K_{\alpha 1}$ radiation. Lattice parameters were determined using the DICVOL[27] program and refined using the STOE software package WinXPow.[28] Temperature-dependent X-ray powder diffraction (TD-XRPD) experiments were performed under air with a STOE STADI P diffractometer equipped with an image plate detector and a STOE capillary furnace (version 0.65.1) using monochromatic Cu-$K_{\alpha 1}$ radiation. Each powder pattern was recorded in the 4–35° range (2θ) at intervals of 10 °C up to 350 °C and intervals of 25 °C from 350–400 °C with duration of 15 min per scan. The temperature ramp between two patterns was set to 2 °C min^{-1}.

Thermogravimetric (TG) analysis was carried out in air (75 mL min^{-1}, 25–900 °C, 4 °C min^{-1}) on a Netzsch STA-409CD. Carbon, hydrogen, and nitrogen contents were determined by elemental chemical analysis on an Eurovektor EuroEA Elemental Analyzer. EDX analysis was performed on a Philips ESEM XL 30. IR spectra were recorded on an ATI Matheson Genesis in the spectral range 4000–400 cm^{-1} using the KBr disk method as well as on an ALPHA-ST-IR Bruker spectrometer equipped with an ATR unit.

Several types of adsorption experiments were carried out using three different gases. Based on the TG data, activation at 130 °C under vacuum for 3 h was used for all measurements. The specific surface area of the dehydrated CAU-1 derivatives was determined by measuring the N_2 sorption isotherms at −196 °C using a BELSORP-max apparatus. Approximately 30 mg of sample were used for each experiment. The CO_2 and H_2O adsorption experiments were carried out at 25 °C up to a pressure of 1 bar using the same instrument.

For the NMR study of the CAU-1 samples liquid- and solid-state NMR experiments were performed. Liquid-state NMR spectra were recorded on a Bruker DRX500 operating at 500 MHz for ^1H. Two different procedures were applied to obtain solution samples for the liquid-state NMR investigations. In the first method, the washed CAU-1 material was directly dissolved in a dilute $NaOD/D_2O$ solution. In the second method the linker was isolated by digesting the framework in 2 M NaOH and reprecipitating by neutralising using 2 M HCl. After filtration, the linker was redissolved in a dilute $NaOD/D_2O$ solution.

The 1D solid-state NMR experiments were carried out on commercial BRUKER Avance DSX-300 and Avance II 300 spectrometers operating at 7.05 T with resonance frequencies of 75.47 MHz for carbon and of 30.41 MHz for nitrogen. 2D experiments were measured on a BRUKER Avance III 400 spectrometer operating at 9.4 T with resonance frequencies for ^1H and ^{13}C of 400.13 MHz and 100.62 MHz. The proton and carbon shifts were referenced relative to tetramethylsilane and the nitrogen shifts to nitromethane. The carbon–proton 2D MAS-J-HMQC[29] experiment of solvothermally synthesised CAU-1 was performed using a 4 mm double-resonance probe with the sample restricted to the inner third of the rotor to increase rf field homogeneity and spinning at 10 kHz rotation frequency. The contact time for the cross-polarisation was set to 5 ms and the delay τ equal to 2 ms. The proton rf field strength was set to 83 kHz during τ (FSLG decoupling) and 100 kHz during acquisition (Spinal64 decoupling). All proton–proton homonuclear and carbon–proton heteronuclear correlation experiments were measured accordingly at 12.5 kHz rotation frequency with a ^1H nutation frequency of 76 kHz for excitation and decoupling (using the eDUMBO sequence during t_1 and the windowed wDUMBO sequence during t_2). The 1D ^{13}C and ^{15}N CPMAS spectra were collected in 4 mm or 7 mm triple resonance probes with spinning speeds between 5 and 8 kHz. These spectra were recorded using a cross-polarization sequence with a nutation frequency of the protons of 77 kHz (sweeping from 50 to 100% power) and a Spinal64 proton decoupling of 63 kHz for the ^{13}C spectra and 89 kHz proton nutation frequency and spinal64 proton decoupling of 71 kHz for the ^{15}N spectra. The relaxation times were checked and the recycle delays set accordingly to 5 s for CAU-1–NH_2, 2.5 s for CAU-1–$NHCOCH_3$ and 2.5 s for CAU-1–$NHCH_3$, respectively.

For the microwave reactions the commercially available microwave synthesizer Biotage Initiator was used. The reaction temperature attained within 1 min corresponds to ramp rates of 2–5 °C s^{-1}. Glass reactor vials (Biotage microwave vial 2–5 mL) with an inner diameter of 14 mm and a volume of 10 mL were used. Temperatures were measured by an internal IR sensor.

Conventional syntheses were carried out in glass reactors (DURAN® glass 25 mL) and Teflon-lined steel autoclaves with a maximum volume of 30 mL.

2.3 Systematic investigation of the influence of reaction time and temperature on the methylation of CAU-1

Based on previous results obtained from the *in situ* EDXRD crystallisation studies the reactions were carried out in a microwave (MW) oven (Biotage Initiator) using 5 mL glass vials.[12a,26] For all reactions a mixture of $AlCl_3 \cdot 6H_2O$ (232 mg, 0.961 mmol) and $H_2BDC–NH_2$ (58 mg, 0.312 mmol) was used, which was suspended in methanol (3.175 mL). The influence of reaction time was studied at 135 °C in a time range of 15–638 min and at 145 °C between 2 and 10 min.

2.4 Synthesis of CAU-1–NH_2, $[Al_4(OH)_2(OCH_3)_4(BDC–NH_2)_3]$

The non-methylated compound CAU-1–NH_2 was synthesised using MW-assisted heating. A mixture of $AlCl_3 \cdot 6H_2O$ (232 mg, 0.961 mmol) and $H_2BDC–NH_2$ (58 mg, 0.312 mmol) was suspended in methanol (3.175 mL) in a 5 mL glass vial. After sealing, the reaction mixture was heated under stirring (300 r s^{-1}) at 145 °C for 3 min. The reaction mixture was rapidly cooled to room temperature. A yellow microcrystalline dispersion was obtained. After centrifugation, the product was redispersed in water (25 mL) to remove the Cl^- ions, which may be present due to the formation of $R–NH_3^+$ groups. This procedure was repeated (three times) until no Cl^- ions could be detected anymore. The final product was dried in air to yield CAU-1–NH_2 (75% for the as-synthesised product and 50% for the activated compound based on aminoterephthalic acid). Elemental analysis of the washed phase: observed, C: 41.22, H: 3.65, N: 5.46; calculated (based on $[Al_4(OH)_2(OCH_3)_4(BDC–NH_2)_3]$), C: 41.84, H: 3.64, N: 5.22%.

2.5 Synthesis of CAU-1–$NHCH_3$, $[Al_4(OH)_2(OCH_3)_4(BDC–NHCH_3)_3]$

The methylated compound was synthesised using MW-assisted heating by increasing the reaction time. A mixture of $AlCl_3 \cdot 6H_2O$ (232 mg, 0.961 mmol) and $H_2BDC–NH_2$ (58 mg, 0.312 mmol) was suspended in methanol (3.175 mL) and heated to 135 °C for 10 h. A yellow microcrystalline product was obtained after filtering and drying in air. Like CAU-1–NH_2, the as-synthesized products contain large amounts of Cl^- ions. To remove these, the raw product was washed several times with water to yield CAU-1–$NHCH_3$. Elemental analysis of the washed phase: observed, C: 44.03, H: 4.18, N: 4.97; calculated (based on $[Al_4(OH)_2(OCH_3)_4(BDC–NHCH_3)_3]$), C: 43.31, H: 4.10, N: 4.98%.

2.6 Post-synthetic modification of CAU-1–NH_2

To $[Al_4(OH)_2(OCH_3)_4(BDC–NH_2)_3]$ (500 mg, 0.626 mmol) acetic anhydride (2 mL, 21.197 mmol) was added. The reaction was carried out in an ultrasonic bath (160 W Bandelin Sonorex RK 100) at room temperature for 3 h leading to the formation of the amide derivative. The product was washed with H_2O and heated in air (80 °C, 2 h) to yield CAU-1–$NHCOCH_3$. Elemental analysis: observed, C: 35.59, H: 3.50, N: 3.63; calculated (based on $[Al_4(OH)_2(OCH_3)_4(BDC\text{-}NHCOCH_3)_3] \cdot xH_2O$; $x \approx 12$) C: 35.68, H: 3.59, N: 3.67%.

2.7 Thermal activation of CAU-1–NH_2

To remove solvent molecules from the pores of CAU-1–NH_2, the samples were treated thermally. Depending on the activation conditions (vacuum *vs.* air) and the applied temperatures (120–190 °C), a substitution of methoxy groups by hydroxy groups in the Al-based brick of the CAU-1–NH_2 framework takes place. At an activation temperature of 190 °C the methoxy groups were fully replaced by hydroxy groups after 24 h and CAU-1–NH_2(OH) ($[Al_4(OH)_6(BDC–NH_2)_3] \cdot xH_2O$) is formed.

3. Results and discussion

3.1 Solid-state NMR investigation of CAU-1 synthesised under conventional heating

The unassigned carbon signal at 27 ppm (see Ahnfeldt *et al.*,[17] Fig. S5b†) gave rise to the question whether the product is phase pure. By performing a carbon–proton 2D MAS-J-HMQC experiment the carbon signals are correlated to signals of directly bonded hydrogen nuclei. In the HMQC spectrum (Fig. 1) the signal at 27 ppm correlates with a proton signal at 2.2 ppm, characteristic of a methyl group, the signal at 57 ppm with the methoxy proton signal at 2.8 pm, and the directly proton bonded aromatic carbons (113, 116, and 132 ppm) correlate with proton signals between 7 and 8 ppm. Non-bonded carbons, like the carboxy (174 ppm) or the quaternary aromatic carbons (153, 137 and 115 ppm), show no correlation to protons in this experiment, but can be seen in the top of Fig. 1 for comparison.

The same proton signals were found in proton–proton homonuclear correlation (HOMCOR) spectra (Fig. 2 and S1†) as well as in carbon–proton heteronuclear (HETCOR) spectra (shown in Fig. S2†). All these 2D spectra exhibit cross-peaks

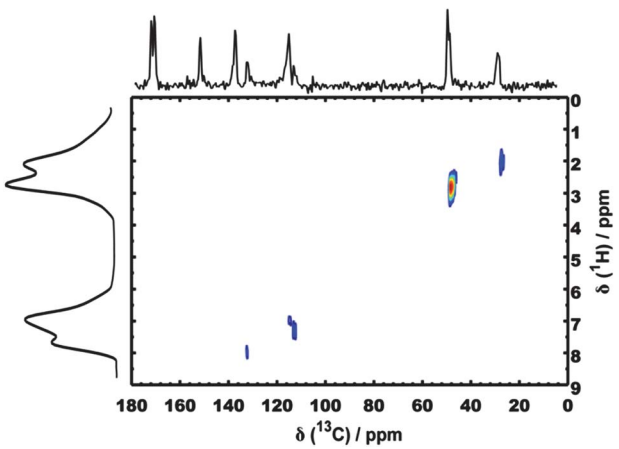

Fig. 1 ^1H-^{13}C-MAS-J-HMQC spectrum of CAU-1 synthesised under conventional heating showing correlations between directly bonded protons to carbon nuclei. For comparison a ^{13}C CP spectrum of the sample, depicting all carbon signals, is shown on top. On the left the homonuclear decoupled ^1H spectrum is shown.

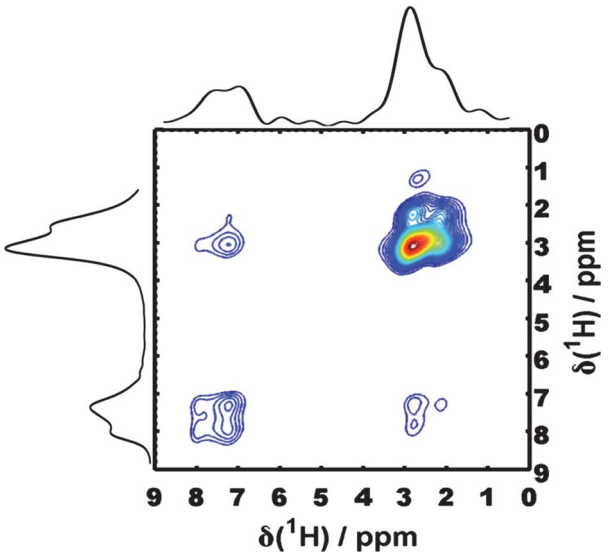

Fig. 2 ^{1}H-^{1}H HOMCOR spectrum of conventionally synthesized CAU-1 with DUMBO decoupling during t_1 and t_2 and a spin diffusion time of 4 ms, showing also longer proton–proton distance correlations.

between either the ^{1}H signal at 2.2 ppm or the ^{13}C signal at 27 ppm and other characteristic resonances. For example in Fig. 2 the ^{1}H signal at 2.2 ppm couples with the resonances in the aromatic region. These experiments therefore allow the assignment of a methyl group as an integral part of the CAU-1 structure. A final clue to its nature is given by the ^{15}N-CPPI experiment (Fig. 3) that shows different nitrogen signals.

The intensity modulation due to a CPPI sequence (Fig. 3, inset) reveals that the ^{15}N resonances at −319 and −323 ppm bear –NH functionalities while the one at −347 ppm seems to be a tertiary N atom. Together with the shift values the signals at −319 and −323 ppm can be assigned to –$NHCH_3$ groups while the one at −347 ppm is probably a –$N(CH_3)_2$ group. By the HMQC experiment we could prove the methyl group to be an integral part of the structure and *via* the CPPI experiment we could prove the methylation of the amino group. The CAU-1 synthesised under conventional heating therefore is methylated at the aminoterephthalic linker molecules. It is worth noting that the occurrence of two different shifts for the $NHCH_3$ groups indicates two different scenarios for the orientation of the functional groups within the pores with one alignment being more probable by a factor of 2. Parameters influencing this methylation reaction are studied in the following.

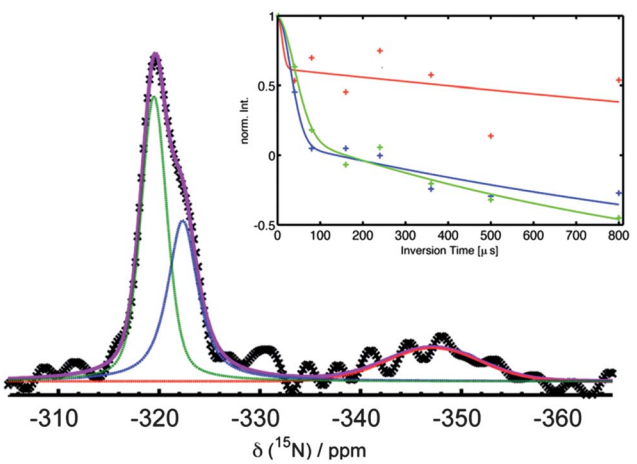

Fig. 3 ^{15}N-CPPI-spectrum and intensity decrease (shown in the inset) for the signals at −319 (green), −323 (blue) and −347 ppm (red).

3.2 Influence of the reaction temperature

The synthesis of CAU-1 under MW-assisted heating was carried out in the temperature range 115–145 °C. The reaction time for each temperature was determined from the *in situ* EDXRD studies on CAU-1 (ref. 26) and corresponds to the time required to reach full crystallisation (ranging from 105 min for 115 °C to 7–9 min for 145 °C, Table S1†). The reaction products were filtered and washed once with water. The XRPD patterns of the reaction products are shown in Fig. S3† and demonstrate that CAU-1 was formed at all reaction temperatures. The corresponding IR spectra of the reaction products are shown in Fig. 4.

The IR spectra of CAU-1 show the characteristic bands for the symmetric and asymmetric stretching modes of the bridging carboxylate group between 1600 and 1400 cm^{-1}. The presence of methoxy groups in the structure of CAU-1 is clearly demonstrated by the asymmetric and symmetric C–H stretching vibrations at 2940 and 2835 cm^{-1} as well as the C–O stretching vibration at ~1080 cm^{-1}. The typical bands for the NH_2 group at ~3500 and 3380 cm^{-1} (symmetric and asymmetric N–H vibrations) are not observed, because they are obscured by a broad intensive band between 3200 and 3600 cm^{-1} due to the presence of water molecules. The characteristic double band for the C_{ar}–N (NH_2) (ar = aromatic) vibration at 1254 and 1334 cm^{-1} can be observed in all spectra.[30] The relatively high intensities of these characteristic amino-bands indicate a large quantity of non-methylated NH_2 groups. This suggests that the reaction temperature has no or only minor influence on the methylation of CAU-1.

3.3 Influence of the reaction time on the degree of methylation at the reaction temperature of 135 °C

To study the influence of the reaction time on the degree of methylation, five reactions were carried out under MW-assisted

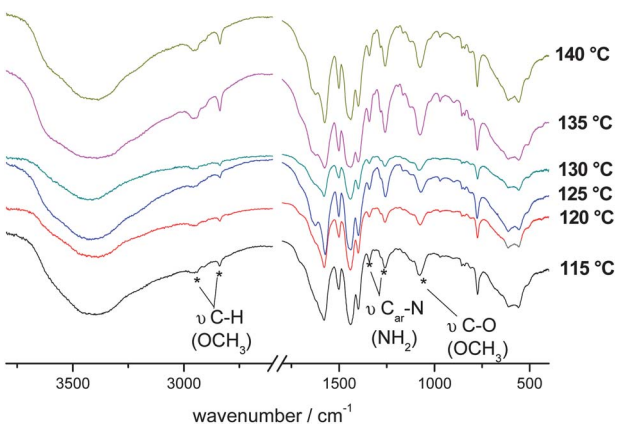

Fig. 4 IR-spectra of the CAU-1 product obtained by MW-assisted heating carried out in the temperature range between 115 and 140 °C.

heating at 135 °C. Reaction times were varied between 15 min and 638 min. The reaction products were characterized by elemental analyses, IR-spectroscopy and ^{1}H liquid-state NMR spectroscopy, which is the most powerful of the three methods. Employing ^{1}H NMR spectroscopy the digested reaction products, which contain only the isolated linker molecules redissolved in a dilute NaOD/D_2O solution, were characterised (Fig. 5). Elemental analyses and IR-spectroscopy were performed on the activated products. Two sets of signals are observed in the ^{1}H NMR spectra which belong to aminoterephthalate and *N*-methylaminoterephthalate ions. The sets of ^{1}H signals are labelled as follows (Scheme 1). The intensity of the resonance corresponding to the protons of the methyl group from the BDC–$NHCH_3^{2-}$ ions at 2.22 ppm in the ^{1}H NMR spectra (Fig. 5) increases with increasing reaction time due to the methylation of the amino groups. The degree of methylation was calculated from the sum of integrals of the aromatic H atoms and the integral of the methyl groups. This procedure is applied to all spectra that are discussed in this study.

The degree of methylation depends strongly on the reaction time. After a reaction time of 15 min only 8% of the amino groups are methylated. This value increases to 47 and 95% after a reaction time of 98 and 638 min, respectively. Furthermore small signals at 2.17 and 2.13 ppm appear in the spectra after a reaction time above 38 min, which indicates some multiple methylation of the amino groups at longer reaction times. Thus, post-synthetic modification, *i.e.* methylation, of CAU-1–NH_2 takes place within the cages. This reaction could be catalysed by Lewis acidic sites of free Al^{3+} ions in the reaction solution.

Focusing on the 6.0–7.3 ppm range the two sets of signals due to the methylated and non-methylated product are clearly distinguishable. Thus the degree of methylation is also visible in the aromatic ^{1}H region. In comparison to CAU-1–NH_2 the ^{1}H signals of the aromatic H atoms of CAU-1–$NHCH_3$ (labelled red) are shifted by about ±0.04 ppm (Fig. 5, left).

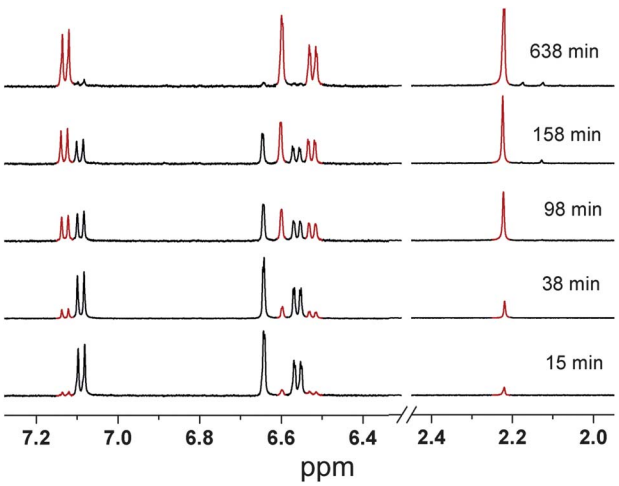

Fig. 5 ^{1}H NMR spectra of the extracted aminoterephthalate linkers collected from the MW-assisted syntheses at 135 °C using reaction times between 15 and 638 min. Each spectrum is normalized to the sum of the aromatic H signals (methylated (black) and non-methylated (red)), the aromatic signals (left) are multiplied by 2.5 relative to the methyl signals (right) for better visualisation.

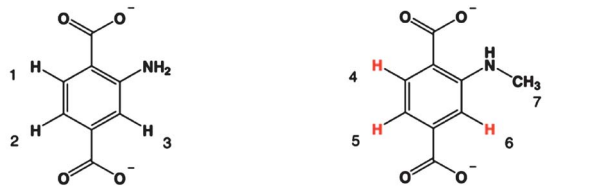

$[Al_4(OH)_2(OCH_3)_4(BDC\text{-}NH_2)_3]$ $[Al_4(OH)_2(OCH_3)_4(BDC\text{-}NHCH_3)_3]$

Scheme 1 Labelling of the ^{1}H signals in methylated and non-methylated aminoterephthalate ions: ^{1}H NMR 500 MHz, (NaOD/D_2O) δ: BDC–NH_2^{2-}: 7.09 (d, 1H, H1 $^3J_{H-H} = 8.1$ Hz); 6.64 (s, 1H, H3); 6.56 (d, 1H, H2 $^3J_{H-H} = 8.1$ Hz); BDC–$NHCH_3^{2-}$: 7.13 (d, 1H, H4 $^3J_{H-H} = 8.0$ Hz); 6.60 (s, 1H, H6); 6.52 (d, 1H, H5 $^3J_{H-H} = 8.0$ Hz); 2.22 (s, 3H, H7).

The methylation of the amino group leads to a low field shift for the protons in the *meta*-position (H4) and to a high field shift for the protons in *ortho*- and *para*-positions (H5, H6).

The results of the ^{1}H NMR investigation are also in good agreement with the elemental analyses of the compounds. Table 1 shows the experimental and calculated CHN values of the products using a reaction time of 38, 98 and 638 min. It should be noted that after washing no water molecules are enclosed in the framework. In addition, the methylation of the amino groups is also clearly demonstrated by the appearance of new vibrational bands in the IR spectra that are associated with the formation of the methylamine functionality (Fig. 6).

The two possible bands due the symmetric and asymmetric stretching vibration of the amino group (ν N–H) at 3520 and 3390 cm^{-1} are clearly visible in the spectra collected for short reaction times (15, 38 min). The N–H double band vanishes and one broad band at 3393 cm^{-1} due to the N–H vibration of the methylamine is observed for the reactions using a longer reaction time. A new signal at 1285 cm^{-1} is observed, which increases at longer reaction times and can be assigned to the C_{ar}–N stretching vibration of the methylamine group.[30] At the same time, the bands due to the C_{ar}–N (NH_2) vibration at 1260 and 1340 cm^{-1} appear with much lower intensities. This indicates the high degree of methylation of the NH_2 groups at longer reaction times.

The IR spectra confirm the results of the ^{1}H NMR spectroscopy that methylation increases at longer reaction times.

3.4 Influence of the reaction time on the degree of methylation at the reaction temperature of 145 °C

To speed up the crystallisation of CAU-1, the reaction temperature was raised to 145 °C. MW-assisted synthesis was stopped after shorter reaction times (2, 3, 5, and 10 min) in order to minimize the degree of methylation. For the NMR measurements the product was directly dissolved in NaOD/D_2O, which allows detecting the methoxy groups. The ^{1}H NMR spectra of the washed products show at longer reaction times an increase in the degree of methylation of the amino groups, as well as the increase of the amount of methoxy groups (2.64 ppm, Fig. S4†). This signal can be assigned to CH_3OD, which is formed by the release of the incorporated methoxy groups from the Al-based brick of the CAU-1 framework. According to the composition $[Al_4(OH)_2(OCH_3)_4(BDC\text{–}NH_2)_3]$ for CAU-1–NH_2 an integral ratio of methoxy H-atoms to aromatic H-atoms = 4 : 3 (= 1.33)

Table 1 Elemental analysis results of CAU-1 synthesised *via* MW-assisted heating at 135 °C for 38, 98 and 638 min. Calculated values correspond to a composition according to $[Al_4(OH)_2(OCH_3)_4(BDC–NH_{2-x}C_xH_{3x})_3]$

Reaction time/min	Degree of methylation (x) (%)	C_{exp} (calc.) (%)	H_{exp} (calc.) (%)	N_{exp} (calc.) (%)
38	16 (0.16)	42.28 (42.21)	3.72 (3.73)	5.09 (5.18)
98	47 (0.47)	42.90 (42.90)	3.92 (3.90)	5.22 (5.10)
638	95 (0.95)	43.31 (43.92)	4.10 (4.15)	4.98 (4.98)

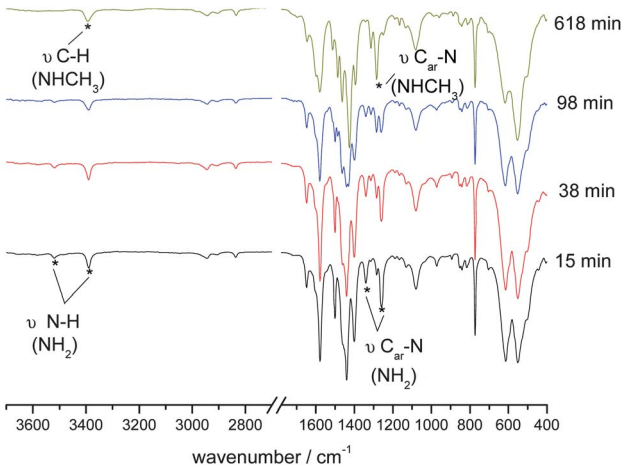

Fig. 6 IR spectra of CAU-1 synthesised *via* MW-assisted heating at the reaction temperature of 135 °C. Four different reaction times were investigated (15, 38, 98 and 638 min).

is expected. Increasing the reaction time from 2 to 10 min leads to integral ratios varying from 1.10 to 1.31, respectively. Thus, short reactions lead only to the partial incorporation of methoxy (83%) groups while after 10 min 99% of the methoxy groups are present. We presume that at very short reaction times structural defects are present. This has also been reported in the synthesis of MOF-5 using short reaction times.[31]

As observed at reaction temperatures of 135 °C, an increase of reaction time leads to a higher degree of methylation of the amino groups, which is clearly visible by an increase of the signal at 2.2 ppm due to the methyl groups. The results are summarized in Table 2.

The lowest degree of methylation of the amino group was found for a reaction time of only two minutes (2%). However, the reaction was not complete and only a very small amount of CAU-1–NH_2 could be obtained (yield < 10% of the washed product, based on aminoterephthalic acid). Using a reaction time of ten minutes leads to a high yield (90%) but also to a much higher degree of methylation (13%).

The results of the NMR investigation fit well with the elemental analyses of the compounds, which are also listed in Table 2. For the products at reaction times of 2 and 3 min water molecules are enclosed within the framework. The best compromise between the product yield and degree of methylation was determined to be at a reaction time of 3 min. In three repeated reactions the dissolved products exhibit the identical degree of methylation (3%), which clearly shows the good reproducibility of the MW-assisted synthesis (Fig. S5†).

3.5 Influence of the heating method and reactor material

In order to investigate the methylation of the amino groups during the CAU-1 synthesis applying conventional heating methods, reactions were performed in Teflon-lined steel autoclaves and glass autoclaves. A mixture of $AlCl_3 \cdot 6H_2O$ (463.5 mg, 1.920 mmol) and $H_2N–H_2BDC$ (116.60 mg, 0.645 mmol) was suspended in methanol (6.175 mL) and heated at 125 °C for 5 h. The washed products were directly dissolved in a dilute NaOD/D_2O solution and characterized by ^1H NMR spectroscopy (Fig. 7). Three sets of signals can be observed in the spectra, which can be assigned to aminoterephthalate, *N*-methylaminoterephthalate, and *N*,*N*-dimethylaminoterephthalate. The signals are discussed for the reaction products obtained in the glass reactor. The labelling of the sets of ^1H signals is listed in Scheme S1† in the ESI. The reaction carried out in a Teflon-lined steel autoclave led to only a small amount of CAU-1–$NHCH_3$ (12%) compared to the reaction performed in a glass autoclave, which shows that 52% of the amino groups are single methylated and 21.5% of the amino groups are twofold methylated (CAU-1–$N(CH_3)_2$). The variation of the degree of methylated amino groups as a function of the use of different reaction vessels may be caused by different heating or diffusion rates within the reactors.

3.6 Influence of the thermal activation process on the composition of CAU-1–NH_2

The TG analysis of CAU-1–NH_2 was performed on the degassed sample (30 min/130 °C at 1×10^{-3} bar) in air. The TG curve is shown in Fig. S6†. A very flat step, corresponding to a weight loss of 10%, is observed between 50 and 370 °C. This weight loss cannot to be due to the presence of incorporated solvent molecules since this would lead to a well defined step in the TG curve. At higher temperatures, above 370 °C, the decomposition of the frameworks takes place and Al_2O_3 is formed. The observed and calculated total weight loss, based on the final mass of Al_2O_3, fit well (obs. 25.1%, calc. 25.5%). To

Table 2 Elemental analyses, degree of incorporation of methoxy and methyl groups in CAU-1 synthesised by MW-assisted heating at 145 °C. Reaction times of 2 to 10 min were used. Calculated values are based on a composition according to $[Al_4(OH)_{2+y}(OCH_3)_{4-y}(BDC–NH_{2-x}C_xH_{3x})_3] \cdot wH_2O$

Time/min	Methoxy groups (y) (%)	Degree of methylation (x) (%)	H_2O formula (w)	C_{exp} (calc.) (%)	H_{exp} (calc.) (%)	N_{exp} (calc.) (%)
2	83 (0.68)	2 (0.02)	2.3	39.31 (39.34)	3.47 (3.84)	5.34 (5.28)
3	88 (0.48)	3 (0.03)	1.3	40.36 (40.37)	3.53 (3.82)	5.14 (5.12)
5	96 (0.16)	6 (0.06)	—	42.84 (41.84)	3.69 (3.69)	5.34 (5.22)
10	99 (0.04)	13 (0.13)	—	41.81 (42.11)	3.70 (3.71)	5.22 (5.19)

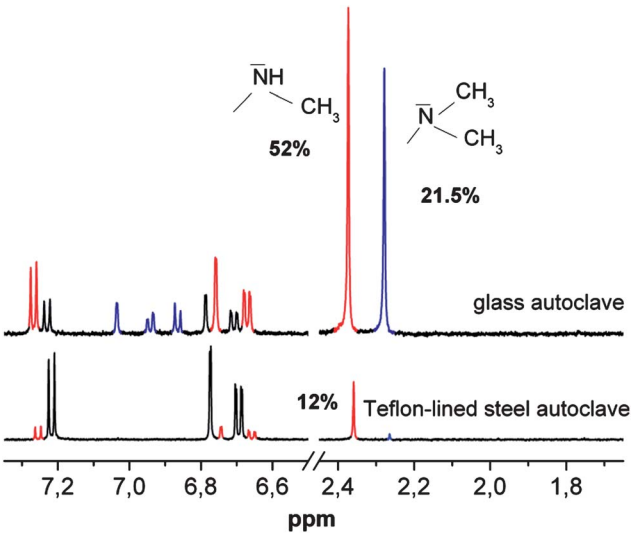

Fig. 7 ^{1}H NMR spectra of CAU-1 prepared by conventional synthesis using a Teflon-lined autoclave (bottom) or a glass autoclave (top). After the washing process both compounds were directly dissolved in a dilute NaOD/D_2O solution. Each spectrum is normalized to the H3, H6, and H10 signals, respectively. Signals due to the linker molecules are coloured as follows: blue: dimethylated, red: methylated and black: non-methylated.

investigate the processes taking place up to 370 °C the influence of the thermal activation process on the composition of CAU-1–NH_2 was studied using the product obtained by MW-assisted synthesis (3 min/145 °C). In the course of this study different activation times, temperatures and atmospheres (vacuum *vs.* air) were used. After thermal treatment the samples were characterized by elemental analyses, IR-spectroscopy and ^{1}H-liquid-state NMR spectroscopy. For the ^{1}H-liquid-state NMR spectroscopy investigations the samples were directly dissolved in a dilute NaOD/D_2O solution. Elemental analyses and IR spectroscopy were performed on the thermally activated products without any further treatment. Fig. S7† shows the ^{1}H spectra of the dissolved CAU-1–NH_2 compounds after thermal treatment under different temperatures, activation times, and activation atmospheres (vacuum *vs.* air). For all five activation procedures, we observed a decrease in the fraction of incorporated methoxy groups retained within the framework (see Table 3). Heating under vacuum at 130 °C for 12 h leads only to the release of a very small fraction of methoxy groups (83% retained) compared to similar heating procedures at 120 °C (55% retained) in air. Even a very short thermal treatment of 30 min at 120 °C leads to a significant removal of methoxy groups (73% retained). While an activation temperature of 190 °C for 12 h leads to an almost complete removal of the incorporated methoxy groups (8% retained), no signal is observed after an activation time of 24 h. Thus methoxy groups are fully replaced by hydroxy groups.

The resulting compound $[Al_4(OH)_6(BDC–NH_2)_3]\cdot xH_2O$, denoted as CAU-1–$NH_2$(OH), contains large amounts of adsorbed water molecules, due to a higher hydrophilicity of the framework. Water molecules from the air are necessary for the substitution of methoxy groups by hydroxy groups. This has also been observed previously for thermal activation procedures of

Table 3 Percentage of incorporated methoxy groups within the structure of CAU-1–NH_2, $[Al_4(OH)_{2+y}(OCH_3)_{4-y}(BDC–NH_{2-x}C_xH_{3x})_3]$, after thermal treatment. The CAU-1 products were synthesised by MW-assisted heating using a reaction time of 3 min at 145 °C

Activation procedure	Methoxy groups (%)	Composition in y and x
—	88	$y = 0.48$; $x = 0.03$
130 °C/12 h (3 mbar)	83	$y = 0.68$; $x = 0.03$
120 °C/0.5 h	73	$y = 1.08$; $x = 0.03$
120 °C/12 h	55	$y = 1.80$; $x = 0.03$
190 °C/12 h	8	$y = 3.68$; $x = 0.03$
190 °C/24 h	0	$y = 4.00$; $x = 0.03$
190 °C/12 h (3 mbar)	83	$y = 0.68$; $x = 0.03$

acidic zeolite catalysts, which contain surface methoxy species.[32,33] The removal of the methoxy groups is also observed by IR spectroscopy.

The IR spectra of CAU-1–NH_2 before and after the thermal treatment in air (190 °C/24 h) are shown in Fig. 8. The two broad bands due to the symmetric and asymmetric modes of C–H stretching vibration of the bridging methoxy groups at 2940 and 2840 cm^{-1} and the C–O stretching vibration of the incorporated methoxy groups at ~1080 cm^{-1} vanish in the spectrum of the heated sample. At the same time, the intensity of the weak signal at ~3700 cm^{-1} due to the bridging OH groups increases. The powder pattern of the washed sample exhibits no significant change in crystallinity after thermal treatment (see Section 3.8 and Fig. 13).

3.7 Post-synthetic modification of CAU-1–NH_2

Using MW-assisted heating for the syntheses of CAU-1 led to non-methylated amino groups at very short reaction times. This should allow the post-synthetic modification of the amino functionality, which has been previously reported, for example, for Al-MIL-53–NH_2 and IRMOF-3.[16,34] For the proof of principle we reacted CAU-1–NH_2 with acetic anhydride, which led to the fully acylated compound CAU-1–$NHCOCH_3$ ($[Al_4(OH)_2(OCH_3)_4(BDC–NHCOCH_3)_3]\cdot xH_2O$) (Scheme 2).

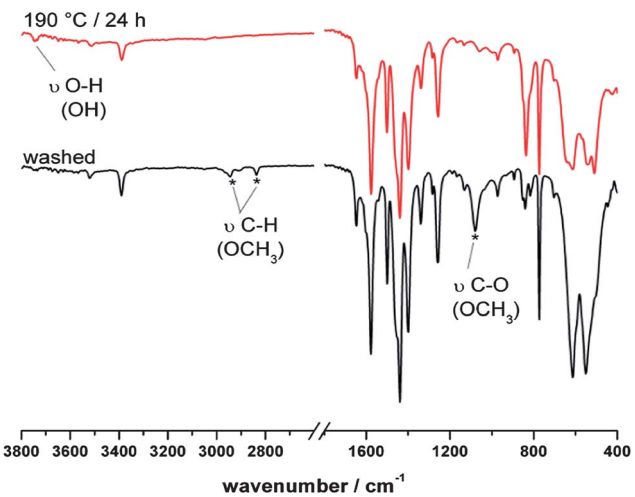

Fig. 8 Comparison of the IR-spectra of washed CAU-1 before (black) and after thermal treatment (190 °C for 24 h in air) (red).

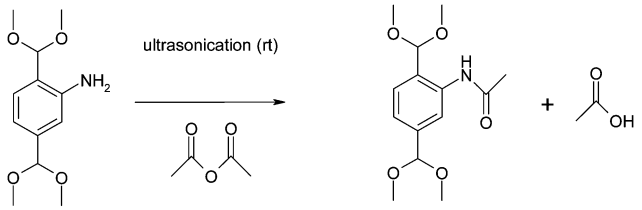

Scheme 2 Post-synthetic modification of CAU-1–NH_2 by reaction with acetic anhydride.

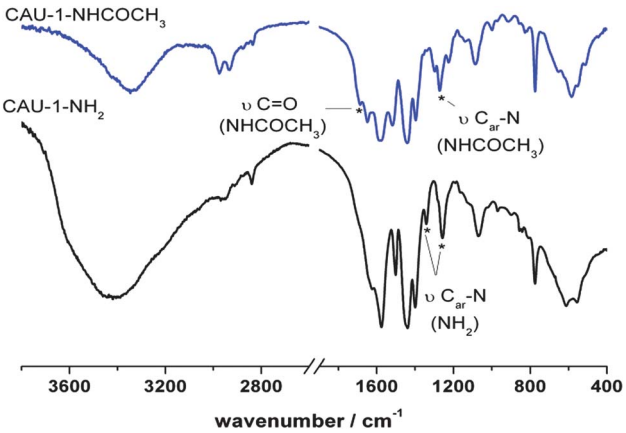

Fig. 9 IR spectra of modified CAU-1 (blue) and unmodified CAU-1–NH_2 (black). The characteristic bands in the spectra are marked with black stars.

Fig. 9 shows the IR spectra of the CAU-1–NH_2 and CAU-1–$NHCOCH_3$. New signals at 1690 and 1274 cm^{-1} in the spectrum of CAU-1–$NHCOCH_3$ are caused by the C=O and the C_{ar}–N stretching vibrations of the amide group respectively.[30] At the same time, the bands due to the C_{ar}–N (NH_2) stretching vibration at 1258 and 1341 cm^{-1} do not appear in the spectrum anymore. This indicates a nearly complete modification of the NH_2 groups.

The results of the IR-spectroscopic measurements of the post-synthetic modification of CAU-1–NH_2 are also confirmed by solid-state ^{13}C and ^{15}N MAS NMR experiments (Fig. 10 and 11).

In contrast to the material obtained by conventional heating (see Ahnfeldt *et al.*,[17] Fig. S5b†), the ^{13}C spectrum of CAU-1–NH_2 shows no signal at 27 ppm (Fig. 10, top). This depicts that there are no –$NHCH_3$ groups present. Upon post-synthetic modification, two new signals at 24 ppm and 178 ppm are observed, which can be assigned to the methyl group of the acetamide and the carbonyl ^{13}C atom, respectively. The signal of the ipso carbon atom, which is closest to the newly formed amide bond, shifts from 150 ppm to 141 ppm.

The ^{15}N CPMAS-NMR spectrum of CAU-1–NH_2 (Fig. 11) exhibits a signal at −316 ppm, which we assigned to the –NH_2 group. The signal due to the N-atom of the amino group shifts in the spectrum of CAU-1–$NHCOCH_3$ to −253 ppm caused by the formation of the amide group. There is no signal left at −316 ppm which confirms a complete modification of the –NH_2 group.

Further structural information for CAU-1–$NHCOCH_3$ could be gained by a series of solid-state NMR experiments like ^{1}H–^{1}H spin diffusion spectra and carbon–proton HETCOR spectra. In Fig. 12 different ^{1}H spin diffusion spectra of CAU-1–$NHCOCH_3$ as a function of the mixing times are shown. The signal assignment for these spectra is as follows: at 0.8 and 1.5 ppm two signals for the methyl protons of the acetyl residue, at 3.0 ppm a signal for the methoxy groups, at 7–8 ppm a broad signal for the aromatic protons and at 9 ppm the NH proton signal.

For very short spin diffusion mixing times (1 μs) no correlation occurs, at short mixing times (700 μs) first spatial proximity can be observed between the signal at 3.0 ppm and 1.5 ppm which we assign to the methoxy groups of the inorganic brick and the methyl group of the acetamide, respectively. This can only be explained by a short distance between the methoxy groups and a part of the linker residues. At medium mixing times (1500 μs) the other correlations begin to develop, whereas even at longer mixing times (4000 μs) the correlation between the signal at

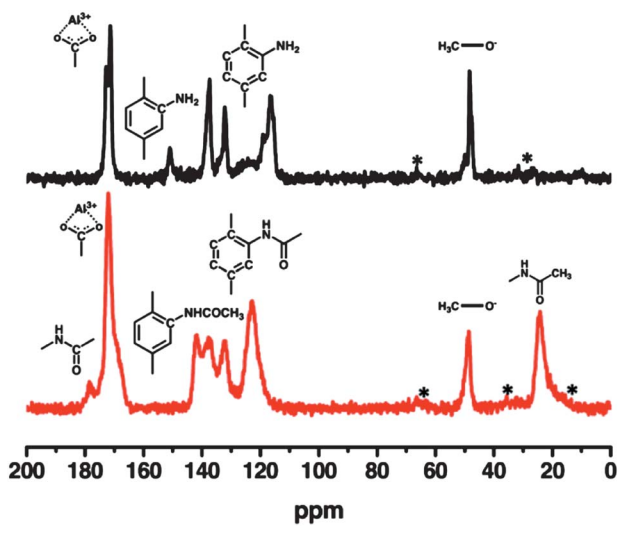

Fig. 10 ^{13}C MAS NMR spectra of CAU-1–NH_2 (black) and CAU-1–$NHCOCH_3$ (red). The signals marked by an asterisk (*) are due to spinning side bands.

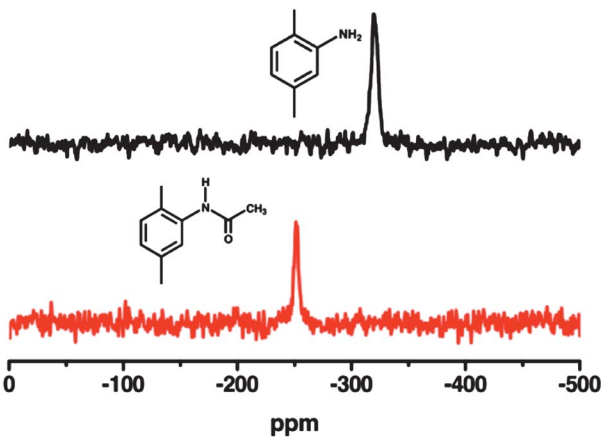

Fig. 11 ^{15}N CPMAS NMR spectra of CAU-1–NH_2 (black) and CAU-1–$NHCOCH_3$ (red).

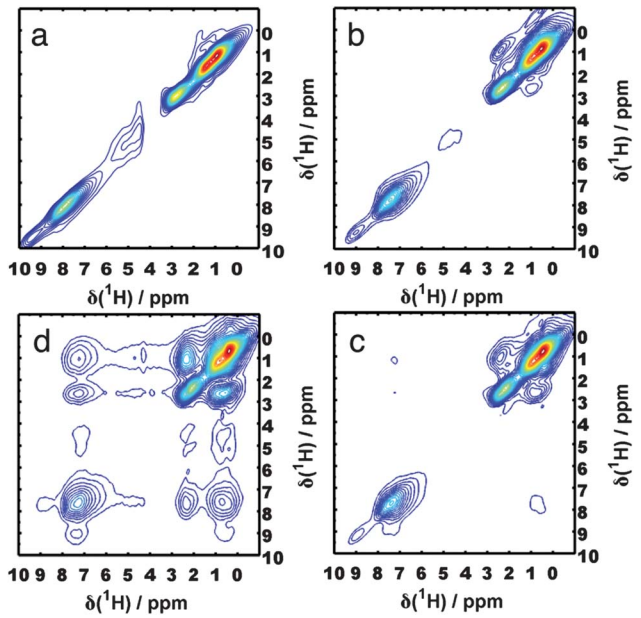

Fig. 12 2D spin diffusion spectra of CAU-1–$NHCOCH_3$ at mixing times of 1 μs (a), 700 μs (b), 1500 μs (c) and 4000 μs (d).

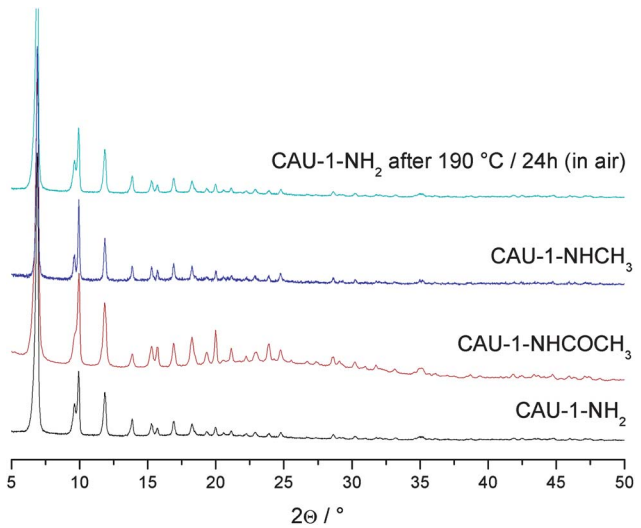

Fig. 13 XRPD patterns of CAU-1–NH_2 (black), CAU-1–$NHCOCH_3$ (red), CAU-1–$NHCH_3$ (blue), and CAU-1–NH_2 after thermal treatment at 190 °C for 24 h in air (green).

Table 4 Refined lattice parameters determined from XRPD data of CAU-1–X (X = –NH_2, –$NHCH_3$, –$NHCOCH_3$) and CAU-1–NH_2(OH), which was heated before the measurement to exchange the incorporated methoxy groups by hydroxy groups (190 °C/24 h in air)

Compound	*a*/Å	*b*/Å	*c*/Å	*V*/Å^3
CAU-1–NH_2	18.319(4)	18.319(4)	17.753(7)	5958(1)
CAU-1–$NHCH_3$	18.331(5)	18.331(5)	17.739(7)	5960(2)
CAU-1–$NHCOCH_3$	18.341(5)	18.341(5)	17.735(4)	5966(1)
CAU-1–NH_2(OH)	18.330(6)	18.330(6)	17.761(7)	5968(1)

3.0 and 0.8 ppm is still weak. We interpret this behaviour as a long distance between methoxy groups and methyl groups of these linker residues. This is only possible if there are different positions for the methyl residues available, like an orientation dependence between an alignment of the linker into the smaller pores (short distances) and into the bigger pores (longer distances). For this model we estimate *via* the intensity ratio of the signals at 1.5 and 0.8 ppm one-third of the linker molecules to be oriented into the small pores and two-thirds into the bigger pores as a possible scenario.

Similar experiments were conducted for CAU-1–$NHCH_3$, but no such behaviour could be observed (see Fig. S1†). This could be explained by the smaller volume of the methyl residues relative to the acetyl residue of CAU-1–$NHCOCH_3$.

3.8 XRPD studies on CAU-1–NH_2, CAU-1–$NHCH_3$, CAU-1–$NHCOCH_3$ and CAU-1–NH_2(OH)

CAU-1–NH_2, CAU-1–$NHCH_3$, and CAU-1–$NHCOCH_3$ could be synthesized with high crystallinity and without crystalline impurities. The thermal treatment of CAU-1–NH_2 at 190 °C for 24 h in air led to a complete replacement of the methoxy by the hydroxy groups. Fig. 13 shows powder patterns of all three products, as well as the one of CAU-1–NH_2 after thermal treatment (190 °C/24 h in air).

To determine the influence of the composition on the crystal structure, the lattice parameters were determined by using WinXPow.[28] Lattice parameter refinements and systematic extinctions led for all compounds to a tetragonal body-centred unit cell with very similar lattice parameters in all four cases (Table 4).

3.9 Temperature-dependent X-ray powder diffraction measurement (TD-XRPD)

For investigating the influence of the different compositions of the compounds on the thermal properties TD-XRPD measurements of all four compounds were performed. The TD-XRPD measurements of CAU-1–NH_2, CAU-1–NH_2(OH), CAU-1–$NHCH_3$ and CAU-1–$NHCOCH_3$ are shown in Fig. 14 and S8–S10†, respectively. In good agreement with the results of the TG

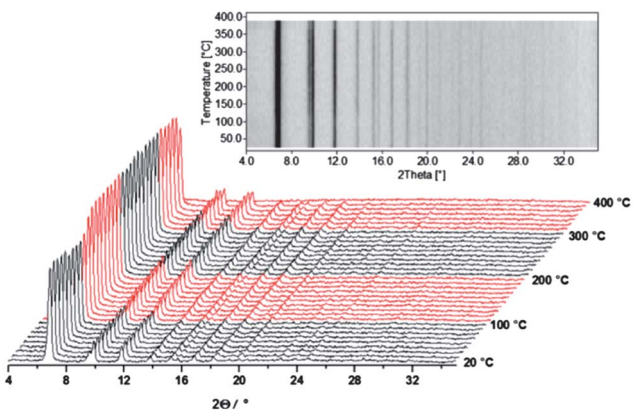

Fig. 14 Temperature-dependent X-ray powder diffraction patterns of CAU-1–NH_2 in air (20–400 °C).

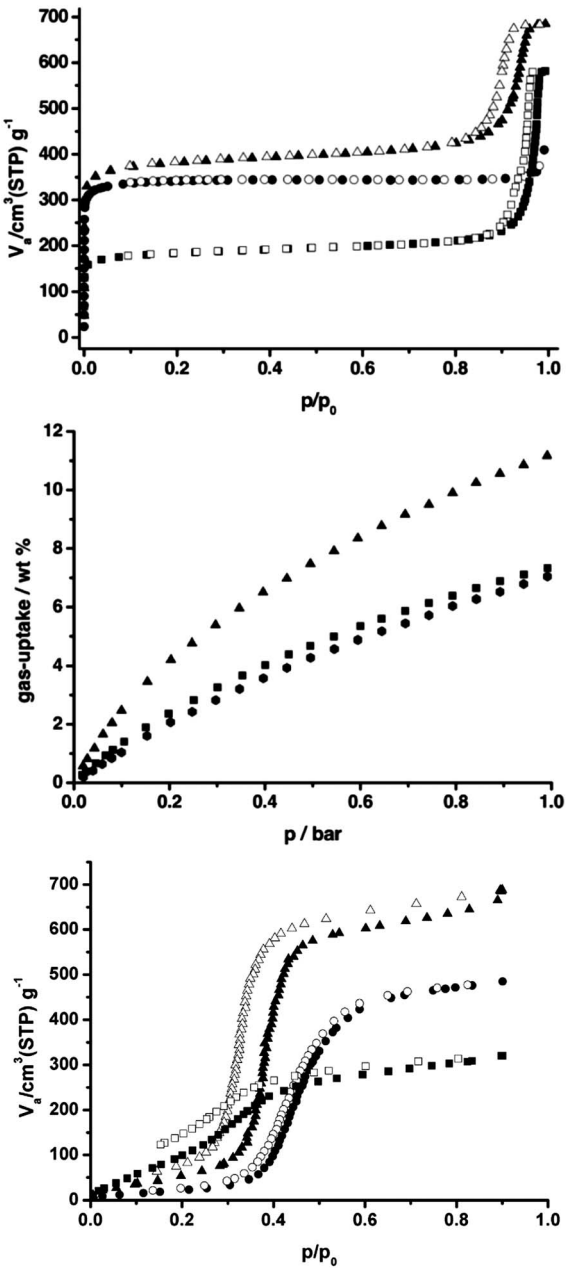

Fig. 15 N_2 (top), CO_2 (middle) and H_2O (bottom) sorption isotherms for CAU-1–NH_2 (● = adsorption, ○ = desorption), CAU-1–$NHCH_3$ (▲ = adsorption, △ = desorption) and CAU-1–$NHCOCH_3$ (■ = adsorption, □ = desorption). The H_2O and CO_2 sorption isotherms were collected at 298 K, N_2 sorption experiments at 77 K.

analysis of CAU-1–NH_2 (Fig. S6†), all investigated compounds show a high thermal stability at least up to 350 °C. At around 100 °C, increased reflection intensities were observed in the TD-XRPD measurements, which are accompanied by the removal of absorbed water molecules. Up to the decomposition of the framework, no changes of the reflection positions are detectable.

However, a comparison of the TD-XRPD measurement of all four CAU-1 derivatives led to the conclusion that the different compositions have no or only a minor influence on their thermal behaviour.

Table 5 Comparison of specific surface area S_A, total pore volume $V(N_2)$ and total pore volume $V(H_2O)$ of CAU-1–NH_2, CAU-1–$NHCH_3$, and CAU-1–$NHCOCH_3$

CAU-1–X	–NH_2	–$NHCH_3$	–$NHCOCH_3$
$S_A/m^2\ g^{-1}$	1530	1340	680
$V(N_2)^a/cm^3\ g^{-1}$	0.64	0.53	0.30
$V(H_2O)^b/cm^3\ g^{-1}$	0.55	0.48	0.25
wt $CO_2{}^c$ (%)	11.2	7.0	7.3

[a] Calculated at $p/p_0 = 0.5$ from the nitrogen adsorption isotherm and 77 K. [b] Calculated at $p/p_0 = 0.9$ from the water adsorption isotherm and 298 K. [c] Calculated at 1 bar and 298 K.

3.10 Sorption study on CAU-1

The three CAU-1 derivatives, CAU-1–NH_2, CAU-1–$NHCH_3$, and CAU-1–$NHCOCH_3$, show different sorption properties depending on the functional group and the adsorptive employed (Fig. 15).

Using nitrogen (Fig. 15, top), Type 1 isotherms are observed for all three compounds. The apparent specific surface area, calculated using the BET equation, decreases strongly from 1530 $m^2\ g^{-1}$ (CAU-1–NH_2) to 680 $m^2\ g^{-1}$ (CAU-1–$NHCOCH_3$) depending on the size of the functional group. Accordingly, the micropore volume also decreases from 0.64 $cm^3\ g^{-1}$ (CAU-1–NH_2) to 0.30 $cm^3\ g^{-1}$ (CAU-1–$NHCOCH_3$). Adsorption experiments with water vapour show a higher uptake for CAU-1–$NHCOCH_3$ at low p/p_0 values compared to CAU-1–NH_2 and CAU-1–$NHCH_3$. This may be due to hydrogen bonding interactions of the amide group, which decrease in the order –$NHCOCH_3$ > –NH_2 > –$NHCH_3$, as well as a higher adsorption potential due to narrower pore sizes. The order is in agreement with the desorption curves of CAU-1–$NHCOCH_3$ and CAU-1–NH_2, where a slight hysteresis due to these stronger interactions with the adsorbate is observed. The micropore volume calculated from the water adsorption isotherms (Fig. 15, bottom) is smaller than the calculated micropore volume from the nitrogen isotherms, as observed for other MOFs like DUT-4 and HKUST-1.[35] The CO_2 sorption measurements of the three compounds (Fig. 15, middle) were carried out at 298 K and up to 1 bar. Under this condition, the maximum uptake was not accomplished. However, the isotherm of CAU-1–NH_2 shows a higher uptake of CO_2 (11.2 wt%) than the isotherms of CAU-1–$NHCOCH_3$ (7.3 wt%) and CAU-1–$NHCH_3$ (7.0 wt%). The higher uptake of CO_2 from the amide functionalized CAU-1 compared to CAU-1–$NHCH_3$ could be explained by stronger host–guest interactions of the adsorbent with CO_2. The results of all sorption measurements are summarised in Table 5.

4. Conclusion

In summary, we have demonstrated that in the field of porous materials the presence of guest molecules, like solvent or uncoordinated linker molecules, can easily result in a misinterpretation of the data. Thus, an extensive characterisation of the reaction products of MOF syntheses is mandatory to fully understand structure–property relationships.

In the case of CAU-1, X-ray diffraction, IR- as well as liquid-state and solid-state NMR-spectroscopy, *in situ* EDXRD,

TD-XRPD, thermogravimetric and elemental analysis, sorption experiments and dynamic light scattering have been applied. Surprisingly, not only the synthesis conditions during the product formation lead to isoreticular products of different compositions, *i.e.*, variation of the degree of methylation, but also the activation procedure needs to be controlled in detail.

We showed the various modifications of the organic linker. By conventional heating methylation of the amino residue occurs depending on the reaction time, whereas by MW-assisted synthesis and short reaction times methylation can be suppressed completely. Even post-synthesis modification is possible *via* acetylation of the amino group.

Also the modification of the inorganic brick is possible during the activation process in air *via* substitution of the methoxy by hydroxy groups.

Liquid- and solid-state NMR spectroscopy proved to be an essential tool for the thorough investigation of the synthesis routes. *Via* solid-state NMR spectroscopy the methylation reaction under conventional synthesis conditions was discovered and the post-synthetic modification as well as the linker orientation were studied.

Acknowledgements

The authors thank Michael Wharmby for cross-reading this article and fruitful discussions. The state of Schleswig-Holstein and the Deutsche Forschungsgemeinschaft (DFG, SPP 1362) "Porous Metal–Organic Frameworks" under the grant STO 643/5-2 and SE 1417/3-2 are gratefully acknowledged for the financial support. The research leading to these results has received funding from the European Community's Seventh Framework Programme (FP7/2007-2013) under grant agreement no. 228862.

Notes and references

1 U. Mueller, M. Schubert, F. Teich, H. Puetter, K. Schierle-Arndt and J. Pastre, *J. Mater. Chem.*, 2006, **16**, 626.
2 P. Horcajada, C. Serre, M. Vallet-Reg, M. Sebban, F. Taulelle and G. Férey, *Angew. Chem., Int. Ed.*, 2006, **45**, 5974.
3 J. Li, R. Kuppler and H. Zhou, *Chem. Soc. Rev.*, 2009, **38**, 1477.
4 J. Y. Lee, O. K. Farha, J. Roberts, K. A. Scheidt, S. T. Nguyen and J. T. Hupp, *Chem. Soc. Rev.*, 2009, **38**, 1450.
5 G. Lu and J. T. Hupp, *J. Am. Chem. Soc.*, 2010, **132**, 7832.
6 M. Gaab, N. Trukhan, S. Maurer, R. Gummaraju and U. Müller, *Microporous Mesoporous Mater.*, 2011, DOI: 10.1016/j.micromeso.2011.08.016.
7 (*a*) H. Reinsch, M. Krüger, J. Wack, J. Senker, F. Salles, G. Maurin and N. Stock, *Microporous Mesoporous Mater.* DOI: 10.1016/j.micromeso.2011.05.029; (*b*) C. Volkringer, T. Loiseau, M. Haouas, F. Taulelle, D. Popov, M. Burghammer, C. Riekel, C. Zlotea, F. Cuevas, M. Latroche, D. Phanon, C. Knöfelv, P. L. Llewellyn and G. Férey, *Chem. Mater.*, 2009, **21**, 5783; (*c*) A. Comotti, S. Bracco, P. Sozzani, S. Horike, R. Matsuda, J. Chen, M. Takata, Y. Kubota and S. Kitagawa, *J. Am. Chem. Soc.*, 2008, **130**, 13664.
8 C. Volkringer, T. Loiseau, N. Guillou, G. Férey, M. Haouas, F. Taulelle, N. Audebrand, I. Margiolaki, D. Popov, M. Burghammer and C. Riekel, *Cryst. Growth Des.*, 2009, **9**, 2927.
9 T. Loiseau, C. Serre, C. Huguenard, G. Fink, F. Taulelle, M. Henry, T. Bataille and G. Férey, *Chem.–Eur. J.*, 2004, **10**, 1373.
10 (*a*) T. Loiseau, C. Mellot-Draznieks, H. Muguerra, G. Férey, M. Haouas and F. Taulelle, *C. R. Chim.*, 2005, **8**, 765; (*b*) I. Senkovska, F. Hoffmann, M. Fröba, J. Getzschmann, W. Böhlmann and S. Kaskel, *Microporous Mesoporous Mater.*, 2009, **122**, 93.
11 (*a*) T. Loiseau, L. Lecroq, C. Volkringer, J. Marrot, G. Férey, M. Haouas, F. Taulelle, S. Bourrelly, P. L. Llewellyn and M. Latroche, *J. Am. Chem. Soc.*, 2006, **128**, 10223; (*b*) C. Volkringer, D. Popov, T. Loiseau, G. Férey, M. Burghammer, C. Riekel, M. Haouas and F. Taulelle, *Chem. Mater.*, 2009, **21**, 5695.
12 (*a*) T. Ahnfeldt, J. Moellmer, V. Guillerm, R. Staudt, C. Serre and N. Stock, *Chem.–Eur. J.*, 2011, **23**, 6462; (*b*) S. Biswas, T. Ahnfeldt and N. Stock, *Inorg. Chem.*, 2011, **50**, 9518; (*c*) D. Himsl, D. Wallacher and M. Hartmann, *Angew. Chem., Int. Ed.*, 2009, **48**, 4639.
13 A. Boutina, S. Couck, F.-X. Coudert, P. Serra-Crespo, J. Gascon, F. Kapteijn, A. H. Fuchs and J. F. M. Denayer, *Microporous Mesoporous Mater.*, 2011, **140**, 108.
14 P. Serra-Crespo, E. V. Ramos-Fernandez, J. Gascon and F. Kapteijn, *Chem. Commun.*, 2011, **47**, 8578.
15 K. K. Tanabe and S. M. Cohen, *Chem. Soc. Rev.*, 2011, **40**, 498.
16 (*a*) T. Ahnfeldt, D. Gunzelmann, T. Loiseau, D. Hirsemann, J. Senker, G. Férey and N. Stock, *Inorg. Chem.*, 2009, **48**, 3057; (*b*) J. Gascon, U. Aktay, M. D. Hernandez-Alonso, G. P. M. van Klink and F. Kapteijn, *J. Catal.*, 2009, **261**, 75.
17 T. Ahnfeldt, N. Guillou, D. Gunzelmann, I. Margiolaki, T. Loiseau, G. Férey, J. Senker and N. Stock, *Angew. Chem., Int. Ed.*, 2009, **48**, 5163.
18 P. Serra-Crespo, E. V. Ramos-Fernandez, J. Gascon and F. Kapteijn, *Chem. Mater.*, 2011, **23**, 2565.
19 Comment: CAU-1 refers to the general framework structure of these compounds. In the following the functionalisation of the $–NH_2$ groups ($–NH_2$, $NHCH_3$, $–N(CH_3)_2$) is explicitly stated to prevent further confusion.
20 J. H. Cavka, S. Jakobsen, U. Olsbye, N. Guillou, C. Lamberti, S. Bordiga and K. P. Lillerud, *J. Am. Chem. Soc.*, 2008, **130**, 13850.
21 M. Dan-Hardi, C. Serre, T. Frot, L. Rozes, G. Maurin, C. Sanchez and G. Ferey, *J. Am. Chem. Soc.*, 2009, **131**, 10857.
22 F. Hinterholzinger, C. Scherb, T. Ahnfeldt, N. Stock and T. Bein, *Phys. Chem. Chem. Phys.*, 2010, **12**, 4515.
23 X. Si, C. Jiao, F. Li, J. Zhang, S. Wang, S. Liu, Z. Li, L. Sun, F. Xu, Z. Gabelica and C. Schick, *Energy Environ. Sci.*, 2011, **4**, 4522.
24 M. Pera-Titus, M. Savonnet and D. Farrusseng, *J. Phys. Chem. C*, 2010, **114**, 17665.
25 M. Savonnet, E. Kockrick, A. Camarata, D. Bazer-Bachi, N. Bats, V. Lecocq, C. Pinela and D. Farrusseng, *New J. Chem.*, 2011, **35**, 1892.
26 T. Ahnfeldt and N. Stock, *CrystEngComm*, 2012, **14**, 505.
27 A. Boultif and D. Louer, *J. Appl. Crystallogr.*, 1991, **24**, 987.
28 *STOE WinXPOW version 2.11*, Stoe & Cie GmbH, Darmstadt, Germany, 2005.
29 A. Lesage and L. Emsley, *J. Magn. Reson.*, 2001, **148**, 449.
30 G. Socrates, *Infrared and Raman Characteristic Group Frequencies: Tables and Charts*, Wiley & Sons, West Sussex, UK, 3rd edn, 2004.
31 U. Ravon, M. Savonnet, S. Aguado, M. E. Domine, E. Janneau and D. Farrusseng, *Microporous Mesoporous Mater.*, 2010, **129**, 319.
32 W. Wang, A. Buchholz, M. Seiler and M. Hunger, *J. Am. Chem. Soc.*, 2003, **125**, 15260.
33 W. Wang and M. Hunger, *Acc. Chem. Res.*, 2008, **41**, 895.
34 Z. Wang and S. M. Cohen, *J. Am. Chem. Soc.*, 2007, **129**, 12368.
35 P. Küsgens, M. Rose, I. Senkovska, H. Fröde, A. Henschel, S. Siegle and S. Kaskel, *Microporous Mesoporous Mater.*, 2009, **120**, 325.

4.2.4 A new family of porous MOFs with a new Al-based brick: $[Al_2(OCH_3)_4(O_2C\text{-}X\text{-}CO_2)]$ (X=aryl)

Das Manuskript wurde zur Publikation bei der Zeitschrift „Dalton Transactions“ eingereicht. Die Zusatzinformation zu diesem Manuskript befindet sich im Anhang 7 auf Seite 214.

In der Publikation wird die Hochdurchsatzuntersuchung des Systems $Al^{3+}/HO_2C\text{-}X\text{-}CO_2H$/NaOH/Methanol (X = C_6H_4, $C_6H_3NH_2$ and $C_{10}H_6$) beschrieben. Die Umsetzung von Terephthalsäure (H_2BDC) mit $Al(NO_3)_3 \cdot 9H_2O$ in Anwesenheit von NaOH führte zu der neuen mikrokristallinen Verbindung CAU-3 $[Al_2(OH_3)_4(BDC)]$. Die Strukturlösung und die Strukturverfeinerung dieser Verbindung erfolgten aus Röntgenpulverdaten.

Die Verbindung weist zwölfkernige $\{Al_{12}(OCH_3)_{24}\}^{12+}$ Cluster auf, die aus zwölf kantenverknüpften AlO_6-Oktaedern zusammengesetzt sind. Die Kantenverknüpfung der AlO_6-Oktaeder erfolgt über Methoxygruppen, während die axialen Sauerstoffatome von verbrückenden Carboxylateinheiten der Terephthalsäure gestellt werden. In einer verzerrten pseudo-kubisch innenzentrierten Anordnung der Cluster verknüpfen jeweils zwölf Terephthalateinheiten zwölf Cluster zu einem dreidimensionalen Netzwerk mit verzerrten oktaedrischen und tetraedrischen Hohlräumen. Die Hohlräume besitzen einen Durchmesser von ~10 und ~11 Å. Unter Verwendung von 2,6-Naphthalindicarbonsäure (H_2NDC) und 2-Aminoterephthalsäure ($H_2BDC\text{-}NH_2$) wurden die isoretikulären Verbindungen CAU-3-NDC und CAU-3-NH_2 synthetisiert. Der Einsatz von H_2NDC führte zu einer Aufweitung der oktaedrischen und tetraedrischen Hohlräume auf einen Durchmesser von ~14 bzw. ~15 Å.

Die optimierten Synthesebedingungen von CAU-3-NDC unterscheiden sich dabei deutlich von den Synthesebedingungen von CAU-3 und CAU-3-NH_2. Es wurde $AlCl_3 \cdot 6H_2O$ als Aluminiumquelle eingesetzt, die Reaktionszeit verkürzt sowie ein geringeres molares Verhältnis Al^{3+} : $HO_2C\text{-}R\text{-}CO_2H$ gewählt. Alle drei Verbindungen wurden mittels Röntgenpulverdiffraktometrie, IR-Spektroskopie, Elementaranalysen, Thermogravimetrie und N_2-Adsorptionsmessungen charakterisiert. Ausgehend von der Struktur von CAU-3 konnten die Gitterparameter von CAU-3-NDC unter anderem mittels der quadratischen Braggschen Gleichung aus den Röntgenpulverdaten

bestimmt werden. Ein Strukturmodell konnte mithilfe des Programms Materials Studio aufgestellt werden. Nach der Anwendung von Kraftfeldmethoden wurde die Struktur mittels Rietveld-Methode verfeinert.
Die drei isoretikulären CAU-3-Verbindungen zeigen ein unterschiedliches Sorptionsverhalten. Das Mikroporenvolumen von CAU-3-NH_2 nimmt im Vergleich zum unfunktionalisierten CAU-3 ab, während das von CAU-3-NDC ansteigt.

Dalton Transactions

Cite this: DOI: 10.1039/c2dt12005d

www.rsc.org/dalton

PAPER

CAU-3: A new family of porous MOFs with a novel Al-based brick: $[Al_2(OCH_3)_4(O_2C\text{-}X\text{-}CO_2)]$ (X = aryl)†

Helge Reinsch, Mark Feyand, Tim Ahnfeldt and Norbert Stock*

Received 21st October 2011, Accepted 7th December 2011
DOI: 10.1039/c2dt12005d

A new family of Al-based MOFs denoted as CAU-3 (CAU = Christian-Albrechts-Universität) was discovered in the solvothermal system Al^{3+}/aryldicarboxylic acid/NaOH/methanol by applying high-throughput-methods. The three compounds reported in this article $[Al_2(OCH_3)_4BDC]$, $[Al_2(OCH_3)_4BDC\text{-}NH_2]$ and $[Al_2(OCH_3)_4NDC]$ (BDC = 1,4-benzenedicarboxylate; NDC = 2,6-naphtalenedicarboxylate) are all based on the same unprecedented inorganic building unit $[Al_{12}(OCH_3)_{24}]^{12+}$, which is a dodecameric cyclic aluminium-methanolate-cluster. The material CAU-3-NDC was found to exhibit the highest surface area as well as the highest micropore volume of all Al-based MOFs reported until now.

Introduction

During the past few years, the research on highly porous MOFs with tailored properties has become a main objective for scientists in the field of porous materials.[1–5] This relatively new class of materials is built up from inorganic vertices, most often metal ions or cationic metal-oxo-clusters, which are connected to each other using polytopic organic linker-molecules. These organic parts of the network usually consist of organic anions often bearing carboxylate- or phosphonate-groups. To create pores by separating the inorganic vertices from each another, the linker molecule is often based on a rigid aromatic unit like benzene or naphthalene. Once the reaction conditions for the formation of such a hybrid compound are known, similar reaction parameters should in principle allow the incorporation of further functionalized and also larger organic molecules into the structure, while keeping the inorganic brick unchanged. This approach towards the synthesis of new compounds is commonly referred to as isoreticular synthesis.[6] There are only few examples for the synthesis of isoreticular families of MOFs, consisting of more than two materials based on the same inorganic building unit.[7–12] An example is the MIL-88-series, which is based on dicarboxylate ions but contains trimeric $M(III)_3\text{-}\mu_3O^{7+}$-clusters, where M(III) stands for a Cr^{3+} or Fe^{3+}. These compounds exhibit enormous changes in their lattice parameters, depending not only upon the metal ion (Fe^{3+}, Cr^{3+}) and the dicarboxylate-molecule, but also on the presence and the nature of guest molecules inside the pores.[9] Another example was reported for the Zr^{4+}-based MOFs called UiO-66, -67, and 68.[10,11] In this case, $Zr_6O_4(OH)_4^{12+}$-clusters are twelvefold connected by linear dicarboxylate ions to form a **fcu**-net, which corresponds to a fcc-packing of inorganic building blocks. Due to their outstanding chemical stability, the functionalized analogues of the UiO-66 (based on 1,4-benzenedicarboxylate) have shown to be ideal candidates for further post-synthetic modification reactions.[12]

One reason for this limited number of examples is due to the complexity of solvothermal reactions. Small changes of the organic linker molecule have often a strong influence on the solubility as well as the acid–base and the coordination properties. Thus, the reaction conditions have to be established and optimized for each organic linker molecule separately. In this context, high-throughput-methods have proven to be a highly valuable tool for the intentional synthesis of MOFs.[13,14] Applying this methodology, we were recently able to synthesize the amino-functionalized Al-MIL-53,[15] a MOF with lozenge-shaped channels bearing NH_2-groups which can be further chemically modified, and Cr-MIL-101-NDC,[16] which exhibits giant pores with a diameter of 4.6 nm. The miniaturization of the reaction vessels, the parallelization of the synthesis and the automated characterization open the opportunity to screen even complex reaction systems with large parameter-spaces. Therefore, chemical trends can be easily identified, and synthesis parameters can be rapidly optimized with a rather low consumption of starting materials.

Recently we have started a systematic high-throughput investigation on the role of the solvent in the synthesis of Al-based MOFs. In contrast to MOFs based on divalent cations, only few Al-based MOFs have been reported in the literature since mostly very small μm-sized crystals have been obtained, which complicates the structure determination. The frameworks of these known porous Al-MOF structures contain only six different

Christian-Albrechts-Universität zu Kiel, Institut für Anorganische Chemie, Max-Eyth-Str. 2, 24118 Kiel, Germany. E-mail: stock@ac.uni-kiel.de; Fax: +49 431 8801775; Tel: +49 431 8801675

† Electronic supplementary information (ESI) available: Crystallographic data, details of the Rietveld refinements and further XRPD data, selected bond lengths, TG curves. CCDC reference numbers 799242–799244 for CAU-3-NDC, CAU-3-BDC, and CAU-3-BDC-NH_2, respectively. For ESI and crystallographic data in CIF or other electronic format see DOI: 10.1039/c2dt12005d

Al–O bricks.[17–23] This rather limited number of structures is in sharp contrast to the diversity of polynuclear species that are known from the solvolysis reactions of aluminium salts.[24,25] For this reason, the field of Al^{3+}-based MOFs still is a promising chemical system for the discovery of new materials. Due to the high thermal and chemical stability of the known Al-based MOFs, as well as to the cost-effective availability of the usually nontoxic starting materials, these yet unknown compounds could be of high interest for commercial applications.

Especially linear dicarboxylic acids have shown to be useful for the synthesis of isoreticular compounds, not only but also due to the commercial availability of a variety of dicarboxylic acids with different size and functionalization. In combination with one-dimensional chains of corner-sharing AlO_6-octahedra, several porous compounds based on the MIL-53 structure are known, showing interesting sorption behaviour as well as high thermal stabilities.[26–30] Another example for a dicarboxylate-based Al-MOF is CAU-1, which contains twelvefold connected octanuclear Al-oxo-clusters.[23,31] Herein we report the synthesis and characterization of a new family of porous MOFs based on linear aryldicarboxylate ions, which contain the novel dodecameric Al-based brick $[Al_{12}(OCH_3)_{24}]^{12+}$.

Experimental

Materials and methods

Chemicals. $AlCl_3{\cdot}6H_2O$ (Riedel-de Haen, ≥99%), $Al(NO_3)_3{\cdot}9H_2O$ (Merck, ≥99%), H_2BDC (Aldrich, ≥98%), $H_2BDC\text{-}NH_2$ (Fluka, ≥98%), NaOH (Baker, ≥97%), methanol (BASF, purum), and *N*,*N*-dimethyl-formamide (BASF, tech.) were used as purchased. 2,6-Naphthalenedicarboxylic acid was synthesized by hydrolysis of dimethyl 2,6-naphthalenedicarboxylate (Aldrich, 98%).

Methods. Most reactions were carried out using our 24-high-throughput reactor system.[32] The upscaled synthesis was performed in custom made Teflon inserts in steel autoclaves with a volume of 30 mL. The high-throughput X-ray analyses were performed in transmission geometry using a STOE HT powder diffractometer equipped with a xy-stage and an image plate detector (IPDS) system (Cu-Kα1 radiation). Temperature dependent X-ray powder diffraction (XRPD) data was measured on a STOE Stadi-P diffractometer in transmission geometry equipped with an image plate detector (IPDS) using Cu-Kα1 radiation. High-precision X-ray powder diffraction data for the structure solution was collected on a STOE Stadi-P powder diffractometer equipped with a linear position sensitive detector (PSD) system (monochromated Cu-Kα1 radiation) in transmission geometry. XRPD data for the structure refinement was recorded on a Panalytical X-pert Highscore diffractometer in reflection-geometry. MIR spectra were recorded on an ATI Matheson Genesis spectrometer in the spectral range of 4000–400 cm^{-1} using the KBr disk method. FT-Raman spectra were recorded on a Bruker IFS 66 FRA 106 in the range of 0–3300 cm^{-1} using a Nd/YAG-Laser (1064 nm). The thermogravimetric analyses were recorded using an NETZSCH STA 409 CD analyzer. The samples were heated in Al_2O_3 crucibles at a rate of 4 K min^{-1} under a flow of air (25 ml min^{-1}). The TG data were corrected for buoyancy and current effects. The molecular modelling software used was Materials Studio 5.0.[33] Sorption experiments were performed using a BEL JAPAN INC. $Belsorp_{max}$.

Synthesis and high-throughput-investigations

Discovery and synthesis optimisation of CAU-3-BDC, $[Al_2(OCH_3)_4BDC]$. The compound CAU-3-BDC (**1**) was discovered in a high throughput-experiment using $AlCl_3{\cdot}6H_2O$, terephthalic acid (H_2BDC), methanol and 2 M methanolic NaOH as starting materials. After the reaction at 125 °C for 5 h, the tendencies in the product formation shown in Fig. 1 could be observed. Exact amounts of starting materials can be found in Table S5.† The molar ratio Al^{3+}:H_2BDC was kept constant at 4, the absolute amount of starting material was increased from row to row and from column to column, the amount of base was raised.

The compound was obtained from a highly diluted basic solution. Under more acidic and more concentrated conditions the well known compounds CAU-1 and MIL-53 are formed. Furthermore an unknown product of very low crystallinity was observed. Although the material obtained under these conditions already exhibited a remarkable porosity (apparent specific surface area of A_{BET} ~1200 m^2 g^{-1}), the crystallinity of the sample was rather low. A detailed high-throughput-investigation (~200 reactions) led to an improved synthesis procedure for CAU-3-BDC and the crystallinity was improved substantially. Therefore, the Al^{3+}-source was varied (nitrate, chloride and perchlorate), as well as the molar ratios and the absolute amounts of starting materials. We also investigated the influence of H_2O on the product formation. While the use of $Al(ClO_4)_3{\cdot}9H_2O$ or the addition of small amounts of water led to the formation of X-ray amorphous products or Al_2O_3, we observed highest crystallinity only for very small concentrations of H_2BDC and large excess of $Al(NO_3)_3{\cdot}9H_2O$ and NaOH. To achieve an optimum of crystallinity we also varied the heating program. The progress during this synthesis optimization is visualized in Fig. 2.

The optimized synthesis procedure of **1** in the 24 reactor system is as follows: a mixture of $Al(NO_3)_3{\cdot}9H_2O$ (45.2 mg, 0.120 mmol), terephthalic acid (H_2BDC; 2.5 mg, 0.015 mmol) and a solution of NaOH in methanol (2 M, 60 µL, 0.120 mmol) was suspended in methanol (1.340 mL). The reactor was heated up to 125 °C in 12 h. The temperature was held for 5 h and the reactor was allowed to cool down to room temperature in 4 h.

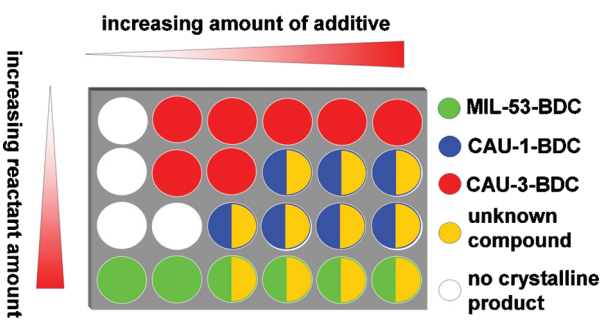

Fig. 1 Results of the high-throughput investigation for the discovery of CAU-3-BDC.

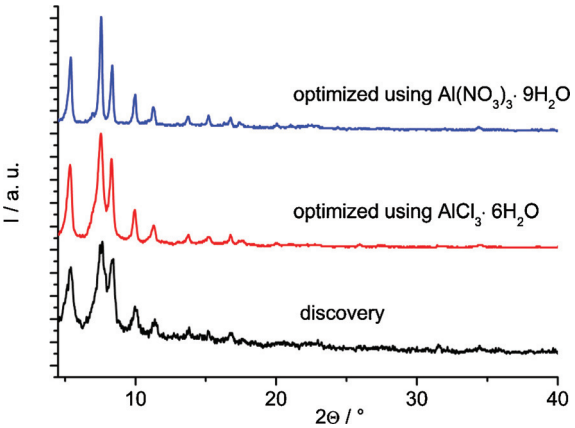

Fig. 2 Improvement of the crystallinity of the products during the HT-assisted synthesis optimization.

Scale-up of the reaction was performed in a 30 mL custom-made autoclave with Teflon insert. For this synthesis, the reaction parameters were stepwise adjusted to the larger reactor.

$Al(NO_3)_3 \cdot 9H_2O$ (540 mg, 1.44 mmol), H_2BDC (40 mg, 0.240 mmol) and a solution of NaOH in methanol (2 M, 720 µL, 1.44 mmol) were suspended in methanol (16.0 mL). The reactor was heated up to 125 °C in 12 h. The temperature was held for 3 h and the reactor was allowed to cool down to room temperature in 1 h.

After the filtration, a white microcrystalline powder was obtained. Thermogravimetric analysis and TEM-images revealed, that a large amount of an X-ray amorphous byproduct was formed. To remove this byproduct, 100 mg of the reaction product were treated with 10 mL of DMF in a microwave oven (Biotage Initiator) at 150 °C for 1 h under stirring. To remove the DMF, the filtrated solid was treated with 10 mL methanol and heated up in the microwave oven to 100 °C for 1 h. The product was dried at room temperature in air, and further activated under vacuum for the sorption experiments (160 °C/12 h/0.1 mbar). Since the crystallinity slightly decreases during this process (Fig. S1), the structure solution and refinement were performed using the XRPD measurements of the "as synthesized" compound. All other analytical data was measured for the activated product stored under ambient conditions prior to the measurements.

Elemental analysis on an activated sample: found: C: 35.43%, H: 4.07%. Calculated values, based on the deduced formula $[Al_2(OCH_3)_4(O_2CC_6H_4CO_2)] \cdot 3.6H_2O$: C: 35.4%, H: 5.7%.

Discovery and synthesis optimisation of CAU-3-BDC-NH_2, [$Al_2(OCH_3)_4$BDC-NH_2]. Starting from the optimized reaction conditions for **1**, the synthesis of the amino-functionalized analogue CAU-3-BDC-NH_2 (**2**) was attempted. Surprisingly, the reaction conditions are very similar. For the optimized synthesis of **2** in the multiclave, a mixture of $Al(NO_3)_3 \cdot 9H_2O$ (52 mg, 0.139 mmol), 2-aminoterephthalic acid (H_2BDC-NH_2, 2.5 mg, 0.014 mmol) and a 2 M solution of NaOH in methanol (69 µL, 0.138 mmol) were suspended in methanol (1.330 mL). The reactor was heated up to 125 °C in 8 h. The temperature was held for 6 h and the reactor was allowed to cool down to room temperature in 1 h.

For the up-scaling of the reaction we used again our 30 mL custom-made autoclave with a Teflon insert. For this synthesis, $Al(NO_3)_3 \cdot 9H_2O$ (540 mg, 1.44 mmol), H_2BDC-NH_2 (40 mg, 0.220 mmol) and a solution of NaOH in methanol (2 M, 720 µL, 1.44 mmol) were suspended in methanol (16.0 mL). The reactor was heated up to 125 °C in 12 h. The temperature was held for 3 h and the reactor was allowed to cool down to room temperature in 1 h.

After the filtration, a yellow microcrystalline product was obtained. Thermogravimetric measurements revealed the presence of an X-ray amorphous byproduct, which was removed by applying the same procedure as for CAU-3-BDC. The crystallinity of CAU-3-BDC-NH_2 decreased slightly during this treatment (Fig. S2†). Therefore, XRPD data of the as-synthesized product was used for the structure refinement while all other analytical data was measured for the activated material. Elemental analysis on an activated sample (160 °C/12 h/0.1 mbar) stored under ambient conditions: found: C: 31.02%, H: 3.81%, N: 1.96%; These values differ from the assumed formula $[Al_2(OCH_3)_4(O_2C\text{-}C_6H_3NH_2\text{-}CO_2)] \cdot 3.6H_2O$ which are calculated to be: C: 34.1%, H: 5.7%, N: 3.3%. After dissolution in D_2O/NaOD we observed in the NMR-spectrum, that CAU-3-NH_2 not only contains aminoterephthalate ions, but also terephthalate anions and N-methylated aminoterephthalate ions. We attribute the discrepancy between the experimental values and the ideal formula to this *in situ* conversion of the linker and to small amounts of X-ray amorphous Al-species (see also TG-measurement). Further investigations of this phenomenon are in progress.

Discovery and synthesis optimisation of CAU-3-NDC, [$Al_2(OCH_3)_4$NDC]. The synthesis of CAU-3-NDC (**3**) needed much more effort, since it is highly sensitive to every single parameter during the synthesis, and every small change leads to the formation of crystalline byproducts, whose structures and compositions are a subject of current research. Without the use of high-throughput-methods, optimization of the synthesis conditions (~800 reactions) would have been hardly possible. Due to the large number of reactions that were performed, a detailed description of the HT-investigations is not given. The varied parameters comprise the Al^{3+}-source (nitrate, chloride and perchlorate) and the molar ratios and absolute amounts of starting materials. Due to the sensitivity of the reaction towards the thermal process, the chemical composition of the starting mixture had to be screened using different heating programs. This finally led to the optimized synthesis of **3** in the 24 reactor system, which is as follows: a mixture of $AlCl_3 \cdot 6H_2O$ (29.3 mg, 0.12 mmol), 2,6-naphtalenedicarboxylic acid (H_2NDC; 7.5 mg, 0.03 mmol) and a 2 M solution of NaOH (52 µL, 0.1 mmol) in methanol was suspended in methanol (448 µL) and heated to 130 °C in 1 h. The temperature was kept for 4 h and the reactor was allowed to cool down in 1 h. The white, as-synthesized product contains traces of sodium chloride (see also structure refinement) and X-ray amorphous byproducts like residual linker molecules in the pores. EDX measurements showed molar ratios of Al: Cl ranging from 2.5 to 3. IR-spectroscopy proved the presence of residual naphthalene dicarboxylic acid. Elemental analysis on a thermally activated sample (160 °C/12 h/0.1 mbar) stored under ambient conditions prior to the measurement:

found: C: 47.97%, H: 3.81%. Calculated values, based on the ideal formula $[Al_2(OCH_3)_4(O_2CC_{10}H_6CO_2)]$: C: 48.9%, H: 4.6%. Although these values are in quite good agreement, the described material still contains the mentioned byproducts.

All measurements were performed with the as-synthesized microcrystalline product. The only activation step for the sorption measurements was heating under vacuum, which hardly influences the crystallinity (Fig. S3†). Several attempts were made, to perform a scale-up of the synthesis and to further activate the as-synthesized compound. The products of the synthesis in larger reactors exhibit a much lower specific surface area, although, based on the XRPD measurements, no differences were observed. Further activation steps were attempted in several solvents, but the raw material decomposes in water, DMF and even ethanol. The solvent treatment in methanol led only to a reduction of the amount of chloride ions.

The absolute amounts synthesized are in all three cases quite low. In the case of CAU-3-BDC and CAU-3-BDC-NH_2, we usually obtain ~25 mg of fully activated sample from one upscaled reaction. One reason is the low overall concentration of the linker molecule that is necessary to obtain the title compounds. The other reason is the elaborate activation procedure to remove the X-ray amorphous byproducts. In the case of CAU-3-NDC, around 8 mg are obtained from one HT-reaction.

Structure determination and refinement

The experimental XRPD pattern of CAU-3-BDC was successfully indexed with Topas Academics[34] as a hexagonal crystal system with the lattice parameters a = 21.0480(4) Å and c = 34.8305(7) Å with a goodness of fit of 23. Based on the extinction conditions, the rhombohedral space group $R\bar{3}m$ was suggested by the program. The structure solution was carried out successfully with the Expo2004[35] software package using Direct Methods. Starting from the space group $R\bar{3}m$, the positions of the aluminum based brick were determined. By recycling these fragments in a new intensity extraction, in addition parts of the BDC^{2-} ion were localized. This starting model was completed by force field calculations with the software package Forcite implemented in Materials Studio 5.0.[33] For the calculations, the universal force field was used without an optimization of the cell parameters. The completed model was refined with Rietveld techniques using Topas Academics.[34] The final Rietveld refinement involved 15 background parameters, 15 atomic parameters, 4 temperature factors, 1 scale factor and 2 cell parameters. The peak shape was modeled using a pearson VII function and anisotropic peak broadening effects were taken into account using a spherical harmonics series. The C–C distances and the C–O distances of the methoxy groups were restrained. The final Rietveld plot shown in Fig. 3 led to satisfying structural model indicators (R_{Bragg} = 0.4%, R_{wp} = 4.76% and GoF = 1.64). Selected bond lengths and the asymmetric unit can be found in the supporting informations in Fig. S4 and Table S1,† respectively.

The structural model of CAU-3-BDC was used for the Rietveld refinement of CAU-3-BDC-NH_2. The difference Fourier calculations showed electron densities at a distance of 1.5 Å from the lateral carbon atoms of the phenyl ring. Assigning these electron densities to a nitrogen atom with a site occupation of 0.25 led to a significant lowering of the R-values R_{bragg} and R_{wp} by 1 and 0.5%. The results of the final Rietveld refinement are shown in Fig. S5.† The C–C distances, C–O distances of the methoxy groups as well as the C–N distances were restrained and an overall temperature factor was used. The refinement led to good structure indicators of R_{Bragg} = 0.59%, R_{wp} = 4.17% and GoF = 1.71. Selected bond lengths are given in Table S2.†

The indexing and lattice parameter refinement of the experimental powder pattern of **3** was carried out with the Stoe WinxPow software package.[36] The hexagonal cell parameters a = 23.1533(5) Å and c = 40.4120(9) Å were obtained. For the construction of a model of CAU-3-NDC, we started from the structure of CAU-3-BDC. The space group was converted to $P1$ and the terephthalate ions were replaced by naphthalene dicarboxylate ions after adjusting the cell parameters to the ones obtained from the indexing process, using Materials Studio 5.0. The model was submitted to a full energy minimization without an optimization of the unit cell constants with the universal force field (UFF) implemented in the software. For this simulation, the aluminum atoms were replaced by iron due to their very similar ionic radii (0.67 *vs.* 0.69) and the missing parameters for octahedrally coordinated aluminum in the parameter set. Van der Waals interactions were represented by a classical 12-6 Lennard Jones potential. The convergence criteria were set to 1.0×10^{-4} kcal mol^{-1} and 0.005 kcal mol^{-1} $Å^{-1}$ and 5.0×10^{-5} Å (displacement) respectively. The obtained structural model possesses lower symmetry than the parent-structure CAU-3-BDC and exhibits the space group $R\bar{3}$, due to the break of the symmetry caused by the naphthalene dicarboxylate ions (atomic coordinates and a simulated powder pattern of this model can be found in Table S3 and Fig. S6†). This structural model was used to carry out the Rietveld refinement. Due to the lower crystallinity and the two-fold number of atomic parameters caused by the lower symmetry, the atomic positions of the NDC^{2-} ions were restrained and an overall temperature factor was used. The final refinement leads to satisfying structure indicators (R_{Bragg} = 4.47%, R_{wp} = 9.41% and GoF = 4.80). The final Rietveld plot is shown in Figure S7† and selected bond lengths are given in Table S4.† Two reflections at 32.62° and 45.42° are observed which are due to NaCl as an impurity. The final parameters of all three refinements are summarized in Table 1.

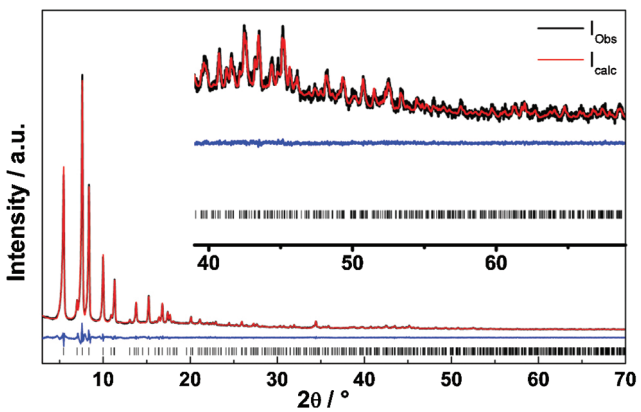

Fig. 3 Final Rietveld-plot for **1**. Measured intensities are in black, calculated intensities are in red, the difference plot is blue. The vertical bars mark the Bragg-positions.

Table 1 Final parameters obtained from the Rietveld-refinements

	CAU-3-BDC	CAU-3-BDC-NH_2	CAU-3-NDC
Empirical formula	$Al_2O_8C_{12}H_{16}$	$Al_2O_8C_{12}N_1H_{17}$	$Al_2O_8C_{16}H_{18}$
M g mol^{-1}	342.21	357.23	368.25
Crystal system	Rhombohedral	Rhombohedral	Rhombohedral
Space group	$R\bar{3}m$	$R\bar{3}m$	$R\bar{3}$
a/pm	2110.51(5)	2093.5(1)	2320.56(2)
c/pm	3488.8(1)	3481.3(2)	4063.51(4)
$V/10^6$ pm^3	13458.1(8)	13214(1)	18950.(3)
Z	18	18	18
R_{wp}/%	4.76	4.17	9.41
R_{Bragg}/%	0.4	0.59	4.47
GoF	1.64	1.71	4.8
weighted Durbin-Watson statistic	0.594	0.312	0.120

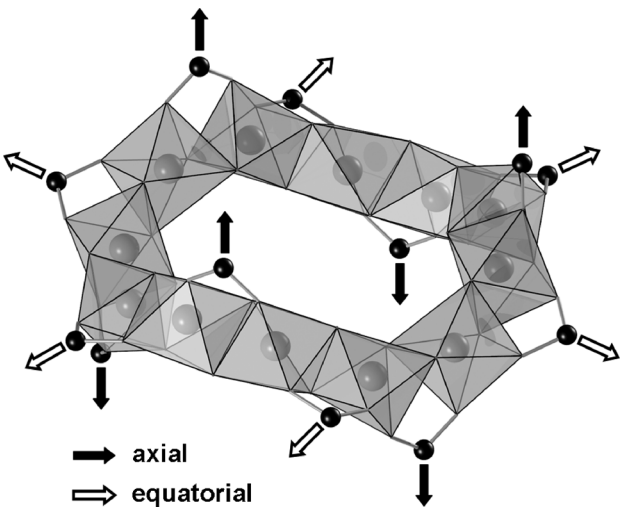

Fig. 4 Dodecameric building unit and its connectivity mode in the framework of CAU-3-BDC. Methyl-groups are omitted for clarity.

Results and discussion

Structural description

The structure of CAU-3-BDC is based on dodecameric $[Al_{12}(OCH_3)_{24}]^{12+}$ cations, to which twelve carboxylate moieties are coordinated, each one bridging two Al-ions (Fig. 4).

Thus, the inorganic units are composed of twelve edge-sharing AlO_6-polyhedra. The edge-sharing oxygen atoms are part of methanolate ions, while the other oxygen-atoms result from the coordination of the bridging carboxylate-groups. Similar dodecameric clusters have been only observed twice in molecular complexes containing the transition metals Fe^{3+} and Mn^{3+}/Cr^{3+} ions.[37,38] To the best of our knowledge this is the first time, that this cluster has been observed in Al chemistry as well as in the chemistry of MOFs. Recently, the Mn^{3+}/Cr^{3+} building block was proposed as a possible brick for the formation of new metal–organic frameworks.[39] Besides the octanuclear cyclic cluster incorporated in the framework of CAU-1,[23] this building unit is the second example of an wheel-shaped aluminium carboxylate, whose occurrence is again strictly limited to the incorporation into a metal–organic framework.

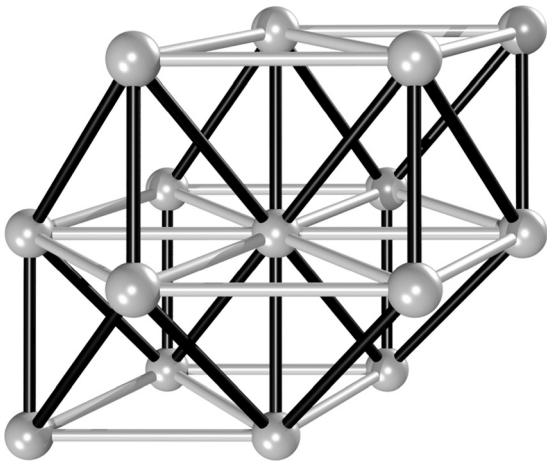

Fig. 5 Schematic representation of a part of the distorted **fcu**-net. The white bonds represent the connectivity in the *xy*-plane of the inorganic brick, the black ones the connectivity along the *z*-axis.

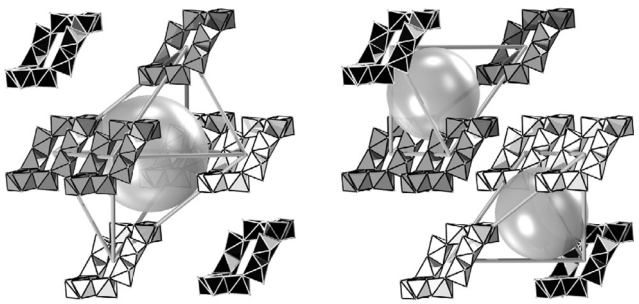

Fig. 6 The two different types of cavities in the **fcu**-framework. Different colours emphasize the ABC stacking of the of the Al-based bricks $[Al_{12}(OCH_3)_{24}]^{12+}$.

The twelvefold connectivity by dicarboxylate units leads to the formation of a **fcu**-net (Fig. 5).

This high connectivity is remarkable, since only few examples of such MOFs have been reported. Besides the well known UiO-66,[10] for example the frameworks of CAU-1[23] and its Ti-analogue MIL-125[40] exhibit this connectivity mode. While the latter two MOFs show a distorted pseudo-bcc packing of clusters, the assembly in CAU-3 leads to a fcc-packing like in UiO-66. Due to the anisotropic shape of the cluster a strongly distorted packing is observed (Fig. S7†).

Accordingly, the $[Al_{12}(OCH_3)_{24}]^{12+}$ clusters are connected sixfold in their *xy*-plane and sixfold alternating in both directions along the *z*-axis of the cyclic cluster. The resulting network contains tetrahedral and octahedral cavities which are strongly distorted due to the anisotropic shape of the Al-containing brick (Fig. 6).

Assuming a spherical shape, the diameters of the tetrahedral and octahedral cavities are approximately 10 and 11 Å (calculated based on van-der-Waals radii), respectively. In reality larger molecules could be accommodated and based on the estimated available free space, the incorporation of rod-shaped guests with maximum length of 27 Å should be possible. The triangular apertures of these cavities differ only slightly in size and should be accessible for molecules up to a diameter of 7 Å.

The dimensionality and shape of the pores differ only slightly for compound **2**, since the amino-group is statistically distributed over the four possible positions of the aromatic ring. The larger linker molecule in **3** leads to an extended, non-interpenetrating framework containing distorted tetrahedral and octahedral cavities of ~14 Å and ~15 Å in diameter, assuming a spherical guest. Based on the structure, rod-shaped guests with maximum length of 38 Å should fit into the octahedral cavities.

Spectroscopic and thermal properties

The vibrational spectra (Fig. 7) of the three title compounds are very similar. The characteristic bands for the carboxylate vibrations around 1580 cm^{-1} and 1420 cm^{-1} clearly show the presence of the dicarboxylate ions coordinating to the Al^{3+}-ions. The aliphatic C–H vibrations at 2950 cm^{-1} and 2840 cm^{-1} are due to the bridging methanolate ions in the Al-based brick. In the case of as synthesized CAU-3-NDC, the absorption band around 1700 cm^{-1} is attributed to residual naphthalene dicarboxylic acid molecules occluded in the pores.

The band at 1250 cm^{-1} (C–N-vibration) in the spectrum of CAU-3-BDC-NH_2 proves the incorporation of aminoterephtalic acid, although the characteristic NH_2-bands around 3450 cm^{-1} are not observed, probably due to the presence of hydrogen-bonded water inside the pores. In the Raman-spectra, especially the aromatic C–C-vibrations between 1640 cm^{-1} and 1380 cm^{-1} are well resolved.

The thermal stability of all three MOFs was investigated in air atmosphere up to at least 800 °C with a heating rate of 4 K min^{-1} (Fig. S9, S10 and S11†). For **1**, the first weight loss of −16.5% corresponds to the removal of incorporated solvent molecules. At higher temperatures (~200 °C), the decomposition of the frameworks and thus the structural collapse proceeds in two steps (calc.: 58.7%, obs.: 60.9%). The product formed in the end is weakly crystalline Al_2O_3. In the case of CAU-3-BDC, we were also able to prove the structural rigidity of the framework during the activation process. Temperature-dependent XRPD data (Fig. 8) demonstrates, that no uncommon cell parameter shifts can be observed.

While the chemical decomposition of **1** shows a stepwise mechanism in the TG curve, the structure of the framework collapses directly during the second weight loss. The increased stability during the TDXRPD experiment compared to the TG-data is attributed to the different experimental set ups.

The decomposition of CAU-3-BDC-NH_2 (**2**) is similar to that of **1**. Like for CAU-3-BDC, the decomposition starts after the removal of adsorbed solvent (10.3%) at a temperature of ~180 °C. The two last weight losses correspond quite well to the decomposition of **2** (calc.: 66.4%, obs.: 62.4%), although the difference could be attributed to a small amount of X-ray-amorphous Al-oxo-species.

The decomposition of **3** during the TG-experiment shows a similar stability (~180 °C), but due to the observed byproducts, we did not attribute the weight losses to defined steps of decomposition.

Sorption properties

For the sorption measurements, the samples were activated in vacuum (10^{-2} mbar) at 160 °C for 12 h. The XRPD patterns of the samples after the sorption experiments can be found in the supporting information (Fig. S1–S3). The nitrogen isotherms (Fig. 9) were measured at 77 K. The BET-method was applied to calculate the apparent surface area and the micropore volumes were calculated from the amount adsorbed at $p/p_0 = 0.5$.

The sorption experiments confirm the tendencies that we expected. The incorporation of the amino-group leads to a decrease of micropore volume as well as apparent surface area,

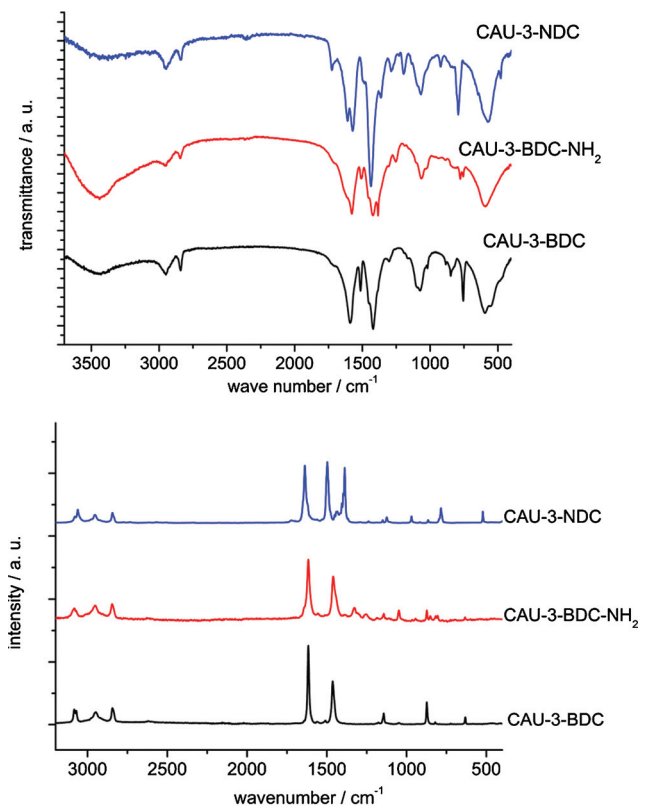

Fig. 7 IR- (top) and Raman-spectra (bottom) of the different CAU-3 MOFs.

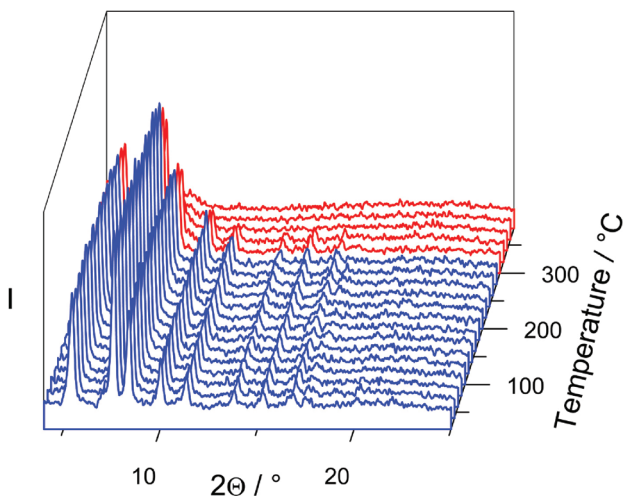

Fig. 8 Temperature-dependent XRPD patterns of CAU-3-BDC (**1**), measured under air.

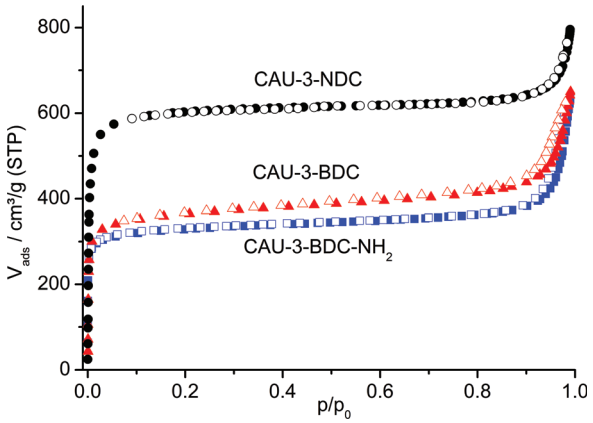

Fig. 9 N_2-Sorption isotherms for **1**, **2** and **3** measured at 77 K.

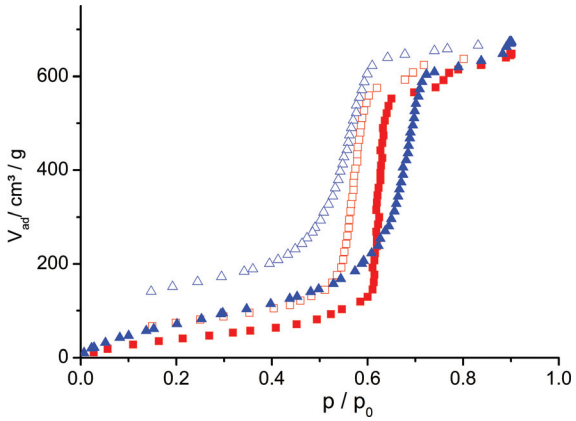

Fig. 10 Water vapour isotherms for **1** and **2** measured at 25 °C. Blue triangles for the NH_2-functionalized compound **2**, red squares for **1**. Empty symbols represent the desorption-, filled symbols represent the adsorption-branch.

Table 2 Apparent specific surface areas and V_{mic} values of the CAU-3-MOFs

Compound	A_{BET} m^2 g^{-1}	$A_{Langmuir}$ m^2 g^{-1}	V_{mic} cm^3 g^{-1}
CAU-3-BDC	1550	1920	0.64
CAU-3-BDC-NH_2	1250	1520	0.53
CAU-3-NDC	2320	2750	0.95

while the enlargement of the linker molecule results in a drastically increased uptake. The BET-surfaces as well as the micropore volumes are summarized in Table 2.

The apparent specific surface areas and the micropore volume measured for CAU-3-NDC **3** are to the best of our knowledge the highest reported so far for any literature known Al-MOF. Changing the adsorbate from N_2 to H_2O, the influence of the functional group is clearly visible (Fig. 10). The use of H_2O vapour leads to strong hysteresis. The absolute amount of adsorbed water is similar for both CAU-3-BDC and CAU-3-BDC-NH_2, but due to the presence of the polar amino group, the adsorbed amount of water vapour at lower partial pressures is higher in CAU-3-NH_2.

Although this is a purely qualitative sorption study, the influence of the amino group with its ability for hydrogen bonding is obvious.

Conclusion

Summarizing our results, we have synthesized three new Al-containing MOFs by applying our high-throughput-methods and characterized them in detail. This new family of MOFs contains an unprecedented brick, $[Al_{12}(OCH_3)_{24}]^{12+}$, which is twelvefold connected by dicarboxylate molecules to form a **fcu**-net. This inorganic unit is the second example for the occurrence of a wheel-shaped aluminium cluster in a metal–organic framework. All three compounds of the CAU-3-family are highly porous and exhibit BET-surface areas larger than 1200 m^2 g^{-1} and micropore volumes higher than 0.5 cm^3 g^{-1}. They are thermally stable up to at least 180 °C in air. The sorption properties are altered upon incorporation of a functional group or a larger linker molecule, respectively.

Acknowledgements

This work has been financially supported by the DFG (SPP 1362). The research leading to these results has received funding from the European Community's Seventh Framework Programme (FP7/2007–20013) under grant agreement n° 228862′.

Notes and references

1 G. Ferey, *Chem. Soc. Rev.*, 2008, **37**, 191.
2 Z. Wang and S. M. Cohen, *Chem. Soc. Rev.*, 2009, **38**, 1315.
3 S. Kitagawa, R. Kitaura and S. Noro, *Angew. Chem., Int. Ed.*, 2004, **43**, 2334.
4 C. Janiak, *Dalton Trans.*, 2003, 2781.
5 R. Long and O. M. Yaghi, *Chem. Soc. Rev.*, 2009, **38**, 1213.
6 O. M. Yaghi, M. O'Keeffe, N. W. Ockwig, H. K. Chae, M. Eddaoudi and J. Kim, *Nature*, 2003, **423**, 705.
7 T. Devic, P. Horcajada, C. Serre, F. Salles, G. Maurin, B. Moulin, D. Heurtaux, G. Clet, A. Vimont, J.-M. Greneche, B. Le Ouay, F. Moreau, E. Magnier, Y. Filinchuk, J. Marrot, J.-C. Lavalley, M. Daturi and G. Ferey, *J. Am. Chem. Soc.*, 2010, **132**, 1127.
8 M. Eddaoudi, J. Kim, N. Rosi, D. Vodak, J. Wachter, M. O'Keeffe and O. M. Yaghi, *Science*, 2002, **295**, 469.
9 C. Serre, C. Mellot-Draznieks, S. Surblé, N. Audebrand, Y. Filinchuk and G. Férey, *Science*, 2007, **315**, 1828.
10 J. H. Cavka, S. Jakobsen, U. Olsbye, N. Guillou, C. Lamberti, S. Bordiga and K. P. Lillerud, *J. Am. Chem. Soc.*, 2008, **130**, 13850.
11 A. Schaate, P. Roy, A. Godt, J. Lippke, F. Waltz, M. Wiebcke and P. Behrens, *Chem.–Eur. J.*, 2011, **17**, 6643.
12 M. Kandiah, S. Usseglio, S. Svelle, U. Olsbye, K. P. Lillerud and M. Tilset, *J. Mater. Chem.*, 2010, **20**, 9848.
13 S. Bauer, C. Serre, T. Devic, P. Horcajada, J. Marrot, G. Férey and N. Stock, *Inorg. Chem.*, 2008, **47**, 7568.
14 P. Maniam and N. Stock, *Inorg. Chem.*, 2011, **50**, 5085.
15 T. Ahnfeldt, D. Gunzelmann, T. Loiseau, D. Hirsemann, G. Férey, J. Senker and N. Stock, *Inorg. Chem.*, 2009, **48**, 3057.
16 A. Sonnauer, F. Hoffmann, M. Fröba, L. Kienle, V. Duppel, M. Thommes, C. Serre, G. Férey and N. Stock, *Angew. Chem., Int. Ed.*, 2009, **48**, 3791.
17 C. Volkringer, D. Popov, T. Loiseau, G. Férey, M. Burghammer, C. Riekel, M. Haouas and F. Taulelle, *Chem. Mater.*, 2009, **21**, 5695.
18 C. Volkringer, D. Popov, T. Loiseau, N. Guillou, G. Ferey, M. Hauuas, F. Taulelle, C. Mellot-Draznieks, M. Burghammer and C. Riekel, *Nat. Mater.*, 2007, **6**, 760.
19 C. Volkringer, T. Loiseau, N. Guillou, G. Ferey, M. Haouas, F. Taulelle, N. Audebrand, I. Margiolaki, D. Popov, M. Burghammer and C. Riekel, *Cryst. Growth Des.*, 2009, **9**, 2927.
20 C. Volkringer, T. Loiseau, M. Haouas, F. Taulelle, D. Popov, M. Burghammer, C. Riekel, C. Zlotea, F. Cuevas, M. Latroche,

D. Phanon, C. Knöfelv, P. L. Llewellyn and G. Ferey, *Chem. Mater.*, 2009, **21**, 5783.
21 C. Volkringer, T. Loiseau, N. Guillou, G. Férey, M Haouas, F. Taulelle, E. Elkaim and N. Stock, *Inorg. Chem.*, 2010, **49**, 9852.
22 C. Volkringer, T. Loiseau, N. Guillou, G. Ferey and E. Elkaım, *Solid State Sci.*, 2009, **11**, 1507.
23 T. Ahnfeldt, N. Guillou, D. Gunzelmann, I. Margiolaki, T. Loiseau, G. Férey, J. Senker and N. Stock, *Angew. Chem., Int. Ed.*, 2009, **48**, 5163.
24 W. Schmitt, E. Baissa, A. Mandel, C. E. Anson and A. K. Powell, *Angew. Chem., Int. Ed.*, 2001, **40**, 3577.
25 E. A. Mainicheva, O. A. Gerasko, L. A. Sheludyakova, D. Y. Naumov, M. I. Naumova and V. P. Fedin, *Russ. Chem. Bull.*, 2006, **55**, 267.
26 T. Loiseau, C. Serre, C. Huguenard, G. Fink, F. Taulelle, M. Henry, T. Bataille and G. Ferey, *Chem.–Eur. J.*, 2004, **10**, 1373.
27 I. Senkovska, F. Hoffmann, M. Fröba, J. Getzschmann, W. Böhlmann and S. Kaskel, *Microporous Mesoporous Mater.*, 2009, **122**, 93.
28 A. Comotti, S. Bracco, P. Sozzani, S. Horike, R. Matsuda, J. Chen, M. Takata, Y. Kubota and S. Kitagawa, *J. Am. Chem. Soc.*, 2008, **130**, 13664.
29 J. Gascon, U. Aktay, M. D. Hernandez-Alonso, G. P. M. Van Klink and F. Kapteijn, *J. Catal.*, 2009, **261**, 75.
30 S. Couck, J. F. Denayer, G. V. Baron, T. Remy, J. Gascon and F. Kapteijn, *J. Am. Chem. Soc.*, 2009, **131**, 6326.
31 T. Ahnfeldt, J. Moellmer, V. Guillerm, R. Staudt, C. Serre and N. Stock, *Chem.–Eur. J.*, 2011, **17**, 6462.
32 E. Biemmi, S. Christian, N. Stock and T. Bein, *Microporous Mesoporous Mater.*, 2009, **117**, 111.
33 Materials Studio Version 5.0, Accelrys Inc., San Diego, CA, 2009.
34 Topas Academics 4.2, Coelho Software, 2007.
35 A. Altomare, M. Cavalli, R. Calandro, C. Cuocci, C. Giacovazzo, A. Gagliardi, A. G. G. Moliterni and R. Rizzi, EXPO2004. Program for Solving Crystal Structures from Powder Data by direct Methods, 2004.
36 STOE WinXPOW version 2.11, Stoe & Cie GmbH, 2005, Darmstadt, Germany.
37 T. C. Stamatatos, A. G. Christou, C. M. Jones, B. J. O'Callaghan, K. A. Abboud, T. A. O'Brien and G. Christou, *J. Am. Chem. Soc.*, 2007, **129**, 9840.
38 M. Helliwell, A. A. Smith, S. J. Teat and R. E. P. Winpenny, *Inorg. Chim. Acta*, 2003, **354**, 49.
39 D. J. Tranchemontagne, J. L. Mendoza-Cortes, M. O'Keeffe and O. M. Yaghi, *Chem. Soc. Rev.*, 2009, **38**, 1257.
40 M. Dan-Hardi, C. Serre, T. Frot, L. Rozes, G. Maurin, C. Sanchez and G. Ferey, *J. Am. Chem. Soc.*, 2009, **131**, 10857.

4.3 In situ-EDXRD-Untersuchungen isoretikulärer CAU-1-Verbindungen

Der modulare Aufbau der Metall-organischer Gerüstverbindungen ermöglicht es, die Größe und Funktionalität der Poren variabel einzustellen. Dabei kann auf einen großen Pool an organischen Linkern und Metallionen zurückgegriffen werden. Das Problem bei der Darstellung isoretikulärer Verbindungen ist, dass neben der Löslichkeit der Reaktanden viele weitere Syntheseparameter (Temperatur, pH-Wert, Zeit, Heizmethode) die Produktbildung stark beeinflussen können. Da bislang sehr wenige Details über die bei der Synthese ablaufenden Kristallisationsprozesse bekannt sind, lässt sich der Einfluss einzelner Parameter auf die Produktbildung nur sehr schwer abschätzen. Auf der Suche nach neuen MOFs wird daher heutzutage fast immer noch ausschließlich empirisch vorgegangen, was mit einem hohen Zeit- und Materialaufwand verbunden ist. Neben der in unserer Arbeitsgruppe verwendeten Hochdurchsatzmethode ist die zeitaufgelöste Untersuchung der Produktbildung eine elegante Methode, bestimmte Reaktionsparameter bei der Synthese zielgerichtet zu untersuchen. Mithilfe von energiedispersiver Röntgenpulverbeugung (EDXRD) sollte das Kristallwachstum zweier isoretikulärer CAU-1-Verbindungen (CAU-1-NH_2 und CAU-1-$(OH)_2$) in situ untersucht werden. Dabei sollte der Einfluss der Heizmethode (MW-unterstützte Synthese vs. konventionelles elektrisches Heizen) und der eingesetzten Linker (H_2BDC-$(OH)_2$, H_2BDC-NH_2) auf die Produktbildung sowie die Kinetik des Kristallisationsprozesses ermittelt werden.

4.3.1 High-throughput and Time-resolved Energy-Dispersive X-Ray Diffraction (EDXRD) Study of the Formation of CAU-1-$(OH)_2$: Microwave and Conventional Heating

Der Beitrag wurde in „Chemistry A European Journal“ im Jahre 2011 veröffentlicht und beschäftigt sich mit der Synthese und Charakterisierung von CAU-1-$(OH)_2$ $[Al_4(OH)_2(OCH_3)_4(BDC\text{-}(OH)_2)_3]\cdot xH_2O$. Im Fokus des Artikels steht die kinetische

Untersuchung des Kristallwachstums von CAU-1-$(OH)_2$ in Abhängigkeit von der verwendeten Heizmethode. Zusätzliche Informationen zum Artikel befinden sich im Anhang 8 ab Seite 224.

Unter Verwendung der Hochdurchsatzmethode erfolgte die Entdeckung und Syntheseoptimierung der dihydroxyfunktionalisierten CAU-1-Verbindung CAU-1-$(OH)_2$. Zur Synthese wurde 2,5-Dihydroxyterephthalsäure (H_2BDC-$(OH)_2$) eingesetzt und als Startpunkt die Syntheseparameter von CAU-1 gewählt. Die Produktbildung von CAU-1-$(OH)_2$ konnte nur in einem sehr kleinen Stabilitätsbereich beobachtet werden. Eine entscheidende Rolle spielte hierbei die richtige Einstellung des pH-Wertes durch Zugabe kleiner Mengen an Natriumhydroxid. Nach der Syntheseoptimierung konnte die Verbindung phasenrein im Gramm-Maßstab hergestellt und mittels IR-Spektroskopie, Röntgenbeugungsexperimenten und Thermogravimetrie charakterisiert werden. Die Sorptionseigenschaften von CAU-1-$(OH)_2$ wurden mit den Gasen Stickstoff, Wasserdampf, Kohlenstoffdioxid und Methan untersucht.
Die Kristallisation von CAU-1-$(OH)_2$ wurde in situ mittels energiedispersiver Röntgenbeugung (EDXRD) im Temperaturbereich von 120 °C–145 °C am HASYLAB, Hamburg, untersucht. Alle Synthesen wurden sowohl in einem MW-Ofen als auch unter Verwendung eines konventionellen elektrisch beheizten Ofens durchgeführt. Es konnte erstmalig ein kommerziell erhältlicher MW-Ofen in einen Synchrotronstrahlengang implementiert werden. Im Vergleich zur konventionellen Heizmethode führte die MW-unterstützte Synthese von CAU-1-$(OH)_2$ zu kürzeren Induktionszeiten sowie einer schnelleren Kristallisation. Die kinetische Auswertung der Messungen mit der Avrami-Eroféev Gleichung deutet an, dass die Kristallisation einem anderen Reaktionsmechanismus folgt als bei der Synthese unter konventionellen Bedingungen. Die Synthese unter Verwendung der konventionellen Heizmethode entspricht einer phasengrenzkontrollierten Produktbildung. Durch eine vermehrte Keimbildung und der damit verbundenen Abnahme an den zum Kristallwachstum beitragenden Reaktanden verläuft die Reaktion in dem MW-Ofen eher diffusionskontrolliert. Aus der Arrheniusauftragung der Geschwindigkeitskonstanten wurde für beide Heizmethoden eine Aktivierungsenergie von ~135(11) $kJ \cdot mol^{-1}$ bestimmt. Die höheren Geschwindigkeitskonstanten für die MW-unterstützte Synthese lassen sich daher

nicht auf ein Absenken der Aktivierungsenergie zurückführen. Eine mögliche Erklärung der beschleunigten Synthesen ist ein höherer Betrag an reaktiven Zentren sowie eine Steigerung der Mobilität der Reaktanden in der Lösung unter MW-Strahlung, was durch einen Anstieg des pre-exponentiellen Faktors gestützt wird.

CHEMISTRY
A EUROPEAN JOURNAL

DOI: 10.1002/chem.201003708

High-Throughput and Time-Resolved Energy-Dispersive X-Ray Diffraction (EDXRD) Study of the Formation of CAU-1-$(OH)_2$: Microwave and Conventional Heating**

Tim Ahnfeldt,[a] Jens Moellmer,[b] Vincent Guillerm,[c] Reiner Staudt,[b] Christian Serre,[c] and Norbert Stock*[a]

Abstract: Aluminium dihydroxyterephthalate $[Al_8(OH)_4(OCH_3)_8(BDC(OH)_2)_6]\cdot x H_2O$ (denoted CAU-1-$(OH)_2$) was synthesized under solvothermal conditions and characterized by X-ray powder diffraction, IR spectroscopy, sorption measurements, as well as thermogravimetric and elemental analysis. CAU-1-$(OH)_2$ is isoreticular to CAU-1 and its pores are lined with OH groups. It is stable under ambient conditions and in water, and it exhibits permanent porosity and two types of cavities with effective diameters of approximately 1 and 0.45 nm. The crystallization of CAU-1-$(OH)_2$ was studied by in situ energy-dispersive X-ray diffraction (EDXRD) experiments in the 120–145 °C temperature range. Two heating methods—conventional and microwave—were investigated. The latter leads to shorter induction periods as well as shorter reaction times. Whereas CAU-1-$(OH)_2$ is formed at all investigated temperatures using conventional heating, it is only observed below 130 °C using microwave heating. The calculation of the activation energy of the crystallization of CAU-1-$(OH)_2$ exhibits similar values for microwave and conventional synthesis.

Keywords: aluminum terephthalate · CAU-1 · metal–organic frameworks · microwave chemistry · X-ray diffraction

Introduction

Metal–organic frameworks (MOFs) belong to the family of crystalline porous materials and are promising multifunctional compounds.[1–3] They are investigated for their potential applications in the fields of gas and liquid separation,[4,5] catalysis,[6,7] drug delivery,[8] as well as electrode materials in batteries.[9] The success of hybrid frameworks is based on the diversity of metal oxide clusters that can be connected by a large variety of organic linkers. It is possible to tune the pore size as well as the chemical properties of such MOFs.[10,11] Although many MOFs are easily hydrolyzed, Al-containing compounds are the focus of intensive research since they exhibit good thermal and chemical stabilities.[12,13] Very promising Al-containing candidates for introducing functional groups are the well-known compounds Al-MIL-53[14–16] and CAU-1.[17] For example, Himsl et al. synthesized a hydroxyl-functionalized Al-MIL-53 that shows a significant increase in hydrogen adsorption after Li doping.[18]

The synthesis of isoreticular frameworks by using functionalized or larger organic linker molecules as starting materials poses challenges, since the different organic linker molecules can drastically influence the reaction conditions due to their different basicity and solubility. A tedious trial-and-error approach is often required to get the pure product. High-throughput (HT) methods are a valuable tool for the systematic and efficient investigation of compositional as well as process parameters in solvothermal reactions.[19–22] Recently, we successfully employed this method to synthesize isoreticular structures of Fe-MIL-53, Fe-MIL-88, Fe-MIL-101, as well as Cr-MIL-101 by using aminoterephthalic acid and 2,6-naphthalenedicarboxylic acid, respectively.[10,23] In the course of these studies, the influence of the solvent, the reaction temperature, and time were investigated. Jhung et al. have recently explored the effect of the type of heating on the formation of Cr-MIL-101, that is, conventional versus microwave heating. At the same temperature, microwave heating leads to smaller crystals, a narrower particle-size distribution, and faster reaction times compared to the synthesis using conventional solvothermal techniques.[24] Only few

[a] T. Ahnfeldt, Prof. N. Stock
Institut für Anorganische Chemie
Christian-Albrechts-Universität
Max-Eyth Strasse 2, 24118 Kiel (Germany)
Fax: (+49) 4318801775
E-mail: stock@ac.uni-kiel.de

[b] J. Moellmer, Prof. R. Staudt
Institut für Nichtklassische Chemie e.V.
04318 Leipzig (Germany)

[c] V. Guillerm, Dr. C. Serre
Institut Lavoisier
Université de Versailles St-Quentin en Yvelines
78035 Versailles (France)

[**] CAU-1-$(OH)_2$ = aluminum dihydroxyterephthalate, $[Al_8(OH)_4(OCH_3)_8(BDC(OH)_2)_6]\cdot x H_2O$.

Supporting information for this article is available on the WWW under http://dx.doi.org/10.1002/chem.201003708.

other studies on the use of microwave heating for the synthesis of MOFs have been reported.[25,26]

Although HT methods allow for the systematic investigation of synthesis fields, no information on the reaction mechanism, the induction time, the reaction rate, or the formation of intermediate phases are obtained. Time-resolved energy-dispersive X-ray diffraction (in situ EDXRD) using white-beam X-rays from a synchrotron source is a powerful method to study crystallization processes since they can penetrate the reaction vessels. Studies on inorganic materials that range from transition-metal oxides to zeolites have been described in the literature.[27–31] Up to now, only three EDXRD MOF crystallization studies—that is, the formation of HKUST-1, Fe-MIL-53, and MOF-14—have been reported.[32,33] In addition, light scattering was used to examine the formation of MOF-5.[34]

Herein, we present the results of the in situ investigation and the detailed characterization of the highly porous compound CAU-1-$(OH)_2$ that contains 2,5-dihydroxyterephthalate ions ($[Al_8(OH)_4(OCH_3)_8$ $(BDC(OH)_2)_6]\cdot x H_2O$). In addition, the in situ crystallization of CAU-1-$(OH)_2$ by means of EDXRD techniques using microwave and conventional heating is described.

Results and Discussion

High-throughput syntheses of CAU-1-$(OH)_2$: For the discovery of CAU-1-$(OH)_2$ high-throughput methods were applied. Solvothermal reactions of $AlCl_3\cdot 6H_2O$ and 2,5-dihydroxyterephthalic acid in methanol were performed by varying chemical (molar ratio of $Al^{3+}/H_2BDC(OH)_2/NaOH$) and process (reaction time, reaction temperature) parameters. The synthesis parameters were chosen based on optimized reaction conditions established for CAU-1 starting with a molar ratio of Al^{3+}/linker = 3:1 in methanol and a reaction temperature of 125 °C.[17] The synthesis optimization of CAU-1-$(OH)_2$ was carried out in a 24-reactor multiclave with a total volume of 2 mL. The synthesis of CAU-1-$(OH)_2$ is very pH-sensitive, and a base, preferentially NaOH, as an additive was necessary to synthesize CAU-1-$(OH)_2$ (Figure S1 in the Supporting Information). The side product NaCl, detected by EDX analysis, can be removed easily by washing with water. To increase the crystallinity of the product, the amount of NaOH, the solvent filling level, and the absolute amount of reagents (concentration) in the system $AlCl_3\cdot 6H_2O/H_2BDC(OH)_2$/MeOH/NaOH was varied. Using large amounts of methanol (1–2 mL), that is, low concentrations, no crystalline product was obtained (Table S1, reactions 1–12, and Figure S2 in the Supporting Information). Highly crystalline CAU-1-$(OH)_2$ was obtained at higher concentrations (Table S1, reactions 13–16, and Figure S3). When varying the amount of NaOH (2 M NaOH in methanol) from 0 up to 60 μL, CAU-1-$(OH)_2$ can only be obtained using 50 μL of the additive (Table S1, reactions 17–24, and Figure S4). The optimized synthesis conditions (see the Experimental Section) were used for the scale up as well as the EDXRD studies that employed microwave and conventional heating. In comparison to the synthesis of CAU-1,[17] a lower molar ratio of Al^{3+}/linker is necessary and a base as additive is needed. The synthesis of CAU-1-$(OH)_2$ was also carried out under higher concentration of reactants. As expected, the powder patterns of CAU-1-$(OH)_2$ and CAU-1 are very similar (Figure S5) and thus only small changes in the lattice parameters are observed (CAU-1-$(OH)_2$: $a=b=$ 18.320(5), $c=17.711(6)$ Å; $V=5945(1)$ Å^3 (Table S2); CAU-1: $a=b=18.3517(1)$, $c=17.7720(1)$ Å; $V=5985.33(8)$ Å^3). The title compound is isoreticular to CAU-1, and its structure consists of eight distorted AlO_6 polyhedra that form the octameric brick $[Al_8(OH)_4(OCH_3)_8]^{12+}$. Within this brick the AlO_6 polyhedra are connected through hydroxide groups (corner-sharing) and methoxide groups (edge-sharing). Each octameric brick is bridged by twelve linker molecules, that is, dihydroxyterephthalate ions, to twelve other eight-ring units and thus a three-dimensional network is formed. A detailed description is given in the literature.[17]

Thermal investigation of CAU-1-$(OH)_2$: The thermal behavior of CAU-1-$(OH)_2$ was studied by thermogravimetric (TG) and temperature-dependent X-ray powder diffraction (TDXRPD) measurements. The TG curve (Figure S6 in the Supporting Information) of CAU-1-$(OH)_2$ shows a two-step weight loss. The first step (50–130 °C) corresponds to the release of approximately 18 water molecules per formula unit (obsd 29.0 %, calcd 27.5 %). At higher temperatures (above 300 °C), the decomposition of the frameworks takes place and Al_2O_3 is formed. Based on the formation of Al_2O_3, the observed and calculated total weight loss compare well. (obsd 82.0 %, calcd 83.1 %). These results are in a good agreement with the temperature-dependent XRPD measurements (Figure S7). Between 70 and 120 °C, a strong change of reflection intensities is observed that corresponds to the desorption of enclosed water molecules. Above 330 °C only an X-ray amorphous product is obtained.

Sorption studies on CAU-1-$(OH)_2$: Based on the TG data, an activation procedure at 130 °C and 10^{-3} mbar for 3 h was used. The N_2 sorption isotherm of CAU-1-$(OH)_2$ exhibits a type-I behavior (Figure 1) according to the IUPAC classification.[35] The apparent specific Brunauer–Emmett–Teller (BET) surface area calculated from the N_2 sorption isotherm is approximately 1350 m^2g^{-1} and the micropore volume is 0.50 cm^3g^{-1}. These values are in good agreement with the data obtained for CAU-1 (1370 m^2g^{-1}, 0.52 cm^3g^{-1}).[17] The result of the H_2O sorption experiment is also shown in Figure 1. The total amount of adsorbed water vapor is approximately 520 cm^3g^{-1} at $p/p_0=0.9$, which is corresponds to 27 wt % of adsorbed water molecules. In contrast to the N_2 sorption isotherm, the water-vapor sorption isotherm shows two adsorption steps, which may be due to the tetragonal and octahedral cages. The desorption shows a slight hysteresis due to the strong intermolecular interaction of the sorbate. CAU-1-$(OH)_2$ exhibits a great stability against water. After the H_2O sorption experiment, the re-

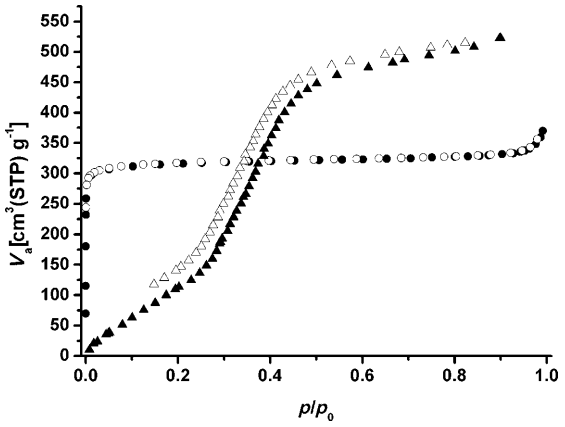

Figure 1. H_2O (298 K, ▲ = adsorption, △ = desorption) and N_2 (77 K, ● = adsorption, ○ = desorption) sorption isotherms of CAU-1-$(OH)_2$.

corded powder pattern of CAU-1-$(OH)_2$ showed no loss of crystallinity. The methane excess uptake of CAU-1-$(OH)_2$ was measured at 25 °C up to 50 bar (Figure 2). Under these conditions, maximum uptake was not fully reached. The

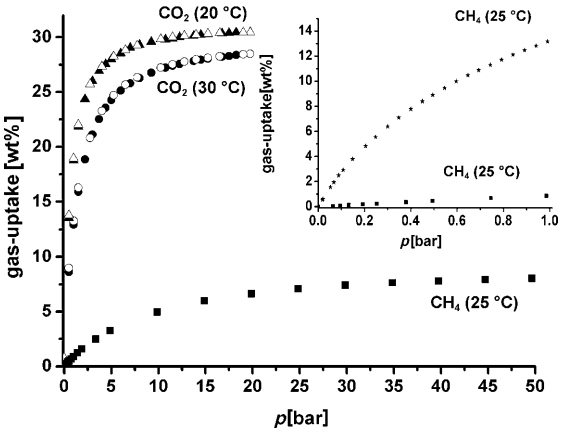

Figure 2. CO_2 and CH_4 sorption isotherms of CAU-1-$(OH)_2$. High-pressure CO_2 sorption isotherms were recorded at 283 and 303 K, and the high-pressure CH_4 isotherm was recorded at 298 K. An additional low-pressure CO_2 sorption experiment was performed at 298 K.

excess methane uptake in CAU-1-$(OH)_2$ at 50 bar corresponds to 8.0 wt %. For comparison, MIL-101 has an uptake of 9.7 wt % at 35 bar.[36] The CO_2 sorption isotherms of CAU-1-$(OH)_2$ are also presented in Figure 2. Two high-pressure measurements were performed at 20 and 30 °C up to 20 bar; the third measurement was carried out at 298 K and up to 1 bar. Under these conditions, maximum uptake was not fully accomplished. However, the isotherm at 20 °C is nearly linear up to 20 bar and shows an uptake of 30.5 wt % CO_2. This value is comparable to those of well-known MOFs like MIL-53(Al) (30.5 wt % at 30 bar and 31 °C)[37] and Cu-BTC (32.0 wt % at 35 bar and 25 °C)[38] and well above those obtained typically with zeolites (e.g., Zeolite 5A: 22.3 wt % at 14 bar and 25 °C).[39] The highest values of CO_2 uptake found for MOFs are around 68.6 wt % (at 50 bar and 25 °C).[40] Looking at the pressure range up to 1 bar, CAU-1-$(OH)_2$ adsorbs at 298 K about 13.1 wt % CO_2, which is relatively high compared to the adsorbed amount of CH_4 (0.9 wt %, Figure 2, inset). This different sorption behavior can be explained by the stronger host–guest interactions of the adsorbent with CO_2.[41,42]

In situ EDXRD investigations: Time-resolved EDXRD measurements of the crystallization of CAU-1-$(OH)_2$ were performed on beamline F3 at HASYLAB (DESY, Hamburg, Germany). The starting reagents were dissolved at the desired reaction temperature, and crystallization of CAU-1-$(OH)_2$ was investigated starting from clear solutions. After the reaction, dispersions with particles between 250 and 1200 nm in diameter, depending on the reaction temperature, and a zeta potential of around 28 mV were obtained. The spectra were recorded at an energy range from 6 to 57 keV. A typical diffraction pattern is shown in Figure S8 in the Supporting information. The four peaks that are observed correspond to the 011, 020, 002, and 121 reflections. The kinetic analyses were done by integrating the 011 reflection, which has the highest intensity. As an example, the results of the crystallization process at 125 °C using conventional heating are shown in Figure 3. The 011 reflection is

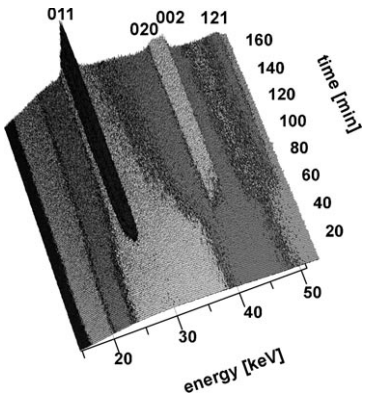

Figure 3. Time-resolved in situ EDXRD data measured during the crystallization of CAU-1-$(OH)_2$ at 125 °C using conventional heating. For clarity, only the section from 15–50 keV is shown.

observed at 27 keV for the conventional setup that corresponds to an interplanar spacing of 12.77 Å. After an induction time of around 50 min, all four product peaks appeared simultaneously (Figure S9) and grew to the maximum intensity within 100 min. The induction time (t_0) represents the time until a detectable size of product particles was formed.[43] During this time nucleation took place. The reaction time corresponds to the period from the first appearance of a reflection to its maximum intensity. The induction time as well as the crystal growth depend strongly on the reaction temperature. To acquire information about the kinetic parameters of the crystallization of CAU-1-$(OH)_2$, the crystallization reactions were carried out at seven different

temperatures in the range 120–145 °C by using conventional and microwave heating. The conventional heating was performed using a setup developed by Bensch et al.[43] For the microwave heating, a new setup was implemented. This was realized by a slight modification of the commercially available Biotage Initiator microwave oven, which was placed in the beam path at beamline F3, HASYLAB (Figure S10). This reactor allows an accurate monitoring of the reaction temperature, stirring rate, and pressure (for details, see the Experimental Section). The comparison of induction and reaction times using conventional and microwave (MW) heating in the crystal growth of CAU-1-(OH)$_2$ between 120–145 °C is shown in Figure 4. For both heating methods,

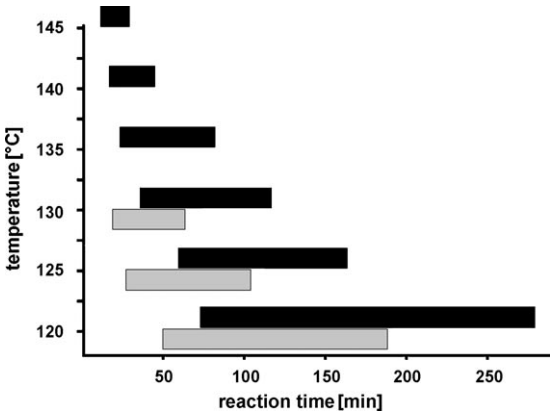

Figure 4. Comparison of induction and reaction times between microwave (gray) and conventional (black) heating for the crystal growth of CAU-1-(OH)$_2$ in the temperature range 120–145 °C.

shorter induction and reaction times with increasing temperature are observed. At the same temperature, the microwave crystallization of CAU-1-(OH)$_2$ is considerably faster; shorter induction as well as reaction times are found. Above 130 °C, conventional heating led to the desired product but no product formation was observed in the microwave reactor. Such a decrease in reaction time using microwave heating instead of conventional heating is generally observed in the literature for organic reactions[44] as well as for MOF synthesis of MIL-53[45] or MIL-101.[24] These studies were performed by quenching the reaction after well-defined reaction times, which can lead to misleading results. According to the literature, the increase in synthesis rates using MW heating are caused by the creation of so-called hot spots, the increase in the heating rate of the reaction mixture or superheating of the reaction mixture.[46,47] In ex situ experiments on the crystal growth of the mircroporous materials silicate-1, VSB-5, and HKUST-1, Jhung et al. also observed accelerated syntheses by microwave irradiation.[48,49] They suggest a higher population of nuclei for microwave syntheses than for conventional syntheses at the same temperature, which leads to a decrease in crystal sizes. These results are in a good agreement with the measured hydrodynamic diameters of CAU-1-(OH)$_2$ synthesized by conventional and MW heating (Figure S12). For the kinetic evaluation of the data, the extent of reaction α and the induction times were determined. The extent of the reaction $\alpha(t)$ is given as the ratio of the intensity at time t to the intensity at time t_∞ [Eq. (1)]:[50]

$$\alpha(t) = I(t)/I(t_\infty)$$

The crystallization kinetics can be calculated using the Avrami–Erofèev expression, which relates $\alpha(t)$ to the reduced time t_{red} ($t_{red} = t - t_0$) as [Eq. (2)]:

$$\ln[-\ln(1-\alpha)] = m\ln(k) + m\ln(t_{red})$$

Plotting $\ln[-\ln(1-\alpha)]$ versus $\ln(t_{red})$ (Sharp–Hancock plot) leads to a straight line if the reaction follows the same mechanism during the complete reaction time.[50] The reaction exponent m can be derived from the slope of the curve, whereas the intercept yields the rate constant k. The plots of extent of crystallization and the corresponding Sharp–Hancock plots are listed in the Supporting Information (Figure S13). The kinetic parameters extracted from the Sharp–Hancock plots are shown in Table 1. The parameter t_0 denotes the starting time for the crystal growth of CAU-1-(OH)$_2$. The Avrami exponent m contains information about the mechanism of the process studied and the growth geometry. Due to the low intensity of the Bragg peaks at the beginning of the reaction, we estimate the error of t_0 according to the reaction rate in the range between ± 5 min for reactions at 115 °C using conventional heating and ± 1 min using MW heating at 130 °C. The error in the determination of the end of reaction was calculated at the scattering of the data at $\alpha = 1$. Here we found an average error of 5 %. Errors involved in fitting the peaks were found to be comparatively small. Altogether, including the error resulting for the determination of the Avrami exponent m by linear regression, a maximum error of ± 0.2 for m and a maximum error of $\pm 3\times10^{-4}$ s^{-1} for the rate constant was found for all reactions. It should be noted that the reaction mechanism models are empirical. Using the Avrami equation is the most commonly employed approach for kinetic studies of solvothermal reactions and has been applied widely to many reaction systems, that is, crystallization of zeolites, thioan-

Table 1. Rate constants (k) and reaction exponents (m) of microwave (MW) and conventional (con) synthesis obtained by evaluation of Sharp–Hancock plots.

$T_{reaction}$	t_0 [min]		k [s^{-1}]		m	
[°C]	MW	con	MW	con	MW	con
120	50	74	9.12×10^{-4}	2.50×10^{-4}	0.74	1.06
125	27	59	1.53×10^{-3}	6.46×10^{-4}	0.66	1.10
130	19	35	2.56×10^{-3}	7.40×10^{-4}	0.74	1.06
135	–	23	–	1.21×10^{-3}	–	1.06
140	–	15	–	2.08×10^{-3}	–	1.06
145	–	11	–	3.18×10^{-3}	–	1.07

timonates, or metal–organic frameworks.[27,28,32] Nevertheless, this method allows one to extract the rate constants and enables the comparison of reactions, for example, at different temperatures. The observed values of Avrami exponents are in the range of 1.0–1.1 and 0.6–0.8 for reactions that use conventional and MW heating, respectively. This indicates a rather diffusion-controlled crystal growth for MW heating and a rather phase-boundary-controlled reaction for conventional heating. The findings are in accordance with studies on the formation of manganese thioantimonates.[43] The high concentration of nucleation sites using MW heating leads to a depletion of the reactants in the reaction mixture. Thus, the rate of reaction depends on how fast the reagents diffuse to the place of crystallization. In the case of conventional heating, the formation of nucleation sites is the most important step and determines the overall rate of crystallization. The rate constants at different temperatures allow for the determination of the Arrhenius activation energy for the crystal growth of CAU-1-$(OH)_2$ as well as the pre-exponential factors (A) for both heating methods (Table S3). Applying the Arrhenius equation and plotting $\ln(k)$ versus $1/T$, the activation energies (E_a) using microwave as well as conventional heating are found in the range of 131–136 kJ (Figure 5). Up to now, no activation energies

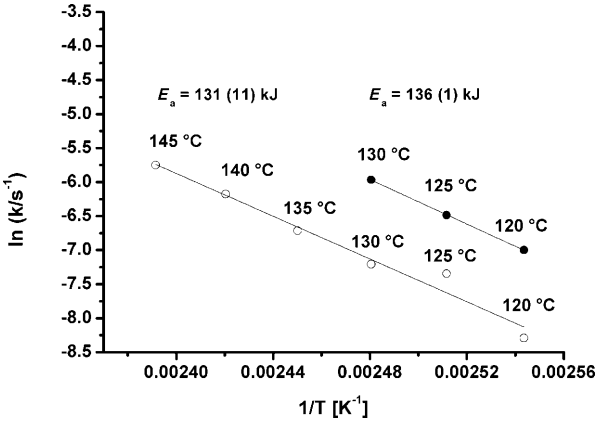

Figure 5. Arrhenius plots to calculate the activation energies for crystal growth of CAU-1-$(OH)_2$ by means of conventional (●) and MW (○) heating.

for the formation of Al-based MOFs have been reported in the literature. For comparison, an activation energy of 53 kJ for phase-boundary-controlled crystallization of layered manganese thioantimonates(III) under conventional conditions was determined.[43] For the diffusion-controlled crystallization of lanthanide phosphonatobutanesulfonates, an activation of 128 kJ was recently published.[51] There are only few studies that compare the influence of microwave-assisted and conventional heating on the crystallization rate, and the described data is not consistent. In ex situ quenching experiments on the crystallization of Fe-MIL-53[45] and AlPO-11,[52] higher activation energies under MW conditions were reported. Nevertheless, MW heating led to an acceleration of the crystallization. This was explained to be due to a large increase of the pre-exponential factor by 6 and 8 orders of magnitude for Fe-MIL-53 and AlPO-11, respectively. In our case, the activation energies do not depend on the heating method and the pre-exponential factor increases by a factor of 15 for microwave-assisted synthesis (Table S3). Possible explanations are the increase of the concentration of reaction sites (number of nuclei) and a higher mobility of the reactants in the microwave field that could lead to an increase of the collision frequency.[49,52,53]

Conclusion

The chemically and thermally stable MOF CAU-1-$(OH)_2$ that contains two -C-OH groups that protrude into the pores has been synthesized by applying our high-throughput methodology. CAU-1-$(OH)_2$ exhibits high porosity and is stable against water. The influence of the reaction temperature and heating method—that is, conventional versus MW heating—on the crystallization of CAU-1-$(OH)_2$ has been investigated by employing in situ EDXRD measurements. Hence, a microwave setup was implemented at beamline F3, HASYLAB, Hamburg. In all crystallization experiments, the induction periods as well as the reaction times are shorter when microwave-assisted heating is employed. Both heating methods yield almost identical activation energies around 135 kJ. The Avrami exponents indicate a phase-boundary-controlled reaction when using conventional heating methods and a diffusion-controlled reaction for the microwave syntheses.

Experimental Section

Chemicals: $AlCl_3 \cdot 6H_2O$ (Riedel-de Haen, $\geq 99\,\%$), 2,5-dihydroxyterephthalic acid ($H_2BDC(OH)_2$; Aldrich, 98 %), methanol (BASF, purum), and NaOH (Merck, $\geq 99\,\%$) were used as purchased.

Synthesis: Pure-phase CAU-1-$(OH)_2$ was formed in the temperature range from 110 to 150 °C without any crystalline byproducts. For the optimized synthesis in the 24-reactor system,[10] a mixture of $AlCl_3 \cdot 6H_2O$ (104.8 mg, 0.433 mmol), $H_2BDC(OH)_2$ (29.9 mg, 0.151 mmol), and 2 M methanolic NaOH (45 μL, 0.09 mmol) was heated at 125 °C in methanol (1000 μL) for 5 h. After filtration, a yellow microcrystalline product was obtained. Scale up of the reaction was performed in a 27 mL Teflon-lined steel bomb using tenfold the amount of the optimized synthesis procedure. The in situ investigations were carried out under stirring in glass vessels with twice the amount of the optimized synthesis. The as-synthesized product of CAU-1-$(OH)_2$ contained large amounts of NaCl. To remove these, the dry yellow microcrystalline raw product was washed on the filter paper several times with water. The sample was dried in air overnight or in an oven at 60 °C for 20 min. After the washing process a yield of 50 % based on the amount of dihydroxyterephthalic acid was obtained (elemental analysis of dehydrated CAU-1-$(OH)_2$ ($[Al_8(OH)_4(OCH_3)_8(BDC(OH)_2)_6]$; obsd: C 39.63, H 3.71; calcd: C 39.35, H 3.07). Dehydration was carried out for 3 h at 130 °C and 1×10^{-3} bar. The absence of chloride and sodium ions was confirmed by EDX analyses. The IR spectrum of CAU-1-$(OH)_2$ (Figure S14 in the Supporting Information) shows the symmetric and asymmetric stretching modes of the bridging carboxylate group at 1598 and 1470 cm^{-1}. The aliphatic C–H stretching vibrations of the methoxy group occurs around 2900 cm^{-1}. The typical

stretching band for the OH groups were not observed due to the presence of water molecules that are involved in O−H···O hydrogen bonding. The band of the C−O stretching vibration of the hydroxyl groups of the incorporated linker molecules appears at 1240 cm^{-1}.

Methods: X-ray powder diffraction patterns were recorded using a STOE STADI P diffractometer equipped with a linear position-sensitive detector using monochromated $Cu_{K\alpha1}$ radiation. Lattice parameters were determined using the DICVOL program[54] and refined using the STOE software package WinXPow.[55] Temperature-dependent X-ray diffraction experiments were performed under air using a STOE STADI P diffractometer equipped with an image plate detector and a STOE capillary furnace (version 0.65.1) using monochromated $Cu_{K\alpha1}$ radiation. Each powder pattern was recorded in the 4–20° range (2θ) at intervals of 10 °C up to 500 °C with a duration of 20 min per scan. The temperature ramp between two patterns was 5 °C min^{-1}. Thermogravimetric (TG) analysis was carried out in air (75 mL min^{-1}, 25–800 °C, 1 °C min^{-1}) using a Netzsch STA-409CD. Carbon, hydrogen, and nitrogen contents were determined by elemental chemical analysis using an Eurovektor EuroEA elemental analyzer. IR spectra were recorded using an ATI Matheson Genesis in the spectral range 4000–400 cm^{-1} using the KBr disk method. The hydrodynamic diameter of the CAU-1-$(OH)_2$ particles were measured by dynamic light scattering using a DelsaNano C apparatus (Beckman & Coulter). EDX analysis was performed using a Philips ESEM XL 30. Several types of adsorption experiments were carried out at three different institutes. Based on the TG data, activation at 130 °C under vacuum for 3 h was used for all measurements. The specific surface area of the dehydrated CAU-1-$(OH)_2$, was determined measuring the N_2 sorption isotherms at −196 °C using a BELSORP-max apparatus. Approximately 100 mg of sample was used for this experiment. The CO_2 adsorption experiments were carried out at 10 and 20 °C up to a pressure of 2 MPa using an HPVA-100 volumetric sorption analyzer (VTI Corporation). The CH_4 isotherm was recorded at 25 °C using a magnetic suspension balance (Rubotherm GmbH, Germany) that can be operated up to 5 MPa. Highly accurate pressure transducers (Newport Omega, Germany) were used in a range from vacuum up to 5 MPa (accuracy 0.05 %). A detailed description of experimental setup for high-pressure adsorption isotherms including buoyancy corrections can be found elsewhere.[56] All wt % values were calculated using the following equation: g(adsorbed gas)/(g(adsorbed gas) + g(adsorbent).

EDXRD experiments: All EDXRD experiments were carried out at the HASYLAB F3 beamline at DESY, Hamburg, Germany. The beamline station receives white synchrotron radiation from a bending magnet with a critical energy of 16.6 keV and gives a positron beam energy of 4.5 GeV. The energy range from 6 to 57 keV exhibits a maximum at about 25 keV. A liquid-nitrogen-cooled solid-state germanium detector with a resolution of about 1 % was used. The in situ investigations were carried out using conventional as well as MW heating. For conventional heating, the reactions were performed in glass tubes in special autoclaves with an internal diameter of 10 mm and a volume of 7 mL. The temperature of the conventional oven can be controlled by a thermocouple within the copper block next to the autoclave and regulated to an accuracy of ±1 K. Several tests showed that the reaction mixture reached the reaction temperature within two minutes.[57] For the microwave reactions, a slightly modified version of the commercially available Biotage Initiator microwave synthesizer was used. The reaction temperature attained within 1 min corresponded to ramp rates of 2–5 °C s^{-1}. Reactor vials with an internal diameter of 14 mm and a volume of 10 mL were used throughout the study. Temperatures were measured using an internal IR sensor. To increase beam intensity on the detector, two holes were drilled into the microwave reaction chamber to assure an unhindered synchrotron beam path through the reaction vessel. With this setup, we are able to recorded time-resolved X-ray powder patterns with acceptable counting statistics within acquisition times of 30 to 120 s. The resulting spectra were evaluated with the tool "calf3," which can be obtained for free at beamline F3. For the data evaluation, the intensive 011 reflection was used. The data are background-corrected and the peaks were fit with Gaussian functions.

Acknowledgements

We thank DESY for the beamtime (project no. II-20080028EC), Andre Rothkirch for the software support, and Mark Feyand for his assistance during the data evaluation. The State of Schleswig–Holstein and the Deutsche Forschungsgemeinschaft (DFG, SPP 1362 "Porous Metal–Organic Frameworks" under the grant STO 643/5-1 and STA 428/17-1) are gratefully acknowledged for the financial support. The research that led to these results has received funding from the European Community's Seventh Framework Programme (FP7/2007–2013) under grant agreement no. 228862.

[1] S. Kitagawa, K. Uemara, *Chem. Soc. Rev.* **2005**, *34*, 109–119.
[2] J. L. C. Rowsell, O. M. Yaghi, *Microporous Mesoporous Mater.* **2004**, *73*, 3–14.
[3] A. K. Cheetham, C. N. R. Rao, R. K. Feller, *Chem. Commun.* **2006**, 4780–4795.
[4] L. Alaerts, M. Maes, P. A. Jacobs, J. F. M. Denayer, D. E. Vos, *Phys. Chem. Chem. Phys.* **2008**, *10*, 2979–2985.
[5] B. Chen, C. Liang, J. Yang, D. S. Contreras, Y. L. Clancy, E. B. Lobkovsky, O. M. Yaghi, S. Dai, *Angew. Chem.* **2006**, *118*, 1418–1421; *Angew. Chem. Int. Ed.* **2006**, *45*, 1390–1393.
[6] M. Fujita, Y. J. Kwon, S. Washizu, K. J. Ogura, *J. Am. Chem. Soc.* **1994**, *116*, 1151–1152.
[7] O. R. Evans, H. L. Ngo, W. Lin, *J. Am. Chem. Soc.* **2001**, *123*, 10395–10396.
[8] P. Horcajada, C. Serre, M. Vallet-Regí, M. Sebban, F. Taulelle, G. Férey, *Angew. Chem.* **2006**, *118*, 6120–6124; *Angew. Chem. Int. Ed.* **2006**, *45*, 5974–5978.
[9] G. Férey, F. Millange, M. Morcrette, C. Serre, M.-L. Doublet, J.-M. Grenèche, J.-M. Tarascon, *Angew. Chem.* **2007**, *119*, 3323–3327; *Angew. Chem. Int. Ed.* **2007**, *46*, 3259–3263.
[10] A. Sonnauer, F. Hoffmann, M. Fröba, L. Kienle, V. Duppel, M. Thommes, C. Serre, G. Férey, N. Stock, *Angew. Chem.* **2009**, *121*, 3849–3852; *Angew. Chem. Int. Ed.* **2009**, *48*, 3791–3794.
[11] A. G. Wong-Foy, A. Matzger, O. M. Yaghi, *J. Am. Chem. Soc.* **2006**, *128*, 3494–3495.
[12] T. Loiseau, L. Lecroq, C. Volkringer, J. Marrot, G. Férey, M. Haouas, F. Taulelle, S. Bourrelly, P. L. Llewellyn, M. Latroche, *J. Am. Chem. Soc.* **2006**, *128*, 10223–10230.
[13] C. Volkringer, D. Popov, T. Loiseau, N. Guillou, G. Férey, M. Haouas, F. Taulelle, C. Mellot-Drazniek, M. Burghammer, C. Riekel, *Nat. Mater.* **2007**, *6*, 760–764.
[14] T. Loiseau, C. Serre, C. Huguenard, G. Fink, F. Taulelle, M. Henry, T. Bataille G. Férey, *Chem. Eur. J.* **2004**, *10*, 1373–1382.
[15] J. Gascon, U. Aktay, M. D. Hernandez-Alonso, G. P. M. van Klink, F. Kapteijn, *J. Catal.* **2009**, *261*, 75–87.
[16] T. Ahnfeldt, D. Gunzelmann, T. Loiseau, D. Hirsemann, J. Senker, G. Férey, N. Stock, *Inorg. Chem.* **2009**, *48*, 3057–3064.
[17] T. Ahnfeldt, N. Guillou, D. Gunzelmann, I. Margiolaki, T. Loiseau, G. Férey, J. Senker, N. Stock, *Angew. Chem.* **2009**, *121*, 5265–5268; *Angew. Chem. Int. Ed.* **2009**, *48*, 5163–5166.
[18] D. Himsl, D. Wallacher, M. Hartmann, *Angew. Chem.* **2009**, *121*, 4710–4714; *Angew. Chem. Int. Ed.* **2009**, *48*, 4639–4642.
[19] S. Bauer, N. Stock, *Angew. Chem.* **2007**, *119*, 6981–6984; *Angew. Chem. Int. Ed.* **2007**, *46*, 6857–6860.
[20] S. Bauer, T. Bein, N. Stock, *Inorg. Chem.* **2005**, *44*, 5882–5889.
[21] N. Stock, T. Bein, *Angew. Chem.* **2004**, *116*, 767–770; *Angew. Chem. Int. Ed.* **2004**, *43*, 749–752.
[22] N. Stock, *Microporous Mesoporous Mater.* **2010**, *129*, 287–295.
[23] S. Bauer, C. Serre, T. Devic, P. Horcajada, J. Marrot, G. Férey, N. Stock, *Inorg. Chem.* **2008**, *47*, 7568–7576.
[24] S. H. Jhung, J.-H. Lee, J. W. Yoon, C. Serre, G. Férey, J.-S. Chang, *Adv. Mater.* **2007**, *19*, 121–124.
[25] Y. K. Hwang, J.-S. Chang, S.-E. Park, D. S. Kim, Y.-U. Kwon, S. H. Jhung, J.-S. Hwang, M.-S. Park, *Angew. Chem.* **2005**, *117*, 562–566; *Angew. Chem. Int. Ed.* **2005**, *44*, 556–660.

[26] S. H. Jhung, J.-H. Lee, P. M. Forster, G. Férey, A. K. Cheetham, J.-S. Chang, *Chem. Eur. J.* **2006**, *12*, 7899–7905.
[27] R. Kiebach, N. Pienack, M. E. Ordolff, F. Studt, W. Bensch, *Chem. Mater.* **2006**, *18*, 1196–1205.
[28] R. I. Walton, F. Millange, D. O'Hare, A. T. Davies, G. Sankar, C. R. A. Catlow, *J. Phys. Chem. B* **2001**, *105*, 83–90.
[29] D. R. Modeshia, R. J. Darton, S. E. Ashbrook, R. I. Walton, *Chem. Commun.* **2009**, 68–70.
[30] D. Croker, M. Loan, B. K. Hodnett, *Cryst. Growth Des.* **2009**, *9*, 2207–2213.
[31] R. J. Francis, S. J. Price, J. S. O. Evans, S. O'Brien, D. O'Hare, S. M. Clark, *Chem. Mater.* **1996**, *8*, 2102–2108.
[32] F. Millange, I. M. Medina, N. Guillou, G. Férey, K. M. Golden, R. I. Walton, *Angew. Chem.* **2010**, *122*, 775–778; *Angew. Chem. Int. Ed.* **2010**, *49*, 763–766.
[33] F. Millange, R. El Osta, M. E. Medina, R. I. Walton, *CrystEngComm* **2011**, *13*, 103–108.
[34] S. Hermes, T. Witte, T. Hikov, D. Zacher, S. Bahnmueller, G. Langstein, K. Huber, R. A. Fischer, *J. Am. Chem. Soc.* **2007**, *129*, 5324–5325.
[35] K. S. W. Sing, D. H. Everett, R. A. W. Haul, L. Mouscou, R. A. Pierotti, J. Rouquerol, T. Siemieniewska, *Pure Appl. Chem.* **1985**, *57*, 603–619.
[36] I. Senkovska, S. Kaskel, *Microporous Mesoporous Mater.* **2008**, *112*, 108–115.
[37] S. Bourrelly, P. L. Llewellyn, C. Serre, F. Millange, T. Loiseau, G. Férey, *J. Am. Chem. Soc.* **2005**, *127*, 13519–1351.
[38] A. R. Millward, O. M. Yaghi, *J. Am. Chem. Soc.* **2005**, *127*, 17998–17999.
[39] D. Saha, Z. Bao, F. Jia, S. Deng, *Environ. Sci. Technol.* **2010**, *44*, 1820–1826.
[40] H. Furukawa, N. Ko, Y. Bok Go, N. Aratani, S. Beom Choi, E. Choi, A. Özgür Yazaydin, R. Q. Snurr, M. O'Keeffe, J. Kim, O. M. Yaghi, *Science* **2010**, *329*, 424–428.
[41] P. L. Llewellyn, S. Bourrelly, C. Serre, A. Vimont, M. Daturi, L. H. Weireld, J.-S. Chang, D.-Y. Hong, Y. K. Hwang, H. S. Jhung, G. Férey, *Langmuir* **2008**, *24*, 7245–7250.
[42] J. Moellmer, E. B. Celer, R. Luebke, A. J. Cairns, R. Staudt, M. Eddaoudi, M. Thommes, *Microporous Mesoporous Mater.* **2010**, *129*, 345–353.
[43] L. Engelke, M. Schaefer, M. Schur, W. Bensch, *Chem. Mater.* **2001**, *13*, 1383–1390.
[44] L. Perreux, A. Loupy, *Tetrahedron* **2001**, *57*, 9199–9223.
[45] E. Haque, N. A. Khan, J. H. Park, S. H. Jhung, *Chem. Eur. J.* **2010**, *16*, 1046–1052.
[46] W. C. Conner, G. Tompsett, K.-H. Lee, K. S. Yngvesson, *J. Phys. Chem. B* **2004**, *108*, 13913–13920.
[47] G. Tompsett, W. C. Conner, K. S. Yngvesson, *ChemPhysChem* **2006**, *7*, 296–319.
[48] S. H. Jhung, T. Jin, Y. K. Hwang, J.-S. Chang, *Chem. Eur. J.* **2007**, *13*, 4410–4417.
[49] N. A. Khan, E. Haque, S. H. Jhung, *Phys. Chem. Chem. Phys.* **2010**, *12*, 2625–2631.
[50] J. H. Hancock, J. D. Sharp, *J. Am. Ceram. Soc.* **1972**, *55*, 74–77.
[51] M. Feyand, C. Näther, A. Rothkirch, N. Stock, *Inorg. Chem.* **2010**, *49*, 11158–11163.
[52] M. Gharibeh, G. A. Tompsett, W. C. Conner, K. S. Yngvesson, *ChemPhysChem* **2008**, *9*, 2580–2591.
[53] J. G. P. Binner, N. A. Hassine, T. E. Cross, *J. Mater. Sci.* **1995**, *30*, 5389–5393.
[54] A. Boultif, D. Louer, *J. Appl. Crystallogr.* **1991**, *24*, 987–993.
[55] *STOE WinXPOW version 2.11*, Stoe & Cie GmbH, Darmstadt, Germany, **2005**.
[56] J. Moellmer, A. Moeller, F. Dreisbach, R. Glaeser, R. Staudt, *Microporous Mesoporous Mater.* **2011**, *138*, 140–148.
[57] R. Kiebach, M. Schaefer, F. Porsch, W. Bensch, *Z. Anorg. Allg. Chem.* **2005**, *631*, 369–374.

Received: December 22, 2010
Published online: April 27, 2011

4.3.2 Synthesis of isoreticular CAU-1 compounds: Effects of linker and heating methods on the kinetics of the synthesis

Die folgende Publikation wurde bei der Zeitschrift „CrystEngComm“ zur Publikation angenommen. Zusätzliche Informationen befinden sich im Anhang 9 ab Seite 243.

Die Kristallisationsgeschwindigkeit Metall-organischer Gerüstverbindungen hängt von vielen Syntheseparametern, wie der Reaktionstemperatur, der Löslichkeit der Reaktanden oder der verwendeten Heizmethode ab. In dieser Arbeit wurde die Synthese von CAU-1-NH_2 in situ mit energiedispersiver Röntgenbeugung (EDXRD) hinsichtlich der Kinetik der Produktbildung untersucht. Die Herstellung von CAU-1-NH_2 erfolgte durch die solvothermale Umsetzung von 2-Aminoterephthalsäure (H_2BDC-NH_2) und $AlCl_3 \cdot 6H_2O$ in Methanol. Ingesamt wurden sieben Reaktionen in dem Temperaturbereich von 115–145 °C durchgeführt. Für die Synthesen wurde ein MW-Ofen (Biotage) verwendet.
Zur Untersuchung des Einflusses der Heizmethode auf den Kristallisationsprozess wurden die Synthesen in einem konventionellen, elektrisch heizenden Ofen wiederholt. Um die Rolle der eingesetzten Linker bei den Synthesen der beiden isoretikulären CAU-1 Verbindungen, CAU-1-NH_2 und CAU-1-$(OH)_2$, zu bestimmen, wurden die Ergebnisse der EDXRD-Untersuchung zudem miteinander verglichen. Beide Studien wurden im gleichen Zeitraum mit einem identischen Setup durchgeführt. Zur Synthese von CAU-1-$(OH)_2$ wurde der Linker 2,5-Dihydroxyterephthalsäure (H_2BDC-$(OH)_2$) eingesetzt. Die Synthesebedingungen von CAU-1 ließen sich nicht 1 : 1 auf die Synthese von CAU-1-$(OH)_2$ übertragen. Zur Darstellung von CAU-1-$(OH)_2$ musste eine konzentriertere Reaktionsmischung verwendet und der pH-Wert der Reaktionsmischung mit NaOH eingestellt werden.
Bei Verwendung der konventionellen Heizmethode konnten CAU-1-NH_2 und CAU-1-$(OH)_2$ über den gesamten Temperaturbereich von 115-145 °C synthetisiert werden. Für beide Verbindungen wurden nahezu identische Induktions- und Reaktionszeiten beobachtet. Die MW-unterstützten Synthesen von CAU-1-$(OH)_2$ und CAU-1-NH_2 weisen hingegen im Vergleich viel kürzere Induktions- und Reaktionszeiten auf, wobei die Synthese von CAU-1-NH_2 deutlich stärker beschleunigt wird. Bemerkenswert ist, dass im MW-Ofen ab einer Reaktionstemperatur von 130 °C kein

CAU-1-$(OH)_2$ mehr erhalten wurde. Die Auswertung der Daten mit der Avrami-Eroféev-Gleichung deutet darauf hin, dass die Kristallisationsgeschwindigkeit der isoretikulären CAU-1-Verbindungen eher von der verwendeten Heizmethode als von den eingesetzten Linkermolekülen abhängig ist. Aus den Arrheniusauftragungen der Geschwindigkeitskonstanten wurden für das Kristallwachstum von CAU-1-NH_2 und CAU-1-$(OH)_2$ die Aktivierungsenergien ermittelt. Für beide Verbindungen wurden sowohl für die Mikrowellensynthesen als auch für die konventionell durchgeführten Synthesen Aktivierungsenergien im Bereich von ~135(11) $kJ \cdot mol^{-1}$ bestimmt. In Übereinstimmung mit der Literatur korrelierten die höheren Geschwindigkeitskonstanten bei den MW-unterstützten Synthesen mit einem Anstieg des pre-exponentiellen Faktors.

.

.

CrystEngComm

Cite this: DOI: 10.1039/c1ce05956d

www.rsc.org/crystengcomm

PAPER

Synthesis of isoreticular CAU-1 compounds: effects of linker and heating methods on the kinetics of the synthesis†

Tim Ahnfeldt and Norbert Stock*

Received 27th July 2011, Accepted 6th October 2011
DOI: 10.1039/c1ce05956d

Two isoreticular aluminium containing metal–organic frameworks, CAU-1-NH_2 and CAU-1-$(OH)_2$, have been synthesized solvothermally using 2-aminoterephthalic and 2,5-dihydroxyterpththalic acid to elucidate the product formation depending on the functionalized carboxylic acids. Here, we focus on the product formation kinetics of the amino-functionalized CAU-1, *i.e.* CAU-1-NH_2. The reactions were studied by *in situ* energy dispersive X-ray diffraction (EDXRD) experiments in the temperature range of 115–145 °C. Both conventional electric (CE) and microwave (MW) -assisted heating were employed. The latter led to shorter induction periods as well as shorter crystallisation times compared to the conventional synthesis. In analogy with the previously reported results of the EDXRD studies of the formation of CAU-1-$(OH)_2$, similar crystal growth rates were observed for both CAU-1-NH_2 and CAU-1-$(OH)_2$ using CE heating. In contrast, MW-assisted synthesis of CAU-1-NH_2 led to a shorter induction period as well as an acceleration of the crystal growth compared to CAU-1-$(OH)_2$. The acceleration in the crystal growth stage of CAU-1-NH_2 can be attributed to a larger pre-exponential factor (about three times that of CAU-1-$(OH)_2$) derived from the Arrhenius plot. However, the activation energy of the crystal growth exhibits similar values for both MW-assisted and CE synthesis of CAU-1-NH_2 and CAU-1-$(OH)_2$.

1. Introduction

Metal–organic frameworks (MOFs) have developed into an important class in the family of porous materials.[1] These crystalline inorganic–organic hybrid compounds are constructed from inorganic bricks and organic linker molecules and form three-dimensional structures. MOFs have been widely investigated for potential applications in the field of gas and liquid separation,[2] catalysis,[3] drug delivery,[4] as well as delivery devices.[5] They are promising multifunctional compounds due to the tunability of size, shape and surface properties of their pores, starting from a wide variety of organic linkers and metal ions. Especially, metal carboxylates have been investigated in detail.[6] Due to their thermal and chemical stability, Al-containing MOFs are in the focus of intensive research.[7] Promising Al-containing candidates for introducing functional groups are the well-known MOFs Al-MIL-53 (ref. 8), Al-MIL-101-NH_2 (ref. 9 and 10) and CAU-1 (ref. 10). For example, the recently reported amino-functionalized Al-MIL-53-NH_2 (ref. 11) and hydroxyl-functionalized Al-MIL-53-OH (ref. 12) exhibit high porosity and are stable against hydrolysis. Al-MIL-53-NH_2 was used for post-synthetic modifications[13] and a lithium doping of Al-MIL-53-OH led to an increase in H_2 adsorption.[12]

The synthesis of isoreticular frameworks using different metal ions, functionalized or larger organic linker molecules as starting materials, is still a challenging task. The reactants can drastically influence the reaction conditions due to their different acidities and solubilities. An exhausting trial and error approach is often required to get the phase-pure products. High-throughput (HT) methods are a valuable tool to explore and optimize synthesis conditions of isoreticular MOFs. The HT-methods allow the systematic and efficient investigation of the effect of reactant compositions, solvents as well as process parameters in solvothermal reactions.[14] Very recently, we have applied the HT-method to introduce hydroxyl groups in the CAU-1 structure using 2,5-dihydroxyterephthalic acid.[15] In the course of this study, the influences of pH value, amount of solvent and overall concentration were examined, which rapidly led to the desired product. Although the HT-method allows the systematic investigation of synthesis fields, no kinetic information such as the reaction mechanism or the reaction rate of the crystallization can be obtained. Exploration of the kinetics of solvothermal reactions leads to a more detailed understanding of the reaction process and is very important for the optimization of synthesis conditions. Most kinetic studies on MOFs focus on the type of heating and were realized by *ex situ* quenching experiments.[16]

Institut für Anorganische Chemie, Christian-Albrechts-Universität zu Kiel, Max-Eyth-Str. 2, D-24118 Kiel, Germany. E-mail: stock@ac.uni-kiel.de
† Electronic supplementary information (ESI) available: Additional characterisation data. Comparison of EDXRD and ADXD data and particle size distribution curves obtained by DLS measurements. DOI: 10.1039/c1ce05956d

The use of different heating sources can lead to an acceleration of synthesis rates as well as affect the product properties. Jhung *et al.* have explored the effect of the heating method on the formation of Fe-MIL-53 using CE, MW-assisted heating as well as ultrasound (US) irradiation.[16] At the same temperature, the rate of crystallization decreases in the order US > MW ≫ CE, which was attributed to increased pre-exponential factors rather than decreased activation energies calculated from Arrhenius plots. The MW-assisted synthesis of HKUST-1 leads generally to smaller particle sizes and faster reaction times compared to the synthesis using conventional solvothermal techniques, which is mainly caused by rapid nucleation *via* MW irradiation.[16] To the best of our knowledge, no report on the product formation of isoreticular MOFs with variation of organic ligands has been reported up to now. However, there exists a report on the product formation of isoreticular MOFs with variation of metal ions. Jhung *et al.* investigated the effect of metal ions (Cr^{3+}, Al^{3+} and V^{3+}) in the synthesis of MIL-53.[17] The synthesis rate increases in the following order: $r_{Cr\text{-}MIL\text{-}53} < r_{Al\text{-}MIL\text{-}53} < r_{V\text{-}MIL\text{-}53}$, which correlates well with the lability of the metal ions. This indicates that the rate of the deprotonation of terephthalic acid is much faster compared to the complexation of deprotonated terephthalic acid to the metal ions. *In situ* experiments enable a more detailed study on the product formation of MOFs, since they allow the observation of possible intermediate phases, the investigation of the decomposition of frameworks and the control over the particle size of the desired products. The following methods have been employed to study the crystallisation process of MOFs: *in situ* light scattering,[18] *in situ* atomic force microscopy,[19] *in situ* surface plasmon resonance spectroscopy,[20] *in situ* small- and wide-angle X-ray scattering (SAXS/WAXS),[21] and time-resolved energy-dispersive X-ray diffraction (*in situ* EDXRD). The *in situ* EDXRD studies require the use of white beam X-rays from a synchrotron and studies on the product formation of inorganic materials ranging from transition metal oxides to zeolites have been described in the literature.[22] Up to now, only a few EDXRD studies on the crystallization of MOFs, *e.g.*, HKUST-1, Fe-MIL-53, and MOF-14, have been reported.[23] Very recently, we have reported an *in situ* time-resolved EDXRD study of the product formation of CAU-1-$(OH)_2$ using MW-assisted and CE heating. Herein, we present the results of the *in situ* EDXRD investigations on CAU-1-NH_2 using the same experimental setup and reaction conditions.

2. Experimental section

CAU-1-NH_2 was synthesised solvothermally similar to the reported method.[10] A mixture of $AlCl_3 \cdot 6H_2O$ (146.1 mg, 0.061 mmol) and H_2BDC–NH_2 (36.5 mg, 0.020 mmol) was suspended in methanol (2 mL). The reactions were carried out under stirring in the temperature range of 115–145 °C. The product formation was studied by *in situ* energy dispersive X-ray diffraction (EDXRD) experiments. All EDXRD experiments were carried out at the HASYLAB F3 beamline at DESY, Hamburg, Germany. The beamline station receives white synchrotron radiation from a bending magnet with a critical energy of 16.6 keV and gives a positron beam energy of 4.5 GeV. The energy range from 6 to 57 keV exhibits a maximum at about 25 keV. A liquid nitrogen cooled solid-state germanium detector with a resolution of about 1% was used. The detector angle was set to approximately 1.9° and the collimator to 0.2 × 0.2 mm^2. Since this setup allows us to monitor only a small part of the reaction mixture continuous stirring is mandatory during the investigation. The statistical distribution of the product is also facilitated by the fact that always colloidal dispersions are formed. The *in situ* investigations were carried out using CE as well as MW-assisted heating. For CE heating the reactions were performed in glass tubes (DURAN® culture tubes) with an internal diameter of 10 mm and a volume of 7 mL. The temperature of the conventional electric oven can be controlled by a thermocouple within the copper block next to the autoclave and regulated to an accuracy of ±1 K. Several tests showed that the reaction mixture reached the reaction temperature within two minutes.[24] The detailed setup is presented in detail in ref. 25. For the MW reactions a slightly modified version of the commercially available MW synthesizer Biotage Initiator was used. The reaction temperature attained within 1 min corresponds to ramp rates of 2–5 °C s^{-1}. Reactor vials (Biotage Microwave Vial 2–5 mL) with an internal diameter of 14 mm and a volume of 10 mL were used throughout the study. Temperatures were measured by an internal IR-sensor. To increase beam intensity on the detector site holes were drilled into the MW reaction chamber to assure an unhindered synchrotron beam path through the reaction vessel. With this set-up we are able to recorded time-resolved X-ray powder patterns with acceptable counting statistics within acquisition times of 30 to 120 s. The resulting spectra were evaluated with the tool "calf3" which can be obtained for free at beamline F3. For data evaluation the intensive 011 reflection was used. The data are background corrected and the peaks are fit with Gaussian functions. The hydrodynamic diameters of the fully crystallized samples were measured by dynamic light scattering after the completion of the reaction using a DelsaNano C apparatus (Beckman & Coulter). The calculation of the particle size distribution (numerical basis) was performed using CONTIN particle size distribution analysis routines as implemented in the Delsa Nano 2.31 software. Angular dispersive X-ray diffraction (ADXD) measurements were recorded using a STOE STADI P diffractometer equipped with a linear position-sensitive detector using monochromated $CuK_{\alpha 1}$ radiation. The synthesis conditions and the results of the kinetic study on the product formation of CAU-1-$(OH)_2$ are reported elsewhere.[15]

3. Results and discussion

Time-resolved EDXRD measurements of the crystallization of the CAU-1 compounds were performed on beamline F3 at HASYLAB (DESY, Hamburg, Germany). The starting reagents are fully dissolved at the desired reaction temperature and therefore the CAU-1 compounds crystallize from clear solutions. After the reaction stable dispersions with particles around 100–500 nm in diameter are obtained. The spectra were recorded at an energy range from 6 keV to 57 keV. The four peaks that are observed correspond to the 011, 020, 002 and 121 reflections (see Fig. S1 in the ESI†). The kinetic analyses were done by integrating the 011 reflection which has the highest intensity. As an example, the results of the crystallization process at 130 °C using CE heating are shown in Fig. 1. The 011 reflection is observed

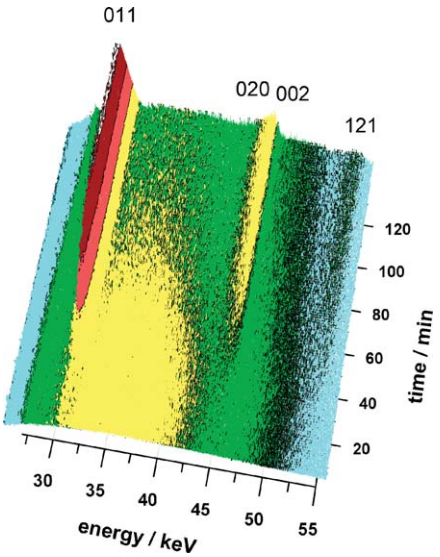

Fig. 1 Time-resolved *in situ* EDXRD data measured during the crystallization of CAU-1-NH_2 at 130 °C using CE heating. For clarity, only the section from 25 to 55 keV is shown.

around 30 keV corresponding to an interlayer spacing of 12.77 Å. After an induction time (t_0) of *ca.* 35 min, all four product reflections are observed and grow simultaneously to their maximum intensity within 110 min (for more detailed information see Fig. S2 in the ESI†). The induction time represents the time until the first product particles are observed in the spectra. During this time nucleation takes place. It has to be kept in mind that numerous factors influence the threshold of a detectable diffraction signal from the product such as the number of product particles, crystallinity, growth rate, possible intermediate phases, measurement time, detector noise and beam intensity.

The crystallisation time (t_{cry}) corresponds to the period from the first appearance of a reflection to its maximum intensity. The induction time as well as the crystal growth depend strongly on the reaction temperature. In order to acquire information about the crystallization kinetics of CAU-1-NH_2, the reactions were carried out at seven different temperatures in the range 115–145 °C. The influence of the applied heating methods was also investigated by performing all reactions under MW-assisted and CE heating. In the course of this study CAU-1-NH_2 based on aminoterephthalic acid and also 2,5-dihydroxyterephthalic acid was investigated. Aminoterephthalic acid and 2,5-dihydroxyterephthalic acid exhibit different acidity and polarity which can have an impact on the crystallization process. Herein we will focus on CAU-1-NH_2 synthesized using aminoterephthalic acid, only making comparisons with the crystallization of 2,5-dihydroxyterephthalic acid functionalized CAU-1-$(OH)_2$. The *in situ* CE heating investigations were performed using experimental methods developed by Bensch *et al.*[25] For *in situ* MW-assisted heating, a new experimental configuration was developed, in which a modified Biotage Initiator MW reactor, which allows monitoring of temperature, pressure and stirring rate, was placed in the beam path.[15]

The comparison of induction and crystallisation times using CE and MW-assisted heating in the formation of CAU-1-NH_2

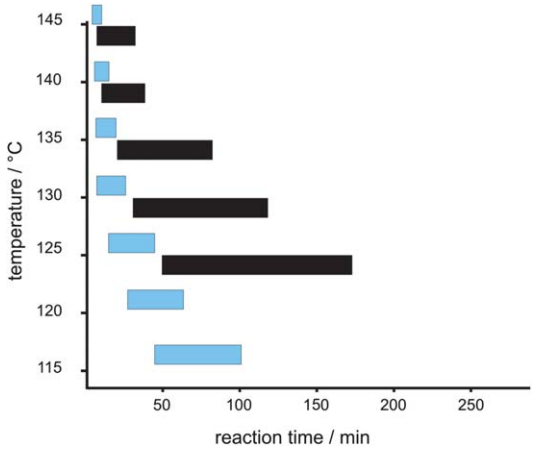

Fig. 2 Comparison of induction and crystallisation times between MW-assisted (blue bars) and CE (black bars) heating for the crystal growth of CAU-1-NH_2 in the temperature range 115–145 °C. No experiments were performed for CE heating at 115 °C or 120 °C due to the slow reaction rate.

between 115 and 145 °C is shown in Fig. 2. For both heating methods, higher temperatures lead to shorter induction and crystallization times. For reactions at the same temperature, MW-assisted heating leads to considerably faster reactions. Such a decrease of reaction time using MW irradiation is also observed for CAU-1-$(OH)_2$ (ref. 15) as well as for solvothermal syntheses of other MOFs, like HKUST-1 (ref. 16*a*), or Fe-MIL-53 (ref. 16*b*). The latter however were performed by quenching the reaction after specific reaction times, which can lead to misleading results. The acceleration is assumed to be caused by a higher and more homogeneous population of nuclei for the MW-assisted syntheses compared to CE syntheses at the same temperature.

The increased nucleation rate leads to a decrease in the particle size of the crystals. In our investigation the decrease of the particle sizes was demonstrated by dynamic light scattering (DLS) measurements of the fully crystallized samples (Fig. 3). The increase of the reaction-temperature leads to a decrease in

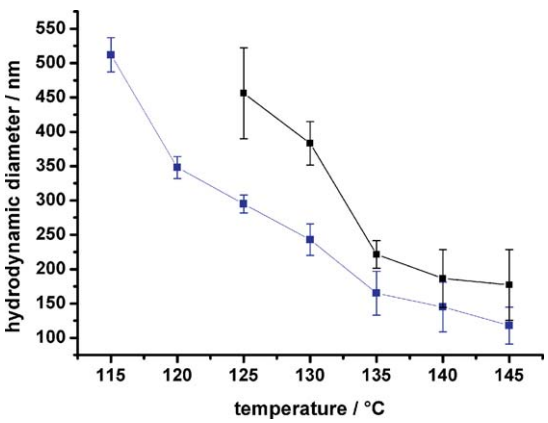

Fig. 3 Comparison of the hydrodynamic diameters of CAU-1-NH_2 particles synthesized by MW-assisted (blue) and CE heating (black) in the temperature range 115–145 °C. Standard deviations are given by error bars.

the hydrodynamic diameter of the CAU-1-NH_2 particles for both heating methods. The MW-assisted synthesis of CAU-1-NH_2 leads to smaller particles compared to the CE synthesis at the same temperature. Above 135 °C only a small decrease in the hydrodynamic diameter of the CAU-1-NH_2 particles was observed for both heating methods. Differential number distribution curves of the hydrodynamic diameters shown in Fig. 3 are given in the ESI (Fig. S2 and S3†).

Fig. 4 shows the induction and crystallisation times for the crystal growth of CAU-1-NH_2 and the previously reported CAU-1-$(OH)_2$ according to the applied heating method.

For reactions at the same reaction-temperature, similar rates are observed for both, CAU-1-$(OH)_2$ and CAU-1-NH_2, under CE heating, though with slightly shorter induction times for the formation of the latter. This indicates that the acidity and the solubility of the linker have no or only a minor influence on the rate of the product formation. The findings are in good agreement with a recent study on the crystallisation of isostructural MIL-53 and MIL-47 compounds containing different metal ions (V^{3+}, Fe^{3+}, and Al^{3+}).[26] These results suggested that the reaction rates are rather influenced by the complexation rate than by the deprotonation rate of the linker.[26] In contrast, applying MW-assisted heating induction and crystallisation times for CAU-1-NH_2 is faster compared to CAU-1-$(OH)_2$. Surprisingly,

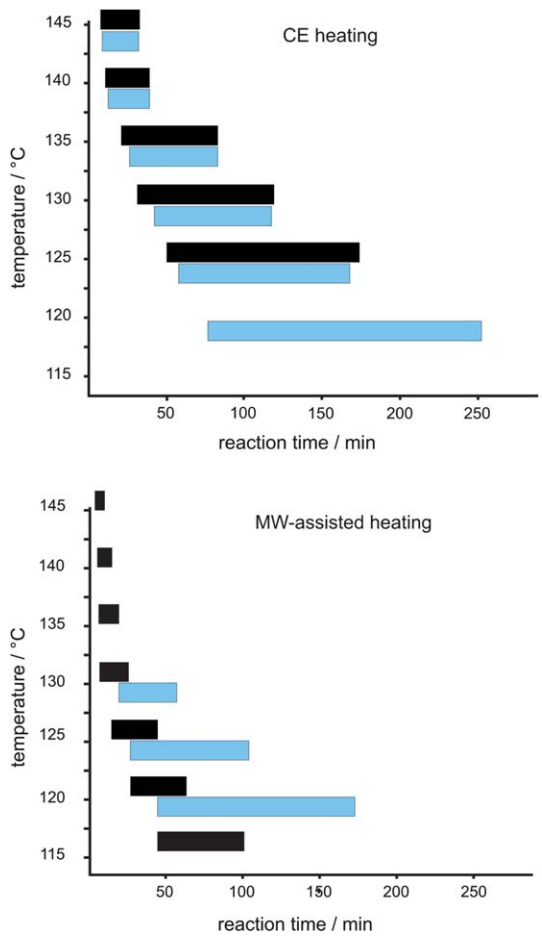

Fig. 4 Comparison of induction and crystallisation times for the crystal growth of CAU-1-NH_2 (black bars) and CAU-1-$(OH)_2$ (blue bars) using CE (top) as well as MW-assisted (bottom) heating.

only non-porous, X-ray amorphous products could be obtained for the MW-assisted synthesis of CAU-1-$(OH)_2$ above 130 °C.

For a kinetic evaluation of the data, the extent of reaction, α, and the induction times, t_0, were determined. The extent of the reaction, $\alpha(t)$, is given as the ratio of the intensity at given time, $I(t)$, to the intensity at t_∞:[27]

$$\alpha(t) = I(t)/I(t_\infty) \quad (1)$$

Due to the low absorption coefficient of *ca.* $\mu = 0.127$ mm^{-1} and the small hydrodynamic diameters of the particles, microabsorption does not substantially affect the reflection intensities. The crystallization kinetics can be calculated using the Avrami–Erofeev expression, which relates $\alpha(t)$ to the reduced time t_{red} ($t_{red} = t - t_0$), where the parameter t_0 denotes the time until the first product particles are observed:

$$\ln[-\ln(1-\alpha)] = m\ln(k) + m\ln(t_{red}) \quad (2)$$

Plotting $\ln[-\ln(1-\alpha)]$ *versus* $\ln(t_{red})$ (Sharp–Hancock plot) leads to a straight line, provided the reaction follows the same mechanism throughout the crystallisation.[27] The reaction exponent m can be derived from the slope of this plot, whilst the intercept yields the rate constant k (plots of the extent of crystallisation and corresponding Sharp–Hancock plots are given in Fig. 5).

Due to an expected large error caused by the short reaction times no kinetic evaluation of the MW-assisted syntheses of CAU-1-NH_2 above a reaction temperature of 135 °C was performed. Nevertheless, the errors were estimated for all other reactions as follows: as a result of the low intensity of the Bragg peaks at the beginning of the reaction, we estimate the error of t_0 according to the reaction rate in the range between ±5 min for reactions at 115 °C using CE heating and ±1 min using MW heating at 135 °C. As an example the determination of t_0 for the

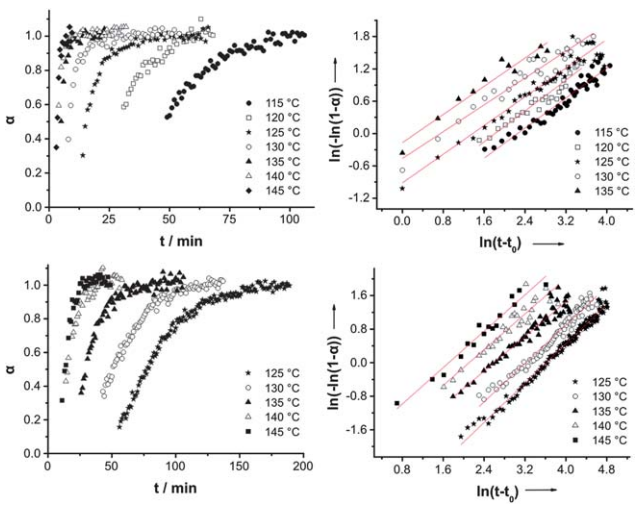

Fig. 5 Kinetic analyses of the crystallization of CAU-1-NH_2 *via* MW-assisted (top row) and CE heating (bottom row). *Left*: plots of the extent of crystallization (α) curves against time (t) obtained by integration of the (011) Bragg peak in the EDXRD spectra. Right: Sharp and Hancock analyses using the Avrami–Erofeev nucleation-growth crystallization model.

MW-assisted heating at 125 °C is shown in Fig. S3 in the ESI†. The error in the determination of the end of reaction was estimated at the scatter of the data at $\alpha = 1$. Here we found an average error of 5%. Errors involved in fitting the peaks were found to be comparatively small. Altogether, including the error resulting in the determination of the Avrami exponent m by linear regression, a maximum error of ±0.2 for m and a maximum error of $\pm 3 \times 10^{-4}$ s^{-1} for the rate constant were found for all reactions. The kinetic parameters derived from the Sharp–Hancock plots and induction times for all temperatures are summarized in Table 1. The Avrami exponent m contains information about the mechanism of the process studied and the growth geometry, though it should be noted that the reaction mechanism models are empirical. The Avrami equation is the most commonly employed approach for kinetic studies of solvothermal reactions and it has been widely applied to many reaction systems, *e.g.* crystallization of zeolites, thioantimonates and metal–organic frameworks.[22b,23,25] This method allows the determination of the rate constants and enables comparison of reactions, *e.g.* at different temperatures. The Sharp–Hancock analysis of the data obtained for CAU-1-NH_2 and CAU-1-$(OH)_2$ suggests uniform kinetics within the observed temperature range for both heating methods, with values of the Avrami exponent in the range of 1.0–1.2 and 0.6–0.9 for CE and MW-assisted heating, respectively (Table 1). These values indicate a diffusion controlled crystal growth mechanism for MW-assisted heating and a phase-boundary-controlled reaction mechanism for CE heating. Using MW-assisted heating seems to lead to a high concentration of nucleation sites, which causes a rapid depletion of the reactants in the reaction mixture. Thus, the rate of reaction depends on how fast the reagents diffuse to the growing crystal. In the case of CE heating the attachment of the reactants, *i.e.* the inorganic brick or metal and linker ions, seems to be rate limiting and thus determines the overall rate of crystallisation.

The rate constants at different temperatures allow the determination of the Arrhenius activation energies (E_a) (Fig. 6) for the crystal growth. For the CE and MW-assisted heating the activation energy (E_a) for the crystallization of CAU-1-NH_2 is found to be 136(6) and 136(5) kJ mol^{-1}, respectively. These values fit well with the values observed for the crystal growth of CAU-1-$(OH)_2$ (131(11) kJ mol^{-1}(CE), 136(1) kJ mol^{-1}(MW)).[15]

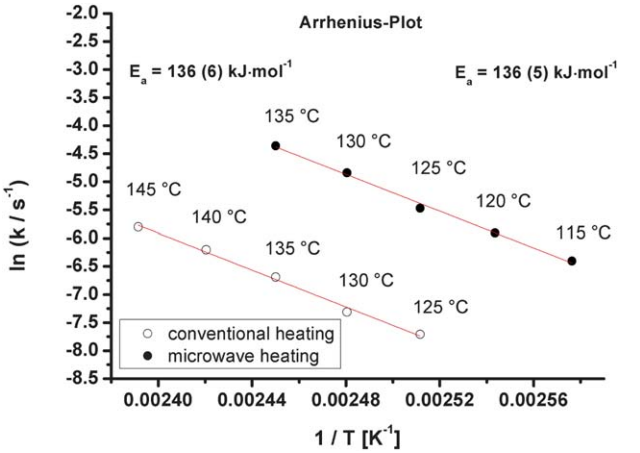

Fig. 6 Determination of Arrhenius activation energies for the crystal growth of CAU-1-NH_2 *via* CE and MW-assisted heating.

The pre-exponential factors (A) are also displayed in Table 1. While similar values for the crystal growth of CAU-1-NH_2 and CAU-1$(OH)_2$ under CE conditions are observed, for MW-assistant heating A increased by a factor of 3 and 10 for CAU-1-$(OH)_2$ and CAU-1-NH_2, respectively. For the calculation of the pre-exponential factors the activation energy of 136 kJ mol^{-1} was used, which is within the error ranges of the Arrhenius plots of the growth rates of CAU-1-NH_2 and CAU-1-$(OH)_2$. Therefore, it can be concluded that the increased rates by MW-assisted heating for the crystal growth of CAU-1-NH_2 and CAU-1-$(OH)_2$, compared to those obtained by CE heating, are due to increased pre-exponential factors instead of lower activation energies.

This could be explained by an increase of the concentration of reaction sites and a higher mobility of the reactants, which cause an increase in the collision frequency.[28]

Table 1 Rate constants k and exponents m obtained from the Sharp–Hancock analysis as well as calculated pre-exponential factors (A) for the crystal growth of CAU-1-NH_2 and CAU-1-$(OH)_2$ in the temperature range 115–145 °C using CE and MW-assisted heating

T/°C	t_0/min (MW)	t_0/min (CE)	k/s^{-1} (MW)	k/s^{-1} (CE)	m (MW)	m (CE)	A/s^{-1} (MW)[a]	A/s^{-1} (CE)[a]
CAU-1-NH_2								
115	43.5		1.66×10^{-3}		0.72		3.33×10^{15}	
120	26.5		2.72×10^{-3}		0.71		3.19×10^{15}	
125	13	49	4.21×10^{-3}	4.49×10^{-4}	0.67	1.14	2.93×10^{15}	3.12×10^{14}
130	7	33	7.92×10^{-3}	6.67×10^{-4}	0.62	1.18	3.31×10^{15}	2.79×10^{14}
135	4	20	1.29×10^{-2}	1.25×10^{-3}	0.65	1.07	3.25×10^{15}	3.17×10^{14}
140	3	9		2.02×10^{-3}		1.06		3.17×10^{14}
145	3	9		3.02×10^{-3}		1.08		2.94×10^{14}
CAU-1-$(OH)_2$								
120	51	74	9.12×10^{-4}	2.50×10^{-4}	0.74	1.06	1.07×10^{15}	2.93×10^{14}
125	27	59	1.53×10^{-3}	6.46×10^{-4}	0.66	1.10	1.06×10^{15}	4.49×10^{14}
130	19	35	2.56×10^{-3}	7.40×10^{-4}	0.74	1.06	1.07×10^{15}	3.09×10^{14}
135		23		1.21×10^{-3}		1.06		3.08×10^{14}
140		16		2.08×10^{-3}		1.06		3.25×10^{14}
145		11		3.18×10^{-3}		1.07		3.10×10^{14}

[a] Values calculated using an activation energy of 136 kJ mol^{-1}.

There are only a few studies comparing the influence of MW-assisted and CE heating on the crystallisation rate and the pre-exponential factor. In *ex situ* quenching experiments on the crystallisation of Fe-MIL-53 (ref. 16*b*), HKUST-1 (ref. 16*a*) and SAPO-11 (ref. 28) higher activation energies under MW conditions were reported. However, no satisfying explanation was given to elucidate the increase of activation energies.

Nevertheless, in all cases MW-assisted heating led to an acceleration of the reaction, which was also explained to be due to a large increase of the pre-exponential factor. For Fe-MIL-53 and SAPO-11 the pre-exponential factor increases by 6 and 8 orders of magnitude, respectively. For SAPO-11 Conner *et al.* speculated that the higher crystallization rates by MW-assisted heating are due to "specific interactions" between microwaves and the precursor species during the nucleation and growth processes.[29]

At present we are also not able to explain in detail the higher pre-exponential factors for the crystallisation of CAU-1-NH_2 and CAU-1-$(OH)_2$ under MW-assisted heating. In addition the larger acceleration (factor 10 *versus* factor 3) observed for CAU-1-NH_2 compared to CAU-1-$(OH)_2$ is not easy to understand. Thermal (hot spots) as well as non-thermal MW effects have been discussed in the literature to explain these effects[30] but are hard to prove. Based on our investigation we suspect that the differences in crystallisation are due to an increase in the nucleation rate upon MW-irradiation. This is supported by the smaller particles obtained in MW-assisted reactions.

4. Conclusions

The influence of the reaction temperature and heating method, *i.e.* conventional electric (CE) *vs.* microwave (MW) heating, on the crystallization of CAU-1-NH_2 has been investigated employing *in situ* EDXRD measurements. In all crystallisation experiments, at the same temperature, the induction periods as well as the crystallisation times are shorter when MW-assisted heating is employed. Both heating methods yield almost identical activation energies around 136 kJ. The Avrami exponents indicate a phase-boundary-controlled reaction using CE heating methods and a diffusion controlled reaction for the MW syntheses. These results are in good agreement with the ones observed in the *in situ* EXRD investigations of CAU-1-$(OH)_2$. Applying CE heating leads to similar induction times, crystallisation rates, pre-exponential factors and activation energies for both compounds, CAU-1-$(OH)_2$ and CAU-1-NH_2. These results suggest that the effects of the linker (deprotonation rate, different functional group) have no or only a minor influence on the rate of the product formation under CE heating. In contrast, syntheses of CAU-1-$(OH)_2$ and CAU-1-NH_2 under MW-assisted heating differ substantially. Whereas CAU-1-NH_2 is formed at all investigated temperatures, CAU-1-$(OH)_2$ is only observed below 130 °C. In addition, the accelerated synthesis for CAU-1-NH_2 is observed compared to CAU-1-OH_2. Based on the kinetic evaluation the difference is apparent by a three times higher pre-exponential factor.

Acknowledgements

We thank DESY for the beam time (project no.: II-20080028 EC), Prof. Bensch for the allocation of the *in situ* equipment, Beatrix Seidelhofer and Dr Nicole Pienack for their support using beamline F3, Andre Rothkirch for the software support and Mark Feyand for his assistance during the data evaluation. The State of Schleswig–Holstein and the Deutsche Forschungsgemeinschaft (DFG, SPP 1362 "Porous Metal–Organic Frameworks" under the grant STO 643/5-1) are gratefully acknowledged for the financial support. The comments of referee 1 are also gratefully acknowledged.

Notes and references

1 (*a*) G. Ferey, *Chem. Soc. Rev.*, 2008, **37**, 191; (*b*) S. Kitagawa and K. Uemara, *Chem. Soc. Rev.*, 2005, **34**, 109; (*c*) J. L. C. Rowsell and O. M. Yaghi, *Microporous Mesoporous Mater.*, 2004, **73**, 3.
2 (*a*) L. Alaerts, M. Maes, P. A. Jacobs, J. F. M. Denayer and D. E. Vos, *Phys. Chem. Chem. Phys.*, 2008, **10**, 2979; (*b*) B. Chen, C. Liang, J. Yang, D. S. Contreras, Y. L. Clancy, E. B. Lobkovsky, O. M. Yaghi and S. Dai, *Angew. Chem., Int. Ed.*, 2006, **45**, 1390; (*c*) L. Hamon, P. L. Llewellyn, T. Devic, A. Ghoufi, G. Clet, V. Guillerm, G. D. Pirngruber, G. Maurin, C. Serre, G. Driver, W. van Beek, E. Jolimaitre, A. Vimont, M. Daturi and G. Férey, *J. Am. Chem. Soc.*, 2009, **131**, 17490.
3 (*a*) L. Hamon, P. L. Llewellyn, T. Devic, A. Ghoufi, G. Clet, V. Guillerm, G. D. Pirngruber, G. Maurin, C. Serre, G. Driver, W. van Beek, E. Jolimaitre, A. Vimont, M. Daturi and G. Férey, *J. Am. Chem. Soc.*, 2009, **131**, 17490; (*b*) B. Chen, C. Liang, J. Yang, D. S. Contreras, Y. L. Clancy, E. B. Lobkovsky, O. M. Yaghi and S. Dai, *Angew. Chem., Int. Ed.*, 2006, **45**, 1390; (*c*) A. Henschel, K. Gedrich, R. Kraehnert and S. Kaskel, *Chem. Commun.*, 2008, 4192.
4 (*a*) P. Horcajada, C. Serre, M. Vallet-Regí, M. Sebban, F. Taulelle and G. Férey, *Angew. Chem., Int. Ed.*, 2006, **45**, 5974; (*b*) P. Horcajada, T. Chalati, C. Serre, B. Gillet, C. Sebrie, T. Baati, J. F. Eubank, D. Heurtaux, P. Clayette, C. Kreuz, J. S. Chang, Y. K. Hwang, V. Marsaud, Y.-N. Bories, L. Cynober, S. Gil, G. Férey, P. Couvreur and R. Gref, *Nat. Mater.*, 2010, **9**, 172.
5 (*a*) W. J. Rieter, K. M. L. Taylor and W. Lin, *J. Am. Chem. Soc.*, 2007, **129**, 9852; (*b*) K. M. L. Taylor, W. J. Rieter and W. Lin, *J. Am. Chem. Soc.*, 2008, **130**, 14358.
6 A. Sonnauer, F. Hoffmann, M. Fröba, L. Kienle, V. Duppel, M. Thommes, C. Serre, G. Férey and N. Stock, *Angew. Chem., Int. Ed.*, 2009, **48**, 3791.
7 (*a*) T. Loiseau, L. Lecroq, C. Volkringer, J. Marrot, G. Férey, M. Haouas, F. Taulelle, S. Bourrelly, P. L. Llewellyn and M. Latroche, *J. Am. Chem. Soc.*, 2006, **128**, 10223; (*b*) C. Volkringer, T. Loiseau, M. Haouas, F. Taulelle, D. Popov, M. Burghammer, C. Riekel, C. Zlotea, F. Cuevas, M. Latroche, D. Phanon, C. Knöfelv, P. L. Llewellyn and G. Férey, *Chem. Mater.*, 2009, **21**, 5783; (*c*) C. Volkringer, T. Loiseau, N. Guillou, G. Férey, M. Haouas, F. Taulelle, N. Audebrand, I. Margiolaki, D. Popov, M. Burghammer and C. Riekel, *Cryst. Growth Des.*, 2009, **9**, 2927; (*d*) C. Volkringer, D. Popov, T. Loiseau, G. Férey, M. Burghammer, C. Riekel, M. Haouas and F. Taulelle, *Chem. Mater.*, 2009, **21**, 5695.
8 T. Loiseau, C. Serre, C. Huguenard, G. Fink, F. Taulelle, M. Henry, T. Bataille and G. Férey, *Chem.–Eur. J.*, 2004, **10**, 1373.
9 P. Serra-Crespo, E. V. Ramos-Fernandez, J. Gascon and F. Kapteijn, *Chem. Mater.*, 2011, **23**, 2565.
10 T. Ahnfeldt, N. Guillou, D. Gunzelmann, I. Margiolaki, T. Loiseau, G. Férey, J. Senker and N. Stock, *Angew. Chem., Int. Ed.*, 2009, **48**, 5163.
11 (*a*) T. Ahnfeldt, D. Gunzelmann, T. Loiseau, D. Hirsemann, J. Senker, G. Férey and N. Stock, *Inorg. Chem.*, 2009, **48**, 3057; (*b*) J. Gascon, U. Aktay, M. D. Hernandez-Alonso, G. P. M. van Klink and F. Kapteijn, *J. Catal.*, 2009, **261**, 75.
12 D. Himsl, D. Wallacher and M. Hartmann, *Angew. Chem., Int. Ed.*, 2009, **48**, 4639.
13 (*a*) C. Volkringer and S. M. Cohen, *Angew. Chem., Int. Ed.*, 2010, **49**, 4644; (*b*) M. Savonnet, D. Bazer-Bachi, N. Bats, J. Perez-Pellitero, E. Jeanneau, V. Lecocq, C. Pinel and D. Farrusseng, *J. Am. Chem. Soc.*, 2010, **132**, 4518; (*c*) S. J. Garibay, Z. Wang and S. M. Cohen, *Inorg. Chem.*, 2010, **49**, 8086.

14 (*a*) S. Bauer and N. Stock, *Angew. Chem., Int. Ed.*, 2007, **46**, 6857; (*b*) S. Bauer, T. Bein and N. Stock, *Inorg. Chem.*, 2005, **44**, 5882; (*c*) N. Stock and T. Bein, *Angew. Chem., Int. Ed.*, 2004, **43**, 749; (*d*) N. Stock, *Microporous Mesoporous Mater.*, 2010, **129**, 287; (*e*) P. M. Forster, N. Stock and T. Bein, *Angew. Chem., Int. Ed.*, 2005, **44**, 7608.
15 T. Ahnfeldt, J. Moellmer, V. Guillerm, R. Staudt, C. Serre and N. Stock, *Chem.–Eur. J.*, 2011, **17**, 6462.
16 (*a*) N. A. Khan, E. Haque and S. H. Jhung, *Phys. Chem. Chem. Phys.*, 2010, **12**, 2625; (*b*) E. Haque, N. A. Khan, J. H. Park and S. H. Jhung, *Chem.–Eur. J.*, 2010, **16**, 1046.
17 N. A. Khan, M. Haque and S. H. Jhung, *Eur. J. Inorg. Chem.*, 2010, 4975.
18 (*a*) S. Hermes, T. Witte, T. Hikov, D. Zacher, S. Bahnmüller, G. Langstein, K. Huber and R. A. Fischer, *J. Am. Chem. Soc.*, 2007, **129**, 5324; (*b*) J. Cravillon, S. Münzer, S.-J. Lohmeier, A. Feldhoff, K. Huber and M. Wiebcke, *Chem. Mater.*, 2009, **21**, 1410; (*c*) J. Cravillon, R. Nayuk, S. Springer, A. Feldhoff, K. Huber and M. Wiebcke, *Chem. Mater.*, 2011, **23**, 2130; (*d*) D. Zacher, J. Lin, K. Huber and R. A. Fischer, *Chem. Commun.*, 2009, 1031.
19 (*a*) M. Shoaee, M. W. Anderson and M. P. Attfield, *Angew. Chem., Int. Ed.*, 2008, **47**, 8525; (*b*) N. S. John, C. Scherb, M. Shoaee, M. W. Anderson, M. P. Attfield and T. Bein, *Chem. Commun.*, 2009, 6294.
20 O. Shekhah, H. Wang, D. Zacher, R. A. Fischer and C. Wöll, *Angew. Chem., Int. Ed.*, 2009, **48**, 5038.
21 J. Juan-Alcañiz, M. Goesten, A. Martinez-Joaristi, E. Stavitski, A. V. Petukhov, J. Gascon and F. Kapteijn, *Chem. Commun.*, 2011, **47**, 8578.
22 (*a*) R. Kiebach, N. Pienack, M. E. Ordolff, F. Studt and W. Bensch, *Chem. Mater.*, 2006, **18**, 1196; (*b*) R. I. Walton, F. Millange, D. ÓHare, A. T. Davies, G. Sankar and C. R. A. Catlow, *J. Phys. Chem. B*, 2001, **105**, 83; (*c*) R. J. Francis, S. J. Price, J. S. O. Evans, S. O'Brien, D. O'Hare and S. M. Clark, *Chem. Mater.*, 1996, **8**, 2102.
23 (*a*) F. Millange, I. M. Medina, N. Guillou, G. Férey, K. M. Golden and R. I. Walton, *Angew. Chem., Int. Ed.*, 2010, **49**, 763; (*b*) F. Millange, R. El Osta, M. E. Medina and R. I. Walton, *CrystEngComm*, 2011, **13**, 103.
24 R. Kiebach, M. Schaefer, F. Porsch and W. Bensch, *Z. Anorg. Allg. Chem.*, 2005, **631**, 369.
25 L. Engelke, M. Schaefer, M. Schur and W. Bensch, *Chem. Mater.*, 2001, **13**, 1383.
26 E. Haque, J. H. Jeong and S. H. Jhung, *CrystEngComm*, 2010, **12**, 2749.
27 J. D. Sharp and J. H. Hancock, *J. Am. Ceram. Soc.*, 1972, **55**, 74.
28 M. Gharibeh, G. A. Tompsett, W. C. Conner and K. S. Yngvesson, *ChemPhysChem*, 2008, **9**, 2580.
29 M. Gharibeh, G. A. Tompsett and W. C. Conner, *Top. Catal.*, 2008, **49**, 157.
30 A. De la Hoz, A. Díaz-Ortiz and A. Moreno, *Chem. Soc. Rev.*, 2005, **34**, 164.

4.4 Zusätzliche Arbeit

4.4.1 3-D coordination polymers based on the TetraThiaFulvaleneTetraCarboxylate (TTF-TC) derivative: synthesis, characterization and oxidation issues

Der folgende Artikel wurde in „Inorganic Chemistry“ publiziert und beschreibt die Synthese und Charakterisierung von dreidimensionalen Koordinationspolymeren auf der Basis von Tetrathiafluvalentetracarbonsäure ($_2$(HOOC)-C_6S_4-$(COOH)_2$ = (TTF-TC)H_4). Zusätzliche Informationen zu dieser Publikation finden sich im Anhang 10 auf Seite 247.

Vier neue dreidimensionale Koordinationspolymere konnten durch Umsetzung von (TTF-TC)H_4 mit verschiedenen Alkalimetallsalzen unter besonderer Berücksichtigung des pH-Wertes und der Reaktionstemperatur dargestellt werden. Folgende Summenformel wurde aus den Einkristallstrukturdaten der Verbindungen erhalten: M_2(TTF-TC)H_2 (M = K, Rb, Cs). Die Substanzen sind redoxaktiv und wurden als Elektrodenmaterial in Lithiumbatterien getestet. Dabei wurde eine gute Reproduzierbarkeit der Ladezyklen festgestellt. Basierend auf oxidierter TTF-TC wurde des Weiteren in einer Elektrokristallisation im wässrigen Medium die dichte Verbindung K(TTF-$TC^{+\bullet}$)H_2 hergestellt, welche über Halbleitereigenschaften verfügt.

Inorganic Chemistry
Article

Inorg. Chem. **2010**, *49*, 7135–7143 **7135**
DOI: 10.1021/ic100950n

3-D Coordination Polymers Based on the Tetrathiafulvalenetetracarboxylate (TTF-TC) Derivative: Synthesis, Characterization, and Oxidation Issues

Thi Le Anh Nguyen,[†] Rezan Demir-Cakan,[‡] Thomas Devic,*[,†] Mathieu Morcrette,[‡] Tim Ahnfeldt,[§] Pascale Auban-Senzier,[∥] Norbert Stock,[§] Anne-Marie Goncalves,[†] Yaroslav Filinchuk,[⊥] Jean-Marie Tarascon,[‡] and Gérard Férey[†]

[†]*Institut Lavoisier, UMR CNRS 8180, Université de Versailles Saint-Quentin-en-Yvelines, 45 avenue des Etats-Unis, 78035 Versailles cedex, France,* [‡]*LRCS UMR CNRS 6007, Université de Picardie Jules Verne, 33 rue Saint-Leu, 80039 Amiens, France,* [§]*Institute of Inorganic Chemistry, Christian-Albrechts-Universität, Otto-Hahn-Platz 6/7, 24118 Kiel, Germany,* [∥]*Laboratoire de Physique des Solides, UMR CNRS 8502, Bât. 510, Université de Paris-Sud, 91405 Orsay, France, and* [⊥]*SNBL at ESRF, 38043 Grenoble, France*

Received May 12, 2010

The reactivity of the redox-active tetracarboxylic acid derived from the tetrathiafulvalene (TTF-TC)H_4 with alkaline cations (K, Rb, Cs) is reported. The exploration of various experimental parameters (temperature, pH) led to the formation of four crystalline three-dimensional coordination polymers formulated M_2(TTF-TC)H_2 (M = K, Rb, Cs), denoted MIL-132(K), MIL-133(isostructural K, Rb), and MIL-134(Cs). Thermogravimetric analysis and thermodiffraction show that all of the solids are thermally stable up to 150−200 °C in the air. In order to exploit the possibility of oxidation of the organic linker in TTF-based compounds, they were employed as positive electrodes in a classical lithium cell. A highly reversible cyclability was achieved at high current density (10 C) with a reasonable performance (∼50 mAh g^{-1}). Finally, combined electro-(sub)hydrothermal synthesis was used to prepare a fifth 3-D coordination polymer formulated K(TTF-TC)H_2 (denoted MIL-135(K)), this time not based on the neutral TTF-TC linker but its radical, oxidized form TTF-$TC^{+\bullet}$. This solid is less thermally stable than its neutral counterparts but exhibits a semiconducting behavior, with a conductivity at room temperature of about 1 mS cm^{-1}.

Introduction

Among the numerous properties which can be hosted by porous coordination polymers, redox activity has recently deserved special attention. Indeed, mixed valence compounds can show high electronic conduction,[1−4] whereas solids stable upon redox reactions[5−7] could lead to enhanced hydrogen sorption[8−12] or can be used as anode electrodes for lithium ion batteries,[13−16] active molds for the preparation of metallic nanoparticles[8,17−19] and conducting polymers,[20,21]

*To whom correspondence should be addressed. E-mail: devic@chimie.uvsq.fr.

(1) Takaishi, S.; Hosoda, M.; Kajiwara, T.; Miyasaka, H.; Yamashita, M.; Nakanishi, Y.; Kitagawa, Y.; Yamaguchi, K.; Kobayashi, A.; Kitagawa, H. *Inorg. Chem.* **2008**, *48*, 9048–9050.
(2) Fuma, Y.; Ebihara, M.; Kutsumizu, S.; Kawamura, T. *J. Am. Chem. Soc.* **2004**, *126*, 12238–12239.
(3) Miyasaka, H.; Motokawa, N.; Matsunaga, S.; Yamashita, M.; Sugimoto, K.; Mori, T.; Toyota, N.; Dunbar, K. R. *J. Am. Chem. Soc.* **2010**, *132*, 1532–1544.
(4) Zeng, M.-H.; Wang, Q.-X.; Tan, Y.-X.; Hu, S.; Zhao, H.-X.; Long, L.-S.; Kurmoo, M. *J. Am. Chem. Soc.* **2010**, *132*, 2561–2563.
(5) Choi, H. J.; Suh, M. P. *J. Am. Chem. Soc.* **2004**, *126*, 15844–15851.
(6) Agusti, G.; Ohtani, R.; Yoneda, K.; Gaspar, A. B.; Ohba, M.; Sanchez-Royo, J. F.; Munoz, M. C.; Kitagawa, S.; Real, J. A. *Angew. Chem. Int. Ed.* **2009**, *48*, 8944–8947.
(7) Ritchie, C.; Streb, C.; Thiel, J.; Mitchell, S. G.; Miras, H. N.; Long, D.-L.; Boyd, T.; Peacock, R. D.; McGlone, T.; Cronin, L. *Angew. Chem., Int. Ed.* **2008**, *47*, 6881–6884.
(8) Cheon, Y. E.; Suh, M. P. *Angew. Chem., Int. Ed.* **2009**, *48*, 2899–2903.
(9) Mulfort, K. L.; Hupp, J. T. *J. Am. Chem. Soc.* **2007**, *129*, 9604–9605.
(10) Mulfort, K. L.; Hupp, J. T. *Inorg. Chem.* **2008**, *47*, 7936–7938.
(11) Dalach, P.; Frost, H.; Snurr, R. Q.; Ellis, D. E. *J. Phys. Chem. C* **2008**, *112*, 9278–9284.
(12) Mulfort, K. L.; Wilson, T. M.; Wasielewski, M. R.; Hupp, J. T. *Langmuir* **2009**, *25*, 503–508.
(13) Férey, G.; Millange, F.; Morcrette, M.; Serre, C.; Doublet, M.-L.; Grenèche, J.-M.; Tarascon, J.-M. *Angew. Chem., Int. Ed.* **2007**, *46*, 3259–3263.
(14) Armand, M.; Grugeon, S.; Vezin, H.; Laruelle, S.; Ribière, P.; Poizot, P.; Tarascon, J.-M. *Nat. Mater.* **2009**, *8*, 120–125.
(15) Xiang, J.; Chang, C.; Li, M.; Wu, S.; Yuan, L.; Sun, J., A *Cryst. Growth Des.* **2008**, *8*, 280–282.
(16) Chen, H.; Armand, M.; Courty, M.; Jiang, M.; Grey, C. P.; Dolhem, F.; Tarascon, J.-M.; Poizot, P. *J. Am. Chem. Soc.* **2009**, *131*, 8984–8988.
(17) Suh, M. P.; Moon, H. R.; Lee, E. Y.; Jang, S. Y. A. *J. Am. Chem. Soc.* **2006**, *128*, 4710–4718.
(18) Moon, H. R.; Kim, J. H.; Suh, M. P. *Angew. Chem., Int. Ed.* **2005**, *44*, 1261–1265.
(19) Hong, B. H.; Bae, S. C.; Lee, C.-W.; Jeong, S.; Kim, K. S. *Science* **2001**, *294*, 348–351.
(20) Yanai, N.; Uemura, T.; Ohba, M.; Kadowaki, Y.; Maesato, M.; Takenaka, M.; Nishitsuji, S.; Hasegawa, H.; Kitagawa, S. *Angew. Chem., Int. Ed.* **2008**, *47*, 9883–9886.
(21) Uemura, T.; Kadowaki, Y.; Yanai, N.; Kitagawa, S. *Chem. Mater.* **2009**, *21*, 4096–4098.

Published on Web 07/02/2010

or for sensing through guest-network charge-transfer interactions.[22−24] The electrochemical synthesis of porous coordination polymers by the electrolysis of copper electrodes has also been proposed,[25,26] and few studies of their electrochemical behaviors have been reported.[13−16,27] Compared to the purely inorganic porous solids, one noticeable advantage of the coordination polymers is that not only the metallic cations but also suitable organic linkers can act as redox centers.[8−12,14−16,19,22,23,28]

Tetrathiafulvalene (TTF) derivatives are sulfur-rich π-electron donors known to form organic molecular conducting or even superconducting salts upon partial oxidation (Scheme 1).[29] Examples of TTF bearing neutral coordinative groups (N, P or S) are numerous,[30] and many coordination complexes have been prepared, mainly with the aim to combine the electronic and magnetic properties of the organic and inorganic moieties in the resulting solids.[31−38] Few coordination polymers (from 1 to 3-D) have been described,[34,35,39−46] mostly involving interactions between d^{10} cations (Cu, Ag) and sulfur atoms of the TTF backbone.[34,39,42−44,46] On the other hand, coordination compounds involving oxygenated anionic binding sites, such as catecholate[47−50] and carboxylate,[51−57] are rare and with few noticeable exceptions[53,55,57] limited to molecular species. This could at first glance appear surprising, since carboxylate linkers are known to afford numerous stable, neutral, and sometimes highly porous 3D coordination networks.[58−61] The reason for this may be found in the presumed low stability of such linkers, which would make them incompatible with the sometimes harsh (temperature, pH) experimental conditions used for the preparation of stable 3-D coordination polymers. We thus focused our attention on the TTF tetracarboxylic acid[62] ((TTF-TC)H_4, see Scheme 1), whose characteristics (high symmetry and potentially strong binding site) appear adequate for the preparation of robust 3-D networks. The reactivity of this linker with divalent cations (Ni,Co) was already studied but led to porous hydrogen-bonded networks of isolated carboxylate anions and inorganic cations.[63,64] For TTF-$Co(H_2O)_6$(TTF-TC)$H_2\cdot 2H_2O$,[64] the partial dehydration was thought to give rise to a coordination compound, although this was not structurally evidenced. Only very recently, a 3-D coordination polymer based on Zn, TTF-TC, and 4,4′-bipyridine as a coligand was reported.[55] Another issue

Scheme 1. (Top) Two-Electron Reversible Oxidation of the TTF Core, As Well As the Shape of the Highest Occupied Molecular Orbital (HOMO) and (Bottom) Tetrathiafulvalenetetracarboxylic Acid ((TTF-TC)H_4) Used in the Present Study[a]

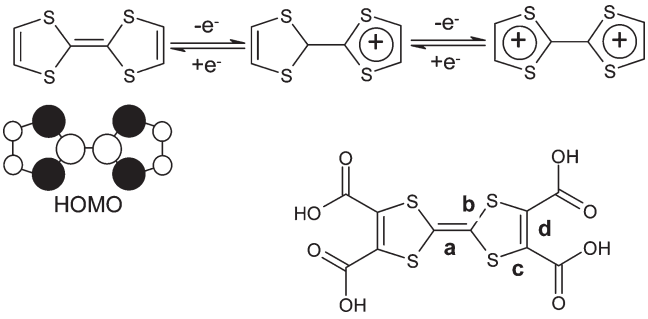

[a] Letters a−d correspond to the bond distances reported in Table 2.

(22) Shimomura, S.; Matsuda, R.; Tsujino, T.; Kawamura, T.; Kitagawa, S. *J. Am. Chem. Soc.* **2006**, *128*, 16416–16417.
(23) Shimomura, S.; Horike, S.; Matsuda, R.; Kitagawa, S. *J. Am. Chem. Soc.* **2007**, *129*, 10990–10991.
(24) Tanaka, D.; Horike, S.; Kitagawa, S.; Ohba, M.; Hasegawa, M.; Ozawa, Y.; Toriumi, K. *Chem. Commun.* **2007**, 3142–4144.
(25) Mueller, U.; Schubert, M.; Teich, F.; Puetter, H.; Schierle-Arndt, K.; Pastré, J. *J. Mater. Chem.* **2006**, *16*, 626-636.
(26) Ameloot, R.; Stappers, L.; Fransaer, J.; Alaerts, L.; Sels, B. F.; De Vos, D. E. *Chem. Mater.* **2009**, *21*, 2580–2582.
(27) Domenech, A.; Garcia, H.; Domenech-Carbo, M. T.; Llabres-i-Xamena, F. *J. Phys. Chem. C* **2007**, *111*, 13701–13711.
(28) Kitagawa, S.; Kawata, S. *Coord. Chem. Rev.* **2002**, *224*, 11–34.
(29) See, for example, the special issue on Molecular Conductors: *Chem. Rev.* **2004**, *104*, 4887−5782 and references therein.
(30) Lorcy, D.; Bellec, N.; Fourmigue, M.; Avarvari, N. *Coord. Chem. Rev.* **2009**, *253*, 1398–1438 and references therein.
(31) Liu, S. X.; Ambrus, C.; Dolder, S.; Neels, A.; Decurtins, S. *Inorg. Chem.* **2006**, *45*, 9622–9624.
(32) Lu, W.; Zhang, Y.; Dai, J.; Zhu, Q.-Y.; Bian, G.-Q.; Zhang, D.-Q. *Eur. J. Inorg. Chem.* **2006**, 1629–1634.
(33) Setifi, F.; Ouahab, L.; Golhen, S.; Yoshida, Y.; Saito, G. *Inorg. Chem.* **2003**, *42*, 1791–1793.
(34) Ichikawa, S.; Mori, H. *Inorg. Chem.* **2009**, *48*, 4643–4645.
(35) Ichikawa, S.; Takahashi, K.; Mori, H.; Yamaura, J.-I. *Solid State Sci.* **2008**, *10*, 1724–1728.
(36) Uzelmeier, C. E.; Smucker, B. W.; Reinheimer, E. W.; Shatruk, M.; O'Neal, A. W.; Fourmigué, M.; Dunbar, K. R. *Dalton Trans.* **2006**, 5229–5268.
(37) Perruchas, S.; Avarvari, N.; Rondeau, D.; Levillain, E.; Batail, P. *Inorg. Chem.* **2005**, *44*, 3459–3465.
(38) Geng, Y.; Wang, X.-J.; Chen, B.; Xue, H.; Zhao, Y.-P.; Lee, S.; Tung, C.-H.; Wu, L.-Z. *Chem.—Eur. J.* **2009**, *15*, 5124–5129.
(39) Ding, Y.; Chen, Q.; Zhong, J.-C.; Munakata, M.; Konaka, H.; Ning, G.-L.; Wang, H.-Z. *Polyhedron* **2008**, *27*, 1393–1400.
(40) Ichikawa, S.; Kimura, S.; Mori, H.; Yoshida, G.; Tajima, H. *Inorg. Chem.* **2006**, *45*, 7575–7577.
(41) Jia, C.; Liu, S.-X.; Ambrus, C.; Neels, A.; Labat, G.; Decurtins, S. *Inorg. Chem.* **2006**, *45*, 3152–3154.
(42) Jia, C.; Zhang, D.; Liu, C.-M.; Xu, W.; Hu, H.; Zhu, D. *New J. Chem.* **2002**, *26*, 490–494.
(43) Lu, W.; Yan, Z.-H.; Dai, J.; Zhang, Z.; Zhu, Q.-Y.; Jia, D.-X.; Guo, W. J. *Eur. J. Inorg. Chem.* **2005**, 2339–2345.
(44) Munakata, M.; Kuroda-Sowa, T.; Maekawa, M.; Hirota, A.; Kitagawa, S. *Inorg. Chem.* **1995**, *34*, 2705–2710.
(45) Olivier, J.; Golhen, S.; Swietlik, R.; Cador, O.; Pointillart, F.; Ouahab, L. *Eur. J. Inorg. Chem.* **2009**, 3282–3290.
(46) Wu, L. P.; Dai, J.; Munakata, M.; Kuroda-Sowa, T.; Maekawa, M.; Suenaga, Y.; Ohno, Y. *Dalton Trans.* **1998**, 3255–3261.
(47) Bellec, N.; Massue, J.; Roisnel, T.; Lorcy, D. *Inorg. Chem. Commun.* **2007**, *10*, 1172–1176.
(48) Massue, J.; Bellec, N.; Chopin, S.; Levillain, E.; Roisnel, T.; Clerac, R.; Lorcy, D. *Inorg. Chem.* **2005**, *44*, 8740–8748.
(49) Xu, C.-H.; Sun, W.; Zhang, C.; Zhou, C.; Fang, C.-J.; Yan, C.-H. *Chem.—Eur. J.* **2009**, *15*, 8717–8721.
(50) Zhu, Q.-Y.; Bian, G.-Q.; Zhang, Y.; Dai, J.; Zhang, D.-Q.; Lu, W. *Inorg. Chim. Acta* **2006**, *359*, 2303–2308.
(51) Gu, J.; Zhu, Q.-Y.; Zhang, Y.; Lu, W.; Niu, G.-Y.; Dai, J. *Inorg. Chem. Commun.* **2008**, *11*, 175–178.
(52) Ebihara, M.; Nomura, M.; Sakai, S.; Kawamura, T. *Inorg. Chim. Acta* **2007**, *360*, 2345–2352.
(53) Zhu, Q.-Y.; Lin, H.-H.; Dai, J.; Bian, G.-Q.; Zhang, Y.; Lu, W. *New J. Chem.* **2006**, *30*, 1140–1144.
(54) Faulkner, S.; Burton-Pye, B. P.; Khan, T.; Martin, L. R.; Wray, S. D.; Skabara, P. J. *Chem. Commun.* **2002**, 1668–1669.
(55) Han, Y.-F.; Li, X.-Y.; Li, J.-K.; Zheng, Z.-B.; Wu, R. T.; Lu, J.-R. *Chinese J. Inorg. Chem.* **2009**, *25*, 1290–1294.
(56) Pointillart, F.; Le Gal, Y.; Golhen, S.; Cador, O.; Ouahab, L. *Chem. Commun.* **2009**, 3777–3779.
(57) Wang, J.-P.; Lu, Z.-J.; Zhu, Q.-Y.; Zhang, Y.-P.; Qin, Y.-R.; Bian, G.-Q.; Dai, J. *Cryst. Growth Des.* **2010**, *10*, 2090–2095.
(58) Férey, G. *Chem. Soc. Rev.* **2008**, *37*, 191–214.
(59) Yaghi, O. M.; O'Keeffe, M.; Ockwig, N. W.; Chae, H. K.; Eddaoudi, M.; Kim, J. *Nature* **2003**, *423*, 705–714.
(60) Kitagawa, S.; Kitaura, R.; Noro, S.-I. *Angew. Chem., Int. Ed.* **2004**, *43*, 2334–2375.
(61) Kepert, C. J. *Chem. Commun.* **2006**, 695–700.
(62) Yoneda, S.; Kawase, T.; Inaba, M.; Yoshida, Z. *J. Org. Chem.* **1978**, *43*, 595–598.
(63) Han, Y.-F.; Li, M.; Wang, T.-W.; Li, Y.-Z.; Shen, Z.; Song, Y.; You, X.-Z. *Inorg. Chem. Commun.* **2008**, *11*, 945–947.
(64) Kepert, C. J.; Hesek, D.; Beer, P. D.; Rosseinsky, M. J. *Angew. Chem., Int. Ed.* **1998**, *37*, 3158–3160.

Table 1. Synthesis Conditions of the MIL-132(K), -133(K, Rb), -134(Cs), and -135(K) Solids

solid	$(TTF\text{-}TC)H_4$ (mmol)	MCl (mmol)	MOH (mmol)	H_2O (mL)	temperature (°C)	current density ($\mu A\ cm^{-2}$)
MIL-132(K)	0.13	0.26	0.2	3	70	0
MIL-133(K)	0.13	0.26	0.1	3	70	0
MIL-133(Rb)	0.13	0.26	1.2	3	100	0
MIL-134(Cs)	0.13	0.26	1.2	3	100	0
MIL-135(K)	0.13	1.70	0.13	15	70	60

is the redox activity of this linker when included in a coordination polymer. Indeed, coordination compounds based on *oxidized* TTF ligands are limited.[31−35,42,45,65−67] This is especially the case for TTF carboxylate derivatives (only one molecular complex reported so far),[56] which are prone to decarboxylation upon oxidation.[68]

Our aim was thus to examine the ability of the $(TTF\text{-}TC)H_4$ linker to act as an organic building block for the preparation of three-dimensional polymers (porous if possible) and to take advantage of its redox activity in the resulting solid. The first part of this study is devoted to the reactivity of the $(TTF\text{-}TC)H_4$ linker with alkaline ions, which are now considered valuable alternatives to transition metal cations for the preparation of coordination polymers.[69−73] Four dense 3-D coordination polymers were produced. In a second part, as these compounds were found to be stable, they were tested as positive electrode materials. Indeed, alkaline-based coordination polymers based on redox active linkers were already shown to be promising alternative electrode materials in lithium-ion batteries.[14−16] Finally, in order to directly prepare coordination polymers based on an oxidized linker, a combined electro-(sub)hydrothermal synthesis was developed. This allows the preparation of a new 3-D solid, which is not based on the neutral TTF-TC however, the oxidized $TTF\text{-}TC^{+\bullet}$ linker, whose electronic conductivity is studied.

Experimental Section

Synthesis. Tetrathiafulvalenetetracarboxylic acid or $(TTF\text{-}TC)H_4$ was prepared in four steps using a synthesis reported by Pittman et al.;[74] slight modifications were made to this procedure, which are given in the Supporting Information. Table 1 summarizes the main characteristics of the optimized synthesis conditions of MIL-132(K), MIL-133(K, Rb), MIL-134(Cs), and MIL-135(K), which are fully described in the Supporting Information.

Characterizations. The Supporting Information contains the details of the different techniques (single-crystal and powder X-ray diffraction, thermal analyses (TGA, thermodiffractometry), infrared spectroscopy, and liquid cyclic voltammetry) used for the characterization of the solids and the measurement of their properties (electronic conductivity and reversible and irreversible electrochemical processes).

Results and Discussion

Synthesis, Structure, and Thermal Behavior of the Non-oxidized Solids. Initial reactions of the tetrathiafulvalenetetracarboxylic acid or $(TTF\text{-}TC)H_4$ with potassium salts focused on variations of temperature and pH. It was noted that temperatures exceeding 100 °C resulted in the decomposition of the linker; however, crystalline materials were observed to form below 100 °C. The temperature was then set to 70 °C, and the pH systemically varied: two phases (later called MIL-132(K) and MIL-133(K); MIL stands for Materials Institut Lavoisier) were identified and isolated (see Figure S1, Supporting Information). The same experimental conditions were then transferred to rubidium and cesium. In each case, only one crystalline phase (MIL-133(Rb) and MIL-134(Cs), respectively) was detected throughout the whole pH and temperature range examined. The structures of the four solids were solved by single-crystal XRD (see the Supporting Information); two (K and Rb-based) are isostructural. The four solids correspond to the general formula $M_2(TTF\text{-}TC)H_2$ (M = K, Rb, Cs), which was further confirmed by chemical analysis. In all cases, two of the four carboxylic acid groups are deprotonated, and the remaining hydroxyl groups are involved in strong intramolecular O−H···O hydrogen bonds (see Table S2, Supporting Information, for distances and angles), while the TTF cores are planar and the C−S and C═C bond distances are in accordance with a neutral oxidation state (Table 2).[75]

For MIL-132(K), which was obtained for a wide range of pH's, two clearly distinguishable sets of K−O distances are observed: five short distances between 2.711(2) and 2.795(2) Å and two long ones (2.925(2) Å and 3.017(2) Å). When only considering the short distances, the potassium environment can be described as square pyramidal. In this case, inorganic chains of edge-sharing $[KO_5]$ polyhedra are defined along [010] (K−K = 3.961(1) Å). Two single chains are linked by the carboxylate functions, which remain bidentate and form dimerized single chains (K−K = 4.415(1) Å), whereas the carboxylic acid groups become monodentate, with C−OH dangling groups (Figure 1). Layers of TTF cores parallel to each other with their long axis perpendicular to the layer develop in the 110 plane with their direction alternating along [001] in a herringbone fashion (Figure S10a, Supporting Information). These layers are reminiscent to the β-type slabs found in molecular conductors[76] but are here built up from uniform 1-D stacks (interplane distance 3.51 Å, shortest S···S distance 3.79 Å) completely isolated from

(65) Avarvari, N.; Fourmigué, M. *Chem. Commun.* **2004**, 1300–1301.
(66) Hervé, K.; Le Gal, Y.; Ouahab, L.; Golhen, S.; Cador, O. *Synth. Met.* **2005**, *153*, 461–464.
(67) Kwon, S.-Y.; Cho, J.-S.; Lee, H.-I.; Lee, U.; Noh, D.-Y. *Inorg. Chim. Acta* **2005**, *8*, 510–512.
(68) Dolbecq, A.; Fourmigué, M.; Batail, P. *Bull. Chem. Soc.* **1996**, *133*, 83–88.
(69) Fromm, K. M. *Coord. Chem. Rev.* **2008**, *252*, 856–885.
(70) Wu, T.; Zhang, J.; Bu, X.; Feng, P. *Chem. Mater.* **2009**, *21*, 3830–3837.
(71) Banerjee, D.; Kim, S. J.; Borkowski, L. A.; Xu, W.; Parise, J. B. *Cryst. Growth Des.* **2010**, *10*, 709–715.
(72) Banerjee, D.; Kim, S. J.; Parise, J. B. *Cryst. Growth Des.* **2009**, *9*, 2500–2503.
(73) Liu, Y.-Y.; Zhang, J.; Xu, F.; Sun, L.-X.; Zhang, T.; You, W.-S.; Zhao, Y.; Zeng, J.; Cao, Z.; Yang, D. *Cryst. Growth Des.* **2008**, *8*, 3127–3129.
(74) Pittman, C. U.; Narita, M.; Liang, Y. F. *J. Org. Chem.* **1976**, *41*, 2855–2860.
(75) Guionneau, P.; Kepert, C. J.; Bravic, G.; Chasseau, D.; Truter, M. R.; Kurmoo, M.; Day, P. *Synth. Met.* **1997**, *86*, 1973–1974.
(76) Mori, T. *Bull. Chem. Soc. Jpn.* **1998**, *71*, 2509–2526.

Table 2. TTF Internal Bond Distances (see Scheme *1* for the definition of a−d) and the Oxidation State of the TTF-TC (Deduced from the Formula) in the Synthesized Solids[a]

solid	*a* (Å)	*b* (Å)	*c* (Å)	*d* (Å)	oxidation state
MIL-132(K)	1.340(5)	1.768(2)	1.747(2)	1.360(3)	0
		1.764(2)	1.752(2)		
MIL-133(K)	1.353(8)	1.756(2)	1.751(3)	1.353(8)	0
MIL-133(Rb)	1.39(2)	1.751(6)	1.750(7)	1.39(1)	0
MIL-134(Cs)	1.37(1)	1.749(4)	1.746(5)	1.35(1)	0
MIL-135(K)	1.401(5)	1.720(3)	1.729(3)	1.359(4)	+1
		1.728(3)	1.734(3)		
$Co(H_2O)_6(TTF\text{-}TC)H_2\cdot 2H_2O$[64]	1.335	1.752	1.745	1.356	0
		1.758	1.748		
$[Co_2(\mu_2\text{-}OH_2)(H_2O)_8][(TTF\text{-}TC)H_2]_2\cdot 2H_2O$[63]	1.344	1.752	1.737	1.350	0
		1.744	1.746	1.334	

[a] For the heaviest cations (Rb, Cs), the large esd's (especially on C=C bonds) mask any clear relation between the bond distances and the oxidation state.

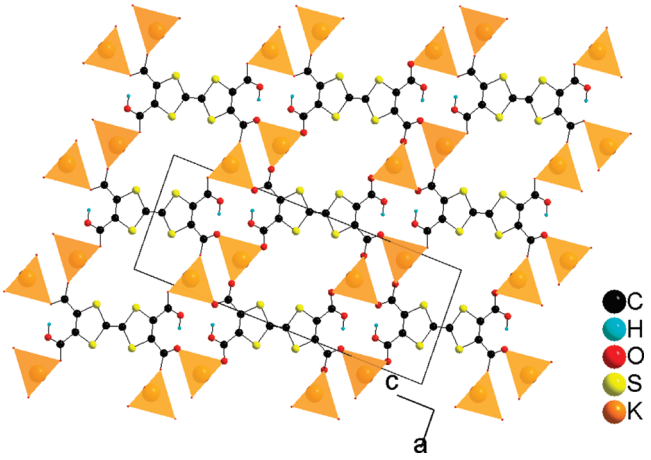

Figure 1. Structure of MIL-132(K), projection down [010].

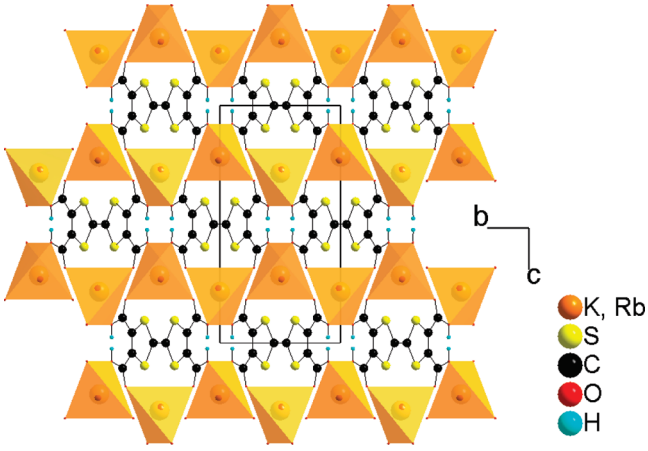

Figure 2. Structure of MIL-133(K, Rb) down [100], which is very similar to the [001] projection of MIL-134(Cs).

each other (shortest interstack S···S distance > 5.8 Å, see Figure S10b).

If one considers the intermediate pH form (final pH around 3, MIL-133(K)), while keeping the same criterion for K−O distances (d < 2.85 Å), four bonds (2.743(2)−2.765(2) Å instead of six when d < 3.25 Å) determine a tetrahedral coordination for K. These tetrahedra are not directly linked to each other, but through $(TTF\text{-}TC)H_2$ linkers defining a 3-D network (Figure 2). Hydrogen atoms are distributed on two sites with 50% occupation. Layers of parallel TTF cores with their long axis parallel to the layer develop in the 110 plane, with an alternating orientation down [001]. Each layer is built up from 1-D staggered stacks of TTFs (interplane distance 3.32 Å, shortest S···S distance 3.96 Å) isolated from each other (shortest interstack S···S contact >6 Å), as shown in Figure S11 (Supporting Information). This finally leads to completely different surroundings of K^+ ions and whole 3-D networks in the two polymorphs. The solid obtained with rubidium is isostructural to MIL-133(K), and longer Rb−O distances (2.879(6)−2.899(6) Å) lead to only a slight increase of the TTF···TTF distance (shortest interplane distance, 3.37 Å; shortest S···S distance, 3.97 Å).

In the case of cesium (MIL-134(Cs)), the compound crystallizes in a different (monoclinic C-centered cell instead of the orthorhombic primitive) but quite similar structure to those of MIL-133(K, Rb). Indeed, almost identical layers of TTFs (interplane distance, 3.33 Å; shortest S···S distance, 3.93 Å) connected through the alkaline cations (Cs−O = 3.086(4)−3.109(5) Å) define the 3-D network (Figure S12, Supporting Information). The structures only differ along the axis of alternation of the organic and inorganic layers (here [010], corresponding to [001] in MIL-133); whereas the direction of the TTFs stacks alternate in MIL-133, it remains unchanged in MIL-134 (Figure 3).

Despite an identical composition ($K_2(TTF\text{-}TC)H_2$), the selective formation of MIL-132 and MIL-133 seems to be driven by the pH; moreover, no thermally induced transition from one polymorph to the other was detected upon heating (see Figure 4). MIL-132(K) has a lower density, and very small 1-D channels (2 × 2.5 $Å^2$ taking into account the van der Waals radii) with sulfur-rich walls running along the K−O−K chain axis are observed (see Figure 1). Nevertheless, no significant adsorption (either nitrogen or hydrogen at 77 K) was measured (see Supporting Information). Attempts to grow the same phase with larger cations (Rb, Cs) in order to increase the size of the pores always led to the formation of a dense phase (MIL-133 and MIL-134, respectively).

The thermal stabilities of the solids were evaluated concomitantly by thermogravimetric analysis (under oxygen) and thermodiffraction (under air). Both techniques indicate that the compounds are stable up to 150−200 °C, whatever the nature of the cation; no mass change and structural transformation are observed below

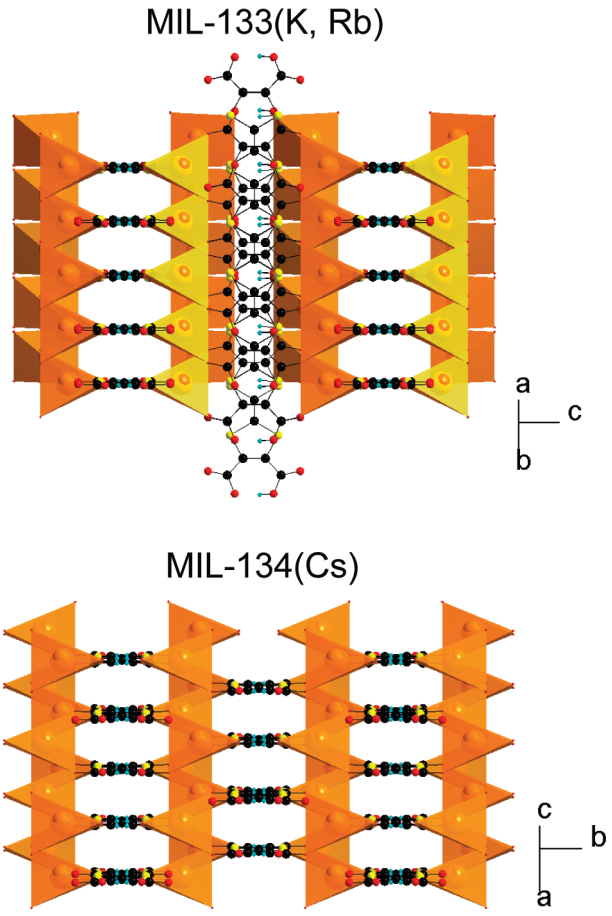

Figure 3. Alternation of inorganic and organic layers in MIL-133(K, Rb) and MIL-134(Cs), illustrating the structural differences between the two solids.

these temperatures (Figure 4). As previously mentioned, no thermally induced structural transition between MIL-132(K) and MIL-133(K) was observed, as can be expected from their largely different crystal structures. Above 200 °C, the solids degrade, eventually yielding crystalline M_2SO_4 (M = K, Rb, Cs), with the associated weight losses in accordance with the proposed formula. The thermal stabilities are slightly lower than the ones usually observed in coordination polymers (typically around 300 °C) and could be related to the destruction of the linker, either through (i) irreversible oxidation (see below) or (ii) thermal decarboxylation.

Redox Behavior. The strong tendency of the TTF cores to pack parallel, as seen in MIL-132/134 or in other coordination polymers,[41] could be used to achieve conductivity upon postsynthetic oxidation. Before considering this, it should be noted that, although the TTF core usually presents two reversible oxidation waves, TTF bearing carboxylic moieties are prone to irreversible decarboxylation upon oxidation,[68] a transformation related to the Kolbe reaction.[77] Nevertheless, a thorough electrochemical study performed on the TTF monocarboxylic acid suggested that the decarboxylation only occurs during the second oxidation step (i.e., the transformation of the radical monocation to the dication, see Scheme 1), whereas the first oxidation step (from the neutral molecule to the radical monocation) is reversible.[78] This was recently confirmed by the preparation of a molecular complex of *oxidized* TTF monocarboxylate.[56] The same trend was observed by Rosseinsky et al. for $(TTF\text{-}TC)H_4$ in water.[64] Cyclic voltammetry performed in DMF (see Figure S6, Supporting Information) led to the same conclusion, with a first reversible process (the width of the half height corresponds to 60 mV)

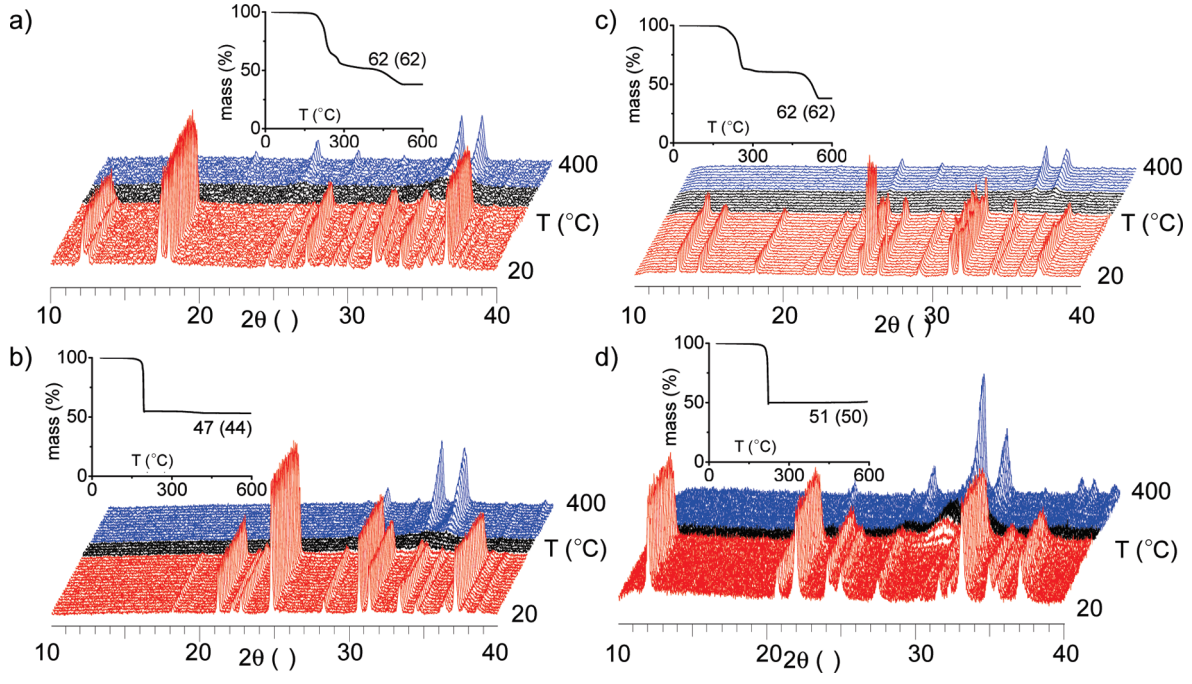

Figure 4. Thermal behavior of the $(TTF\text{-}TC)H_2$-based solids: (a) MIL-132(K), (b) MIL-133-(Rb), (c) MIL-133(K), and (d) MIL-134(Cs). Thermodiffractograms from room temperature to 400 °C: red, as-synthesized solid; black, amorphous intermediate; blue, M_2SO_4; M = K, Rb, Cs (λ(CoKα) = 1.7890 Å). Inset: Thermogravimetric analysis from room temperature to 600 °C; experimental and theoretical (in parentheses) weight losses are also reported.

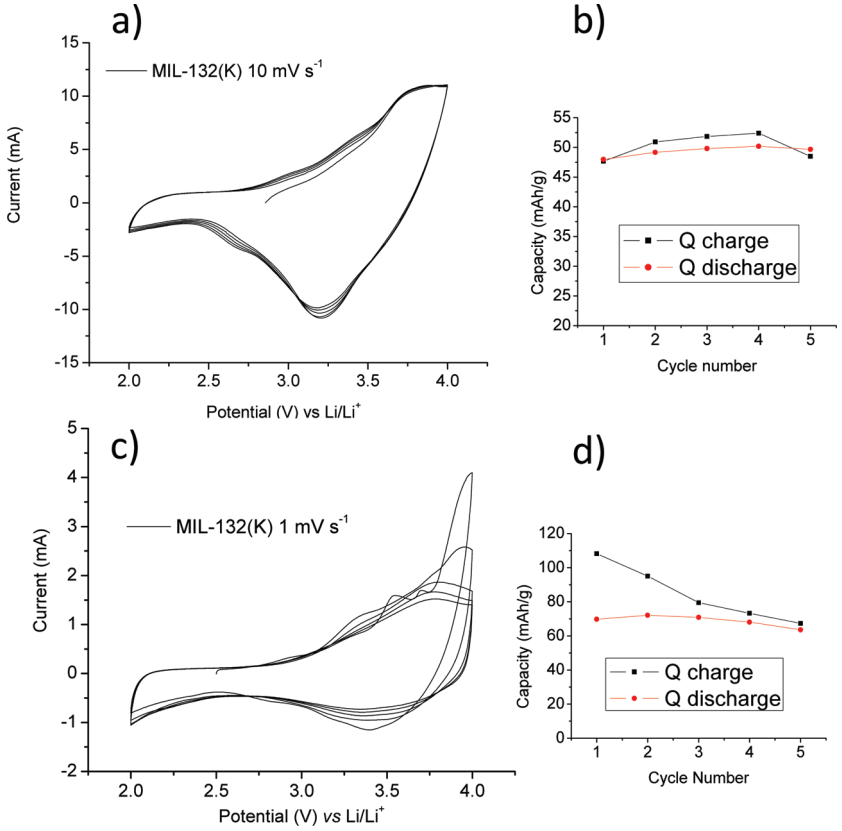

Figure 5. Oxidation behavior of MIL-132(K): (a) solid-state cyclic voltammetry between 2 and 4 V vs Li/Li^+ at 10 mV s^{-1}, (b) charge/discharge capacities upon cycling between 2 and 4 V vs Li at 10 mV s^{-1}, (c) solid-state cyclic voltammetry between 2 and 4 V vs Li at 1 mV s^{-1}, (d) charge/discharge capacities upon cycling between 2 and 4 V vs Li at 1 mV s^{-1}.

followed by a second irreversible oxidation ($E_{1/2}{}^1 = 0.53$ V and $E_{1/2}{}^2 = 0.80$ V vs SCE, respectively).

The direct chemical oxidation of MIL-132(K) and -133(K) was explored initially. Exposure to vapors of iodine or bromine led either to no change (iodine) or to amorphous products (bromine). These results may be explained in terms of relative redox potentials: where iodine is too weak an oxidant to react with $(TTF\text{-}TC)H_2{}^{2-}$, bromine leads to the second, irreversible, oxidation. Electrochemical oxidation, which allows a better control of the redox state, was thus considered. To test the potential applicability of the materials, we investigated the compounds as positive electrode materials in a classical two-electrode Swagelok-type cell using 1 M $LiPF_6$ containing ethylene carbonate/dimethyl carbonate (EC/DMC) electrolyte, in which metallic lithium foil was used as the negative and reference electrode. Prior to the test, the active materials were hand-milled with 30% w/w Ketjen black carbon (as conductive additives) in an agate mortar.

According to solid-state cyclic voltammogram experiments at different voltage sweep rates, all compounds (MIL-132(K), MIL-133(K, Rb), and MIL-134(Cs)) exhibit a similar behavior. Here, only MIL-132(K) will be discussed in detail (see Figure S7, Supporting Information, for the others). Solid-state cyclic voltammetry curves of MIL-132(K) at a 10 mV s^{-1} sweep rate present one highly reversible redox couple (Figure 5a) between 2 and 4 V vs Li/Li^+, with a charge capacity around 50−60 mAh g^{-1} (Figure 5b). The reversible charge/discharge processes could be related to the first oxidation of the TTF core (theoretical capacity of MIL-132(K) is 59 mAh g^{-1} when 1 e^- insertion is concerned). At a lower sweep rate (1 mV s^{-1}), at the same voltage range, an irreversible second oxidation of the TTF core is achieved (Figure 5c; theoretical capacity for MIL-132(K) is 118 mAh g^{-1} when 2 e^- insertion is concerned) but which drastically decreased upon cycling and finally reached the value of the first oxidation of the TTF core (Figure 5d). Note that the same irreversible oxidation wave was observed at the solution-state cyclic voltammogram with the TTF tetracarboxylic acid (Figure S6, Supporting Information).

Galvanostatic charge−discharge experiments were performed in order to explore the maximum Li storage ability with a large number of cycles at different current densities and different voltage ranges. Figure 6a shows the charge−discharge profile of MIL-132(K) with a 10 C rate (which corresponds to the current required to completely charge/discharge an electrode in 6 min) at potential values between 2.3 V and 3.75 V. The curve presents continuous dependence on the potential versus composition that can be assessed to a typical solid solution reaction where reversible 0.6 e^- insertions were clearly observed. Rate performance (Figure 6b) also depicted the highly reversible capacity of MIL-132(K) at both 10 and 2 C. Initially, the cell was cycled at a 10 C rate, and the potential was increased stepwise to 3.8 V where the

(77) See for example: Grimshaw, J. *Electrochemical reactions and mechanisms in organic chemistry*; Elsevier: Amsterdam, The Netherlands, 2000.
(78) Idriss, K. A.; Chambers, J. Q. *J. Electroanal. Chem.* **1980**, *109*, 341–352.

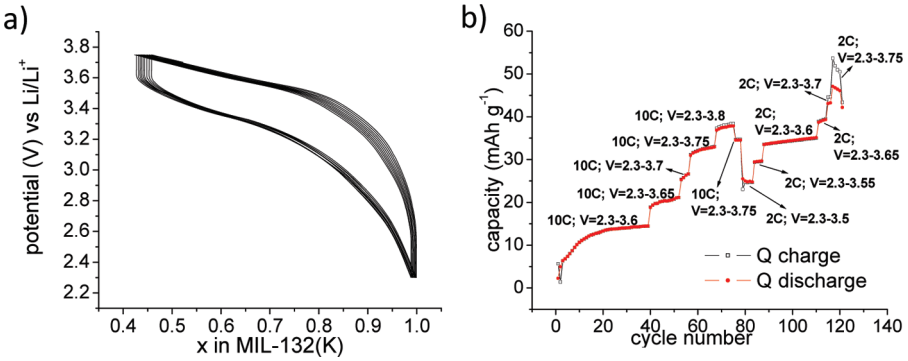

Figure 6. (a) Galvanostatic charge−discharge profile of MIL-132(K) at constant 10 C current density for the voltage range between 2.3 and 3.75 V. (b) Rate performance of MIL-132(K) at both 10 and 2 C with different voltage ranges.

capacity reached 40 mAh g^{-1}. The reversibility is demonstrated by the fact that the capacity is reached again once the potential is lowered to 3.75 V. At a slightly lower C rate (herein 2 C), irreversible capacity loss should not be neglected in the voltage range 2.3−3.7 V, which is presumably due to the decarboxylation of the carboxylic acid groups, as is known to happen during the second oxidation step.

In such a system, oxidation of the molecule backbone requires additional anion insertion (from the electrolyte; PF_6^-) or departure of the cations (from the structure; K^+, Rb^+, or Cs^+) in order to maintain the electroneutrality of the structure. Herein, this phenomenon is still not clear, although the structure turns out to be a completely amorphous phase after charge−discharge processes. Also, a clear structural change is observed when the material (e.g., MIL-132(K)) is contacted with the electrolyte, resulting in a badly crystallized structure (Figure S8, Supporting Information). This phenomenon of an electrolyte effect as well as a better understanding of the role of irreversible capacity loss at low rates (< 2 C) are ongoing studies in our laboratories and will be a subject for another upcoming paper.

However, even considering the unanswered questions surrounding the electrochemical studies, the promising capacities at high-rate performances must be underlined. It is also really important to stress that these new compounds are synthesized in their reduced state (discharge state of a positive electrode). Thus, they are compatible with Li-ion technology since they will provide their electrons during the first charge. Moreover, the average potential, 3.6 V, versus lithium is also comparable or even higher than that of other inorganic compounds (e.g., $LiFePO_4$). Indeed by comparison with the conventional inorganic cathode materials such as $LiFePO_4$ or $LiCoO_2$ (unless further modified), the new TTF based 3D organic frameworks are beneficial electrode materials especially when high-current-regime-required purposes are concerned.

Electrocrystallization. Electrocrystallization is often considered the method of choice for the preparation of crystalline TTF radical salts, allowing both a high purity and a good reproducibility.[79] Nevertheless, as already stated,[30] the use of this technique for the preparation of complexes based on *oxidized* TTF derivatives is rather limited,[33,45,65,66] chemical oxidation being the preferred method.[31,32,34,35,42,56,67] A plausible reason could be the lower stability of the complexes once the TTF-based ligands are oxidized. Indeed, whereas chemical oxidation often allows simultaneous coordination and oxidation processes to occur (for example, using Cu(II) as both a metal and oxidant source[32,34,35,67]), the electrocrystallization is performed on presynthesized complexes[33,65,66] (except in one recent case[45]). Indeed, formation of crystalline products which could require a "high" temperature is usually not accessible using conventional electrocrystallization setups. This problem could be circumvented by the combination of electrocrystallization and solvothermal techniques. Coupled electro-hydrothermal systems were developed, mainly for the preparation of polycrystalline films,[80−89] rods,[90] or single crystals of oxides.[91−93] We used here the same technique for the preparation of crystalline coordination polymers based on *oxidized* linkers. Using an autoclave equipped with two platinum electrodes, we were able to directly transfer the experimental conditions used for the preparation of MIL-132(K) and MIL-133(K) to our galvanostatic electrocrystallization experiments.

Whereas at pH's higher than 3 only a small amount of MIL-132(K) is observed, experiments performed at a low pH (1.5−3) produce a black crystalline solid on the anode (later denoted MIL-135(K)), presenting an XRD powder

(79) Batail, P.; Boubekeur, K.; Fourmigué, M.; Gabriel, J. C. P. *Chem. Mater*. **1998**, *10*, 3005–3015.
(80) Ban, S.; Maruno, S. *J. Biomed. Mater. Res. A* **1998**, *42*, 387–395.
(81) Han, K.-S.; Krtil, P.; Yoshimura, M. *J. Mater. Chem*. **1998**, *9*, 2043–2048.
(82) Kajiyoshi, K.; Sakabe, Y. *J. Am. Ceram. Soc*. **1999**, *82*, 2985–2992.
(83) Kajiyoshi, K.; Yanagisawa, K. *J. Phys.: Condens. Matter* **2004**, *16*, S1351–S1360.
(84) Kajiyoshi, K.; Yanagisawa, K.; Feng, Q.; Yoshimura, M. *J. Mater. Sci*. **2006**, *41*, 1535–1540.
(85) Lee, Y.; Watanabe, T.; Takata, T.; Kondo, J. N.; Hara, M.; Yoshimura, M.; Domen, K. *Chem. Mater*. **2005**, *17*, 2422–2426.
(86) Watanabe, T.; Cho, W.-S.; Suchanek, W. L.; Endo, M.; Ikuma, Y.; Yoshimura, M. *Solid State Sci*. **2001**, *3*(1−2), 183–188.
(87) Yoshimura, M.; Suchanek, W. *Solid State Ionics* **1997**, *98*, 197-208.
(88) Yoshimura, M.; Suchanek, W.; Han, K.-S. *J. Mater. Chem*. **1999**, *9*, 77–82.
(89) Yoshimura, M.; Urushihara, W.; Yashima, M.; Kakihana, M. *Intermetallics* **1995**, *3*, 125–128.
(90) Park, S. K.; Park, J. H.; Ko, K. Y.; Yoon, S.; Chu, K. S.; Kim, W.; Do, Y. R. *Crys. Growth Des*. **2009**, *9*, 3615–3620.
(91) Liu, L.; Wang, X.; Bontchev, R.; Ross, K.; Jacobson, A. J. *J. Mater. Chem*. **1999**, *9*, 1585–1589.
(92) Wang, X.; Liu, L.; Bontchev, R.; Jacobson, A. J. *Chem. Commun*. **1998**, 1009–1010.
(93) Wang, X.; Liu, L.; Jacobson, A. J.; Ross, K. *J. Mater. Chem*. **1999**, *9*, 859–861.

pattern different from those of both MIL-132(K) and MIL-133(K) (see Figure S3, Supporting Information). The optimization of the experimental parameters (pH and current density, see Figure S2, Supporting Information) afforded a solid suitable for single-crystal analysis. One can note that this optimized current density is higher (about 10 times) than the one usually used for the preparation of TTF-based molecular materials at ambient temperature, which could be related to the higher solubility and diffusion rate of the precursors at high temperatures (here, 70 °C).

The structural resolution reveals a 1:1 TTF-TC/K stoichiometry. The linker adopts the diprotonated state previously observed in the other solids ((TTF-TC)H_2), including the formation of strong intramolecular O−H···O hydrogen bonds (see Table S2, Supporting Information). When compared with MIL-132(K) and MIL-133(K), the internal C−S and C=C bond distances respectively decrease and increase, as expected from the shape of the HOMO when oxidation of the TTF core occurs (see Table 2 and Scheme 1).[75] The solid could thus be formulated K(TTF-TC$^{+\bullet}$)H_2. The TTF-TC core is shown to be oxidized, but not decarboxylated, as anticipated from cyclic voltammetry measurements.

If one takes into account the same criterion for K−O distances as the one used to describe MIL-132(K) and MIL-133(K), the potassium cations appear to be six-coordinated (K−O = 2.707(2)−2.823(2) Å) in a slightly distorted octahedral environment. They are not directly connected to each other but through bridging carboxylate groups down [100] to define chains. These chains arrange in layers in the 001 plane, alternating down [001] with organic slabs (Figure 7) to finally define a 3-D coordinated network.

The organic layers of (TTF-TC)H_2 are once again reminiscent of the β-type topology found in molecular conductors, i.e., built up from *uniform* 1-D stacks of TTF (interplane distance, 3.45 Å; shortest S···S distance, 3.66 Å) closer to each other (shortest interstack S···S contact is 3.76 Å along [010]) than in MIL-132(K) (see Figure 9a and b). Nevertheless, if one compares the arrangement of the oxidized TTF in MIL-135(K) and in typical molecular conductors, some differences emerge. Whereas the packing of the TTF cores is mainly driven by the optimization of the HOMO−HOMO overlap in molecular conductors (and in some cases additional supramolecular interactions such as hydrogen bonds),[94] the intrinsic rigidity afforded by the coordination of the inorganic cation constrains, at least partially, the packing of the TTF cores. Indeed, although fully oxidized TTFs (+1 oxidation state) usually tend to form an eclipsed dyad to maximize the HOMO−HOMO overlap,[95] the packing observed in MIL-135(K) corresponds only to a poor overlap (see Figures 9b and Figure S13, Supporting Information).

The thermal behavior of MIL-135(K) was investigated using the same conditions as those used for the solids based on the nonoxidized (TTF-TC)H_2 linker. This solid

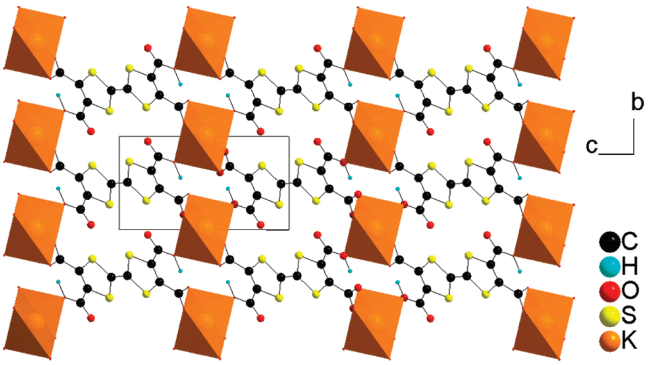

Figure 7. Structure of K(TTF-TC$^{+\bullet}$)H_2 or MIL-135(K), projection down [100].

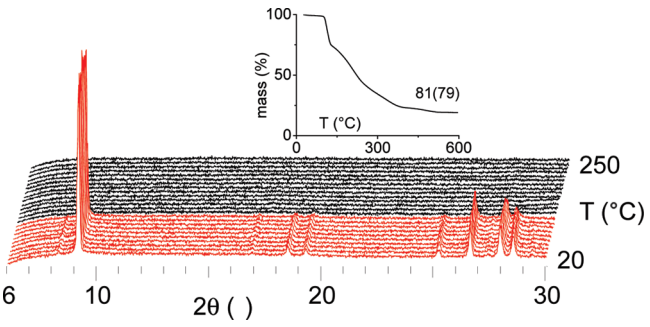

Figure 8. Thermal behavior of MIL-135(K). Thermodiffractogram from room temperature to 250 °C: red, as-synthesized solid; black, amorphous intermediate (λ(CoKα) = 1.7890 Å). Inset: Thermogravimetric analysis from room temperature to 600 °C; experimental and theoretical (in parentheses) weight losses are also reported.

is rigid and stable up to about 100 °C and is thermally destroyed above this temperature to give K_2SO_4 (Figure 8), with a weight loss in agreement with the proposed formula. Compared to MIL-132(K) and MIL-133(K), MIL-135(K) thus presents a lower thermal stability, which is probably related to the higher reactivity of the oxidized TTF-TC$^{+\bullet}$ core.

Finally, the electronic conductivity of a single crystal of MIL-135(K) was investigated from room temperature to 180 K and is shown in Figure 9c. The solid exhibits a semiconducting behavior with a rather low room-temperature conductivity ($\sigma_{RT} \sim 1$ mS cm^{-1}) in comparison with molecular TTF-based materials and an activation energy of 2400 K (0.22 eV). This result is not completely unexpected considering the oxidation state of the TTF core (+1) and the bad TTF···TTF overlap, which prevent an efficient electronic delocalization along the stacks of TTF molecules (see Figures 9a and b).

Conclusion

The use of (TTF-TC)H_4 as an organic building block for the preparation of 3-D coordination polymers was investigated. Although this linker appears less stable than the commonly used hydrocarbonated polycarboxylates, the synthesis of coordination polymers is achievable, providing that some precautions are taken into account, mainly in terms of temperature and pH of the reaction mixture. The reaction of (TTF-TC)H_4 with alkaline ions indeed led to four 3-D solids formulated M_2(TTF-TC)H_2 (M = K, Rb, Cs)

(94) Fourmigué, M.; Batail, P. *Chem. Rev.* **2004**, *104*, 5379–5418.
(95) Devic, T.; Domercq, B.; Auban-Senzier, P.; Molinié, P.; Fourmigué, M. *Eur. J. Inorg. Chem.* **2002**, 2844–2849.

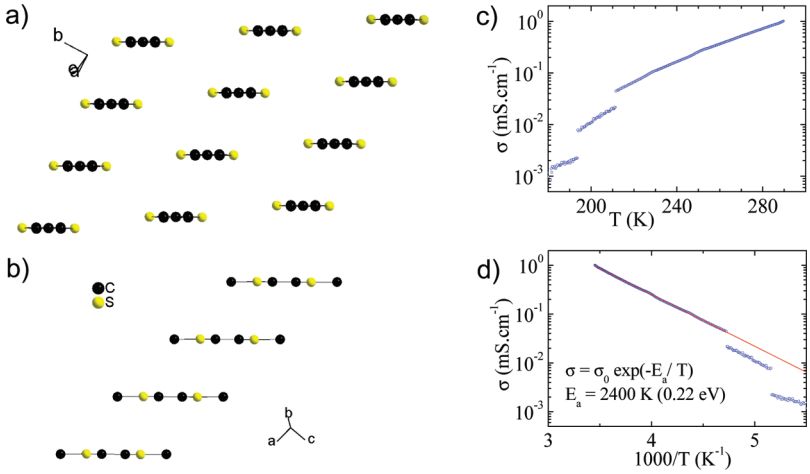

Figure 9. Left: Organic part in MIL-135(K): (a) View or the organic slab along the long axis of the TTFs molecules, reminiscent of a β layer in the 110 plane; (b) view of the uniform 1-D stack along the short axis of the TTF molecules (carboxylate groups are omitted for clarity). Right: (c) temperature dependence of the electronic conductivity of MIL-135(K); (d) fit of the data to a law of the type $\sigma = \sigma_0 \exp(-E_a/T)$.

crystallizing in three different structure types. All the solids demonstrated a reasonable thermal stability in the air but no permanent porosity. They were shown to act as positive electrode materials in lithium batteries exhibiting good cyclabilities. Although the capacities are still moderate with regard to fulfilling lithium batteries market requirements, the TTF-based redox-active compounds are promising potential materials, especially at high current densities. Finally, the direct synthesis of coordination polymers based on the *oxidized* TTF-TC was investigated using a combined electrocrystallization−(sub)hydrothermal approach. This technique allows the preparation of a new compound formulated $K(TTF\text{-}TC^{+\bullet})H_2$ in which the TTF core is oxidized while maintaining its molecular integrity. This dense solid exhibits a semiconducting behavior. Further work will mainly be driven by the use of transition metals in place of alkaline ions and the development of the combined electrocrystallization−hydrothermal approach in the prospect of producing truly conductive, multifunctional, porous coordination polymers.

Acknowledgment. The authors acknowledge the MENRT and the ANR for financial support (Ph.D. grant for T.L.A. N. and project "CONDMOFs", respectively), the ESRF for providing access to the beamline BM01A, Dr. N. Avarvari for providing some organic precursors, Dr. S. Miller for his help in hydrogen sorption experiments, and Pr. C. Pasquier for fruitful discussions.

Supporting Information Available: Full synthetic procedures, characterization, and complete XRD data (experimental details, structural description, cif files). This material is available free of charge via the Internet at http://pubs.acs.org.

5 Zusammenfassung

In der vorliegenden Arbeit wurden poröse, aluminiumhaltige Metall-organische Gerüstverbindungen unter solvothermalen Bedingungen dargestellt und charakterisiert (Tab. 5.1). Unter Einsatz der Hochdurchsatztechnik wurde eine Vielzahl neuer und isoretikulärer Al-MOFs synthetisiert sowie der Einfluss chemischer und physikalischer Reaktionsparameter auf deren Bildung systematisch untersucht. Für die Charakterisierung der Verbindungen konnten in den Poren vorliegende, nicht umgesetzte Reaktanden durch individuelle Aktivierungsprozeduren zerstörungsfrei und unter Erhalt der Kristallinität aus dem Gerüst entfernt werden.

Durch die umfassende Charakterisierung der Verbindungen konnten Informationen über deren Zusammensetzung, Porosität und thermische Stabilität erhalten werden. Diese Erkenntnisse ermöglichten zudem, die chemische Zusammensetzung und die Partikelgrößen von CAU-1 ($[Al_4(OH)_{2+z}(OCH_3)_{4-z}(BDC\text{-}NH_{2-y}(CH_3)_y)_3]\cdot xH_2O$ mit $z \leq 4$ und $y = \leq 2$), eines hochporösen Al-MOF, in situ sowie durch postsynthetische Modifizierung gezielt einzustellen. Im Rahmen dieser Untersuchungen wurde zudem der Einfluss der Heizmethode auf die Produktbildung mit Hilfe der in situ-EDXRD-Methode untersucht. Für diese Messungen ist erstmalig ein kommerziell erhältlicher MW-Reaktor in einen Synchrotronstrahlengang implementiert worden.

Tab. 5.1 Liste der in dieser Arbeit hergestellten Verbindungen.

Nr.	Verbindung	CCDC Nummer	
1	$[Al(OH)(BDC\text{-}NH_2)]\cdot 0.9H_2O$, (**Al-MIL-53-$NH_2$ (lt)**)	-	Ind., Charak.
2	$[Al(OH)(BDC\text{-}NHCHO)]\cdot H_2O$, (**Al-MIL-53-NHCHO**)	-	Ind., Charak.
3	$[Al(OH)(BDC\text{-}NO_2)]\cdot 0.6H_2O$, (**Al-MIL-53-$NO_2$ (lt)**)	-	Ind., Charak.
4	$[Al(OH)(BDC\text{-}(OH)_2)]\cdot H_2O$, (**Al-MIL-53-$(OH)_2$ (lt)**)	-	Ind., Charak.
5	$[Al_{1-y}/Cr_y(OH)(BDC)]\cdot xH_2BDC$ (y < 0.1), (**Al/Cr-MIL-53 (as)**)	-	Ind., EDX
6	$[Al_4(OH)_2(OCH_3)_4(BDC\text{-}NH_{2-y}(CH_3)_y)_3]\cdot xH_2O$ (y < 0.5), (**CAU-1**)	723320	PD
7	$[Al_4(OH)_2(OCH_3)_4(BDC\text{-}NH_2)_3]\cdot xH_2O$, (**CAU-1-$NH_2$**)	**-**	Ind., Charak.
8	$[Al_4(OH)_2(OCH_3)_4(BDC\text{-}NHCOCH_3)_3]\cdot xH_2O$, (**CAU-1-$NHCOCH_3$**)	**-**	Ind., Charak.
9	$[Al_4(OH)_2(OCH_3)_4(BDC\text{-}NHCH_3)_3]\cdot xH_2O$, (**CAU-1-$NHCH_3$**)	**-**	Ind., Charak.
10	$[Al_4(OH)_6(BDC\text{-}NH_2)_3]\cdot xH_2O$, (**CAU-1-$NH_2$(OH)**)	**-**	Ind., Charak.
11	$[Al_4(OH)_2(OCH_3)_4(BDC\text{-}(OH)_2)_3]\cdot xH_2O$, (**CAU-1-$(OH)_2$**)	**-**	Ind., Charak.
12	$[Al_2(OCH_3)_4(NDC)]\cdot xH_2O$, (**CAU-3-NDC**)	**-**	Ind., Charak.

PD: Strukturlösung aus Synchrotronpulverdaten; Ind.: Pulverdiffraktogramm konnte indiziert werden; Charakterisierung: Zusammensetzung wurde mittels IR-Spektroskopie, Thermogravemetrie und Elementaranalyse bestimmt.

1. Übersicht zur Darstellung, Modifizierung und Charakterisierung aluminiumhaltiger MIL-53-Verbindungen auf der Basis von Terephthalsäurederivaten

Auf der Basis funktionalisierter Terephthalsäurederivate (H_2BDC-X mit X= -NH_2, -NO_2, -$(OH)_2$) und verschiedener Aluminiumquellen ($AlCl_3 \cdot 6H_2O$, $Al(NO_3)_3 \cdot 9H_2O$, $Al(ClO_4)_3 \cdot 9H_2O$) konnten isoretikuläre Verbindungen des porösen Netzwerks MIL-53 erhalten werden. Die Synthesen dieser Verbindungen wurden so optimiert, dass phasenreine Produkte im Gramm-Maßstab erhalten werden konnten. Die Synthesebedingungen konnten dabei nicht 1:1 übertragen werden. Mögliche Ursachen hierfür stellen die unterschiedliche Acidität, thermische Stabilität und Löslichkeit der verwendeten Terephthalsäurederivate dar. Die aminofunktionalisierte Al-MIL-53-NH_2-Verbindung konnte durch eine postsynthetische Formylierung der Aminogruppen mit Ameisensäure chemisch modifiziert werden.

Die Struktur von Al-MIL-53 enthält Ketten eckenverknüpfter AlO_6-Oktaeder, die über Terephthalateinheiten zu einem flexiblen, dreidimensionalen Netzwerk miteinander verbunden sind. Das Netzwerk weist eindimensionale Kanäle auf, deren Durchmesser je nach Funktionalisierung und den in den Kanälen eingelagerten, Molekülen variiert. Die funktionellen Gruppen (-NH_2, -NO_2, -$(OH)_2$, -NHCHO) haben außerdem einen großen Einfluss auf die Flexibilität des Netzwerks und dessen Sorptionseigenschaften.

Die Flexibilität des Gerüstes von Al-MIL-53 wurde mittels ESR-Spektroskopie in Abhängigkeit von der Temperatur genauer untersucht. Für diese Untersuchung musste Al-MIL-53 mit Cr(III)-Ionen dotiert werden, um paramagnetische Zentren in der Verbindung zu erzeugen. Hierfür wurden der Reaktionsmischung kleine Mengen von $Cr(NO_3)_3 \cdot 9H_2O$ beigemengt.

2. $[Al(OH)(BDC\text{-}NH_2)]\cdot 0.9H_2O$

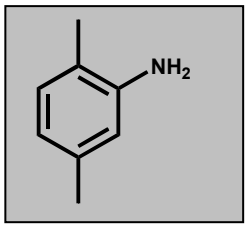

Ausgehend von 2-Aminoterephthalsäure ($H_2BDC\text{-}NH_2$) und $AlCl_3\cdot 6H_2O$ wurde $[Al(OH)(BDC\text{-}NH_2)]\cdot 0.3H_2BDC\text{-}NH_2$ (Al-MIL-53-NH_2 (as)) unter hydrothermalen Bedingungen dargestellt. Die in den Poren eingelagerten freien Aminoterephthalsäuremoleküle wurden durch thermische Behandlung in DMF bei 150 °C unter Bildung von $[Al(OH)(BDC\text{-}NH_2)]\cdot 0.95DMF$ (Al-MIL-53-NH_2 (DMF)) gegen DMF-Moleküle ausgetauscht. Im Anschluss konnten die DMF-Moleküle an Luft bei einer Temperatur von 130 °C vollständig aus dem Gerüst entfernt werden. Während des Abkühlprozesses wurden Wassermoleküle aus der Luft adsorbiert und die hydratisierte Form Al-MIL-53-NH_2 (lt) ($[Al(OH)(BDC\text{-}NH_2)]\cdot 0.9H_2O$) gebildet. Die Gitterparameter von Al-MIL-53-NH_2 (lt) sowie aller anfallenden Zwischenprodukte wurden durch Indizierung der Röntgenpulverdiffraktogramme bestimmt. Die Zusammensetzungen der jeweiligen Verbindungen konnten mithilfe von IR-Spektroskopie, Thermogravimetrie, Elementaranalyse und Festkörper-NMR-Spektroskopie ermittelt werden. Die Porosität von Al-MIL-53-NH_2 wurde durch N_2-Sorptionsexperimente nachgewiesen.

3. $[Al(OH)(BDC\text{-}NHCHO)]\cdot H_2O$

Die Verbindung $[Al(OH)(BDC\text{-}NHCHO)]\cdot H_2O$ (Al-MIL-53-NHCHO) konnte durch die postsynthetische Modifizierung von $[Al(OH)(BDC\text{-}NH_2)]\cdot 0.9H_2O$ mit Ameisensäure bei einer Reaktionstemperatur von 70 °C erhalten werden (Abb. 5.1).

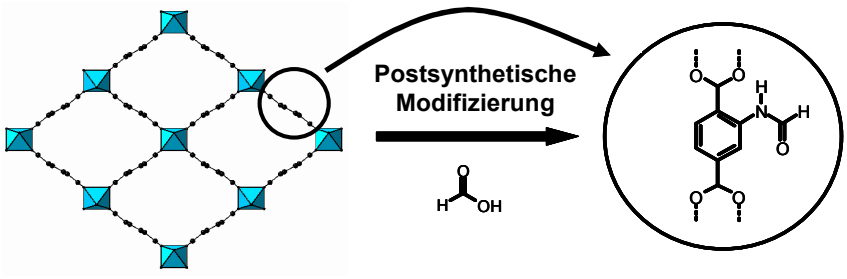

Abb. 5.1 Schematische Darstellung der postsynthetischen Modifizierung von MIL-53-NH_2 mit Ameisensäure.

Mit Hilfe von ^{13}C- und ^{15}N-MAS-NMR-Spektroskopie wurde ein Formylierungsgrad von > 80% der Aminogruppen nachgewiesen. Die Verbindung wurde des Weiteren

mit IR-Spektroskopie, Thermogravimetrie und Elementaranalyse charakterisiert. Die Bestimmung der Gitterparameter erfolgte durch Indizierung des Röntgenpulverdiffraktogramms.

4. $[Al(OH)(BDC\text{-}NO_2)]\cdot 0.6H_2O$

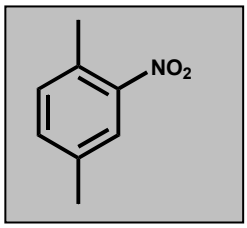

Die nitrofunktionalisierte Al-MIL-53 Verbindung wurde unter hydrothermalen Bedingungen durch Umsetzung von 2-Nitroterephthalsäure ($H_2BDC\text{-}NO_2$) mit $Al(NO_3)_3\cdot 9H_2O$ bei 170 °C erhalten. Das Rohprodukt wurde zweimal thermisch bei 80 °C im großen Überschuss mit Methanol behandelt, um in den Poren eingelagerte Nitroterephthalsäuremoleküle auszutauschen. Im Anschluss konnte bei einer Temperatur von 150 °C das in den Kanälen eingelagerte Methanol vollständig aus dem Gerüst entfernt werden. Nach dem Abkühlen der Substanz an der Luft wurde die Verbindung $[Al(OH)(BDC\text{-}NO_2)]\cdot 0.6H_2O$ (Al-MIL-53-NO_2 (lt)) erhalten. Die Gitterparameter von Al-MIL-53-NO_2 (lt) wurden durch Indizierung des Röntgenpulverdiffraktogramms bestimmt. Die Zusammensetzung konnte mittels IR-Spektroskopie, Thermogravimetrie und Elementaranalyse ermittelt werden.

5. $[Al(OH)(BDC\text{-}(OH)_2)]\cdot H_2O$

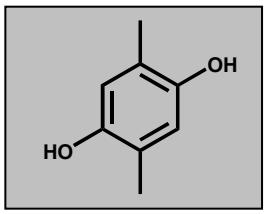

Die Umsetzung von 2,5-Dihydroxyterephthalsäure ($H_2BDC\text{-}(OH)_2$) mit $Al(ClO_4)_3\cdot 9H_2O$ in DEF bei 125 °C führte zu dem hydroxyfunktionalisierten MOF $[Al(OH)(BDC\text{-}(OH)_2)]\cdot x$DEF (Al-MIL-53-$(OH)_2$ (as)). In einem Methanol/Wasser-Gemisch wurden die in den Poren des Rohproduktes eingelagerten DEF-Moleküle bei 100 °C vollständig gegen Wassermoleküle ausgetauscht. Dabei wurde die wasserreiche, offenporige Form von Al-MIL-53-$(OH)_2$ erhalten ($[Al(OH)(BDC\text{-}(OH)_2)]\cdot xH_2O$ mit x~5-6). Diese wandelt sich an Luft (langsam) bzw. durch thermische Behandlung (schnell) in die Al-MIL-53-OH_2 (lt)-Form ($[Al(OH)(BDC\text{-}(OH)_2)]\cdot H_2O$) um, welche geschlossene Poren aufweist. Die chemische Zusammensetzung von Al-MIL-53-$(OH)_2$ (lt) wurde mittels IR-Spektroskopie, Thermogravimetrie und Elementaranalyse ermittelt. Die Gitterparameter von Al-MIL-53-$(OH)_2$ (as) und Al-MIL-53-OH_2 (lt) wurden durch die Indizierung der Pulverdiffraktogramme bestimmt.

6. $[Al_{1-y}/Cr_y(OH)(BDC)]\cdot xH_2BDC$ (y < 0.1)

Zur Darstellung von $[Al_{1-y}/Cr_y(OH)(BDC)]\cdot xH_2BDC$ (y < 0.1) (Al/Cr-MIL-53 (as)) wurden Terephthalsäure und $Al(NO_3)_3\cdot 9H_2O$ mit kleinen Mengen $Cr(NO_3)_3\cdot 9H_2O$ hydrothermal bei einer Temperatur von 210 °C umgesetzt. Das Produkt wurde mittels Röntgenpulverdiffraktometrie untersucht, wobei eine geringe Verunreinigung der Probe mit γ-AlOOH festgestellt wurde. Zur Entfernung der in den Kanälen eingelagerten freien Terephthalsäuremoleküle wurde Al/Cr-MIL-53 (as) bei 430 °C an der Luft kalziniert und dabei Al/Cr-MIL-53(Al/Cr)deh ($[Al_{1-y}/Cr_y(OH)(BDC)]$ (y < 0.1)) erhalten.

7. Gerüstflexibilität der Al-MIL-53-X Verbindungen

Die Gerüstflexibilität der funktionalisierten Al-MIL-53-X-Verbindungen wurde mittels TD-XRPD-Messungen in Glaskapillaren untersucht. Für die Verbindungen Al-MIL-53-NO_2, Al-MIL-53-CH_3, Al-MIL-53-Br und Al-MIL-53-Cl konnte ein Übergang von der geschlossen- in die offenporige Form beobachtet werden. Die Temperatur, ab der der Phasenübergang einsetzt, sowie dessen Geschwindigkeit unterscheidet sich je nach Verbindung stark. In Abbildung 5.2 sind die Ergebnisse der TD-XRPD-Untersuchungen graphisch zusammengefasst.

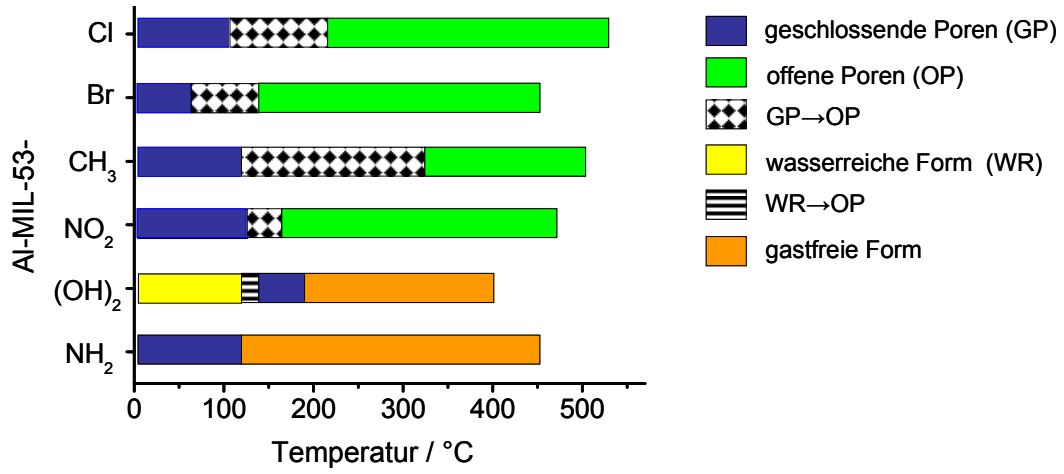

Abb. 5.2 Zusammenfassung der Ergebnisse der TD-XRPD Messungen aller im Rahmen dieser Arbeit untersuchten Al-MIL-53-X-Verbindungen.

Für Al-MIL-53-NO_2 erstreckt sich der Phasenübergang von der geschlossen- in die offenporige Form über einen Temperaturbereich von 130–160°C. Im Vergleich zu Al-

MIL-53-CH_3, Al-MIL-53-Br und Al-MIL-53-Cl verläuft dieser Phasenübergang mit einer deutlich höheren Geschwindigkeit. Für die Verbindungen Al-MIL-53-$(OH)_2$ und Al-MIL-53-NH_2 konnte durch eine rein thermische Behandlung kein Übergang in die offenporige Form beobachtet werden.

8. Sorptionseigenschaften der Al-MIL-53-X-Verbindungen

Die Sorptionseigenschaften der Al-MIL-53-X-Verbindungen wurden mittels Sorptionsexperimenten mit den Messgasen N_2, CO_2 und H_2O untersucht. In Abbildung 5.3 sind die Ergebnisse für Al-MIL-53-NH_2, Al-MIL-53-NO_2 und Al-MIL-53-$(OH)_2$ gezeigt. Die Menge an adsorbiertem Gas hängt dabei, je nach Probe und Messbedingungen, unter anderen von folgenden Faktoren ab:

1. Wechselwirkungen der funktionellen Gruppen mit dem Adsorbat
2. Flexibilität des Gerüstes
3. kinetischer Durchmesser des Messgases

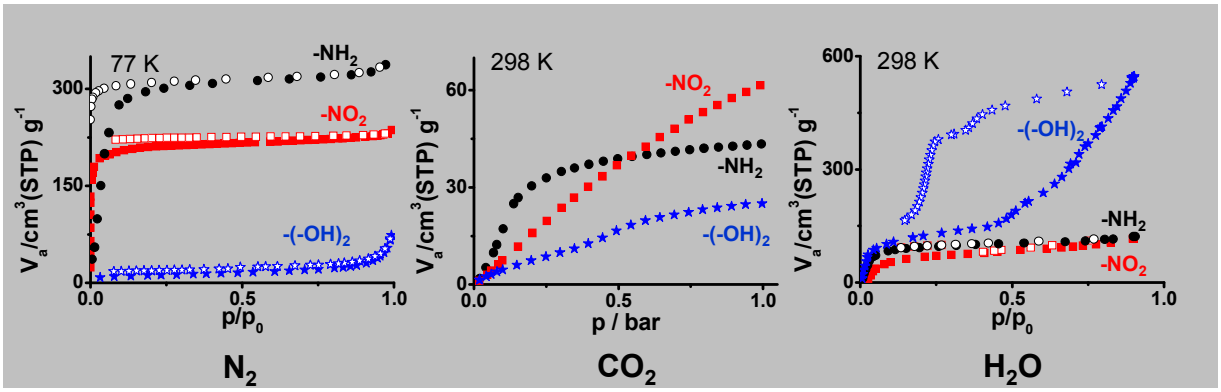

Abb. 5.3 N_2 (links), CO_2 (Mitte), und H_2O (rechts) Sorptionsexperimente von Al-MIL-53-NH_2 (schwarz), Al-MIL-53-NO_2 (rot), und Al-MIL-53-$(OH)_2$ (blau).

9. Übersicht zur Darstellung, Charakterisierung und Modifizierung von CAU-1 und CAU-3

Zu Beginn der Doktorarbeit wurde unter Einsatz der Hochdurchsatzmethode der Einfluss des Lösemittels und der Aluminiumquelle auf die Produktbildung aluminiumhaltiger MOFs untersucht. Die Verwendung der Lösemittel Methanol und DMF ermöglichte das Auffinden neuer Verbindungen. In DMF wurden unter Verwendung von Aminoterephthalsäure die aluminiumhaltigen Verbindungen Al-MIL-53-NH_2 und Al-MIL-101-NH_2 erhalten. Eine sehr geringe Konzentration der Reaktionsmischungen sowie der Einsatz von $AlCl_3 \cdot 6H_2O$ begünstigte die Bildung von Al-MIL-101-NH_2. Bei der Verwendung von Methanol als Lösemittel führte die Variation der Konzentration der Reaktanden und des pH-Wertes zu den Verbindungen CAU-1 ($[Al_4(OH)_2(OCH_3)_4(BDC\text{-}NH_{2\text{-}y}(CH_3)_y)_3] \cdot xH_2O$ mit $y = \leq 2$) und CAU-3 ($[Al_2(OCH_3)_4(NDC)] \cdot xH_2O$). Die Wahl der Aluminiumquelle war dabei ebenfalls von entscheidender Bedeutung. Die zwölffach verknüpften Netzwerke von CAU-1 und CAU-3 enthalten neue anorganische Baueinheiten (CAU-1: $\{Al_8(OH)_4(OCH_3)_8)^{12+}\}$; CAU-3: $\{Al_{12}(OCH_3)_{24})^{12+}\}$), bei denen das Lösemittel in Form von Methoxygruppen in das Gerüst eingebaut ist. Die Verwendung größerer oder zusätzlich funktionalisierter Linkermoleküle ermöglichte die Darstellung der isoretikuläreren Verbindungen CAU-3-NDC und CAU-1-$(OH)_2$.

Die Verbindung CAU-1 wurde mittels Röntgenpulverbeugung, NMR- und IR-Spektroskopie, Elementaranalyse, Thermogravimetrie, dynamischer Lichtstreuung und Sorptionsexperimenten im Detail charakterisiert. Die Auswertung der gesammelten Daten zeigte, dass die chemische Zusammensetzung von CAU-1 gezielt in situ sowie post-synthetisch modifiziert werden konnte. Die Aminogruppen der organischen Baueinheit konnten zum einen direkt durch Variation der Reaktionszeit und Reaktionstemperatur schrittweise methyliert und zum anderen nachträglich chemisch mit Essigsäureanhydrid zu Acetamidgruppen umgesetzt werden. Des Weiteren konnten durch eine thermische Behandlung an Luft die Methoxygruppen kontrolliert aus der anorganischen Baueinheit entfernt und gegen Hydroxygruppen ausgetauscht werden. Der Einsatz der in situ-EDXRD-Methode ermöglichte zudem, den Einfluss der Heizmethode auf die Produktbildung von CAU-1 zu untersuchen sowie dessen Partikelgrößen in einem Bereich von 100–500 nm einzustellen.

10. Struktur von CAU-1 und CAU-3

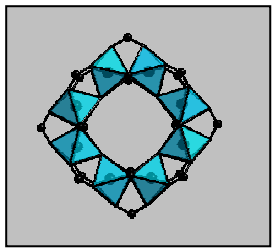

CAU-1 ist aus verzerrten AlO_6-Oktaedern aufgebaut, welche kanten- bzw. eckenverknüpft oktamere Baueinheiten $\{Al_8(OH)_4(OCH_3)_8)^{12+}\}$ ausbilden. Die Oktamere werden über zwölf Aminoterephthalationen mit zwölf weiteren Oktameren zu einem dreidimensionalen Netzwerk verknüpft. Die Anordnung der Oktamere in der Struktur von CAU-1 lässt sich von einem kubisch innenzentrierten Gitter ableiten und führt zu Bildung tetraedrischer und oktaedrischer Hohlräume. Diese Holräume besitzen einen effektiven zugänglichen Durchmesser von 4.5 Å beziehungsweise 10 Å.

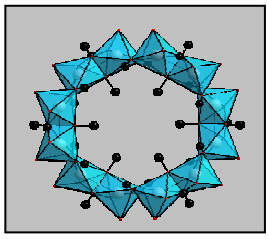

Das Gerüst von **CAU-3-NDC** ist aus zwölfkernigen $\{Al_{12}(OCH_3)_{24})^{12+}\}$ Clustern aufgebaut, die aus kantenverknüpften AlO_6-Oktaedern zusammengesetzt sind. Die Kantenverknüpfung der AlO_6-Oktaeder erfolgt über die Sauerstoffatome der Methoxygruppen. In einer verzerrten pseudo-kubisch innenzentrierten Anordnung der Cluster ist ein Cluster mit jeweils zwölf weiteren Clustern über Naphthalindicarboxylateinheiten zu einem dreidimensionalen Netzwerk verknüpft. Das Netzwerk weist verzerrte tetraedrische und oktaedrische Hohlräume mit Durchmessern von ~14 und ~15 Å auf.

In der Tabelle 5.2 sind die Gitterparameter von CAU-1-NH_2 und CAU-3-NDC angegeben.

Tab. 5.2 Gitterparameter der CAU-1-Derivate und CAU-3-NDC

Al-MOF	Kristallsystem	a / Å	b / Å	c / Å	V / Å^3
CAU-1-NH_2	tetragonal	18.319(4)	18.319(4)	17.753(7)	5958(1)
CAU-1-$NHCH_3$	tetragonal	18.331(5)	18.331(5)	17.739(7)	5961(2)
CAU-1-$NHCOCH_3$	tetragonal	18.341(5)	18.341(5)	17.735(4)	5966(1)
CAU-1-NH_2(OH)	tetragonal	18.330(6)	18.330(6)	17.761(7)	5968(1)
CAU-1-$(OH)_2$	tetragonal	18.320(5)	18.320(5)	17.711(6)	5945(1)
CAU-3-NDC	romboedrisch	23.205(1)	23.205(1)	40.635(1)	18950(3)

11. Synthese und Aktivierung

Der Einfluss der Synthese- und Aktivierungsbedingung auf die chemische Zusammensetzung von CAU-1 wurde mittels ^{1}H NMR- und IR-Spektroskopie systematisch untersucht. Für diese Untersuchungen wurde $AlCl_3 \cdot 6H_2O$ mit 2-Aminoterephthalsäure in einem Verhältnis von 3 : 1 unter solvothermalen Bedingungen in Methanol in einem MW-Ofen umgesetzt.

Bei der Verbindung CAU-1-NH_2 können sowohl die anorganische Baueinheiten als auch die organischen Linkermoleküle modifiziert werden. Die Variation der Reaktionszeit und Reaktionstemperatur erlaubt die Kontrolle über den Methylierungsgrad der Aminogruppen. Sehr kurze Reaktionszeiten führen zu unmethylierten CAU-1-NH_2, während bei längeren Reaktionszeiten CAU-1-$NHCH_3$ erhalten wird (Abb. 5.4, links).

Die thermische Behandlung von CAU-1-NH_2 ermöglicht die Zusammensetzung der Al-haltigen Baueinheit zu ändern. Schrittweise können die Methoxygruppen gegen Hydroxygruppen bei 190 °C an Luft ausgetauscht werden (Abb. 5.4, rechts). Die Geschwindigkeit dieser Austauschreaktion hängt stark von der verwendeten Temperatur ab. Der Austausch führt zu keiner signifikanten Änderung der Struktur oder der thermischen Stabilität, wenngleich die Ergebnisse der Elementaranalyse und TD-XRPD-Messung zeigen, dass die Proben hydrophilere Poren aufweisen.

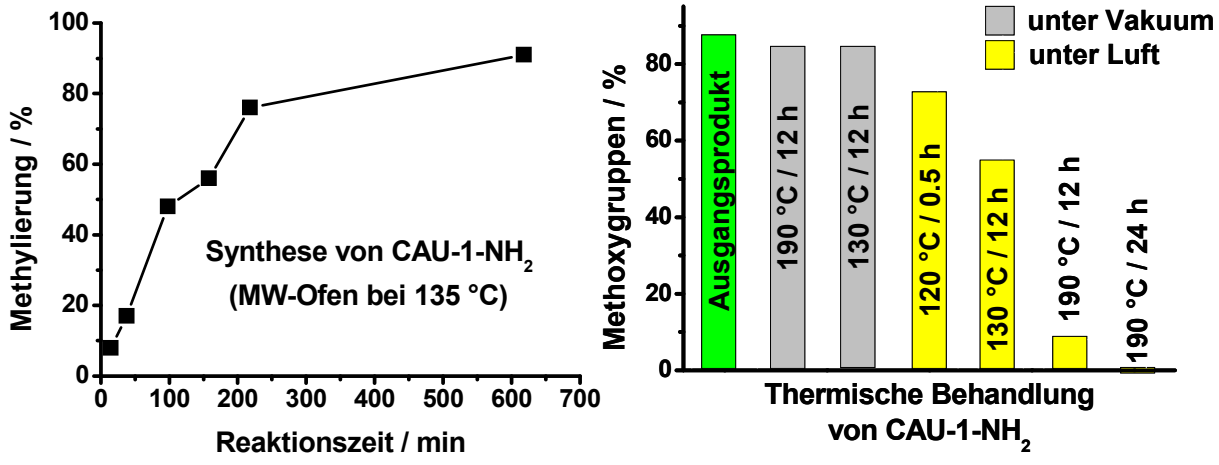

Abb. 5.4 Methylierung der Aminogruppen während der Synthese von CAU-1-NH_2 bei einer Reaktionstemperatur von 135 °C (links). Prozent der im Gerüst von CAU-1-NH_2 enthaltenden Methoxygruppen nach der thermischen Behandlung der Probe (rechts). Die Methoxygruppen werden dabei durch Hydroxygruppen ausgetauscht. Die Charakterisierung erfolgte in beiden Fällen mittels ^{1}H-NMR-Spektroskopie.

Die im Rahmen dieser Arbeit dargestellten CAU-1-Derivate wiesen nach der Synthese große Mengen an Chloridionen auf, welche durch Waschen mit Wasser entfernt werden konnten. Bei sowie CAU-3-NDC führte diese Behandlung zu einem drastischen Verlust der Kristallinität.

12. CAU-1-NH_2

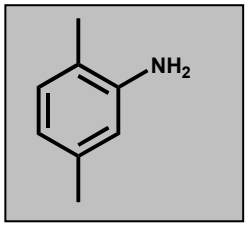

CAU-1-NH_2 ($[Al(OH)_2(OCH_3)_4(BDC\text{-}NH_2)_3]\cdot xH_2O$) konnte unter solvothermalen Bedingungen im MW-Ofen erhalten werden. Dazu wurde die in Absatz 11 beschriebene Reaktionslösung 3 min bei 145 °C erhitzt und im Anschluss rasch auf Raumtemperatur abgekühlt. Das Vorliegen unfunktionalisierter Aminogruppen konnte mit ^{15}N-MAS-NMR- und IR-Spektroskopie nachgewiesen werden. Die Ergebnisse wurden mittels Elementaranalyse und Thermogravimetrie bestätigt. Dabei wurde festgestellt, dass die Menge der in die Verbindung eingelagerten Wassermoleküle sehr stark mit der äußeren Umgebung (Temperatur und Luftfeuchtigkeit) variiert.

13. CAU-1-$NHCOCH_3$

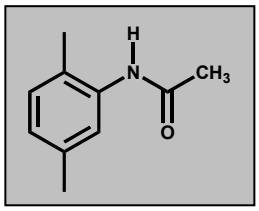

Die Verbindung CAU-1-$NHCOCH_3$ ($[Al_4(OH)_2(OCH_3)_4(BDC\text{-}NHCOCH_3)_3]\cdot xH_2O$) wurde im Ultraschallbad durch Umsetzen von CAU-1-NH_2 mit Essigsäureanhydrid dargestellt. Anfallende Nebenprodukte wurden durch Waschen mit Wasser und anschließende thermische Behandlung entfernt. Die Acylierung der Aminogruppen wurde mit IR-Spektroskopie sowie ^{13}C- und ^{15}N-MAS-NMR- Spektroskopie nachgewiesen. Die Umsetzung zum Amid erfolgte mit nahezu 100% Ausbeute.

14. CAU-1-$NHCH_3$

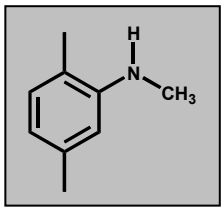

Für die Herstellung von $[Al_4(OH)_2(OCH_3)_4(BDC\text{-}NHCH_3)_3]\cdot xH_2O$ (CAU-1-$NHCH_3$) wurde die unter Punkt 11 verwendete Reaktionsmischung 10 h bei 135 °C im MW-Ofen umgesetzt. Mittels ^{1}H NMR-Spektroskopie wurde eine nahezu vollständige Einfachmethylierung der Aminogruppen nachgewiesen. Die Verbindung wurde mit Röntgenpulverbeugung, IR-Spektroskopie und Elementaranalyse charakterisiert.

15. CAU-1-NH_2(OH)

Durch eine thermische Behandlung von CAU-1-NH_2 bei 190 °C für 24 h an Luft konnte die Verbindung CAU-1-NH_2(OH) ($[Al_4(OH)_6(BDC\text{-}NH_2)_3]\cdot xH_2O$) dargestellt werden. Dabei wurden alle in das Gerüst eingebauten Methoxygruppen gegen Hydroxygruppen ausgetauscht. Das vollständige Entfernen der Methoxygruppen konnte mittels ^{1}H NMR- und IR-Spektroskopie sowie Elementaranalyse nachgewiesen werden. Eine schematische Darstellung der Austauschreaktion ist in Abbildung 5.5 gezeigt.

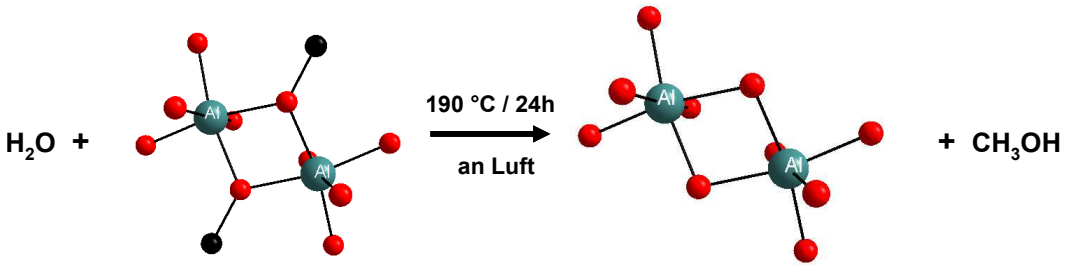

Abb. 5.5 Schematische Darstellung der Austauschreaktion der Methoxygruppen durch Hydroxygruppen bei thermischer Behandlung von CAU-1-NH_2 an Luft. In der Abbildung sind zwei kantenverknüpfte AlO_6-Oktaeder aus den an der Reaktion beteiligten anorganischen Baueinheiten gezeigt.

16. CAU-1-$(OH)_2$

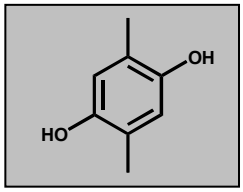

Die hydroxyfunktionalisierte Verbindung CAU-1-$(OH)_2$ ($[Al_4(OH)_2(OCH_3)_4(BDC\text{-}(OH)_2)_3]\cdot xH_2O$) konnte durch die solvothermale Umsetzung von $AlCl_3\cdot 6H_2O$ und 2,5-Diydroxyterephthalsäure ($(H_2BDC\text{-}(OH)_2)$) in Methanol in Anwesenheit von NaOH erhalten werden. Eine Synthese von CAU-1-$(OH)_2$ im Gramm-Maßstab konnte etabliert werden. Die Verbindung wurde mittels

Röntgenpulverdiffraktometrie, IR-Spektroskopie, Thermogravimetrie und Elementaranalyse charakterisiert. Das Sorptionsverhalten von CAU-1-$(OH)_2$ wurde mit den Gasen CO_2, N_2 und CH_4 untersucht.

17. CAU-3-NDC

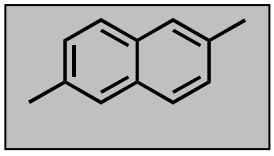

In dem Lösemittel Methanol konnte aus $AlCl_3 \cdot 6H_2O$ und 2,6-Napthalindicarbonsäure (H_2NDC) in Gegenwart von NaOH unter starker Verdünnung der Reaktionsmischung die Verbindung CAU-3-NDC ($[Al_2(OCH_3)_4(NDC)] \cdot xH_2O$) dargestellt werden. Die Charakterisierung der Verbindung erfolgte durch IR-Spektroskopie, Thermogravimetrie, N_2-Sorptionsexperimente und Elementaranalyse.

18. In situ EDXRD Untersuchungen

Mithilfe von in situ-EDXRD-Experimenten wurde das Kristallwachstum von CAU-1-NH_2 und CAU-1-$(OH)_2$ in Abhängigkeit von der Reaktionstemperatur und der verwendeten Heizmethode untersucht. Nach der Auswertung der Daten wurden folgende Trends hinsichtlich der Kinetik der Kristallisation beobachtet:

1. Wie zu erwarten, führt ein Anstieg der Reaktionstemperatur zu höheren Geschwindigkeitskonstanten. Gleichzeitig werden durch höhere Reaktionstemperaturen sowie der Verwendung eines MW-Ofens Produktpartikel mit einem kleineren hydrodynamischen Radius erhalten. Die Partikelgrößen sind für CAU-1-NH_2 in einem Bereich von 100–500 nm bzw. für CAU-1-$(OH)_2$ im Rahmen von 200–1000 nm einstellbar.
2. Bei gleicher Reaktionstemperatur werden im Mikrowellen-Ofen kürzere Induktions- und Reaktionszeiten beobachtet als bei der Verwendung der konventionellen Heizmethode.
3. Im MW-Ofen verläuft der Kristallisationsprozess von CAU-1-NH_2 wesentlich schneller als der von CAU-1-$(OH)_2$, während unter Verwendung der konventionellen Heizmethode für beide Verbindungen ähnliche Induktions- und Reaktionszeiten beobachtet werden (Abb. 5.6).

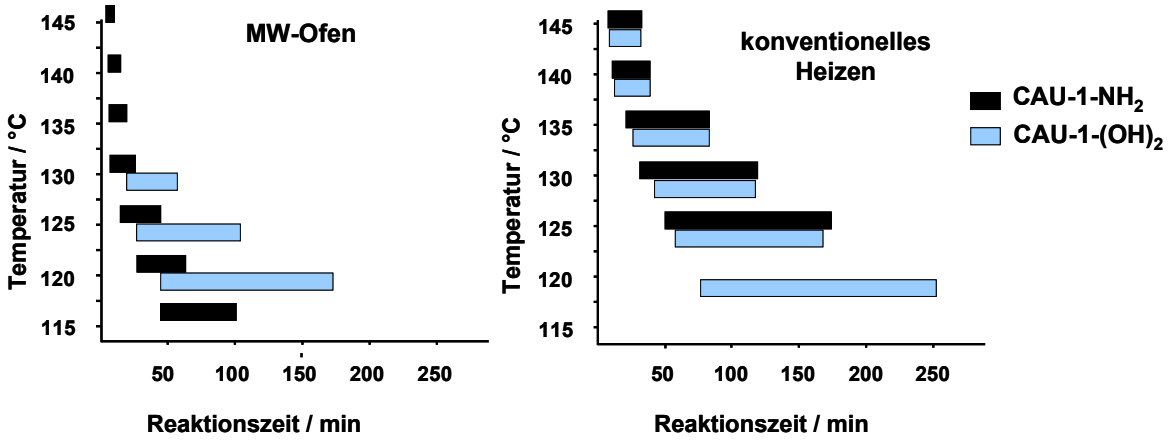

Abb. 5.6 Vergleich der Induktions- und Reaktionszeiten für das Kristallwachstum von CAU-1-NH_2 und CAU-1-$(OH)_2$ unter Verwendung eines MW-Ofen (links) sowie konventioneller Heizmethode (rechts).

4. Die aus der Arrheniusauftragung ermittelte Aktivierungsenergie von ~136(11) $kJ \cdot mol^{-1}$ für das Kristallwachstum von CAU-1 und CAU-1-$(OH)_2$ ist unabhängig von der verwendeten Heizmethode.

6 Ausblick

Die Vielzahl neuer isoretikulärer Al-MIL-53-Verbindungen, die im Rahmen dieser Arbeit auf der Basis von Terephthalsäurederivaten erhalten werden konnten, zeigt, dass Al-MIL-53 besonders geeignet ist funktionelle Gruppen in ein dreidimensionales Netzwerk einzubauen. In Abhängigkeit von den funktionellen Gruppen sollten unterschiedliche Wirt-Gast-Wechselwirkungen im Gerüst vorliegen. Bislang ist allerdings unklar wie, die funktionellen Gruppen im Gerüst angeordnet sind. Im Falle von Al-MIL-53-NHCHO wird dies zurzeit mittels ^{13}C MAS NMR-Spektroskopie im Detail untersucht. Dazu wurde unter anderem Al-MIL-53-NH_2 mit ^{13}C-angereicherter Ameisensäure in das entsprechende Formamid (Al-MIL-53-$NH^{13}CHO$) umgewandelt. Im Zuge dieser Studie wird zudem die Wirt-Gast-Wechselwirkung in Al-MIL-53-X anhand von Al-MIL-53-$NH^{13}CHO$ (Protonendonator) und Aceton (Protonenakzeptor) untersucht.

Poröse Verbindungen wie Al-MIL-53-X sollten Stoffgemische durch unterschiedliche Wechselwirkungen mit dem Gerüst bzw. mit den in das Gerüst eingefügten funktionellen Gruppen voneinander trennen können. Hierzu laufen bereits erste Versuche mit Al-MIL-53-NH_2 und Al-MIL-53-NO_2, bei denen die selektive Adsorption von C_8-Alkylaromaten untersucht wird. Erste Ergebnisse zeigen, dass Al-MIL-53-NH_2 im Gegensatz zu dem unmodifizierten Al-MIL-53 ein *o*-Xylol/*m*-Xylol-Gemisch in einer verdünnten Heptanlösung voneinander trennen konnte. Für die Verbindung Al-MIL-53-NO_2 wurde sogar eine selektive Aufnahme von *o*-Xylol beobachtet, da *m*-Xylol, *p*-Xylol und Ethylbenzol nicht in die Poren eindringen konnten. In weiteren Experimenten soll Al-MIL-53-NHCHO untersucht werden, um mögliche Trends bezüglich des Adsorptionsverhaltens der unterschiedlich modifizierten Al-MIL-53-Derivate aufzudecken.

Zur gezielten Beeinflussung der Wirt-Gast-Wechselwirkungen in einem funktionalisierten MOF ist es denkbar einen selektiven chemischen Sensor in das Gerüst einzubauen. Als ein solcher Sensor könnten UV-aktive Moleküle, wie z. B. Azoverbindungen, dienen, welche kovalent an funktionelle Gruppen im Gerüst gebunden werden. Die cis/trans-Stellung der im Gerüst verankerten Azoverbindung sollte sich durch eine geeignete Wellenlänge schalten lassen, um so die Größe, den

Zugang und die Adsorptionseigenschaften der Poren zu variieren. Die meisten funktionalisierten MOFs besitzen jedoch zu kleine Poren, um größere, als Sensormaterial verwendbare Moleküle, in das Gerüst einzubauen. Dieses Problem könnte durch den Einsatz großer Liganden bei den Synthesen isoretikulärer Al-MIL-53- und CAU-1-Verbindungen gelöst werden. Die Verwendung aminofunktionalisierter Linkermoleküle bietet sich an, da sich solche MOFs aufgrund der hohen Nukleophilie der Aminogruppe besonders leicht nachträglich chemisch modifizieren lassen. Die Abbildung 6.1 zeigt potentielle Dicarbonsäuren, deren Aminoderivate bei der Synthese eingesetzt werden könnten.

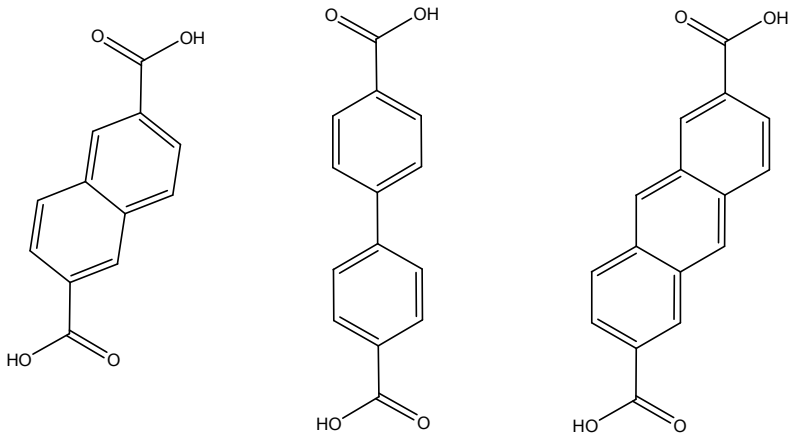

Abb. 6.1 Potentielle Linker zur Vergrößerung der Poren isoretikulärer Al-MIL-53- und CAU-1-Verbindungen.

Die im Rahmen dieser Arbeit erhaltende Verbindung Al-MIL-101-NH_2 bietet aufgrund ihrer großen Porenöffnungen und eingebauten Aminogruppen ebenfalls ein hohes Potential, um große schaltbare Moleküle kovalent zu binden. Erste Vorversuche zeigten, dass die Aminogruppen unter Verwendung von Phenylisocyanat in die entsprechenden Harnstoffgruppen überführt werden können, allerdings weisen die Produkte eine geringe Kristallinität auf.

Die Speicherung von Gasen und die Trennung von Stoffgemischen sind intensiv erforschte Gebiete in der Festkörperchemie. Durch die Vielzahl an Modifizierungsmöglichkeiten, der bemerkenswert hohen Porosität sowie thermischen und chemischen Stabilität eignet sich das CAU-1-Gerüst hervorragend als Modellsubstanz, um das Sorptionsverhalten gegenüber einer Vielzahl von Gasen zu untersuchen.

An der im Rahmen dieser Arbeit erhaltenden Verbindung Al-MIL-53-$(OH)_2$ zeigten Himsl et al., dass durch eine basengesteuerte Lithiumdotierung der Hydroxygruppen die Menge an adsorbiertem Wasserstoff erhöht werden konnte. Die in diesem Versuch verwendete Lithiumbase LDA war jedoch sterisch zu anspruchsvoll, um auch in die Poren von CAU-1-$(OH)_2$ einzudringen. Durch ein thermisches Entfernen der Methoxygruppen sollte der Zugang zu den Poren vergrößert sowie die Zahl der zum Austausch zur Verfügung stehenden Hydroxygruppen erhöht werden können.

Entgegen des akademischen Fokus auf funktionalisierte Metall-organische Gerüstverbindungen sind für die Industrie eher unfunktionalisierte Netzwerke auf der Basis kostengünstiger Linker wie Terephthalsäure oder Naphthalindicarbonsäure interessant. Beim Einsatz unfunktionalisierter Dicarbonsäurelinker in den systematischen Hochdurchsatzuntersuchungen des Systems Al^{3+}/Linker/MeOH/NaOH traten neben CAU-3 und CAU-3-NDC mit H_2NDC, H_2BDC und H_2BPDC drei weitere hochporöse aluminiumhaltige Gerüstverbindungen auf. Eine Indizierung der Pulverdiffraktogramme konnte aufgrund der geringen Zahl an Reflexen bzw. der schwachen Kristallinität der Verbindung nicht durchgeführt werden. Es hat sich gezeigt, dass der pH-Wert bei der Bildung neuer Strukturen in diesen Systemen eine entscheidende Rolle spielt. Unter Verwendung verschiedener organischer oder anorganischer Basen sollte es möglich sein, die Kristallinität der Produkte zu erhöhen. Ebenso wie bei der Synthese von CAU-3-NDC scheint zudem das Gegenion des Aluminiumsalzes einen großen Einfluss auf die Produktbildung zu besitzen. Dieses gilt es im Detail zu untersuchen.

Eine immer häufiger verwendete Synthesemethode zur Darstellung anorganisch-organischer Hybridverbindungen stellt die MW-Synthese dar. Diese ermöglicht neben einer drastischen Verkürzung der Synthesezeit die Herstellung homogener Nanopartikel. Die für die MW-unterstützten Synthesen charakteristischen schnelleren Aufheizraten und das homogenere Erwärmen der Reaktionsmischungen können zudem zu anderen Reaktionsverläufen führen. In ersten Vorversuchen konnten in einem MW-Ofen erstmalig CAU-1 auf der Basis von Terephthalsäure und Al-MIL-53-COOH unter Verwendung von Trimilitsäure erhalten werden. Beide Verbindungen waren bisher unter konventionellen Heizmethoden nicht zugänglich. Mithilfe eines Hochdurchsatzmikrowellenofens sollte es möglich sein, Stabilitätsfelder neuer

Verbindungen zu erschließen und den Einfluss einzelner Reaktionsparameter effizienter zu untersuchen.

Die Kristallisation isoretikulärer CAU-1 Verbindungen im MW-Reaktor wurde bereits unter Verwendung von in situ-EDXRD-Methoden untersucht. Bemerkenswerterweise hing dabei die Kristallisationsgeschwindigkeit der CAU-1-Derivate von den funktionellen Gruppen der Linkermoleküle ab. Zur Bestätigung dieser Beobachtung sollte die Kristallisation weiterer isoretikulärer CAU-1-Verbindungen untersucht werden. Potentielle Linker stellen $H_2BDC\text{-}CH_3$, $H_2BDC\text{-}NO_2$ und $H_2BDC\text{-}OH$ dar, die sich hinsichtlich ihrer Polarität stark von den bisher verwendeten Linkern ($H_2BDC\text{-}NH_2$) und ($H_2BDC\text{-}(OH)_2$) unterscheiden. Eine erfolgreiche Synthese der methylfunktionalisierten CAU-1-Verbindung unter Verwendung von Methylterephthalsäure ($H_2BDC\text{-}CH_3$) konnte bereits unter ähnlichen Reaktionsbedingungen durchgeführt werden. Diese Untersuchungen könnten wichtige Erkenntnisse über den Einfluss funktioneller Gruppen bei der Synthese von isoretikulären Verbindungen liefern und das Auffinden neuer Al-MOFs beschleunigen.

7 Anhang

Anhang 1:

Synthesis and modification of a functionalized 3D open-framework structure with MIL-53 topology

Tim Ahnfeldt,[a] Daniel Gunzelmann,[b] Thierry Loiseau,[c], Dunja Hirsemann,[b] Jürgen Senker,[b] Gerard Férey,[c] and Norbert Stock[,a]*

[a] Institute of Inorganic Chemistry, Christian-Albrechts-Universität, Otto-Hahn-Platz 6/7, 24118 Kiel, Germany

[b] Institute of Inorganic Chemistry, University of Bayreuth, Universitätsstr. 30, 95447 Bayreuth Germany

[c] Institut Lavoisier, UMR CNRS 8180, Université de Versailles St-Quentin en Yvelines, 45 Avenue des Etats-Unis, 78035 Versailles, France

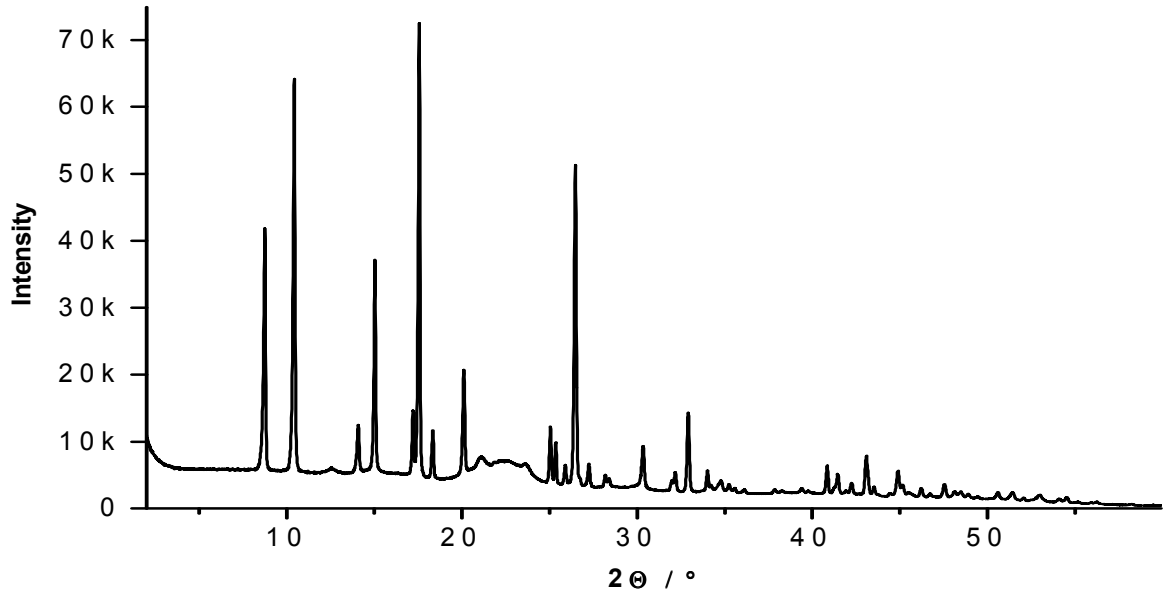

Fig. S1. Powder XRD pattern of MIL-53-NH_2(as)

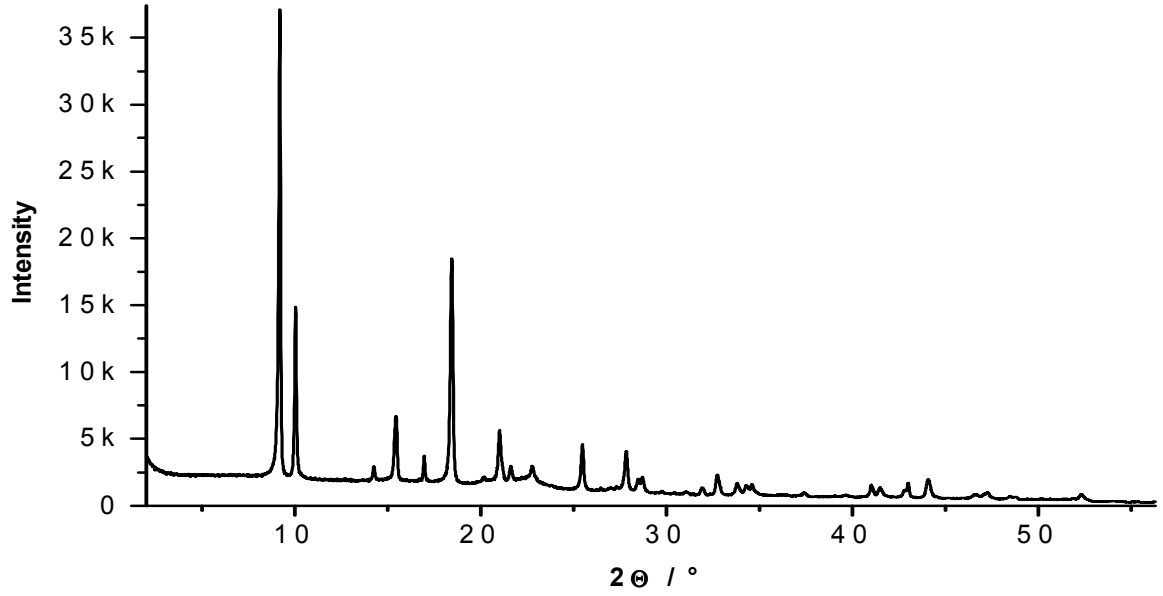

Fig. S2. Powder XRD pattern of MIL-53-NH_2(DMF).

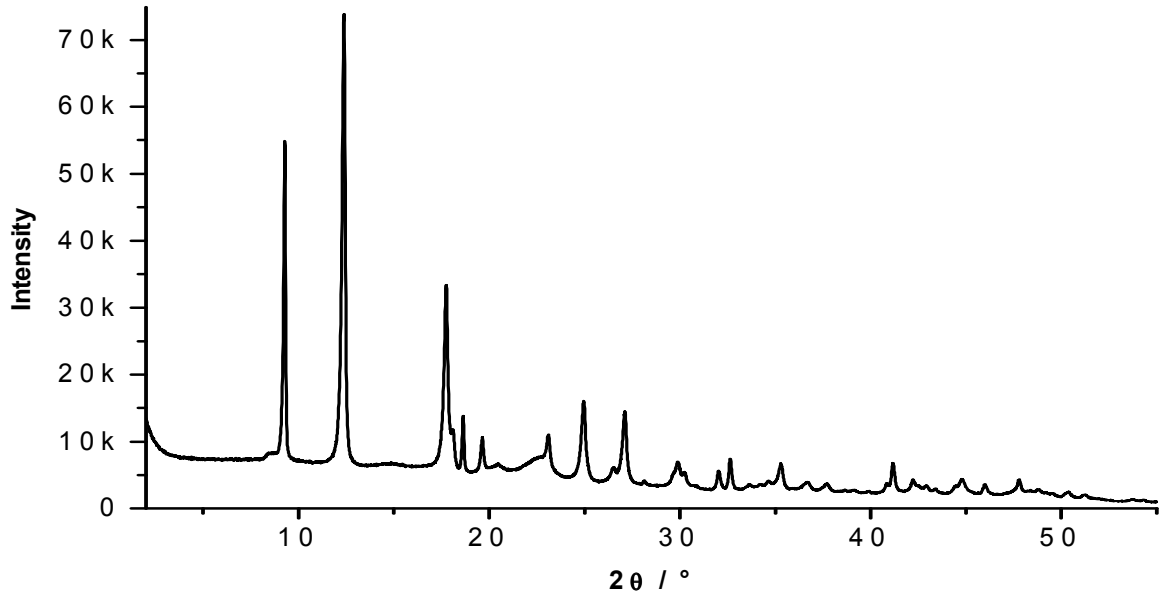

Fig. S3. Powder XRD pattern of MIL-53-NH_2(lt).

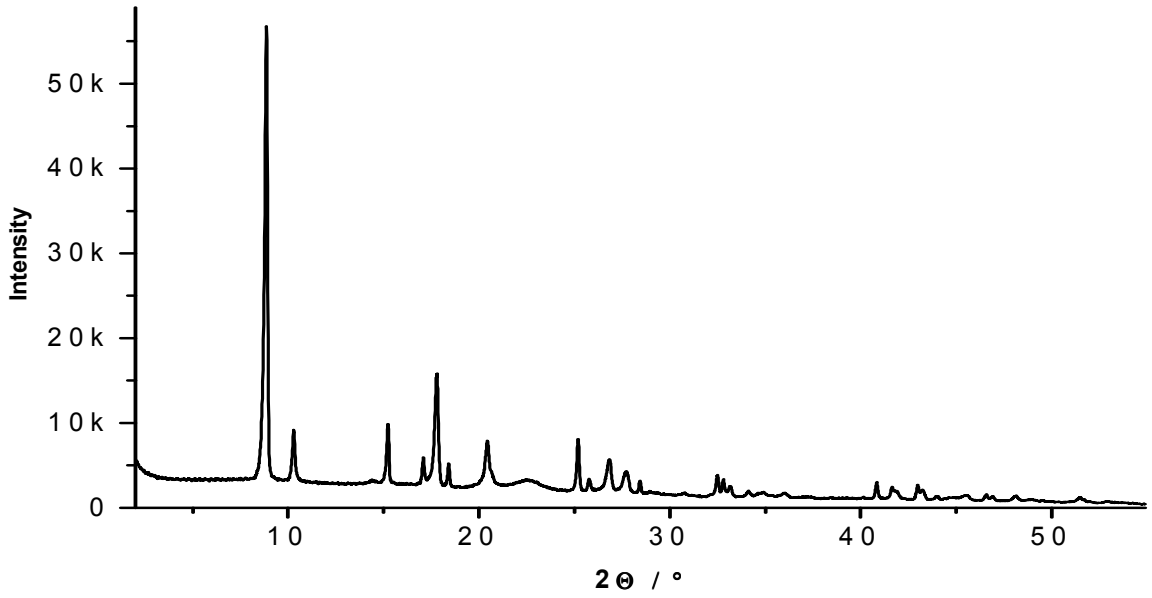

Fig. S4. Powder XRD pattern of MIL-53-NHCHO.

Anhang 2:

Supporting Information For

New Functionalized Flexible Al-MIL-53-X (X = -Cl, -Br, -CH_3, -NO_2, -$(OH)_2$) Solids: Syntheses, Characterization, Sorption and Breathing Behaviour

*Shyam Biswas, Tim Ahnfeldt, and Norbert Stock**

* To whom correspondence should be addressed. E-mail: stock@ac.uni-kiel.de. Tel: (+)49-4318801675. Fax: (+)49-4318801775.

Table of Contents:

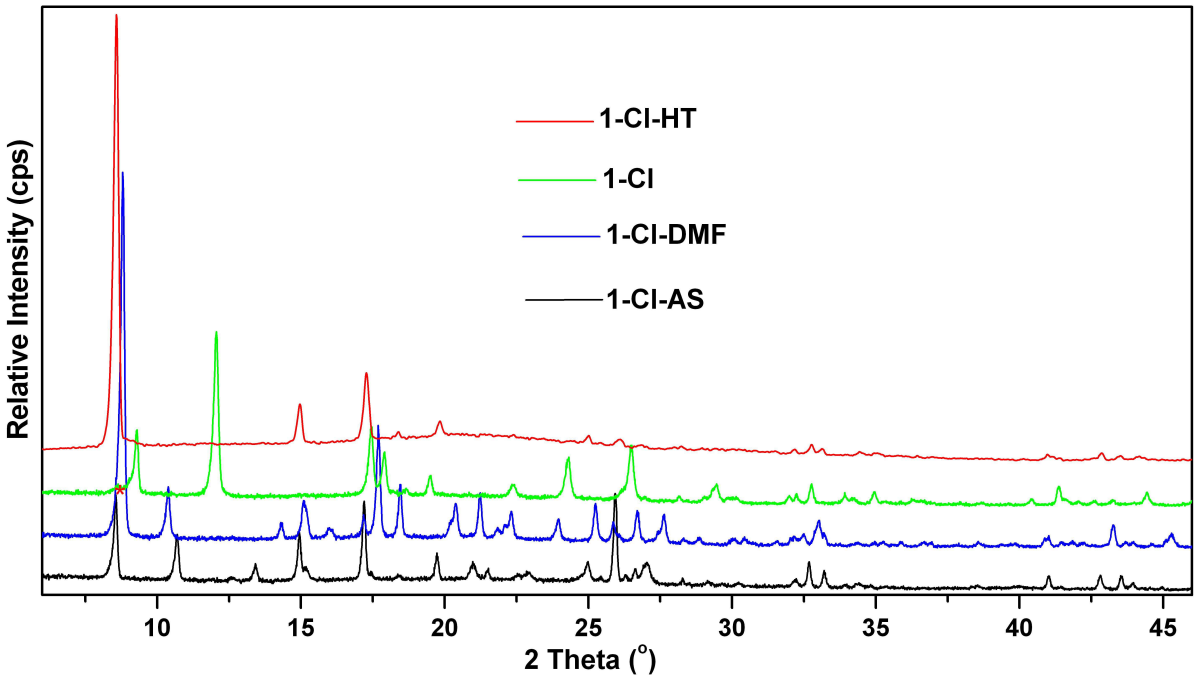

Figure S1. XRPD patterns of **1-Cl** in different forms: AS (black); after guest-exchange with DMF (blue); NP (green); HT (red). The diffraction peak marked with red star corresponds to HT-form. It was ignored during indexing the respective pattern.

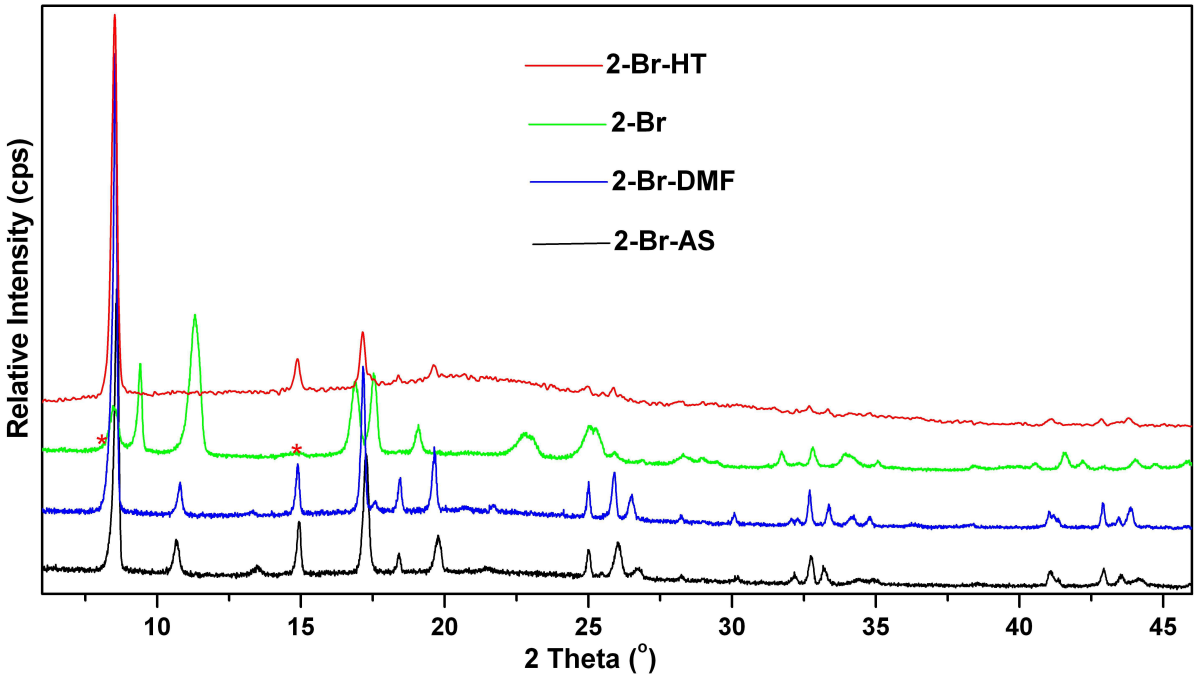

Figure S2. XRPD patterns of **2-Br** in different forms: AS (black); after guest-exchange with DMF (blue); NP (green); HT (red). The diffraction peaks marked with red stars correspond to HT-form. They were ignored during indexing the respective pattern.

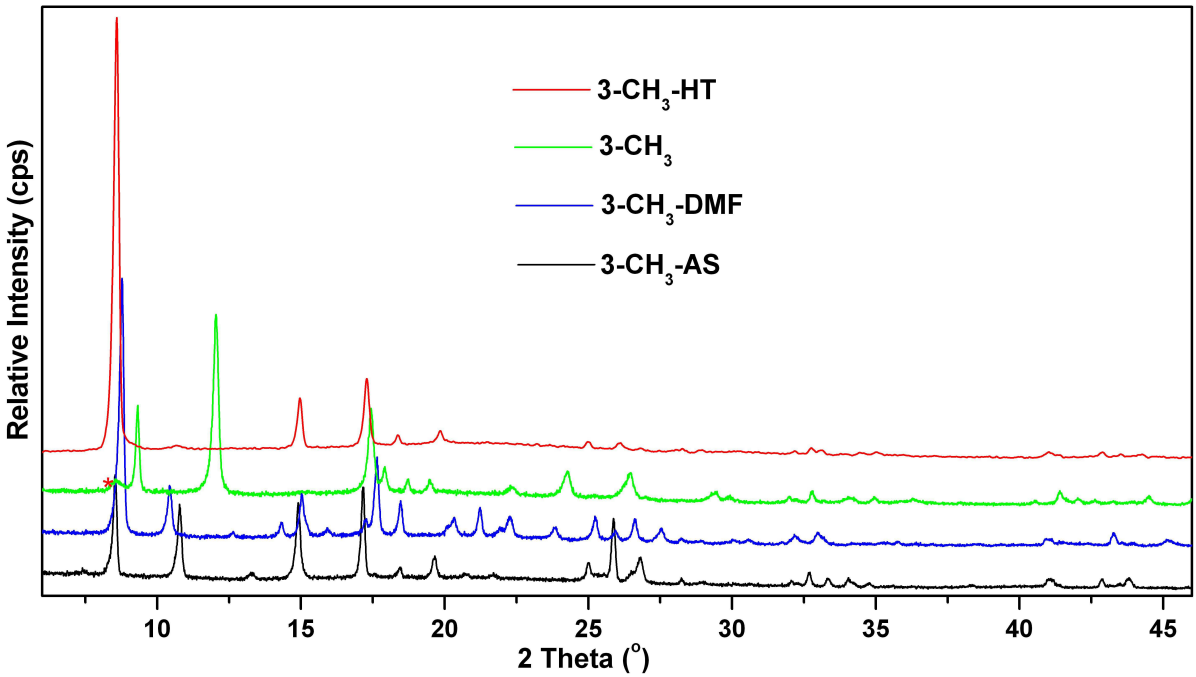

Figure S3. XRPD patterns of **3-CH$_3$** in different forms: AS (black); after guest-exchange with DMF (blue); NP (green); HT (red). The diffraction peak marked with red star corresponds to HT-form. It was ignored during indexing the respective pattern.

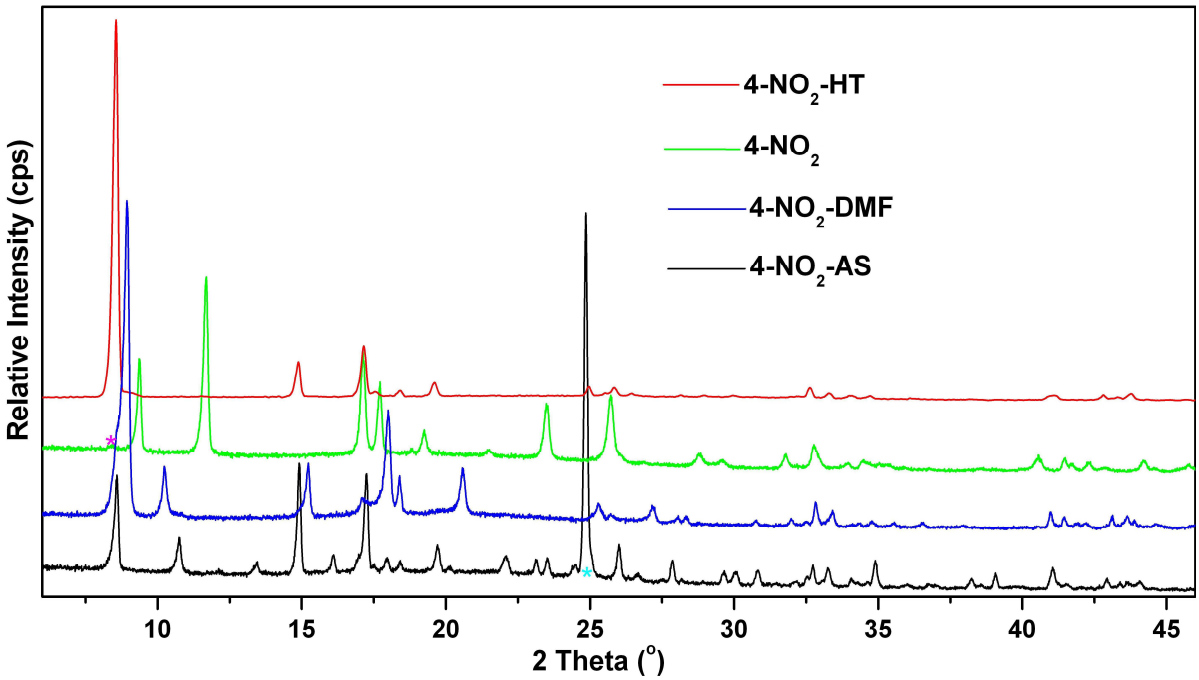

Figure S4. XRPD patterns of **4-NO_2** in different forms: AS (black); after guest-exchange with DMF (blue); NP (green); HT (red). The diffraction peaks marked with magenta and cyan stars correspond to HT-forms and recrystallized BDC-NO_2 linker, respectively. They were ignored during indexing the respective patterns.

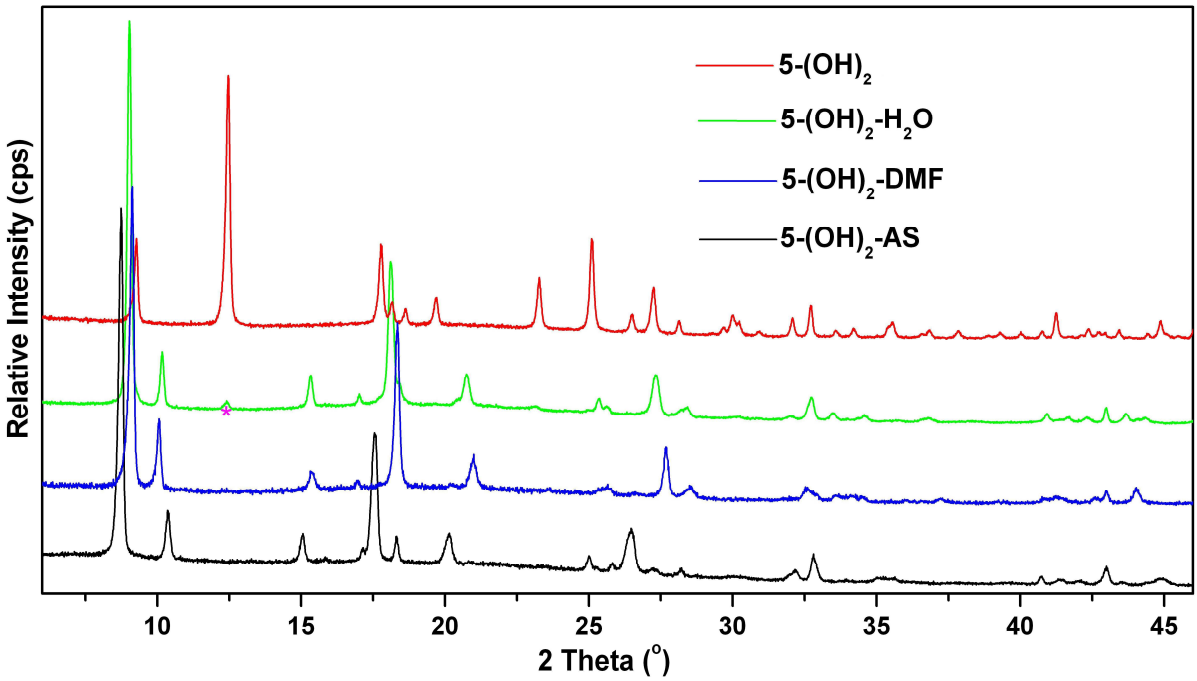

Figure S5. XRPD patterns of **5-(OH)$_2$** in different forms: AS (black); after guest-exchange with DMF (blue); after guest-exchange with H_2O/CH_3OH (50:50, v/v) followed by washing with H_2O (green); HT (red). The diffraction peak marked with magenta star corresponds to NP-form. It was ignored during indexing the respective pattern.

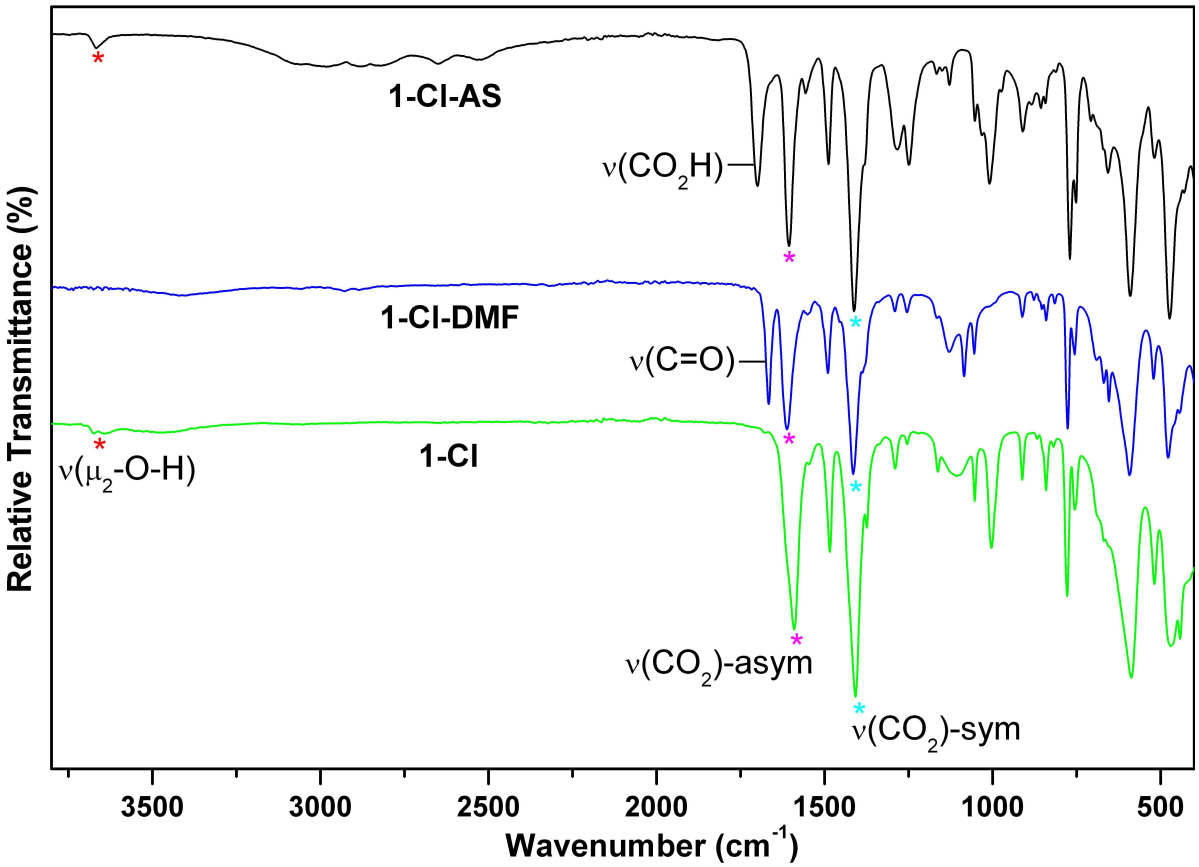

Figure S6. FT-IR spectra of **1-Cl** in different forms: AS (black); after guest-exchange with DMF (blue); NP (green) (asym: asymmetric, sym: symmetric).

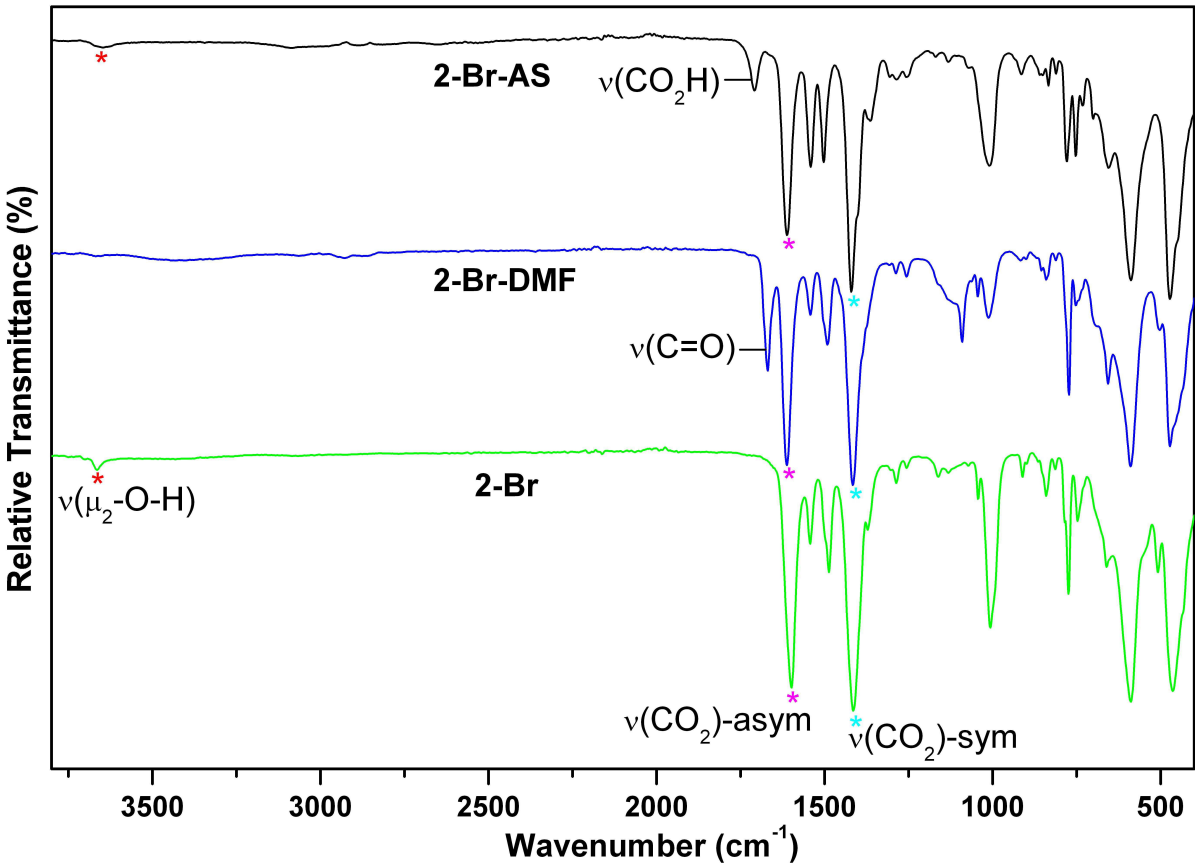

Figure S7. FT-IR spectra of **2-Br** in different forms: AS (black); after guest-exchange with DMF (blue); NP (green) (asym: asymmetric, sym: symmetric).

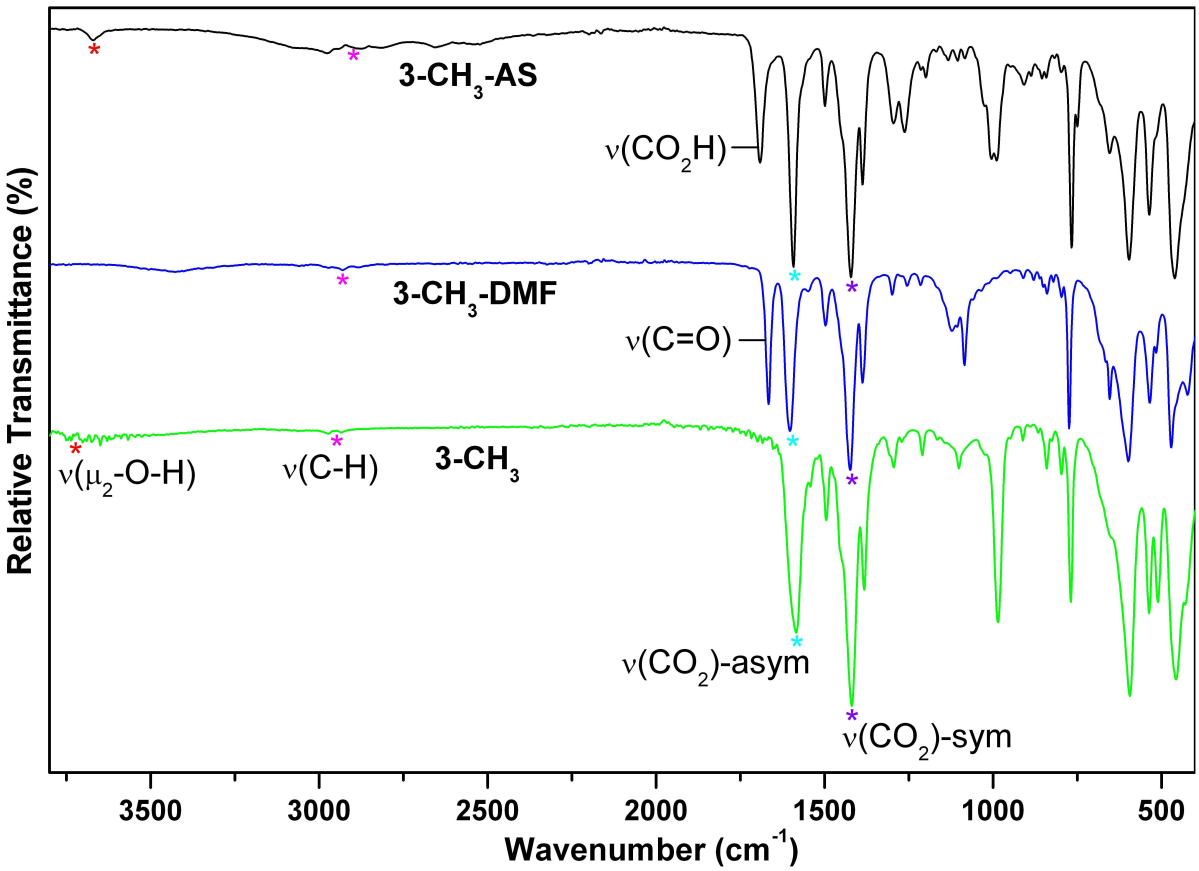

Figure S8. FT-IR spectra of **3-CH_3** in different forms: AS (black); after guest-exchange with DMF (blue); NP (green) (asym: asymmetric, sym: symmetric).

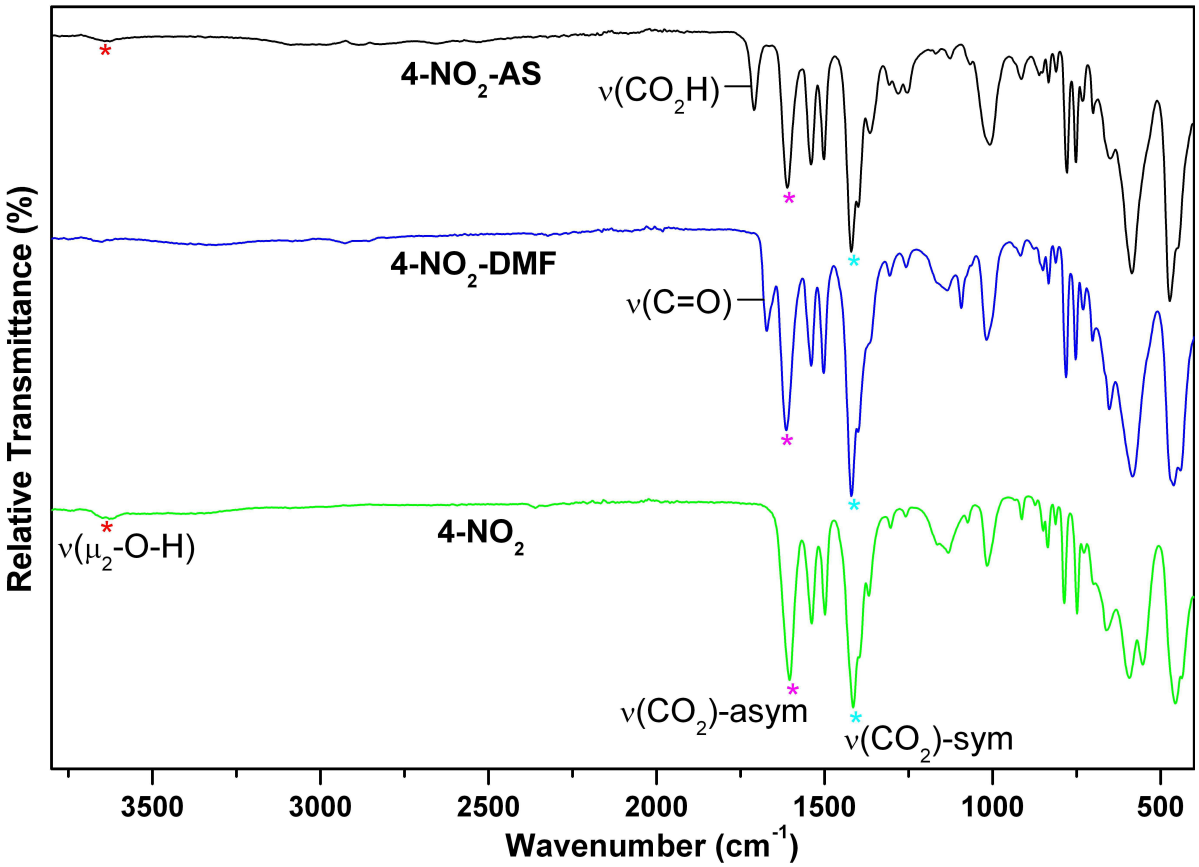

Figure S9. FT-IR spectra of **4-NO$_2$** in different forms: AS (black); after guest-exchange with DMF (blue); NP (green) (asym: asymmetric, sym: symmetric).

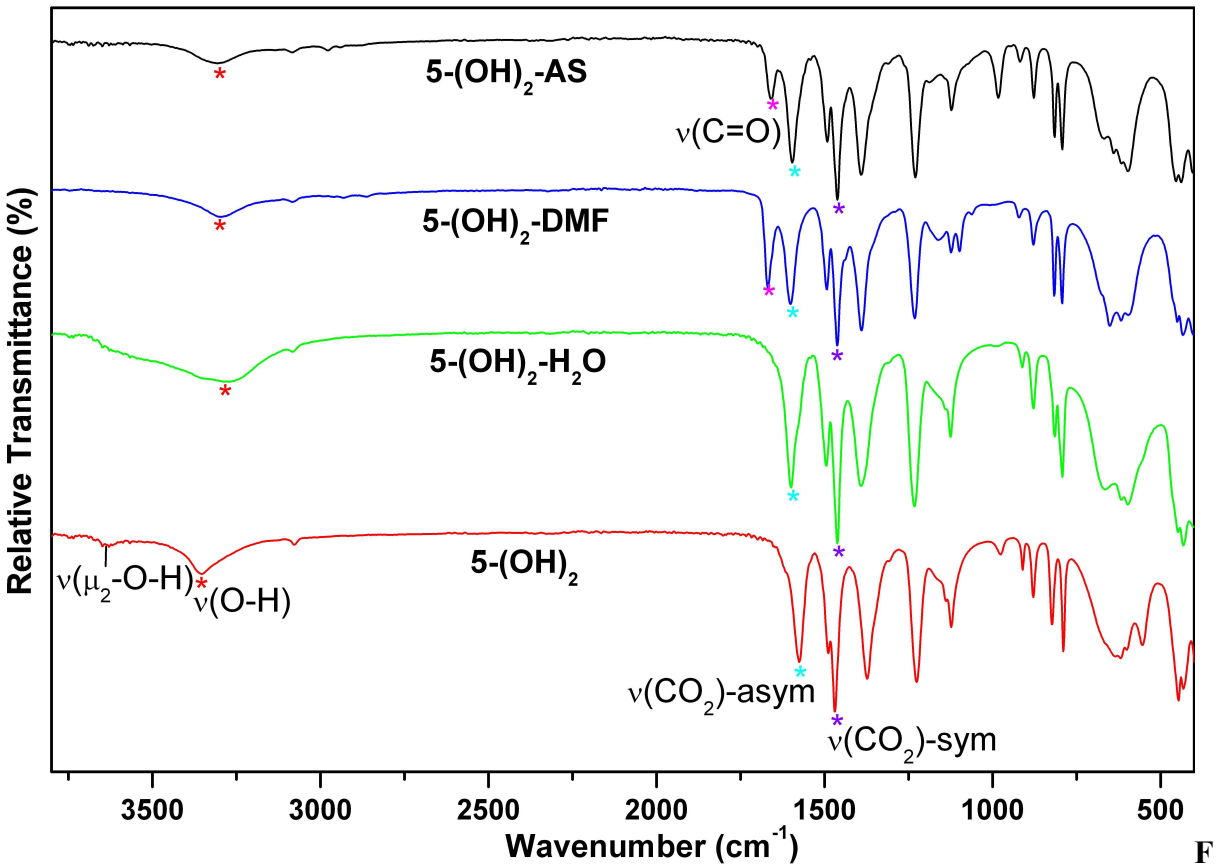

Figure S10. FT-IR spectra of **5-(OH)$_2$** in different forms: AS (black); after guest-exchange with DMF (blue); after guest-exchange with H_2O/CH_3OH (50:50, v/v) followed by washing with H_2O (green); NP (red) (asym: asymmetric, sym: symmetric).

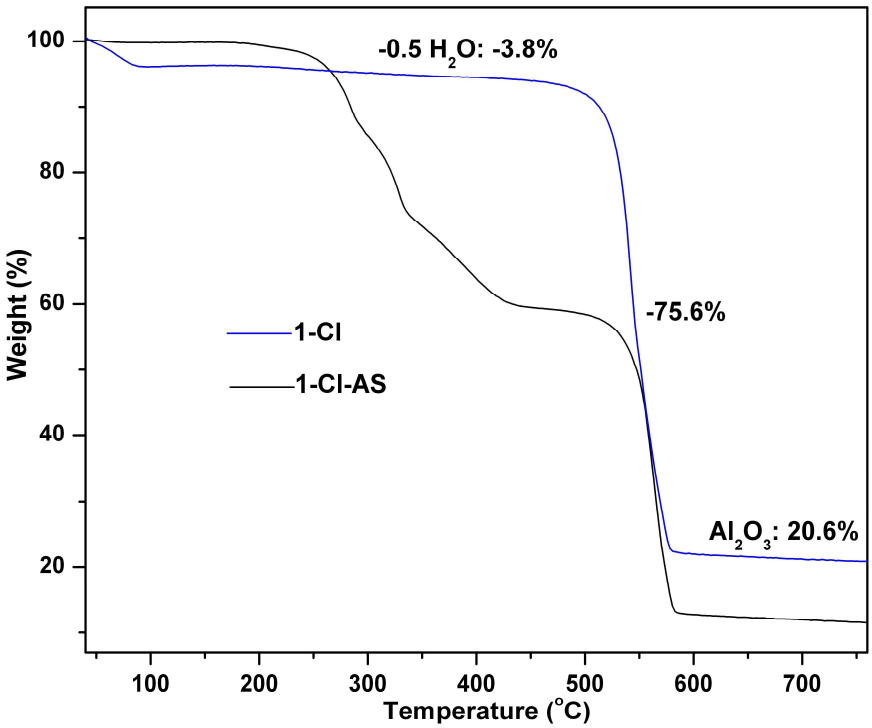

Figure S11. TG analyses under air atmosphere of **1-Cl** in AS (black) and NP (blue) forms.

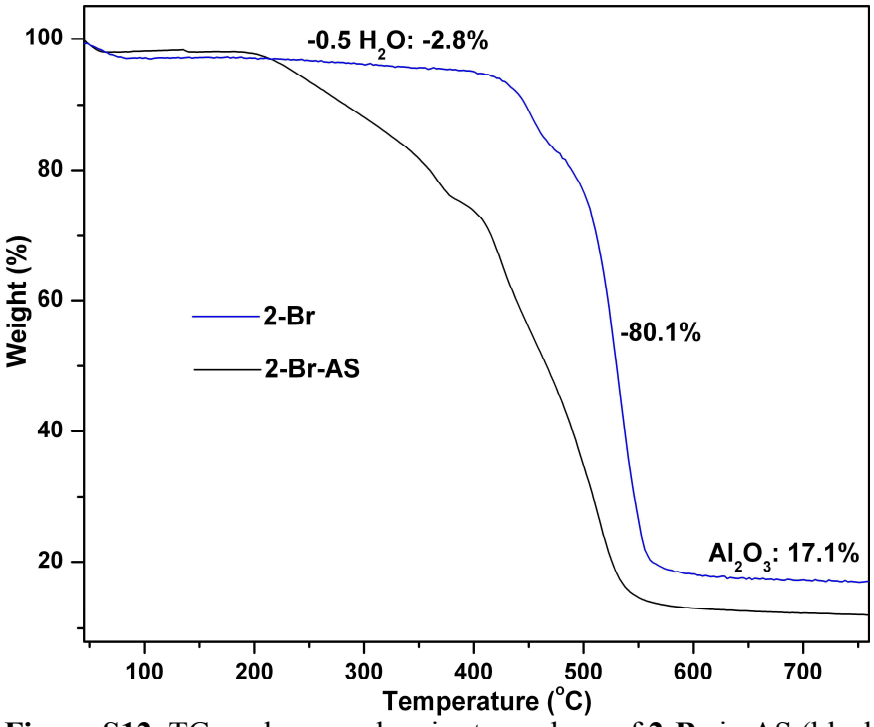

Figure S12. TG analyses under air atmosphere of **2-Br** in AS (black) and NP (blue) forms.

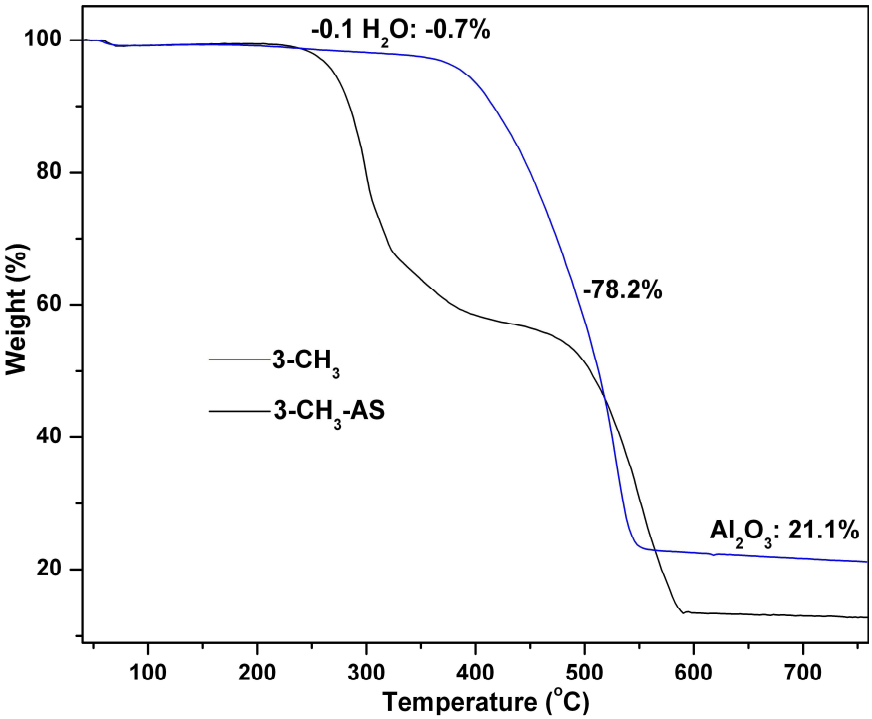

Figure S13. TG analyses under air atmosphere of **3-CH_3** in AS (black) and NP (blue) forms.

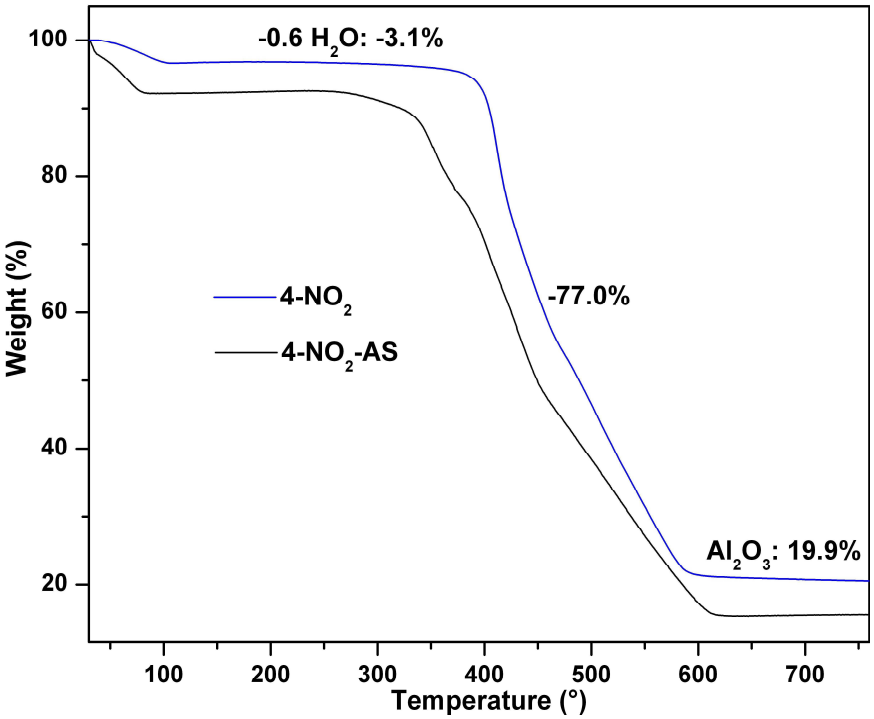

Figure S14. TG analyes under air atmosphere of **4-NO_2** in AS (black) and NP (blue) forms.

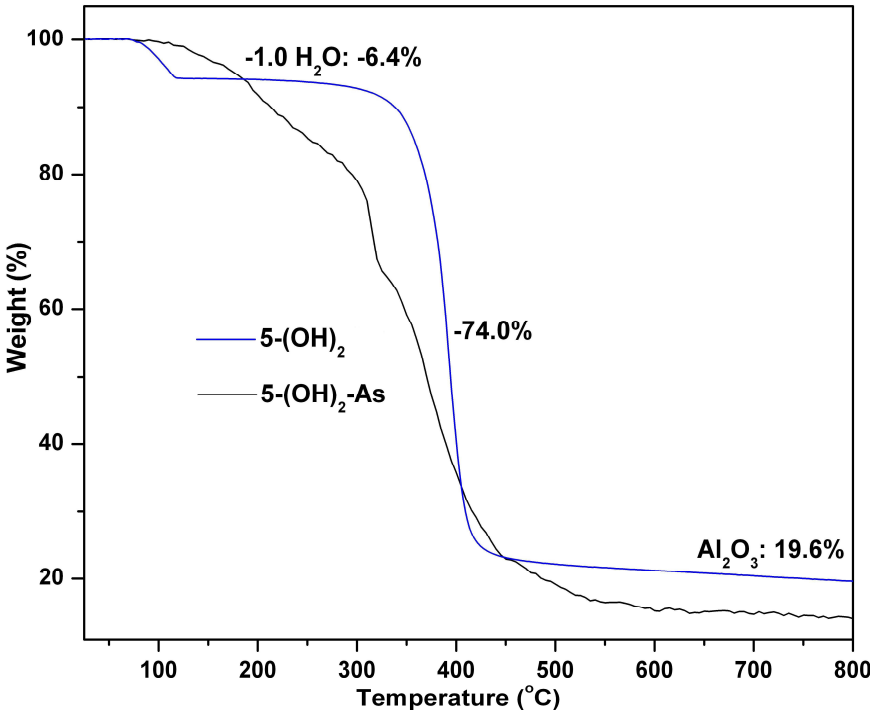

Figure S15. TG analyses under air atmosphere of **5-(OH)$_2$** in AS (black) and NP (blue) forms.

Table S1. weight loss steps in TG curves for the NP forms of the Al-MIL-53-X compounds and their assignments.

Compound	No. of H_2O Molecules Removed in 1st Weight Loss Step	1st Weight Loss (%): Obs. / Cal.	2nd Weight Loss (%)	Amount of Residual Al_2O_3 (%): Obs. / Cal.
1-Cl	0.5	3.8 / 3.3	75.6	20.6 / 20.8
2-Br	0.5	2.8 / 3.0	80.1	17.1 / 16.9
3-CH_3	0.1	0.7 / 0.8	78.2	21.1 / 21.3
4-NO_2	0.6	3.1 / 4.0	77.0	19.9 / 19.2
5-$(OH)_2$	1.0	6.4 / 6.9	74.0	19.6 / 19.7
Al-MIL-53[1]	1.0	7.0 / 7.9	70.0	23.0 / 21.9

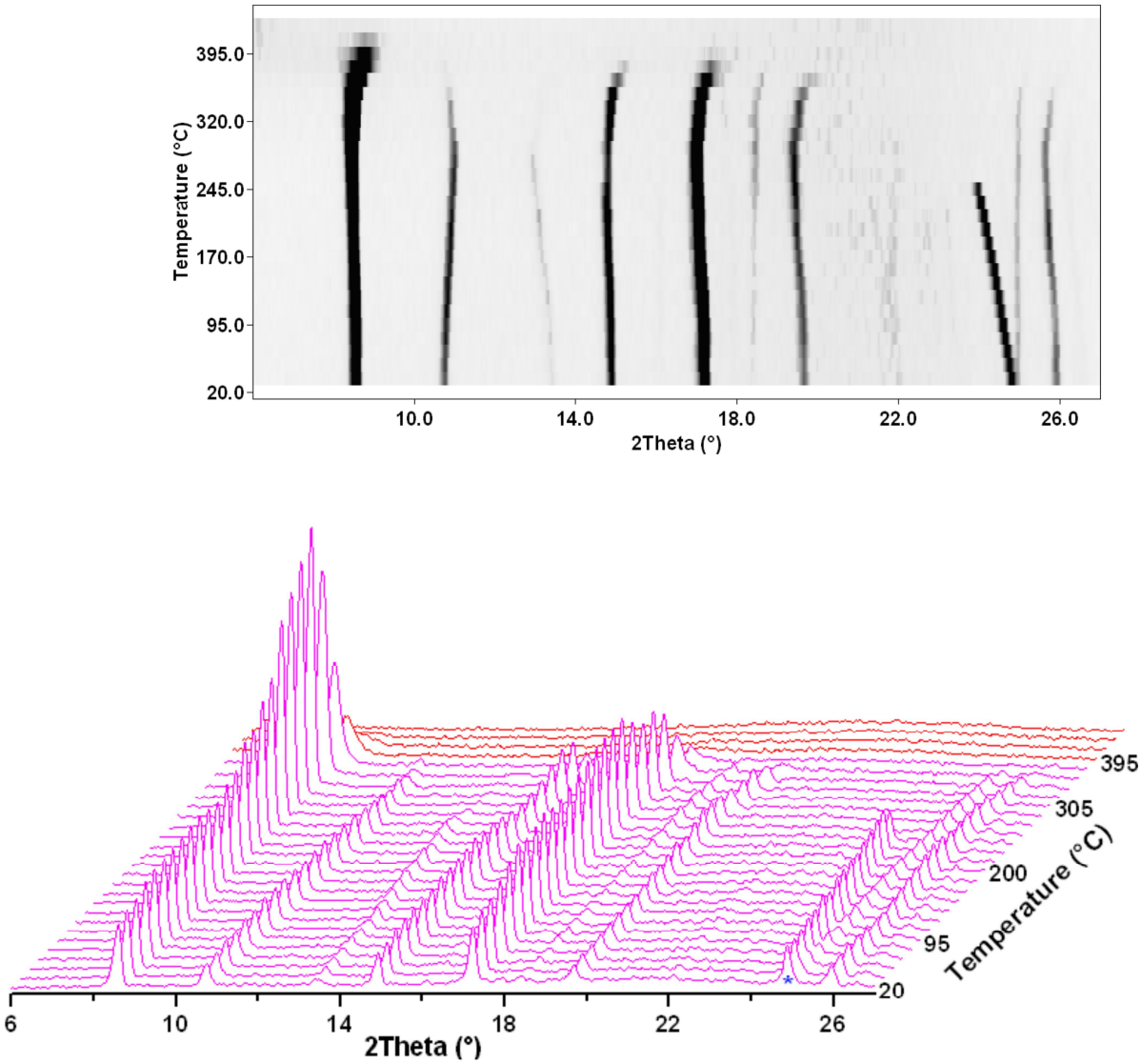

Figure S16. TDXRPD patterns of of **4-NO_2-AS** under air atmosphere (CuKα radiation, λ = 1.5406 Å) in the range 20-425 °C. The top view of the patterns is shown on the top. Each pattern was recorded at intervals of 15 °C. Magenta patterns: AS-form; red patterns: decomposed form. The diffraction peak marked with blue star which exists in the range 20-245 °C, corresponds to recrystallized BDC-NO_2 linker.

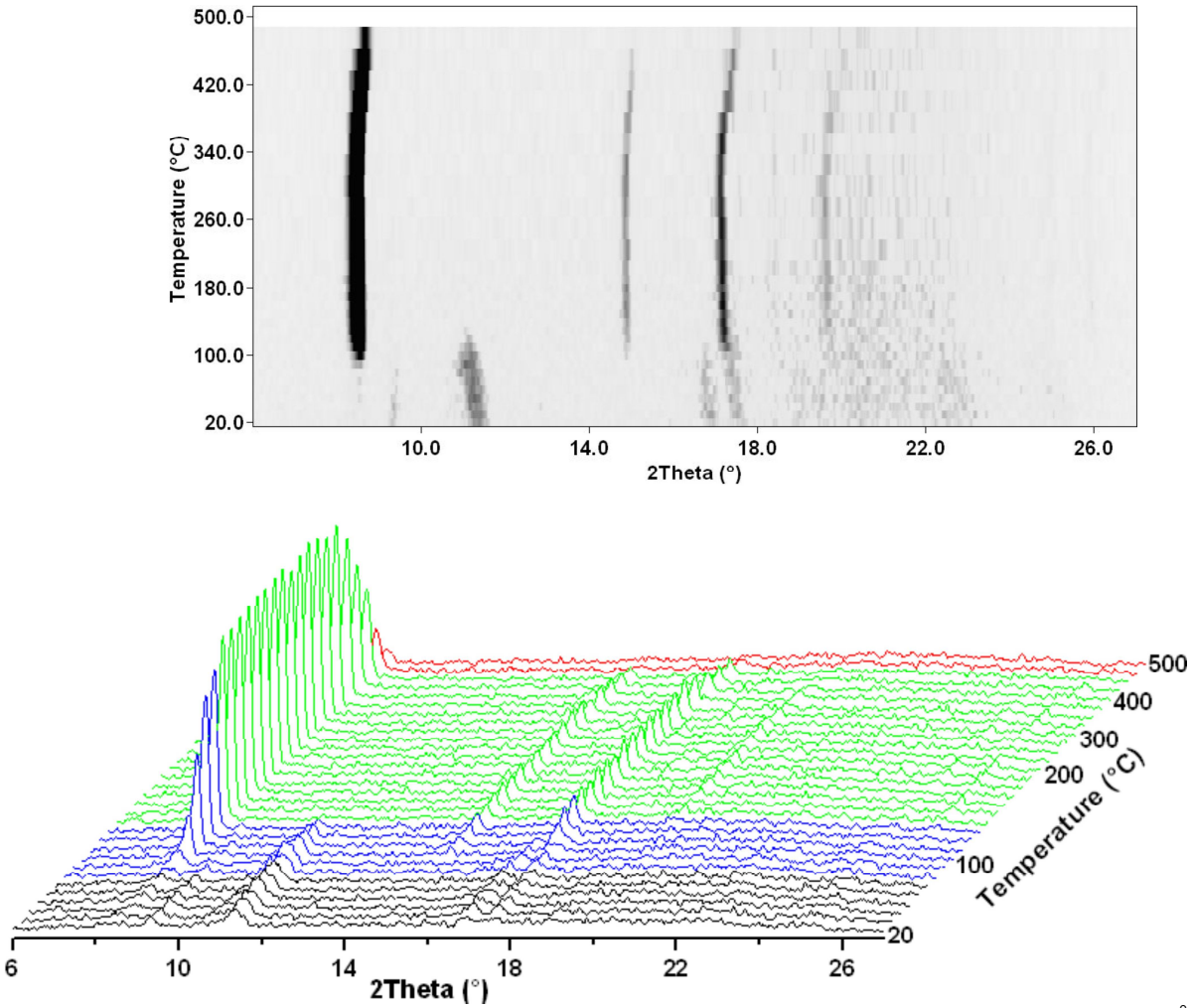

Figure S17. TDXRPD patterns of **2-Br** under air atmosphere (CuKα radiation, λ = 1.5406 Å) in the range 20-500 °C. The top view of the patterns is shown on the top. Black patterns: NP-form; blue patterns: mixture of NP and HT-forms; green patterns: HT-form; red patterns: decomposed form.

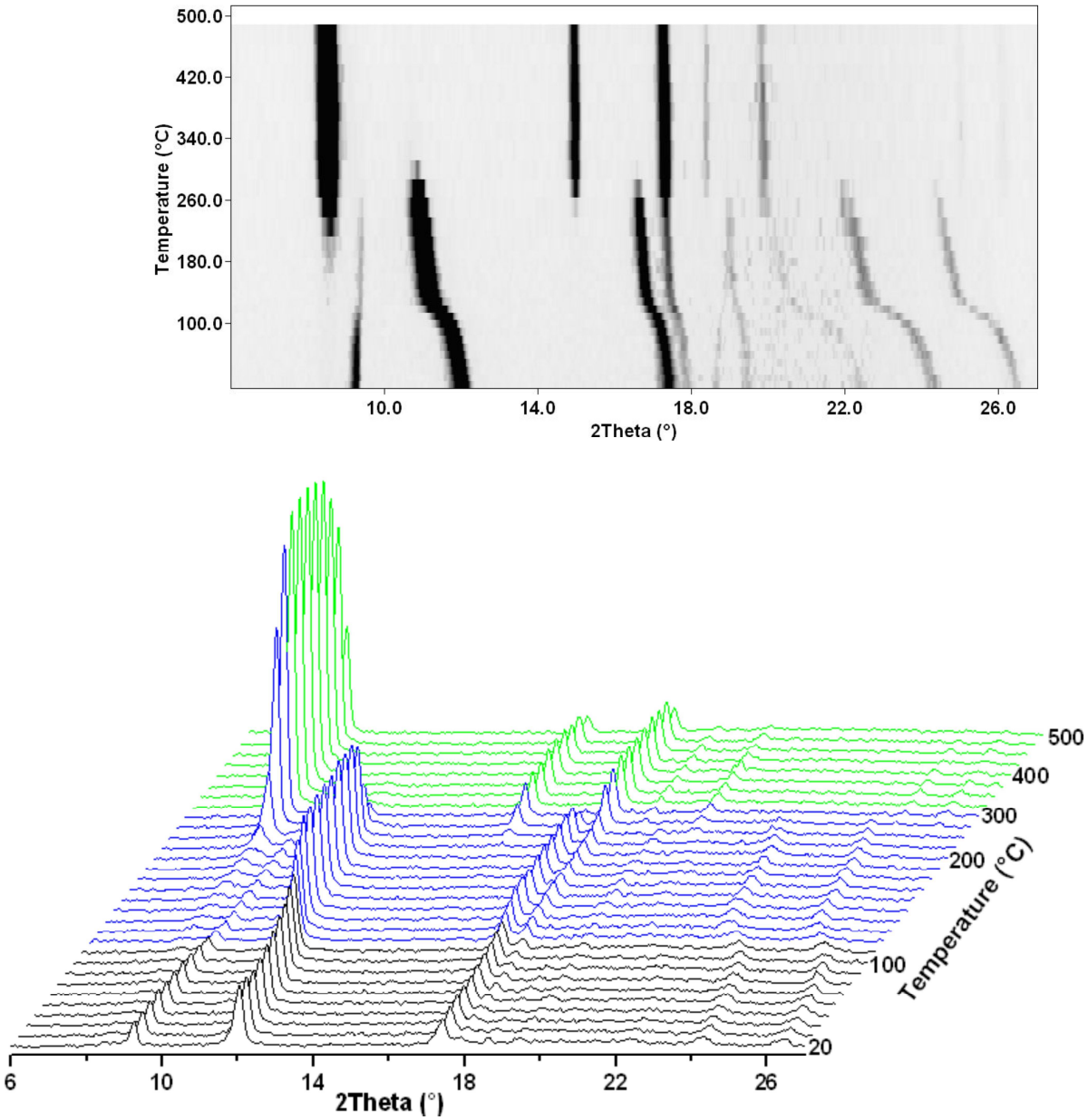

Figure S18. TDXRPD patterns of **3-CH_3** under air atmosphere (CuKα radiation, λ = 1.5406 Å) in the range 20-500 °C. The top view of the patterns is shown on the top. Black patterns: NP-form; blue patterns: mixture of NP and HT-forms; green patterns: HT-form.

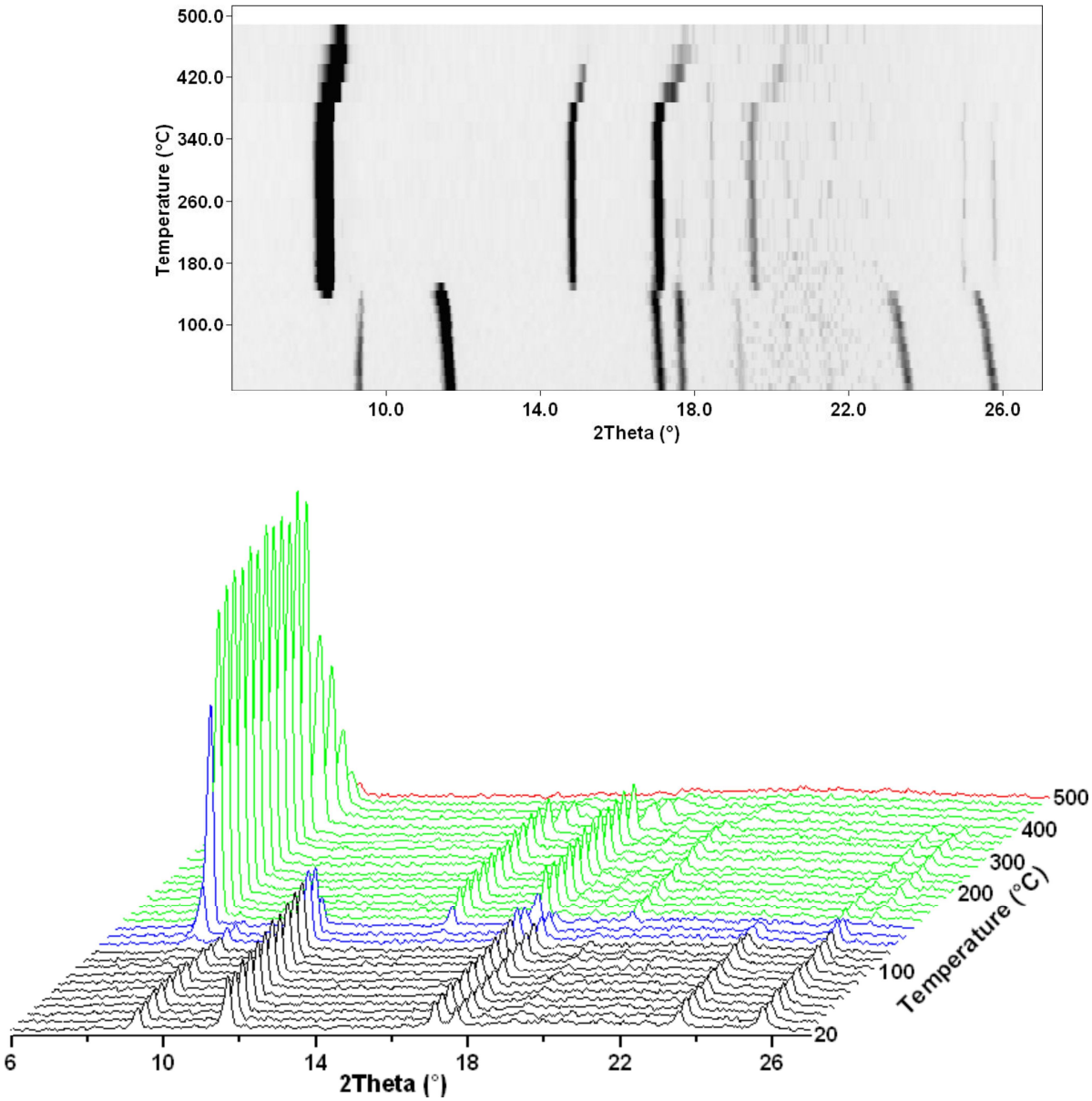

Figure S19. TDXRPD patterns of **4-NO_2** under air atmosphere (CuKα radiation, λ = 1.5406 Å) in the range 20-500 °C. The top view of the patterns is shown on the top. Black patterns: NP-form; blue patterns: mixture of NP and HT-forms; green patterns: HT-form; red pattern: decomposed form.

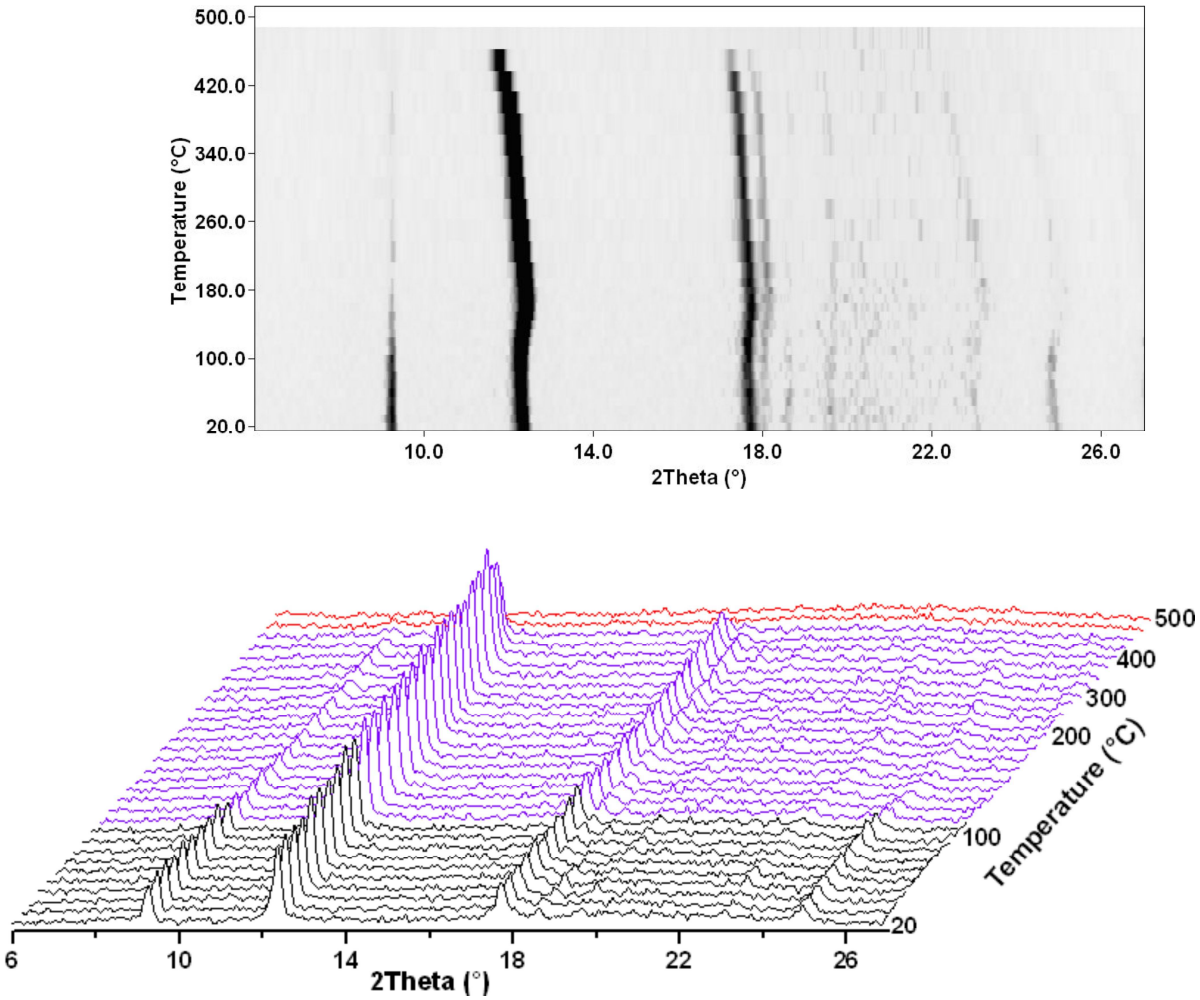

Figure S20. TDXRPD patterns of Al-MIL-53-NH_2 under air atmosphere (CuKα radiation, λ = 1.5406 Å) in the range 20-500 °C. The top view of the patterns is shown on the top. Black patterns: NP-form; violet patterns: NP-form with positions of some of the Bragg peaks shifted; red patterns: decomposed form.

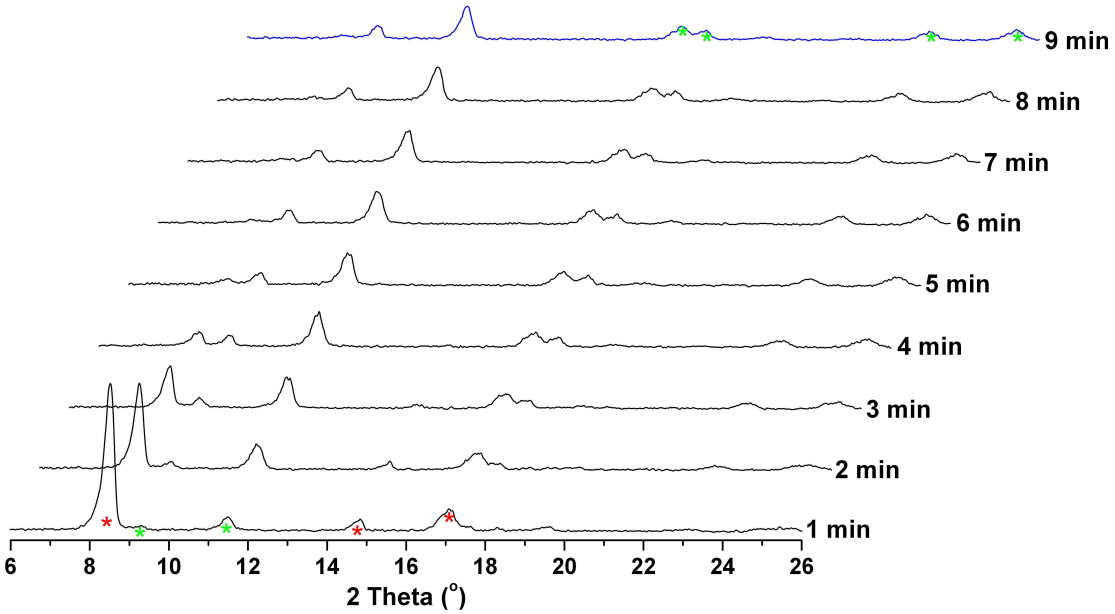

Figure S21. Time-dependent XRPD patterns of **4-NO_2** under air atmosphere (CuKα, λ = 1.5406 Å). The sample was heated at 180 °C under vacuum for 2 h and subsequently the powder patterns were collected at room temperature under air atmosphere. The diffraction peaks marked with red and green stars correspond to HT and NP-form of the compound. Black patterns: mixture of NP and HT-forms; blue pattern: NP-form.

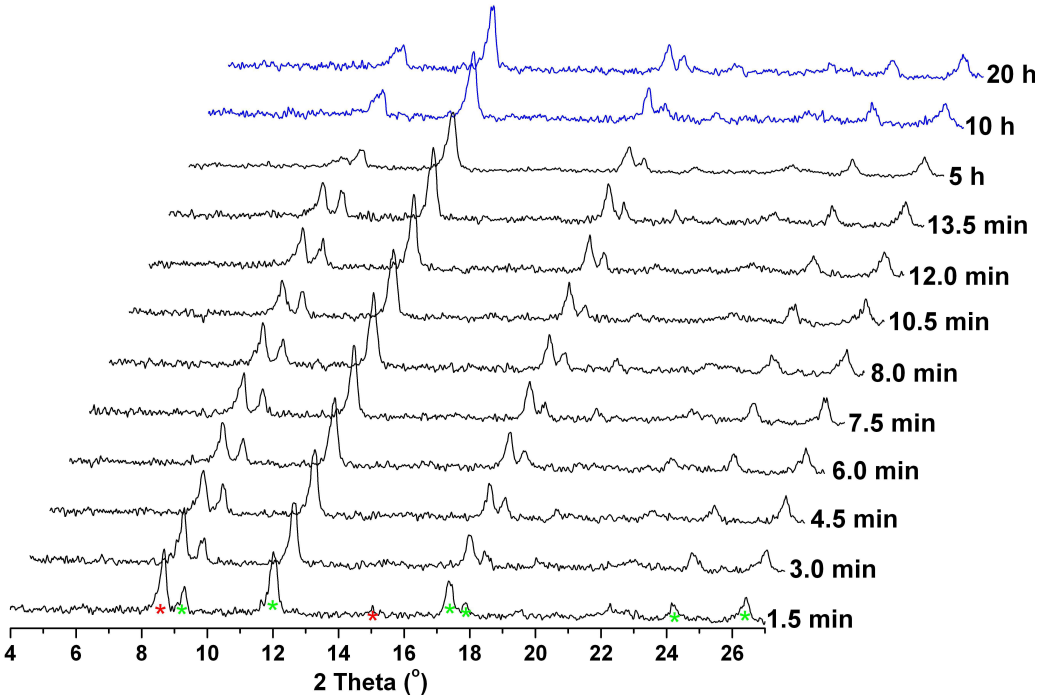

Figure S22. Time-dependent XRPD patterns of **1-Cl** under air atmosphere (CuKα, λ = 1.5406 Å). The sample was heated at 180 °C under vacuum for 2 h and subsequently the powder patterns were collected at room temperature under air atmosphere. The diffraction peaks marked with red and green stars correspond to HT and NP-form of the compound. Black patterns: mixture of NP and HT-forms; blue patterns: NP-form

.

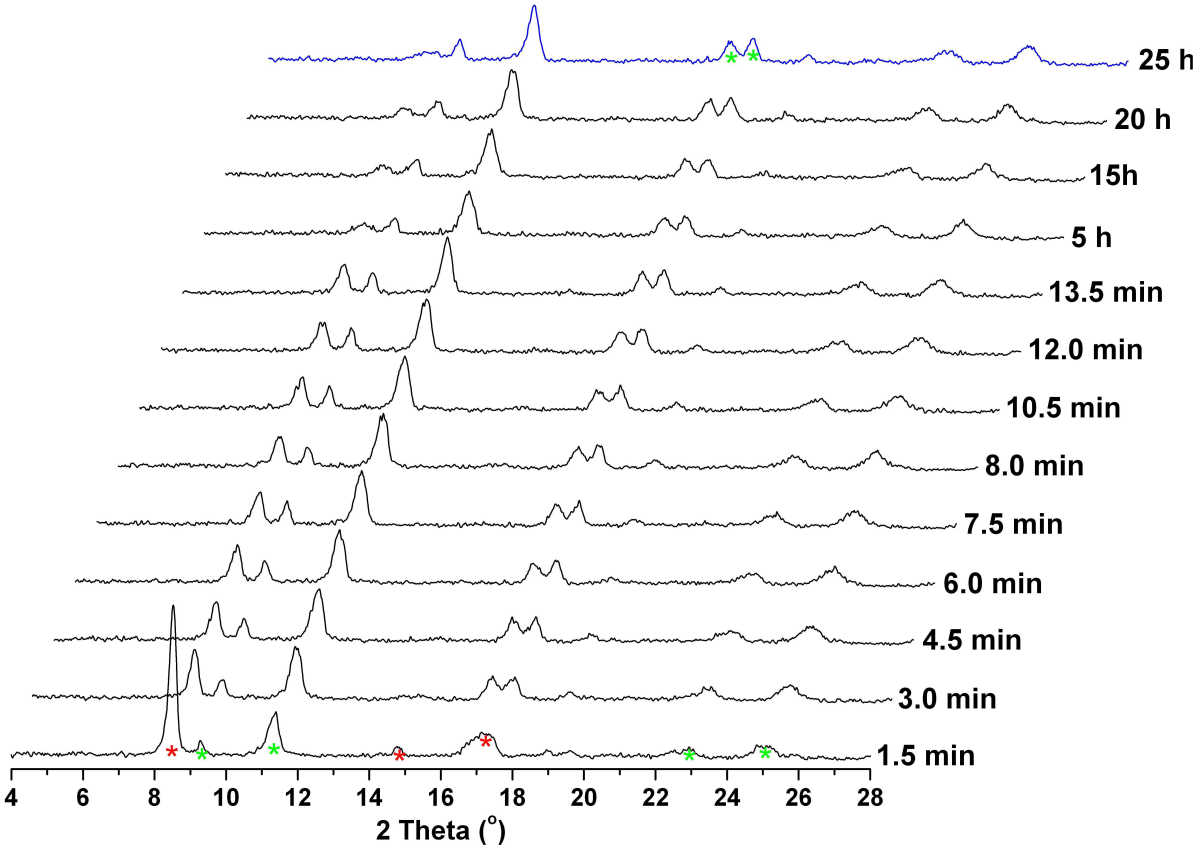

Figure S23. Time-dependent XRPD patterns of **2-Br** under air atmosphere (CuKα, λ = 1.5406 Å). The sample was heated at 180 °C under vacuum for 2 h and subsequently the powder patterns were collected at room temperature under air atmosphere. The diffraction peaks marked with red and green stars correspond to HT and NP-form of the compound. Black patterns: mixture of NP and HT-forms; blue pattern: NP-form.

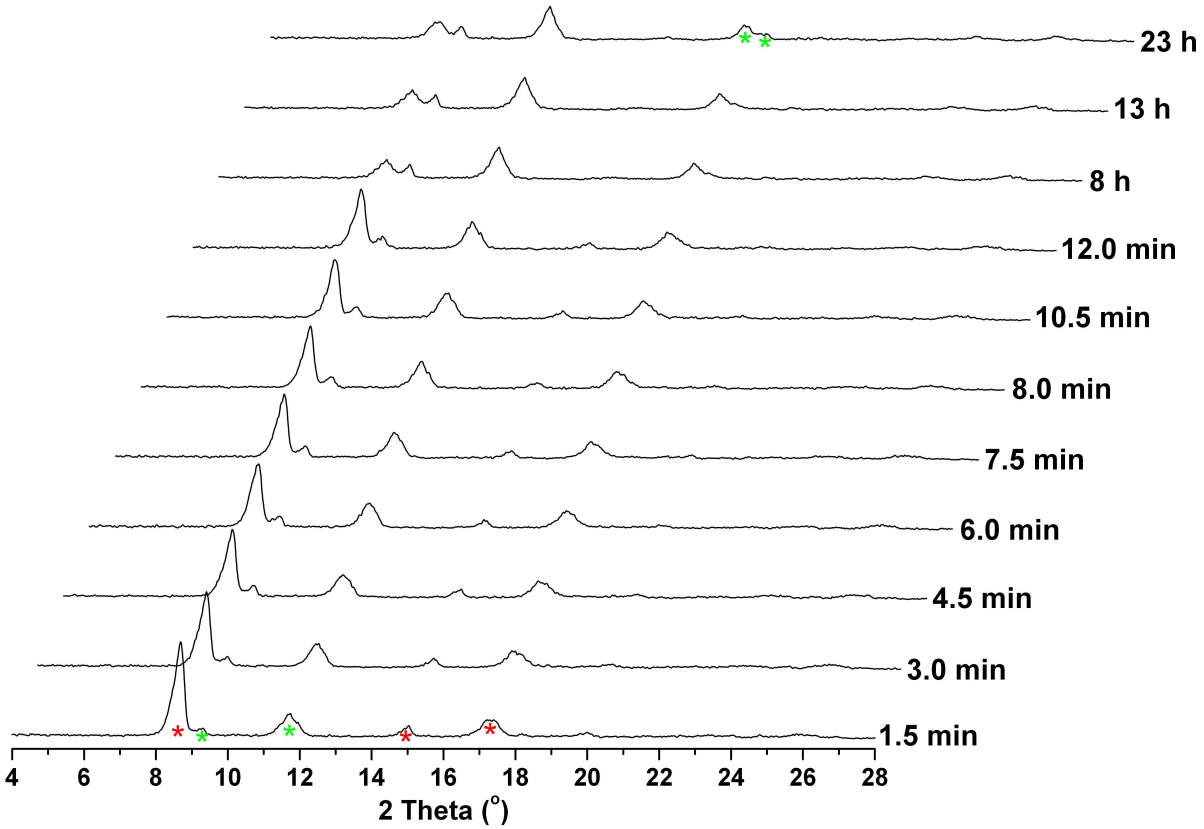

Figure S24. Time-dependent XRPD patterns of **3-CH$_3$** under air atmosphere (CuKα, λ = 1.5406 Å). The sample was heated at 180 °C under vacuum for 2 h and subsequently the powder patterns were collected at room temperature under air atmosphere. All the patterns represent a mixture of NP and HT-forms. The diffraction peaks marked with red and green stars correspond to HT and NP-form of the compound.

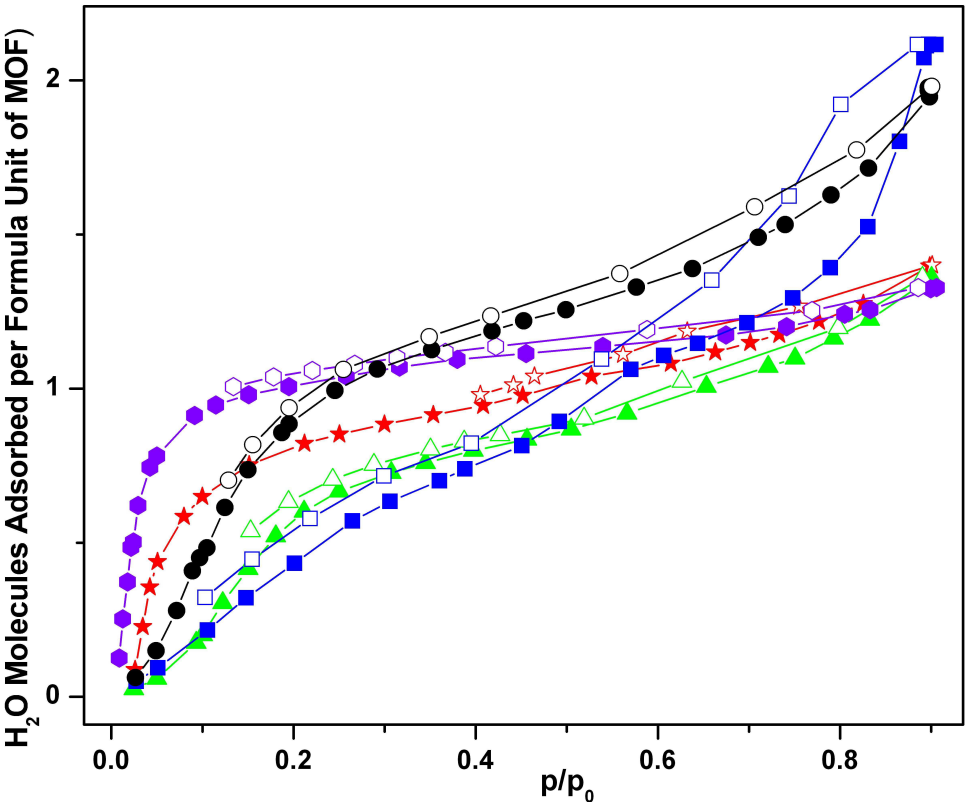

Figure S25. H_2O adsorption (solid symbols) and desorption (empty symbols) isotherms for the thermally activated **1-Cl** (black, circles), **2-Br** (blue, squares), **3-CH_3** (green, triangles), **4-NO_2** (red, stars), and Al-MIL-53-NH_2 (violet, hexagons) measured at 25 °C.

Table S2. Elemental analyses for different forms of Al-MIL-53-X compounds.

Compound	Molecular Formula	$C_{obs.}$ / $C_{cal.}$ (%)	$H_{obs.}$ / $H_{cal.}$ (%)	$N_{obs.}$ / $N_{calc.}$ (%)
1-Cl-AS	[Al(OH)(BDC-Cl)]·0.85 (H_2BDC-Cl)	42.92 / 43.03	2.05 / 2.01	-
1-Cl-DMF	[Al(OH)(BDC-Cl)]·1.1(DMF)	42.01 / 42.02	3.57 / 3.65	4.60 / 4.77
1-Cl	[Al(OH)(BDC-Cl)]·0.5(H_2O)	38.35 / 38.19	1.97 / 2.00	-
2-Br-AS	[Al(OH)(BDC-Br)]·0.4 (H_2BDC-Br)·0.5(H_2O)	34.39 / 34.14	1.73 / 1.79	-
2-Br-DMF	[Al(OH)(BDC-Br)]·1.1(DMF)	36.79 / 36.94	3.43 / 3.20	4.30 / 4.19
2-Br	[Al(OH)(BDC-Br)]·0.5 (H_2O)	32.33 / 32.46	2.46 / 1.70	-
3-CH_3-AS	[Al(OH)(BDC-CH_3)]·0.9 (H_2BDC-CH_3)·0.2(H_2O)	52.94 / 53.19	3.59 / 3.34	-
3-CH_3-DMF	[Al(OH)(BDC-CH_3)]·1.1 (DMF)	48.64 / 48.83	4.74 / 4.89	5.10 / 5.09
3-CH_3	[Al(OH)(BDC-CH_3)]·0.1(H_2O)	48.23 / 48.27	3.09 / 3.24	-
4-NO_2-AS	[Al(OH)(BDC-NO_2)]·0.22 (H_2BDC-NO_2)·1.4(H_2O)	35.91 / 36.09	2.36 / 2.45	5.34 / 5.26
4-NO_2-DMF	[Al(OH)(BDC-NO_2)]·1.0 (DMF)	40.46 / 40.50	3.57 / 3.39	8.39 / 8.58
4-NO_2	[Al(OH)(BDC-NO_2)]·0.6(H_2O)	36.35 / 36.40	1.77 / 1.99	5.23 / 5.30
5-$(OH)_2$-AS	[Al(OH)(BDC-$(OH)_2$)]·0.7 (H_2BDC-$(OH)_2$)	43.45 / 43.12	2.31 / 2.44	-
5-$(OH)_2$-DMF	[Al(OH)(BDC-$(OH)_2$)]·1.0 (DMF)	41.93 / 42.18	3.96 / 3.86	4.68 / 4.47
5-$(OH)_2$-H_2O	[Al(OH)(BDC-$(OH)_2$)]·5.5 (H_2O)	28.57 / 28.32	4.53 / 4.75	-
5-$(OH)_2$	[Al(OH)(BDC-$(OH)_2$)]·1.0 (H_2O)	37.27 / 37.22	2.74 / 2.73	-

Table S3. Frequencies of infrared bands[a] for different forms of Al-MIL-53-X compounds.

Compound	Infrared Frequencies (cm^{-1})
1-Cl-AS	3666 (w), 3426 (br), 2648 (w), 2523 (w), 1704 (s), 1615 (vs), 1552 (w), 1489 (m), 1416 (vs), 1286 (m), 1249 (m), 1166 (w), 1129 (w), 1056 (w), 1009 (m), 910 (w), 842 (w), 774 (s), 659 (w), 597 (s), 519 (w), 482 (s)
1-Cl-DMF	3648 (w), 1667 (m), 1611 (vs), 1549 (w), 1490 (m), 1414 (vs), 1290 (w), 1254 (w), 1131 (w), 1086 (w), 1054 (w), 1003 (w), 911 (w), 853 (w), 840 (w), 775 (s), 755 (w), 653 (w), 590 (vs), 516 (w), 471 (vs), 439 (sh), 417 (w)
1-Cl	3672 (br), 1590 (vs), 1484 (m), 1407 (vs), 1377 (sh), 1291 (w), 1164 (w), 1105 (br), 1055 (w), 1003 (m), 915 (w), 838 (w), 775 (s), 752 (w), 587 (vs), 518 (m), 471 (s), 444 (sh)
2-Br-AS	3646 (br), 3085 (br), 1708 (w), 1611 (s), 1541 (m), 1502 (m), 1420 (vs), 1363 (w), 1285 (w), 1256 (w), 1009 (s), 913 (w), 850 (w), 769 (m), 748 (m), 731 (w), 659 (w), 597 (vs), 477 (vs)
2-Br-DMF	3431 (br), 2927 (w), 1668 (s), 1612 (vs), 1541 (w), 1491 (m), 1415 (vs), 1287 (w), 1255 (w), 1090 (m), 1044 (w), 1011 (m), 916 (w), 840 (s), 811 (w), 656 (sh), 589 (vs), 502 (sh), 472 (vs)
2-Br	3663 (br), 1598 (vs), 1542 (w), 1486 (m), 1414 (vs), 1371 (sh), 1286 (w), 1255 (w), 1161 (w), 1042 (sh), 1006 (s), 910 (w), 840 (w), 773 (s), 773 (w), 747 (w), 660 (sh), 858 (vs), 508 (w), 463 (vs)
3-CH_3-AS	3669 (w), 2976 (br), 2655 (br), 1691 (s), 1592 (vs), 1498 (m), 1421 (vs), 1387 (m), 1295 (m), 1262 (m), 1199 (w), 1009 (s), 989 (s), 905 (w), 852 (w), 797 (vs), 654 (w), 602 (vs), 539 (s), 472 (vs),
3-CH_3-DMF	2972 (w), 2930 (w), 1665 (s), 1602 (vs), 1497 (w), 1423 (vs), 1387 (m), 1299 (w), 1254 (w), 1218 (w), 1123 (w), 1083 (m), 838 (w), 797 (w), 775 (s), 653 (w), 598 (vs), 534 (m), 471 (s), 422 (w)
3-CH_3	2971 (w), 2933 (w), 1584 (s), 1495 (w), 1419 (vs), 1382 (m), 1294 (w), 1209 (w), 1101 (w), 985 (s), 840 (w), 797 (w), 770 (s), 594 (vs), 536 (m), 510 (m), 457 (s), 426 (sh)
4-NO_2-AS	3640 (br), 1709 (m), 1610 (s), 1540 (m), 1501 (m), 1420 (vs), 1401 (sh), 1364 (w), 1286 (w), 1254 (w), 1008 (s), 915 (w), 858 (w), 832 (w), 785 (m), 753 (m), 701 (w), 649 (w), 586 (vs), 477 (vs)
4-NO_2-DMF	3649 (w), 2929 (w), 2852 (w), 1671 (w), 1613 (s), 1539 (m), 1502 (m), 1419 (vs), 1400 (sh), 1306 (w), 1257 (w), 1136 (w), 1092 (w), 1015 (m), 916 (w), 834 (w), 811 (w), 782 (m), 751 (m), 731 (w), 702 (w), 653 (sh), 583 (vs), 459 (vs), 441 (sh)
4-NO_2	3627 (br), 1603 (vs), 1538 (m), 1498 (m), 1414 (vs), 1368 (sh), 1286 (w), 1254 (w), 1132 (br), 1073 (w), 1019 (m), 910 (w), 833 (w), 779 (m), 752 (m), 592 (s), 553 (s), 455 (vs)
5-$(OH)_2$-AS	3291 (br), 2979 (w), 1657 (m), 1601 (s), 1491 (m), 1460 (vs), 1391 (vs), 1230 (vs), 1186 (w), 1120 (m), 984 (w), 919 (w), 879 (m), 816 (s), 790 (s), 669 (sh), 639 (sh), 617 (sh), 597 (s), 453 (sh), 436 (s), 406 (sh)
5-$(OH)_2$-DMF	3295 (br), 3082 (w), 2931 (w), 2860 (w), 1668 (s), 1604 (s), 1494 (m), 1459 (vs), 1389 (vs), 1232 (vs), 1162 (w), 1127 (m), 1097 (m), 923 (w), 878 (m), 818 (s), 789 (s), 649 (vs), 614 (sh), 597 (sh), 451 (sh), 434 (vs), 402 (vs)
5-$(OH)_2$-H_2O	3276 (br), 3083 (w), 1604 (s), 1494 (m), 1459 (vs), 1389 (s), 1232 (s), 1121 (m), 911 (w), 876 (m), 812 (w), 789 (m), 667 (s), 620 (sh), 597 (s), 451 (sh), 428 (vs), 397 (sh)

5-$(OH)_2$	3630 (br), 3356 (m), 3076 (w), 1677 (w), 1579 (s), 1489 (sh), 1468 (vs), 1371 (vs), 1227 (vs), 1140 (sh), 1123 (m), 910 (w), 879 (m), 822 (s), 789 (s), 617 (s), 602 (sh), 551 (m), 445 (s), 430 (s), 394 (m)

[a] Abbreviations: s = strong; vs = very strong; m = medium, w = week, sh = shoulder.

Table S4. Selected infrared frequencies (cm^{-1}) for different forms of Al-MIL-53-X compounds and their assignments.

Compound	Asymmetric Stretching of $–CO_2$ Group	Symmetric Stretching of $–CO_2$ Group	Stretching of $–CO_2H$ Group	Carbonyl Stretching of DMF or DEF	C-H Stretching of $–CH_3$ Group	Stretching of -OH Group
1-Cl-AS	1611	1415	1706	-	-	3666
1-Cl-DMF	1615	1416	-	1667	-	3666
1-Cl	1588	1411	-	-	-	3660
2-Br-AS	1604	1421	1702	-	-	3647
2-Br-DMF	1615	1416	-	1672	-	3659
2-Br	1599	1416	-	-	-	3665
3-CH_3-AS	1592	1422	1691	-	2975, 2940	3671
3-CH_3-DMF	1598	1422	-	1664	2972, 2930	3676
3-CH_3	1587	1422	-	-	2969, 2934	3650
4-NO_2-AS	1609	1416	1708	-	-	3630
4-NO_2-DMF	1615	1422	-	1675	-	3650
4-NO_2	1604	1411	-	-	-	3630
5-$(OH)_2$-AS	1592	1461	-	1658		3640, 3303
5-$(OH)_2$-DMF	1598	1461	-	1669	-	3650, 3292
5-$(OH)_2$-H_2O	1598	1461	-	-	-	3636, 3330
5-$(OH)_2$	1576	1472	-	-	-	3638, 3352

[1] Loiseau, T.; Serre, C.; Huguenard, C.; Fink, G.; Taulelle, F.; Henry, M.; Bataille, T.; Férey, G. *Chem.-Eur. J.* **2004**, *10*, 1373.

Anhang 3

Supporting Information:

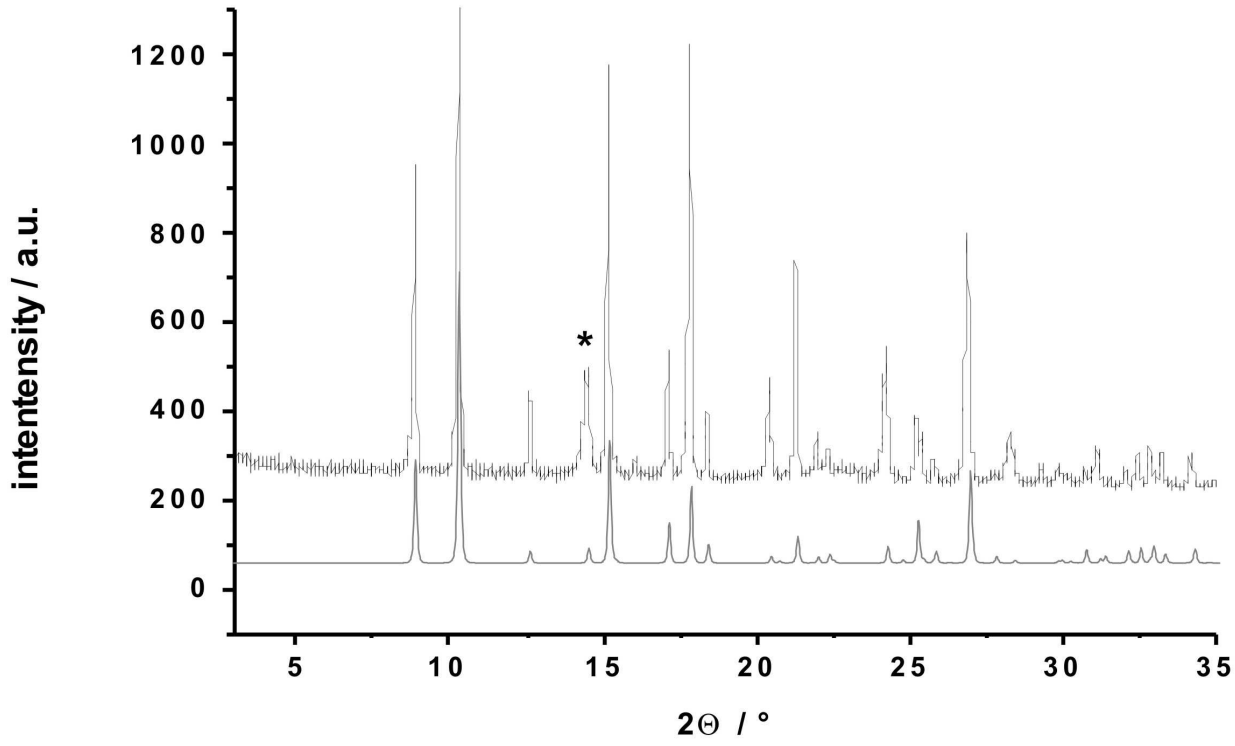

Figure S1: PXRD pattern of the as synthesized materials MIL-53(Al/Cr) (top) and MIL-53(Al)[19] (bottom). The reflection from minor impurities of γ-AlOOH is marked by an asterisk.

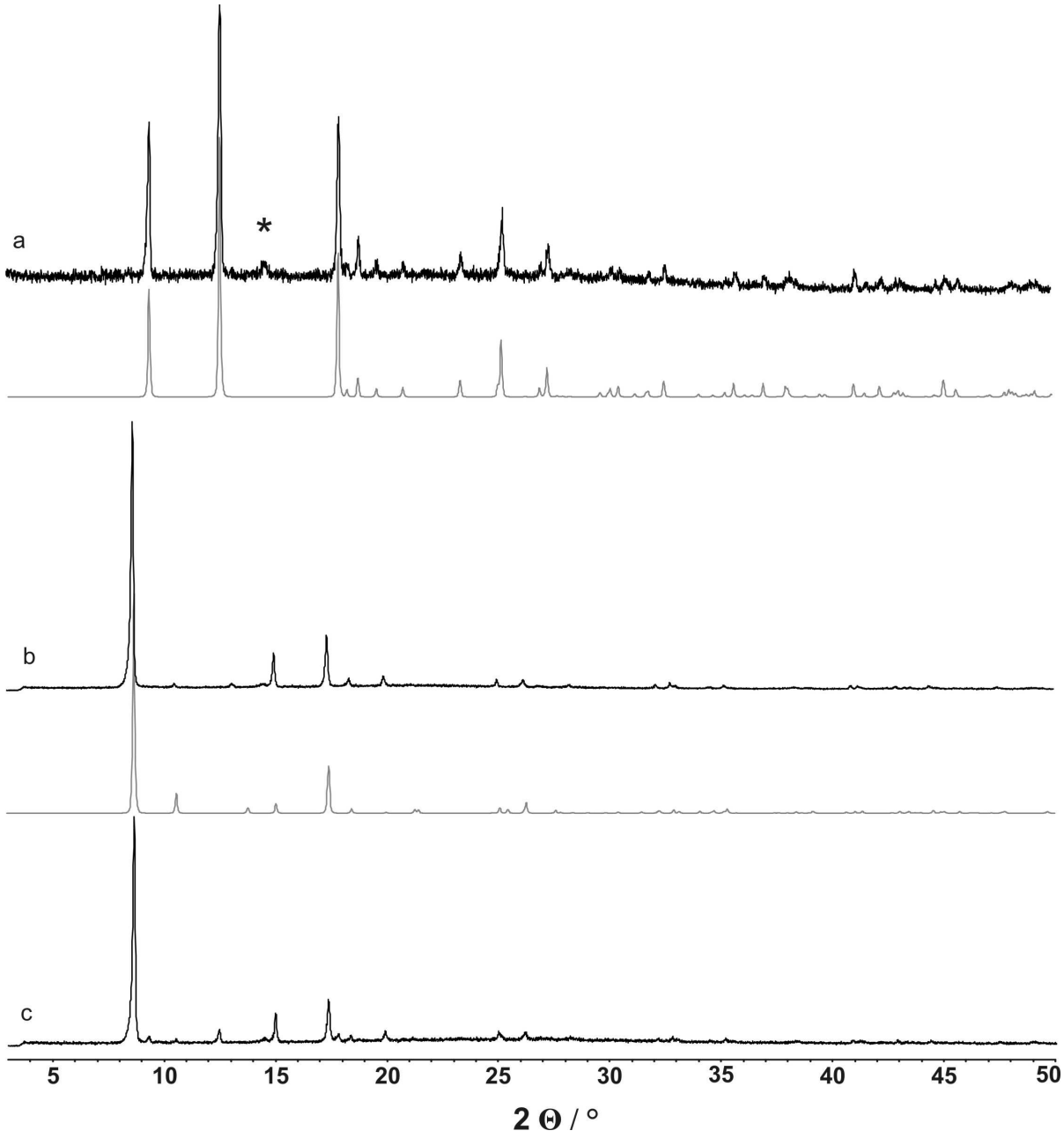

Figure S2: Powder XRD pattern of calcined MIL-53(Al/Cr): (a) kept under ambient conditions, (b) dehydrated and (c) dehydrated MIL-53(Al/Cr) after a complete set of EPR experiments. Grey lines show the powder XRD pattern of the LT and HT phase[19] of MIL-53(Al). The reflection from minor impurities of γ-AlOOH is marked by an asterisk.

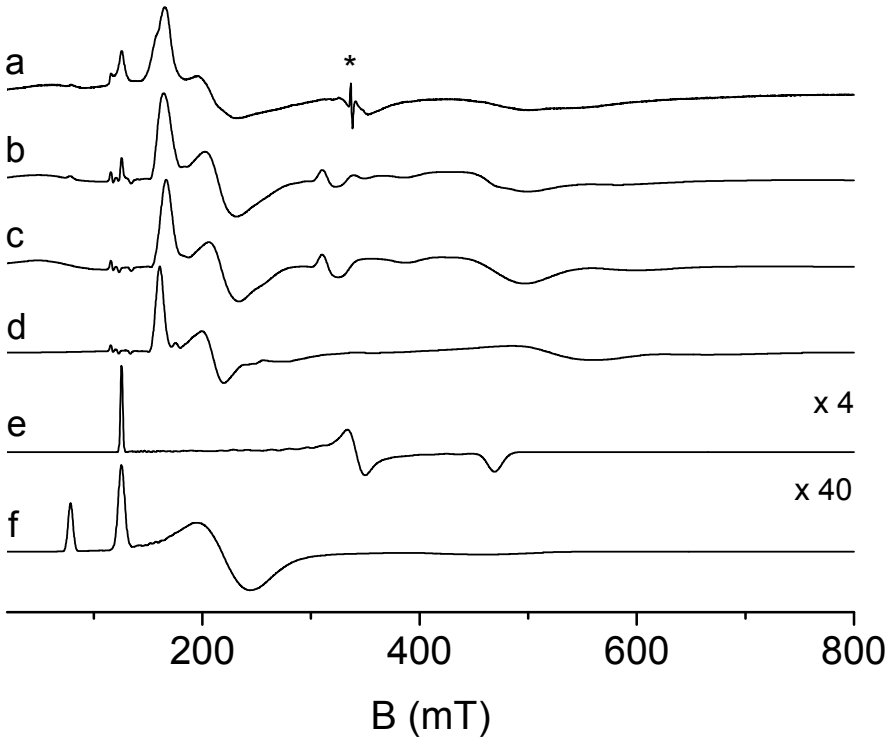

Figure S2: X-band ESR spectra of MIL-53(Al/Cr)as at 6 K: (a) experimental spectrum, (b) sum of simulated spectra, (c) species A(as), (d) species B(as), (e) species C(as), and (f) Fe^{3+} impurity species. The asterisk indicates a free radical signal. The simulation parameters of the Cr(III) species are given in Table I of the manuscript. The spin Hamiltonian parameters for the Fe(III) ions with $S = 5/2$ are $g = 2.003(2)$, $D > 30$ GHz, $E/D = 0.145(7)$, $\Delta E > 1.5$ GHz, relative contribution to total spectrum less than 1 %.

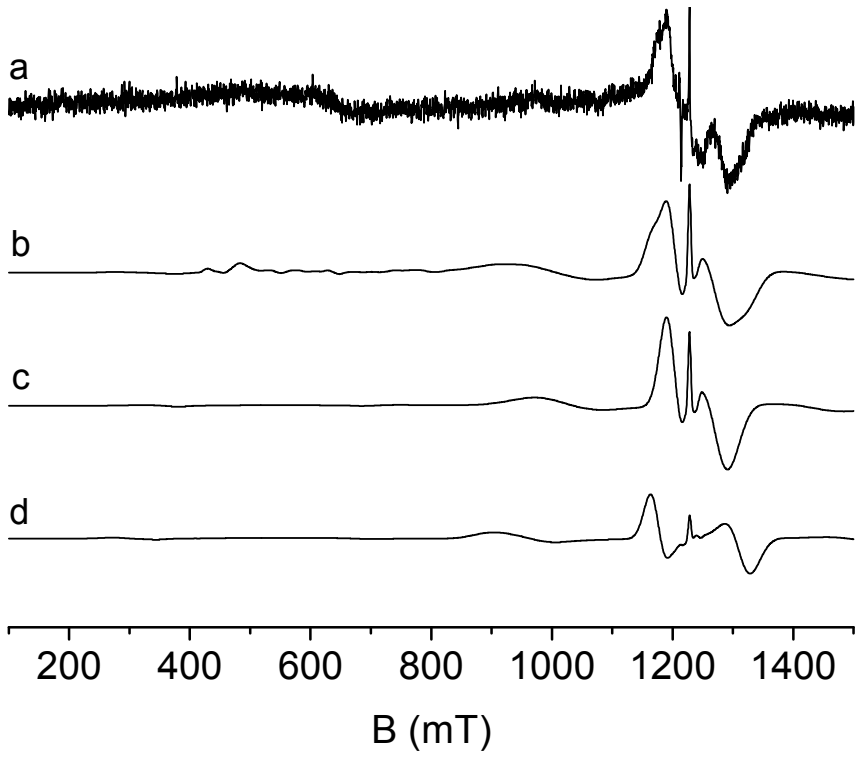

Figure S3: Q-band ESR spectra of MIL-53(Al/Cr)as at 295 K: (a) experimental spectrum, (b) sum of simulated Cr(III) spectra, (c) species A(as), and (d) species B(as). The simulation parameters of the Cr(III) species are given in Table I of the manuscript.

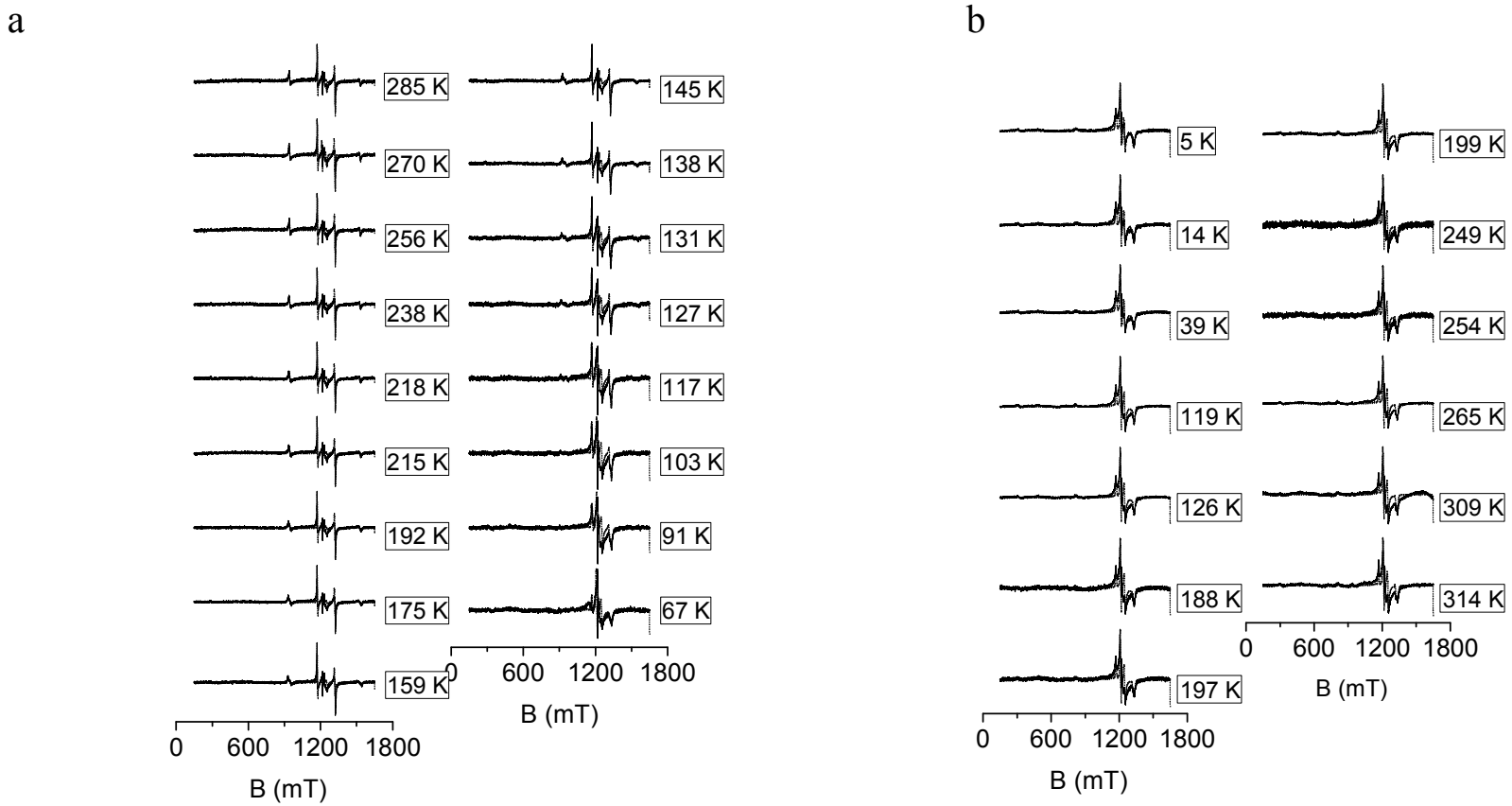

Figure S5: Temperature-dependent experimental (solid lines) and simulated (dashed lines) Q-band ESR spectra of MIL-53(Al/Cr)deh at Q-band for (a) decreasing and (b) increasing temperatures .

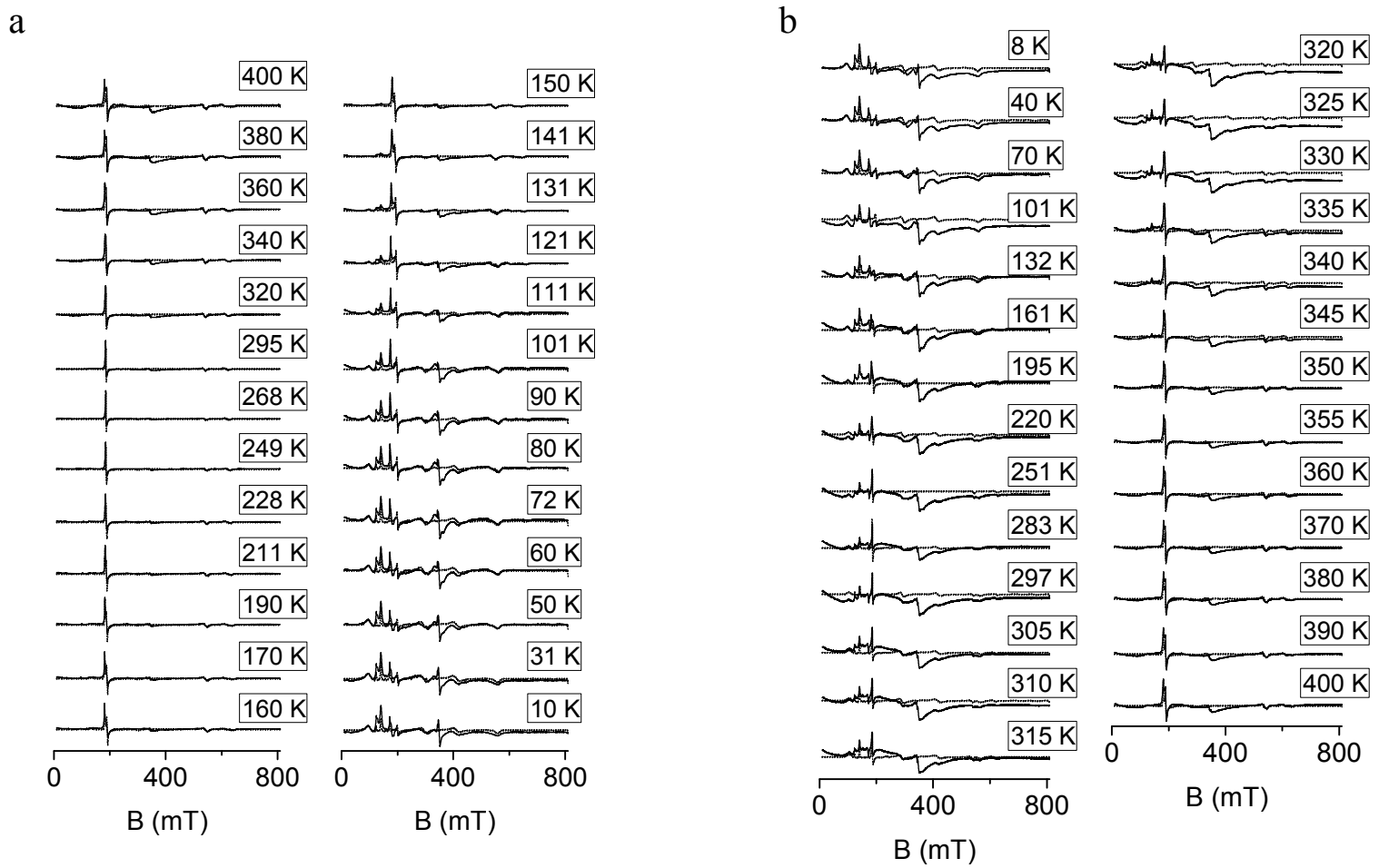

Figure S6: Temperature-dependent experimental (solid lines) and simulated (dashed lines) Q-band ESR spectra of MIL-53(Al/Cr)deh at X-band for (a) decreasing and (b) increasing temperatures .

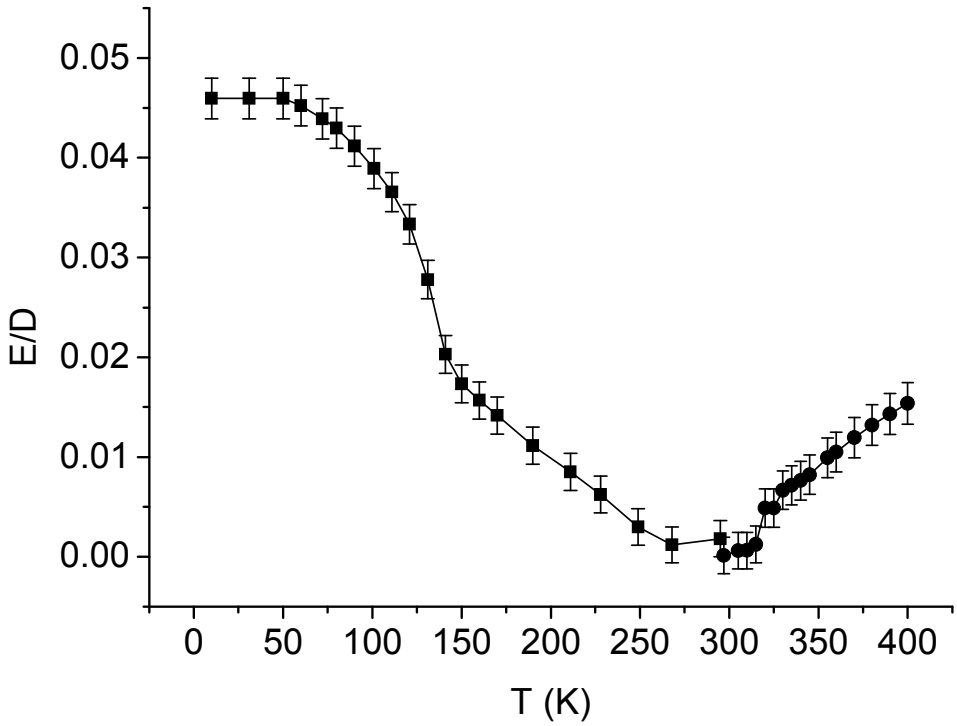

Figure S7: Temperature dependence of the ratio *E*/*D* of the Cr(III) ions in the HT phase of MIL-53(Al/Cr)deh. No hysteresis effects have been observed for the ratio *E*/*D*.

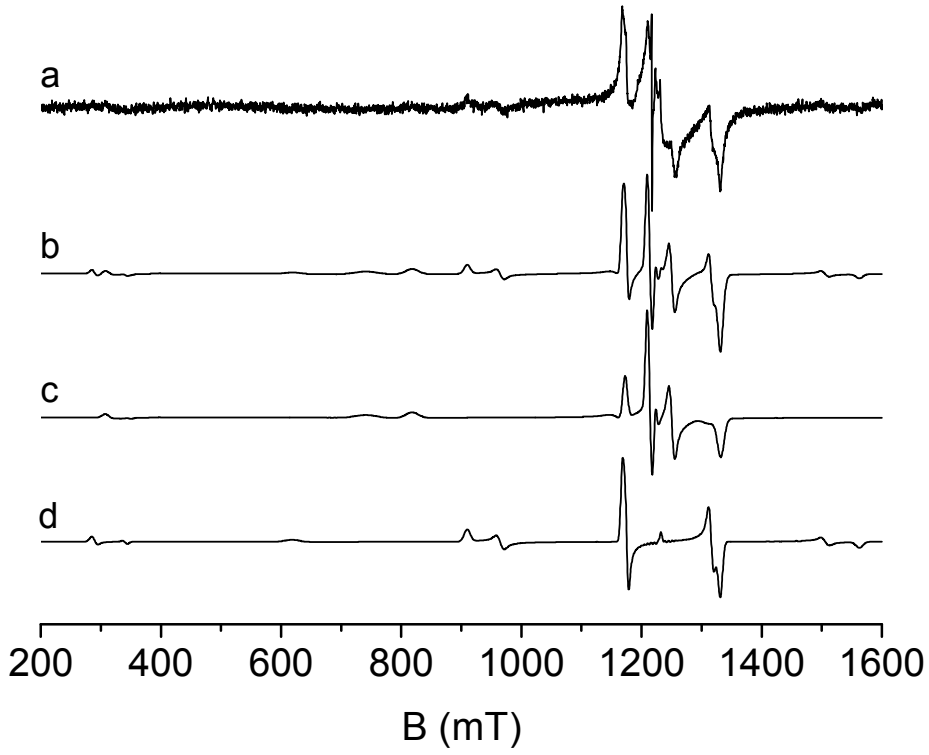

Figure S8. Q-band ESR spectra of MIL-53(Al/Cr)deh at 117 K showing the superposition of the Cr(III) ESR spectra from the HT and LT phases: (a) experimental spectrum, (b) sum of simulated Cr(III) spectra, simulated Cr(III) spectrum of (c) LT and (d) HT phase.

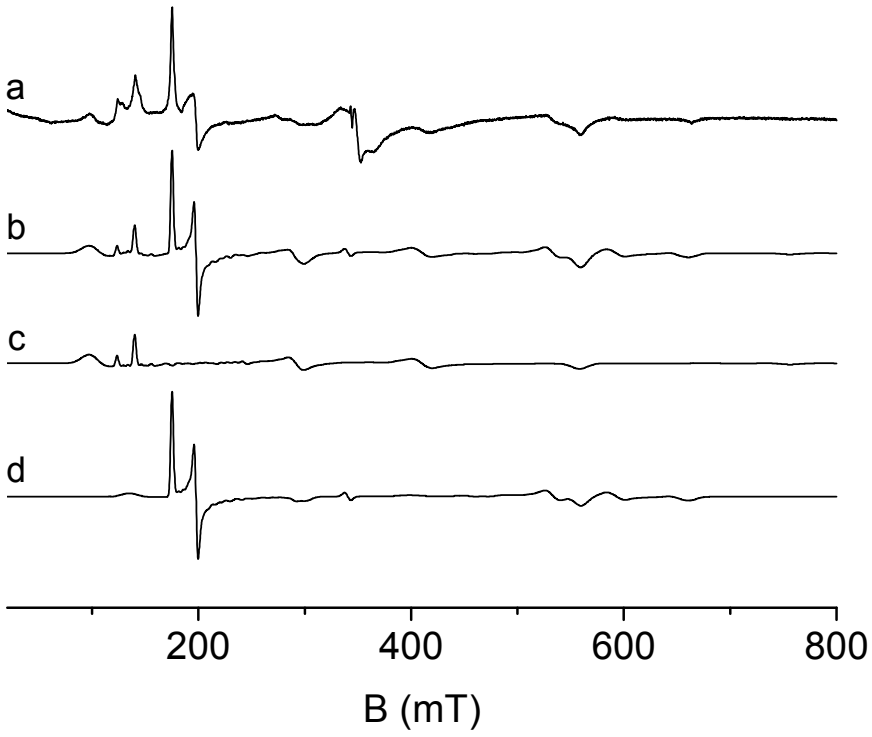

Figure S9. X-band ESR spectra of MIL-53(Al/Cr)deh at 111 K showing the superposition of the Cr(III) ESR spectra from the HT and LT phases: (a) experimental spectrum, (b) sum of simulated Cr(III) spectra, simulated Cr(III) spectrum of (c) LT and (d) HT phase.

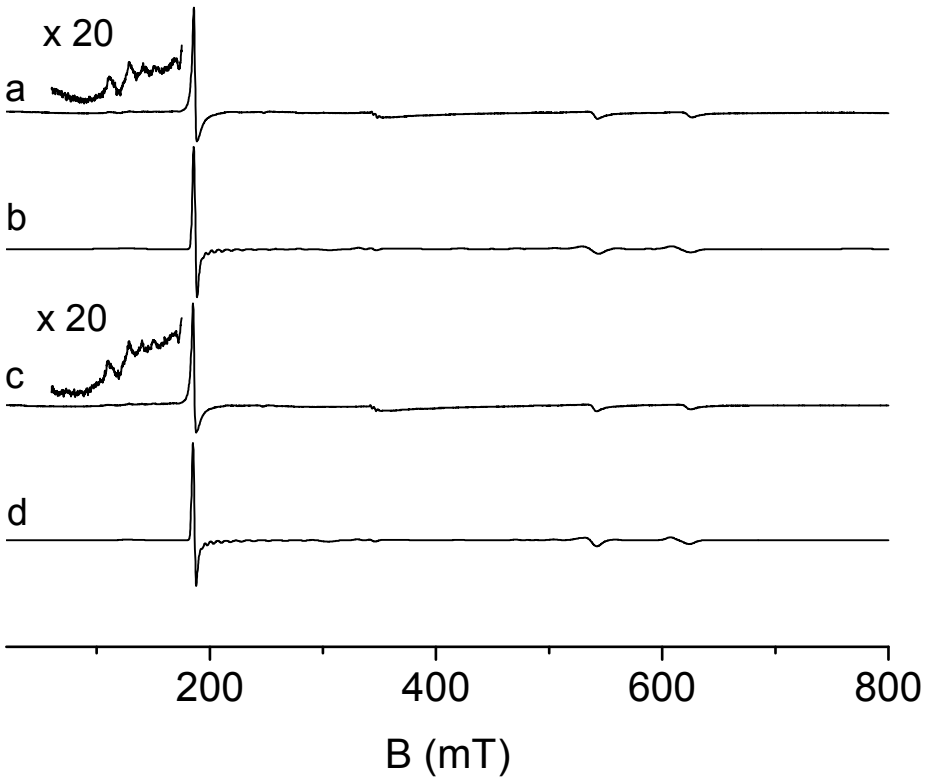

Figure S10. X-band ESR spectra of MIL-53(Al/Cr)deh in the HT phase recorded at 295 K: (a) experimental and (b) simulated Cr(III) spectra recorded before the hysteresis cycle, (c) experimental and (d) simulated Cr(III) spectra recorded after a full hysteresis cycle. The amplified spectral regions show the signature signals of Cr(III) ions from a minor LT phase fractions that seems to be unaffected by the thermal hysteresis.

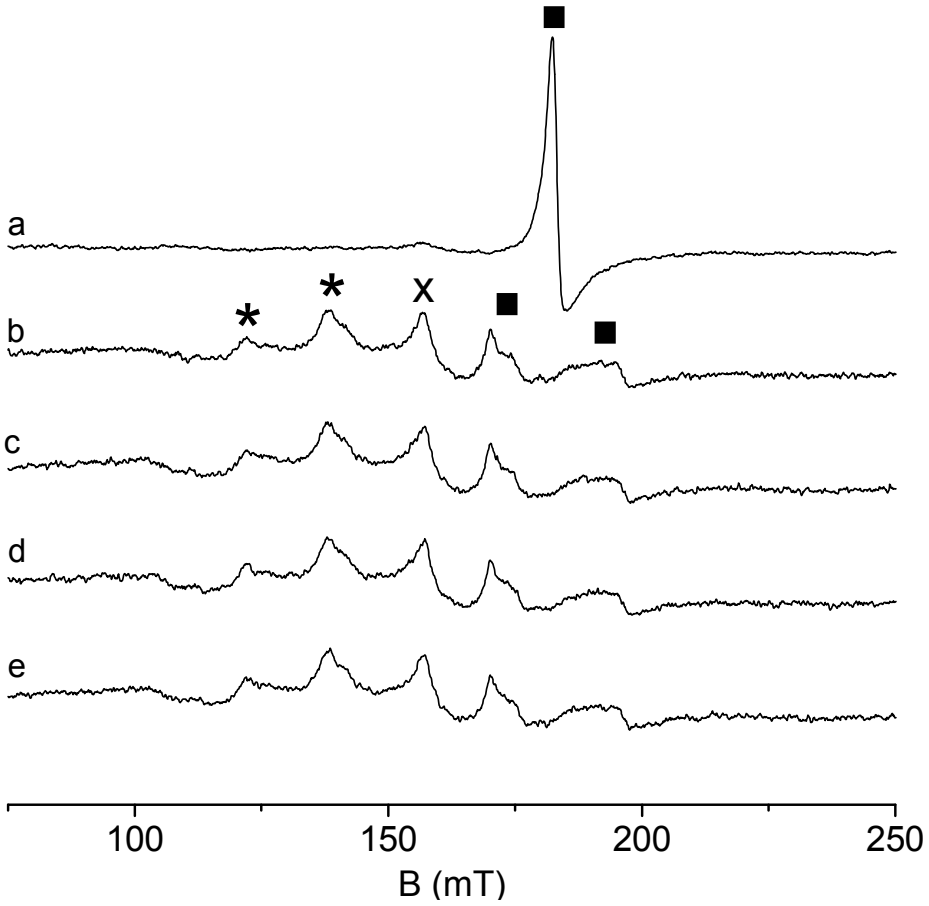

Figure S11. X-band ESR spectra of MIL-53 (Al/Cr) deh recorded (a) at 295 K in the HT phase and at 77 K measured (b) 3 min, (c) 18 min, (d) 33 min, and (e) 43 min after exposing the sample to low temperatures. Squares and asterisks indicate signals of Cr(III) ions in the HT and LT phases, respectively. The line indicated by a cross is an impurity high spin Fe(III) signal from the cryostat.

Anhang 4:

Supporting Information

CAU1 - A new 12-connected porous metal-organic framework with an unprecedented Al-containing brick: $[Al_4(OH)_2(OCH_3)_4(H_2N\text{-}BDC)_3]\cdot xH_2O$

Tim Ahnfeldt,[a] Nathalie *Guillou,*[b] *Daniel Gunzelmann,*[c] *Thierry Loiseau,*[b] *Gerard Férey,*[b] *Jürgen Senker,*[c] *and Norbert Stock*[*,a]

[a] Institute of Inorganic Chemistry, Christian-Albrechts-Universität, Otto-Hahn-Platz 6/7, 24118 Kiel, Germany

[b] Institut Lavoisier, UMR CNRS 8180, Université de Versailles St-Quentin en Yvelines, 45 Avenue des Etats-Unis, 78035 Versailles, France

[c] Inorganic Chemistry I, University of Bayreuth, Universitätsstr. 30, 95447 Bayreuth Germany

(1) General Information

Chemicals. $AlCl_3 \cdot 6H_2O$ (Riedel-de Haen, ≥99%), $Al(NO_3)_3 \cdot 9H_2O$ (Merk, ≥99%), $H_2N\text{-}H_2BDC$ (Fluka, ≥98%), methanol (BASF, purum), acetonitrile (Riedel-de Haen, ≥99%), ethanol (Walter, abs. 99%), and N,N-dimethyl-formamide (BASF, tech.) were used as purchased.

Reactions were carried out using our 24-high-throughput reactor system.[1] The high-throughput X-ray analyses were performed in transmission geometry using a STOE HT powder diffractometer equipped with a xy-stage and a linear position sensitive detector (PSD) system using monochromated Cu-Kα1 radiation. MIR spectra were recorded on an ATI Matheson Genesis spectrometer in the spectral range of 4000-400 cm^{-1} using the KBr disk method. FT-Raman spectra were recorded on a Bruker IFS 66 FRA 106 in the range of 0-3300 cm^{-1} using a Nd/YAG-Laser (1064 nm). The thermogravimetric analysis was recorded using an NETSCH STA 409 CD analyzer. The samples were heated to 900°C in Al_2O_3 crucibles at a rate of 4 K min^{-1} under a flow of air (75 ml min^{-1}). The TG data were corrected for buoyancy and current effects. Nitrogen sorption experiments were performed using a BEL JAPAN INC. $Belsorp_{max}$ at 77 K. For the sorption experiments CAU-1 was heated over night at 130 °C in vacuum (10^{-3} mbar)

(2) Measured and simulated powder XRD patterns of the phases observed in this study The discovery library lead to the formation of four different phases. In addition to pure phase Al-MIL-53-NH_2 (Fig. S1a) a mixture of Al-MIL-101-NH_2 and Al-MIL-53-NH_2 (Fig. S1b) is observed. Due to the breathing effect of MIL-53 the position of the reflexes of the simulated powder pattern vary from both measured powder pattern. In experiment TA25_10, containing a reaction mixture of methanol, $AlCl_3 \cdot 6H_2O$ and aminoterephthalic acid, poorly crystalline CAU-1, can be observed (Fig. S1c). At a molar ratio Al^{3+} : $H_2N\text{-}H_2BDC$ = 1 : 1, an unknown phase is formed in addition to CAU-1 which exhibits a reflection at 4.2 °(2θ) (Fig. S1d). The powder patterns in Fig. S1e and Fig. S1f summarize the results of the synthesis optimization of Al-MIL-101-NH_2 and CAU-1. Crystalline MIL-101 was obtained at very low concentrations of the reaction mixture. Highly crystalline CAU-1 is formed at a molar ratio $Al^{3+}/H_2N\text{-}H_2BDC$ = 3 : 1.

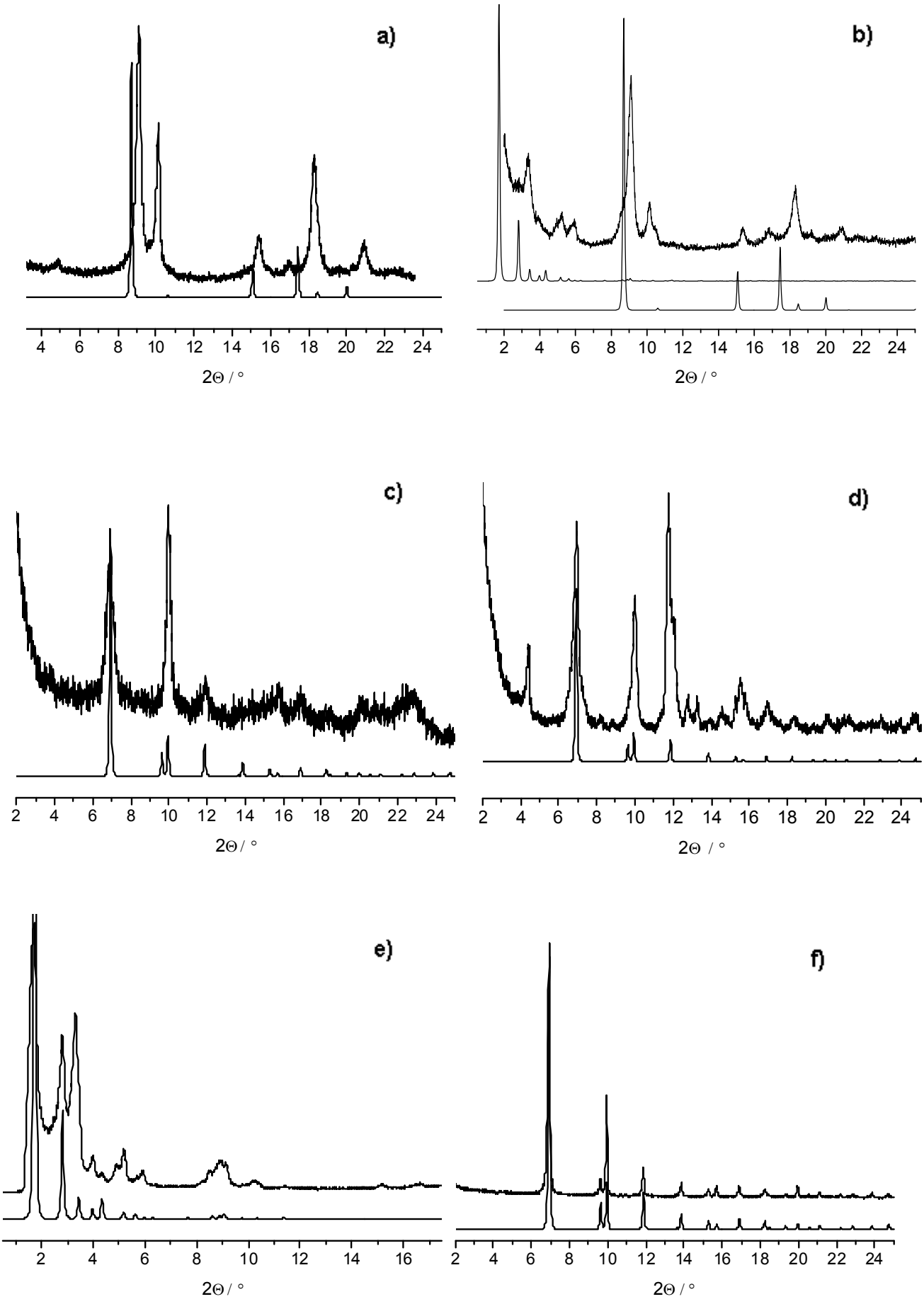
a)
b)
c)
d)
e)
f)
2Θ / °

Figure S1. XRD patterns of the four phases observed in the high-throughput investigation of the system Al^{3+} / H_2N-H_2BDC / solvent at a reaction temperature of 125 °C. Fig. S1a, top: TA25_1 (Al-MIL-53-NH_2 (DMF)), bottom: sim. Al-MIL-53.[2] Due to the breathing effect of MIL-53-NH_2 the position of the reflexes of the simulated powder pattern vary from the measured powder pattern. Fig. S1b, top: TA25_6 (mixture of Al-MIL101-NH_2 and Al-MIL-53-NH_2), middle: sim. Cr-MIL-101[8], bottom: sim. Al-MIL-53.[2] Fig. S1c, top: TA25_10 (CAU-1), bottom: sim. CAU-1. Fig. S1d, top: TA25_11 (mixture of CAU-1 and an unknown phase), bottom: sim. CAU-1. Fig. S1e, top: optimized Al-MIL-101-NH_2, bottom: sim. Cr-MIL-101[8]. Fig. S1f, top: optimized CAU-1, bottom: sim. CAU-1.

(3) Result of the Rietveld Refinement

High-precision X-ray powder diffraction data were collected on ID31 of the ESRF from powdered sample contained in a 1 mm diameter glass capillary (see manuscript, Figure 3). The beamline receives X-rays from the synchrotron source (which operates with an average energy of 6 GeV and a current beam of typically 100 mA) from an undulator device. The incident X-ray wavelength was 0.79989667 Å using an incident beam size of 2.0 mm (horizontal) × 1.0 mm (vertical). The sample was rapidly spun during data collection to ensure good powder averaging. Extractions of the peak positions, pattern indexing, Fourier calculations and Rietveld refinements were carried out with the TOPAS program.[3] A tetragonal unit was found unambiguously with satisfactory figure of merit (*GoF* = 110) using the LSI-Indexing method. Systematic extinctions were consistent with the *I* Bravais lattice and the *I*4/*mmm* space group was chosen to solve the structure. A list of 823 reflections was extracted in the angular range 1 – 45 °(2θ). According to the degree of diffraction overlap, 42.39 % of these reflections were statistically considered as independent and the whole structural model (except for disordered N atoms of the carboxylate groups) was found unambiguously from the E-map with the highest figure of merit. The atomic coordinates were then used as the starting model in the Rietveld refinement. O2 located at about 1.5 Å from another Fourier peak was assigned to an oxygen atom of a methanol group. N atoms were then found by difference Fourier calculations as disordered on the four possible positions for the both independent organic moieties. The occluded water molecule was first located away from the framework on a 4*e* Wyckoff position, but a strong residual peak remained on the difference Fourier map near this position on a 16*n* site. It was assumed that the water molecule was in fact disordered on this 16*n* Wyckoff position with ¼ occupancy. That allowed decreasing significantly the R_{Bragg} value and led to hydrogen interactions between Ow1 and the bridging hydroxyl O1. At the final stage, Rietveld refinement involved the following parameters: 30 atomic coordinates, 5 thermal factors, 1 scale factor, 1 zero point, 2 cell parameters, 20 background parameters and 8 ones to model the evolution of diffraction lines shape. The anisotropic line

broadening effect was modeled by using spherical harmonics series combined with the Finger *et al.* asymmetric model. Soft restraints were maintained on the C-N and some few C-C bond lengths and C-C-N angles. The final Rietveld plot (Figure 3) corresponds to satisfactory crystal structure model indicator (R_{Bragg} = 0.025) and profile factors (R_P = 0.053 and R_{WP} = 0.070).

(4) IR- and Raman-Spectroscopy

CAU-1 was characterized by IR and Raman spectroscopy (Figure S2). The incorporation of aminoterephthalic acid in CAU-1 is supported by the C=O vibrations at 1600 cm^{-1} and 1430cm^{-1}. The presence of uncoordinated aminoterephthalic acid can excluded since no vibration around 1700 cm^{-1} is observed. The aliphatic C-H stretching-vibrations of the methoxy group occurs around 2900 cm^{-1}. The typical bands for the NH_2 group at 3497 and 3385 cm^{-1} are not observed due to the presence of water molecules which could also be involved in N-H···O hydrogen bonding.

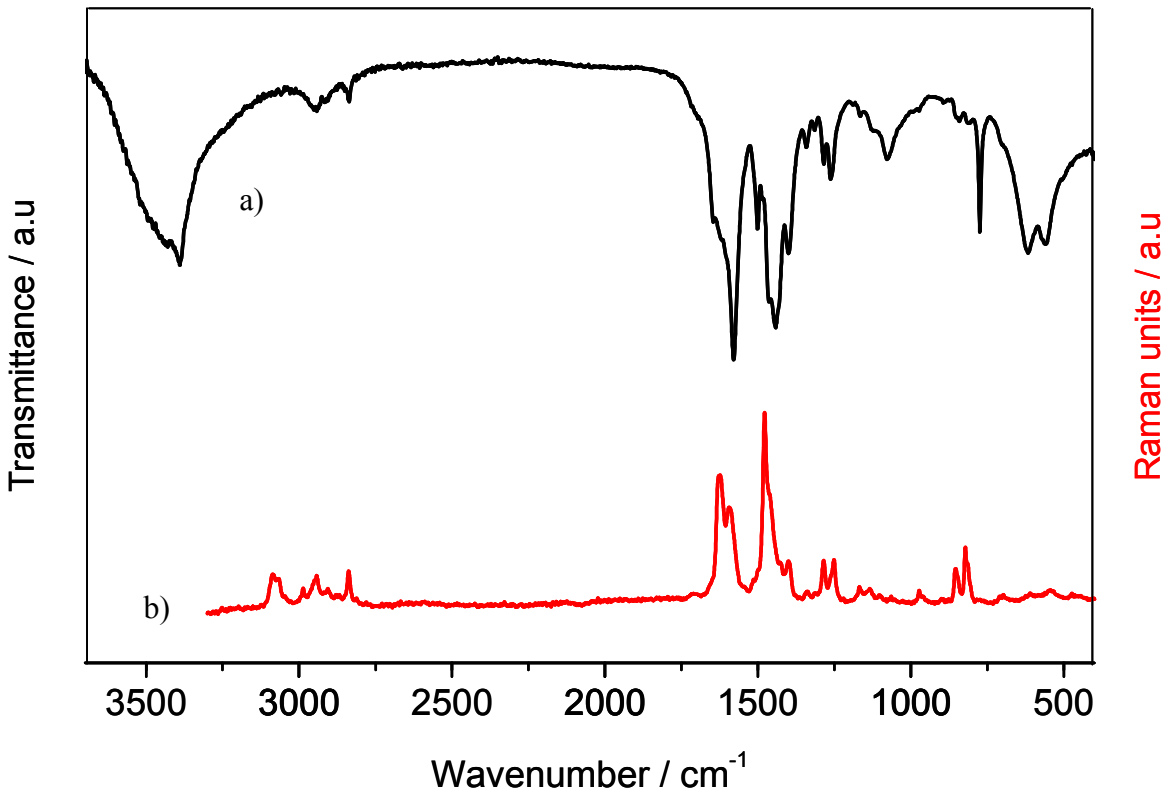

Figure S2. IR-spectrum (top) and Raman-spectrum (bottom) of CAU-1.

(5) Solid-State NMR-Spectroscopy

The ^{1}H, ^{13}C, and ^{15}N MAS NMR spectra of CAU-1 are displayed in Figure S3a), b) and c). The ^{1}H spectrum (S3 a) exhibits two signals at δ = 2.9 and ~7 ppm. The high-field signal can be attributed to the edge-bridging methanolate and the corner-bridging hydroxide groups as well as the incorporated water molecules. The low-field resonances were assigned to the aromatic CH atoms and the NH_2-groups of the aminoterephthalate units, respectively. The ^{13}C NMR spectrum of CAU-1 exhibits one signal at δ = 48 due to the methanolate groups, six between δ = 152 and 115 ppm due to the C atoms of the phenyl ring and one signal at δ = 172 ppm which is due to the carboxylate groups. The signals marked by an asterix (*) are due to rotational side bands. The signal at 27 ppm could not be assigned up to now. The ^{15}N NMR spectrum of CAU-1 exhibit a signal in the region of δ = -325 to -330 ppm, which can be unequivocally assigned to a NH_2–group.

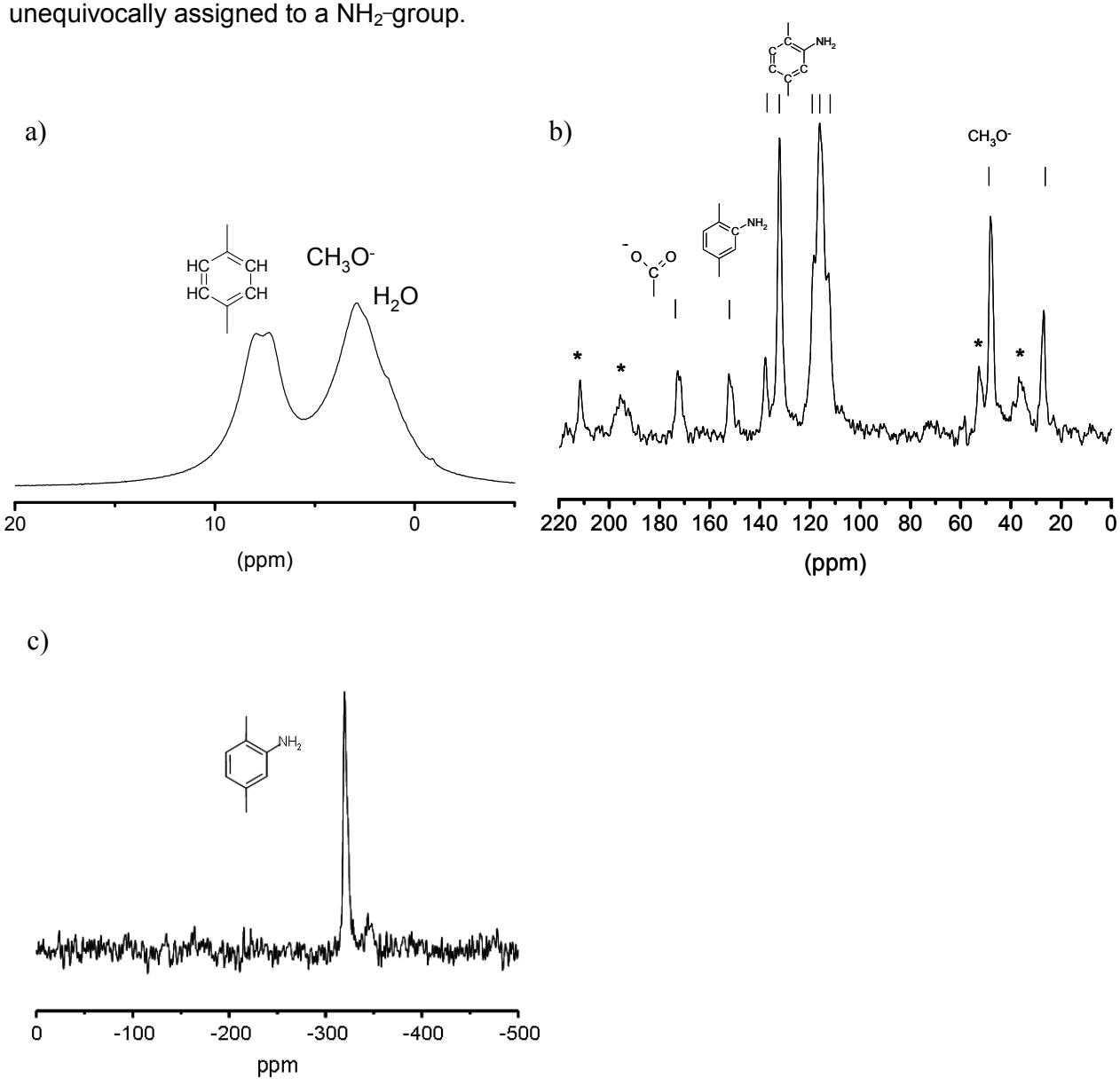

Figure S3. NMR spectra of CAU-1 (a) ^{1}H, (b) ^{13}C, (c) ^{15}N.

(6) Thermal Analysis

The thermal stability of CAU-1 was investigated in air atmosphere up to 800°C with a heating rate of 4 K min^{-1} (Figure S4). The first loss of -6% is due to incorporated water molecules and corresponds to the loss of three mol of water per formula unit (calc. -6.3%). At higher temperatures, the decomposition of the frameworks begins and at the end of the measurement Al_2O_3 is formed (total weight loss, obs. 76%, calc. 76.1). The water content of CAU-1 varies considerably depending on the actual environment (temperature, humidity, etc.) in the lab. The results of this thermal analysis are in good agreement with the temperature depending X-ray experiment and the CHN-analysis.

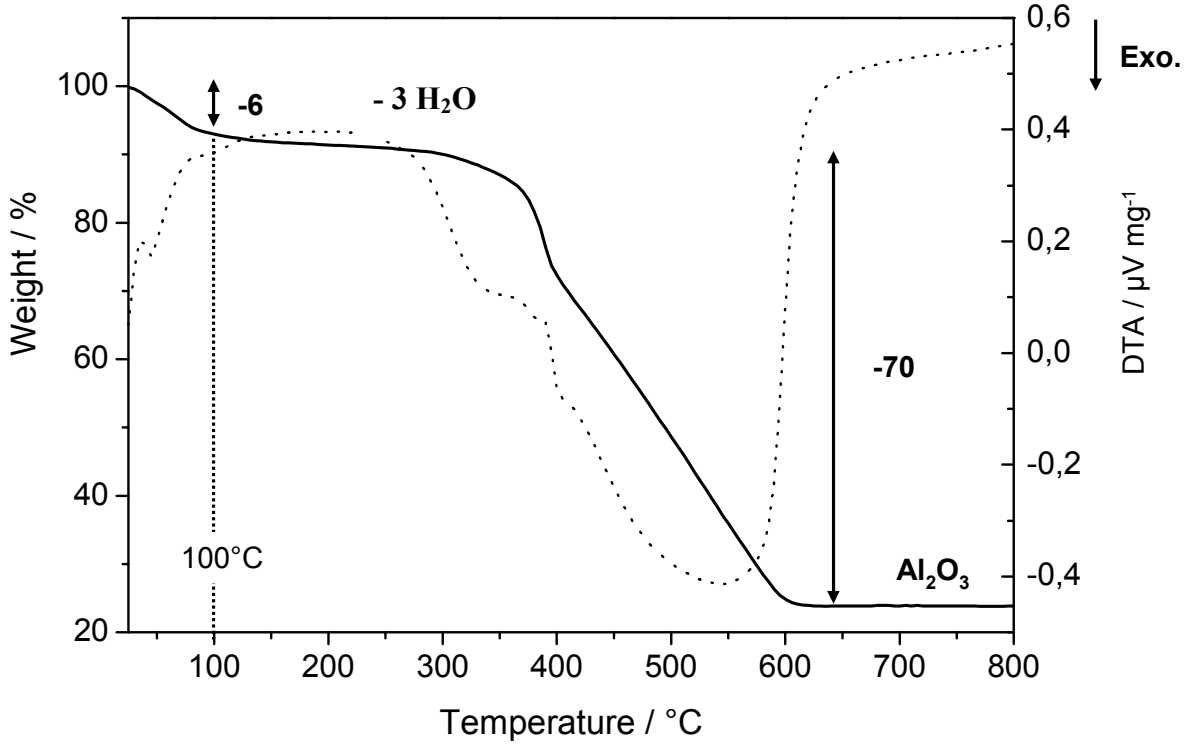

Figure S4. TG investigation of $[Al_4(OH)_2(OCH_3)_4(H_2N\text{-}BDC)_3]\cdot xH_2O$ in air (heating rate of 4 K min^{-1}).

(7) List of High-Throughput Reactions

Table S3. Discovery library: molar ratios and dispensed amounts of the high-throughput investigation of the system Al^{3+} / H_2N-H_2BDC / solvent at a reaction temperature 125 °C and a reaction time of 5 h.

Sample	Al : H_2N-H_2BDC	H_2N-H_2BDC / mg (mmol)	$AlCl_3 \cdot 6H_2O$/ mg (mmol)	$Al(NO_3)_3 \cdot 9H_2O$/ mg (mmol)	Solvent 1.235 mL
TA25_1	2 : 1	11.7 (0.064)		48.0 (0.128)	DMF
TA25_2	1 : 1	23.2 (0.128)		48.0 (0.128)	DMF
TA25_3	1 : 2	69.7 (0.384)		72.0 (0.192)	DMF
TA25_4	2 : 1	11.7 (0.064)	31.1 (0.128l)		DMF
TA25_5	1 : 1	23.2 (0.128)	31.1 (0.128)		DMF
TA25_6	1 : 2	69.7 (0.384)	46.4 (0.2)		DMF
TA25_7	2 : 1	11.7 (0.064)		48.0 (0.128)	MeOH
TA25_8	1 : 1	23.2 (0.128)		48.0 (0.128)	MeOH
TA25_9	1 : 2	69.7 (0.384)		72.0 (0.192)	MeOH
TA25_10	2 : 1	11.7 (0.064)	31.1 (0.1)		MeOH
TA25_11	1 : 1	23.2 (0.128)	31.1 (0.1)		MeOH
TA25_12	1 : 2	69.7 (0.384)	46.4 (0.2)		MeOH
TA25_13	2 : 1	11.7 (0.064)		48.0 (0.128)	EtOH
TA25_14	1 : 1	23.2 (0.128)		48.0 (0.128)	EtOH
TA25_15	1 : 2	69.7 (0.384)		72.0 (0.192)	EtOH
TA25_16	2 : 1	11.7 (0.064)	31.1 (0.1)		EtOH
TA25_17	1 : 1	23.2 (0.128)	31.1 (0.1)		EtOH
TA25_18	1 : 2	69.7 (0.384)	46.4 (0.2)		EtOH
TA25_19	2 : 1	11.7 (0.064)		48.0 (0.128)	Acetonitril
TA25_20	1 : 1	23.2 (0.128)		48.0 (0.128)	Acetonitril
TA25_21	1 : 2	69.7 (0.384)		72.0 (0.192)	Acetonitril
TA25_22	2 : 1	11.7 (0.064)	31.1 (0.1)		Acetonitril
TA25_23	1 : 1	23.2 (0.128)	31.1 (0.1)		Acetonitril
TA25_24	1 : 2	69.7 (0.384)	46.4 (0.2)		Acetonitril

For the synthesis optimization of CAU-1 a focused library was set up and the molar ratio $AlCl_3 \cdot 6H_2O$: H_2N-H_2BDC as well as the overall concentration of the starting materials were varied (Table S4). The crystallinity of the resulting products changes drastically. Very crystalline CAU-1 was obtained at a molar ratio $AlCl_3 \cdot 6H_2O$: H_2N-H_2BDC = 3 : 1. The overall concentration has also a strong effect on the product formation and the higher concentrations lead to an increase of crystallinity of CAU-1.

Table S4. Molar ratios and dispensed amounts of the high-throughput synthesis optimization of CAU-1 at a reaction temperature of 125 °C and a reaction time of 5 h.

Sample	Al : H_2N-H_2BDC	H_2N-H_2BDC / mg (mmol)	$AlCl_3 \cdot 6H_2O$/ mg (mmol)	Concentration	Methanol
TA84_1	4 : 1	5.8 (0.032)	31.1 (0.128l)	x1	1.235 mL
TA84_2	3 : 1	7.3 (0.043)	31.1 (0.128)	x1	1.235 mL
TA84_3	2 : 1	11.6 (0.064)	31.1 (0.128)	x1	1.235 mL
TA84_4	1 : 1	23.2 (0.128)	31.1 (0.128)	x1	1.235 mL
TA84_5	1 : 2	23.2 (0.128)	15.5 (0.064)	x1	1.235 mL
TA84_6	1 : 3	23.2 (0.128)	10.4 (0.043)	x1	1.235 mL
TA84_7	1 : 4	23.2 (0.128)	7.8 (0.032)	x1	1.235 mL
Sample	Al : H_2N-H_2BDC	H_2N-H_2BDC / mg (mmol)	$AlCl_3 \cdot 6H_2O$/ mg (mmol)	Concentration	Solvent
TA84_10	1 : 1	46.4 (0.256)	62.2 (0.256)	x2	1.235 mL
TA84_11	1 : 1	92.8 (0.512)	124.4 (0.512)	x4	1.235 mL
TA84_12	1 : 1	11.6 (0.064)	15.5 (0.64)	x0.5	1.235 mL
TA84_13	1 : 1	5.8 (0.032)	7.8 (0.032)	x0.25	1.235 mL
TA84_14	1 : 1	2.3 (0.013)	3.1 (0.013)	x0.01	1.235 mL

(8) Description of the crystal structure of $[Al_4(OH)_2(OCH_3)_4(H_2N\text{-}BDC)_3]\cdot xH_2O$

The structure of CAU-1 contains 8-ring units composed of eight distorted AlO_6-octahedra that are connected through hydroxide groups (corner-sharing) and two methanolate groups (edge-sharing) (Fig. S5). These wheel-shaped 8-rings are connected through 12 phenyl rings to 12 other 8-rings. Thus a 12-connected net is formed. The arrows in Figure S5 indicate the direction of the connection. The arrangement of the 8-rings can be derived from the (tetragonally distorted) cubic centered packing motive. The positions of the metal ions are occupied by the 8-ring units (Fig. S6). This arrangement leads to the formation of distorted octahedral and tetrahedral holes (Fig. S6 and S7). Thus, per unit cell two octahedral and four tetrahedral holes are formed (Fig. S7). The connection between the 8-ring units is accomplished by the phenyl ring (Fig. S8) and the final structure (Fig. S9) is formed.

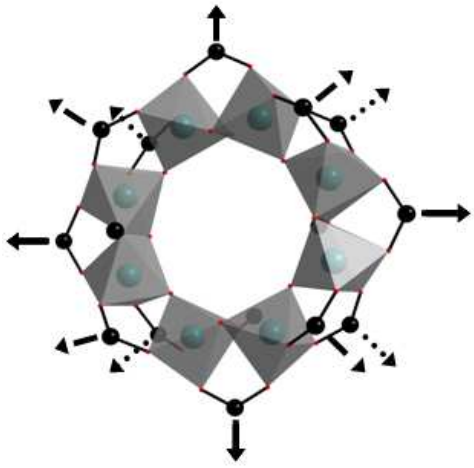

Figure S5. 8-ring unit of corner-sharing (μ-OH) and edge-sharing (μ-OCH_3) AlO_6 octahedra.

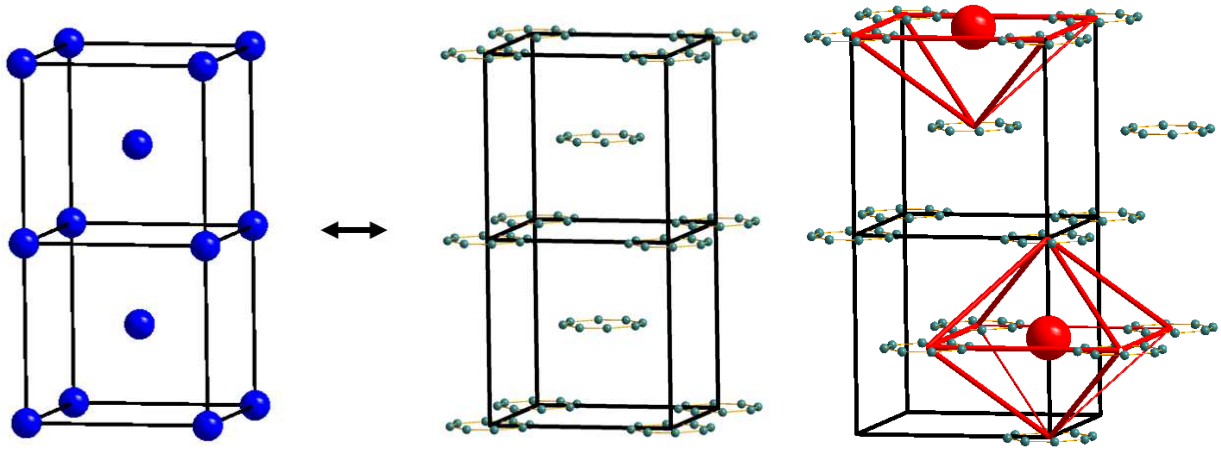

Figure S6. The positions of the atoms in a (distorted) cubic centered packing (left) are occupied by the 8-ring units (middle, only the Al atoms are shown). Due to this arrangement distorted octadedral holes (right) are formed.

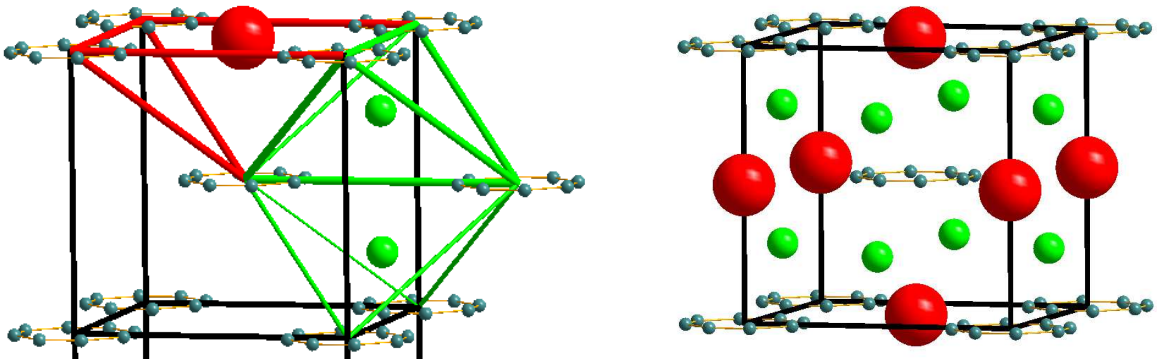

Figure 7. The arrangement of the 8-rings leads to the formation of distorted octahedral and tetrahedral holes shown in red and green, respectively.

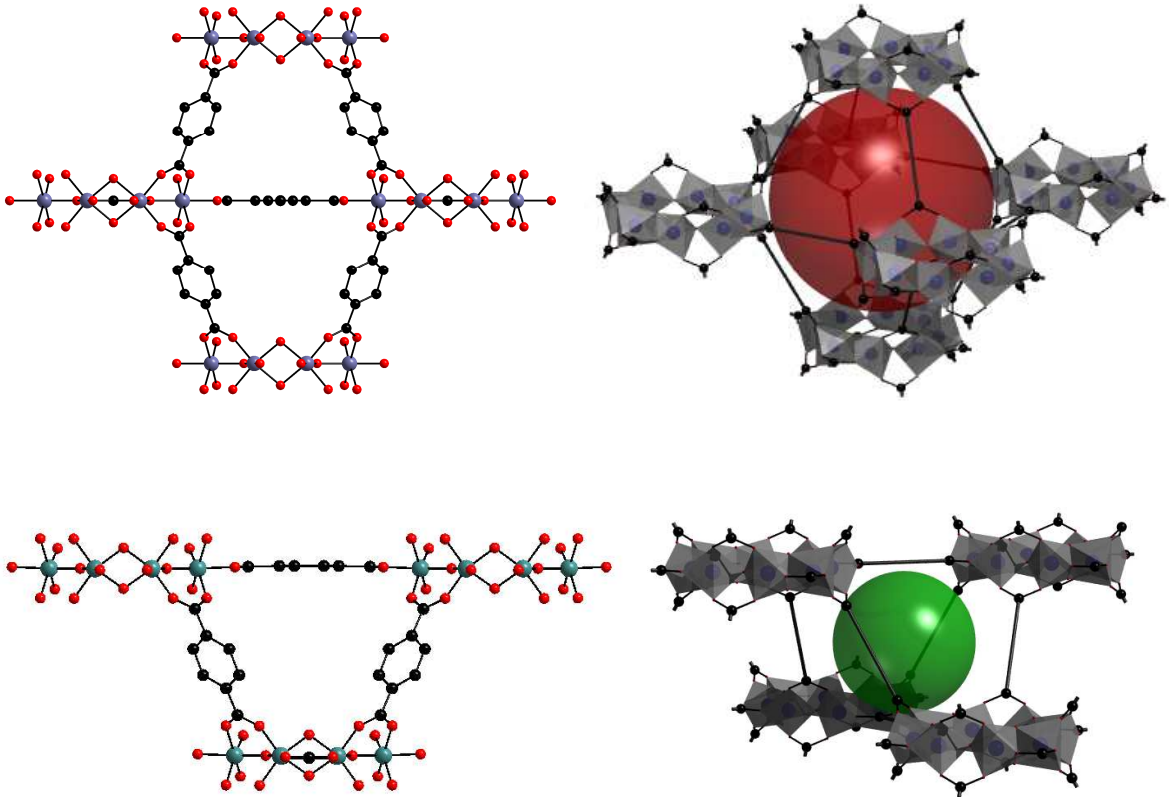

Figure 8. Distorted octahedral (top) and distorted tetrahedral cages (bottom). On the left site the stick and ball model is show. On the right site the phenyl rings are replaced by a line. The holes are presented as red and green balls.

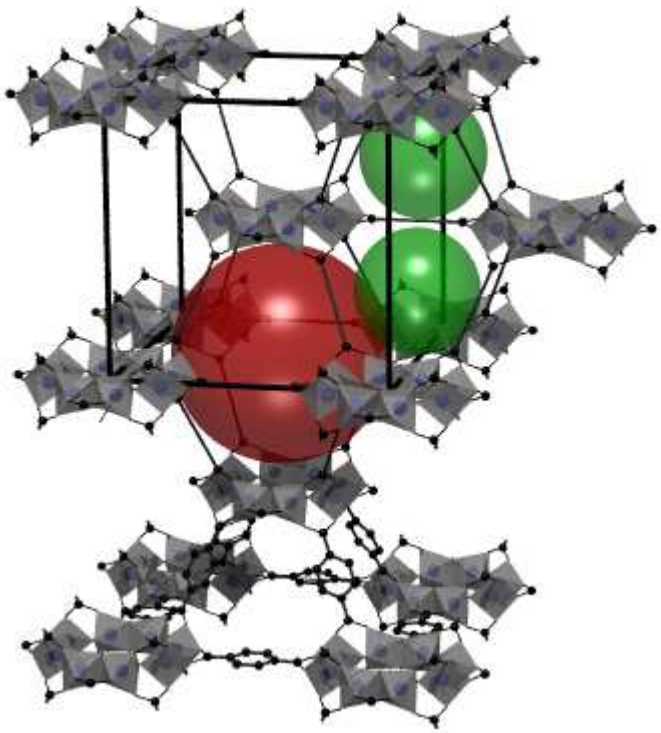

Figure 9. Structure of CAU-1. The 8-ring units are presented. These are connected by the phenyl rings (lower part). Thus distorted octahedral (red) and tetrahedral (green) holes are formed. For clarity the phenyl rings are replaced by a line in the upper part of the figure. Thick, black lines represent the unit cell edges.

References

[1] A. Sonnauer, F. Hoffmann, M. Fröba, L. Kienle, V. Duppel, M. Thommes, C. Serre, G. Férey, N. Stock, *Angew. Chem., Int. Ed.* **2009**, *48*, 3791.

[2] T. Loiseau, C. Serre, C. Huguenard, G. Fink, F. Taulelle, M. Henry, T. Bataille, G. Férey, *Chem. Eur. J.* **2004**, *10*, 1373.

[3] Topas V4.1: General Profile and Structure Analysis Software for Powder Diffraction Data Bruker AXS Ltd, **2004**.

Anhang 5:

Supplementary material (ESI) for PCCP

Supporting Information for the Article

Oriented growth of the functionalized metal-organic framework CAU-1 on –OH- and –COOH-terminated self-assembled monolayers

Florian Hinterholzinger,[a] Camilla Scherb,[a] Tim Ahnfeldt,[b] Norbert Stock,[b] and Thomas Bein*[a]

Department of Chemistry and Biochemistry, University of Munich (LMU),

Butenandtstr. 11 (Gerhardt-Ertl-Building, E), 81377 Munich (Germany).

bein@lmu.de

Supplementary material (ESI) for PCCP

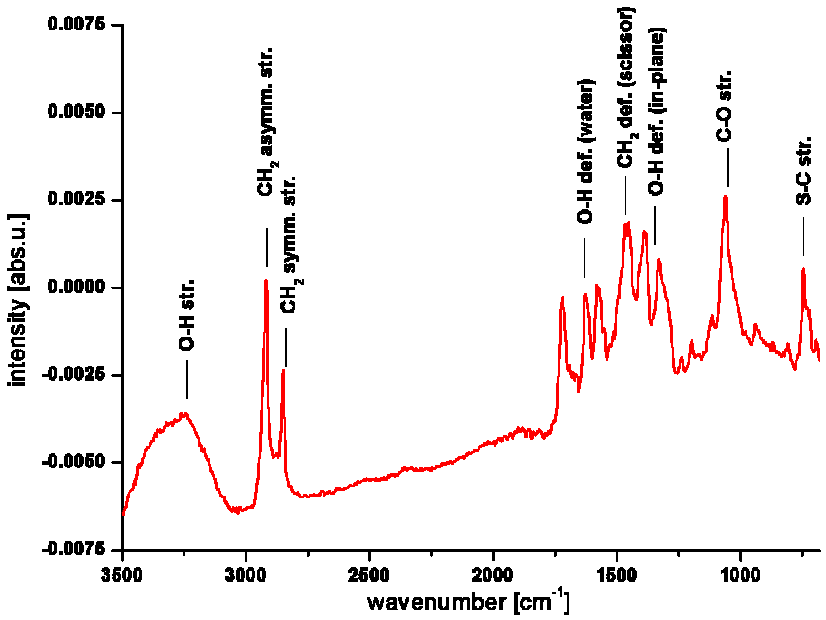

Figure S1. RAIR-spectrum of a 16-mercaptohexadecanol (MHD) self-assembled monolayer on a gold substrate.

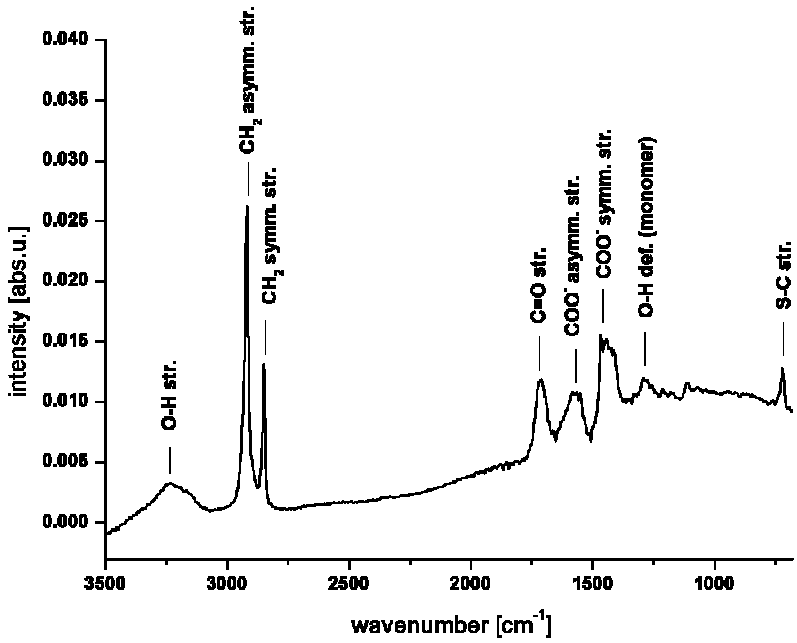

Figure S2. RAIR-spectrum of a 16-mercaptohexadecanoic acid (MHDA) self-assembled monolayer on a gold substrate.

Supplementary material (ESI) for PCCP

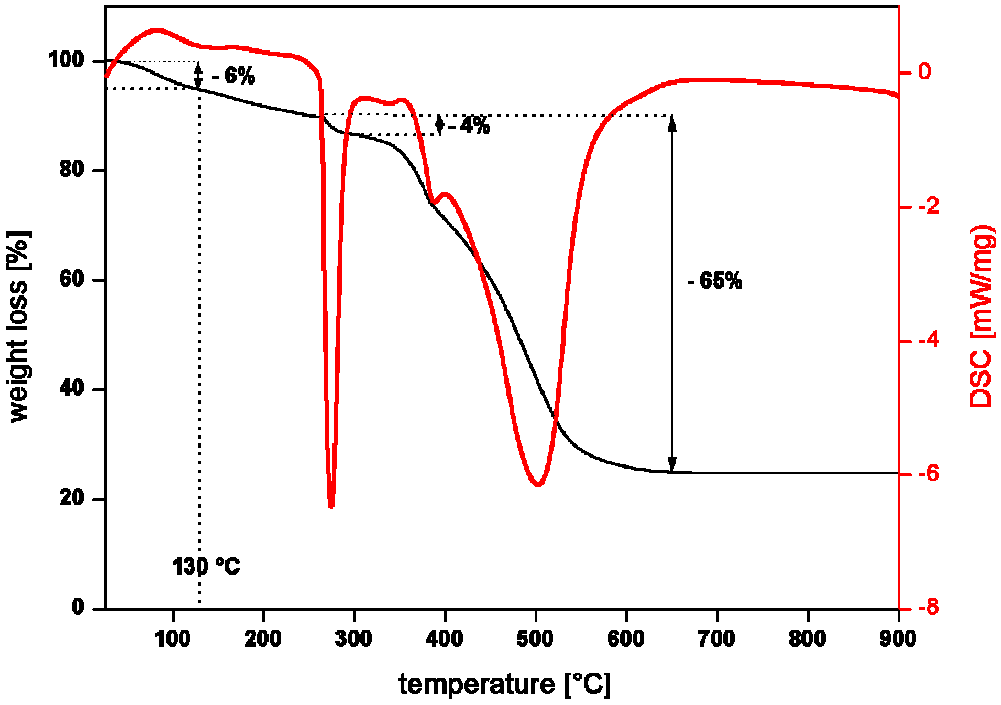

Figure S3. TGA and DSC data of bulk CAU-1 showing the solvent removal and decomposition of the product.

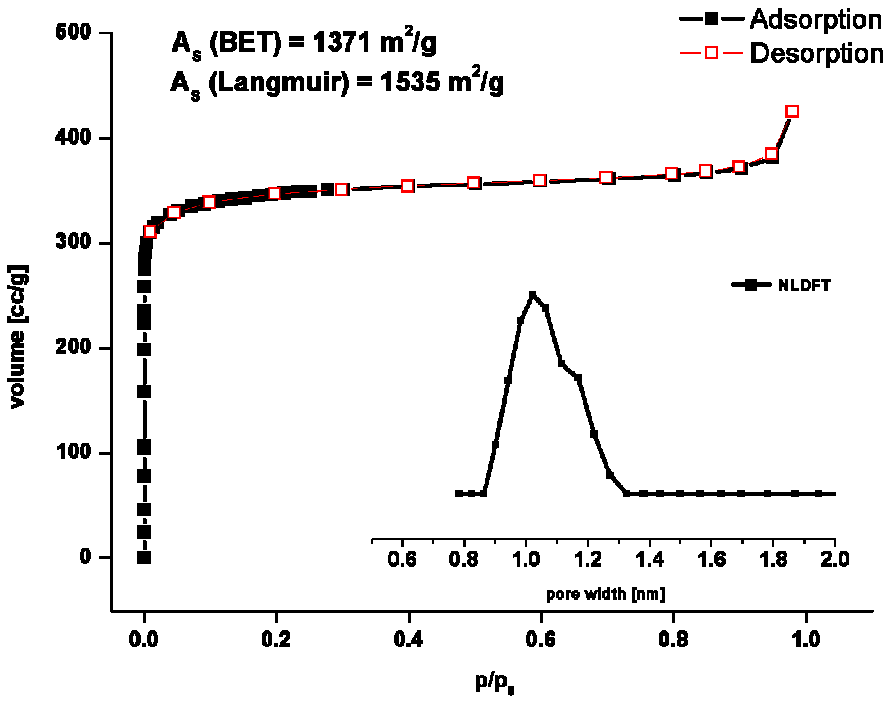

Figure S4. Physisorption measurement performed with nitrogen at 77 K for bulk CAU-1 showing a type I isotherm, the specific surface area (BET) and the pore size distribution (NLDFT).

Supplementary material (ESI) for PCCP

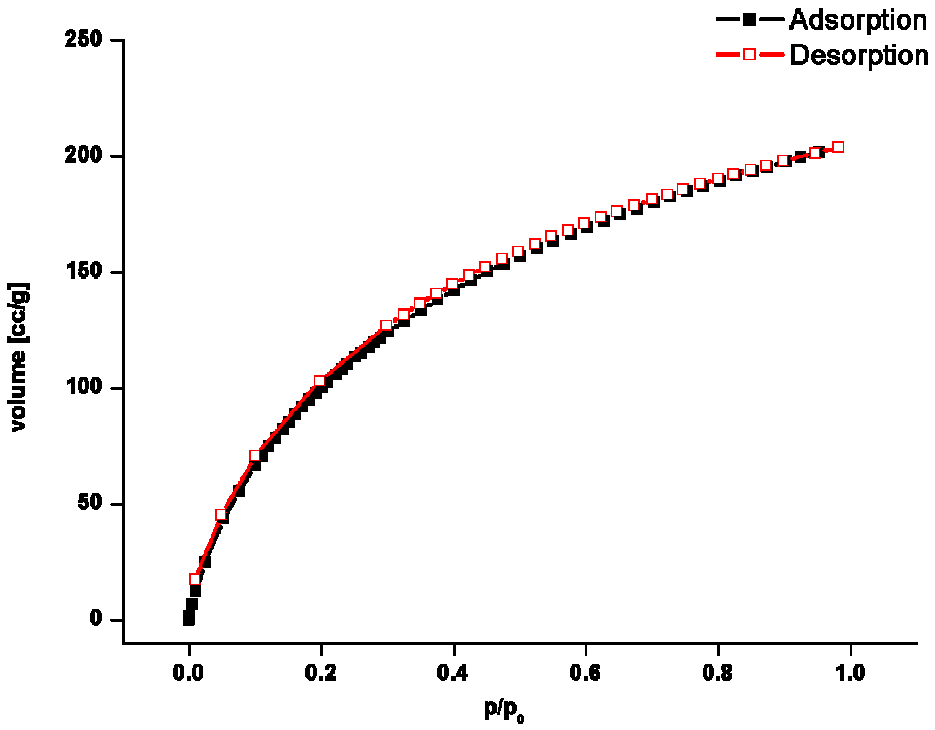

Figure S5. Physisorption measurement performed with H_2 at 77 K for bulk CAU-1.

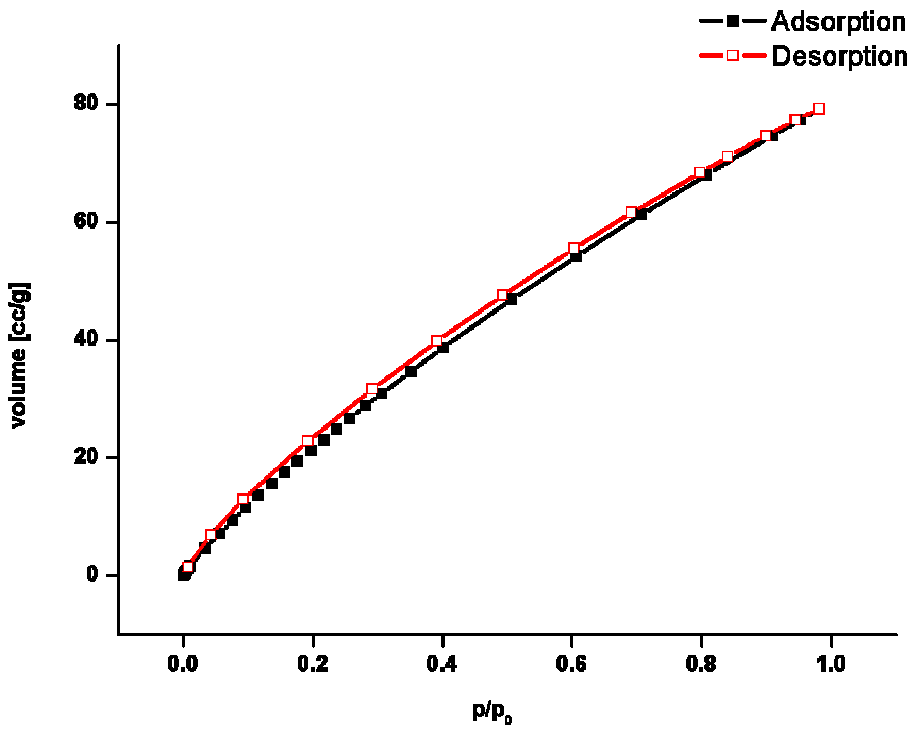

Figure S6. Physisorption measurement performed with CO_2 at 273 K for bulk CAU-1.

Supplementary material (ESI) for PCCP

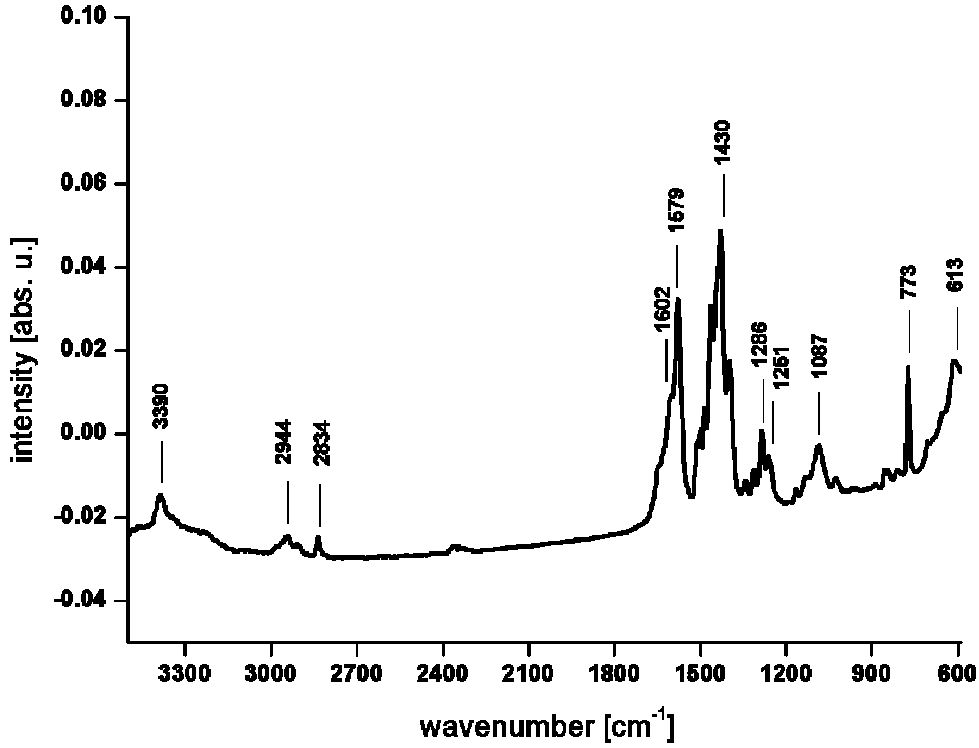

Figure S7. IR spectrum of bulk CAU-1.

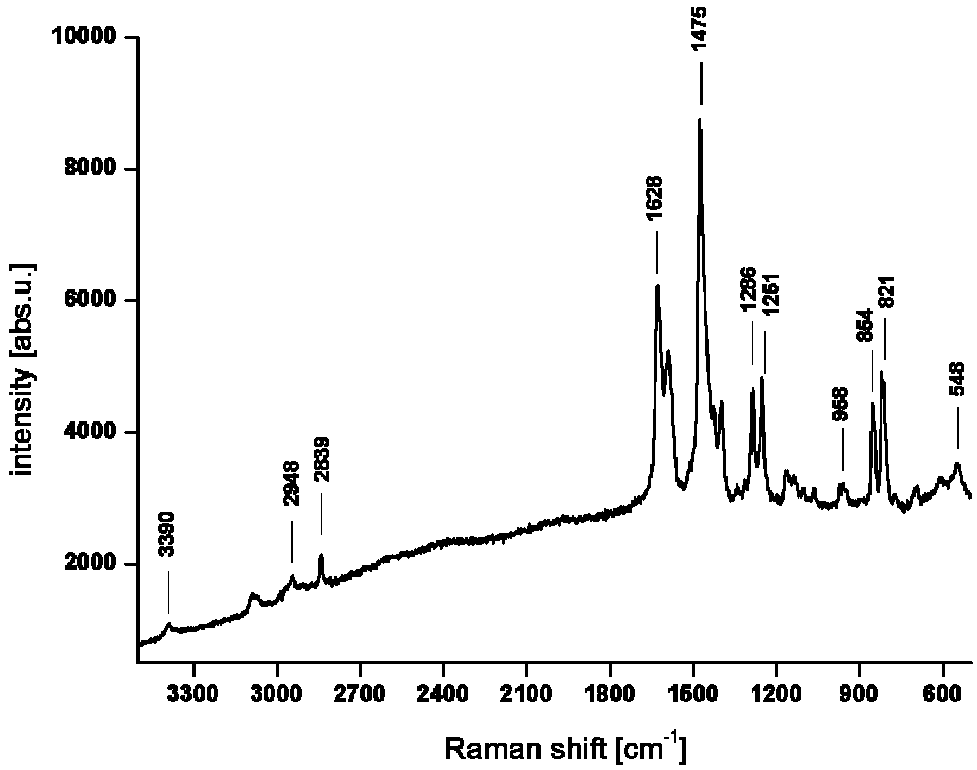

Figure S8. Raman spectrum of bulk CAU-1.

Supplementary material (ESI) for PCCP

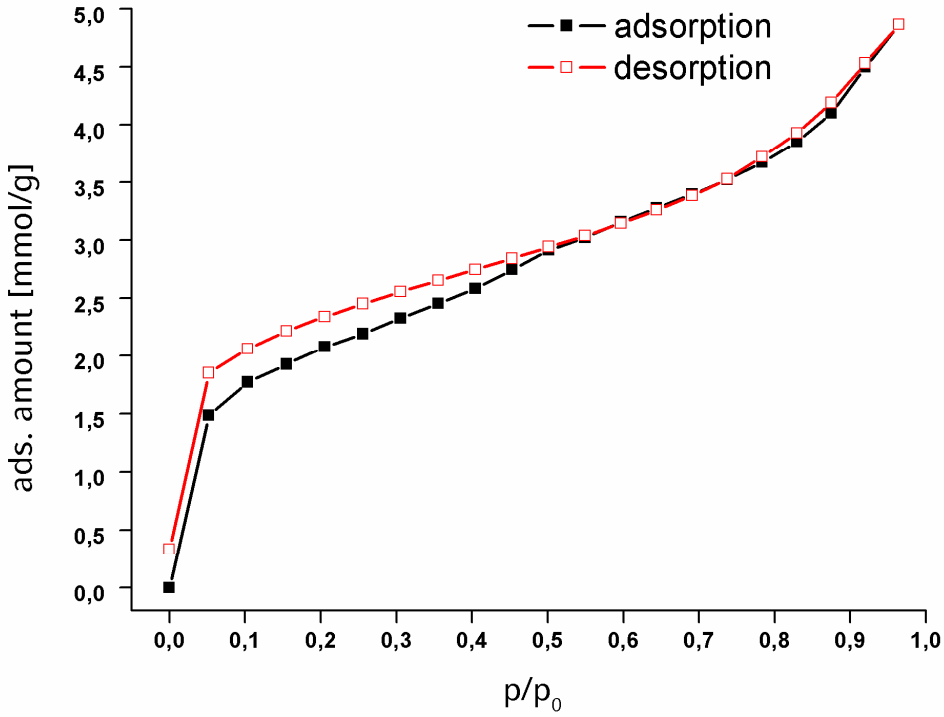

Figure S8. EtOH sorption isotherms recorded from a CAU-1 thin film with preferred [011] orientation.

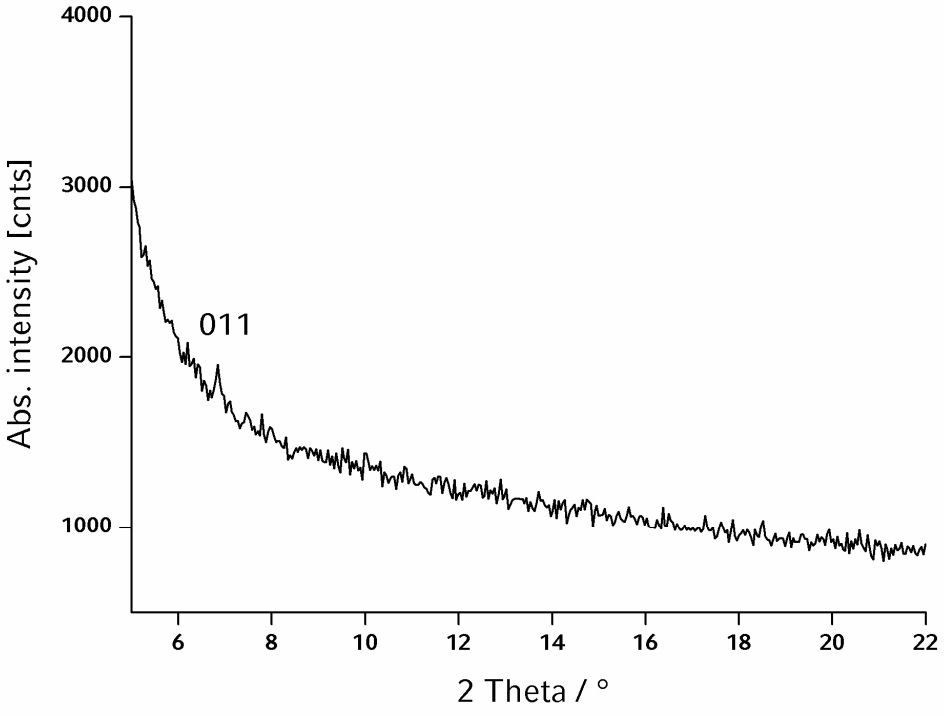

Figure S9. X-ray diffraction pattern of CAU-1 (**A**) crystals with preferred [011] orientation on a MHDA SAM-functionalized QCM chip. The small signal to noise ratio is attributed to the small area of the gold electrode.

Anhang 6:

Supporting Information

Controlled modification of the inorganic and organic brick in an Al-based MOF by direct and post-synthetic synthesis routes

Tim Ahnfeldt,[a] Daniel Gunzelmann,[b] Julia Wack,[b] Jürgen Senker[b,*] and Norbert Stock[a,*]

[a]Insitut für Anorganische Chemie, Christian-Albrechts-Universität, Max-Eyth Straße 2, 24118 Kiel, Germany

[b]Anorganische Chemie III, Universität Bayreuth, Universitätsstraße 30, 95447 Bayreuth, Germany

Electronic Supplementary Material (ESI) for CrystEngComm

1. Proton-proton homonuclear spin diffusion spectra of CAU-1-NHCH$_3$, and CAU-1-NH$_2$

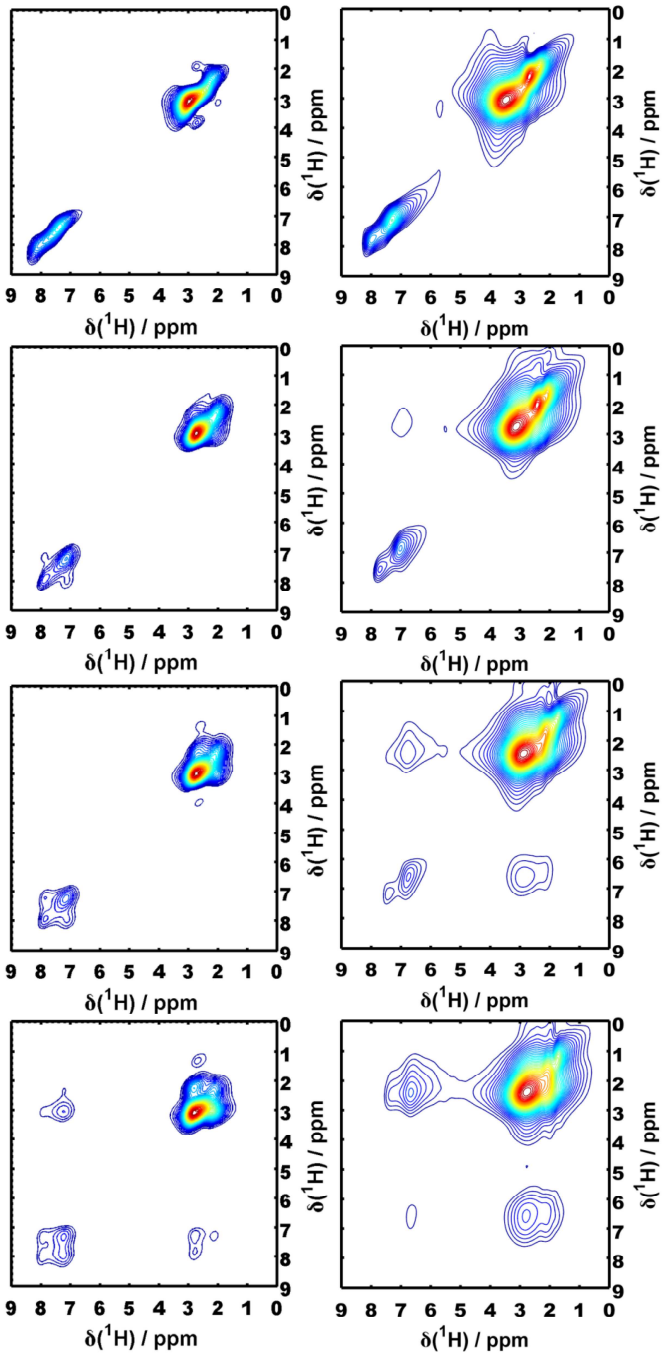

Fig. S1 Proton-Proton Spin-Diffusion Spectra of CAU-1-NHCH$_3$ (left), and CAU-1-NH$_2$ (right) at Spin Diffusion mixing times of 1 µs (top), 700 µs, 1500 µs and 4000 µs (from top to bottom).

Electronic Supplementary Material (ESI) for CrystEngComm

2. Carbon-proton HETCOR spectra of CAU-1-NHCH$_3$ and CAU-1-NHCOCH$_3$

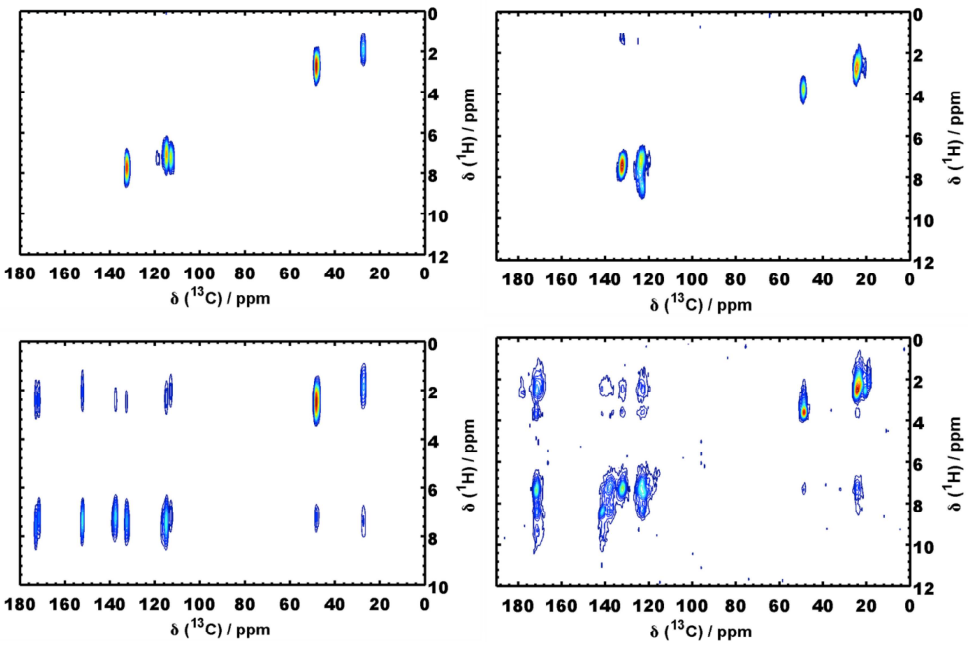

Fig. S2 Carbon-proton HETCOR spectra of CAU-1-NHCH$_3$ (left) and CAU-1-NHCOCH$_3$ (right) at contact times of 75 µs (top) and 1000 µs (bottom) showing short and long distance correlations, respectively.

Electronic Supplementary Material (ESI) for CrystEngComm

3. Reaction times to reach full crystallisation (α = 1) determined from the EDXRD studies for MW-assisted reactions

CAU-1 was synthesized by MW-assisted heating in the temperature range 115 - 145 °C. The reaction time for each temperature was determined from EDXRD studies on the product formation of CAU-1-NH_2 and corresponds to the time required to reach full crystallisation, i.e. extent of crystallisation, α = 1 (Table S1).[1]

Tab. S1 Reaction times to reach full crystallisation (α = 1) determined from the EDXRD studies for MW-reactions carried out in the temperature range between 115-145 °C. Values taken form reference [1].

reaction temperature / °C	reaction time / min
115	105
120	65-70
125	42
130	25
135	16
140	10
145	7-9

Electronic Supplementary Material (ESI) for CrystEngComm

4. X-ray powder diffraction (XRPD) patterns of CAU-1 obtained by MW-assisted heating at different temperatures

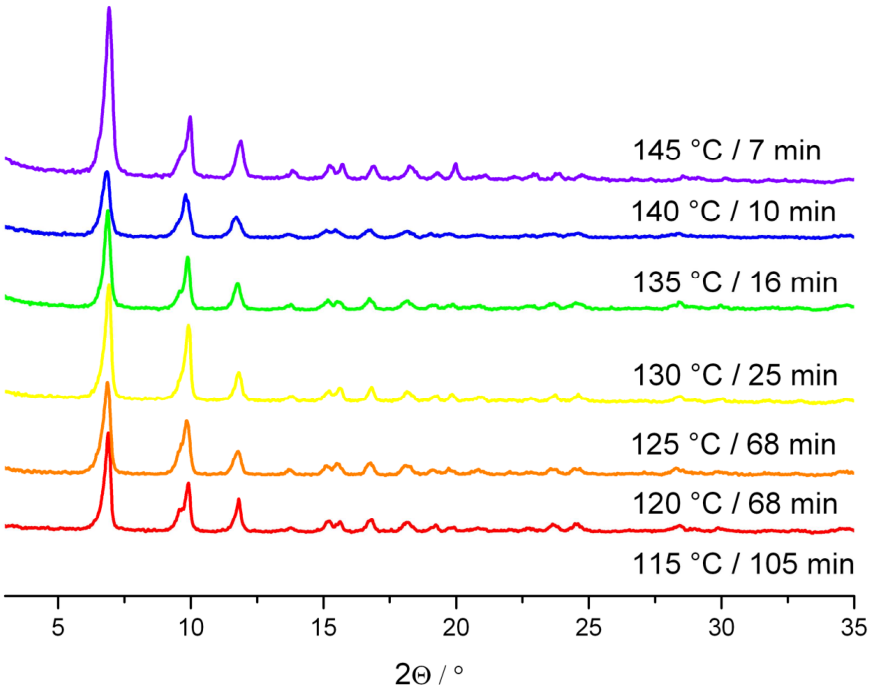

Fig. S3 X-ray powder diffraction (XRPD) patterns for CAU-1 obtained by MW-assisted heating carried out in the temperature range between 115 °C – 145 °C.

Electronic Supplementary Material (ESI) for CrystEngComm

5. Time dependence of the methylation of the MW-assisted synthesis at 145 °C

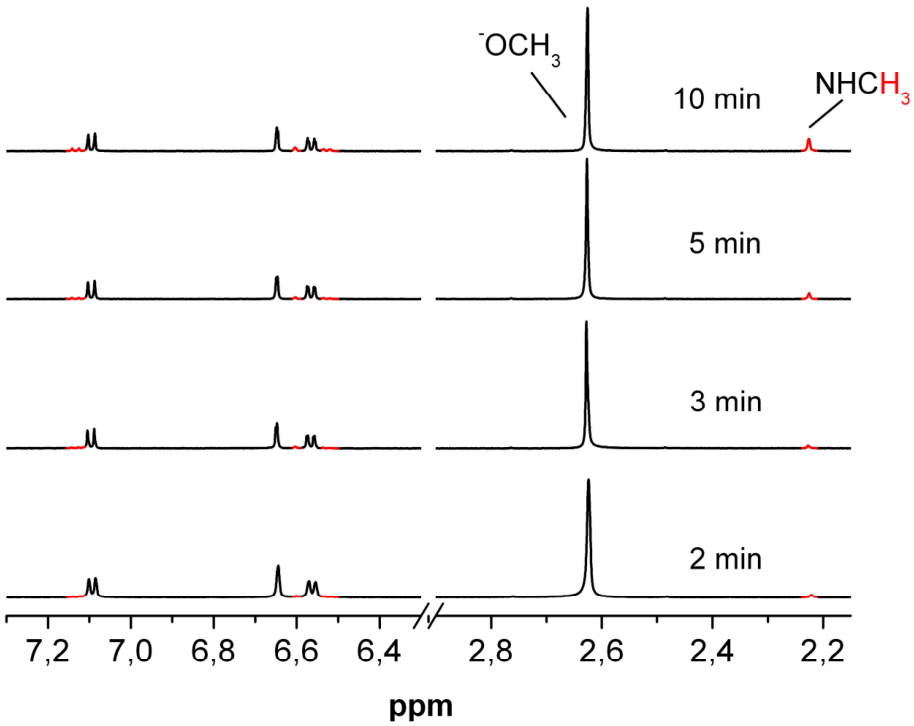

Fig. S4 ^{1}H NMR spectra of the dissolved CAU-1 samples collected from MW-assisted syntheses at 145 °C using reaction times between 2 and 15 min. Each spectrum is normalized to the sum of the aromatic H signals (methylated and non-methylated). Signals due to methylated CAU-1 are highlighted red.

Electronic Supplementary Material (ESI) for CrystEngComm

6. Accuracy of ^{1}H NMR spectra and reproducibility of the MW-assisted synthesis of CAU-1-NH$_2$

In three repeated reactions under identical condition (3min a-c) all directly dissolved products exhibit the identical degree of methylation in the ^{1}H NMR spectra, which clearly shows the good reproducibility of the synthesis and the measurements.

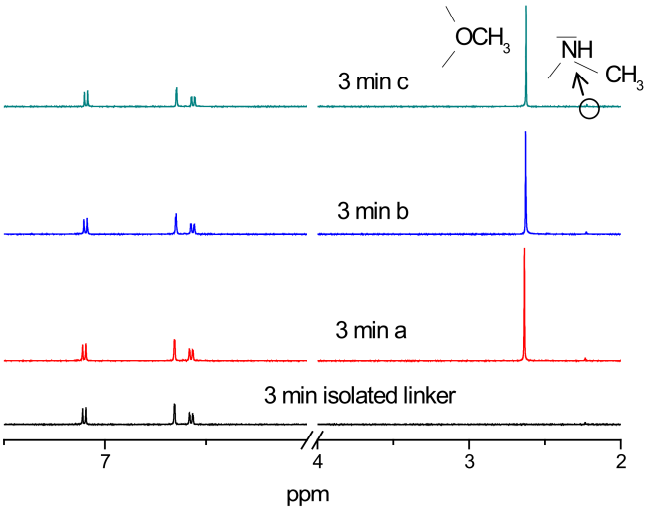

Fig. S5 ^{1}H NMR spectra of the isolated aminoterephthalic acid linker (black) and directly dissolved CAU-1 (red, blue and green) prepared by MW-assisted synthesis at 145 °C using a reaction time of 3 min. Each spectrum is normalized to the sum of aromatic H signals (methylated and unmethylated).

The integral ratios methoxy H-atoms : aromatic H-atoms of the products (3 min a-c) are between 1.14 and 1.21 (1.33 calc.). Thus, approximately 88% of the methoxy groups are incorporated in the framework after this reaction time according to the formula sum. We presume that syntheses at very short reaction times may lead to CAU-1-NH$_2$ for which a small fraction (12%) of the methoxy groups is replaced by OH-groups. Nevertheless, the product is still very crystalline and exhibits high thermal and chemical stability, such as CAU-1-CH$_3$ and CAU-1-CHCOCH$_3$.

Electronic Supplementary Material (ESI) for CrystEngComm

7. Labelling of the set of ^{1}H signals of the reaction product carrying out under conventional heating method using a glass reactor

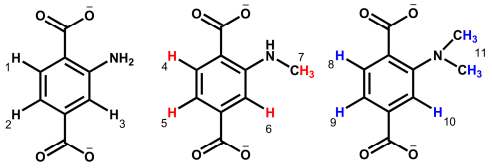

Scheme S1 Labelling of the ^{1}H signals in dimethylated, methylated and non-methylated CAU-1. ^{1}H NMR 500 MHz, (NaOD/D_2O) δ: **BDC-NH_2^{2-}:** 7.23 (d, 1H, H_1 $^{3}J_{H\text{-}H}$ = 8.2Hz); 6.79 (s, 1H, H_3); 6.71 (d, 1H, H_2 $^{3}J_{H\text{-}H}$ = 8.1Hz); **BDC-$NHCH_3^{2-}$:** 7.27 (d, 1H, H_5 $^{3}J_{H\text{-}H}$ = 8.0Hz); 6.76 (s, 1H, H_6); 6.52 (d, 1H, H_5 $^{3}J_{H\text{-}H}$ = 8.0Hz); 2.37 (s,3H,H_7); **BDC-$N(CH_3)_2^{2-}$:** 7.04 (s, 1H, H_{10}); 6.94 (d, 1H, H_9 $^{3}J_{H\,H}$ = 8.0Hz); 6.87 (d, 1H, H_8 $^{3}J_{H\,H}$ = 7.9Hz); 2.28 (s, 6H, H_{11})

Electronic Supplementary Material (ESI) for CrystEngComm

8. TG-curve of CAU-1-NH_2

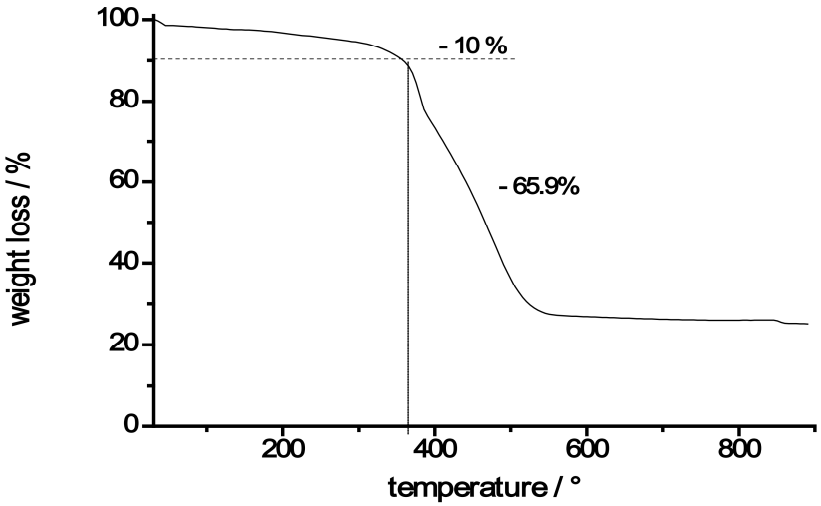

Fig. S6 TG-curve of CAU-1-NH_2 synthesized via MW-heating (3min / 145°C). The sample was measured in air with a heating rate of 4K / min and was degassed (30 min / 130 °C) before the measurement.

Electronic Supplementary Material (ESI) for CrystEngComm

9. Activation process screened by ^{1}H NMR

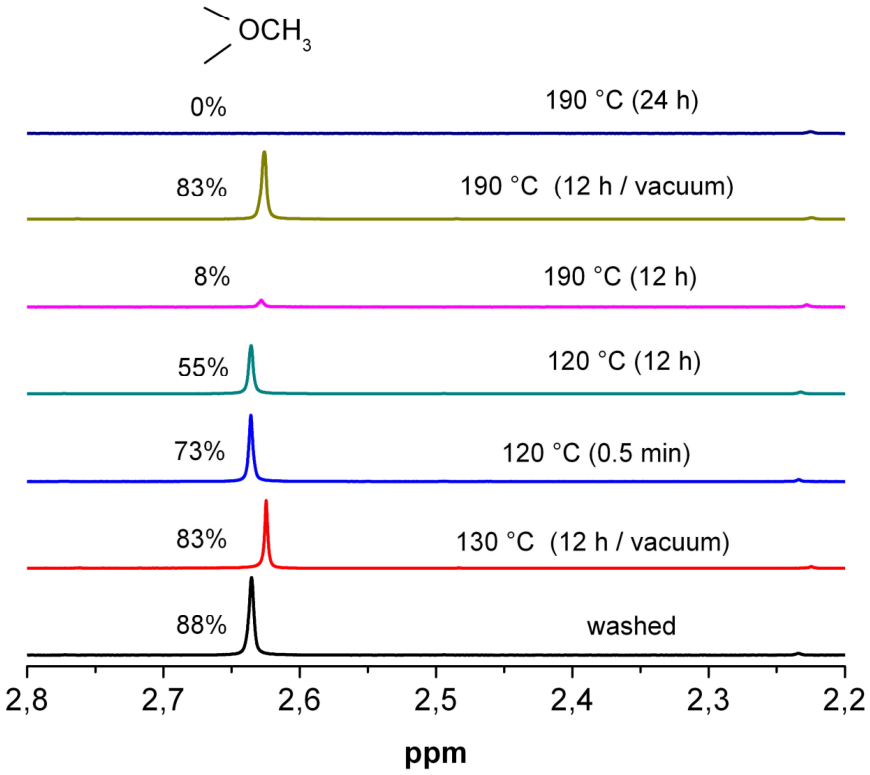

Fig. S7 ^{1}H NMR spectra of differently activated CAU-1-NH_2 compounds prepared by MW-synthesis. After the washing process the compounds were treated using different activation procedures. Each spectrum is normalized to the sum of aromatic H signals (methylated and non-methylated, not shown).

Electronic Supplementary Material (ESI) for CrystEngComm

10. Temperature-dependent X-ray powder diffraction measurements (TD-XRPD)

The TD-XRPD measurements of CAU-1-NH_2(OH), CAU-1-$NHCH_3$ and CAU-1-$NHCOCH_3$ are shown in Figure S8-S10. The data were obtained under air with a STOE STADI P diffractometer equipped with an image plate detector and a STOE capillary furnace (version 0.65.1) using monochromated Cu-$K_{\alpha 1}$ radiation. Each powder pattern was recorded in the 4-35° range (2θ) at intervals of 10 °C up to 350 °C, and interval of 25 °C from 350-400 °C with duration of 15 min per scan. The temperature ramp between two patterns was set to 2 °C min^{-1}.

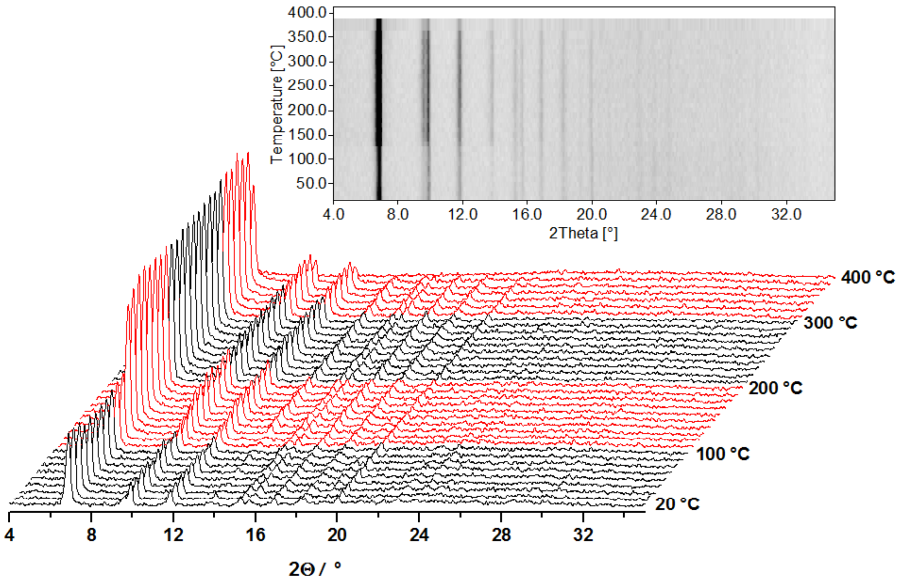

Fig. S8 Temperature-dependent X-ray powder diffraction patterns of CAU-1-NH_2(OH), $[Al_4(OH)_6((BDC\text{-}NH_2)_3]\cdot xH_2O$, in air (20 - 400 °C).

Electronic Supplementary Material (ESI) for CrystEngComm

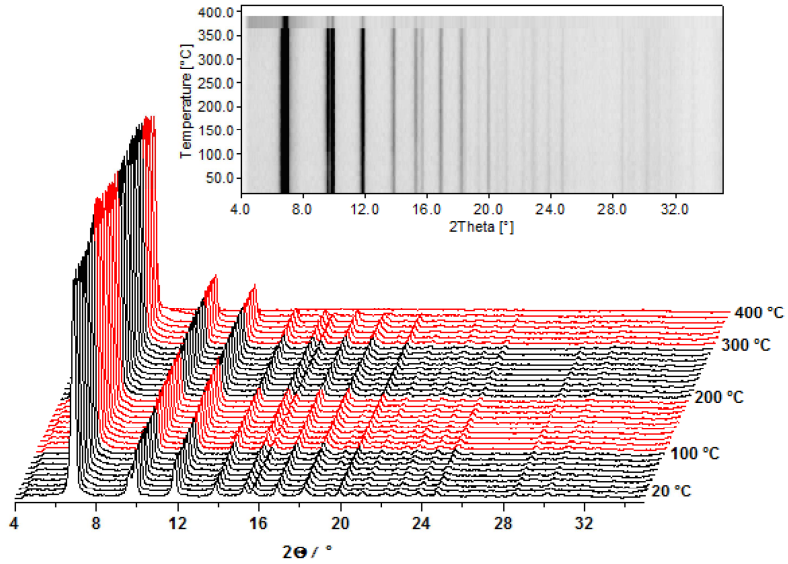

Fig. S9 Temperature-dependent X-ray powder diffraction patterns of CAU-1-$NHCH_3$, $[Al_4(OH)_2(OCH_3)_4(BDC\text{-}NHCH_3)_3]\cdot xH_2O$, in air (20 - 400 °C).

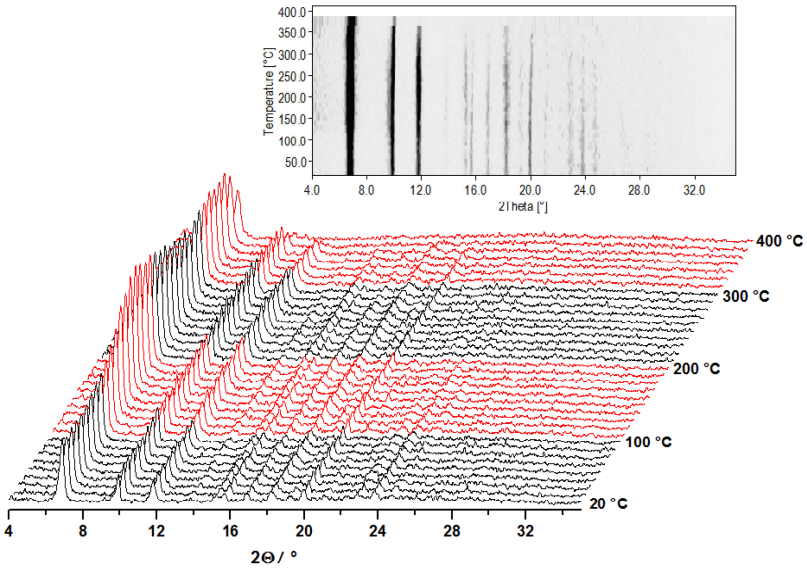

Fig. S10 Temperature-dependent X-ray powder diffraction patterns of CAU-1-$NHCOCH_3$, $[Al_4(OH)_2(OCH_3)_4(BDC\text{-}NHCOCH_3)_3]\cdot xH_2O$, in air (20 - 400 °C).

Literature

[1] T. Ahnfeldt, N. Stock, *CrystEngComm*, **2011**, doi:110.1039/c1ce05956d

Anhang 7:

Supporting Information

CAU-3: A new family of porous MOFs with a novel Al-based brick: $[Al_2(OCH_3)_4(O_2C\text{-}X\text{-}CO_2)]$ (X=aryl)

Helge Reinsch, Mark Feyand, Tim Ahnfeldt and Norbert Stock

Institute of Inorganic Chemistry, Christian-Albrechts-Universität, Max-Eyth-Straße 2, 24118 Kiel, Germany

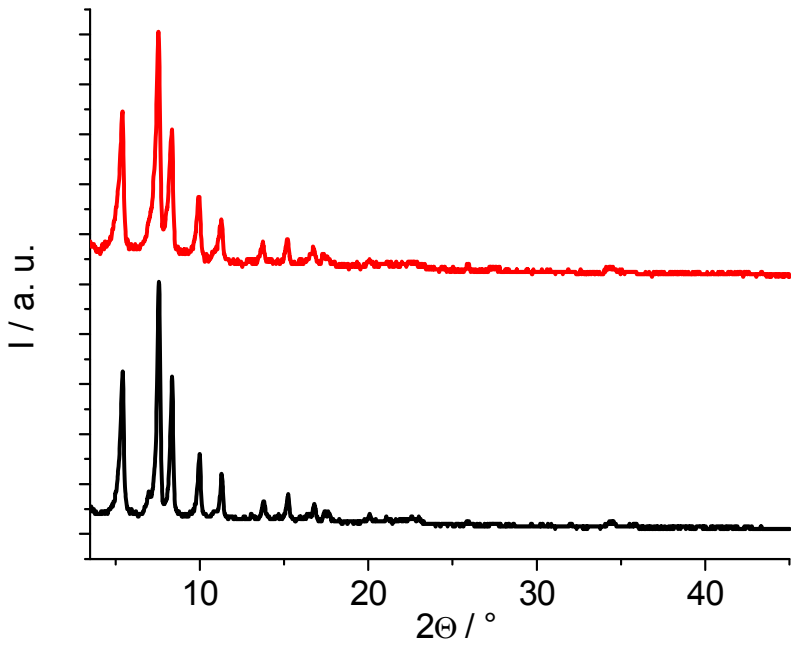

Figure S1: Powder pattern of an as-synthesized sample of CAU-3-BDC (black), and a sample after activation procedure and sorption measurement (red).

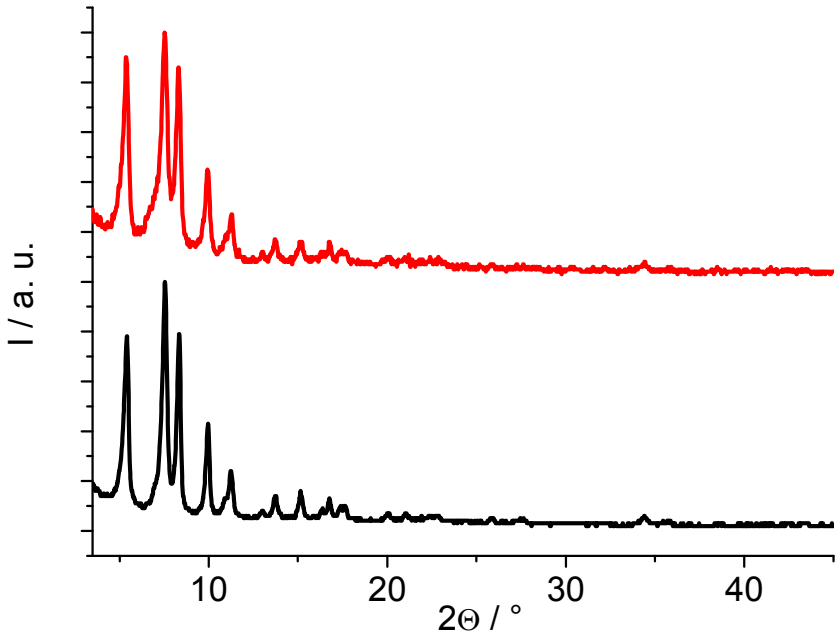

Figure S2: Powder pattern of an as-synthesized sample of CAU-3-BDC-NH_2 (black), and a sample after activation procedure and sorption measurement (red).

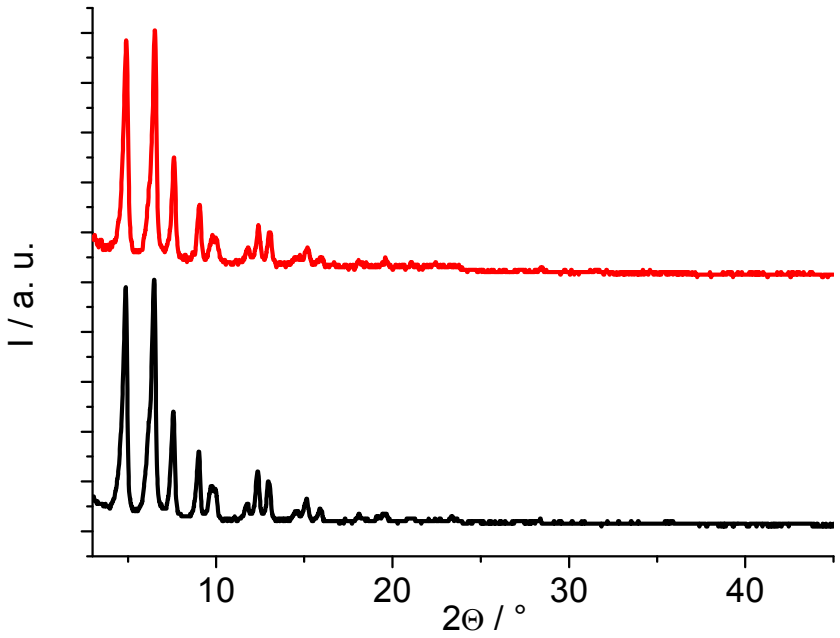

Figure S3: Powder pattern of an as-synthesized sample of CAU-3-NDC (black), and a sample after activation procedure and sorption measurement (red).

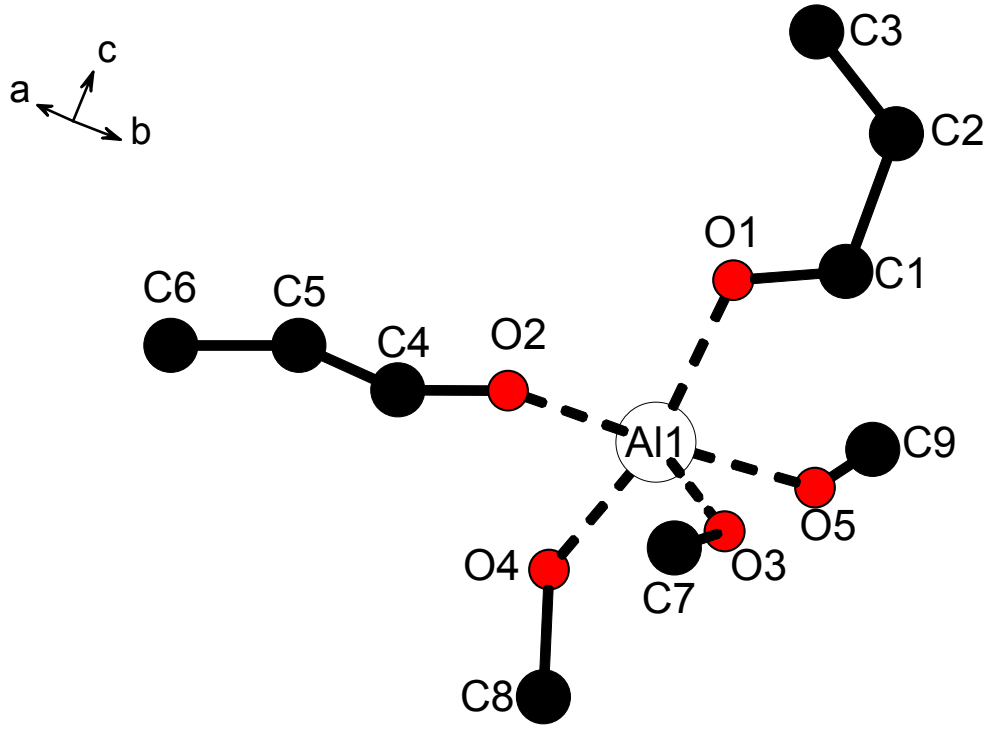

Figure S4: Asymmetric unit of CAU-3-BDC with numbering scheme.

Table S1: Selected bond lengths in CAU-3-BDC [Å].

Atom 1	*Atom 2*	*d / Å*
Al1	O1	1.96(1)
	O2	1.98(2)
	O3	1.92(1)
	O4	1.83(1)
	O5	1.89(2)
O1	C1	1.22(2)
C1	C2	1.54(1)
C2	C3	1.39(1)
O2	C4	1.23(1)
C5	C6	1.37(1)
O3	C7	1.47(3)
O4	C8	1.46(2)
O5	C9	1.51(3)
C9	O5	1.51(3)

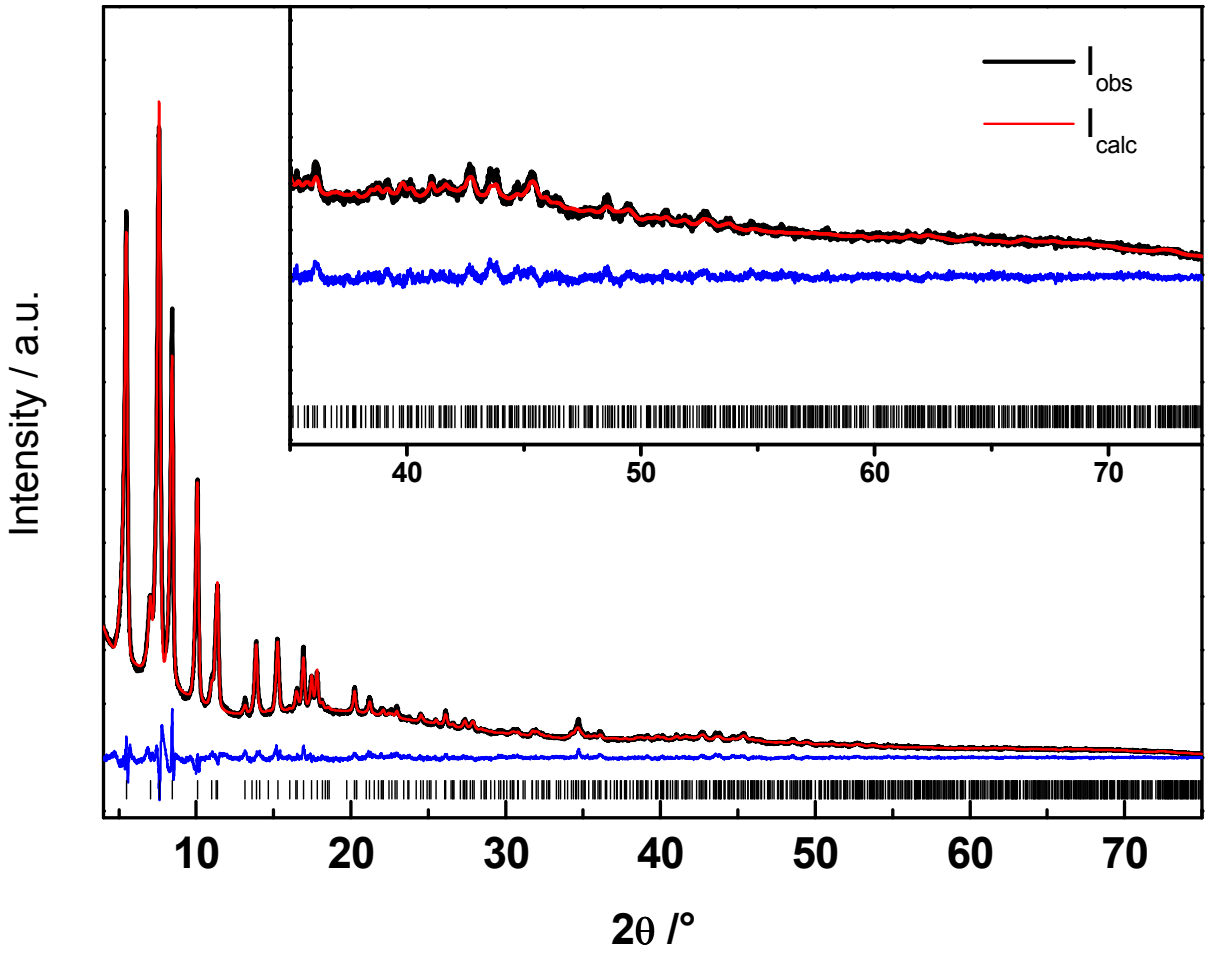

Figure S5: Final Rietveld plot of the refinement of CAU-3-BDC-NH_2. The observed intensities are shown in black, the calculated intensities are shown in red. The difference curve is shown below in blue, vertical bars mark the Bragg positions. The insert shows a plot enlargement from 35 -75 °2θ.

Table S2: Selected bond lengths in CAU-3-BDC-NH_2 [Å].

Atom 1	*Atom 2*	*d / Å*
Al1	O1	1.99(2)
	O2	1.80(2)
	O3	1.74(2)
	O4	1.87(3)
	O5	1.99(4)
O1	C1	1.23(5)
C1	C2	1.60 (2)
C2	C3	1.38 (6)
C3	C3	1.39(3)
O2	C4	1.39(5)
C4	O2	1.39(3)
	C5	1.53(9)
C5	C6	1.33(5)
N1	C3	1.5 (1)
N2	C6	1.5(1)

Table S3: Atomic coordinates of CAU-3-NDC obtained from the force field calculations using Materials Studio 5.0.

Symbol	*x/a*	*y/b*	*z/c*
M1	0.25217	0.05104	0.51501
O2	0.27995	0.07593	0.55811
O3	0.32005	0.02894	0.51211
O4	0.21924	0.01434	0.47145
C5	0.26741	0.0306	0.44692
C6	0.24497	0.90175	0.2889
C7	0.24115	0.91213	0.32179
C8	0.19049	0.86321	0.34061
C9	0.14677	0.7935	0.29296
C10	0.19805	0.84234	0.27414
M11	0.0794	0.26015	0.48371
O12	0.11136	0.28559	0.44055
O13	0.06741	0.33477	0.4861
O14	0.04232	0.23563	0.52706
C15	0.05494	0.18882	0.54084
C16	0.5384	0.61932	0.48658
C17	0.47766	0.56072	0.48441
C18	0.47197	0.50052	0.49396
C19	0.58885	0.55858	0.50829
C20	0.59464	0.61894	0.49844
C21	0.29241	0.12878	0.57297
O22	0.31378	0.14379	0.50389
C23	0.34838	0.16804	0.47475
O24	0.18921	0.08691	0.51862
C25	0.15431	0.07905	0.54788
C26	0.31919	0.97871	0.49943
H27	0.31796	0.05445	0.456
H28	0.26201	0.06152	0.42827
H29	0.26215	0.9876	0.43382
H30	0.28504	0.94023	0.27504
H31	0.27804	0.9583	0.33253
H32	0.11043	0.7473	0.28205
H33	0.10738	0.20825	0.54132
H34	0.03412	0.14329	0.52646
H35	0.04152	0.18272	0.56665
H36	0.54135	0.665	0.47882
H37	0.43518	0.56247	0.47513
H38	0.63177	0.55735	0.51734
H39	0.31608	0.15723	0.45372
H40	0.3848	0.15121	0.47182
H41	0.3791	0.22248	0.47602
H42	0.1003	0.04938	0.54346
H43	0.16228	0.12602	0.55768
H44	0.16881	0.05767	0.56752

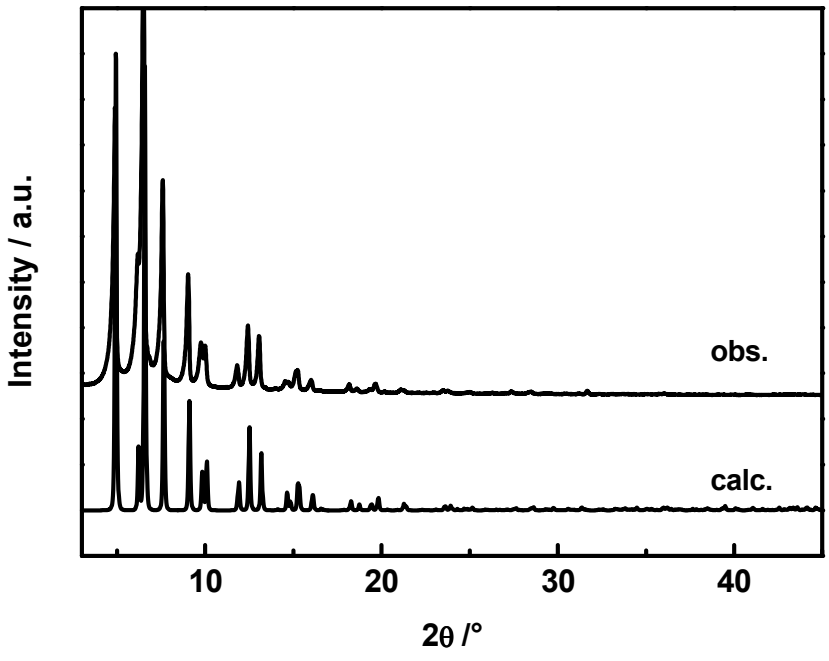

Figure S6: Calculated and observed powder pattern of CAU-3-NDC obtained from force field calculation.

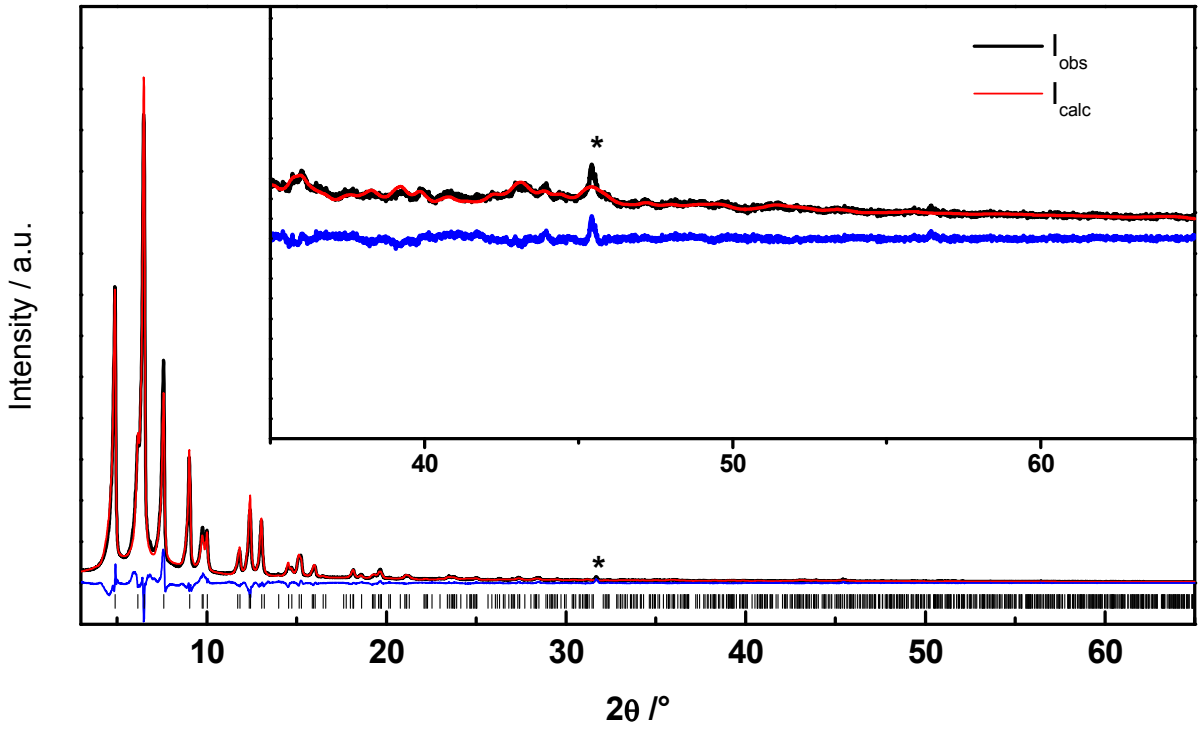

Figure S7: Final Rietveld plot of CAU-3-NDC. The asterisks correspond to NaCl as a by-product. The observed intensities are shown in black, the calculated intensities are shown in red. The difference curve is shown below in blue, vertical bars mark the Bragg positions. The insert shows a plot enlargement from 35 -65 °2θ.

Table S4: Selected bond lengths of CAU-3-NDC [Å]

Atom 1	Atom 2	d /
Al1	O1	1.8(2)
	O4	1.8(2)
	O5	1.9(2)
	O6	1.9(2)
	O7	1.8(1)
	O8	2.0(3)
Al2	O2	1.8(2)
	O3	1.8(1)
	O5	2.0(3)
	O6	1.9(3)
	O7	1.9(2)
	O8	2.0(2)
O1	C1	1.2(4)
O2	C1	1.2(4)
C1	C2	1.4(3)
C2	C3	1.4(1)
	C6	1.4(4)
C3	C4	1.4(3)
C4	C5	1.3(3)
C5	C5	1.3(4)
	C6	1.5(6)
O3	C7	1.2(3)
O4	C7	1.2(2)
C7	C8	1.5(2)
C8	C9	1.3(6)
	C12	1.4(6)
	C7	1.5(2)
C9	C10	1.3(4)
C10	C11	1.3(7)
C11	C12	1.3(4)
O5	C13	1.4(2)
O6	C16	1.3(4)
O7	C14	1.3(2)
O8	C15	1.4(2)

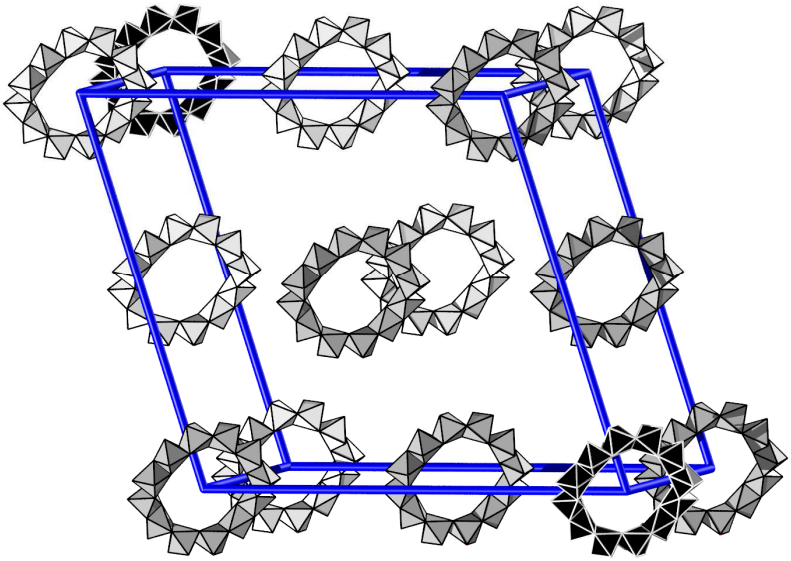

Figure S8: Pseudo-fcc-arrangement of the inorganic units. The colours emphasize the ABC-stacking,

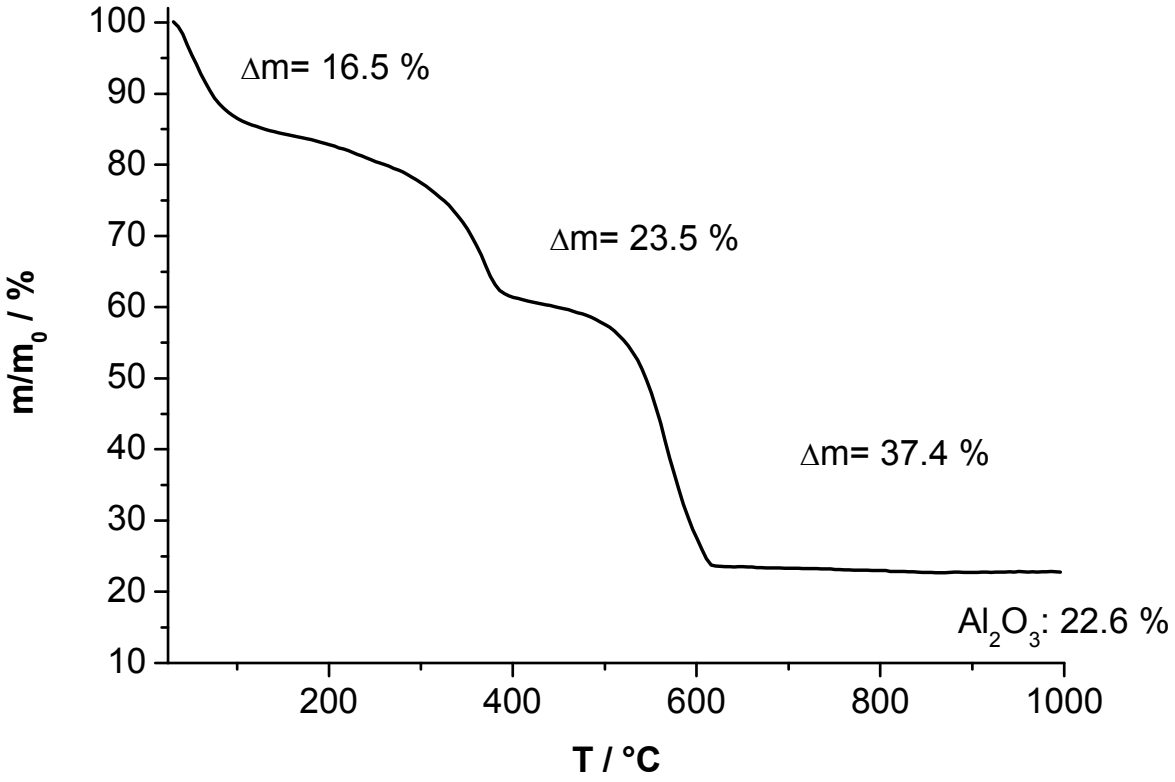

Fig. S9: TG-curve for CAU-3-BDC (**1**).

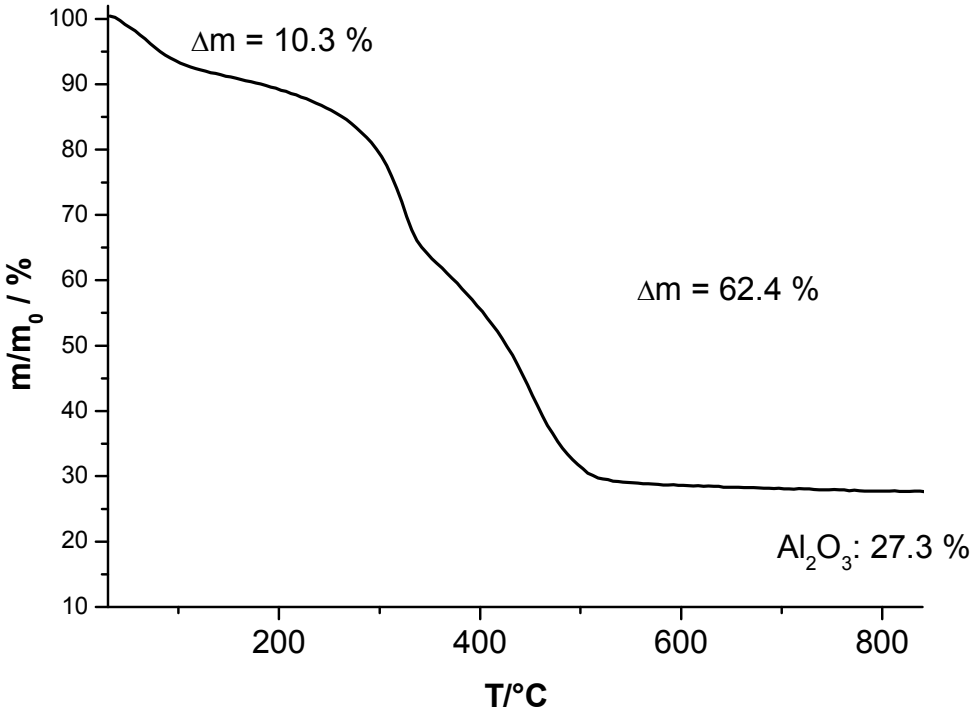

Figure S10. TG-diagram of the decomposition of CAU-3-BDC-NH_2 (**2**).

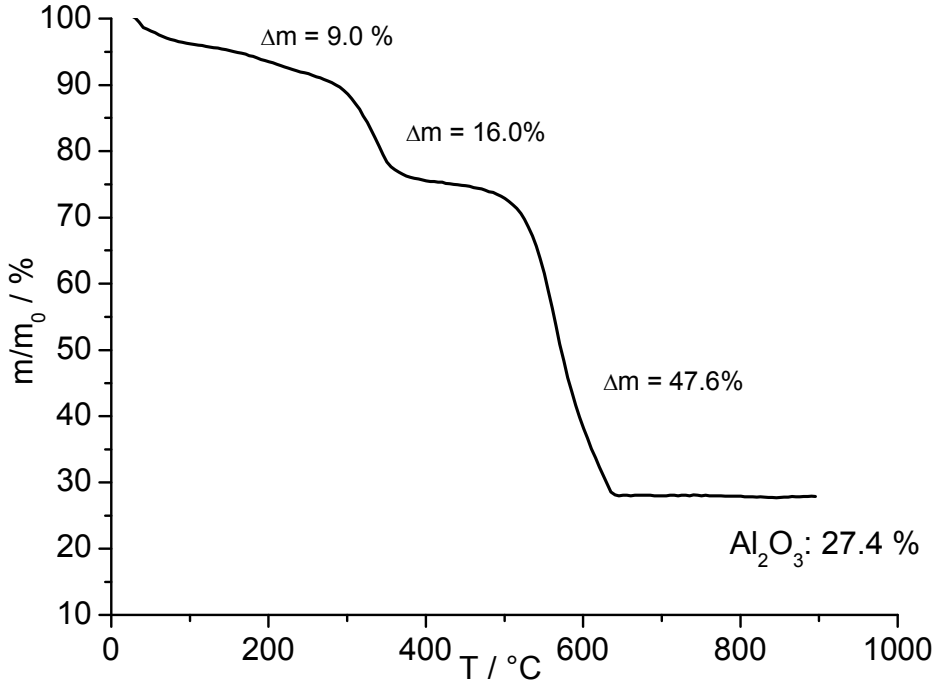

Figure S11. TG-diagram of the decomposition of CAU-3-NDC (**3**).

Table S5: Exact amounts of starting materials used in the discovery of CAU-3-BDC.

Reaktor No.	molar ratio H_2BDC	molar ratio $AlCl_3 \cdot 6H_2O$	molar ratio NaOH	amount H_2BDC [µmol]	amount $AlCl_3 \cdot 6H_2O$ [µmol]	amount NaOH [µmol]	mass H_2BDC [mg]	mass $AlCl_3 \cdot 6H_2O$ [mg]	volume NaOH [µL]	volume MeOH [µL]
1	0,25	1	0,5	32	128	64	5	31	32	1368
2	0,25	1	0,75	32	128	96	5	31	48	1352
3	0,25	1	1,25	32	128	160	5	31	80	1320
4	0,25	1	1,5	32	128	192	5	31	96	1304
5	0,25	1	1,75	32	128	224	5	31	112	1288
6	0,25	1	2	32	128	256	5	31	128	1272
7	0,25	1	1	32	128	130	5	31	65	935
8	0,25	1	1	32	128	130	5	31	65	1185
9	0,25	1	1	32	128	130	5	31	65	1435
10	0,50	2	2	64	256	260	11	62	130	870
11	0,50	2	2	64	256	260	11	62	130	1120
12	0,50	2	2	64	256	260	11	62	130	1370
13	0,50	2	1	64	256	128	11	62	64	1336
14	0,50	2	1,25	64	256	160	11	62	80	1320
15	0,50	2	1,50	64	256	192	11	62	96	1304
16	0,50	2	1,75	64	256	224	11	62	112	1288
17	0,50	2	2	64	256	256	11	62	128	1272
18	0,50	2	2,5	64	256	320	11	62	160	1240
19	1	4	1,55	128	512	198	21	124	99	1301
20	1	4	2,18	128	512	279	21	124	140	1260
21	1	4	2,81	128	512	360	21	124	180	1220
22	1	4	3,43	128	512	439	21	124	220	1180
23	1	4	4,06	128	512	520	21	124	260	1140
24	1	4	4,68	128	512	599	21	124	300	1100

Anhang 8:

Supporting Information

(1) High-throughput syntheses of CAU-1-$(OH)_2$

(2) Experimental XRD powder pattern of CAU-1-$(OH)_2$

(3) Thermal investigation of CAU-1-$(OH)_2$

(4) Sorption study of CAU-1-$(OH)_2$

(5) Experimental EDXRD pattern of CAU-1-$(OH)_2$

(6) Microwave set up of the in-situ EDXRD investigation of CAU-1-$(OH)_2$

(7) Hydrodynamic diameters of the CAU-1-$(OH)_2$ particles after microwave and conventional syntheses

(8) Calculated pre-exponential factors for CAU-1-$(OH)_2$ syntheses by applying the Arrhenius equation

(9) Plots of extent of crystallization and the corresponding Sharp-Hancock plots

(10) IR-spectrum of CAU-1-$(OH)_2$

(1) High-throughput syntheses of CAU-1-$(OH)_2$

Reactions were carried out using our 24-high-throughput reactor system.[1] The high-throughput X-ray analyses were performed in transmission geometry using a STOE HT powder diffractometer equipped with an xy-stage and an image-plate detector. Based on the optimized synthesis conditions established for the amino-functionalized CAU-1[2], a molar ratio of $AlCl_3 \cdot 6H_2O$: $H_2BDC(OH)_2$ = 3.5 : 1, a reaction temperature of 125 °C and a reaction time of 5 h were chosen as starting parameters. The following parameters were investigated: the amount of NaOH and the concentration of reagents. The exact amounts of reactants used are listed Table S1.

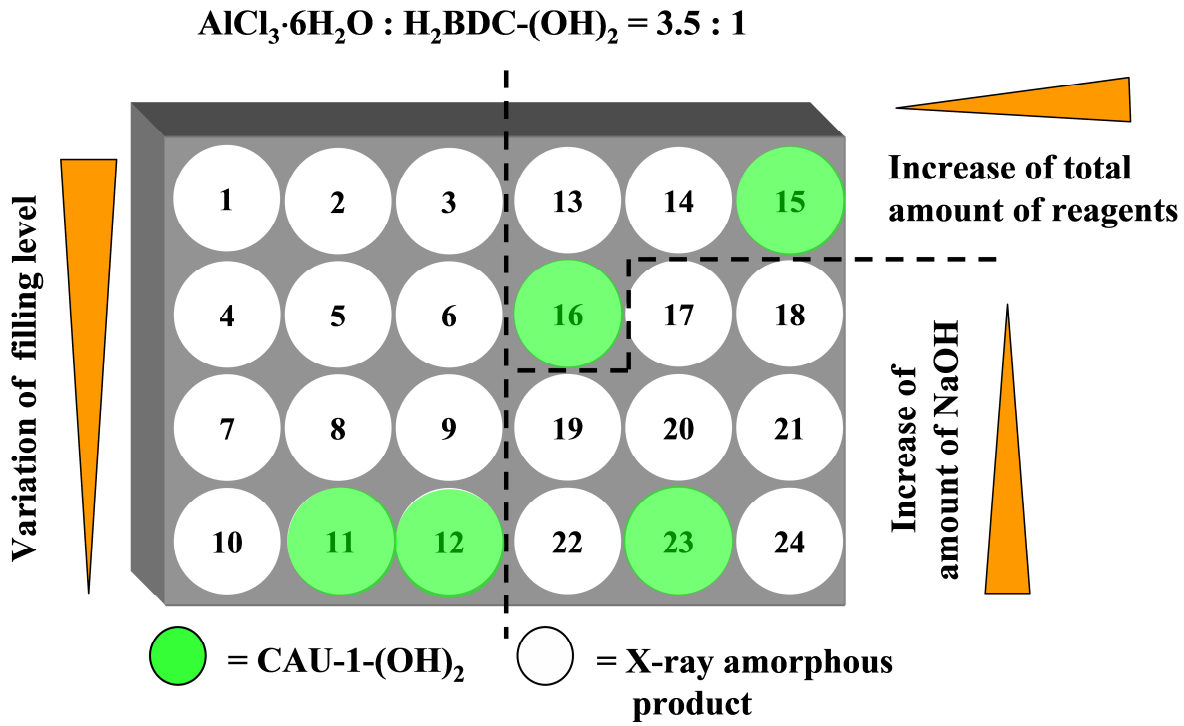

Figure S1. Results of the high-throughput investigation of the system $AlCl_3 \cdot 6H_2O$/ $H_2BDC(OH)_2$ /MeOH/NaOH at 125 °C.

Table S1. Molar ratios and exact amounts of reactants used in the high-throughput investigation of the system $AlCl_3 \cdot 6H_2O$/ $H_2BDC(OH)_2$ /MeOH/NaOH at a reaction temperature 125 °C and a reaction time of 5 h.

Reactions 1-12: Variation of filling level and overall concentration by changing the amount of methanol used:

reaction mixture	$AlCl_3 \cdot 6H_2O$ / mg	$H_2BDC(OH)_2$ / mg	MeOH / µl	2M NaOH in MeoH / µl
1	34.7	9.5	2000	15
2	34.7	9.5	1900	15
3	34.7	9.5	1800	15
4	34.7	9.5	1700	15
5	34.7	9.5	1600	15
6	34.7	9.5	1500	15
7	34.7	9.5	1300	15
8	34.7	9.5	1200	15
9	34.7	9.5	1100	15
10	34.7	9.5	1000	15
11	34.7	9.5	800	15
12	34.7	9.5	600	15

Reactions 10-13: Variation of total amount of educts (i.e. concentration):

reaction mixture	$AlCl_3 \cdot 6H_2O$ / mg	$H_2BDC(OH)_2$ / mg	MeOH / µl	2M NaOH in MeoH / µl
13	34,7	9,5	1000	15
14	69,5	19,1	1000	30
15	104,7	29,8	1000	45
16	139	39,8	1000	60

Reactions 14-19: Variation of amount of NaOH:

reaction mixture	$AlCl_3 \cdot 6H_2O$ / mg	$H_2BDC(OH)_2$ / mg	MeOH / µl	2M NaOH in MeoH / µl
17	34.7	9,5	800	0
18	34.7	9,5	800	5
19	34.7	9,5	800	10
20	34.7	9,5	800	20
21	34.7	9,5	800	30
22	34.7	9,5	800	40
23	34.7	9,5	800	50
24	34.7	9,5	800	60

The XRPD patterns of reaction mixtures (10, 11, 12), (13, 14, 15, 16) and (22, 23, 24) are shown in Figures S3, S4 and S5:

The XRPD patterns of reaction mixtures (10, 11, 12), (13, 14, 15, 16) and (22, 23, 24) are shown in Figures S3, S4 and S5:

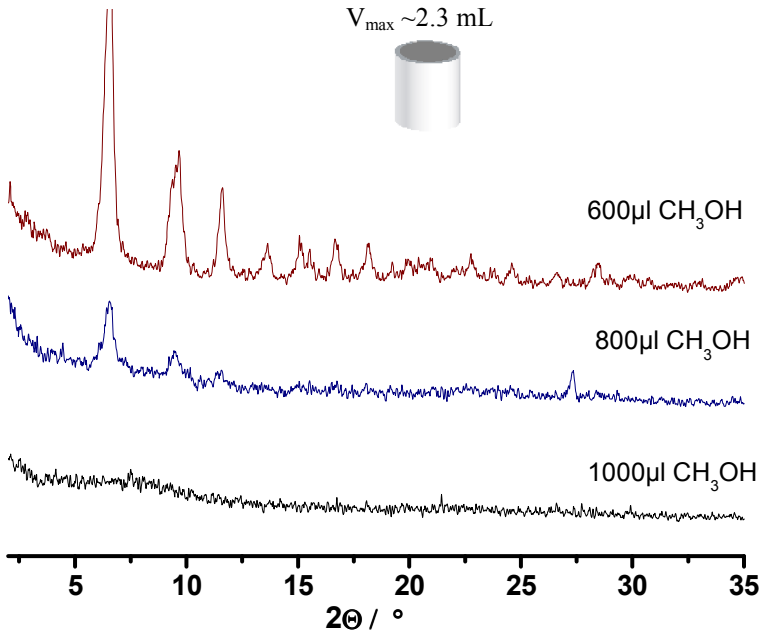

Figure S2. XRPD patterns of the products of reaction mixtures 10 (bottom), 11 (middle) and 12 (top).

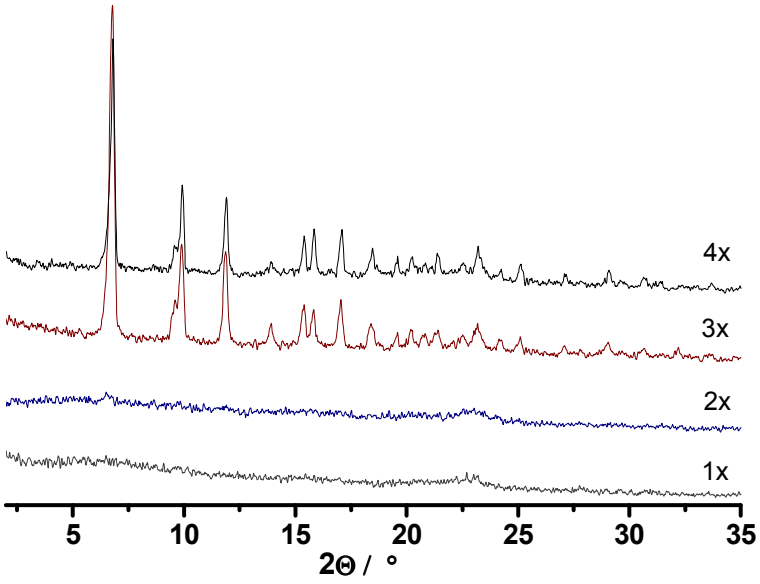

Figure S3. XRPD patterns of products of reaction mixtures 13, 14, 15, and 16 (from bottom to top). The concentration of the reaction mixtures is increased in four steps.

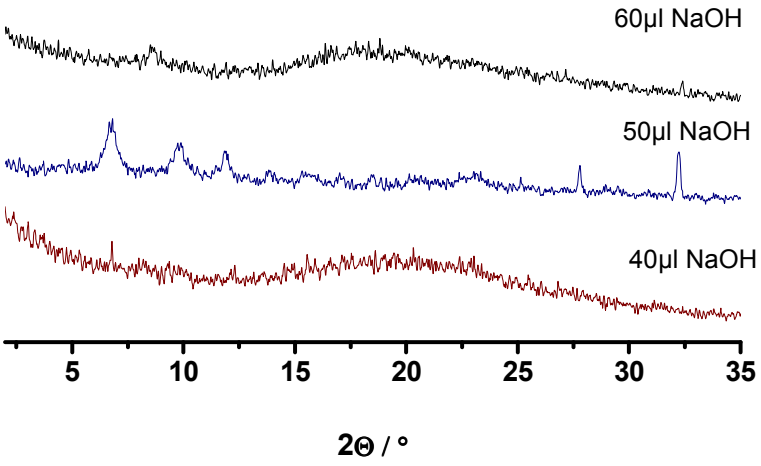

Figure S4. XRPD patterns of the products of reaction mixtures 22 (bottom), 23 (middle) and 24 (top). The amount of added NaOH (2M in methanol) was increased.

(2) Experimental XRPD pattern of CAU-1-$(OH)_2$

CAU-1-$(OH)_2$ could be synthesized with high crystallinity and without crystalline impurities; Lattice parameters of the unit cell were determined by using WinXPOW[3]. Lattice parameter refinement and systematic extinctions led to a tetragonal body-centered unit cell (FOM (F30) = 33.2 (0.012, 75) with $a = b = 18.320(5)$ and $c = 17.711(6)$ Å. The results of the lattice parameter refinement of CAU-1-$(OH)_2$ are listed in Table S2.

Comparison of the powder pattern of CAU-1$(OH)_2$ with the powder pattern of CAU-1. (Figure S5).

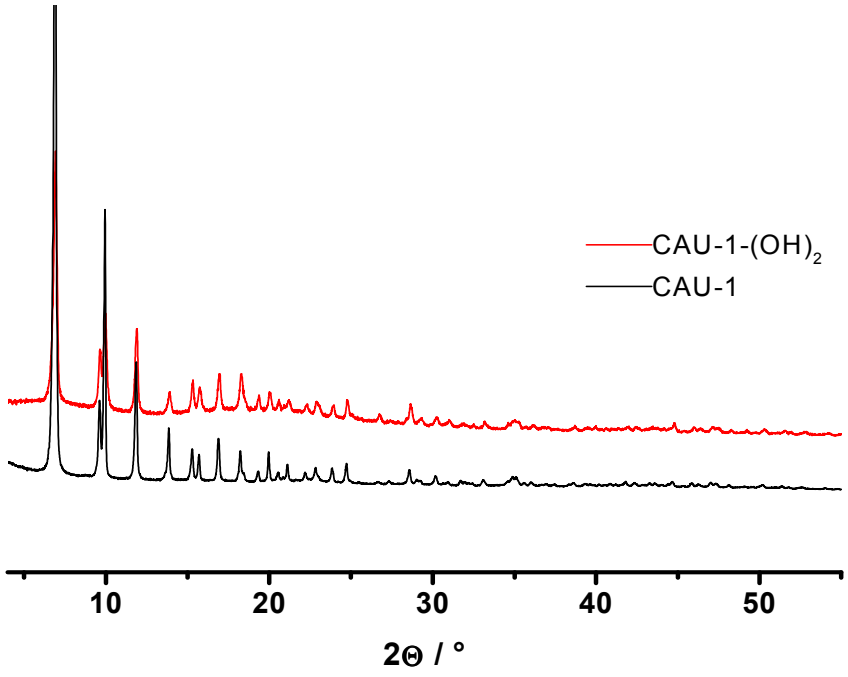

Figure S5. XRPD pattern of CAU-1-$(OH)_2$ (red) and CAU-1 (black)

Table S2. Results of the lattice parameter refinement for CAU-1-$(OH)_2$.

Lattice parameters of CAU-1-$(OH)_2$									
Symmetry				**a / Å**		**b / Å**		**c / Å**	**V / Å^3**
Tetragonal I				18.320(5)		18.320(5)		17.711(6)	5945(1)
List of the observed and calculated reflections of CAU-1-OH_2									
	$2\theta_{obs.}$	h	k	l	$2\theta_{cal.}$	obs.- cal.	int.	$d_{obs.}$	$d_{cal.}$
1	6.92	1	0	1	6.936	-0.0167	100	12.7643	12.7337
2	9.649	2	0	0	9.648	0.0013	32	9.159	9.1602
3	9.97	0	0	2	9.98	-0.0099	43.9	8.8644	8.8557
4	11.887	2	1	1	11.892	-0.0053	38.8	7.4394	7.4361
5	13.896	2	0	2	13.898	-0.0016	17.1	6.3676	6.3669
6	15.316	3	1	0	15.281	0.0343	20.8	5.7805	5.7934
		3	0	1	15.335	-0.0194	5.7733		
7	15.749	1	0	3	15.758	-0.0095	18.6	5.6226	5.6192
8	16.946	2	2	2	16.946	3E-4	23.5	5.228	5.228
9	18.29	3	1	2	18.284	0.0052	23.6	4.8468	4.8481
10	19.363	4	0	0	19.364	-0.0018	15.8	4.5805	4.5801
11	20.021	0	0	4	20.037	-0.0166	16.9	4.4315	4.4278
12	20.589	3	3	0	20.551	0.0371	14.2	4.3105	4.3182
		4	1	1	20.592	-0.0032	4.3098		
13	21.198	1	1	4	21.188	0.01	14.2	4.1879	4.1899
14	22.295	2	0	4	22.282	0.013	12.8	3.9842	3.9865
15	22.912	3	3	2	22.894	0.018	13.9	3.8783	3.8813
16	23.92	4	2	2	23.914	0.0056	12.6	3.7172	3.718
17	24.786	5	1	0	24.76	0.0265	14.7	3.5892	3.5929
		5	0	1	24.794	-0.0074	3.5881		
18	26.742	5	1	2	26.755	-0.0131	9.5	3.331	3.3293
19	27.419	2	1	5	27.409	0.01	7.5	3.2502	3.2514
20	28.656	5	0	3	28.651	0.0049	12.9	3.1127	3.1132
21	29.348	4	4	2	29.34	0.0082	8.2	3.0408	3.0416
22	30.243	0	0	6	30.253	-0.0096	8.5	2.9528	2.9519
		5	0	1	24.794	-0.0074	3.5881		
23	31.017	1	1	6	31.048	-0.0308	7.4	2.8809	2.8781
24	31.838	2	0	6	31.825	0.0137	6.3	2.8084	2.8096
25	32.535	6	2	2	32.495	0.0398	5.8	2.7499	2.7532
26	33.176	6	3	1	33.164	0.0118	7.2	2.6982	2.6992
27	34.63	7	1	0	34.592	0.0381	6.5	2.5881	2.5909
		7	0	1	34.617	0.0131	2.5891		
28	35.01	5	3	4	34.99	0.0202	7.5	2.5609	2.5624
29	35.717	6	0	4	35.69	0.0273	5.3	2.5118	2.5137
30	36.197	4	0	6	36.173	0.0237	5.4	2.4796	2.4812
		6	3	3	36.211	-0.0144	2.4787		
31	36.834	3	3	6	36.854	-0.0204	4.7	2.4382	2.4369
32	37.148	2	1	7	37.16	-0.0117	5.1	2.4183	2.4175

33	38.663	6	5	1	38.69	-0.0272	5.4	2.327	2.3254
34	39.427	5	1	6	39.477	-0.0502	5.1	2.2836	2.2808
35	39.955	8	1	1	39.969	-0.0139	5.3	2.2547	2.2539
36	40.322	7	1	4	40.298	0.0234	4.6	2.235	2.2362
37	40.637	8	0	2	40.661	-0.0239	4.5	2.2184	2.2171
38	41.371	1	1	8	41.339	0.0316	4.7	2.1807	2.1823
		4	4	6	41.352	0.0191	2.1816		
		6	5	3	41.386	-0.0149	2.1799		
39	41.929	8	2	2	41.889	0.0397	5.4	2.153	2.1549
		2	0	8	41.949	-0.0203	2.152		
		5	3	6	41.961	-0.0327	2.1514		
40	42.435	7	5	0	42.408	0.0266	5.3	2.1284	2.1297
		8	3	1	42.429	0.0056	2.1287		
41	43.452	5	0	7	43.428	0.0236	4.7	2.0809	2.082
42	44.783	9	1	0	44.759	0.024	6.6	2.0221	2.0232
		9	0	1	44.779	0.0039	2.0223		
43	45.392	8	4	2	45.411	-0.0198	4	1.9964	1.9956
44	46.005	9	1	2	45.978	0.0275	5.2	1.9712	1.9723
		3	3	8	46.033	-0.0283	1.9701		
45	46.38	1	0	9	46.367	0.0129	4.8	1.9562	1.9567
		6	5	5	46.39	-0.01	1.9558		
46	47.139	6	4	6	47.16	-0.0207	5.3	1.9264	1.9256
		9	0	3	47.191	-0.0514	1.9244		
47	48.278	5	1	8	48.244	0.0332	4	1.8836	1.8848
		9	2	3	48.286	-0.008	1.8833		
48	49.222	7	7	0	49.194	0.0279	4.3	1.8497	1.8506
		9	4	1	49.213	0.0092	1.85		
49	49.722	10	0	0	49.727	-0.0049	3.5	1.8322	1.832
50	50.29	10	1	1	50.274	0.0156	4.5	1.8128	1.8134
		7	7	2	50.33	-0.0397	1.8115		
51	51.558	0	0	10	51.56	-0.0026	4.1	1.7712	1.7711
		9	3	4	51.592	-0.0343	1.7701		
52	51.873	10	2	2	51.891	-0.0186	3.5	1.7612	1.7606
53	52.791	5	0	9	52.758	0.0324	3.5	1.7327	1.7337
		9	2	5	52.779	0.0115	1.7331		
54	54.233	8	1	7	54.211	0.0227	3.3	1.69	1.6906
55	54.994	6	4	8	54.969	0.0252	2.8	1.6684	1.6691
		9	1	6	54.979	0.0151	1.6688		
56	55.545	8	7	3	55.499	0.0453	2.7	1.6531	1.6544
		4	0	10	55.589	-0.0448	1.6519		
57	57.844	8	8	2	57.839	0.0045	2.8	1.5928	1.5929
		8	0	8	57.887	-0.0429	1.5917		
58	58.867	8	2	8	58.838	0.0282	3.1	1.5675	1.5682
		7	7	6	58.848	0.0185	1.568		
59	60.533	9	6	5	60.545	-0.0118	2.4	1.5283	1.528

(3) Thermal investigation on CAU-1-$(OH)_2$

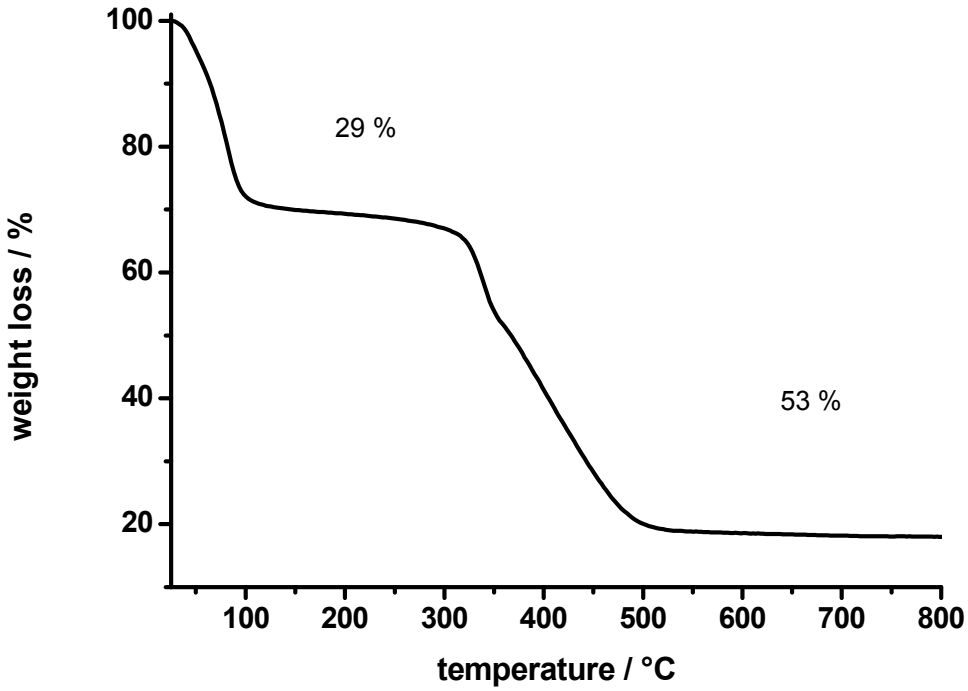

Figure S6. TG-curve of CAU-1-$(OH)_2$ under air with a heating rate of 4K / min.

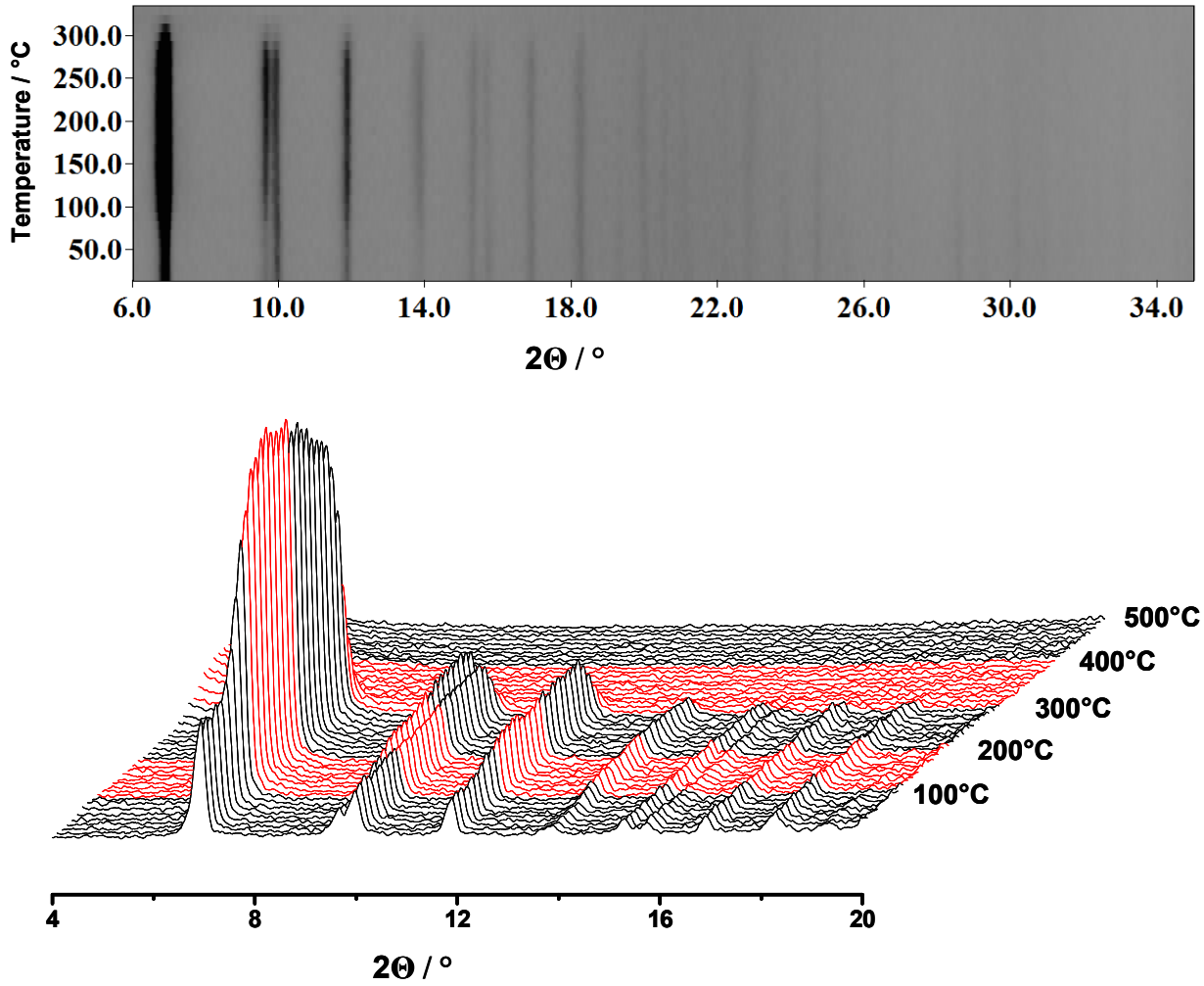

Figure S7. Top: Temperature-dependent X-ray powder pattern of CAU-1-$(OH)_2$ in air (top-view); bottom: temperature-dependent X-ray powder pattern of CAU-1-$(OH)_2$ in air (20-500 °C).

(4) Sorption study on CAU-1-(OH)$_2$

Comparison of this data with the results of a sorption study on the MOFs HKUST-1, MIL-100 (Fe), MIL-101 and DUT-4.[4]

Table S2. Comparison of specific surface area S_A (calculated using the BET equation), total pore volume V_{N2} and total pore volume V_{H2O} of CAU-1-(OH)$_2$ with data from other highly porous MOFs.

Material	S_A ($m^2 \cdot g^{-1}$)	V_{N2} ($cm^3 \cdot g^{-1}$)[a]	V_{H2O} ($cm^3 \cdot g^{-1}$)[b]	CH_4 (wt.%)[c]
CAU-1-(OH)$_2$	1350	0.50	0.42	7.6
HKUST-1	1340	0.72	0.55	14.3
MIL-100 (Fe)	1549	0.82	0.81	
MIL-101	3017	1.61	1.28	9.7
DUT-4	1360	0.79	0.28	
ZIF-8	1255	0.64	0.02	

[a] Calculated at $p/p_0 = 0.9$ from nitrogen adsorption isotherm and 77 K.

[b] Calculated at $p/p_0 = 0.9$ from water adsorption isotherm and 298 K.

[c] Calculated at 35 bar and 298 K.

The surface area of CAU-1-(OH)$_2$ fits well in the values of the other investigated microporous compounds. In addition, the total pore volume calculated from the water adsorption isotherm is smaller than the calculated micropore volume from the nitrogen adsorption. This may be due to hydrophobic areas in CAU-1-(OH)$_2$.

(5) Experimental EDXRD pattern of CAU-1-$(OH)_2$

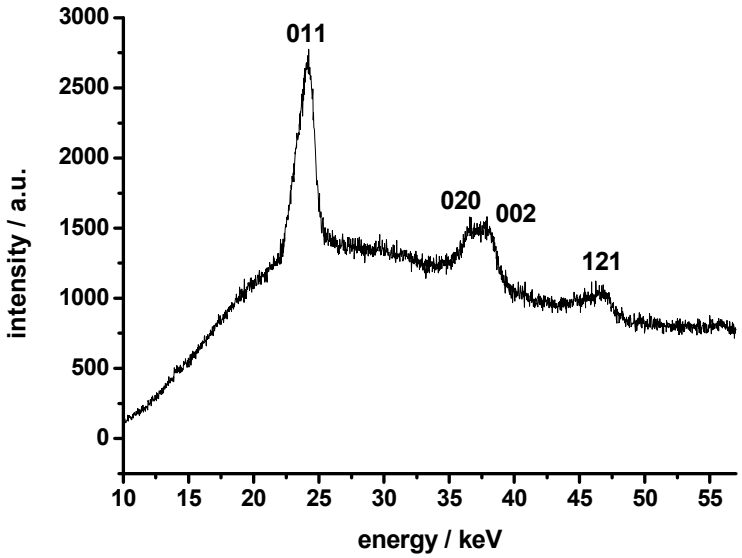

Figure S8. Experimental EDXRD pattern of CAU-1-$(OH)_2$ (130 °C microwave synthesis after 50 min).

The plots of extent of crystallization (α) vs. time (t) obtained from the analysis of the four observed Bragg peaks show that the integration leads to very similar curves. (Figure S9) Due to the lower intensities of the 020, 002 and 121 peaks larger scattering of the data points is observed.

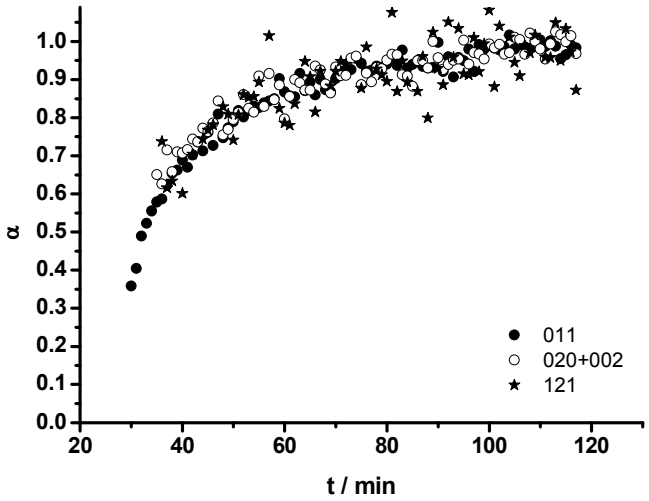

Figure S9. Plots of extent of crystallization (α) vs. time (t) obtained by integration of the 011, 020, 002 and 121 Bragg peaks during the microwave synthesis of CAU-1-$(OH)_2$ at 130 °C. The areas of the 020 and 002 Bragg Peaks were treated as single Peak due to a nearly complete overlapping of the Bragg peaks.

(6) Microwave set up of in-situ EDXRD investigations of CAU-1-$(OH)_2$

The microwave reactor Biotage Initiator (Figure S10) records the reaction temperature, heating power and pressure during the reaction. The stirring rate was digitally adjusted to 300 rpm. In addition, the reactions were also performed under stirring in a conventional oven using the same reaction mixtures and temperatures. This set-up is described in reference [5].

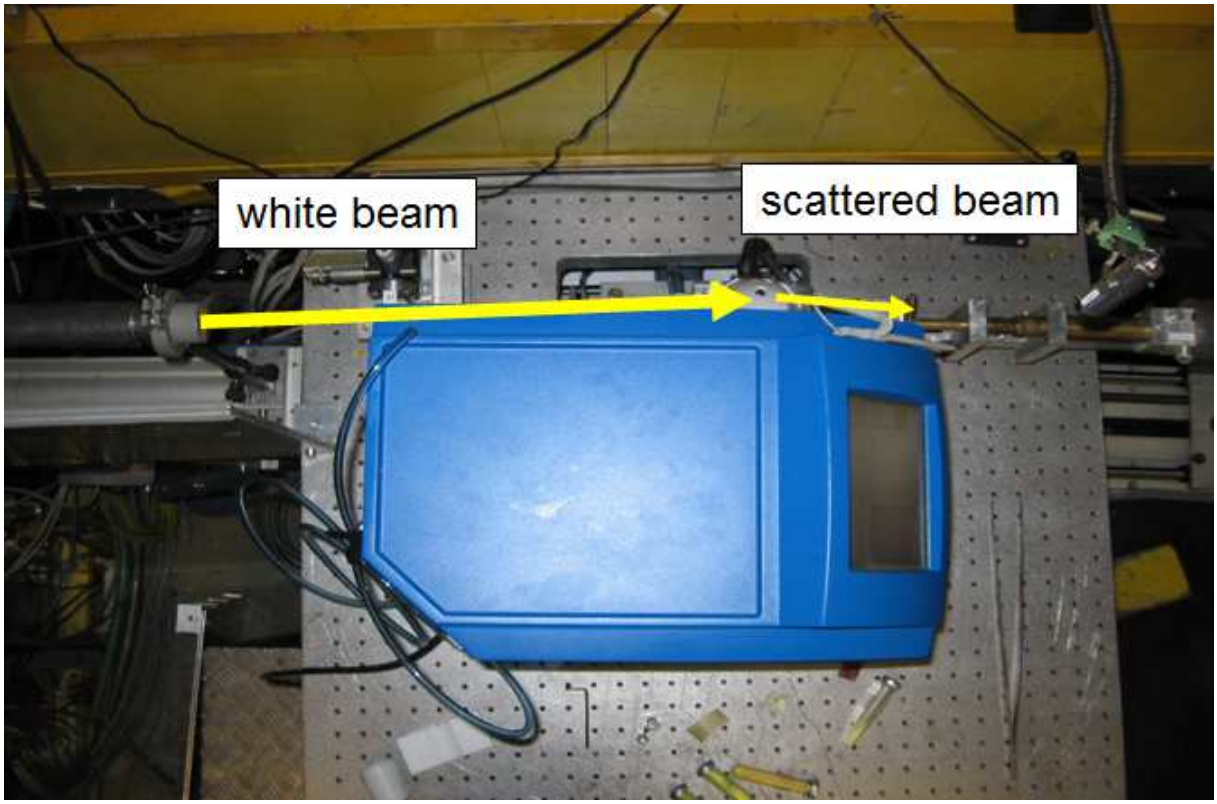

Figure S10. Implementation of the microwave reactor Biotage Initiator at beamline F3, HASYLAB, Hamburg for the in-situ EDXRD measurements.

The temperature of the conventional oven can be controlled by a thermocouple within the copper block next to the autoclave and regulated to an accuracy of ±1 K. Several test showed, that the reaction mixture reached the reaction temperature within two minutes.[6] The reactants can be mixed by a magnetic stirrer with a maximum rotational speed of 1000 rpm. The speed cannot be adjusted exactly since no digital readout is given.

To estimate the influence of different stirring rates on the synthesis of CAU-1-$(OH)_2$ the microwave assisted synthesis was additionally carried out at a stirring rate of 900 rpm for the reaction temperature of 130 °C. The plots of extent of crystallization (α) vs. time (t) obtained by integration of the 011 reflection of these two reactions are very similar.(Figure S11) However, the first appearance of the Bragg peaks was observed two minutes earlier for the synthesis using a stirring rate of 900 rpm. This is probably due to a faster dissolution of the reactants

at the beginning of the reaction using the higher stirring rate (the crystallisation takes place from a clear solution).

The conventional and the microwave assisted reactions were carried out in slightly different glass vessels (Duran® culture tube 12 x 100 mm(conventional) and Biotage® microwave vials 2-5mL (microwave)). They have a similar geometry and therefore similar surface : volume ratios. Thus, no or only a minor influence on the kinetic of the reaction is expected.

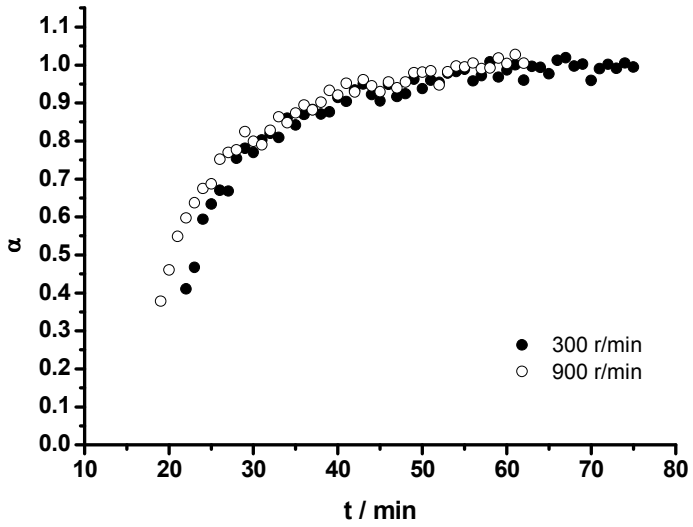

Figure S11. Plots of extent of crystallization (α) vs time (t) obtained by integration of the 011 Bragg peak during the microwave synthesis of CAU-1-$(OH)_2$ at 130 °C using a rotational speed of 300 and 900 rpm.

(7) Hydrodynamic diameter of the CAU-1-$(OH)_2$ particles after microwave and conventional syntheses

The hydrodynamic diameters of the CAU-1-$(OH)_2$ particles after microwave and conventional syntheses were measured (Figure S12) with dynamic light scattering using a DelsaNano C apparatus (Beckman & Coulter). Therefore, all syntheses were repeated with the ascertained reaction times from the in-situ EDXRD measurements. Increasing temperature leads to a decrease of the hydrodynamic diameter of the CAU-1-$(OH)_2$ particles for both heating methods. The microwave assisted synthesis of CAU-1-$(OH)_2$ leads to smaller particles compared to the conventional synthesis at same temperature. Above 130 °C no crystalline product was observed in the microwave assisted syntheses.

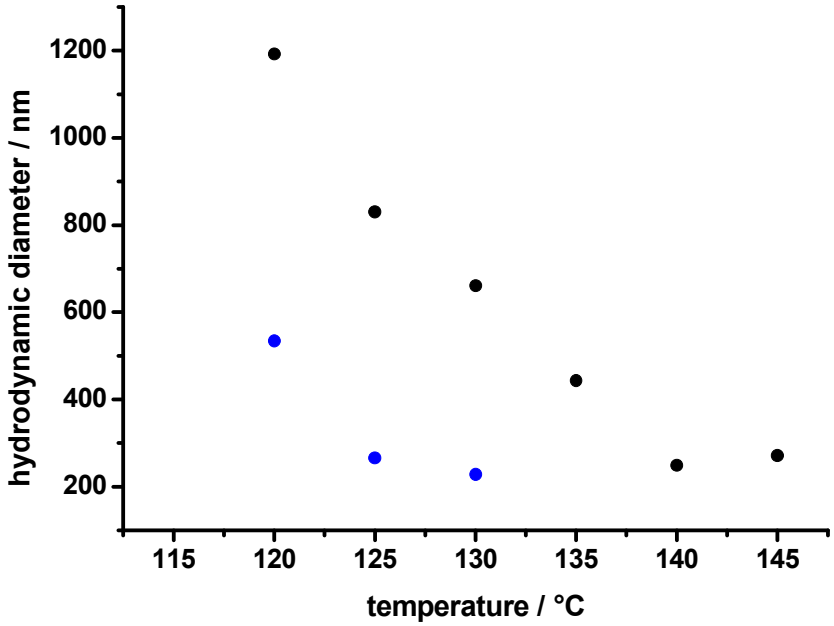

Figure S12. Comparison of the hydrodynamic diameters of CAU-1 particles synthesized by microwave (blue) and conventional heating (black) in the temperature range 120 - 145 °C.

(8) Plots of extent of crystallization and the corresponding Sharp-Hancock plots

For the crystallization curves (Figure S13, left) of CAU-1-$(OH)_2$ the area of the 011 reflections was integrated, which have the highest intensity of the observed Bragg peaks in the recorded spectra. The induction time as well as the crystal growth depends strongly on the reaction temperature. An increase of the reaction temperature leads to shorter crystallization and reaction times. At higher temperatures the reaction (nucleation and crystallisation) proceeds much faster. The minimal recording time per spectrum is 1 minute in order to get a good signal to noise ratio. Thus for the reactions at high temperatures rather large α values are observed as the first value. For reactions applying microwave heating no product formation of CAU-1-$(OH)_2$ was observed for reaction temperatures above 130 °C. The Avrami-Erofèev nucleation-growth model was used for the kinetic evaluation of the data. [7] The linear Sharp-Hancock plots obtained from the crystallization curves of CAU-1-$(OH)_2$ are shown in Figure S13 (right). The Avrami equation fits the kinetic linear Sharp-Hancock plots obtained from crystallization curves describing the crystallization of CAU-1-$(OH)_2$.

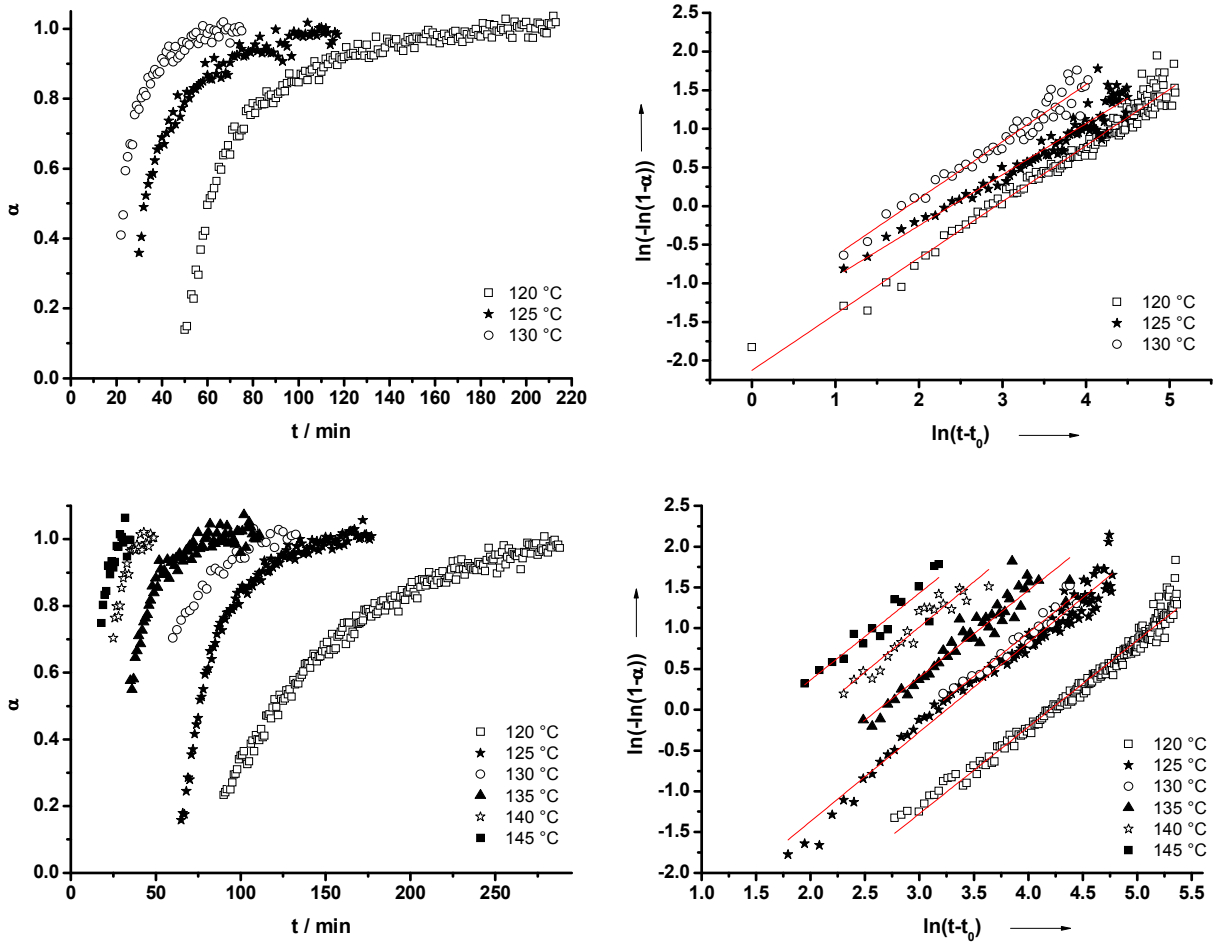

Figure S13. Kinetic analyses of the crystallization of CAU-1-$(OH)_2$ obtained via microwave and conventional heating. Left: Plots of extent of crystallization (α) curves against time (t) obtained by integration of the 011 Bragg peak in the EDXRD spectra during microwave (top) and conventional (bottom) reactions. Right: Analyses by the method of Sharp and Hancock to fit with the Avrami–Eroféev nucleation-growth crystallization model for microwave (top) and conventional (bottom) reactions.

(9) Calculated pre-exponential factors for CAU-1-$(OH)_2$ syntheses applying Arrhenius equation.

Table S3. Calculated pre-exponential factors (A) for the crystal growth of CAU-1-$(OH)_2$ in the temperature range 120 - 145 °C using conventional and microwave heating method.

reaction temperature	A [s^{-1}] (con)	A [s^{-1}] (mw)
120 °C	$6.34 \cdot 10^{13}$	$1.07 \cdot 10^{15}$
125 °C	$9.92 \cdot 10^{13}$	$1.06 \cdot 10^{15}$
130 °C	$6.96 \cdot 10^{13}$	$1.07 \cdot 10^{15}$
135 °C	$7.07 \cdot 10^{13}$	
140 °C	$7.59 \cdot 10^{13}$	
145 °C	$7.35 \cdot 10^{13}$	

(10) IR-spectrum of CAU-1-$(OH)_2$

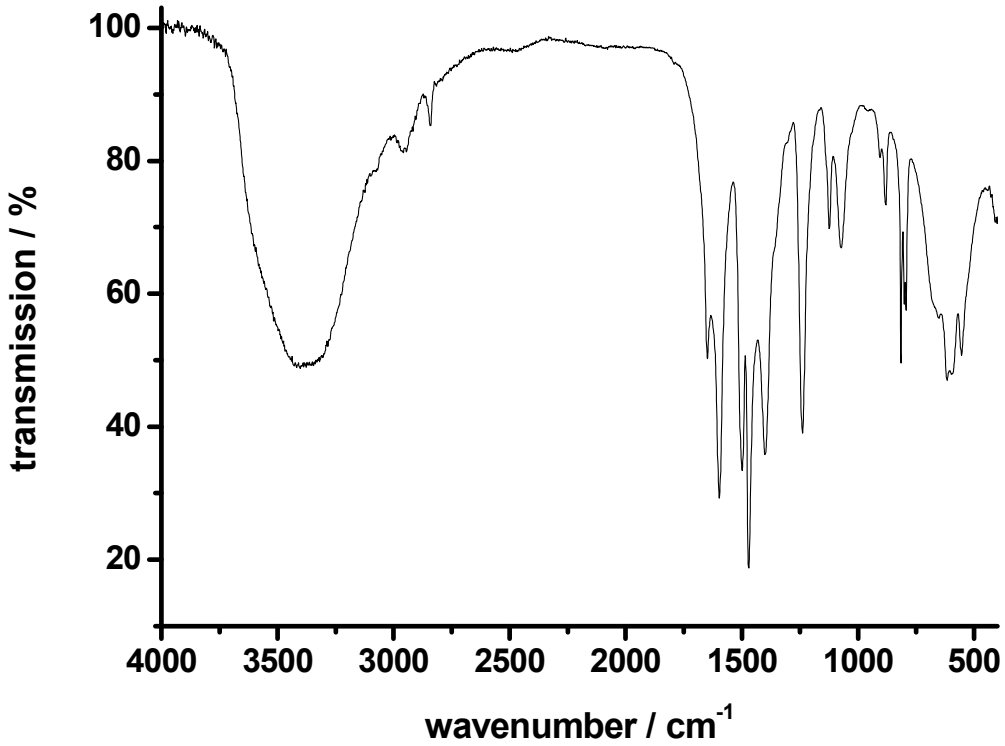

Figure S14. IR-spectrum of CAU-1-$(OH)_2$.

Literature

[1] A. Sonnauer, F. Hoffmann, M. Fröba, L. Kienle, V. Duppel, M. Thommes, C. Serre, G. Férey, N. Stock, *Angew. Chem.* **2009**, 121, 3849-3852; *Angew. Chem. Int. Ed.* **2009**, *48,* 3791-3794.
[2] T. Ahnfeldt, N. Guillou, D. Gunzelmann, I. Margiolaki, T. Loiseau, G. Férey, J. Senker, N. Stock, *Angew*. *Chem*. **2009**, *121*, 5265–5268; *Angew. Chem. Int. Ed.* **2009**, *48*, 5163-5166.
[3] *STOE WinXPOW version 2.11*, Stoe & Cie GmbH, Darmstadt, Germany, **2005**.
[4] P. Küsgens, M. Rose , I. Senkovska, H. Fröde , A. Henschel, S. Siegle S. Kaskel, *Micropor. Mesopor. Mater.* **2009**, *120*, 325-330.
[5] L. Engelke, M. Schaefer, M. Schur, W. Bensch, *Chem. Mater*. **2001**, *13*, 1383-1390.
[6] R. Kiebach, M. Schaefer, F. Porsch, W. Bensch, *Z. Anorg. Allg. Chem.* **2005**, *631*, 369-374.
[7] J. D. Sharp, J. H. Hancock, *J. Am. Ceram. Soc.* **1972**, *55*, 74-77.

Anhang 9:

Supporting Information

Synthesis of isoreticular CAU-1 compounds: Effects of linker and heating methods on the kinetics of the synthesis

Tim Ahnfeldt, Norbert Stock

Comparison of the EDXRD and the ADXD measurement

The EDXRD patterns of CAU-1-NH_2 were recorded using a nitrogen-cooled germanium solid-state detector positioned at approximately 1.90° 2theta. The detector contains 2048 channels, which recording the data in an energy range of 6-57 keV. The beam is collimated to a dimension of 20µm x 20µm by wolfram-collimators. The d-spacing is given by the equation:

$$E = 6.199/(d \sin\Theta)$$

The energy calibration of the detector was performed using a glass containing a series of heavy elements with well separated fluorescence lines. The angle of the detector in the conventional and MW set-up, were calibrated using the set of Bragg peaks measured from a pre-made sample of CAU-1-NH_2. A comparison of an EDXRD with an ADXD measurement is given in Figure S1.

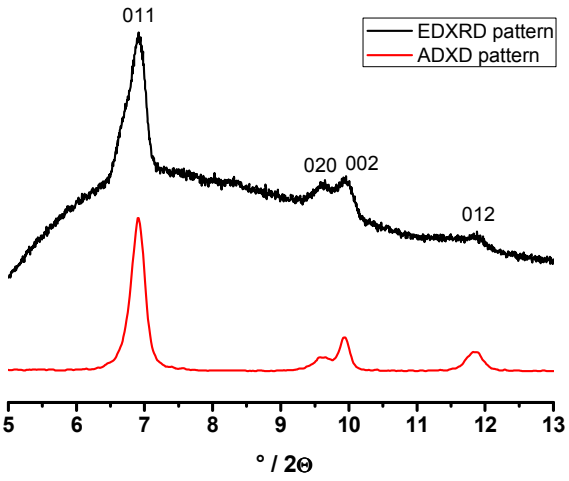

Figure S1: Comparison of ADXD data recorded from a dry sample of CAU-1-NH_2 synthesised at 140 °C using MW-assisted heating (bottom) and the corresponding EDXRD measurement during in-situ crystallisation study (top).

Preferred orientation

To exclude the presence of preferred orientation the 011, 020, 002 and 012 Bragg reflections of the EDXRD measurements were used to calculate the extent of crystallization (α) (conventional synthesis of CAU-1-NH_2 at 145 °C). The corresponding curves α(t) are shown in Figure 2. Since superimposable curves are obtained the presence of preferred orientation can be excluded.

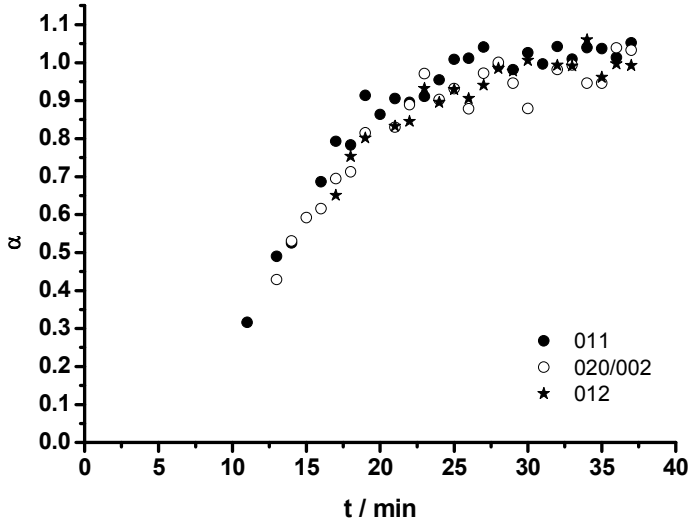

Figure S2. Plots of extent of crystallization (α) vs. reaction time (t) obtained by integration of the 011, 020, 002 and 012 Bragg peaks during the conventional synthesis of CAU-1-NH_2 at 145 °C. The areas of the 020 and 002 Bragg peaks were treated as a single peak due to a nearly complete overlap.

Determination of t_0

The parameter t_0, which is the time until the first crystallites are observed in the EDXRD spectra, is one of the key parameter for the kinetic modelling using the Avrami-Eroféev expression. Therefore, the determination of t_0 was done very carefully for each measurement. As an example the determination of t_0 is shown for the micro-wave-assisted synthesis of CAU-1-NH_2 at 125 °C. The data were accumulated in 1 min intervals. Between a reaction time of 12 min and 14 min the first product peaks appears in the EDXRD spectra (Figure S3, top) at ~23 keV. Due to the low intensity of the Bragg peaks at the beginning of the reaction, the exact time of t_0 was often difficult to determine. Hence, in addition contour plots of the EDXRD spectra were calculated to verify the estimated t_0 values (Figure S3, bottom). In good agreement a time of 13 min was determined for t_0 for the MW-assisted synthesis of CAU-1-NH_2 at 125 °C using both methods.

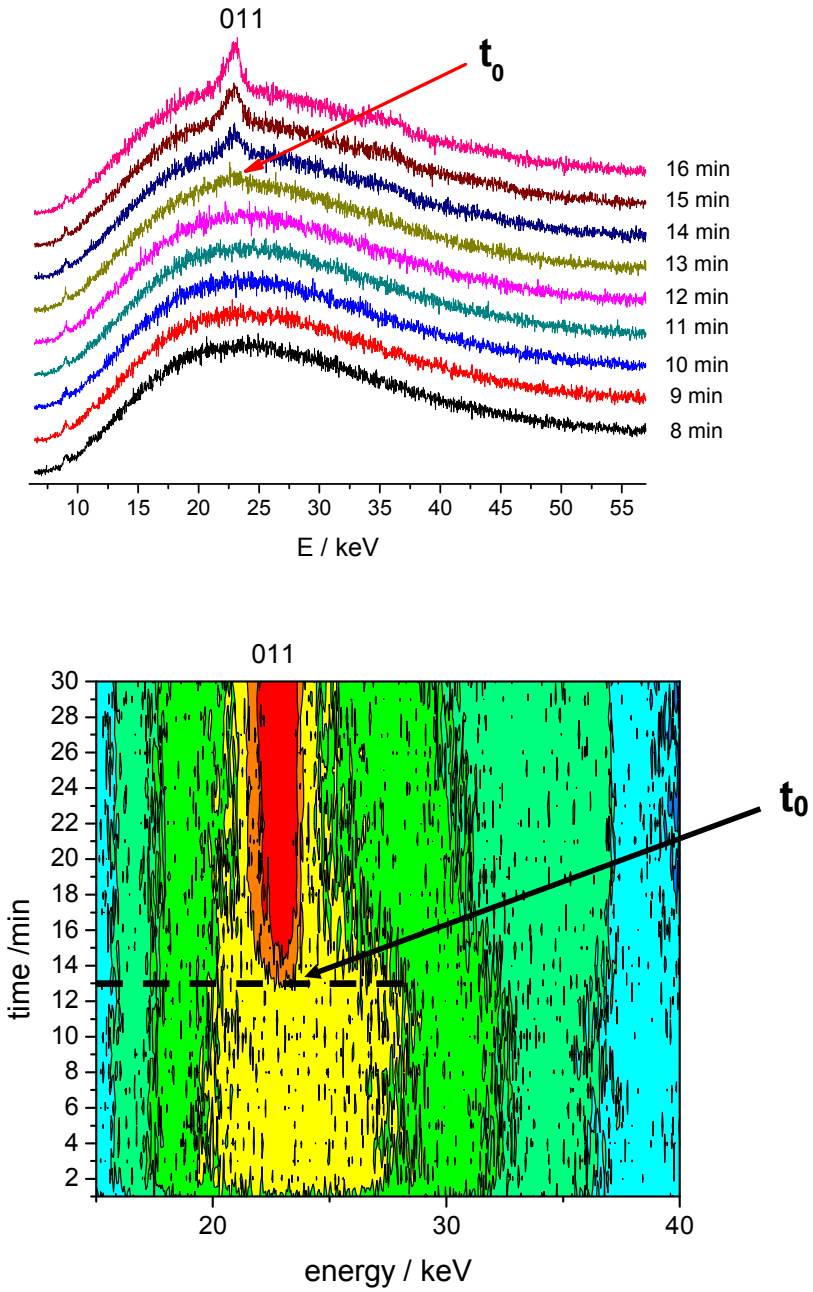

Figure S3. Plots of the EDXRD spectra (top) and the contour plot (bottom) of the MW-assisted synthesis of CAU-1-NH_2 to determine t_0. For both methods the 011 Bragg Peak occurs at a reaction time of 13 min at ~23 keV.

Dynamic light scattering

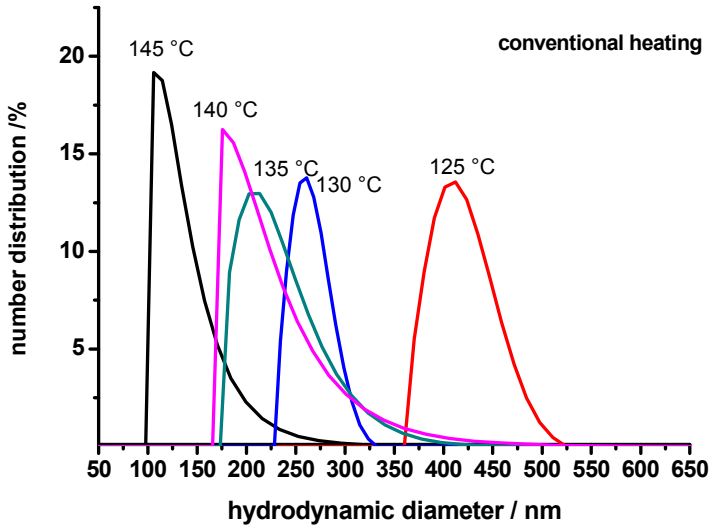

Figure S2: Differential number distribution curves of the hydrodynamic diameters of CAU-1 particles synthesized by conventional electrical heating as determined by dynamic light scattering measurements.

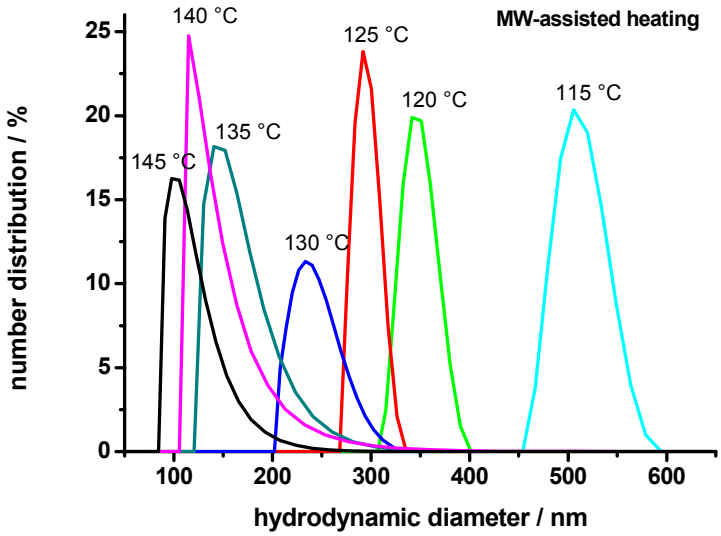

Figure S3: Differential number distribution curves of the hydrodynamic diameters of CAU-1 particles synthesized by MW-assisted heating as determined by dynamic light scattering measurements.

Anhang 10:

SUPPORTING INFORMATION

3-D coordination polymers based on the Tetra-ThiaFulvaleneTetraCarboxylate (TTF-TC) derivative: synthesis, characterization and oxidation issues

Thi Le Anh Nguyen,[a] Rezan Demir-Cakan,[b] Thomas Devic,[a] Mathieu Morcrette,[b] Tim Ahnfeldt,[c] Pascale Auban-Senzier,[d] Norbert Stock,[c] Anne-Marie Goncalves,[a] Yaroslav Filinchuk,[e] Jean-Marie Tarascon,[b] Gérard Férey.[a]*

[a] Institut Lavoisier, UMR CNRS 8180, Université de Versailles Saint-Quentin-en-Yvelines, 45 avenue des Etats-Unis, 78035 Versailles cedex, France ; [b] LRCS UMR CNRS 6007, Université de Picardie Jules Verne, 33 rue Saint-Leu, 80039 Amiens, France; [c] Institute of Inorganic Chemistry, Christian-Albrechts-Universität, Otto-Hahn-Platz 6/7, 24118 Kiel, Germany; [d] Laboratoire de Physique des Solides, UMR CNRS 8502, Bât. 510, Université de Paris-Sud, 91405 Orsay, France; [e] SNBL at ESRF, 38043 Grenoble, France.

AUTHOR EMAIL ADDRESS devic@chimie.uvsq.fr

Content

1. Synthesis

1.1 (TTF-TC)H_4

The TetraThiaFulvalene tetracarboxylic acid ((TTF-TC)H_4, **6**) was synthesized in four steps following a procedure closely related to the one published by Pittmann et al.,[1] as shown in Scheme S1. The 4,5-dimethyloxycarbonyl-1,3-dithiole-2-thione (**3**) was prepared from ethylenetrithiocarbonate (Aldrich) and dimethylacetylenedicarboxylate[2] (Aldrich) and subsequently reacted with mercury(II) acetate to afford the corresponding dithiole-2-one[3] (**4**). Self-coupling in the presence of trimethylphosphite afforded the tetramethytetrathiafulvalenetetracarboxylate[1] (**5**). Further hydrolysis with lithium hydroxide followed by acidification[4] yielded to the desired tetrathiafulvalenetetracarboxylic acid **(6)**.

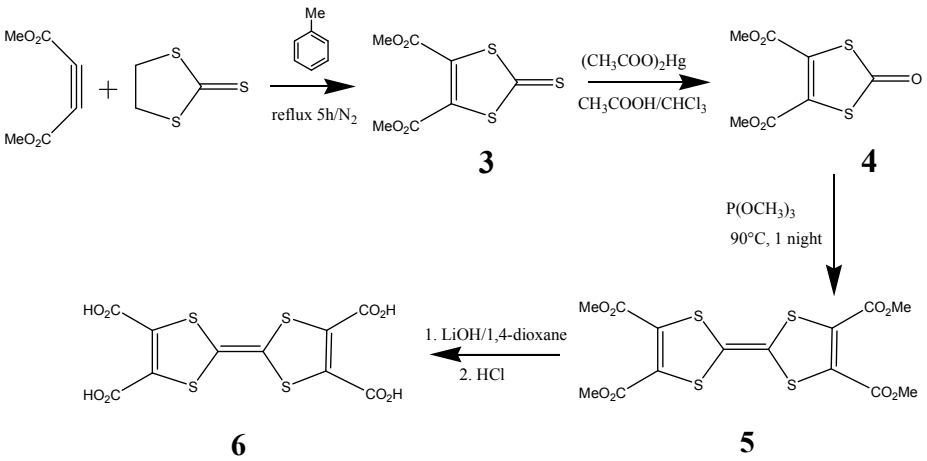

Scheme S1. Synthesis of (TTF-TC)H_4.

1.2 M_2(TTF-TC)H_2 (M = K, Rb, Cs) or MIL-132(K), -133(K,Rb) and -134(Cs)

Both forms of K_2(TTF-TC)H_2 (MIL-132: monoclinic, and MIL-133: orthorhombic) were synthesized using a mixture of (TTF-TC)H_4, potassium chloride (99%), potassium hydroxide (2M) and H_2O (3 mL) in a molar ratio 1:2:x:1270 ($0.75 < x < 2.5$). All the reactants were

placed in a 24 mL Teflon-lined steel autoclave, stirred for a few minutes and then heated at 70°C for 20 hours, cooled down to room temperature and kept at this temperature for 24 hours. The pH was monitored before and after the reaction, and always decreases during the reaction. The red crystals were filtered, washed with water and acetone and dried under air. The polymorphic MIL-132 and -133 were obtained at different pH, as shown in Figure S1. The monoclinic phase (MIL-132) was collected in a wide range of pH (typically x = 1.5) while the orthorhombic one (MIL-133) was only obtained in a pure form at intermediate pH (typically x = 0.75).

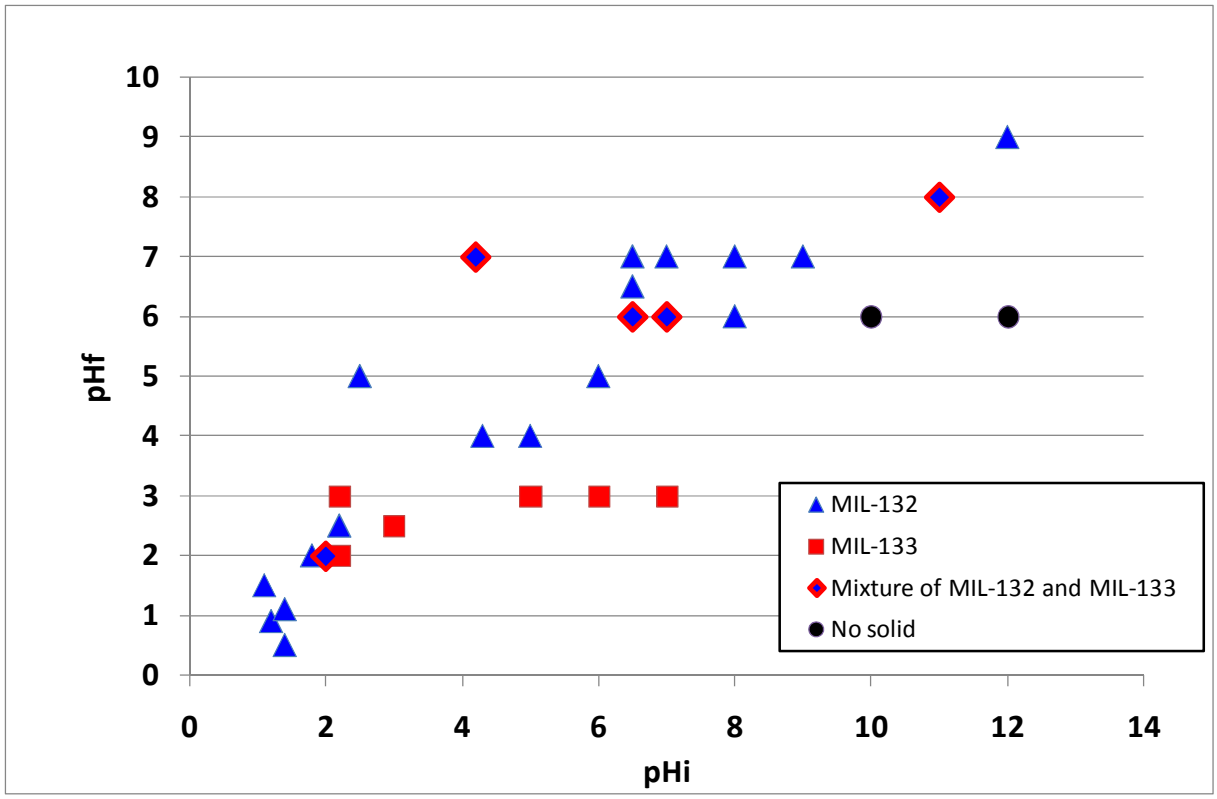

Figure S1. Formation of the polymorphic MIL-132(K) and MIL-133(K) *vs.* initial and final pHs.

The same procedure was used for the preparation of MIL-133(Rb) and MIL-134(Cs), but at a higher temperature (T = 100°C). Various composition (TTF-TC)H_4:MCl:MOH:H_2O 1:2:x:1270 were tested ($0 < x < 14$, 3 < initial pH < 10), but only one phase was observed for both Rb and Cs. The best yield was obtained for $x \sim 9$.

1.3 K(TTF-TC)H_2 or MIL-135

MIL-135(K) was prepared using a teflon lined steel autoclave equipped with two platinum electrodes (diameter 0.5 mm, active length about 2 cm). In order to avoid the fast diffusion of oxidized species, the electrodes were separated by a glass filter, a procedure commonly used for conventional electrocristallization.[5] A constant current density was applied using a 363 Princeton Applied Research potentiometer. A mixture of (TTF-TC)H_4, potassium chloride (99%), hydrochloric acid (1M) and H_2O (15 mL) in a molar ratio 1:13:1:6350 (initial pH = 3) was divided in the two compartments. The system was heated at 70°C for 17hrs, while a constant current density of 130 µA cm^{-2} was applied. After cooling down to room temperature, MIL-135(K) was recovered on the anode as a black crystalline. Higher temperature and current density above 350 µA.cm^{-2} lead to amorphous solid, whereas no solid product is observed at low current density (<50 µA.cm^{-2}), as shown in Figure S2.

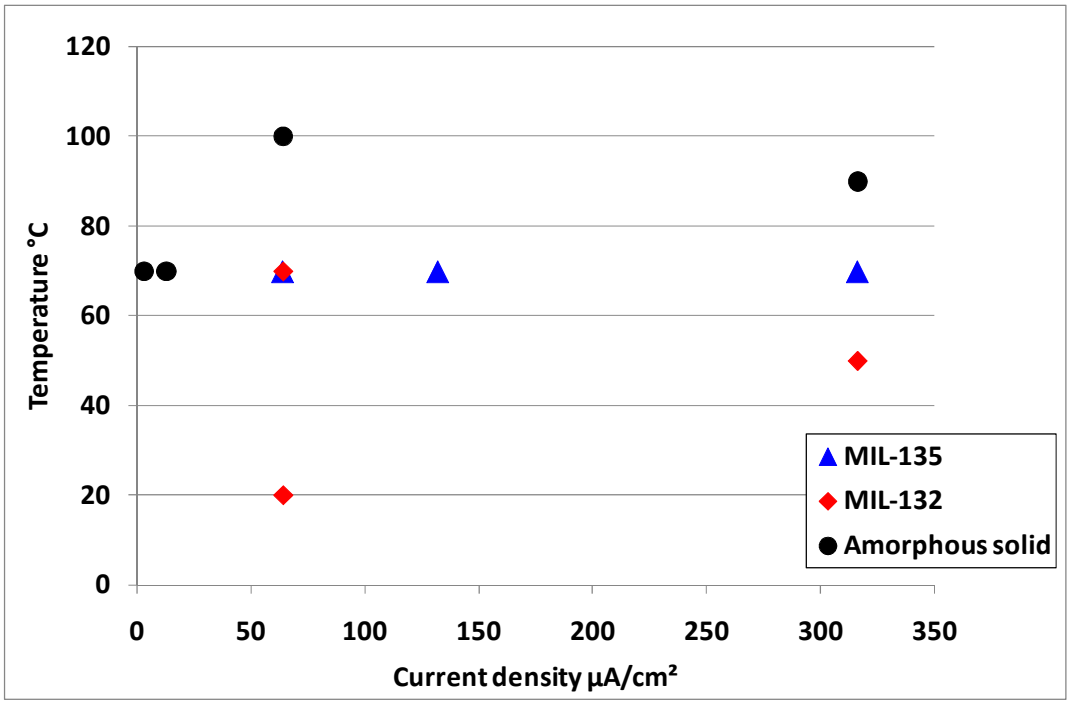

Figure S2. Effect of the temperature and pH on the formation of MIL-135(K).

2. Characterization

2.1 Single crystals X-Ray analysis

Single crystals of MIL-132(K), MIL-133(K, Rb), MIL-134(Cs) and MIL-135(K) were mounted with paratone oil on a nylon cryoloop. MIL-132(K) was measured at 200K at the European Synchrotron Research Facilities (ESRF, Grenoble, France) on BM01A (λ = 0.699765 Å), using a MAR345 image plate detector; whereas the other solids (MIL-133(K, Rb), MIL-134(Cs) and MIL-135(K)) were measured at 293K on a Siemens Smart diffractometer equipped with a Mo anode, a graphite monochromator and a CCD camera detector. The data reduction was performed with the Crysalis softwares for MIL-132 and SAINT for the other solids; the absorption correction was performed with the SADABS software. All structures were solved and refined by full-matrix least-squares techniques, based on F^2, using the SHELX software package.[6] All non hydrogen atoms were refined anisotropically, hydrogen atoms were found on the Fourier map and refined, sometimes (Rb, Cs) with constrains on the O-H (0.85-0.9 Å) and O···H (1.55 Å) distances. For MIL-133(K, Rb) and MIL-134(Cs), the occupancy of the hydrogen atom was found to be 50% because of statistical disorder. Crystallographic data are summarized in Table S1.

Table S1. Crystallographic data and refinement parameters for the TTF-TC based solids.

	MIL-132(K)	**MIL-133(K)**	**MIL-133(Rb)**	**MIL-134(Cs)**	**MIL-135(K)**
Empirical formula	$C_{10}H_2K_2O_8S_4$	$C_{10}H_2K_2O_8S_4$	$C_{10}H_2O_8Rb_2S_4$	$C_{10}H_2Cs_2O_8S_4$	$C_{10}H_2KO_8S_4$
Formula weight ($g.mol^{-1}$)	456.56	456.56	549.30	644.18	417.46
Temperature (K)	200	293	293	293	293
Wavelength (Å)	0.699765	0.71073	0.71073	0.71073	0.71073
Crystal system	monoclinic	orthorhombic	orthorhombic	monoclinic	triclinic
Space group	$P2_1/n$	Pnnm	Pnnm	C2/m	P-1
Unit cell dimension (Å)	a = 8.8268(6)	a = 6.0005(8)	a = 5.968(5)	a = 9.992(3)	a = 5.1094(7)
	b = 3.9607(3)	b = 7.943(1)	b = 8.150(6)	b = 16.770(4)	b = 6.0771(9)

	c = 22.639(1) β = 92.595(6)°	c = 15.584(2)	c = 16.170(13)	c = 5.936(1) β = 123.390(4)°	c = 11.099(2) α = 89.659(3)° β = 86.035(3)° γ = 86.061(3)°
Volume ($Å^3$)	790.64(9)	742.8(2)	786.4(11)	830.4(4)	342.99(9)
F(000)	456	456	528	600	209
Crystal size (mm)	0.08x0.02x0.01	0.30x0.12x0.05	0.25x0.15x0.08	0.30x0.20x0.04	0.30x0.15x0.03
Theta range for data collection(°)	3.60-26.75	2.61-28.29	2.52-30.52	2.43-28.30	1.84-29.56
Limiting indices	-11 < h < 11 -5 < k < 5 -28 < l < 28	-6 < h < 8 -8 < k < 10 -20 < l < 20	-8 < h < 8 -11 < k < 9 -22 < l < 19	-6 < h < 13 -22 < k < 22 -7 < l < 7	-5 < h < 7 -8 < k < 8 -15 < l < 12
Reflections collected	7876	4654	5228	2874	2593
R_{int}	0.0377	0.0415	0.1032	0.0364	0.0184
Refinement method	Full-matrix least square on F^2				
Data/restraints/parameters	1647/0/112	961/0/60	1211/2/60	1060/1/60	1862/0/109
Goodness-of-fit on F^2	1.123	1.234	1.013	1.164	1.108
Final R indices [I>2σ(I)]	R_1 = 0.0291; wR_2 = 0.0723	R_1 = 0.0473; wR_2 = 0.1077	R_1 = 0.0657; wR_2 = 0.1574	R_1 = 0.0443; wR_2 = 0.0906	R_1 = 0.0422; wR_2 = 0.1081
R indices (all data)	R_1 = 0.0346; wR_2 = 0.0874	R_1 = 0.0571; wR_2 = 0.1116	R_1 = 0.1580; wR_2 = 0.1996	R_1 = 0.0498; wR_2 = 0.0926	R_1 = 0.0602; wR_2 = 0.1289
Largest diff. peak and hole	0.426 and -0.383 $e^-.Å^{-3}$	0.359 and -0.442 $e^-.Å^{-3}$	0.769 and -1.048 $e^-.Å^{-3}$	0.992 and -1.102 $e^-.Å^{-3}$	0.638 and -0.385 $e^-.Å^{-3}$

2.2 Powder X-Ray diffraction

X-Ray powder diffraction patterns of were collected at 293 K on a Siemens D5000 Diffractometer working in the (θ-θ) mode by using CuKα radiation. X-ray thermodiffractometry was performed under static air in an Anton Parr HTK16 high temperature device of a Siemens D-5000 diffractometer (θ-θ mode, CoKα radiation) equipped with a M Braun linear position sensitive detector (PSD). The thermal behavior has been studied in the 20-400°C range with 10°C intervals. The room temperature experimental powder diffraction diagrams and the theoretical ones for all the solids are reported in Figure S3.

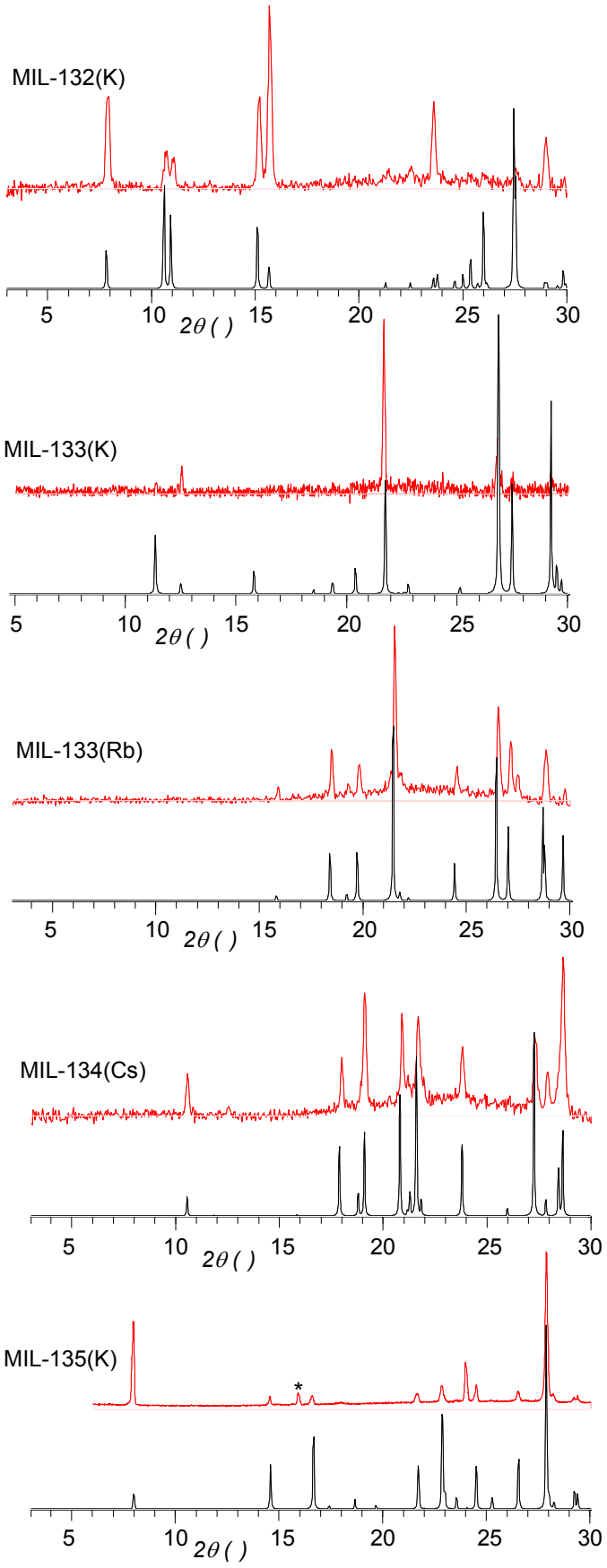

Figure S3. Theoretical (black) and experimental (red) powder X-Ray diagrams of the studied solids (λ(CuKα) = 1.5406 Å). Note that in most cases the compounds were obtained as plate-

lets, leading to a strong preferential orientation and thus a discrepancy between the experimental and theoretical peaks intensities. *: unidentified impurity.

2.3 Elemental analyses

- MIL-132(K): calculated C 26.31%, H 0.44%, S 28.09%, K 17.13%; found C 26.20%, H 0.44%, S 28.21%, K 16.36%.

- MIL-133(K): calculated C 26.31%, H 0.44%, S 28.09%, K 17.13%; found C 25.77%, H 0.58%, S 26.42%, K 16.78%.

- MIL-133(Rb): calculated C 21.86%, H 0.37%, S 23.35%, Rb 31.12%; found C 21.22%, H 0.37%, S 20.54%, Rb 28.83%.

- MIL-134(Cs): calculated C 18.64%, H 0.31%, S 19.91%, Cs 41.26%; found C 18.38%, H 0.34%, S 16.62%, Cs 39.30%.

2.4 Infra red analysis

IR spectra were recorded on a Fourier Transform Nicolet Magna-IR 550 spectrometer in KBr pellets in the 350-4000 cm^{-1} region. The following abbreviations are used: s, strong; m, medium; w, weak; br, broad. Residual water (from KBr) and CO_2 (from air) were visible at 3340 and 2350 cm^{-1} respectively (see Figure S4).

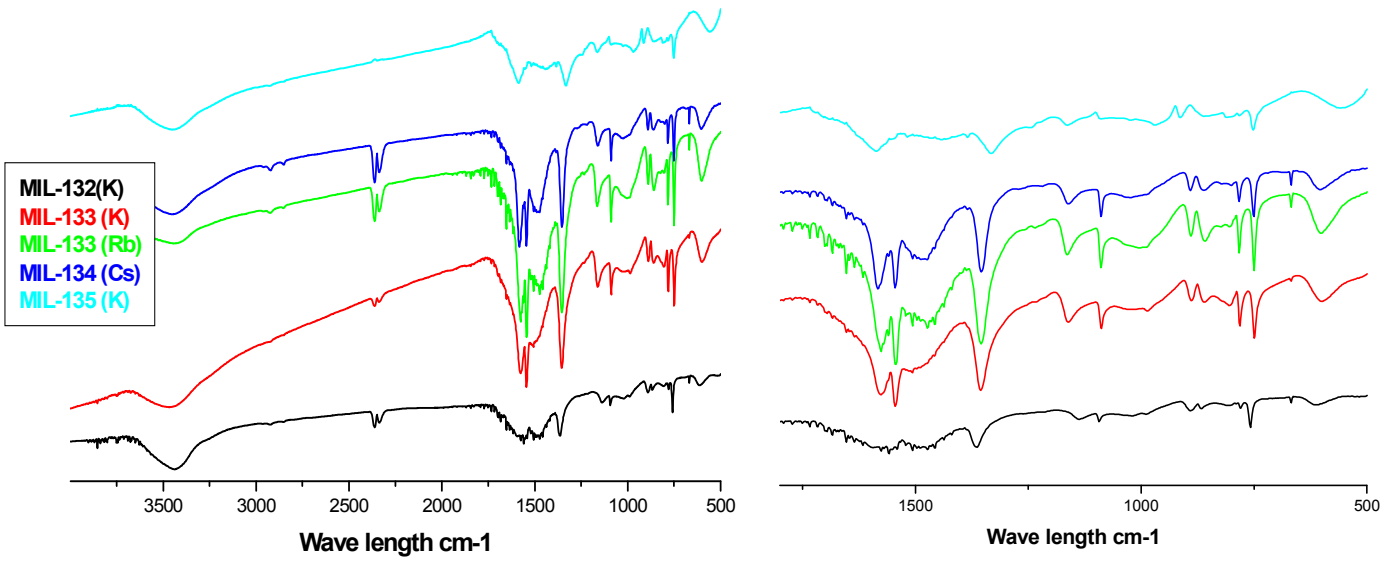

Figure S4. Infra-red spectra of of MIL-132(K), MIL-133(K), MIL-133(Rb), MIL-134(Cs) and MIL-135(K).

- MIL-132(K): 1685 (sh), 1569.8 (w), 1550.5 (s), 1479.2 (s), 1361.5 (s), 1137.8 (m), 1091.5 (m), 1022.1 (w), 987.4 (w), 891.0 (m), 867.8 (w), 804.2 (w), 779.1 (m), 757.9 (s).
- MIL-133(K): 1575.6 (s), 1544.7 (s), 1496.5 (sh), 1355.7 (s), 1161.0 (m), 1087.7 (m), 1016.3 (w), 987.4 (w), 889.0 (m), 860.1 (w), 804.2 (w), 781.0 (m), 750.2 (s).
- MIL-133(Rb): 1577 (s), 1545 (s), 1506 (m), 1475 (m), 1477 (m), 1358 (s), 1167 (m), 1090 (m), 890 (m), 864 (w), 783 (m), 750 (s), 607 (s).
- MIL-134(Cs): 1583 (s), 1545 (s), 1537 (w), 1506 (w), 1496 (w), 1358 (s), 1165 (s), 1090 (s), 891 (m), 862 (m), 783 (m), 752 (s), 667 (s), 609 (m).
- MIL-135(K): 1585(s), 1333 (s), 1244 (w), 1165 (w), 970 (m), 914 (s), 862 (m), 810 (m) 781 (m), 752 (s), 557 (s).

2.5 Thermogravimetric analyses

Thermogravimetric analyses were performed on a TA-instrument 2050 under O_2 atmosphere between room temperature and 600°C in an aluminum crucible (heating speed 3°C/min)

using 5-10 mg of solid. The remaining product (MSO_4, M = K, Rb, Cs) was identified by powder XRD.

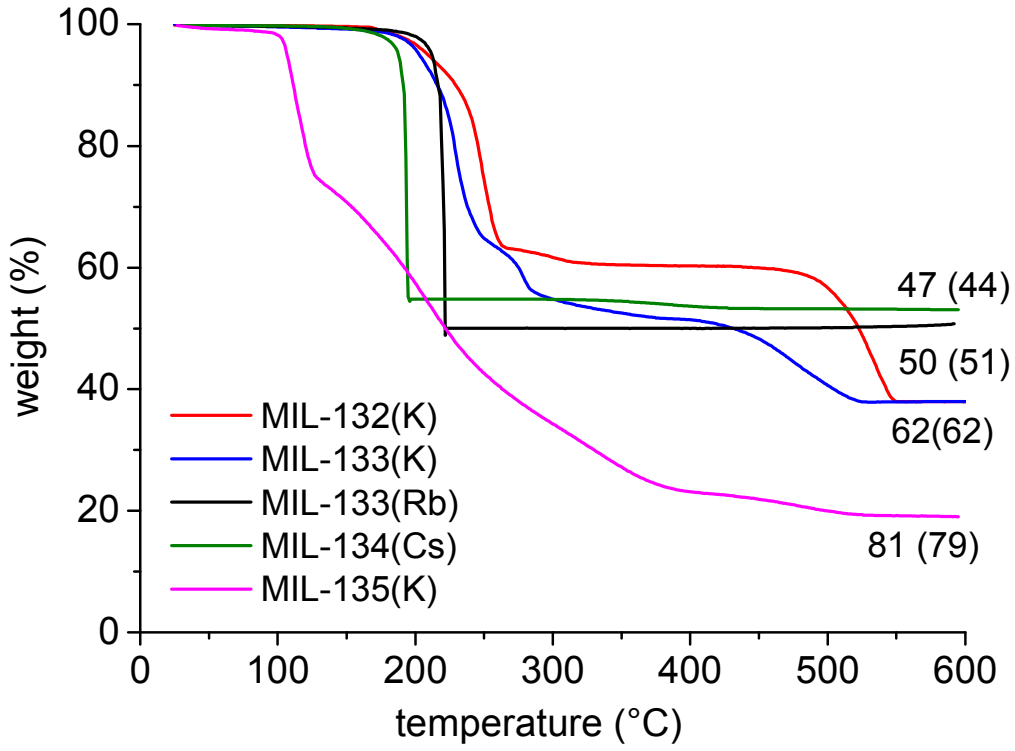

Figure S5. Thermogravimetric analyses of MIL-132(K), MIL-133(K), MIL-133(Rb), MIL-134(Cs) and MIL-135(K). Experimental and theoretical weight losses (in parenthesis) are also reported.

2.6 Electrochemistry

- In solution: cyclic voltammetry of $(TTF\text{-}TC)H_4$ has been performed in a three-electrode cell equipped with two platinum wires as working (diameter 1 mm) and counter-electrodes and an SC electrode as a reference. The electrolytic media involved a 0.03 $mol.L^{-1}$ solution of $(n\text{-}Bu_4N)PF_6$ in DMF (concentration of $(TTF\text{-}TC)H_4$ = 2.10^{-3}M). Electrochemical experiments have been carried out with an EGG PAR 2263A potentiometer with a sweep rate of 50 $mV\ s^{-1}$; the pack Par PowerSuite 2.56 was used to process the data (Figure S6).

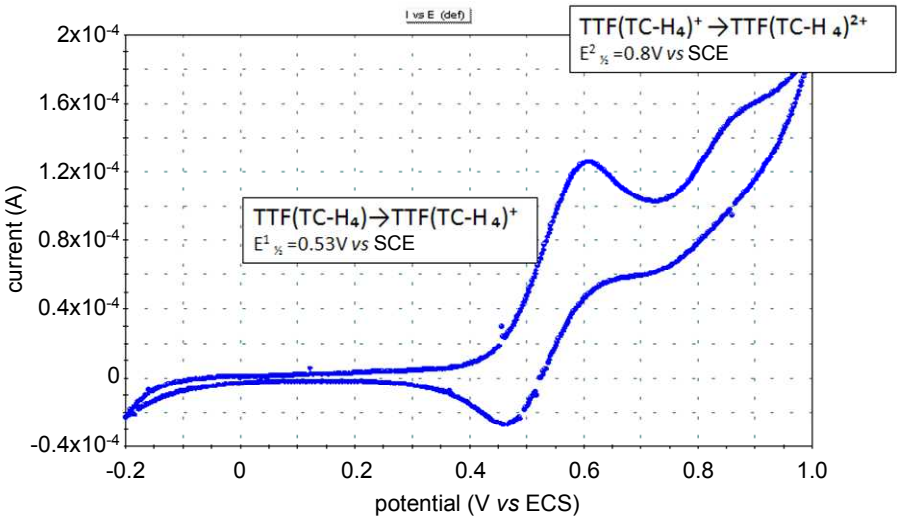

Figure S6. Cyclic voltametry of (TTF-TC)H_4 *vs*. SCE.

- In the solid state:

Cyclic voltammetry of MIL-132(K), MIL-133(K, Rb) and MIL-134(Cs) was performed using a VMP potentiostat in the potential range of 2.0 to 4.0 V (vs. Li) with scan rates of 10mVs^{-1} and 1mVs^{-1}. Experiments were carried out using two-electrode Swagelok-type™ cells. The working electrodes were prepared by mixing 70 wt% of the active materials (MIL series) and 30 wt % of Ketjen black carbon (as conductor) with an agate mortar. The glass fiber (GF/D) from Whatman® was used as a separator and pure lithium foil (Aldrich) was used as counter electrode. The electrolyte consisted of a solution of 1 M $LiPF_6$ in ethylene carbonate (EC)/dimethyl carbonate (DMC) (1:1 by volume). The cells were assembled inside an argon-filled glove box.

Galvanostatic charge-discharge experiments were tested using the same electrode cell as described above at the current densities of 10C and 2C with different voltage values ranging from 2.3-3.8V.

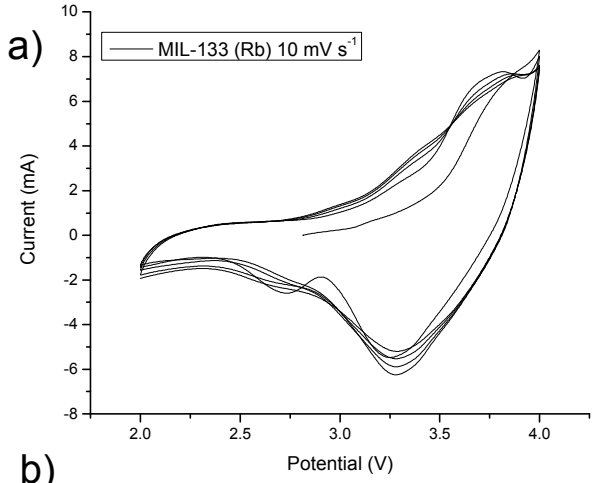
a)
MIL-133 (Rb) 10 mV s-1
Current (mA)
Potential (V)

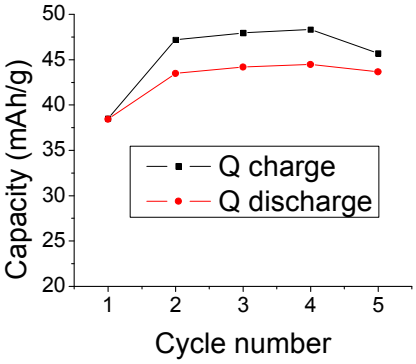
Capacity (mAh/g)
Q charge
Q discharge
Cycle number

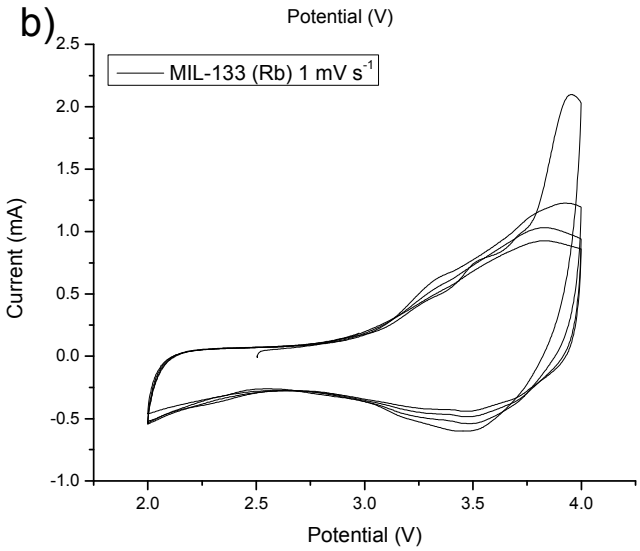
b)
MIL-133 (Rb) 1 mV s-1
Current (mA)
Potential (V)

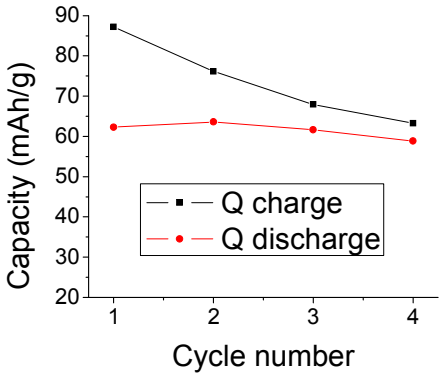
Capacity (mAh/g)
Q charge
Q discharge
Cycle number

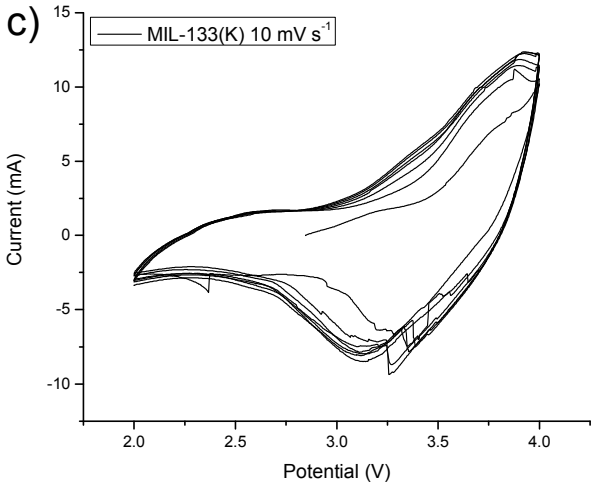
c)
MIL-133(K) 10 mV s-1
Current (mA)
Potential (V)

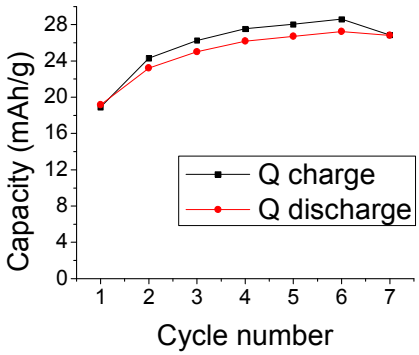
Capacity (mAh/g)
Cycle number
Q charge
Q discharge

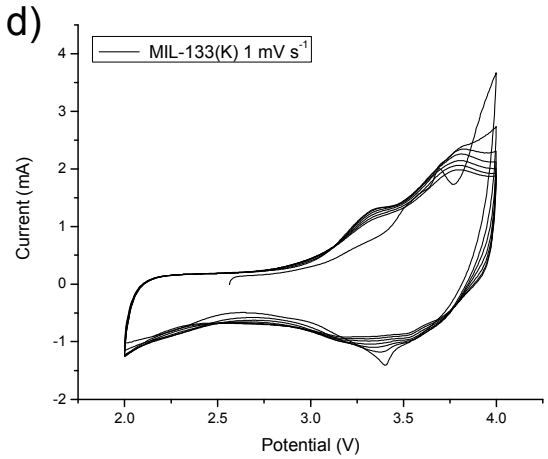
d)
MIL-133(K) 1 mV s-1
Current (mA)
Potential (V)

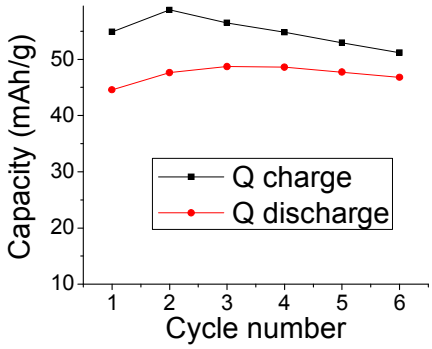
Capacity (mAh/g)
Cycle number
Q charge
Q discharge

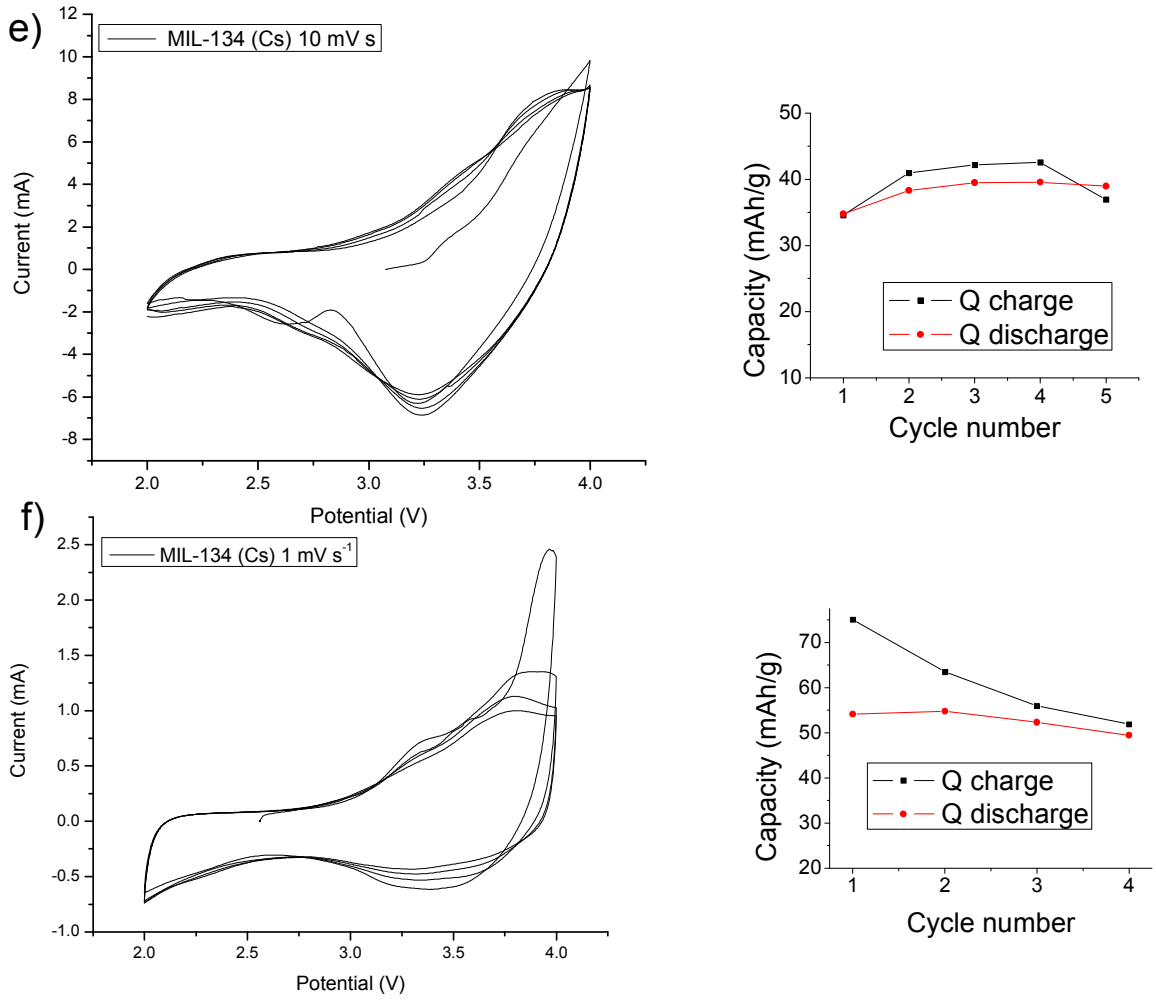

Figure S7. Solid cyclic voltammetry and charge/discharge capacities upon cycling between 2 and 4V *vs.* Li. a) MIL-133(Rb) at 10 mV s^{-1} voltage sweep rate, b) MIL-133(Rb) at 1 mV s^{-1} voltage sweep rate, c) MIL-133(K) at 10 mV s^{-1} voltage sweep rate, d) MIL-133(K) at 1 mV s^{-1} voltage sweep rate, e) MIL-134(Cs) at 10 mV s^{-1} voltage sweep rate f) MIL-134(Cs) at 1 mV s^{-1} voltage sweep rate

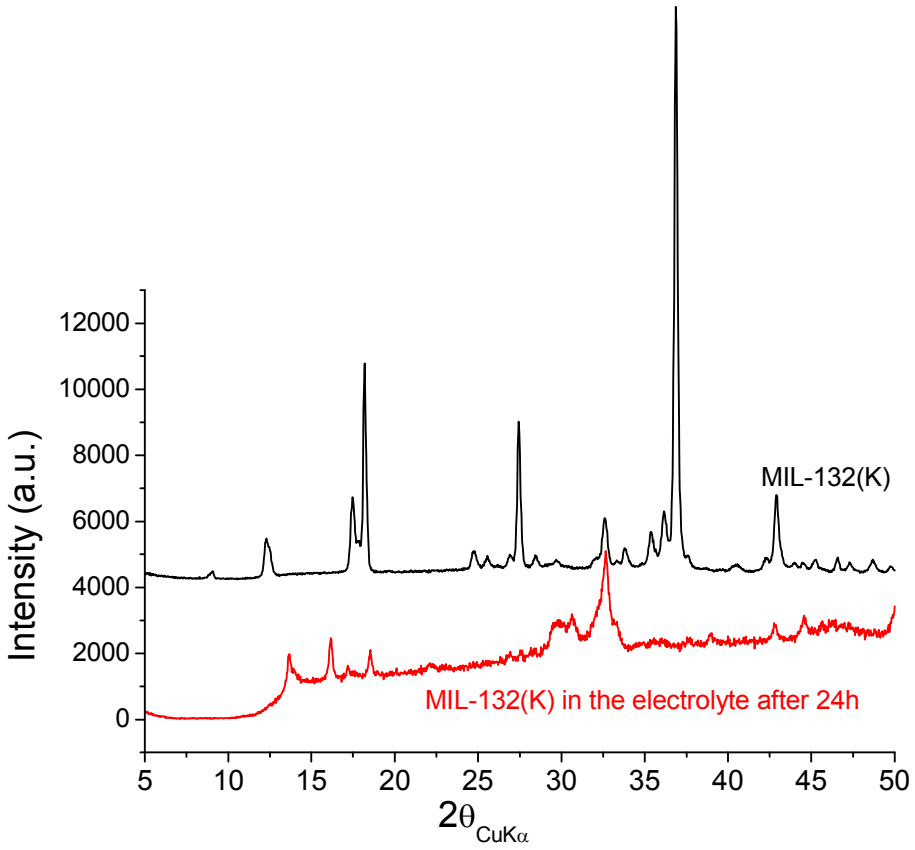

Figure S8. Comparison of the X-ray profile of pristine MIL-132(K) (black) and after 24h duration in the electrolyte (red)

2.7 Conductivity measurements

The electronic conductivity of MIL-135(K) has been extracted from a two points conductance measurement performed on single crystals. A Keithley 487 has been used to apply a constant voltage and measure the current through two contacts made by silver paint on both ends of the crystal. The linearity of V-I curves has been checked at room temperature for applied voltage varying between -4 and +4 V and the temperature dependence of the conductivity was measured with an applied voltage of 1 V. Considering the small size of the crystals (total length < 200 µm, thickness < 10µm) the accuracy on the absolute value of the conductivity is poor, the room temperature value varies from 0.8 up to 2 $mS.cm^{-1}$ depending on the crystal and the size of the contacts.

2.8 Surface area measurement.

Experiments were performed at 77K on a Belsorb Mini apparatus using nitrogen as the probing gas. MIL-132(K) and -133(K) samples (50 mg) were outgassed at room temperature under primary vacuum for one night prior to measurement. No accessible microporosity was detected (Figure S7).

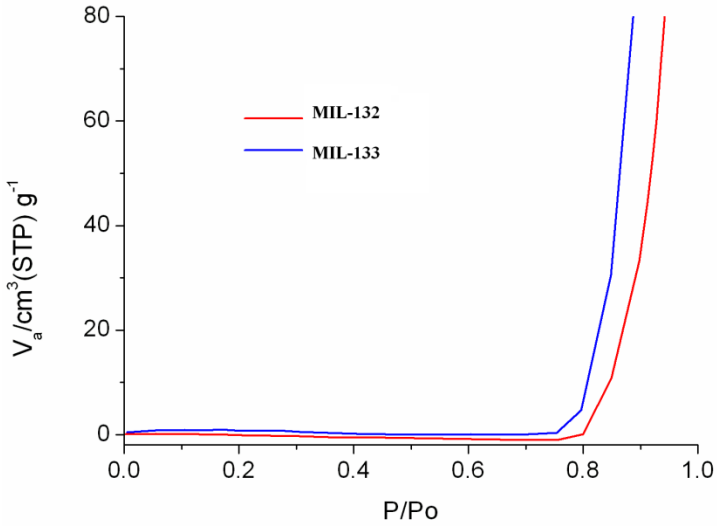

Figure S9. N_2 adsorption isotherms of MIL-132(K) and MIL-133(K) measured at 77 K.

3. Crystal structures

3.1 Intramolecular hydrogen bonds

Table S2. Geometric characteristics of the intramolecular O-H···O hydrogen bonds.

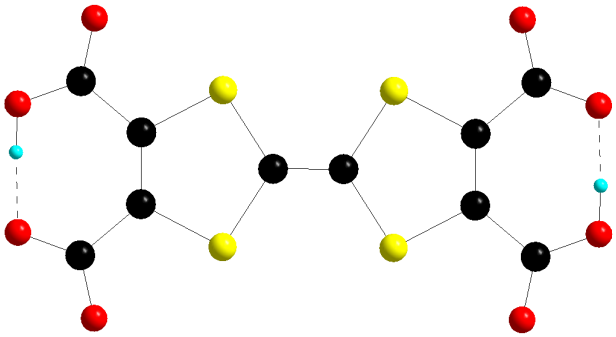

Compound	d(O···O) (Å)	d(H···O) (Å)	angle (O-H···O) (°)
MIL-132(K)	2.433(2)	1.493	172.8
MIL-133(K)	2.406(5)	1.578	174.0
MIL-133(Rb)	2.422(11)	1.566	171.5
MIL-134(Cs)	2.409(9)	1.508	174.0
MIL-135(K)	2.436(3)	1.296	170.7

3.2 Bond valence calculations[7]

Table S3. Bond valence calculations for the alkaline cations. The M-O bonds taken into account for the structural description (see main text) are highlighted in grey.

Solid	M-O (except *: M-S) distance (Å) M = K, Rb, Cs	valence bond
MIL-132 (K)	2.711(2)	0.21
	2.721(2)	0.20
	2.722(2)	0.20
	2.784(2)	0.17
	2.795(2)	0.17
	2.925(2)	0.12
	3.017(2)	0.09
	3.682(1)*	0.05
	total	**1.21**

MIL-133 (K)	2.743(2)	0.19
	2.743(2)	0.19
	2.765(2)	0.18
	2.765(2)	0.18
	3.202(2)	0.06
	3.202(2)	0.06
	3.550(1)*	0.07
	3.550(1)*	0.07
	total	**1.00**
MIL-133 (Rb)	2.878(6)	0.19
	2.878(6)	0.19
	2.899(6)	0.18
	2.899(6)	0.18
	3.264(6)	0.07
	3.264(6)	0.07
	3.667(3)*	0.02
	3.667(3)*	0.02
	total	**0.92**
MIL-134 (Cs)	3.090(5)	0.16
	3.090(5)	0.16
	3.120(6)	0.15
	3.120(6)	0.15
	3.503(6)	0.05
	3.503(6)	0.05
	3.540(7)	0.05
	3.540(7)	0.05
	3.838(2)*	0.02
	3.838(2)*	0.02
	total	**0.86**
MIL-135(K)	2.707(2)	0.21
	2.707(2)	0.21
	2.718(2)	0.20
	2.718(2)	0.20
	2.823(2)	0.15
	2.823(2)	0.15
	3.393(3)	0.03
	3.393(3)	0.03
	total	**1.20**

3.3Alternative views of the structures.

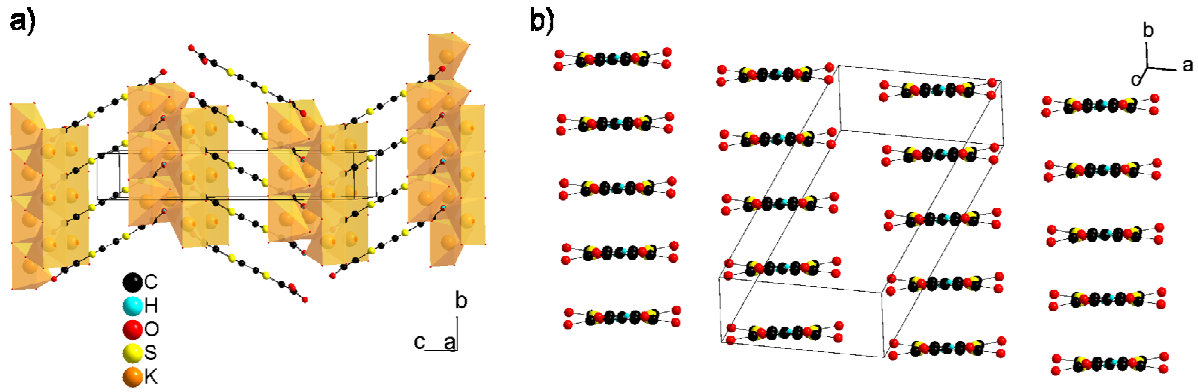

Figure S10. Views of MIL-132(K) along the TTF a) short and b) long axis, highlighting the herringbone arrangement and the β-type layer in the 011 and 110 planes respectively.

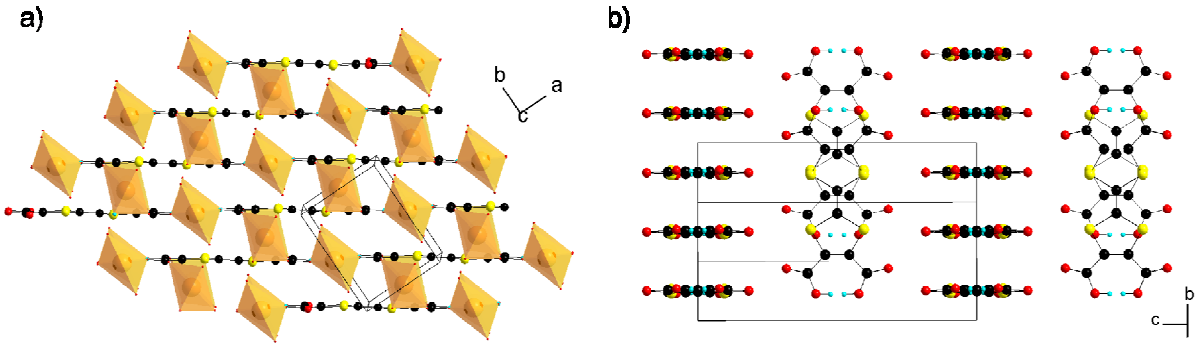

Figure S11. Views of MIL-133 along the TTF a) short and b) long axis, highlighting the layers of parallel TTFs developing in the 110 plane, and alternating perpendicularly along [001].

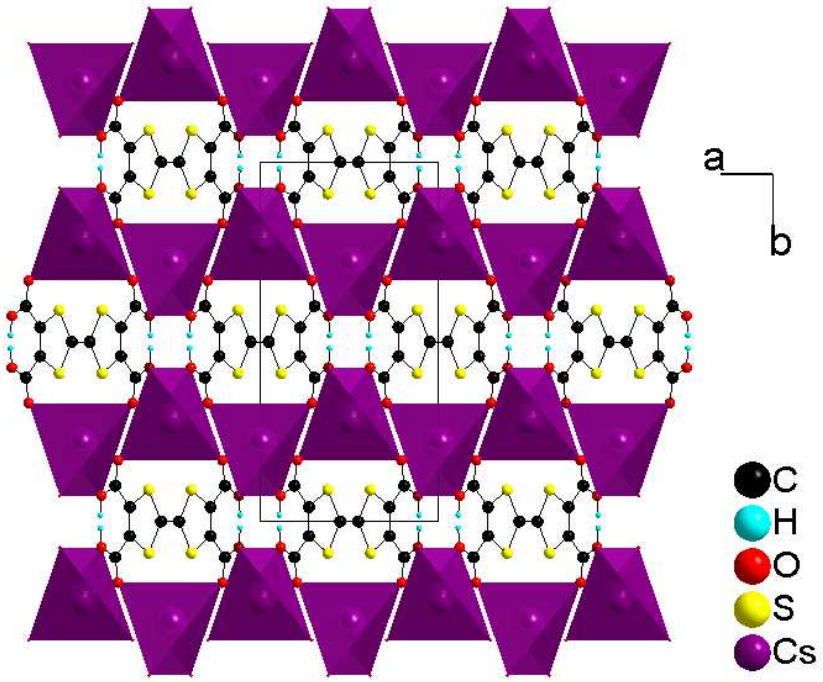

Figure S12. View of MIL-134(Cs) along along [001].

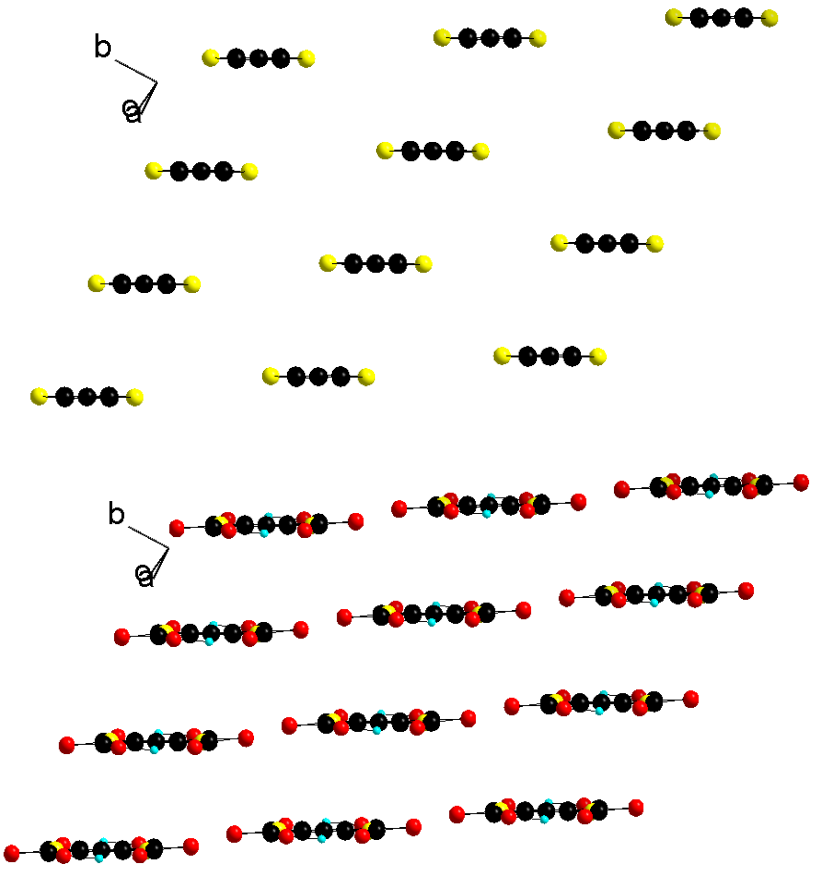

Figure S13. View of the organic slab in MIL-135(K), which is reminiscent of the β-type layers found in molecular conductors. Top: carboxylate group omitted, bottom: carboxylate groups pictured.

References

[1] Pittman, C. U.; Narita, M.; Liang, Y. F., *J. Org. Chem.* **1976**, *41*, 2855-2860.

[2] Easton, D. B. J.; Leaver, D., *Chem. Commun.* **1965**, 585-586.

[3] Challenger, F.; Mason, E. A.; Holdsworth, E. C.; Emmott, R., *J. Chem. Soc.* **1953**, 292-304.

[4] Heuzé, K.; Fourmigué, M.; Batail, P., *J. Mater. Chem. 1999*, **9**, 2373-2379.

[5] Batail, P.; Boubekeur, K.; Fourmigue, M.; Gabriel, J. C. P., *Chem. Mate.* **1998,** *10*, 3005-3015.

[6] Sheldrick, G. M. *Acta Cryst.* **2008**, *A64*, 112-114.

[7] Brese, N. E.; O'Keeffe, M., *Acta. Cryst.* **1991**, *B47*, 192-197.

8 Publikationen / Tagungsbeiträge

Publikationen

1. „Synthesis and Modification of a Functionalized 3D Open-Framework Structure with MIL-53 Topology"
   T. Ahnfeldt, D. Gunzelmann, T. Loiseau, D. Hirsemann, G. Férey, J. Senker, N. Stock, *Inorg. Chem*. **2009**, *48*, 3057.

2. „$[Al_4(OH)_2(OCH_3)_4(H_2N\text{-}bdc)_3]\cdot xH_2O$: A 12-Connected PorousMetal–Organic Framework with an Unprecedented Aluminum-Containing Brick"
   T. Ahnfeldt, N. Guillou, D. Gunzelmann, I. Margiolaki, T. Loiseau, G. Férey, J. Senker, N. Stock, *Angew. Chem*. *Int. Ed.* **2009**, *121*, 5163.

3. „Oriented growth of the functionalized metal-organic framework CAU-1 on -OH- and -COOH- terminated self-assembled monolayers"
   F. Hinterholzinger, C. Scherb, T. Ahnfeldt, N. Stock, T. Bein, *Phys. Chem. Chem. Phys.* **2010**, *12*, 4515.

4. „3-D Coordination Polymers Based on the Tetrathiafulvalenetetracarboxylate (TTF-TC) Dervative: Synthesis, Characterization, and Oxidation Issues"
   T.L.A. Nguyen, R. Demir-Cakan, T. Devic, M. Morcrette, T. Ahnfeldt, P. Auban-Senzier, N. Stock, A.-M. Goncalves, Y. Filinchuk, J.-M. Tarascon, G. Férey, *Inorg. Chem*. **2010**, *49*, 7135.

5. „Structural Phase Transitions and Thermal Hysteresis in the Metal-Organic Framework Compound MIL-53 As Studied by Electron Spin Resonance Spectroscopy"
   M. Mendt, B. Jee, N. Stock, T. Ahnfeldt, M. Hartmann, D. Himsl, A. Pöppl, *J. Phys. Chem. C* **2010**, *114*, 19443.

6. „Reinvestigation of the M-II (M = Ni, Co)/TetraThiafulvaleneTetraCarboxylate System Using High-Throughput Methods: Isolation of a Molecular Complex and Its Single-Crystal-to-Single-Crystal Transformation to a Two-Dimensional Coordination Polymer"
T.L.A. Nguyen, R. Demir-Cakan, T. Devic, M. Morcrette, T. Ahnfeldt, P. Auban-Senzier, N. Stock, A.-M. Goncalves, Y. Filinchuk, J.-M. Tarascon. G. Férey, *Inorg. Chem.* **2010**, *49*, 10710.

7. „High-Throughput and Time-Resolved Energy-Dispersive X-Ray Diffraction (EDXRD) Study of the Formation of CAU-1-$(OH)_2$: Microwave and Conventional Heating"
T. Ahnfeldt, J. Moellmer, V. Guillerm, R. Staudt, C. Serre, N. Stock, *Chem. Eur. J.* **2011**, *17*, 6462.

8. „New Functionalized Flexible Al-MIL-53-X (X = -Cl, -Br, -CH_3, -NO_2, -$(OH)_2$) Solids: Syntheses, Characterization, Sorption and Breathing Behavior"
S. Biswas, T. Ahnfeldt, N. Stock, *Inorg. Chem*. **2011,** *50*, 9518.

9. „Synthesis of isoreticular CAU-1 compounds: Effects of linker and heating methods on the kinetics of the synthesis"
T. Ahnfeldt, N. Stock, *CrystEngComm*, **2012**, *14*, 505.

10. „A new family of porous MOFs with a new Al-based brick: [$Al_2(OCH_3)_4(O_2C$-X-$CO_2)$] (X=aryl)"
H. Reinsch, M. Feyand, T. Ahnfeldt, N. Stock, *Dalton Trans*., **2012**, *41*, 4164.

11. „Controlled modification of the inorganic and organic brick in an Al-based MOF by direct and post-synthetic synthesis routes"
T. Ahnfeldt, D. Gunzelmann, J. Wack, J. Senker, N. Stock, *CrystEngComm*, **2012**, DOI: 10.1039/C2CE06620C.

Vorträge

12. „Synthesis and Characterization of a Functionalized 3D Open-Framework Structure with MIL-53 Topology"
T. Ahnfeldt, N. Stock, Norddeutsches Doktorandenkolloquium, **2007**, Bremen.

13. „Synthesis and Characterization of Functionalized 3D Open-Framework Structures with MIL-53 and MIL-101 Topology„
T. Ahnfeldt, N. Stock, Arbeitsgruppenvortrag, **2007**, Versailles.

14. „CAU-1: A New 12-Connected Porous Metal-Organic Framework"
T. Ahnfeldt, N. Stock, Deutsche Zeolithtagung, **2009**, Kiel.

15. „Synthesis and Characterization of Highly Porous Aluminium Containing Frameworks"
T. Ahnfeldt, N. Stock, AC-Kolloquium, **2010**, Kiel.

Posterpräsentationen

16. „Synthesis and modification of a functionalized 3D open-framework structure with MIL-53 topology"
T. Ahnfeldt, J. Senker, S. Lutschinger, T. Loiseau, G. Férey, N. Stock, Deutsche Zeolithtagung, **2008**, Halle.

17. „In situ EDXRD investigation on the formation of isoreticular CAU-1 compounds and determination of their sorption properties"
T. Ahnfeldt, M. Feyand, N. Stock, Deutsche Zeolithtagung, **2010**, München.

18. „In situ EDXRD investigation of the formation of isoreticular CAU-1 compounds and determination of their sorption properties"
T. Ahnfeldt, N. Stock, MOF Konferenz, **2010**, Marseille.

Curriculum Vitae

Der Lebenslauf ist in der Online-Version aus Gründen des Datenschschutzes nicht enthalten.

Eidesstattliche Erklärung

Hiermit versichere ich an Eides statt, dass ich die vorliegende Arbeit selbständig – abgesehen von der wissenschaftlichen Beratung durch meinen Lehrer – und nur unter Verwendung der angegeben Hilfsmittel angefertigt habe. Die Dissertation wird ausschließlich an dieser Stelle zur Promotion vorgelegt.

Kiel, November 2011